Schweizerische Eidgenossenschaft
Confédération suisse
Confederazione Svizzera
Confederaziun svizra

National Centre for Climate Services NCCS

CH2018 - Climate Scenarios for Switzerland

Technical Report

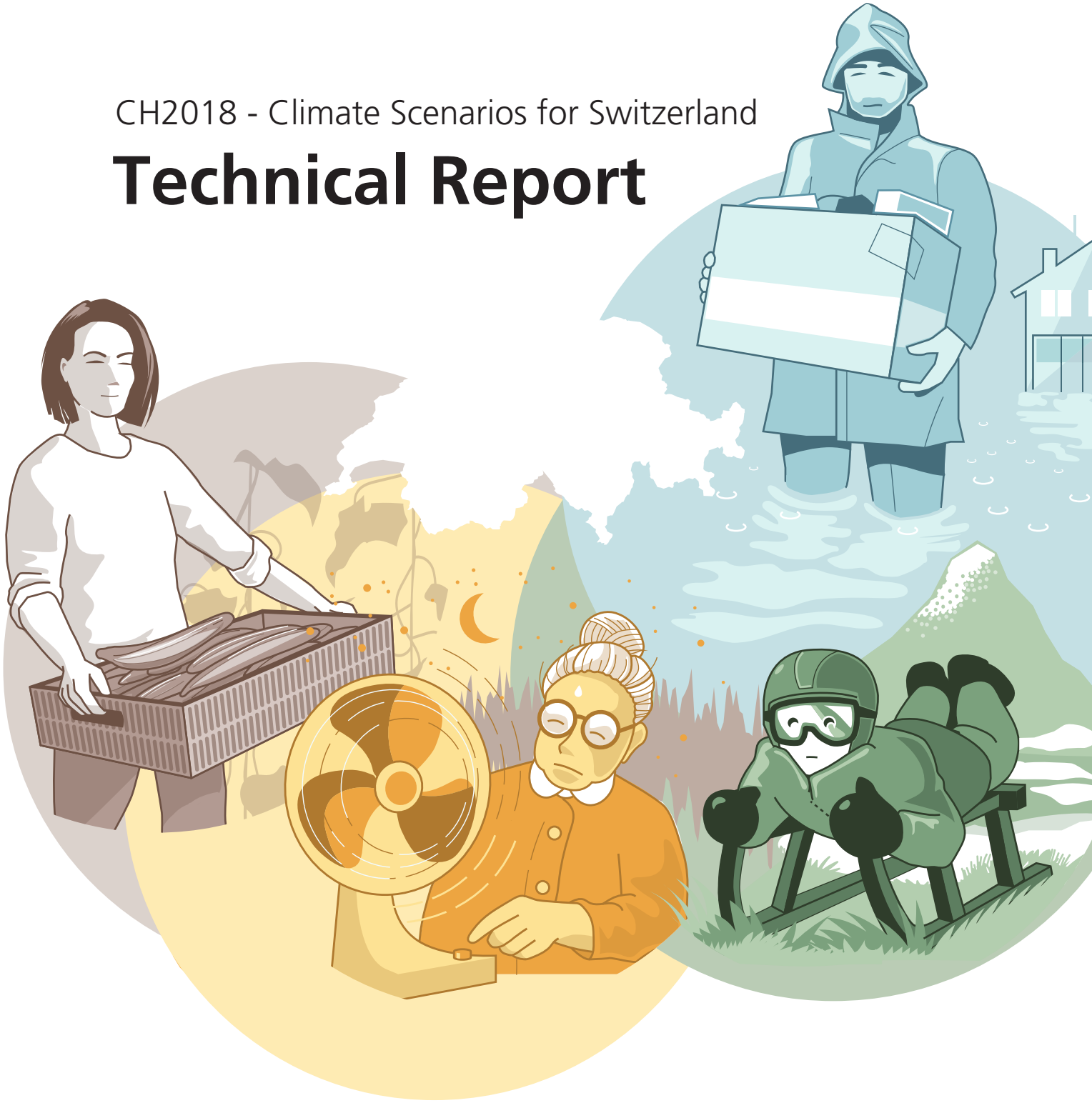

Schweizerische Eidgenossenschaft
Confédération suisse
Confederazione Svizzera
Confederaziun svizra

Swiss Confederation

Federal Department of Home Affairs FDHA
Federal Office of Meteorology and Climatology MeteoSwiss

MeteoSwiss

ETH zürich

C2SM Center for Climate Systems Modeling

UNIVERSITÄT BERN

sc | nat
Science and Policy
Platform of the Swiss Academy of Sciences

ProClim
Forum for Climate and Global Change

Imprint

Authors (in alphabetical order)

1. Introduction
Lead authors: Mischa Croci-Maspoli[2], Christoph Schär[1]
Contributing: Christina Schnadt Poberaj[3]

2. The CH2018 framework
Lead authors: Andreas M. Fischer[2], Kuno M. Strassmann[3]
Contributing: Sven Kotlarski[2] (Box 2.1), Christoph Schär[1] (Box 2.1), Silje Sørland[1] (Box 2.1), Elias M. Zubler[2]

3. Current climate and recent change
Lead author: Simon C. Scherrer[2], Cornelia Schwierz[2]
Contributing: Stefan Brönnimann[4,5], Ana Casanueva[2], Sophie Fukutome[2], Michael Graf[4,5], Olivia Martius[4], Christoph C. Raible[6,5], Mathias Trachsel[4,5]

4. Seasonal mean changes
Lead authors: Reto Knutti[1], Silje Sørland[1]
Contributing: Andreas M. Fischer[2], Sven Kotlarski[2], Hans-Ruedi Künsch[7], Mark Liniger[2], Jan Rajczak[1], Christoph Schär[1], Curdin Spirig[3], Kuno M. Strassmann[3], Elias M. Zubler[2]

5. Localized projections
Lead authors: Sven Kotlarski[2], Jan Rajczak[1]
Contributing: Ana Casanueva[2], Iris Feigenwinter[2], Mark Liniger[2]

6. Climate extremes and climate indices
Lead authors: Erich M. Fischer[1], Christoph Schär[1]
Contributing: Nikolina Ban[1] (6.6, Box 6.1), David N. Bresch[8] (6.1), Ana Casanueva[2] (6.5), Iris Feigenwinter[2] (6.3), Michael Graf[4,5] (6.9), Martin Hirschi[1] (6.7), Sven Kotlarski[2] (6.3), Mark Liniger[2] (6.3, 6.5), Christoph C. Raible[5,6] (6.9), Jan Rajczak[1] (6.3, 6.6), Simon C. Scherrer[2] (6.9), Sonia I. Seneviratne[1] (6.7), Richard Wartenburger[1] (6.8)

7. Natural climate variability, detection, and attribution
Lead authors: Erich M. Fischer[1], Reto Knutti[1]
Contributing: Iselin Medhaug[1]

8. Comparison with earlier climate change scenarios in Switzerland
Lead author: Jan Rajczak[1]
Contributing: Andreas M. Fischer[2], Curdin Spirig[1], Kuno M. Strassmann[3]

9. The CH2018 scenario datasets
Lead authors: Christina Schnadt Poberaj[3], Kuno M. Strassmann[3]
Contributing: Andreas M. Fischer[2], Curdin Spirig[1]

10. The CH2018 scenarios in use
Lead author: David N. Bresch[8]
Contributing: Mathias Bavay[10] (10.2.2), Paolo Burlando[10] (10.2.3), Fabienne Dahinden[1] (10.1), Simone Fatichi[10] (10.2.3), Iris Feigenwinter[2] (10.1), Andreas M. Fischer[2] (10.2.3, 10.4), Sven Kotlarski[2] (10.1), Christoph Marty[9] (10.2.2), Nadav Peleg[10] (10.2.3), Ole Rössler[4,5] (10.2.1), Maurice Skelton[8] (10.3), Kuno M. Strassmann[3] (10.4)

11. Synthesis and future perspectives
Lead authors: Christoph Schär[1], Simon C. Scherrer[2], Cornelia Schwierz[2]
Contributing: Andreas M. Fischer[2], Kuno M. Strassmann[3], Sven Kotlarski[2], Michiko Hama[2]

Editors

Andreas M. Fischer[2], Kuno M. Strassmann[3]

Editorial and technical support

Urs Beyerle[1,3], Iris Feigenwinter[2,3], Moritz Pickl[2,3] Curdin Spirig[1], Joel Zeder[1,3], Elias Zubler[2]

Steering Group

Mischa Croci-Maspoli[2], Reto Knutti[1], Mark Liniger[2] Christoph Schär[1], Cornelia Schwierz[2]

Affiliations:
[1] Institute for Atmospheric and Climate Science, ETH Zürich
[2] Federal Office of Meteorology and Climatology MeteoSwiss
[3] Center for Climate Systems Modeling (C2SM)
[4] Institute of Geography, University of Bern
[5] Oeschger Centre for Climate Change Research (OCCR), University of Bern
[6] Climate and Environmental Physics (CEP), University of Bern
[7] Seminar for Statistics, ETH Zürich
[8] Institute for Environmental Decisions, ETH Zürich
[9] Institute for Snow and Avalanche Research SLF
[10] Institute of Environmental Engineering, ETH Zürich

How to cite this report:

CH2018 (2018), CH2018 – Climate Scenarios for Switzerland, Technical Report, National Centre for Climate Services, Zurich, 271 pp.
ISBN: 978-3-9525031-4-0

Table of contents

Executive Summary

The Swiss Climate Scenarios CH2018

This report is the result of a joint effort by several Swiss institutions under the umbrella of the National Center for Climate Services (NCCS), with major inputs from MeteoSwiss, ETH Zurich, the Center for Climate Systems Modeling (C2SM), the University of Bern, and the Institute for Snow and Avalanche Research (SLF/WSL). It provides the most accurate, up-to-date, and coherent climate information available to support assessments of climate change impacts and decisions about adaptation and mitigation in Switzerland. It builds on previous scenario efforts and assesses past and future changes in the physical climate system of Switzerland.

The conclusions of this report reflect the consensus of the Swiss climate science community, supported by international reviewers. The report is based on the most recent set of global and regional climate models, combined with high-quality observations and process understanding of global and regional climate change. It considers the research and results of many international projects. The data is provided free of charge for anyone to use and includes future changes at various spatial and temporal resolutions for research on climate impacts (www.climate-scenarios.ch). The CH2018 scenarios encompass projections of a number of variables, addressing changes in mean climate and extreme events (along with uncertainty estimates where possible) for different regions, different future time periods, and different scenarios of socio-economic development. The past and current climate in Switzerland is documented using observational data, which serve as a reference for future climate change.

Climatological overview

Switzerland lies in the zone of the westerlies in the northern mid-latitudes. Cyclones and fronts bring moist air from the nearby Atlantic Ocean and Mediterranean Sea to Switzerland, interspersed with phases of high pressure with stable weather. Together with the complex topography of the Alps, this creates a diverse climate with large elevation gradients, spatial heterogeneity, and small-scale phenomena.

The climate in Switzerland has changed, already affecting various economic sectors; such impacts will continue in the future. These sectors include critical infrastructure such as bridges, dams, and water-resource systems, agriculture and forestry, tourism, energy supply and use, and public health, all of which react to changes in the climate mean state as well as to extreme events. Decisions on adaptation measures will therefore benefit from a better characterization of the associated existing risks and new opportunities, including representations of uncertainty and confidence, based on a set of future climate scenarios for Switzerland.

Past trends

Warming in Switzerland is unequivocal. Surface air temperature has increased in all regions of Switzerland since the start of the instrumental record in 1864. Nine of the ten warmest years have occured in the twenty-first century. The amounts of snow and ice have diminished, and hot days and heavy precipitation have become more frequent and more intense. For some quantities, no changes have been observed thus far, either because the expected signal has not yet emerged from the large variability (e.g., summer drying) or because it is not yet clear whether these quantities are affected by climate change (low stratus, storms, hail).

Long-term high-quality measurements and proxy reconstructions of weather and climate exist for up to the last 150 and 330 years, respectively. Despite large natural variability on timescales of years to decades, a robust climate change signal is found for several variables.

- Near-surface air temperature has increased by about 2.0 °C between 1864 and 2017, compared to 0.9 °C globally, with most of the warming taking place since the 1980s. The 1988 to 2017 summer average is by far the warmest 30-year period since the start of reliable climate reconstructions in 1685. This warming has led to more frequent and more intense heatwaves, whereas cold periods have become less frequent.
- The zero-degree line in winter has shifted upward by about 300 - 400 meters since the 1960s, and the volume of Alpine glaciers has decreased by about 60 % since the 1850s. Since the 1970s, the number of snow days and snowfall days have decreased by about 20 % at about 2000 m a.s.l. to 50 % below 800 m a.s.l.
- The vegetation period is two to four weeks longer today than in the 1960s.
- Winter precipitation has increased by about 20 % to 30 % since 1864, although part of that change may be natural variability. There is robust evidence that heavy precipitation has become more frequent (+30 %) and more intense (+12 %) since the beginning of the 20th century.
- Sunshine duration, a proxy for global radiation, shows a significant decline of -15 % between the 1950s and around 1980, followed by a significant increase of +20 % up to the present day.

In the observational record, no robust signals for long-term trends are found for summer precipitation, droughts, wind speed, or low stratus. For these quantities, it is either unclear at this point how they are affected by climate change, or the expected anthropogenic signal has not yet emerged from observed large natural variability (e.g., summer drying). The observational basis is too short or insufficient to make robust inferences about past changes in small-scale phenomena such as thunderstorms, tornadoes, and hail.

For quantities for which the expected future climate trends are small or considered unreliable, accounting for present-day climate variability provides the best estimate of potential climate-related impacts.

Future changes in mean climate

Results described as “likely” generally mean that there is a >66 % probability that the actual outcome will be within the range given. Unless indicated otherwise, this is based on the range of outcomes spanned by 90 % of the models (5 % quantile to 95 % quantile) to account for structural model uncertainties not covered by the ensemble of models. Likely ranges for the whole of Switzerland are calculated as a median across the upper and lower bounds, evaluated for each of the five regions separately. Values are rounded to the nearest 0.1 °C and 1 %. An overview of key climate indicators is provided in Appendix 1.

Global warming in response to further greenhouse gas emissions will continue over the course of the 21st century, but natural variability can regionally mask, dampen, or amplify the human-induced warming, particularly on timescales of decades. In the long term, temperatures in Switzerland will very likely rise with unmitigated climate change irrespective of natural variability, and the warming will likely be larger than in the global mean.

Anthropogenic warming by the end of the century relative to today will be about three times larger in a scenario without mitigation than in a strong mitigation scenario. Changes in many climate variables (e.g., precipitation, snow cover) approximately scale with warming.

Warming in Switzerland will likely be in the range of 2.1 - 3.4 °C above pre-industrial levels (0.6 - 1.9 °C with respect to the reference period 1981 - 2010) for a scenario that will likely limit global mean warming to 2 °C (RCP2.6). Unmitigated warming (RCP8.5) by the end of the century may reach up to 6.9 °C in the annual mean since the pre-industrial era (5.4 °C since the reference period 1981 - 2010).

In the long term, unmitigated climate change will likely cause mean precipitation over Switzerland to decrease during the warmer seasons and to increase during the colder seasons. The summer decrease until the end of the century will likely be -43 % to +2 % outside of the Alps, and the winter change will likely be in the range of 2 % to 24 % throughout the country. Lower elevations (below 2000 m a.s.l.) will very likely experience a reduction in snowfall sums and snow cover.

- Based on climate model simulations, Europe will experience substantial further warming. This warming varies spatially and is projected to be strongest over northern Europe during the winter and southern Europe during the summer. Temperature is estimated to increase in all seasons and regions in Switzerland during the 21st century, with a stronger warming in summer than in winter. The strength of the warming at the end of the century (2070 - 2099) relative to the reference period (1981 - 2010) highly depends on the emission scenario considered, with a summer increase of 0.7 - 2.4 °C for the mitigation scenario RCP2.6 compared to 4.1 - 7.2 °C for the unabated emissions scenario RCP8.5. Thus, the warming from now until the end of the century will be about three times larger without mitigation.
- Precipitation is projected to increase in high northern latitudes and decrease in southern Europe. Long-term warming will likely cause precipitation over Switzerland to increase during the colder seasons and decrease during the warmer seasons, but large natural variability can mask or enhance these forced trends for several decades. Precipitation changes depend on the season, region, and the emission scenario considered. For RCP8.5, the multi-model median increase in winter precipitation by the end of the century ranges from 12% in the western Alps to 22 % in southern Switzerland, and the decrease in summer precipitation ranges from 10 % in the eastern Alps to 24 % in western Switzerland.
- Warming will cause substantial reductions in both snowfall and snow cover over the Swiss territory. At low elevations and for the RCP4.5 and RCP8.5 emission scenarios, mean September - May snowfall sums will likely decrease by more than -50 % by the end of the century. Mean winter snow cover is projected to decline strongly by the end of the century, with decreases exceeding -80 % at low elevations for RCP8.5.
- The goal of the Paris Agreement is to hold the global temperature increase “well below” 2 °C, while pursuing efforts to limit it to 1.5 °C relative to pre-industrial levels. RCP2.6 is an illustrative case of a scenario with global mean warming likely below 2 °C. For this scenario, Switzerland will likely experience a further annual mean warming of 0.6 - 1.9 °C relative to the 1981 - 2010 reference period. Adding the observed temperature increase (1.5 °C between 1864 - 1900 and 1981 - 2010) suggests a total warming of 2.1 - 3.4 °C. A difference of 0.5 °C in the global mean temperature target (e.g., between 1.5 °C and 2 °C) would result in a difference of about 0.6 - 0.7 °C in Switzerland.
- For local projections, the gap between the coarse climate model resolution and the station scale is bridged by statistical techniques. The resulting products consist of daily data for several meteorological variables, which are available as time series for a large number of stations in Switzerland as well as fields on a regular 2 x 2 km grid. The localized data are consistent with those at larger scales but provide more detail and are suitable for local climate-impact modeling. However, careful consideration of their strengths, weaknesses, and limitations is required.

Changes in extremes and extreme indices

Anthropogenic climate change affects the characteristics of weather and climate extremes in Switzerland. heatwaves and extremely hot days and nights have become more frequent. These trends will likely continue. It is the the most rare and most extreme events for which the changes are largest. The low-altitude areas of the Swiss Plateau, Ticino, and the lower Alpine valleys experience the greatest increase in the number of days with high heat stress and of tropical nights. This increase accelerates with every additional degree of warming, such that the increase without mitigation is many times larger than with mitigation.

In summer, both a reduction in wet days and a tendency toward drier soils and longer periods without rain are likely in response to strong warming.

There is consistent evidence from observations, theoretical understanding, and climate models that despite large natural variability, heavy rainfall extremes have become more frequent and intense, and that this trend will continue in a warming climate.

Since most damages depend nonlinearly on the magnitude of extreme events, every degree of warming will disproportionately increase the overall potential risk from climate extremes.

- As a result of warming, the frequency, intensity, and character of many extreme events will also change, in particular for hot days, heatwaves, cold waves, and heavy precipitation. The projected changes fit into continental-scale patterns and are mostly consistent with recent observational trends. At the scale of Switzerland, there is substantial decadal and year-to-year variability in extremes. Thus, the climate change signal in extremes may be dampened or amplified by variability for years to several decades. Depending on the type of extreme considered, the anthropogenic signal may only emerge at a substantial level of warming in RCP4.5 and RCP8.5 by the middle to end of the 21st century. Future changes in weather patterns, storms, thunderstorms, and hail are unclear.
- Like central and southern Europe, Switzerland is a hotspot for changes in summer temperature extremes. As summer warming continues, there will be more frequent, more intense, and longer-lasting heatwaves and extremely hot days (very high confidence). Under RCP8.5, the hottest summer days are projected to warm by 3.9 - 9.4 °C, and very hot days that on average occur on about one day per summer today are projected to occur during 2 to 5 weeks per summer by the end of the 21st century, depending on the model and region. Along with warming mean temperatures, there will be more frequent days with heat stress (high temperature and humidity) and more warm nights (very high confidence). These changes will be largest at low elevations where the population density is typically highest and where heat stress may be further amplified by urban heat island effects. Particularly for unmitigated climate change, heat stress is projected to reach levels that have not been observed in Switzerland over the past century, and probably not since the beginning of reliable climate reconstructions in 1685. The number of days with high heat stress increases non-linearly with warming, becoming about 3 to 5 times more frequent for RCP8.5 than for RCP2.6. Under RCP8.5, half of the summer days in low-altitude areas of Ticino might exhibit high heat stress risk by the end of the 21st century.
- In addition to increasing mean winter temperatures, the number of intense cold waves, frost days, and ice days will decrease (very high confidence), but cold winter periods will continue to occur for several more decades due to the very high variability of winter temperatures.

- For substantial levels of warming, there will be more frequent and intense heavy precipitation events overall (high confidence). Heavy rainfall is projected to intensify in all seasons, but particularly in the winter half year, for all event categories from hourly downpours to multi-day events. The long-term trend will be associated with high variability, and heavy rainfall will continue to occur on an irregular basis. The intensity of peak events will increase much more strongly than mean precipitation and may increase even in seasons with decreasing mean precipitation. For the RCP8.5 scenario and the end of the century, day-long heavy precipitation events (100-year return levels) are projected to increase by 10 - 25 %, depending on the season and region (multi-model medians).
- Confidence in heavy rainfall intensification is now substantially higher than in earlier reports, based on the evidence from observations, the attribution of increases in heavy precipitation on larger scales, and a new generation of climate models that run at unprecedented resolution.
- During the summer season, the projected changes in the intensity of heavy precipitation events on daily to hourly time scales are consistent with an increase of 6 - 7 % per degree warming, the change in the water-holding capacity of warmer air. Thus, the projected intensification of heavy precipitation events is approximately proportional to the warming and is correspondingly smaller for the mitigation scenarios.
- During the winter season, the partitioning between solid (snow) and liquid (rain) precipitation will change in favor of liquid precipitation. The associated intensification of heavy rainfall has implications for the risk of flooding, whereas the frequency of heavy snowfall events is projected to decrease at low to mid-altitudes (< 2000 m a.s.l.).
- In summer, a reduction in wet days and a tendency toward longer dry spells (meteorological droughts, i.e., periods with no rain) is expected in response to strong warming (RCP8.5 at the end of the 21st century, low to medium confidence). In addition, there will be an increasing evaporative demand, which is projected to lead to more pronounced agricultural droughts (drier soils, medium confidence). In comparison to temperature and precipitation extremes, the extent of the drying remains more uncertain.

Natural variability and emerging anthropogenic trends

The human influence on the climate system is clear, and anthropogenic greenhouse gases are likely the dominant cause of the observed warming in Switzerland over the past 50 - 100 years. The observed warming in Switzerland is much too large to be plausibly explained by natural climate variability alone. Because warming is predominantly anthropogenic, human influence has likely also contributed to trends seen in many other climate variables that respond to temperature.

- The emerging human-induced influence on climate must be considered against the backdrop of substantial natural (in part solar and volcanic, but mostly internal unforced) variability on timescales of years to several decades. This poses challenges in detecting climate change and attributing it to anthropogenic causes, evaluating models against observed trends, and quantifying uncertainties in future changes, in particular on local scales where variability is substantial. Nevertheless, the observed warming in Switzerland over the past 50 - 100 years is much larger than could plausibly be explained by natural climate variability alone. It is unlikely that natural variability (internal variability and forced natural variability) can explain more than half of the observed warming.
- On the spatial scales considered, natural variability largely occurs as the result of strong variability in mid-latitude circulation. It can partially mask or amplify the forced changes caused by anthropogenic emissions, as it has in the past. As a consequence, short-term trends are poor indicators of the magnitude of climate change, and apparent regime shifts, step changes, disaster gaps and the clustering of events, and strong increases or decreases in event frequency or magnitude when estimated as trends over short periods are expected to occur on local scales even without anthropogenic forcing. Although global society can in principle influence emissions, model uncertainty and in particular internal unforced variability will remain substantial, calling for adaptation measures that are robust under a wide range of outcomes.

- At least half of the observed annual and seasonal warming in Switzerland over the past 50 to 100 years is likely due to anthropogenic emissions. This conclusion is supported by the unusual magnitude and pace of the past warming relative to natural variability, the attribution of warming to anthropogenic emissions at continental to global scales with very high confidence, and the process understanding of land warming faster than the global average.

The CH2018 scenarios in use

The CH2018 scenarios are an important source of data for impact research and for defining adaptation strategies, bringing together the most up-to-date collection of climate change information for Switzerland. The dialog between providers and users of the scenarios will continue past 2018 under the umbrella of the recently founded National Center for Climate Services (NCCS).

- As the most up-to-date collection of climate change information for Switzerland, the CH2018 scenarios are an important source of data for impact research and for the definition of adaptation strategies.
- Use cases illustrate the potential of the CH2018 scenario data to explore the consequences of climate change in Switzerland. The data can, for example, be used to find so-called “climate analogs”, which suggest that the future Swiss climate is similar to the present-day climate near the northern Mediterranean coastline. An application to runoff shows that the transient evolution of climate variables should be taken into account in order to develop realistic expectations of future streamflow. Simulations of snow pack for the Swiss Alps reveal that combined temperature and precipitation change is an adequate predictor of the response. Finally, weather generators such as the recently developed Advanced WEather GENerator (AWE-GEN-2d) are promising tools for overcoming some of the limitations of the downscaling method used in CH2018.
- The choice of methods and datasets depends on the application and most often requires a collaboration between climate experts and stakeholders. A stakeholder dialog has been initiated to provide continued support and ensure close collaboration with users of the CH2018 scenarios. This interaction between providers and users of the CH2018 scenarios will be continued under the umbrella of the recently founded National Center for Climate Services (NCCS).

What is new and different in CH2018?

- The projections in CH2018 are based on the latest generation of climate models, a larger number of models, simulations run at higher resolution, and improved methods that reflect the advancements in science since the previous scenario assessment CH2011. Although there are some quantitative differences, the climate change projections of the CH2018 scenarios generally confirm the findings of CH2011. Results are provided for three emission scenarios from the Representative Concentration Pathway (RCP) family to reflect recent societal and technological trends and ensure consistency with global climate assessments, but the range covered by the scenarios is similar to that in CH2011 and does not alter the conclusions.
- A larger set of variables on different scales and a more quantitative assessment of climate extremes and climate impact-relevant indices is provided. Projections at observation stations for a complete set of seven meteorological variables (including temperature, precipitation, relative humidity, global radiation, and near-surface wind) are now available for 58 stations and at daily resolution for the period 1981 to 2099 based on a quantile mapping method that incorporates statistical downscaling and bias-correction steps.
- Daily gridded data are now available from models statistically downscaled to a 2 km x 2 km grid, including daily mean, maximum, and minimum temperature and precipitation, as well as gridded temperature indices including hot days, summer days, tropical nights, frost days, and ice days. Indices of temperature and precipitation extremes, precipitation frequency, and drought are provided for five regions covering Switzerland. These projections facilitate the assessment of climate change and its

impacts at the local to regional scale.

- The various products are based on different methods, but consistency across scales and variables is ensured to the degree possible. Due to the complexity of the CH2018 climate scenarios, there is no single physically consistent scenario for “strong climate change”. The strongest changes in summer hot spells, extreme winter precipitation, or any other parameter are not all found in the same simulations. Thus, the behavior of individual simulations should be considered when deriving an impact-specific climate change scenario from the range of CH2018 projections.
- Compared to previous assessments, the new models and methods indicate wetter winters and a less pronounced mean summer drying. The uncertainty ranges for precipitation changes have increased somewhat with the new set of projections, but the CH2018 scenarios are fully compatible with the expert judgement interpretation of CH2011 that the projected ranges encompass the true changes with a likelihood of at least 66 % for temperature and at least 50 % for precipitation. The temperature projections are similar to those in CH2011, but in any case the use of the most recent datasets and scenarios is strongly recommended to increase confidence in the results and facilitate comparisons across studies.
- The projections provided here are subject to uncertainties. The uncertainty assessment is based on the results of multiple models but also incorporates arguments of physical understanding, the results of recently developed high-resolution models, the results of other model ensembles, studies on continental to global scales, and consistency with observed changes. The uncertainties are most challenging for extremes, for projections at local scales, and for the influence of natural climate variability. Research on global and high-resolution regional models, process understanding, and model evaluation must continue, and the development of improved statistical methods and the support for long-term observation networks represent key areas that need to be strengthened in the future. For future scenario efforts, an even stronger link to climate impacts, adaptation, and stakeholders could further increase the relevance of the results to decision-makers and society.

1. Introduction

Anthropogenic climate change is one of the most significant challenges currently faced by humankind. Climate change impacts the atmosphere-ocean-land system by causing global warming, changes in global and regional snow and ice cover, sea level rise, an increase in the occurrence of extreme events (such as heat waves, floods, and droughts), and changes in the distribution of global freshwater resources. Climate change is already evident in Switzerland: Glaciers are retreating, temperatures and the frequency of heatwaves are rising, and there is increasing concern about additional detrimental impacts. Changes in the climate system will likely be far-reaching and affect our environment, urban and rural settlements, agricultural productivity, tourism, health, energy and hydropower production, etc. Climate change might potentially even challenge international stability. We are only beginning to understand the extent of these implications.

In light of these challenges, it is imperative to reconsider our long-term planning and adapt to those factors that can be anticipated (climate adaptation). To this end, federal, cantonal, and local authorities, as well as policy makers and other stakeholders, require a solid basis for decision making in the form of climate change projections. Climate projections also provide information on the extent to which climate change can be reduced, for instance through appropriate steps toward reducing greenhouse gas emissions (climate mitigation), and on potential trade-offs between mitigation and adaptation. Climate projections are thus an essential requirement for decision-making at international, national and sub-national levels.

The current “CH2018 Climate Scenario” report – hereafter referred to as CH2018 – presents the latest projections of how climate change in Switzerland will likely unfold in the future. The report provides a solid foundation for adaptation to the impacts of climate change in Switzerland. It addresses a broad constituency, from educated citizens and stakeholders who desire detailed information about climate change, to engineers, politicians, and decision makers who are planning the next generation of our infrastructure, to scientists who are assessing the implications of climate change in specific areas of the natural environment and society.

The development of climate change scenarios for Switzerland started about two decades ago [40]. The first comprehensive national report CH2007 [246] was published in 2007, followed by a second report in 2011 (CH2011) [56]. The current CH2018 report serves as a follow-up to these two previous Swiss reports. The past reports have served as the basis for impact studies in several areas, among them a report on the implications of climate change on hydropower utilization [317], the Swiss climate adaptation strategy [116], and a comprehensive report on a wide range of climate change impacts in Switzerland (CH2014 [57]). The CH2011 results have also been extensively used by a recent report on climate change and its effects in Switzerland (“Brennpunkt Klima Schweiz”; [307]).

Seven years between reports may not seem very long, but there are many reasons why a new report is critically required. Like weather forecasts, which are issued on a daily basis to account for the most recent weather evolution, climate projections need to be regularly updated every few years, in order to take into account the most recent observational data and latest scientific methods and understanding. In comparison to the previous CH2011 report, the most significant innovations are as follows: First, there are now seven additional years of observational data (2011 - 2017), allowing us to situate the projections in an updated climatological context. Second, a new generation of global and regional climate model simulations has become available, representing recent progress in state-of-the-art climate modeling (CMIP5 and EURO-CORDEX; see Box 2.1). These simulations are available in much larger numbers compared to CH2011, and feature more recent model versions and higher spatial resolution. Third, new scientific knowledge and

findings have become available, among them the Fifth Assessment Report of the Intergovernmental Panel on Climate Change [168]. Fourth, new scenarios of greenhouse gas and aerosol emissions have become available (the so-called RCP scenarios, replacing the former SRES scenarios). Fifth, there is an increased understanding of user needs related to a number of socio-economic impacts. The current CH2018 report reflects these innovations. In comparison to CH2011, there is also much more detailed information in a number of key areas (e.g., extreme events); moreover some of the projections and uncertainty estimates have moderately changed, and additional data sets are provided to better serve future climate change impact studies.

The CH2018 report is embedded in a global climate service framework (the Global Framework for Climate Services, GFCS), an initiative that originated in the 2009 Geneva World Climate Conference of the World Meteorological Organization (WMO). The GFCS seeks “to guide the development and application of science-based climate information and services in support of decision-making in climate sensitive sectors”. A further purpose of the GFCS is the implementation of climate-service frameworks on regional, national, and sub-national levels.

In 2013, the Swiss government officially adopted the regular provision of climate scenarios for Switzerland as one of the measures outlined in its National Plan for Adaptation to Climate Change [116]. This mandate has been assigned to the Federal Office of Meteorology and Climatology MeteoSwiss. The Swiss National Center for Climate Services (NCCS), founded in 2015, takes up this initiative by coordinating the development and propagation of Swiss national climate services. The parties involved in the NCCS include the Federal Office of Meteorology and Climatology (MeteoSwiss), the Federal Office for the Environment (FOEN), the Swiss Federal Office for Civil Protection (FOCP), the Federal Office for Agriculture (FOAG), the Federal Office of Public Health (FOPH), the Federal Food Safety and Veterinary Office (FSVO), the Swiss Federal Institute of Technology in Zurich (ETH Zurich), and the Swiss Federal Institute for Forest, Snow and Landscape Research (WSL). Acting as an interface between producers and users of climate information, the NCCS encourages dialogue and fosters the collaborative development of climate services. A prominent example of such work are the current CH2018 Climate Scenarios, which also involved the Center for Climate Systems Modeling (C2SM, Zurich), the Oeschger Centre for Climate Change Research of the University of Bern, and the Forum for Climate and Global Change (ProClim, Bern).

The report is organized as follows: Chapter 2 presents the framework of CH2018 and details the key methodological procedures. Chapter 3 provides an assessment of the past evolution of the Swiss climate based on instrumental observations as well as climate reconstructions from proxy information. Chapters 4 to 6 present the climate projections for the next 100 years, addressing regional mean changes (Chapter 4), statistical scenarios at high resolution and at station locations (Chapter 5), and an assessment of changes in extreme events, covering in particular temperature and heat stress extremes, as well as changes in heavy precipitation and drought events (Chapter 6). Chapters 7 to 10 provide further analyses and information. This includes an assessment of natural variations in the context of projected anthropogenic changes (Chapter 7), an intercomparison with previous Swiss climate change scenarios (Chapter 8), technical details on available datasets provided with this report (Chapter 9), and recommendations on the use of the scenario datasets (Chapter 10). Chapter 11 concludes the report and discusses future perspectives.

2. The CH2018 framework

Summary

The Swiss climate scenarios CH2018 are climate change projections based on the recent EURO-CORDEX ensemble of regional climate simulations. These simulations project climate change for three alternative "Representative Concentration Pathways" (RCPs) that explore future anthropogenic forcing of climate change ranging from unabated emissions (RCP8.5) to an ambitious mitigation pathway to keep global warming below 2 °C with respect to pre-industrial levels (RCP2.6). An intermediate case with mitigation insufficient to reach the 2 °C target is also considered (RCP4.5). The CH2018 projections consist of several datasets derived through various methods that provide robust and relevant information on climate change in Switzerland:

- Mean seasonal changes show the main characteristics of possible future climate change in Switzerland.
- Localized projections provide highly spatially and temporally detailed data for research on the impacts of climate change.
- Projections of both climate extremes and climate indices provide information on long-term changes in the occurrence or prevalence of specific impact-relevant weather situations such as extreme precipitation or heat stress.

For a robust quantification of climatic changes, averages over five model regions covering Switzerland (eastern and western regions for both the area north of the Alps and the Alpine area, and a region south of the Alps) and three scenario periods spanning the 21st century (centered on the years 2035, 2060, and 2085) are used. Historical and ongoing climate change in Switzerland is documented using observational data, which serve as a reference for future climate change.

This chapter describes the framework of data and analysis that underpins the CH2018 climate scenarios and explains the rationale of the approach taken here. In this overview section, the main components and concepts of CH2018 are introduced. The keywords set in bold are explained in more detail in the following sections of this chapter.

CH2018 harnesses the advances achieved since the last generation of Swiss Climate Change Scenarios CH2011 [56] in the areas of observations, climate simulations, and scientific understanding (Chapter 1). Although the conclusions from CH2011 are generally confirmed by CH2018, the new set of scenarios imparts a wealth of new and more user-oriented information on future climate change in Switzerland (Chapter 8). The CH2018 climate scenarios are primarily derived from the new EURO-CORDEX ensemble of **climate simulations** with Regional Climate Models (RCMs) (Box 2.1). The RCM simulations of EURO-CORDEX cover a common model domain centered on western Europe, ranging from northern Scandinavia to northern Africa and from the Atlantic to the Black Sea (Figure 2.3). The boundary conditions for this model domain are prescribed by simulations with "driving" Global Climate Models (GCMs), and this nested GCM-RCM combination is referred to as a *model chain*. The RCMs thus translate the coarse global GCM projections to a resolution that represents the main topographical features of Switzerland, a process referred to as *dynamical downscaling*.

The climate change simulations used in this report are conditioned on scenarios of anthropogenic forcing (greenhouse gases, aerosols, and land use) over the 21st century, the **Representative Concentration Pathways (RCPs)** [168]. As these RCPs primarily represent different levels of future greenhouse gas emissions, they are referred to here as "emission scenarios". Estimates based on these simulations are referred to as climate change *projections*. Projections are not predictions of future climate change, since the underlying RCPs are scenarios of unspecified probability and depend on political choices as well as on socio-economic factors.

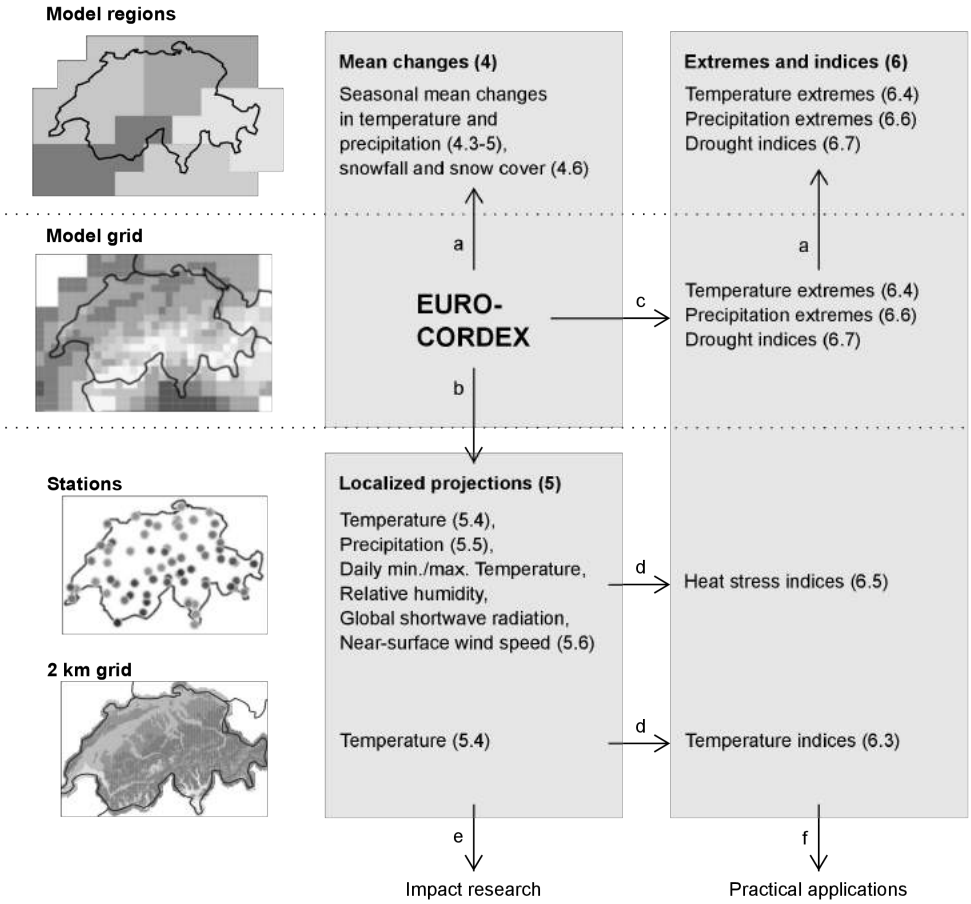

Figure 2.1. Schematic overview of the CH2018 framework, showing the results derived from the EURO-CORDEX ensemble of climate simulations and the corresponding chapters, arranged by level of spatial aggregation. The arrows indicate (a) regional aggregation, (b) statistical downscaling, (c) the derivation of extreme events and indices from RCM simulations and (d) from localized projections, (e) the application of localized projections in impact research, and (f) practical applications of the derived extremes and indices, e.g., for adaptation purposes.

To extract robust and relevant climate change projections from the underlying set of simulations, a range of different datasets has been produced (Figure 2.1). Users attribute relevance to a high spatial and temporal resolution and quantitative information specific to their climate exposure, e.g., concerning extreme events [230]. A basic characterization of the main features of climate change in Switzerland is obtained using averages in time and space. The simulated climate variables are averaged seasonally and over periods of 30 years to filter out daily and interannual stochastic variation and reveal the long-term climate change signal. Changes with respect to the **reference period** 1981 - 2010 are calculated for three CH2018 **scenario periods** spanning the 21st century. The seasonal changes over Switzerland are considered in a European context in order to facilitate understanding of the large-scale changes and complement the assessments for Switzerland. Changes are further aggregated spatially to summarize the main traits, assess the model uncertainty in terms of ensemble spread, and emphasize large-scale information (Figure 2.1, a). This aggregation increases robustness against outliers among models, different simulations, and individual grid cells. Spatial averages are shown for five **model regions** covering Switzerland and adjacent territory. The regions used for aggregation correspond to those used in the earlier CH2011 report [56].

Localized projections of climate variables are often more relevant for impacts and adaptation than aggregate results or relatively coarse model output. With a maximal resolution of 12.5 km, the RCMs of EURO-CORDEX still poorly resolve the topographic and climatological landscape of Switzerland (e.g., the inner Alpine valleys are not represented). Accordingly, data characterizing the local scale are derived by the *statistical downscaling* of RCM simulations (Figure 2.1, b). The localized CH2018 projections are statistically downscaled by **quantile mapping**, a method that matches the distributions of simulated and observed climate variables and applies the correction derived from observations to the projections of future climate

(Figure 2.1). This yields absolute values in transient data with daily resolution. Such localized data is particularly valuable for research on the impacts of climate change (Figure 2.1, e), although changes in extremes extracted from this downscaled data can be subject to large uncertainties and must be evaluated for the specific application (Chapter 5.7).

Seasonal mean changes do not capture all types of events that may cause climate change-related impacts. To characterize climate change in more relevant terms, CH2018 considers climate extremes and indices in addition to seasonal means. Indices statistically describe changes in extreme events or events that are characterized by the exceedance of some significant threshold (for example, freezing temperature). Extreme value analyses and percentile-based indices are derived from the unmodified RCM simulations (Figure 2.1, c) to avoid any distortions created by processing steps such as statistical downscaling. For indices related to absolute temperature thresholds, downscaled temperatures are used, as these best capture the strong dependency of local temperatures on topography (Figure 2.1, d). These derived quantities are closely related to the impacts of climatic changes. Indices are also frequently tailored to the susceptibility of specific sectors and thus extract information that is particularly relevant for adaptation to climate change (Figure 2.1, f).

In summary, CH2018 follows a multi-pronged approach to provide robust and relevant information on climate change in Switzerland. The various products are derived using different methods according to their specific requirements. As a consequence, consistency among the diverse types of data is not guaranteed and must be separately assessed (Chapter 4.7). A more detailed tabulation of the variables considered in each of the results is given in Figure 2.1.

To put the climate projections in context, historical and ongoing climate change in Switzerland is documented using **observational data**. The observed climate in different parts of Switzerland is described using measurement data from selected stations, gridded data, and averages over climatological regions (Figure 2.1, a). In addition to direct observations of climate variables, which start in the year 1864, indirectly inferred information from measurements of climate proxies is used, reaching back to 1685 (Chapter 3.3). The observational record serves as a reference for future climate change. In addition, the variability of the current climate provides an indication of climate-related risks today. For quantities whose expected future climate trends are small or considered unreliable, accounting for present-day climate variability provides the best estimate of potential climate-related impacts.

2.1. Climate simulations

For areas with complex topography such as Switzerland, the resolution of general circulation models (GCMs) is far too low to produce an accurate representation of local climatic features. Regional climate models (RCMs) allow for refinement of the larger-scale GCM information by explicitly representing higher-resolution atmospheric and surface processes (*dynamical downscaling*). The RCMs of the EURO-CORDEX ensemble used here (Box 2.1) simulate climate within a limited region and at a higher horizontal resolution. To “drive” the RCM simulations, GCM output is used to prescribe the boundary conditions of the RCM simulation domain. The GCM- and RCM-simulated climates at a particular location may differ substantially due to the important role of small-scale topography and atmospheric processes in the hydrological cycle.

Box 2.1: Coordinated global and regional climate simulations

Global and regional climate models (GCMs and RCMs) are used to assess how the climate is responding to various external forcings such as solar variability, volcanic eruptions, and anthropogenic greenhouse gas emissions This information can tell us why the climate has changed in the past and how it may be changing in the future. These models are based on a governing system of equations that is integrated forward in time on a computational mesh. The accuracy of the integration depends upon the horizontal and vertical grid spacing. Typical GCMs operate at horizontal resolutions of around 100 km; RCMs, at 10 - 25 km. GCMs use a global mesh and generally represent the coupled atmosphere/ocean/land system. RCMs operate on regional domains (see Figure 2.3), are driven by a GCM, and usually do not include a dynamical representation of the oceans. RCMs are particularly attractive in regions affected by complex topography and coastlines, and studies have demonstrated that they can provide added value to the lower-resolution GCMs not only with regard to spatial climate variability and extremes, but also in terms of mean climatologies over large regions (e.g., [78, 177, 335, 344]).

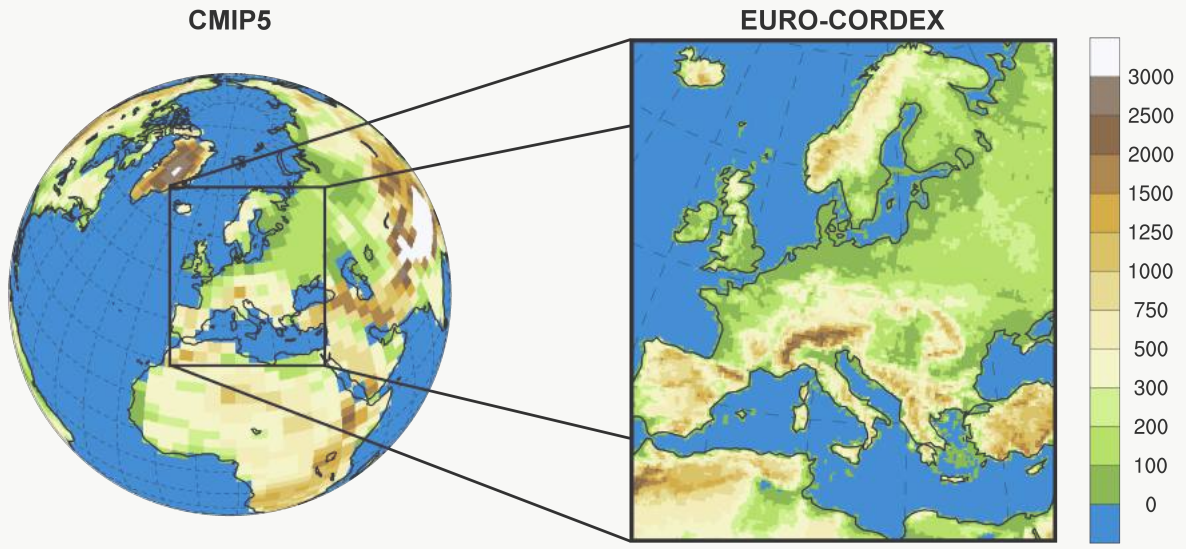

Figure 2.3. Domains and approximate topography of global (CMIP5, left) and regional (EURO-CORDEX, right) coordinated modeling efforts (in m a.s.l.).

More than 20 years ago, the climate modeling community began to coordinate their numerical experiments. This coordination encompasses the choice of emission scenarios and the duration of the simulations, as well as certain technical aspects of the simulations (e.g., the treatment of volcanoes). Such coordination is essential to enable thorough comparisons between different model simulations, to evaluate model skill, to ensure that differences between simulations reflect the model uncertainty rather than technical aspects of the simulations, and to provide climate projections. The most recent set of simulations available include the CMIP5 GCM and the CORDEX RCM simulations.

On the level of GCMs, coordination takes place within the framework of the Coupled Model Intercomparison Project, which has completed its fifth phase (CMIP5; [336]); this endeavor is organized by the World Climate Research Programme (WCRP). The inter-comparison framework defines a standardized experimental design. For CMIP5, it included a new set of emission scenarios, namely four different Representative Concentration Pathways (RCPs). The IPCC's Fifth Assessment Report (AR5 [168]) relied heavily on model results simulating the different RCP emission scenarios. In total, climate modeling groups from more than 30 different institutions have participated in CMIP5.

Thus far, the CMIP5 dataset is the most comprehensive climate model ensemble at the global scale. Because the comparatively coarse GCM grid spacing often requires a further downscaling of GCM data in order to produce climate projections at regional scales, dynamical downscaling by RCMs has become common practice. As with GCMs, the application of RCMs is a resource-intensive exercise that requires appropriate modeling expertise, and individual modeling groups can typically only afford to carry out a few simulations.

The regional counterpart of the CMIP5 intercomparison project is the Coordinated Regional Climate Downscaling Experiment CORDEX ([130]; www.cordex.org), also led by the WCRP. One of the goals of CORDEX is to provide comprehensive regional climate projections for all land areas of the globe. This is achieved by running a comprehensive set of RCMs driven by various CMIP5 GCMs and assuming different RCP forcing scenarios under a controlled setup, which enables comparability of the individual experiments. The CORDEX design is thus similar to the CMIP5 experimental design but targets regional scales. Statistical downscaling approaches are also considered. The number of available RCM simulations varies widely among the regional CORDEX domains; the largest sets of simulations that are currently available for public use are for the African, Mediterranean, and European domains. This last domain is coordinated through the EURO-CORDEX effort, the European branch of CORDEX (www.euro-cordex.net). EURO-CORDEX involves more than 30 European modeling centers (among them ETH Zurich), applying more than 10 different RCMs on a pan-European model domain. The current EURO-CORDEX database consists of more than 80 simulations at grid spacings of 12 km (EUR-11) and 50 km (EUR-44).

The output data of the CMIP5 and CORDEX simulations is publicly available via the Earth System Grid Federation system (ESGF; https://esgf.llnl.gov) and forms the backbone of the CH2018 scenarios.

Box 2.2: User needs and stakeholder dialog

In the run-up to CH2018, a comprehensive survey was conducted to allow a better understanding of the users of climate scenarios and their needs [230]. The survey addressed organizations from climate-relevant sectors and involved representatives from administration, research, and private companies across Switzerland. The survey consisted of group interviews with key stakeholders, a questionnaire answered by more than one hundred users, and two workshops on dissemination. Additionally, the survey results were consolidated at a national symposium with approximately 150 participants from research, public administration, and practice. These results indicated that a dedicated approach is necessary to reach beyond the needs of research and provide relevant information to practitioners in adaptation to climate change and climate change politics. To make the CH2018 findings accessible to this user group, which has little exposure to climate science, comprehensibility, clarity, and support are paramount. One way this goal is approached is through a stakeholder dialog, an important instrument for transforming the scenarios from “pure” climate information into a climate service. Various key stakeholders from within and beyond the Swiss adaptation community were included. In the long term, this stakeholder dialog should become institutionalized within the National Centre for Climate Services. In addition, a “sounding board” group composed of representatives from research institutions as well as public service accompanied the project, giving feedback on its status and direction at regular intervals.

In the survey, many of the users of climate scenarios called for expansion of the range of data offered. Among the most frequent requests was the need for quantitative information on changes in extremes. Compared to the previous generation of climate scenarios, CH2011, which treated extreme events in a mostly qualitative way (Chapter 8), CH2018 has made substantial progress in accommodating this need. Another requirement that was emphasized by users involves the consistency of the scenario data across different atmospheric variables. For instance, agricultural impacts depend on heat and dryness as a combined phenomenon; similarly, the potential for renewable energy depends on both wind speed and insolation. By conserving the relation of data products within individual simulations, consistency is greatly improved upon in CH2018. The survey further highlights the challenge of communicating uncertainty to different user groups: Whereas scientific users can deal with comprehensive and differentiated quantifications of different kinds of uncertainty, practitioners tend to be overwhelmed by this complexity, requiring uncertainty information in a reduced form better suited to their purposes.

Like earlier climate scenario assessments for Switzerland, this report builds upon the latest RCM projections for Europe produced in the internationally coordinated projects of leading European climate institutes. Compared to the predecessor set of RCM projections (ENSEMBLES; [352]), the new ensemble from EURO-CORDEX includes simulations at a higher spatial resolution (12 km compared to 25 km in ENSEMBLES); it also contains a larger number of dynamically downscaled GCMs and a larger number of simulations for three explicitly simulated emission scenarios (instead of one). The new EURO-CORDEX simulations have been validated and compared to the ENSEMBLES simulations for Europe (e.g., [197, 177]). Although the main patterns of climatic changes and systematic model errors are comparable between the two generations of RCM sets, the new simulations at 12 km show new features, such as maximum daily precipitation intensities that exceed those in ENSEMBLES [177]. Even so, the most recent EURO-CORDEX RCM generation is subject to limitations and inaccuracies – for instance, concerning the treatment of atmospheric aerosols and their effect on the near-surface climate (Chapter 4.2). In addition, the resolution of 12 km is still too coarse to make these simulations suitable for studies on sub-daily climate variability (e.g., sub-daily summer rainfall extremes).

The RCP8.5 simulations from EURO-CORDEX form the core of the CH2018 projections, as climatic changes are expected to be the most clear under this scenario, and because fewer simulations are available for the other RCPs (Chapter 5). For the purpose of multi-model analysis, simulations available at both resolutions are considered redundant, and only the higher-resolution model is retained. The selected set of 21 different RCP8.5 simulations includes nine different GCM and seven different RCM versions (including two different versions of one RCM; see Table 4.1). The climate projections cover a range corresponding to the spread of the joint set of simulations for each forcing scenario. This projected range represents both model uncertainty and uncertainty arising from the internal variability of the climate system. In order to estimate uncertainty ranges consistently for the other RCPs, a corresponding set of simulations should be used. To achieve this, given the smaller number of simulations for RCP4.5 and RCP2.6, missing simulations are substituted by pattern scaling (Chapter 4).

2.2. Representative Concentration Pathways

In this report, climate change in Switzerland is estimated for three of the Representative Concentration Pathways (RCPs) used in the latest assessment report issued by the IPCC [168]. The three RCPs used here range from a mitigation scenario implying swift and substantial reductions in global emissions (RCP2.6) to continued emission growth until the end of the century. The RCPs are named after the level of radiative forcing (RF in Wm^{-2}) reached by the end of the century (Table 2.1, Figure 2.4).

Table 2.1. RCPs used within this report, their main characteristics in terms of radiative forcing (RF), CO_2-equivalent concentration (CO_2eq), global mean surface temperature change (GMT), and relationship to the emission scenarios used in CH2011.

Scenario	Pathway	Global changes until 2100 relative to 1850 to 1900	Corresponding CH2011 scenario
RCP8.5	Unabated emissions	Continuously increasing RF (8.5 W m^{-2}, 1370 ppm CO_2eq) and GMT (4 - 5 °C)	A2
RCP4.5	2°C-non-compliant mitigation	Emissions decline after 2050, stabilization of RF (4.5 W m^{-2}, 650 ppm CO_2eq), increasing GMT (~2.5 °C)	-
RCP2.6	2°C-compliant mitigation	Implies strong reduction of greenhouse gas emissions early in the 21st century, peak and decline of RF (2.6 W m^{-2}, 490 ppm CO_2eq), stabilization of GMT (< 2 °C)	RCP3PD

RCPs are primarily used to explore the climatic consequences of the emissions of long-lived greenhouse gases, the most important of which is CO_2. However, as the name implies, RCPs are defined in terms of the concentrations of these gases. In addition to the long-lived greenhouse gases, RCPs also specify time series of emissions of aerosols and chemically active gases, as well as land use/land cover over the course of the 21st century. The implied CO_2 emissions corresponding to each RCP are only known within considerable uncertainty, mainly related to imperfect knowledge of the uptake of CO_2 by the ocean and the land biosphere (carbon cycle uncertainty; e.g., [62]). In the present report, RCPs are also referred to as *emission scenarios* in this sense. It should be noted, however, that carbon cycle uncertainty is not accounted for explicitly here. In contrast, the SRES scenarios [164] used in CH2011 [56] and the third and fourth IPCC reports [165, 166] were defined in terms of *emissions*. Thus, any climate projection based on the SRES scenarios requires assumptions regarding the carbon cycle and is associated with the corresponding uncertainties (see also Chapter 2.7).

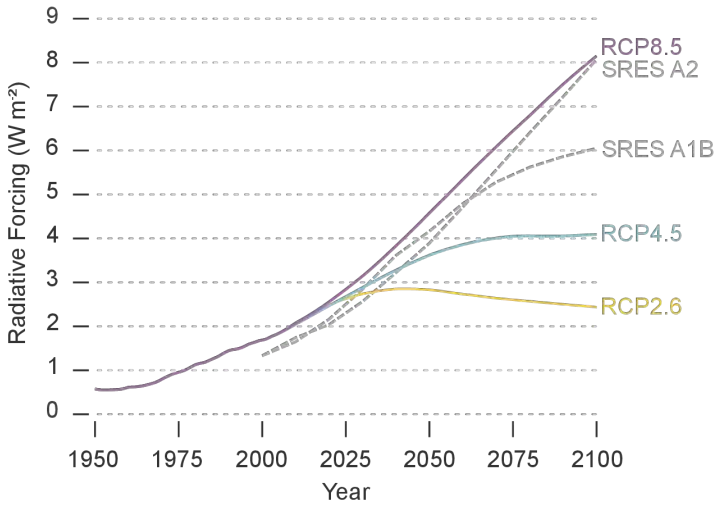

Figure 2.4. Radiative forcing with respect to pre-industrial levels for the three RCPs used in this report (colored lines). The dashed grey lines show the two SRES scenarios that were used in CH2011. RCP2.6 was also included in CH2011, but is labeled "RCP3PD" for historical reasons. The atmospheric CO_2 concentration and RF corresponding to the SRES emission scenarios can only be calculated within some uncertainty related to the uptake of CO_2 by the ocean and the land biosphere [224]; the RF shown for the SRES emission scenarios do not account for this carbon cycle uncertainty. The RF shown at the end of the century does not exactly correspond to the nominal forcing levels of the RCPs, as forcing was implemented in terms of greenhouse gas concentrations or emissions, which results in slightly different RF in the various models. Figure adapted from [168].

The RCPs used in this report are also relevant for political mitigation targets. The Paris Agreement of the Conference of the Parties to UNFCCC states the aim of "holding the increase in the global average temperature to well below 2°C above pre-industrial levels and to pursue efforts to limit the temperature increase to 1.5 °C above pre-industrial levels, recognizing that this would significantly reduce the risks and impacts of climate change." The RCP2.6 scenario is unlikely to exceed 2 °C warming within the 21st century (relative to 1850 to 1900) [169] and has been accepted by signatory governments as representing the policy case in which global mean temperature is limited to 2 °C warming over pre-industrial levels. In this report, the projections for RCP2.6 are compared to the implications of global warming of exactly 1.5 °C and 2 °C for Switzerland (Box 4.1), using a pattern-scaling approach (Chapter 4).

2.3. Reference period and scenario periods

For a robust quantification of climatic changes over a small region such as Switzerland, averages over sufficiently long time periods must be considered to filter out short-term variability. CH2018 uses averages over 30-year periods, corresponding to the definition of climatological standard normals used by the World Meteorological Organization (WMO).

The current official normal period 1981 - 2010 recommended by WMO and implemented at MeteoSwiss is used as the *reference period* against which future climatic changes are calculated. Additionally, the official WMO climate normal period 1961 - 1990 is used as a historical base period for assessment of observed variability, trends, and extremes (Chapter 3.3). Three future periods are used to project climate change: 2020 - 2049, 2045 - 2074, and 2070 - 2099. For simplicity, these periods are denoted by the corresponding central year of the time window (i.e., 2035, 2060, and 2085).

The CH2018 time periods correspond to those used for the previous generation of Swiss climate scenarios CH2011 [56], with the exception of a shift of one year in the reference period (from 1980 - 2009 to 1981 - 2010) to match the norm period used by WMO and MeteoSwiss. The reference period is also consistent with the 20-year-long reference period used in the IPCC AR5 report, which has the same central year (1995). Although this reference period is somewhat outdated and does not include the latest years of observation, it was retained for the following reasons: First, consistent time periods permit comparability with earlier publications and are preferred by most users [230]. Furthermore, as projections start in 2005, a later reference period would affect the consistency between boundary conditions and observations in the reference period.

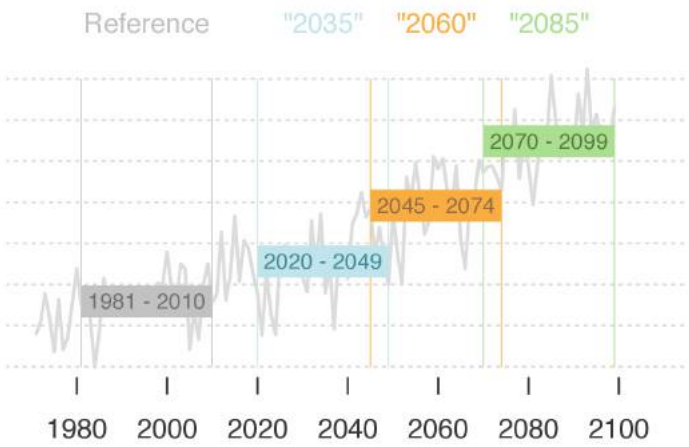

Figure 2.5. Reference period and the three future periods consisting of 30 years each.

Some of the changes discussed in CH2018 are analyzed in reference to pre-industrial times. For this purpose, the pre-industrial reference period 1864 - 1900 is chosen. This is the official period used by MeteoSwiss; it represents a compromise between the commonly used period 1850 - 1900 (e.g., by the IPCC), a standard 30-year period, and the instrumental station data available in Switzerland (beginning in 1864).

2.4. Model regions

For robust estimates of simulated changes and uncertainty, climate data are aggregated spatially for five model regions (Figure 2.6): Northeastern Switzerland (CHNE), western Switzerland (CHW), southern Switzerland (CHS), western Swiss Alps (CHAW), and eastern Swiss Alps (CHAE). The CH2018 model regions divide Switzerland and some adjacent territory into climatically distinctive parts. The regions are similar in size, which ensures comparable stochastic variability in the regional averages. They are also similar to those used in CH2011 and follow-up products [56, 100], differing only where the grids of the underlying climate models do not coincide. This allows for a quantitative comparison between CH2018 and CH2011 (see Chapter 8).

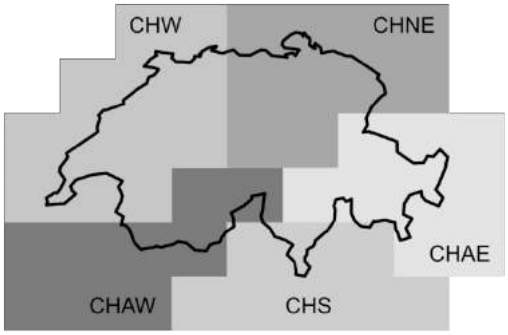

Figure 2.6. The five CH2018 model regions covering Switzerland and adjacent territories.

2.5. Quantile Mapping

Although the new generation of RCM simulations from EURO-CORDEX provides information at a spatial resolution of 12 km, often this is still too coarse for local impact assessments. Furthermore, the RCM simulations are prone to substantial biases [197], especially over complex topography such as the Alps. Over recent years, numerous statistical techniques have been developed to downscale climate model simulations to the local scale and correct for bias [212]. CH2018 applies the commonly used method of *quantile mapping* for statistical downscaling. Assuming a constant relationship between spatial averages on the model grid scale and local values, a transfer function is calculated that aligns the simulation with the local observations over the observational period. Thus, if the simulations are biased at the model grid scale (i.e., biases that have not previously been removed), quantile mapping implicitly corrects for such biases as well. If quantile mapping is applied to a simulation at the same spatial scale as the observational reference, it functions as a bias-correction method only. In this report, quantile mapping is applied to station observations as well as gridded observations at 2 km to derive localized climate projections. The quantile-mapped projections preserve the daily granularity and transient nature of the native RCM simulations throughout the common simulation period 1981 - 2100. A typical application of such data is for climate change impact models, which require high-resolution input. However, the suitability of these data for a specific application must be evaluated in each case, as some of their properties, such as changes in extremes, can be subject to large uncertainties. A detailed description of the QM method and its limitations is given in Chapter 5.7.

2.6. Observational data

The primary sources of the observational data used for CH2018 are the long-term meteorological measurements of temperature and precipitation and other variables from the station network of the Federal Office of Meteorology and Climatology MeteoSwiss. In the cases of daily temperature and precipitation, these data have been homogenized to account for station relocation, changes in measurement instruments, and other factors. For some stations, the data reach back as far as 1864 [21]. They thus represent a unique opportunity to identify changes in the climate at the local scale. Despite the relatively long observational record, there is considerable uncertainty in the amount of systematic (forced) climate change occurring at one location as opposed to the random result of natural variability. This applies in particular to very rare events whose return period approaches the length of the measurement record and which may never have been observed at a given location. This problem also arises with variables that do not have a very long measurement record. Nevertheless, the totality of observations over Switzerland permits the identification of of both extreme events and changes in variables other than mean temperature..

Instrumental measurements are complemented by proxy data that convey information on the climate going further back in time. Documentary evidence, tree rings, and other proxy records provide reconstructed temperature and precipitation data for the Swiss Plateau and the Alpine region dating back to 1685.

In order to validate RCMs over Europe, gridded observational data at the resolution of the climate models (12 and 50 km) are necessary. For temperature and precipitation, the commonly applied E-OBS dataset [150]

is available. Because E-OBS has a resolution of only 25 km and entails certain deficiencies (in particular, for daily precipitation intensities over complex topography such as the Alps [157, 172])., it is substituted by high-resolution data of better quality for Alpine areas. This approach ensures that the highest-quality gridded datasets available for Switzerland and the surroundings are used, while still providing a gridded dataset for the whole of Europe. The dataset used for the Alpine region is the operational gridded dataset of 2-km resolution produced at MeteoSwiss. For precipitation, the MeteoSwiss dataset is based on the method developed by [125] to derive gridded values from the daily rain gauge observation network over Switzerland. The MeteoSwiss precipitation data is complemented by the Alpine Precipitation Grid Dataset (APGD; [173]) of 5-km resolution outside of Switzerland.

2.7. Uncertainty assessment

The CH2018 climate projections for each emission scenario are based on an ensemble of models. The central tendency of this ensemble may be suitable for a best-guess estimate given the available information, and its spread provides an indication of uncertainty due to model imperfections and natural variability [286]. However, this uncertainty is conditional on the largely arbitrary selection of models in the ensemble (see Chapter 4.7). As the models of the EURO-CORDEX ensemble are interrelated to varying degrees and are not guaranteed to comprise all theoretically plausible model formulations, the ensemble range cannot be expected to capture the full scientific uncertainty of the climate change signal. This is commonly expressed by the phrase “ensemble of opportunity” (e.g., [193]).

To characterize the range of the CH2018 climate projections, an empirical quantile range capturing 90 % of the model spread is used (from the estimated 5 % to the 95 % quantile, Figure 2.7; see Chapter 4.2 for details). The 90 % quantile range is a common choice for characterizing ensemble spread (e.g., used in IPCC AR5 [168]) and represents a compromise between underrepresentation of the range (for a narrower range) and sensitivity to individual simulations (for a wider range).

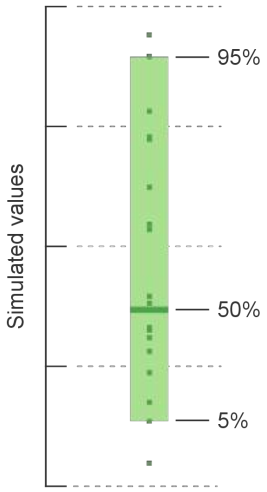

Figure 2.7. Representation of uncertainty showing values from individual simulations (dots), the multi-model median value (bold line), and the estimated 90 % quantile range (colored bar). The 90 % range is calculated such that its upper and lower bounds correspond to the second highest and second lowest values for an ensemble with 21 members.

This range descriptively characterizes the uncertainty represented by the model ensemble and must be interpreted in the context of broader expert knowledge. In other words, the 90 % range of the model spread does not indicate a probability of 90 %. Thus, it is not a “very likely” range as such and cannot be used to identify statistically significant changes. This is analogous to the interpretation of the model-based uncertainty ranges in CH2011 ([56]). As each projected variable and index has an individual uncertainty, the corresponding ranges are related to different levels of likelihood. Throughout this report, the likelihood of the actual outcome falling in the projected 90 % range is assumed to be 66 % unless otherwise noted. However, it is not possible to quantify, for example, a likely outcome across the full parameter space (e.g., different variables, different seasons, different indices). Thus, the interpretation of the CH2018 model range may deviate from the “likely” rule depending on the quantity assessed, as specified in the corresponding sections.

Furthermore, the projected ranges remain fundamentally scenario-based and governed by assumptions. The Representative Concentration Pathways (RCPs; Chapter 2.2), which represent uncertainty in the future anthropogenic influence on climate in the EURO-CORDEX simulations and in CH2018, are “plausible descriptions of how the future may develop based on a coherent and internally consistent set of assumptions about key driving forces and relationships” [168]. With climate simulation, the uncertainty of climate response is introduced as a second dimension of uncertainty (Figure 2.8). Whereas climate uncertainty is due to physical processes and their scientific descriptions, the uncertainty captured by the RCPs is related both to socio-economic dynamics and political choice regarding climate change mitigation. Finally, the fact that carbon cycle uncertainty is not considered in the RCPs or in EURO-CORDEX (Chapter 2.2) implies that the CH2018 projections do not fully characterize all possible outcomes of climate policies from unabated emissions to ambitious mitigation. In particular, a high-emissions path such as the SRES scenario A2 may not be as similar to RCP8.5 as suggested by Figure 2.4, but could instead result in substantially higher radiative forcing; likewise, meeting the 2 °C target of RCP2.6 may prove to be even more difficult than expected based on standard assumptions on carbon uptake.

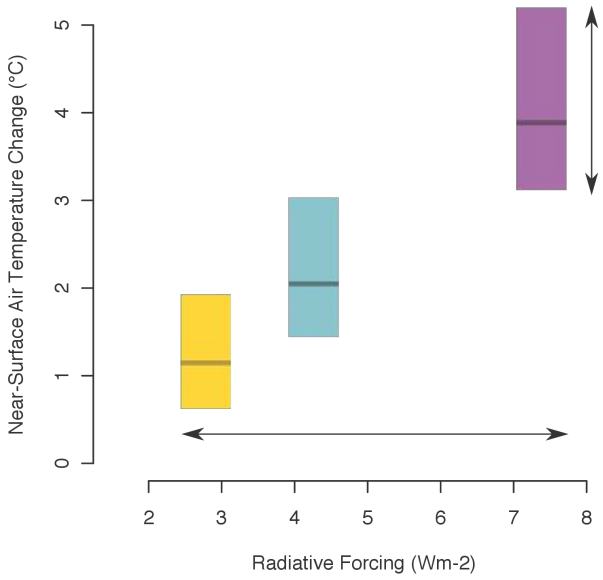

Figure 2.8. Mean surface temperature change averaged over Switzerland vs. radiative forcing (RF). RF uncertainty represented by RCPs is on the horizontal axis; climate change uncertainty, on the vertical axis.

3. Reference climate and recent change

Summary

Switzerland is situated in the zone of the westerlies in the northern mid-latitudes. Cyclones and fronts bring moist air from the nearby Atlantic Ocean and seas to Switzerland, intermitted by phases of high pressure with stable weather. The complex topography of the Alps creates a diverse climate with large altitudinal and spatial gradients and small-scale phenomena. Detailed information on the country's past and present climate is presented for temperature, heat stress, precipitation, snow, and wind.

Long-term high-quality measurements of the climate exist for the last 150 years, and reconstructions for some variables are available for the last 330 years. Despite large natural variability on timescales of years to decades, a robust climate-change signal is found for several variables.

- Near-surface air temperature has increased by about 2.0 °C between 1864 and 2017, compared to 0.9 °C globally, with most of the warming taking place since the 1980s. The 1988 to 2017 summer average is by far the warmest 30-year summer average since the start of reliable reconstructions in 1685. This warming has led to more frequent and more intense heat waves; meanwhile, cold periods have become less frequent. The zero-degree line has risen by 300 m to 400 m since the 1960s.
- The temperature increase has had pronounced effects on the cryo- and biosphere. The volume of Alpine glaciers has decreased by about 60 % since the 1850s. Since the 1970s, the number of snow days and snowfall days has decreased by about 20 % at about 2000 m a.s.l. to 50 % below 800 m a.s.l. The vegetation period and pollen season are two to four weeks longer today than in the 1960s.
- Winter precipitation has increased by about 20 % to 30 % since 1864, although part of this apparent change may be due to natural variability. There are robust signals that heavy precipitation has become more frequent (+30 %) and more intense (+12 %) since the beginning of the 20th century.
- Sunshine duration, a proxy for global radiation, shows a significant decline of -15 % between the 1950s and around 1980, followed by a significant increase of +20 % to the present day.

No robust signals on long-term trends in the observational record are found for summer precipitation, droughts, wind speed, or low stratus. For these quantities, it is either unclear at this point how they are affected by climate change, or the expected anthropogenic signal has not yet emerged from the observed large natural variability (e.g., summer drying). The observational basis is too short or insufficient to make robust inferences about past changes in small-scale phenomena such as thunderstorms, tornadoes, and hail.

Comprehensive knowledge of the past and present-day climate and its variability is indispensable in the process of securing a reference for potential future climate change, validating and correcting climate models, and assessing the significance of the observed and projected trends. A comparison of observed and modeled trends in the past is essential in efforts to reveal the driving physical processes. In addition, high-quality long-term observational datasets are key for the estimation of the range of variability intrinsic to the climate system. This further allows estimation of natural variability and assessment of the significance of the projected changes.

In this chapter, the large-scale setting and relevant drivers of the Swiss climate are introduced first (Chapter 3.1). The main features and the mean state – setting the reference for the projected changes – are then described in Chapter 3.2. Finally, the observed variability and recent changes are presented in Chapter 3.3, using observations and some reconstructions from climate proxies.

3.1. Drivers of the Swiss climate

3.1.1. Introduction

The general characteristics of the Swiss climate are mainly determined by Switzerland's geographical position and the corresponding dynamical processes dominant in this climate zone. The local characteristics can be strongly modified by the complex topography of the Alps. In this section, the focus is on the large-scale setting and variability, the effects of the Alps, and local feedbacks.

3.1.2. Large-scale setting and variability

Switzerland and the Alps are situated in the northern mid-latitudes and the so-called "temperate climate zone" [221]. The synoptic-scale flow is strongly determined by the eastward passage of fronts, cyclones, and anticyclones determining the day-to-day weather variation, albeit with pronounced seasonal differences (e.g., [5]). In winter (DJF), large pressure gradients and considerable variability in the pressure field are caused by low- and high-pressure systems and fronts impinging upon the Alpine region (Figure 3.1). The latter effect is illustrated by the percentage share of the ten "Grosswettertypen" based on the geopotential height at 500 hPa (GWT10 Z500) [263, 229], which indicates that the flow for both summer and winter is dominated by advection from the west, northwest, and southwest, as well as from the north.

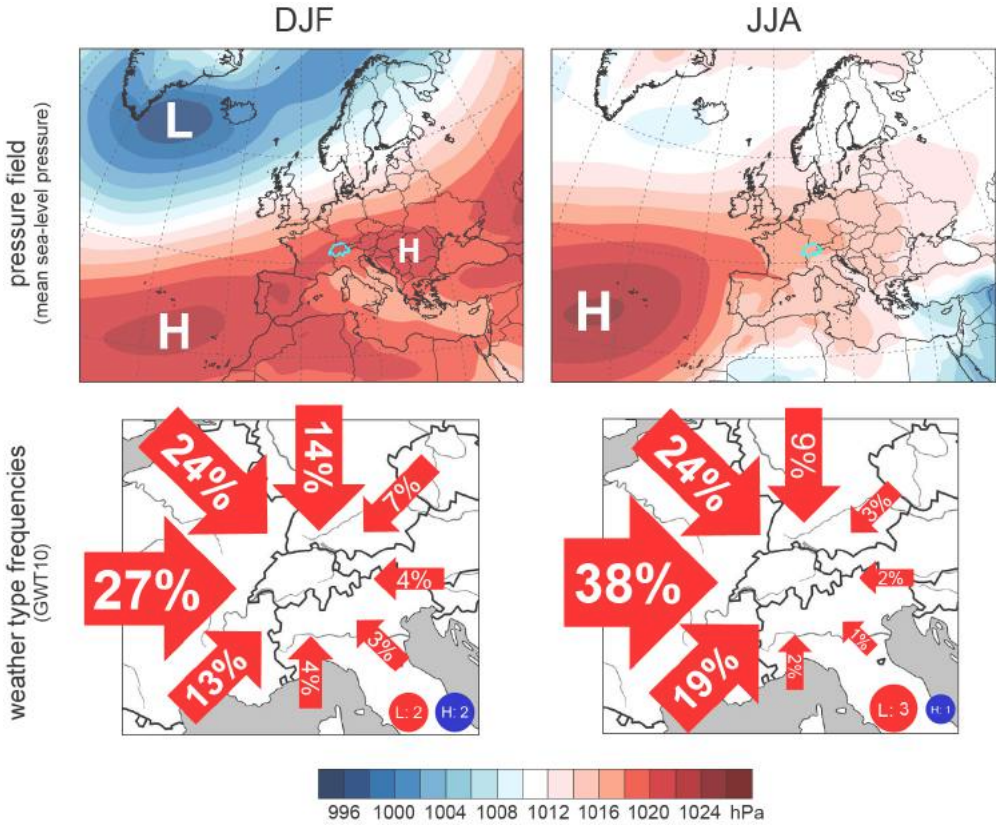

Figure 3.1. Seasonal mean sea-level pressure (hPa) over Europe (top) and the portion of incident flow (bottom) expressed as the percentage share of the ten GWT10 Z500 weather types over Switzerland for winter (left, December to February) and summer (right, June to August). The GWT10 Z500 types represent flow from the N: north, NE: north-east, E: east, SE: south-east, S: south, SW: southwest, W: west, NW: northwest, and L: low pressure, H: high pressure. The period considered is 1981 - 2010. The Swiss borders are shown in light blue in the top panels.

The day-to-day variability of sea-level pressure is large, and the distribution is negatively skewed (long left tail) in winter (standard deviation ~10 hPa, Figure 3.2). The small values are caused by low-pressure systems impinging upon the Alps. In summer, the variability is much smaller (~4 hPa), and the distribution is highly symmetrical (Figure 3.2). In summary, the difference between the winter and summer pressure distributions nicely illustrates the strong seasonality typical of a mid-latitude climate.

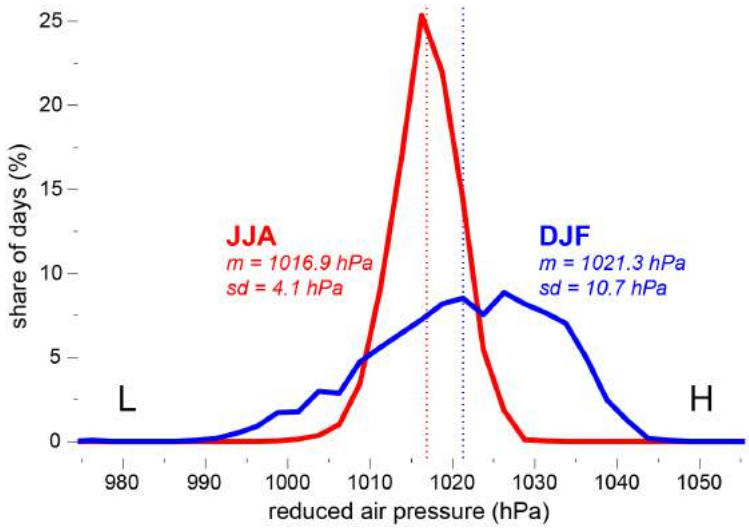

Figure 3.2. Distributions of the daily reduced sea-level air pressure at the Zurich/Fluntern station for winter (December to February, blue) and summer (June to August, red). The mean pressure (m, dotted vertical lines and numbers) is higher and the pressure is much more variable (standard deviation sd, numbers) in winter compared to summer. The values have been binned into 2.5 hPa bins to compute the share of days per bin. L stands for "low pressure", H for "high pressure".

On the monthly and seasonal scale, the effect of weather systems is usually expressed by the dominant modes of flow variability using pressure fields (e.g., [364, 14]). The most prominent mode in the Euro-Atlantic region is the North Atlantic Oscillation (NAO), which explains about one-third of the variance in sea-level pressure in winter [363, 161, 368] and also substantial fractions of temperature and precipitation variability. Other common modes explaining considerable amounts of temperature and precipitation variability (e.g., [51]) are the East Atlantic (EA) pattern, the East Atlantic/Western Russia (EAWR) pattern (sometimes also called the Eurasia-2 pattern), and the Scandinavian (SCAN) pattern (also called the Eurasia-1 pattern) [14].

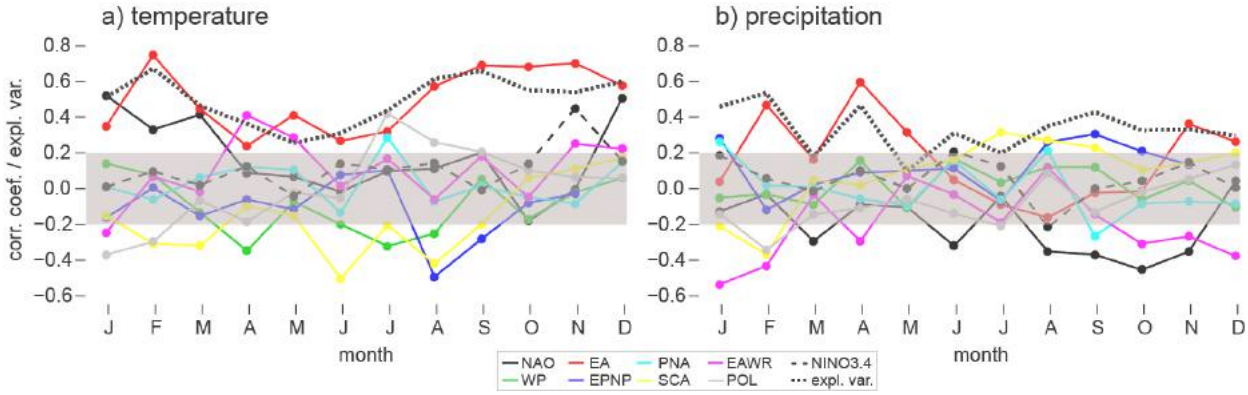

Figure 3.3. Influence of the eight major modes of climate variability of the Northern Hemisphere and the El Niño Southern Oscillation (ENSO, shown as NINO3.4 index) on Swiss temperature and precipitation variability for the time period 1950 - 2017. Shown is the Pearson correlation of the corresponding mode with northern Swiss temperature (a) and precipitation (b). The dashed bold black lines indicate the fraction of the variance explained by a stepwise linear regression model using the eight major climate modes of the Northern Hemisphere plus ENSO as the explaining time series. The grey band shows the range of insignificant correlations (p=0.05). The monthly climate mode indices used here are produced by the Climate Prediction Center of NCEP/NOAA (ftp.cpc.ncep.noaa.gov/wd52dg/data/indices/). NAO: North Atlantic Oscillation, EA: East Atlantic Pattern, PNA: Pacific/North American pattern, EAWR: East Atlantic/West Russia pattern, WP: West Pacific pattern, EPNP: East Pacific/North Pacific pattern, SCA: Scandinavian pattern, POL: Polar/Eurasia pattern.

Figure 3.3 gives an overview of the influence of the major modes of climate variability on Swiss temperature and precipitation variability. The EA-like pattern (red line) has a substantially larger influence on the interannual Swiss temperature variability than the NAO (black line; cf. [294]). The influence of the NAO is somewhat more pronounced at higher altitudes and in southern Switzerland, especially in winter (not shown). For winter and spring precipitation, the blocking-like EAWR (purple line) and EA (red line) patterns explain substantial fractions of interannual variability. The eight major climate modes of the

Northern Hemisphere explain about 50 - 70 % of interannual Swiss winter temperature variability and 30 - 55 % of interannual Swiss winter precipitation variability (dashed red lines in Figure 3.3). The direct influence of the most dominant global climate mode, the El Niño Southern Oscillation (ENSO, shown as Nino3.4 index, dashed black line), on Switzerland is generally small. Some studies have hypothesized a more significant impact of the ENSO on Europe in the past (e.g., [119, 43]).

In summer (JJA), the pressure gradients are much smaller than in winter, and the Azores high is the dominant large-scale pressure system, leading to reduced variability over Switzerland (cf. Figure 3.1). The flow is still dominated by advection from westerly directions and from the north, but the influence of modes of flow variability is reduced. Consequently, local processes and feedbacks become important, as the following section explains.

3.1.3. Effects of the Alps

The Alps with their complex topography considerably influence the Swiss weather and climate (see [304] for an overview). The synoptic systems impinging upon the Alps are strongly modified, leading to effects often associated with severe weather such as frontal bending and lee cyclogenesis south of the Alps. Regional wind systems and gravity waves are triggered. The two most well-known regional wind systems are the Föhn (e.g., [329]), which is a flow crossing the main ridge, and the Bise [366], an example of deflected flow. Other examples of deflected flow in the greater Alpine region are the Mistral [259] and the Bora [327, 137]. Several smaller-scale features such as thermally driven circulation (mountain-valley flow; e.g., [247]), lee waves, and deep convective clouds are also common.

The interplay between the flow and the complex topography leads to spatially highly variable meteorological fields. This is especially the case for precipitation, where factors such as orographic enhancement, rain shadow effects, and enhanced convective activity modify the precipitation field. Due to low temperatures, a substantial amount of precipitation falls as snow, especially at higher altitudes that feature glaciers and permafrost (e.g., [160]). Favored by cold-air pooling, fog and low stratus are often found in the pre-Alpine basins in the winter half year.

3.1.4. Local feedback processes

Especially in summer, when large-scale pressure gradients are small (cf. Figure 3.1), local feedbacks can generate small-scale climate variability and extreme weather events. An important feedback in this respect is the soil moisture-temperature feedback. This is known to be a strong driver of temperature extremes in many regions across the globe with a transition climate (i.e., between humid and arid) and could strongly affect future temperature extremes in Europe and Switzerland as well (cf. [313, 111, 315, 156, 239] and Chapter 6.7 for more details). Another feedback coming into play in spring and summer, especially at higher altitudes, is the snow-albedo feedback, which can modify spring temperatures at the snowline by a few tenths of a degree [293, 384].

3.2. Reference climate

This section introduces the Swiss reference climate, which has already been influenced by climate change. The climate-change signal is discussed in detail in Chapter 3.3. The reference climate is the same as or as similar as possible to the mean reference state of the CH2018 scenarios (the 30-year reference period 1981 - 2010; cf. Chapter 2.3). The variables of near-surface (2-meter) temperature, mean, heavy, and extreme precipitation, snowpack, and wind are considered in detail. For other variables, additional resources are provided. The observational network density available is different for each variable, but is generally very dense compared to most other mountainous regions in the world (cf. Chapter 2.6).

3.2.1. Temperature and heat stress

Switzerland spans an altitude range from 193 m a.s.l. to 4634 m a.s.l. Accordingly, the temperature range in Switzerland is large. The lowest temperature officially measured by MeteoSwiss in Switzerland was -42.5 °C in La Brévine (1048 m a.s.l.) on January 12, 1987; the highest temperature was +41.5 °C in Grono (382 m asl)

on August 11, 2003 (source: MeteoSwiss). Most regions on the Swiss Plateau have experienced absolute minima between -20 °C and -25 °C and absolute maxima between +35 °C and +40 °C in the reference period. Temperatures above 40 °C have only been recorded once in Switzerland thus far.

Figure 3.4 shows normal values (averages over the reference period) for the monthly mean of daily maximum, mean, and minimum temperature at four Swiss meteorological stations situated in four different climatic zones (southern Swiss lowlands at ~300 m a.s.l., Swiss Plateau at ~550 m a.s.l., eastern Swiss Alps at ~1600 m a.s.l., and central Alps at almost 3600 m a.s.l.). The temperature has a strong seasonal cycle, with minima in January or February and maxima in July. The seasonal cycle is somewhat less pronounced at the high-altitude stations than at the low-altitude stations. At higher altitudes (> ~2000 m a.s.l.), the monthly mean temperature minima (TN) are below 0 °C during most of the year. At very high altitudes (> 3500 m a.s.l.), the monthly mean temperature maxima (TX) rises above 0 °C only in the summer months (cf. Figure 3.5, bottom left). At low altitudes, in contrast, monthly mean temperatures ™ are close to 0 °C only in the coldest winter months (cf. Figure 3.5, top center), whereas in summer, monthly mean temperature maxima (TX) can reach almost 25 °C in northern Switzerland and even higher in southern Switzerland (Figure 3.5, bottom left).

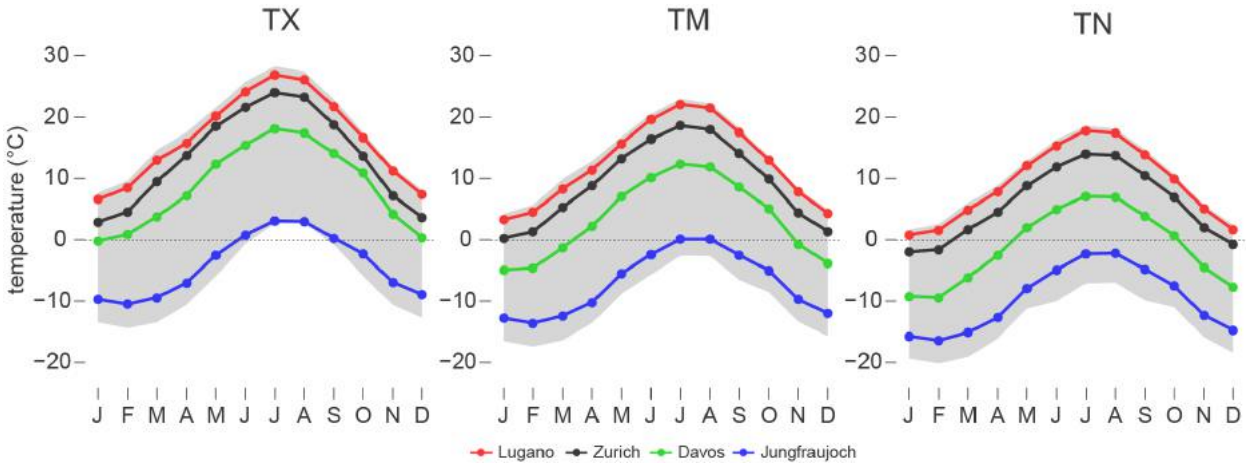

Figure 3.4. Monthly normal values (mean of period 1981 - 2010) for daily maximum (TX, left), mean (TM, center), and minimum (TN, right) temperature in °C at four Swiss stations: Lugano (red, 273 m a.s.l.), Zürich/Fluntern (black, 556 m a.s.l.), Davos (green, highest city in the Swiss Alps at 1594 m a.s.l.), and Jungfraujoch (blue, high mountain station at 3580 m a.s.l.). The grey band shows the range of all values in Switzerland using the MeteoSwiss gridded temperature products [123].

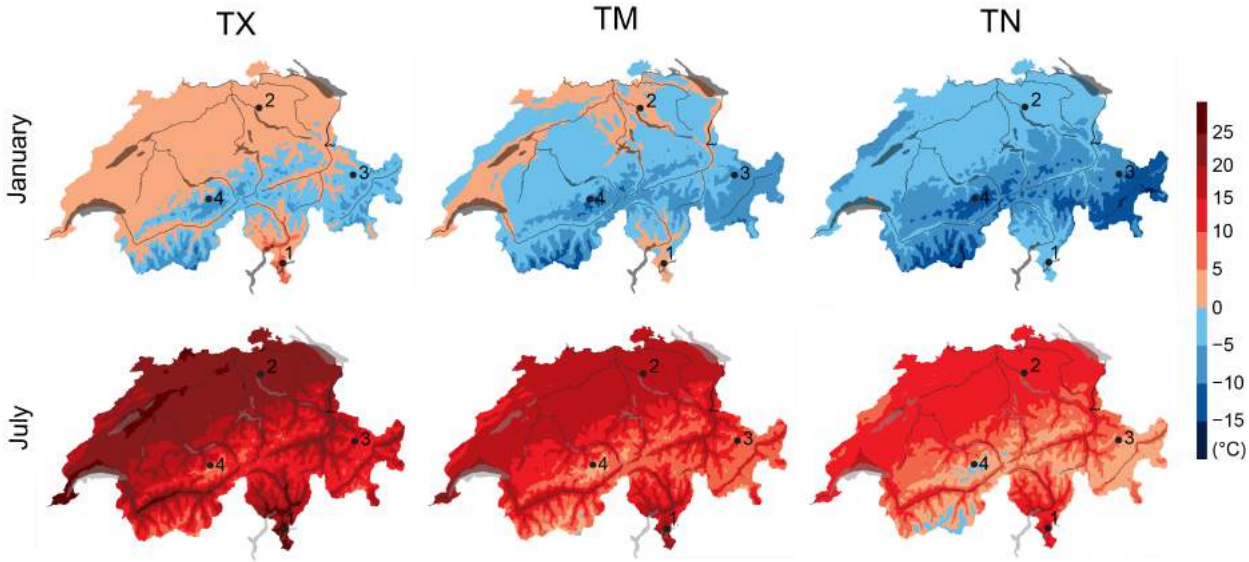

Figure 3.5. Maps of monthly normal values (mean of period 1981 - 2010) for maximum (TX, left column), mean (TM, middle column), and minimum (TN, right column) temperature in °C for January (top row) and July (bottom row). The dots and numbers show the locations of the four stations used in Figure 3.4: 1: Lugano, 2: Zürich/Fluntern, 3: Davos, and 4: Jungfraujoch. Data: MeteoSwiss gridded temperature products [123].

Very high temperatures during the night and day greatly affect human health and well-being. Heat exposure can raise the core body temperature and thus cause heat-related illnesses and impact productivity [188]. The effect of temperature on the human body is enhanced by the relative humidity. When the external temperature is high, the only way for the body to stay at a healthy temperature is through loss of heat via sweat evaporation. However, high external air humidity and certain clothing (e.g., protective clothing worn in certain jobs) limit sweat evaporation, forcing core body temperature to rise [348]. Under such circumstances, the combination of external heat exposure and internal heat production generated from metabolic processes can provoke heat stress [386]. There are many heat stress indices in the literature that attempt to quantify heat stress in a single value (see [28, 63] for a review). In this report, the Wet Bulb Temperature (TW) has been selected to describe heat stress conditions [321, 74, 253]. TW is the temperature an air parcel would attain if cooled at constant pressure until saturation by the evaporation of water into it; it equals the air (dry bulb) temperature when relative humidity is 100 %. TW can be measured by covering a standard thermometer bulb with a wet cloth and fully ventilating it. In contrast to more sophisticated heat stress indices, such as the Wet Bulb Globe Temperature [204] or the Universal Thermal Climate Index [201], TW can be easily derived from temperature and humidity by means of thermodynamic equations [72] or, as in this report, by the empirical formula derived in [333]. The highest TW values recorded on Earth are close to 35 °C, which is considered the limit of survivability for a fit human being [321, 253]. This value would greatly reduce the possibility of evaporation at skin level to cool the body, since the skin (usually at 35 °C or below) must be cooler than the body core (around 37 °C) in order for metabolic heat to be conducted to it. In this report, three heat-stress-derived indices are considered (based on daily maximum values of TW): summer mean and maximum TW, and the number of summer days with TW above 22 °C. This threshold is chosen to account for intense heat stress, as it approximately corresponds to the observed summer 98th percentile of TW in Zurich and Geneva and the 92nd percentile in Lugano in the reference period.

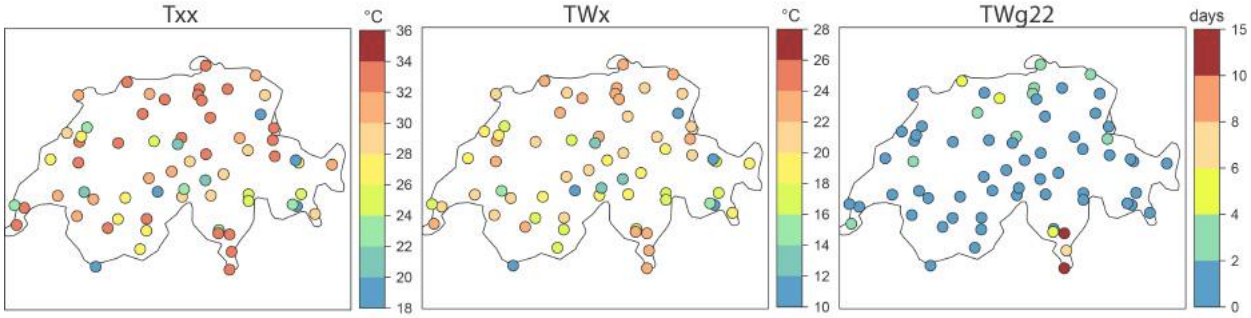

Figure 3.6. Observed values at 67 Swiss stations for the mean annual maximum temperature (TXx) and wet bulb temperature (TWx), both in °C, and the number of days with TW above 22 °C (TWg22) in summer (JJA) for the period 1981 - 2010.

Unlike the highest daily maximum temperature per year (*TXx*), which shows a markedly orographic spatial pattern, the highest daily heat stress (*TWx*) is between 18 °C and 24 °C at most of the non-mountainous stations (Figure 3.6). The threshold of 22 °C is, on average, only exceeded in a few locations, with the largest values in the low-lying stations in Ticino (7 days in Lugano and 12 in Magadino/Cadenazzo and Stabio). Unlike temperature, no gridded product is available for the heat stress indices at the moment, due to the lack of gridded specific humidity.

3.2.2. Precipitation

Although landlocked, Switzerland is still fairly close to the Atlantic Ocean and the Mediterranean Sea, which are important sources of humidity. Nevertheless, a transition from an oceanic (wet) climate in the western parts of the country to a more continental (dry) climate in the eastern parts can be observed within Switzerland. In addition, the complex Alpine topography leads to a large spatial variability in precipitation [125, 302, 173]. The annual precipitation sums vary by a factor of about five, from less than 600 mm in certain valleys in Valais in southwestern Switzerland to more than 3000 mm annually at some high-altitude regions of the central Swiss Alps. There are considerable differences in the annual cycles of precipitation sums in the different climatic regions, as illustrated by the histograms in Figure 3.7. The western Jura

mountains and western Plateau regions exhibit almost no annual cycle. Most other regions show a summer maximum, which is more pronounced in the eastern parts of the country. There, summer amounts of precipitation are larger by a factor of two or three compared to winter amounts. In the southern Alps, two maxima in spring and autumn are observed. All these characteristics are well explained by the dominant flow regimes (cf. Chapter 3.1) and convection activity in summer [173].

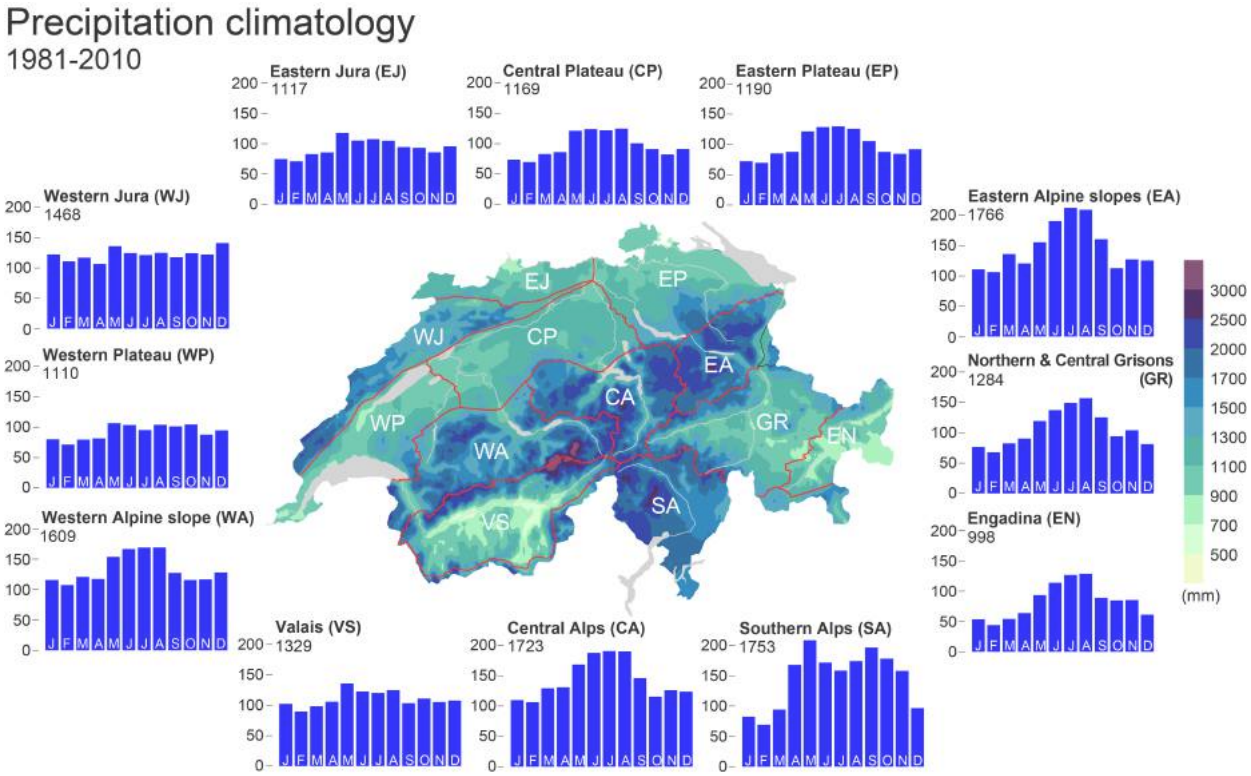

Figure 3.7. Gridded annual mean precipitation and monthly sums for the twelve Swiss climate regions after [227]. Regional annual means based on the gridded data are shown in the upper left corner of each barplot. Units: mm. Time period: 1981 - 2010. Data: MeteoSwiss gridded precipitation product RhiresM (see here for details).

To illustrate heavy and extreme precipitation in Switzerland, the 50-year return levels of 5-day, 1-day, 1-hour, and 10-minute precipitation are presented (cf. Figure 3.8; for technical details, see [129]). Note that the values shown on the maps have considerable uncertainty (often ±10 - 30 % or more for the 95 % confidence interval for a 1-day precipitation event for a 1-day precipitation event; cf. climate-extremes.ch for details). The most extreme precipitation events occur in Ticino on the southern side of the Alps, regardless of the duration of rainfall accumulation. In contrast, the inner-Alpine valley floors, especially the Rhone and Inn valleys, experience the most moderate heavy precipitation events within Switzerland. North of the Rhone and Rhine valleys, the spatial distribution of heavy precipitation varies with the duration of rainfall accumulation considered. For accumulations longer than a day, the northern Alpine rim and the Jura mountains experience heavier precipitation than the Plateau, whereas for sub-daily precipitation extremes, heavy precipitation generally does not seem to depend on altitude.

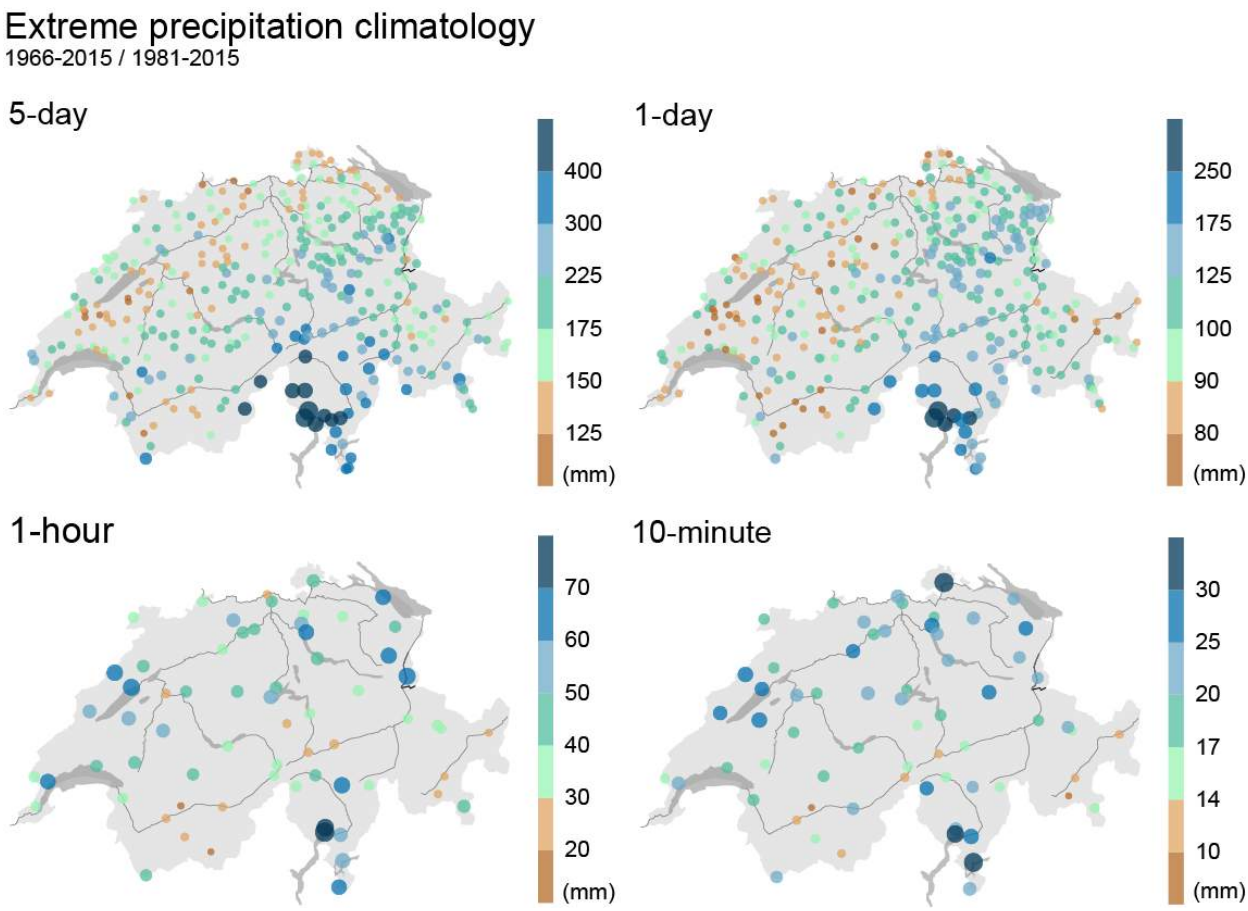

Figure 3.8. 50-year return values of 5-day (top left), 1-day (top right), 1-hour (bottom left), and 10-minute (bottom right) precipitation sums (in mm). Note that the color scale is different for each panel. The size of the circles is proportional to the return value and shows the same information as the color scale. The analysis period considered is 1966 - 2015 for the 1-day and 5-day sums and 1981 - 2015 for the 10-minute and 1-hour sums.

Another pertinent question is in which season the maxima occur and what processes lead to extreme events. For the 10-minute and 1-hour durations, the most extreme precipitation events in a year are generally associated with thunderstorms and, all over Switzerland, occur mostly in the summer months (source: MeteoSwiss). In contrast, the 1-day and 5-day durations exhibit more complex patterns (cf. [347] and MeteoSwiss). In summer, a high frequency of heavy 1-day and 5-day precipitation events along the northern Alpine rim and on the Plateau coincides with the tracks of thunderstorms, as revealed by the lightning climatology (see MeteoSwiss Website). In autumn, the high proportion of heavy precipitation events in Ticino reflects frequent situations in which a southerly flow of humid Mediterranean air impinges on the southern flank of the Alps. Interestingly, a considerable proportion of annual maxima occurs in winter in the Rhone valley and along the eastern flank of the Jura mountains.

> Much more information on Swiss precipitation extremes including a thorough assessment of their uncertainties can be found on the website climate-extremes.ch.

3.2.3. Snow

Due to the geographical location and the Alpine topography of Switzerland, a substantial fraction of precipitation falls as snow, and the water is stored for some time before it is released as meltwater. In CH2018, the analysis is restricted to basic features of snowfall and snow cover. Snow variables related to runoff, etc., are addressed in detail in the upcoming Hydro-CH2018 report.

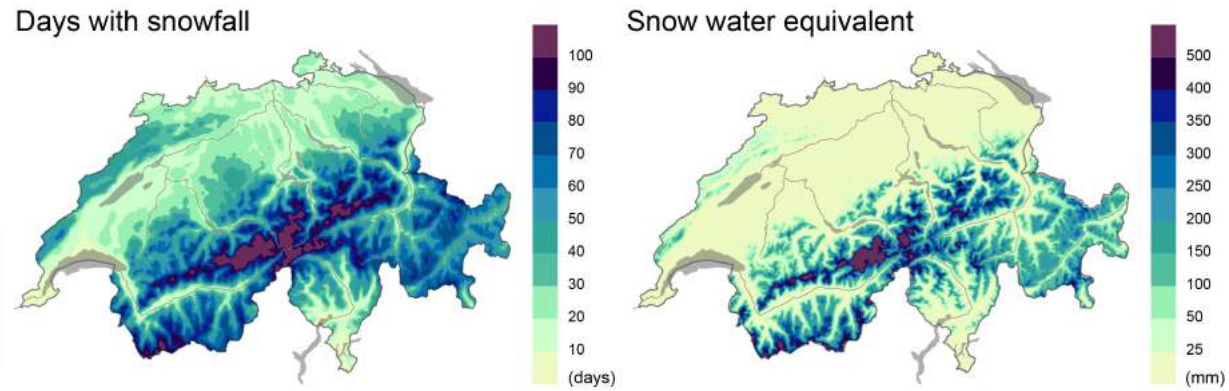

Figure 3.9. 1981 - 2010 snow climatology for the extended winter season (September - May). Left: Mean number of days with measurable snowfall based on [398] (days with new snow sum ≥ 1 cm). Right: Mean snow water equivalent (in mm, courtesy of T. Jonas, WSL).

The number of days with measurable snowfall strongly depends on altitude, with more days at higher altitudes (Figure 3.9). On the Swiss Plateau, roughly 10 to 30 days with snowfall are found in the September to May period. In the Alpine region, this number is higher, ranging between 30 and 120 days in most regions. In southern Switzerland, in the Rhone valley, and in the Lake Geneva region, the mean number of days with snowfall is less than 10. In terms of the mean snow water equivalent (SWE) [207], only a few millimeters of snow water are recorded on the Swiss Plateau and other low-altitude regions. In contrast, SWE values in the Alps are between 100 mm and 300 mm, with the highest values (up to 600 mm) in the Bernese and central Alps (Gotthard region).

3.2.4. Wind

Winds in Switzerland are forced by the large-scale flow patterns but are strongly altered by the country's complex topography and therefore exhibit considerable spatial variation (cf. Figure 3.10, left). Monthly mean wind data from MeteoSwiss has been homogenized for climate analysis (cf. [22]). The observed annual mean wind speed in the reference period (1981 - 2010) ranges between 0.93 m s^{-1} (Disentis) and 8.57 m s^{-1} (Chasseral). The highest mean wind speed is observed over the Jura mountain peaks, followed by the Alpine mountains with slightly lower values. The lowest mean wind speed is measured in the lowlands of the Swiss Plateau, Ticino, and some inner-Alpine valleys. Most stations in northern Switzerland and on mountain peaks experience the strongest mean winds during wintertime. In the southern Alps, Ticino, and many Alpine valleys, the maximum occurs in spring, in some inner-Alpine valleys, in summer (cf. also [135]).

The strong wind gusts (98th percentile of daily maximum wind speed) range between 13.5 m s^{-1} (Disentis) and 43.9 m s^{-1} (Jungfraujoch; cf. Figure 3.10, right). Note that the uncertainty of wind-gust measurements is considerable, especially for the high percentiles presented here. Furthermore, the exact location and exposition of the measurement station plays a considerable role, complicating the spatial interpretation of strong wind gusts. The strongest gusts generally occur on high Alpine mountain peaks (up to 44 m s^{-1}), on the Jura mountain crests (up to 36 m s^{-1}), and, albeit weaker gusts, in typical Föhn valleys (up to 29 m s^{-1}). The weakest gusts, at around 15 m s^{-1}, are observed in some inner-Alpine valleys and the lowlands of Ticino.

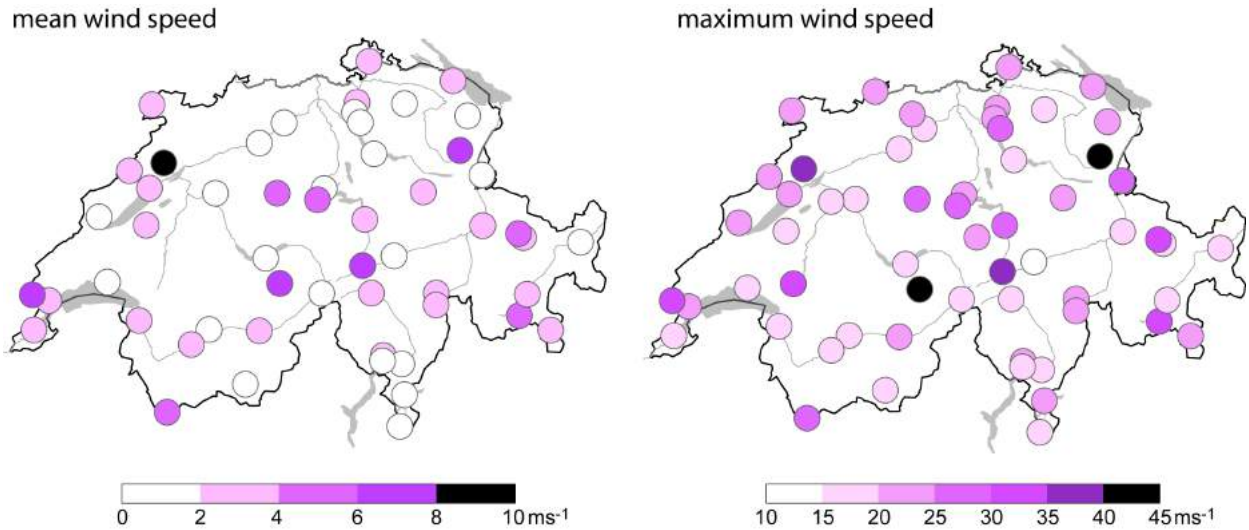

Figure 3.10. Mean wind speed (left) based on homogeneous data, and daily maximum wind speed (98th percentile, right) based on original data. Values are in m s^{-1} and are shown for the 1981 - 2010 reference period.

An analysis of the quality-checked strongest wind gusts since 1981 shows that the top-10 gusts in Switzerland are produced by a variety of wind types (cf. Figure 3.11). Winter storms are the most important causes, especially in northern Switzerland. In most regions, seven or more of the ten strongest events are caused by winter storms. In the northwestern parts of Switzerland, as many as all top-10 events are caused by winter storms. The main wind direction of winter storms is west or west-southwest. Wind gusts related to thunderstorms are in the top 10 at certain stations, mostly along the northern Alpine slopes, in the inner-Alpine valleys, and in southern Switzerland. North of the Alps and in inner-Alpine areas, the general wind direction of thunderstorm-related gusts is west, whereas in southern Switzerland, gusts show no preferred wind direction. In major Alpine valleys, most of the top-10 wind gusts are caused by the Föhn. Here, the wind direction is strongly affected by the orientation of the valley. In the Lake Geneva region, the Bise (from north-easterly directions) [366] is also be responsible for some top-10 wind gusts.

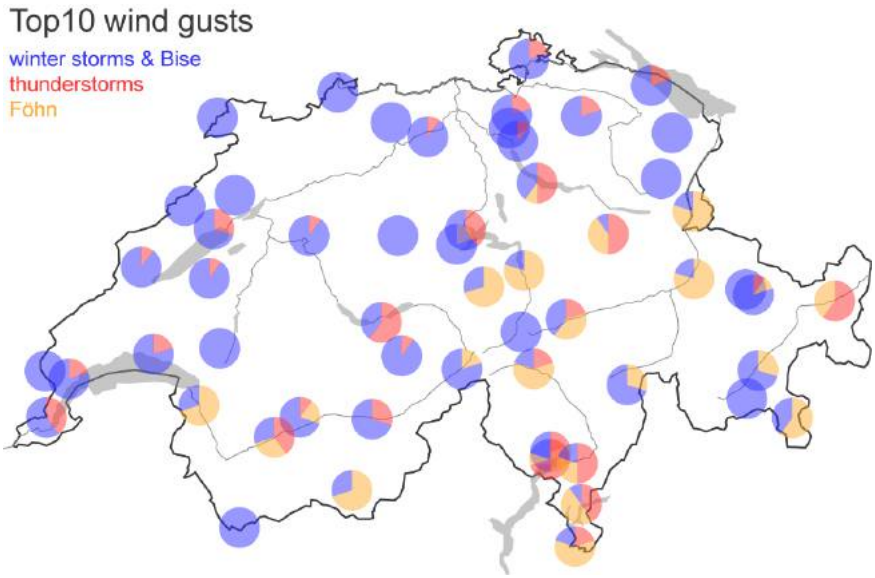

Figure 3.11. Classification of the top-10 wind-gust events at Swiss wind stations in the 1981 - 2017 period into "winter storms and Bise" (blue), "thunderstorms" (red), and "Föhn" (yellow).

For more information on the reference climate 1981 - 2010 (more parameters, gridded datasets, climate sheets at stations, climate indices, etc.) please visit the MeteoSwiss website meteoswiss.ch. For snow, also consult the website of the WSL Institute for Snow and Avalanche Research SLF (slf.ch).

3.3. Observed variability and recent change

3.3.1. Introduction

Possibly the most informative way to analyze the climate and especially its change over time is to examine the observed climate evolution. We restrict most of our analysis to the instrumental record covering the last 150 years, as this is the period in which the anthropogenic influence on the global climate became increasingly important. For summer temperatures and winter storms, reliable reconstructions based on documentary evidence and climate proxies going back to the year 1685 are used. For all other variables, the data source is high-quality observational climate data from the Swiss meteorological network, which was established in the year 1864. These long time frames, more than 150 years of measurements and more than 300 years for some reconstructions, are crucial for the correct identification of natural and anthropogenically forced changes in the climate system and the assessment of how strong the projected future changes will be. In the following sections, the variability and trends since the start of measurements/reconstructions are discussed. Extreme indices and their change signals are then presented. For a discussion of detection and attribution, the reader is referred to Chapter 7. For most analyses in this section, the period 1961 to 1990 is used as a reference period. This period, which should not be confused with the reference period 1981 to 2010 for climate projections, is still the valid standard normal period used by WMO and is often utilized for analyses related to climate change.

3.3.2. Temperature

Near-surface air temperatures in Switzerland exhibit large interannual to decadal variability. However, there is a pronounced long-term trend in the temperature data of almost 2.0 °C of warming between 1864 and 2016, or ~1.3 °C per 100 years using a linear trend estimate (Figure 3.12). The largest increases have occurred since the late 1980s. This trend has been discussed in many studies (e.g., [21, 274, 9, 55]). Warming in Switzerland amounts to more than twice the global warming rate of 0.9°C in the same time period (Figure 3.12). It is also greater than the warming of the Northern Hemisphere's land regions, which is about 1.3°C, and is on the upper end of the warming rates over the European domain based on global observational datasets like CRUTEM4, GHCNv3, GISSTEMP, and BEST [237, 145, 202, 280]. Nine of the ten warmest years since measurements began in 1864 have been recorded in the 21st century (cf. Figure 3.13). There has been no year with temperatures below the 1961 - 1990 mean in the last 30 years, and the annual temperature anomalies with respect to the period 1961 - 1990 are largely similar all across the country. Note that due to the strong recent trends, the 1981 - 2010 mean is about 0.8 °C higher than the 1961 - 1990 mean (cf. the different axis in Figure 3.12).

The long-term temperature trends show pronounced differences between regions and elevations on the seasonal scale ([21], and F. Isotta, 2018, personal communication). The Swiss Plateau warmed more than the Alpine regions in winter, but the opposite effect is found for summer. In spring and autumn, the warming is regionally more homogeneous. For most regions, the warming is somewhat stronger in autumn than in spring. It is not yet clear whether these differences are related to climate change, as has been proposed for some mountain regions in the world (e.g., [258]), or whether they are primarily caused by internal variability [55, 9]. On shorter timescales (a few decades), some signals of elevation-dependent temperature trends have been identified – for example, a strong cooling of high-altitude winters. These can be explained by natural variability producing unusual atmospheric flow conditions (cf. [10, 290] and Chapter 7). Slightly stronger temperature trends have also been identified near the snow line in spring, pointing to a small effect of the snow-albedo feedback (cf. [55, 299]).

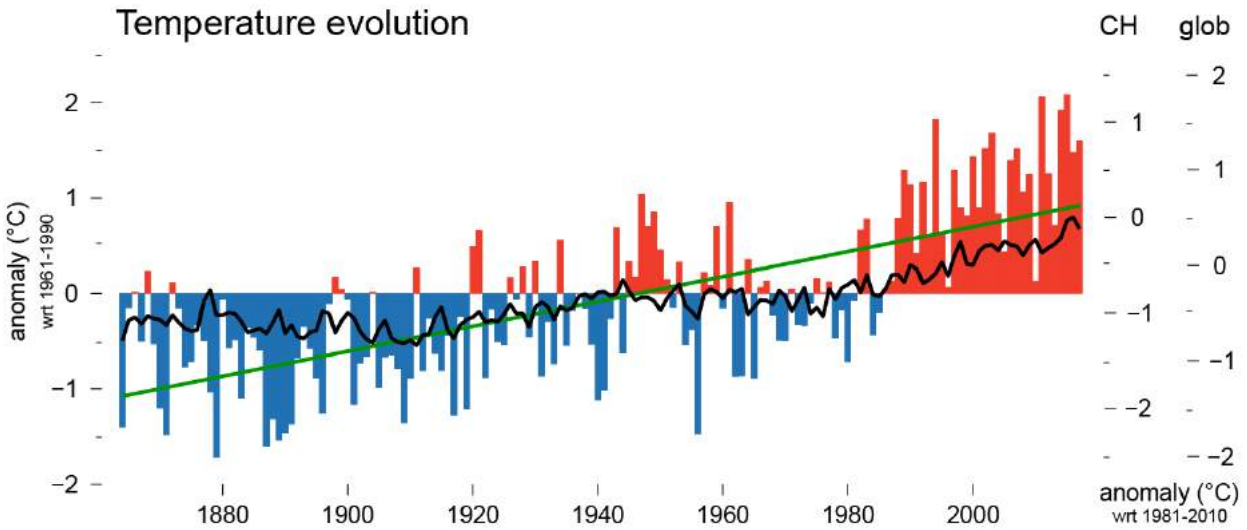

Figure 3.12. Evolution of Swiss and global annual mean temperatures, shown as deviation from the means for 1961 - 1990 (left axis) and 1981 - 2010 (right axes, left: Swiss series (CH) and right: global (glob)), the time frame used as reference period for the climate scenarios. The Swiss mean values (computed after [20]) are shown as bars with values above the 1961 - 1990 mean in red and values below the 1961 - 1990 mean in blue. The global values stem from the HadCRUT dataset (version 4.6.0.0, [237]) and are shown as a black line. The linear trend fit to the Swiss values is shown in green. Units: °C.

The observed Swiss temperature trend reflects an anthropogenic climate-change signal that is strongly modified by natural variability. The influence of natural variability is hard to quantify on regional and local levels (cf. Chapter 7 for more details). It is therefore important to note that the recent temperature increases can not be simply extrapolated into the future.

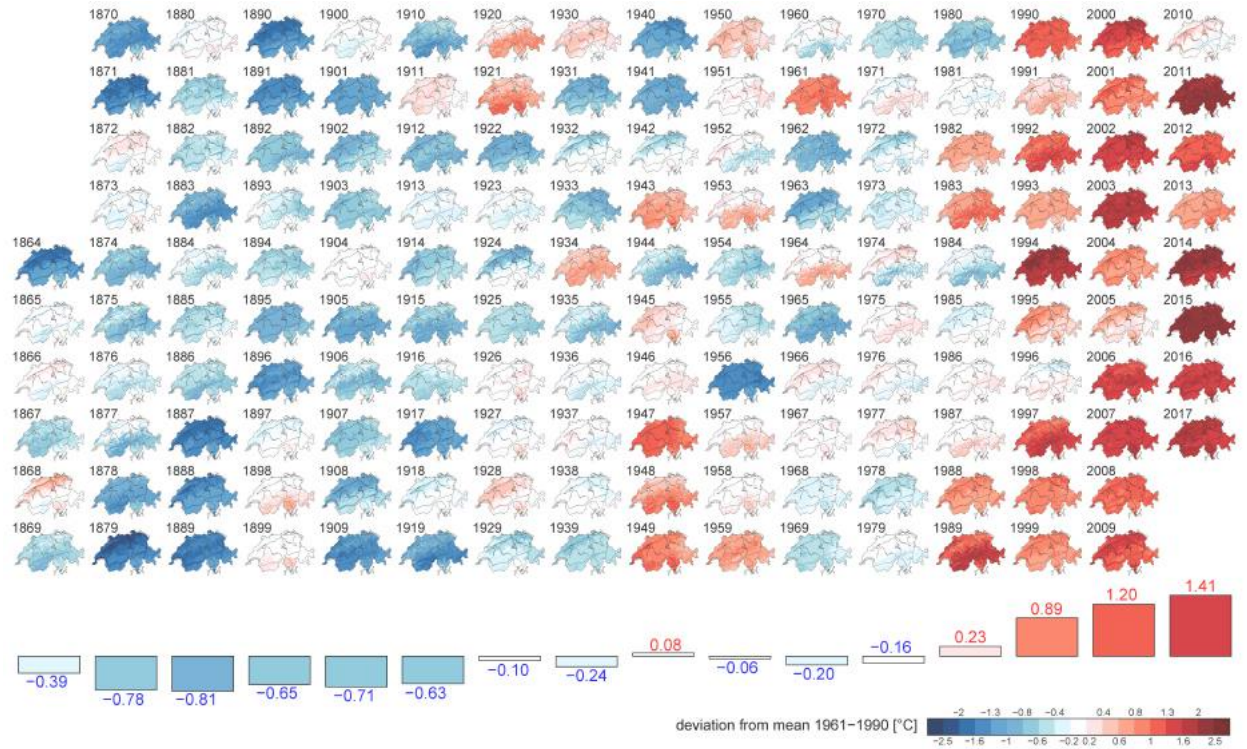

Figure 3.13. Maps of temperature deviation (in °C) from the mean for 1961 - 1990 for each year from 1864 until 2017 and decadal means for Switzerland (bars and numbers in the lower part). Years/decades above the mean are shown in red; years below the mean are shown in blue. Scale: -2.5 °C to 2.5 °C. Gridding method after [123], reconstruction by Isotta and Frei (in preparation).

There have also been significant changes in temperature extremes in the period 1864 - 2016. The coldest day, week, and two-week period warmed by +3.2 °C to 3.6 °C; this is considerably more than the increase for the warmest day, week, and two-week period, which (only) warmed by between +1.2 °C and 1.4 °C (cf. the slopes in the left and right panels of Figure 3.14). A possible reason for the smaller increases in the

temperature maxima is the declining sunshine duration and global radiation until about 1980 (see Chapter 3.3.6 for details). Not only the trend but also the variability in the cold extremes is considerably larger than that of the hot extremes. Very intense cold spells have been registered in 1929, 1956, 1963, 1985, and 1987. The trends in hot extremes for the period 1864 - 2016 reported here are somewhat lower than those in [298] for the the period 1901 - 2015. The frequency of hot periods has also changed significantly; notably, the rarer the event, the stronger the increase. [298] concluded that the number of days exceeding the 90th percentile of the 1961 - 1990 period increased by 94 % between 1901 and 2015 – and those exceeding the 95th and 99th percentile increased by 138 % and 212 %, respectively, in the same period – consistent with the findings of [77].

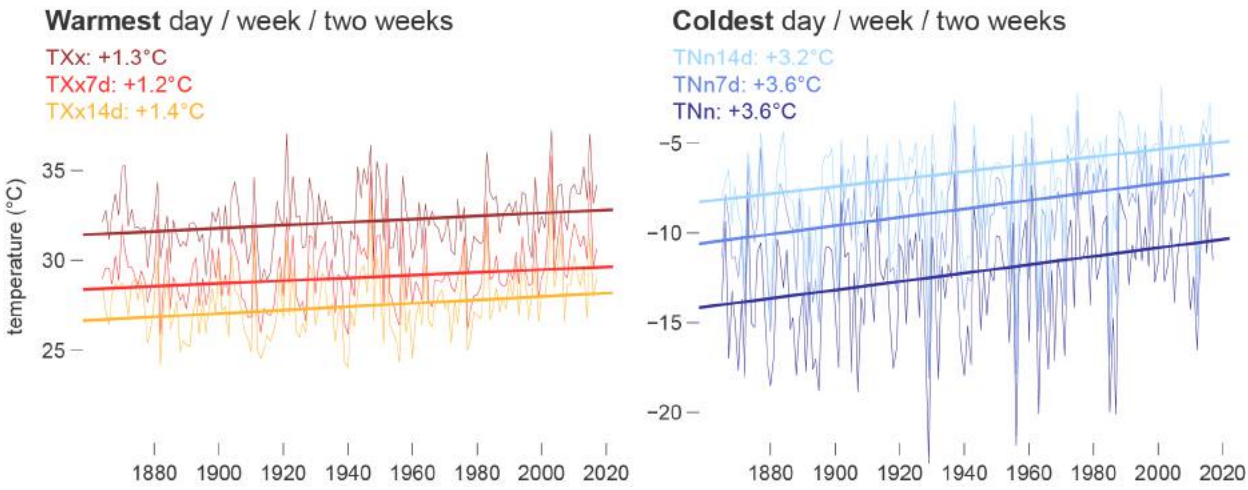

Figure 3.14. Time series of the warmest day (TXx, dark red), warmest week (TXx7d, red), and warmest 2-week period (TXx14d, orange) in the left panel and of the coldest day (TNn, dark blue), coldest week (TNn7, medium blue), and coldest 2-week period (TNn14d, light blue) in the right panel. Shown are the evolution of annual values (thin lines), a 20-year Gaussian smoother (bold line), the Theil-Sen linear trends (cf. [388], dashed lines), and the trend numbers (since 1864, in °C) on the Swiss Plateau (four-station mean for Zürich/Fluntern, Basel/Binningen, Bern/Liebefeld, and Genève-Cointrin).

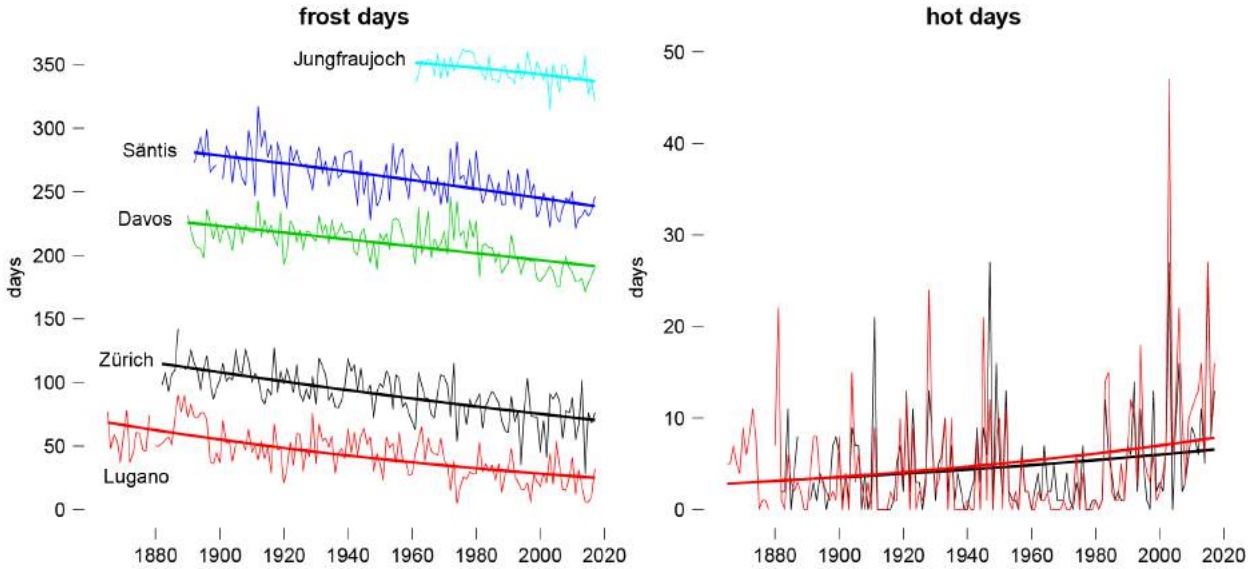

Figure 3.15. Evolution of the number of frost days (T_{min} < 0 °C, left) and the number of hot days (T_{max} ≥ 30 °C, right) for five Swiss stations (Lugano (red), Zürich (black), Davos (green), Säntis (dark blue), and Jungfraujoch (light blue)) since measurements began. The trend lines show fits using a logistic regression (e.g., [124]). Note that there have not yet been any hot days at the high-altitude stations of Davos, Säntis, and Jungfraujoch.

For practical purposes, threshold-based indices such as *frost days* (T_{min} < 0 °C) and *hot days* (T_{max} ≥ 30 °C) are often used (e.g., [392]). Figure 3.15 shows the changes in *frost days* (left) and *hot days* (right) since the measurements started in the 19th century. There is a distinct and highly significant decrease in the annual number of *frost days* at all altitude levels, with moderate changes of -5 % to -20 % since 1961 at high altitudes and the strongest declines, of the order of -60 %, at low altitudes (cf. also [231]). In contrast, strong

increases in the number of *hot days* are found. In the 1960s, only 1 to 3 *hot days* per year were observed in Zurich and Lugano, but these numbers have increased to about 10 days on average today.

Another intuitive temperature index is the altitude of the zero-degree line (degree Celsius), which can be defined using upper-air data or surface station data (cf. [36, 231]). This line has risen by 300 to 400 m or by roughly 150 to 200 m $°C^{-1}$ warming in the period from 1961 to today [231]. This change corresponds well to theoretical expectations based on an altitude shift in an atmosphere with a moist-adiabatic lapse rate of 0.5 °C to 0.67 °C per 100 m, which is very close to the current-day lapse rate in the Swiss Alps (cf. [200]). The long-term evolution of the zero-degree line in the winter season since 1864 shows a strong upward trend, but also substantial decadal variability (cf. Figure 3.16).

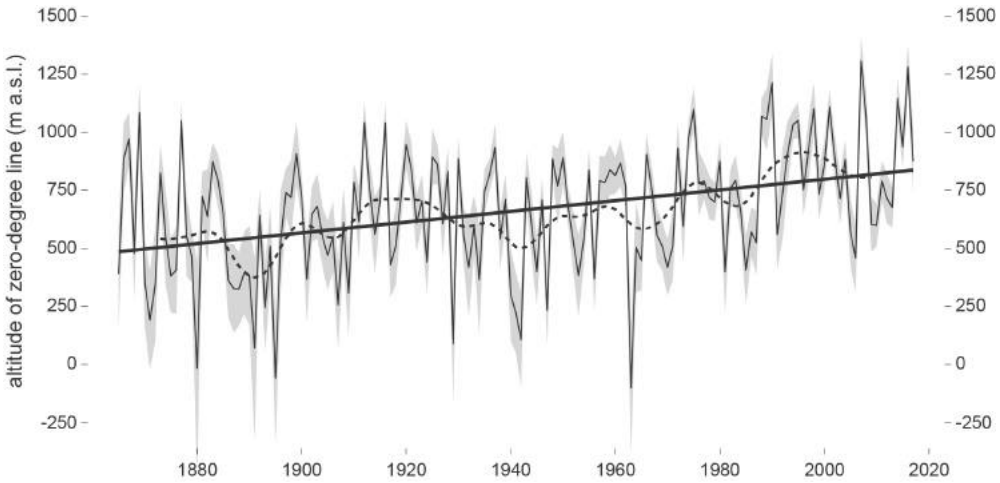

Figure 3.16. Evolution of the altitude of the winter (DJF) zero-degree line in Switzerland from 1864 to 2017 assessed from surface station temperatures (cf. [231] for methodological details). The black curve shows the best estimate; the grey range, the uncertainty of the value. The bold black line denotes the linear trend over the entire period, and the dotted line depicts the smoothed evolution using a 20-year Gaussian smoother.

Box 3.1: Summer temperature record since 1685

In addition to early instrumental measurements, which in Switzerland reach back to the mid-19 th century, summer (JJA) temperatures for the Swiss Plateau and the Alpine region have been reconstructed based on documentary evidence, tree rings, and other proxies [261, 53, 49]. The present assessment starts in 1685, in the middle of the Little Ice Age (LIA), a cold phase well described in the literature (e.g., [367]). For this period, various climate proxies agree relatively well, which is not always the case for earlier times.

The annual time series of summer mean (June to August) temperature from two different multi-proxy reconstructions using different techniques and focusing on different proxies (F, [121], and T, [345]) are shown together with the MeteoSwiss observational data (M, [20]) and the multi-station means of the Historical Instrumental climatological Surface Time series of the greater ALPine region (HISTALP, H, [48]) in Figure 3.17, a).

All series show a slight increase from the 17th to the mid-20th century, followed by a steep increase since the 1980s. Several particularly warm and cold summers stand out. The coldest summers occurred in the 1810s and include the “year without a summer” following the Tambora eruptions [268, 41]. The summers of 2003 and 2015 stand out as the warmest summers [306]. The summer 2018 not shown in Figure 3.17 ranked third and summer 2017 fourth. Since 1987, no individual summer has been colder than the 1961 - 1990 average. Summers were warmer around 1800 than in the decades before and after, particularly in the instrumental series (H). Possible instrumental biases (overheating of temperature screens, particularly in summer) have been discussed as a possible cause [120], but these have been taken into account in the dataset shown [48]. For a quantitative comparison to present climate reference periods (1961 - 1990 or 1981 - 2010), 30-year moving averages and confidence intervals are shown in Figure 3.17.

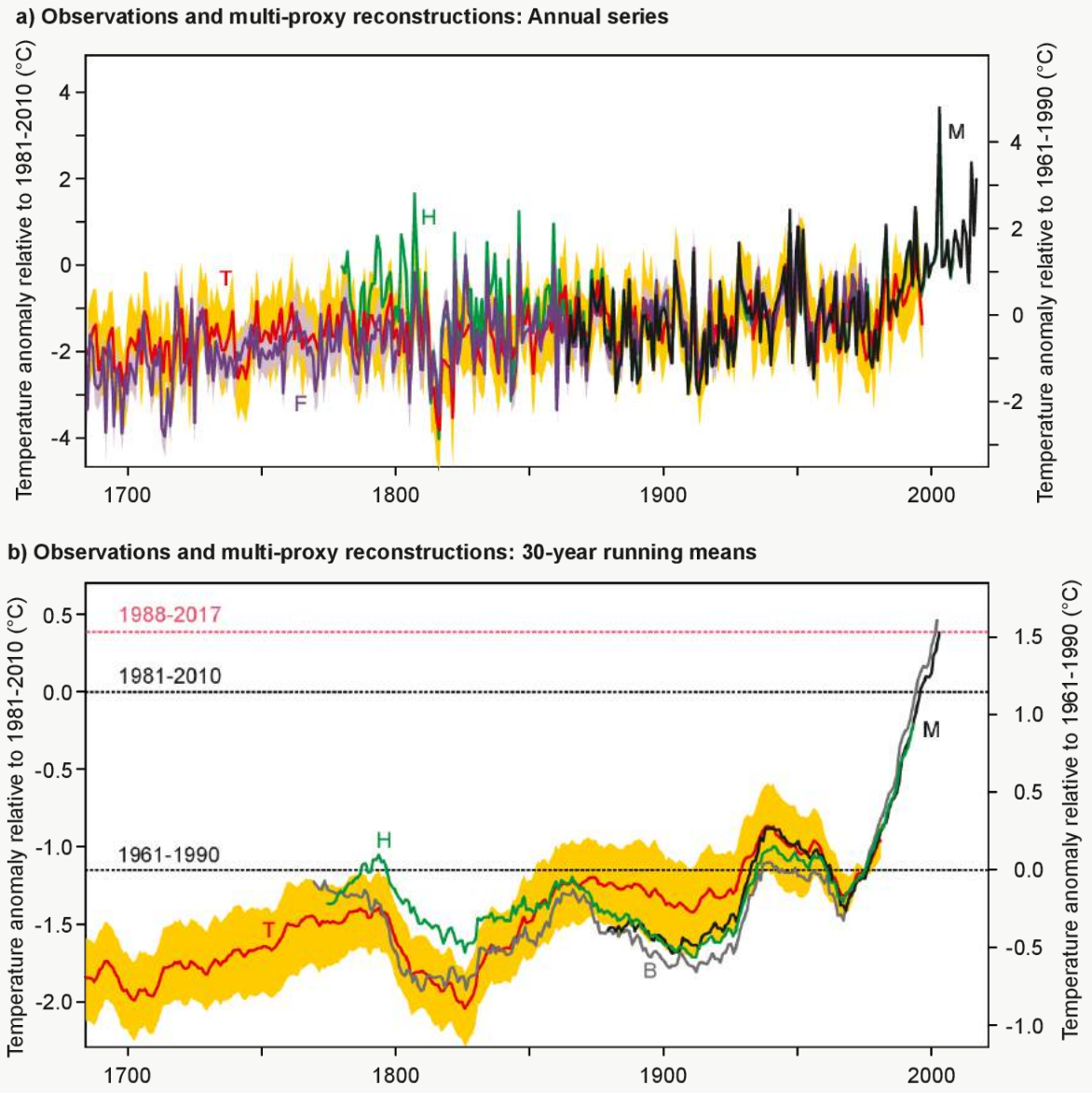

Figure 3.17. Time series of summer (JJA) temperature in the area of Switzerland/Alps. Top: Multi-proxy reconstructions by Trachsel et al. (2012) [345] (T, including 95 % confidence interval) and from a data assimilation by Franke et al. (2017) [121] (F, for the closest grid point up to 1975, ensemble mean, and range). Also shown are early instrumental measurements (H, HISTALP, [48] for the area 46° - 48°N/6° - 10°E) and the MeteoSwiss multi-station mean (M). Anomalies are indicated with respect to the 1981 - 2010 climatology (left axis) and the 1961 - 1990 climatology, which was used for calibration (the red dashed line indicates the most recent 30-year mean in M). Bottom: 30-year running means for the Trachsel et al. (2012) [345] reconstruction (T, red) with 95 % confidence interval (yellow), HISTALP (H, green), MeteoSwiss multi-station mean according to Begert and Frei (2018) [20] (M, black), and the series of Basel since 1755 (B, grey). The confidence interval for T accounts for the calibration of proxy data to an instrumental target; other uncertainties (e.g., associated with tree-ring measurements) are not accounted for.

The Trachsel et al. (2012) [345] summer temperatures are lower than the HISTALP temperatures between 1780 and 1830 (T, red in Figure 3.17, b), a period for which uncertainties in instrumental series are still high [48, 37, 178]. The coldest 30-year anomalies are found around 1700 during the so-called “Late Maunder Minimum”. During that time, summers were on average 0.8±0.3 °C colder than the 1961 - 1990 climatology or 2.2±0.3 °C colder than the most recent 30-year period (1987 - 2016). The figure further shows that the 1961 - 1990 average is unlikely to have ever been reached by any 30-year period during the LIA. Likewise, summer temperatures similar to those around 1980 (0.2 °C above 1961 - 1990) are unlikely to have been reached before the 1920s. The CH2018 reference period (1981 - 2010) is much warmer than the warmest period in the reconstruction. The recent 30-year period, 1988 - 2017, is 1.5 °C warmer than 1961 - 1990. In the longest Swiss instrumental series (from Basel), it is as much as 1.6 °C warmer than any 30-year period prior to 1961 - 1990.

3.3.3. Precipitation and drought

Due to the different precipitation regimes in Switzerland (cf. Figure 3.7), it is advisable to subdivide the trend analysis into different regions. Scherrer et al. (2016) [297] demonstrated that there are trend differences between the regions north and south of the main Alpine divide. Considerable and significant precipitation increases in the period from 1864 to the present day are only found in northern Switzerland (Swiss Plateau) for winter (~+20 % per 100 years, $p < 0.001$; Figure 3.18). In southern Switzerland, the trends are smaller and not significant (~+10 % per 100 years, p-value=0.20). In spring and autumn, no significant trends are found. In summer, trends are very close to zero (cf. [231]).

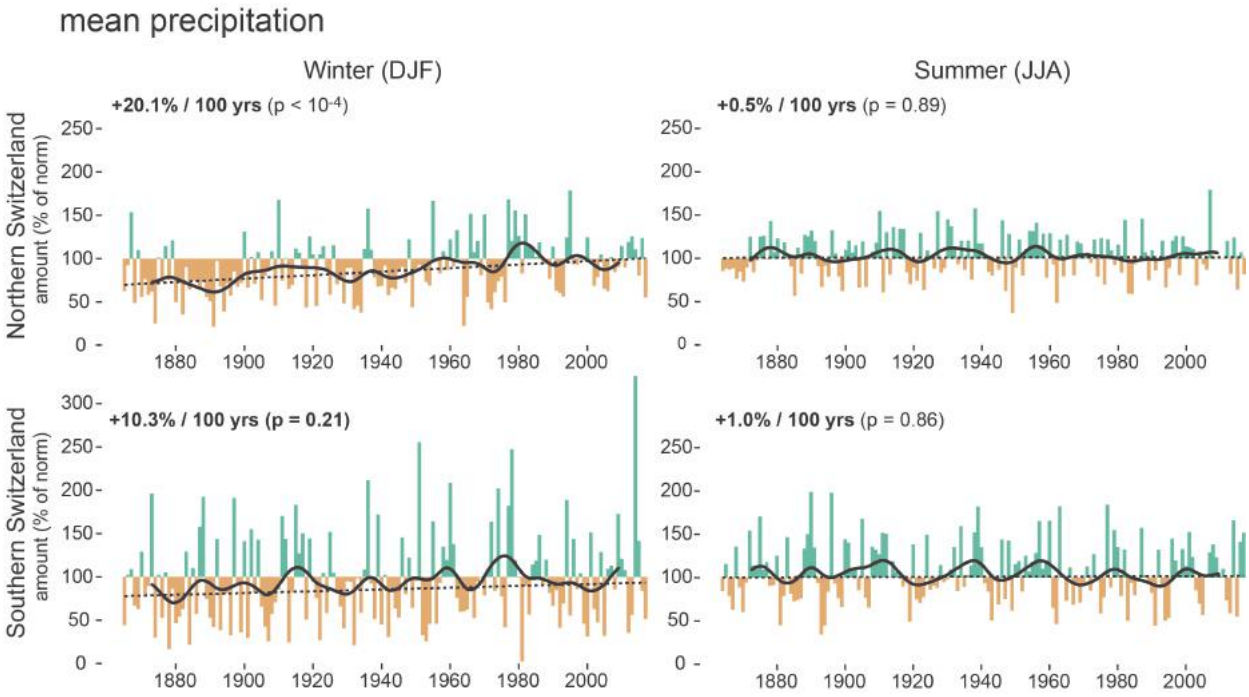

Figure 3.18. Precipitation from 1864 to 2017 for northern Switzerland (mean of Bern, Genève, Basel, and Zürich, top row) and southern Switzerland (Lugano, bottom row). Shown are seasonal amounts for winter (DJF, left) and summer (JJA, right) in percent of the 1961 - 1990 norm. Also shown are a 20-year Gaussian smoother (solid line) and the Theil-Sen linear trend fit (cf. [388], dashed line).

Reconstructions of summer precipitation for the Alps based on documentary data [261], early instrumental data [48], or multiple proxies [53] allow the identification of individual wet or dry years (or clusters of years), such as the dry summers around 1800 and those in the late 1940s. These data exhibit large uncertainties that are barely quantifiable, making trend estimates highly imprecise. It can additionally be noted that none of the existing reconstructions shows a clear long-term trend [39].

Extreme precipitation is rare by definition and subject to large interannual to decadal variability. It is therefore difficult to detect changes in extreme precipitation in the relatively short observational record (e.g., [64]). Consequently, the present analysis is restricted to heavy precipitation events that are rare in the sense that they occur on average only one to three days a year. Changes in both the intensity and the frequency of precipitation are of concern. Here, intensity trends are analyzed in terms of daily maximum precipitation sums (*Rx1d*; cf. [392]), and frequency trends in terms of the number of days exceeding the all-day 99th percentile (#R99e; cf. [298]). Intensity has increased by on average 12 % or 7.7 % per °C of warming since 1901 (Figure 3.19, a), a value close to that expected from the thermodynamic dependence of the water-holding capacity of air on temperature as described by the Clausius-Clapeyron scaling (e.g., [346]) and similar to the mean for a global dataset of several thousand stations [371]. Among the time series examined, 91 % show an increase, a fraction far greater than what would be expected by chance. The frequency of heavy precipitation events (1961 - 1990 period, 99th percentile; Figure 3.19, b) has increased by on average of 26.5 % since 1901. Over 92 % of the series show an increase, again a fraction far greater than what would be expected by chance.

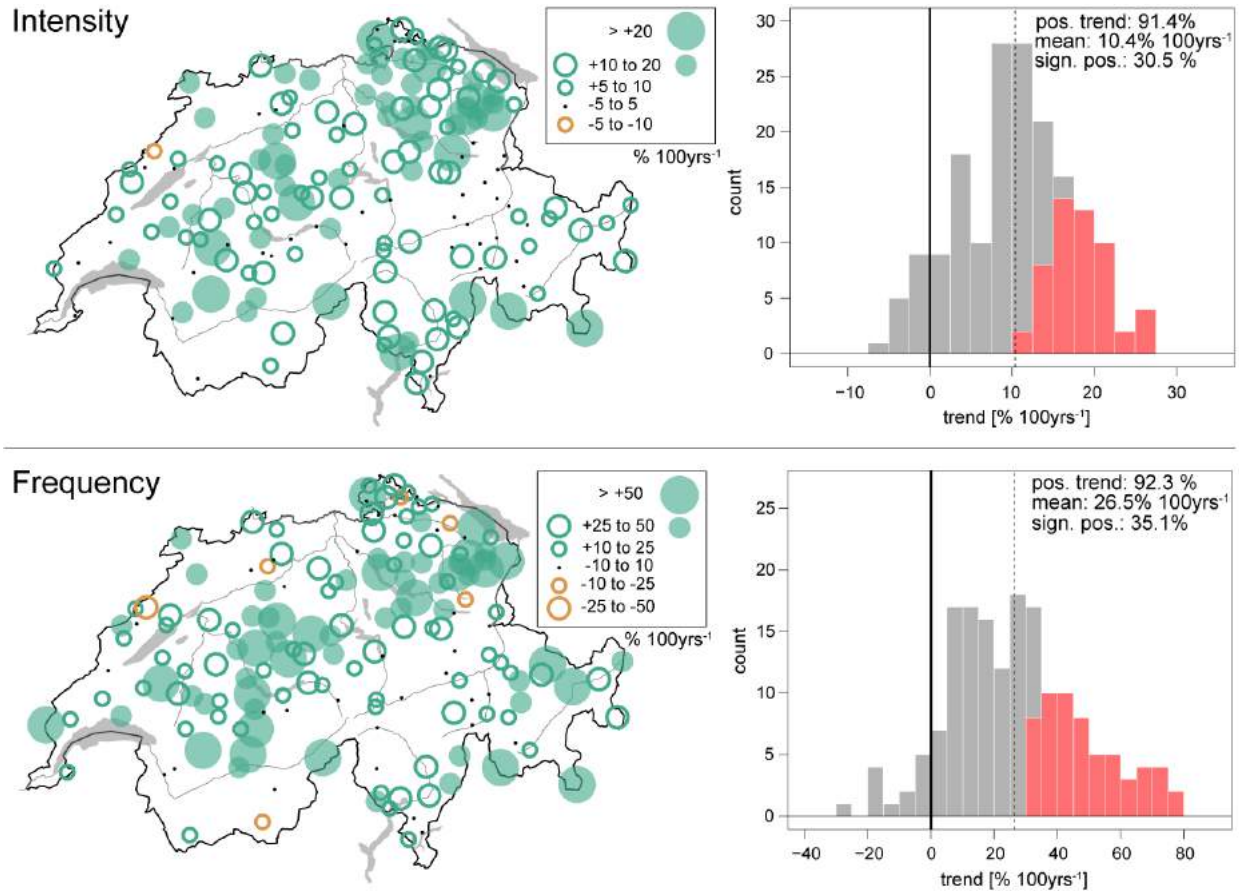

Figure 3.19. Observed 1901 - 2014 trends at ~170 Swiss precipitation stations of heavy precipitation, showing the annual daily maximum precipitation as the intensity measure (top), and of heavy precipitation frequency, showing the number of days exceeding the 1961 - 1990 all-day 99th percentile (bottom). Units are in percent per 100 years. Filled circles and red histogram bars indicate trends that are statistically significant at the 5 % level. Figure adapted from [298].

Drought can have a large impact on several sectors, including agriculture [381], water resources management, and energy production. The definition of drought is not straightforward and depends on the perspective of the stakeholders (cf. Chapter 6.7 for more information). Switzerland has experienced several meteorological and agricultural droughts since 1901 (i.e., 1911, 1945, 1947, 1949, 1952, 1959, 1962, 1976, 2003, 2011, 2015 and 2018; cf. [50, 309, 373, 251, 232]).

The evolution of agricultural droughts in the summer half year in Switzerland is described here using the Standardized Precipitation-Evapotranspiration Index (SPEI; cf. [357]). In addition to precipitation, the SPEI incorporates the effects of evapotranspiration on drought via a parametrization using air temperature. Here, evapotranspiration is parameterized by the potential evapotranspiration after [343]. This approach is known to have a tendency to overestimate changes in droughts, as the applied estimate of potential evaporation tends to be overestimated under high temperatures [320] and ignores several other important drivers of potential evaporation (radiation, wind, humidity), and because potential evaporation is a strong overestimate of actual evapotranspiration [233]. Several other drought indices exist, as analyzed in section Chapter 6.7. Nonetheless, in the absence of long measurement records of evapotranspiration or soil moisture [315], SPEI estimates can provide a first evaluation of the potential drying resulting both from precipitation deficits and from atmospheric demand for evapotranspiration.

There are no long-term SPEI trends, but the increasing evaporation due to positive temperature trends contributes to a negative but non-significant tendency. There is considerable decadal variability in the evolution of the SPEI on the Swiss Plateau (Figure 3.20), and most of the known drought years can be identified (cf. also [231, 232]). The strongest events in the summer half year according to the SPEI are 1865, 1911, 1947, 1949, 2003 and 2018 in northern Switzerland and 1870, 1893, 1921, 1962, and 2003 in southern Switzerland.

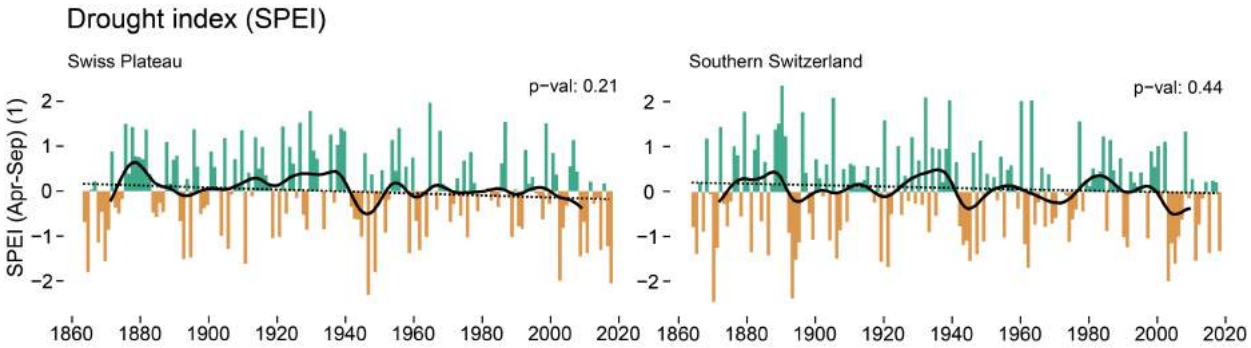

Figure 3.20. Standardized Precipitation-Evapotranspiration Index (SPEI) computed for the summer half year (April - September) 1864-2018 for the Swiss Plateau (left, average over the four stations of Zürich/Fluntern, Basel/Binningen, Bern/Liebefeld, and Genève-Cointrin) and for southern Switzerland (right, Lugano station). Also shown is a 20-year Gaussian smoother (thick lines) and the Theil-Sen linear trend fit (dashed line). The reference period for the SPEI computation is 1864 to 2018.

3.3.4. Snow and ice

In Switzerland, time series of new snow are available since the late 19th century for some stations. Snow height measurements, in contrast, are only more recently available but can be reconstructed with reasonable accuracy from new snow, temperature, and precipitation back to the late 19th century (cf. [299]. Long data series are required to put recent changes into context with natural variability and anthropogenic climate change [296, 294]. The snow series have been quality checked but not homogenized, and the influence of non-climatic artifacts cannot be entirely ruled out everywhere.

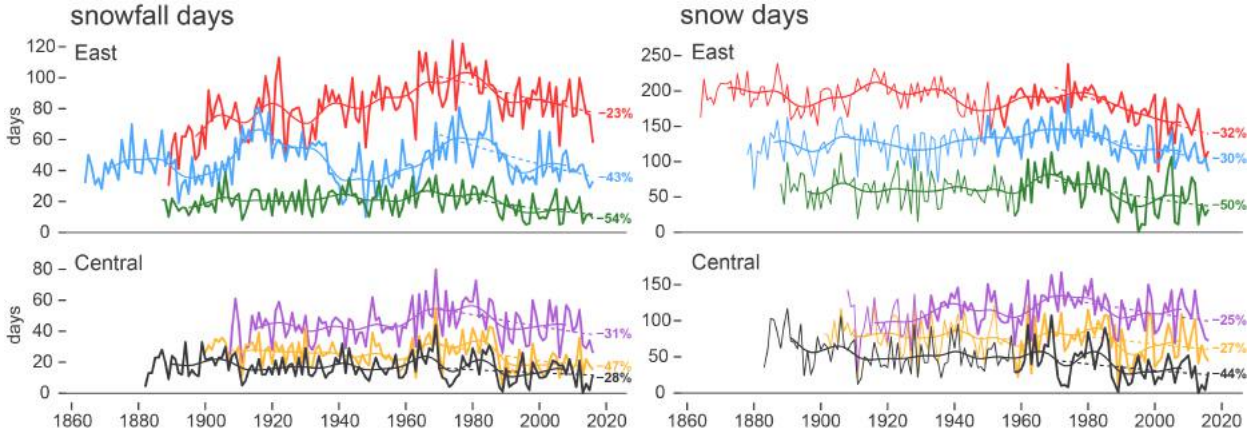

Figure 3.22. Number of days with snowfall (daily new snow sum ≥ 1 cm) per snow year (September 1 to August 31, left) and number of days with snowpack (daily snow height ≥ 1 cm) per snow year (right). The annual values are shown as a bold line; the thin line represents a 20-year Gaussian smoother. Top: Eastern Switzerland stations (Sils-Maria: red, Elm: blue, Chur: green). Bottom: Central Switzerland stations (Einsiedeln: purple, Meiringen: orange, Luzern: black). The dashed lines and numbers show the linear trends in the period 1970 - 2016.

For most stations, the lowest values and unprecedented negative trends in the snowfall and snow day records were observed in the late 1980s and 1990s (Figure 3.22; [299]). [217] and [316] demonstrate that after 1980, a shift-like decrease in the Swiss snow regime resulted in a reduction of the ratio of snowfall days to precipitation days by as much as 50 % below 800 m a.s.l. At higher elevations, around 2000 m a.s.l., the decrease is around 20 % since 1970. Very similar numbers are found for the number of snow days (cf. Figure 3.22, right panel) and by [189] for snow cover duration. This decrease is due to earlier snowmelt rather than to later snow onset. As demonstrated by time series of snow water equivalent, the large majority of sites in the Alps (even at the highest elevations) have seen a reduction in snow mass, which is more pronounced for spring than for winter (cf. [218]). Finally, it should be noted that not all snow variables show clear trends. The maximum new snow sums, for example, show no clear trends as yet (cf. [299]). Note also that the recent shift-like trends are often the result of the combined effect of forced trends and large natural variability (Chapter 7).

Changes in ice (glaciers, permafrost, lake ice) have not been assessed in this report. However, it has been shown in the literature that the Swiss and Alpine glacier area and volume have declined substantially ([391, 16, 143, 162, 112]). According to [391], the Alpine glaciers lost 35 % of their total area between 1850 and the 1970s, and almost 50 % by the year 2000. The Alpine glacier volume decreased by about 60% since the 1850s (e.g., [143]). [162] estimates the Alpine glacier volume losses in the period from 1900 to 2011 at about 96±13 km^3. In Switzerland alone, the glacier volume loss from 1980 to 2010 has been estimated to be 22.51±1.76 km^3 ([112]). The ice cover on Swiss lakes has also been significantly reduced since the mid-1980s (cf. [153]).

3.3.5. Wind

Wind speed and its potential changes are of interest for a wide range of applications (e.g., energy production, storms, warning systems). A decrease in wind speed was observed at most stations in Switzerland over the period 1981 - 2016 (cf. Figure 3.23). The absolute trends range from -0.21 m s^{-1} per 10 years (Chasseral) to less than 0.01 m s^{-1} per 10 years (Luzern). The most pronounced negative absolute trends were observed in the Jura mountains, parts of Valais, Grisons, and Ticino. The trends are significant ($p < 0.05$ using a Mann-Kendall trend test; cf. [388]) at most stations in Ticino, at some stations in Valais and Grison, at a few stations on the Swiss Plateau, on Chasseral, and in Interlaken. In order to judge whether these trends are extraordinary, it is important to put them into context with decadal variability.

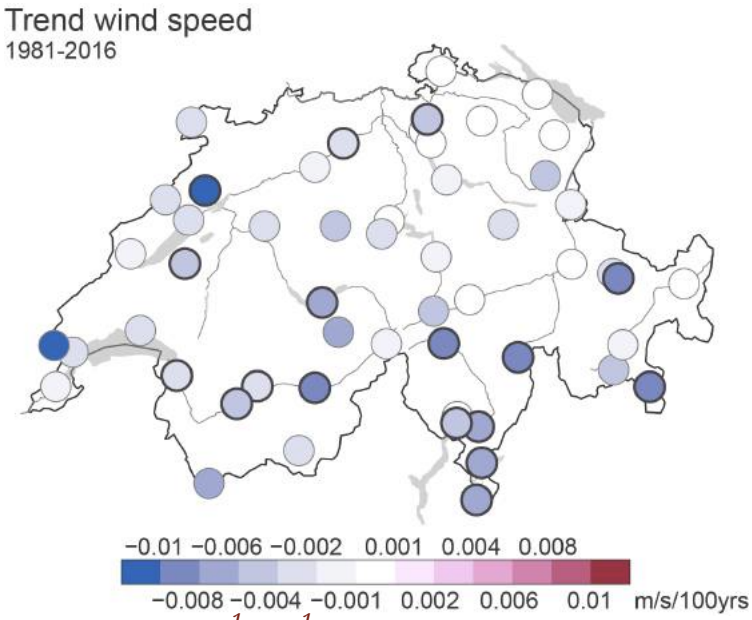

Figure 3.23. Linear trend of wind speed in m s^{-1} $year^{-1}$ for the period 1981 - 2016 based on homogeneous data. A thick black border on the symbol indicates that the trend is statistically significant at the 0.05 level (Mann-Kendall).

Switzerland has one long measurement series of wind speed, which is based on anemometer data from Zurich. From this record, evaluated hourly, homogenized daily maximum wind speed data have been derived [350]. Figure 3.24 shows the 96th percentile of daily maximum wind speed per winter half year (October - March) from 1851 to 2018. The year-to-year variations are in good agreement (though completely independent) with the 96th percentile of daily maximum wind speed from the Twentieth Century Reanalysis (20CR) Version 2c [67] for the grid point closest to Zurich. The Pearson (Spearman) correlation coefficient between measurements and 20CR is 0.56 (0.51). Both series display relatively pronounced multidecadal variability [42, 370]. The wind speeds in the 1981 - 2016 period are well within the band of the decadal variability since the mid-19th century.

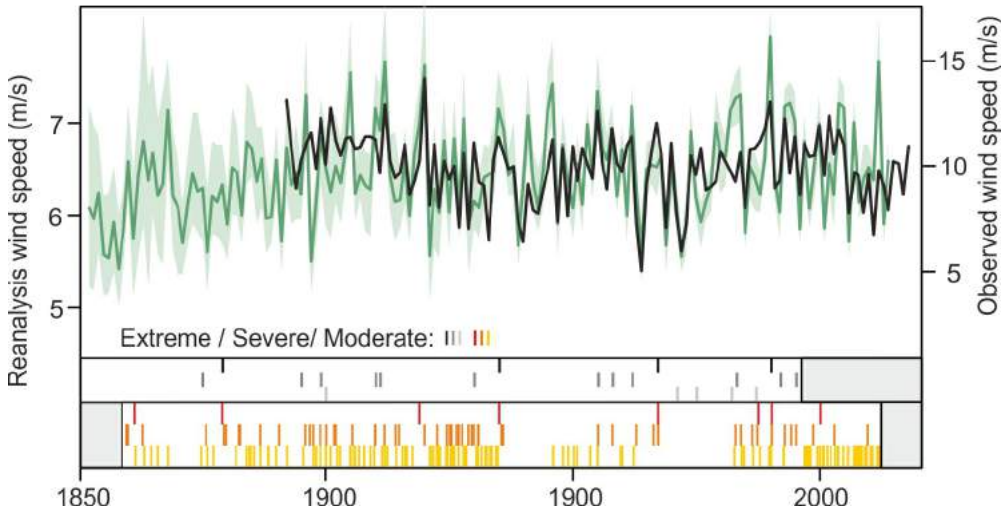

Figure 3.24. Winter windstorms in Switzerland 1851 - 2018. Top: 96th percentile of daily maximum wind speed in October to March in observations from Zurich (black) and the closest grid point in the Twentieth Century Reanalysis (green). The green shading shows the range of the 96th percentile in each of the 56 ensemble members of the reanalysis. Note that the scale is different, as maximum three-hourly wind speeds in the reanalysis are lower than maximum hourly wind speeds in the observations. Bottom: Occurrence of extreme, severe, and moderate windstorms in the catalogs of [38] in grayscale and [332] in color.

This strong decadal variability is also found in the independent damage-based storm catalog [332] and a windstorm catalog based on documentary data ([38], which excludes Föhn storms). Although the damage-based catalog might lack some of the moderate storms due to changes in the sources, very large events are unlikely to be missing. All sources agree that there have been decades or multi-decadal periods with more windstorms (e.g., ca. 1860 - 1875, 1890 - 1920, 1980 - 2000) and periods with fewer windstorms (e.g., 1940s to 1970s). The latter period is important, as it encompasses the “disaster gap” (cf. [262]), a period in which natural disasters were uncommon, and which had a strong influence on risk perception in Switzerland during a time of economic growth.

The long-term evolution of the Föhn, a typical topographic wind in the Swiss Alps, has been analyzed using the almost 150-year series of Altdorf [277]. The number of Föhn hours shows pronounced decadal variability but no clear long-term trend.

3.3.6. Sunshine, fog, and low stratus and small-scale phenomena

Sunshine duration is highly correlated (Spearman correlation r > 0.9 on the annual scale) with the amount of shortwave radiation reaching the ground [291, 351] and is therefore strongly influenced by cloudiness, but also to some degree by the transparency of the atmosphere to sunlight (air quality) in clear sky conditions. The long-term evolution of sunshine is of great interest also because it has a strong influence on temperature extremes. For the Swiss Plateau, four long series are available for analysis dating back to the late 19th century. Pronounced decadal variability and trends are found in the series from the Swiss Plateau and the southern Switzerland series of Lugano (cf. Figure 3.25). The values decrease from relatively high levels at the end of the 19th century and reach a distinct minimum around 1980. After 1980, the values increase strongly, rising back to the level of the maxima of the late 19th century in recent years. This is well in line with a widespread decrease in surface solar radiation between the 1950s and 1980s (global dimming) and a partial recovery more recently at many locations (brightening) [380, 378, 379]. The origins of these variations are mainly related to anthropogenic air-quality modifications through changes in aerosol emissions governed by economic developments and air pollution regulations. A preliminary analysis of observations of cloudiness shows that sunshine duration and cloudiness are highly anti-correlated (r ~-0.85 on the annual scale). To date, the contribution of changes in cloudiness and aerosols is not clear, although there are indications that changes in cloudiness alone cannot explain the strong increase in sunshine duration [291]. The high Alpine peak station Säntis shows no clear trend and no clear dimming or brightening effect since the late 1950s (Figure 3.25).

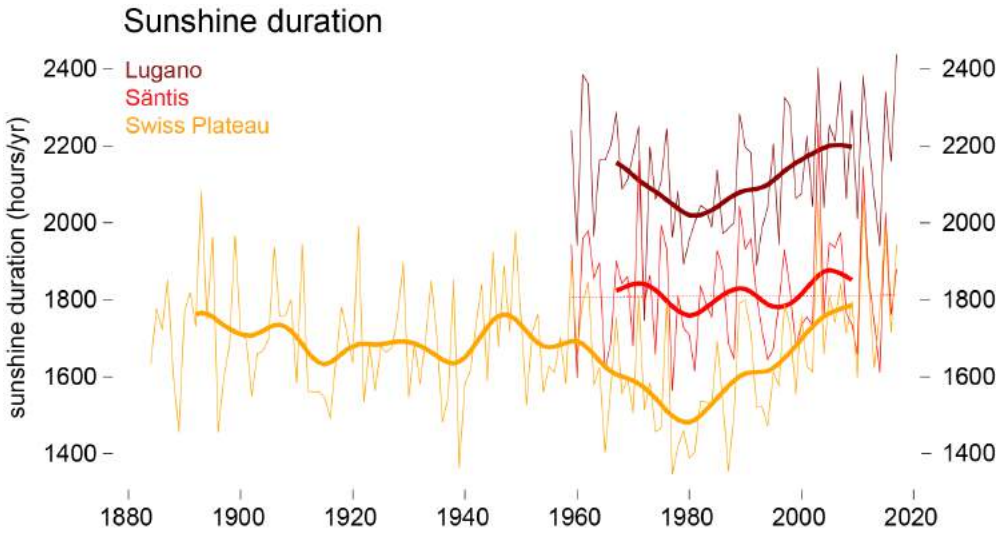

Figure 3.25. Observed evolution of averaged sunshine duration (in hours) since 1864 for the Swiss Plateau (mean of Zürich/Fluntern, Basel/Binningen, Bern/Liebefeld, and Genève-Cointrin, orange) and from 1959 onward for an Alpine peak (Säntis, red) and southern Switzerland (Lugano, brown). Shown are annual values (thin line), a 20-year Gaussian smoother (bold line), and a linear trend estimator for the Swiss Alpine peaks (dashed line).

Analyses of fog and low stratus series have found no clear long-term trend, but there is pronounced decadal variability with a maximum frequency in the late 1980s and early 1990s, followed by a minimum in the late 2000s [295]. A large fraction of the interannual variability and trends in fog and low stratus can be explained by the primarily natural variability of weather types [283]. It should be noted that for fog alone (using horizontal visibility), declining trends have been reported for the last few decades [361].

There is a large number of small-scale phenomena for which the available data series are too short or incomplete to make robust and reliable inferences on changes over the observational period. These include thunderstorms, hail, and tornadoes, but also pollen.

4. Seasonal mean changes

Summary

Consistent with past trends, the latest generation of climate models projects substantial further warming in the long term in all seasons for Europe in response to greenhouse-gas emissions. The warming signals have spatial variations, with an enhanced warming projected over northern Europe during winter and southern Europe during summer. Switzerland is located close to the line at which the distinct and in part opposing precipitation changes in northern and southern Europe occur. As a result, estimates of precipitation changes across models may not agree on the sign of change in some regions. Based on the analysis presented in this chapter, the main robust findings are:

- Temperatures are projected to increase in all seasons and regions in Switzerland during the 21st century. Warming will be larger in summer than in winter, although the strength of the warming at the end of the century (2070 - 2099) relative to the reference period (1981 - 2010) depends on the emission scenario considered. For the low-emission scenario (RCP2.6), Switzerland will likely experience a temperature increase of 0.7 - 2.4 °C (0.6 - 2.0 °C) in summer (winter). For the high-emission scenario (RCP8.5), the temperature increase in Switzerland will likely be between 4.1 and 7.2 °C (3.1 and 5.4 °C) in summer (winter).
- Precipitation is projected to increase in high northern latitudes and decrease in southern Europe. In accordance with these larger-scale trends, long-term warming will likely cause precipitation over Switzerland to increase during the colder seasons and decrease during the warmer seasons, but large natural variability may mask or enhance these forced trends for several decades. Precipitation changes depend on the season, the region, and the emission scenario considered. For RCP8.5, the multi-model median increase in winter precipitation ranges from 12 % in the western Alps to 22 % in southern Switzerland, and the decrease in summer precipitation ranges from 10 % in the eastern Alps to 24% in western Switzerland. The summer decrease until the end of the century will likely be in the range of -5 % to -40 % outside of the Alps, and the winter change will likely be in the range of 2 % to 24 % throughout the country.
- On the spatial scales considered, natural variability (largely as the result of strong variability in mid-latitude circulation) is important. It can partially mask or amplify the forced changes in temperature, precipitation, and other variables caused by anthropogenic emissions, as it has done in the past.
- Warming will cause substantial reductions in both snowfall and snow cover over the Swiss territory. At low elevations and for the RCP4.5 and RCP8.5 emission scenarios, mean September - May snowfall sums will likely decrease by more than -50 % by the end of the century. Mean winter snow cover is projected to decline strongly by the end of the century, with losses exceeding -80 % at low elevations for RCP8.5.
- The goal of the Paris Agreement is to hold the global temperature increase “well below” 2 °C, while pursuing efforts to limit it to 1.5 °C relative to pre-industrial levels. RCP2.6 is an illustrative case of a scenario with global mean warming likely below 2 °C. For this scenario, Switzerland will likely experience an additional annual mean warming of 0.6 - 1.9 °C relative to the 1981 - 2010 reference period. Adding the observed temperature increase (1.5 °C between 1864 - 1900 and 1981 - 2010) suggests a total warming of 2.1 - 3.4 °C. A difference of 0.5 °C in the global mean temperature target (e.g., between 1.5 °C and 2 °C) would result in a difference of about 0.6 - 0.7 °C in Switzerland.
- Uncertainty ranges caused by natural variability and model choice are similar in magnitude to differences across emission scenarios. Although society can in principle influence global emissions, model uncertainty and in particular internal unforced variability will remain substantial, calling for adaptation measures that are robust under a wide range of outcomes.
- The robustness of the climate projections is investigated by comparing different sets of models, including weighted ensembles constrained by past climatology and trends. All methods and data sources show projected changes in temperature and precipitation that are consistent within the stated uncertainty ranges, but the individual best estimates depend on the method applied.

4.1. Introduction

The first part of this chapter sets the European context, using maps of seasonal changes in temperature and precipitation (Chapter 4.4, Chapter 4.5). It serves as a reference for the subsequent sections, which provide a more detailed analysis based on localized projections and derived quantities. To make robust inferences on the spatial scale of Switzerland, the simulated future changes are aggregated into seasons and regions, thereby filtering out small-scale variability and increasing the signal-to-noise ratio [147]. Chapter 4.6 describes changes in snow cover, while Chapter 4.7 provides best estimates and uncertainty ranges for seasonal temperature and precipitation for Switzerland. An overview of key climate indicators is provided in Appendix 1.

The assessment of future climate change is challenging due to the different sources of uncertainties involved: uncertain anthropogenic forcing, model imperfections, and natural variability (Chapter 7, [191, 279, 147]). Model-based projections are evaluated conditional on an emission scenario [193] and provide an estimated range of future changes for that scenario (the scenarios used here are the Representative Concentration Pathways, or RCPs; Chapter 2.2). Natural variability is explicitly included in these projections by considering 30-year periods from regional climate models, to the extent that these models correctly represent natural variability. Especially on small spatial scales, in the near term, and for variables such as precipitation, natural variability is the largest contribution to the total uncertainty. Finally, climate simulations are subject to model uncertainty related to the fact that individual climate models simulate different magnitudes of climate change, in particular at the regional scale [147]. Even though each climate model is based on the same governing physical equations (see Box 2.1), models exhibit structural differences related to the processes included ("structural uncertainty") and how they are parameterized, leading to a spread in the model projections ("parameter uncertainty"). Thus, part of the spread between climate models is due to differences in the models' sensitivities to anthropogenic forcings. Model spread in general is not representative of the overall uncertainty, and common model bias must be accounted for. One suitable framework for this purpose is provided by a Bayesian probabilistic methodology, which combines observations and model projections with a subjective prior assumption [45]. This framework was used to derive the CH2011 climate scenarios (Chapter 8; [99]). In contrast, the CH2018 climate scenarios provide uncertainty ranges based on empirical quantiles of seasonal mean changes (Chapter 4.2, Chapter 2.7). This allows the descriptive uncertainty ranges to be applied consistently, from seasonal mean changes to climate indices and extremes. The Bayesian algorithm (Box 4.2) in its current form is used to support the uncertainty assessments for mean temperature and precipitation, but it cannot be applied to other derived quantities. In Chapter 4.7, a comparison between the projected CH2018 ranges and the uncertainty estimates from this Bayesian analysis and other methods is presented, and recommendations on how to interpret and use the provided seasonal mean projections are provided.

4.2. Methods

4.2.1. Climate model ensemble

The climate model ensemble used in CH2018 is a selection of regional climate simulations from the EURO-CORDEX initiative (Box 2.1, Chapter 2.1). The future climate change projections presented in this report (Chapter 4, Chapter 5, and Chapter 6) are based on this set of simulations (see also Chapter 2.1, Figure 2.1).

EURO-CORDEX is an initiative that coordinates the dynamical downscaling of the CMIP5 global climate model (GCM) simulations for three emission scenarios (RCPs; Chapter 2.2) with regional climate models (RCMs; Chapter 2.1). Dynamical downscaling is a technique employed to increase the resolution of climate simulations by using a GCM to prescribe the initial and lateral boundary conditions for a higher-resolution RCM nested into the GCM grid. Such a GCM-RCM combination is referred to as a *model chain*. The dynamical downscaling method was originally developed in the context of short- and medium-range numerical weather prediction, but is now a common and well-established method for producing climate projections at regional scales [80, 284, 131, 197]. It should be noted that the RCM results are dependent on the quality of the

driving GCM. For instance, if an RCM is downscaling a GCM with large errors in the circulation over the region of interest, the downscaled results will be influenced by this bias in the large-scale field. However, it has been shown that RCMs systematically correct some of the bias in the GCMs [185, 335], supporting the use of a GCM-RCM model chain.

The EURO-CORDEX simulation protocol defines a common model grid for the RCMs, specifically a spherical grid with regular angular spacing and a rotated pole, placed such that the grid cells are of similar size. The ensemble contains simulations at two horizontal resolutions: 0.44°(EUR-44 ensemble), corresponding to grid spacing of about 50 km, and 0.11°(EUR-11 ensemble), corresponding to about 12 km.

The dataset used for CH2018 includes 68 simulations with 7 RCMs, driven by 12 GCM simulations (including different GCMs and different initial condition members of the same GCM). The ensemble prioritizes RCP8.5 and reflects a trade-off between speed and accuracy in the two different RCM horizontal resolutions (Table 4.1). For RCP8.5, 25 % of the 12x7 possible GCM-RCM combinations are simulated at 50-km resolution and 12 % at 12-km resolution. The number of RCMs driven by the same GCM varies from one GCM to another. Consequently, the ensemble mean and range a priori cannot be assumed to provide a balanced representation of model uncertainty (see http://www.euro-cordex.net for more information about EURO-CORDEX and the full simulation list), and the interpretation of the ensemble will potentially need to consider model quality, model dependence, and consistency with observed trends (see Chapter 4.7 for a discussion).

This set of simulations (Table 4.1) corresponds to the full EURO-CORDEX ensemble available in May 2017, except for simulations excluded due to quality issues. A quality check has revealed that some simulations exhibit problematic values in limited regions relevant for Switzerland. These issues were communicated to the respective modeling groups (see http://www.euro-cordex.net) . Simulations showing substantial and unrealistic snow accumulation over the Alps were removed from the model set used in CH2018 (`ICHEC-EC-EARTH_r1i1p1_KNMI-RACMO22E` (EUR-11), `MOHC-HadGEM2-ES_r1i1p1_KNMI-RACMO22E` (EUR-11)). Additionally, a number of simulations were omitted based on recommendations from their creators. Simulations from one model chain were omitted due to a strong wet bias, a strong increase in summer precipitation along the northern Alpine rim, and a very low correlation with its driving GCM (`IPSL-IPSL-CM5A-MR_r1i1p1_IPSL-INERIS-WRF331F`). Moreover, 9 RCM simulations were excluded due to errors detected in the CNRM-CM5 GCM forcing files. Assessing the quality of individual simulations and tracking technical issues in model intercomparisons remain challenging tasks. Chapter 4.7 includes a discussion about the impact of the choice of GCMs and RCMs on uncertainties in the estimated projections, in which the exclusion of the RCM simulations downscaling the CNRM-CM5 GCM was found to affect the CH2018 results to a considerably.

Additional quality issues discovered in some simulations are noisy precipitation (change) patterns (all simulations of the RCMs `SMHI-RCA4` and `DMI-HIRHAM5`) and unrealistically high snow accumulation at isolated grid points (all simulations of the RCMs `SMHI-RCA4` and `DMI-HIRHAM5` of the EUR-11 ensemble). These issues were judged to be minor, and their influence was reduced by smoothing the output fields with a spatial filter (Appendix 1.2).

Finally, for the EURO-CORDEX simulations in the CH2018 ensemble that were not available on the common model grid in accordance with the EURO-CORDEX simulation protocol (i.e., they were only available on a non-standard grid), a conservative remapping to the CORDEX grid was carried out (`CNRM-CERFACS-CNRM-CM5_r1i1p1_CNRM-ALADIN53`, `CNRM-CERFACS-CNRM-CM5_r1i1p1_HMS-ALADIN52`, `MOHC-HadGEM-ES_r1i1p1_ ICTP-RegCM4-3`, `MPI-M-MPI-ESM-LR_r1i1p1_MPI-CSC-REMO2009` (EUR-11), `MPI-M-MPI-ESM-LR_r2i1p1_MPI-CSC-REMO2009` (EUR-11)).

For the analysis of snowfall and snow cover changes, additional criteria for model selection apply (see Chapter 4.6). The corresponding underlying set of EURO-CORDEX model chains differs from the set presented in Table 4.1 (see Table 13.5 and Table 13.6). Hence, the results for snowfall and snow cover are not

fully consistent with the results for temperature and precipitation. Furthermore, reduced model ensembles are employed for the heat stress analysis and for some variables in the downscaled scenarios, as not all EURO-CORDEX model chains provide data for all of the required variables (specifically, minimum and maximum temperature, global radiation, relative humidity, and wind speed).

The EURO-CORDEX archive (and, accordingly, the CH2018 ensemble of RCM simulations) represents the state of the art in continental-scale regional climate modeling. However, there are limitations on its use, and there is the risk of potential inaccuracies. For instance, a well-known deficiency of the EURO-CORDEX RCMs is their predominant cold bias in most seasons over large parts of Europe, including the Alps [197]. It has been suggested that this cold bias is related to topography and to physical processes involving convection or microphysical parameterization schemes [354]. Another limitation of the EURO-CORDEX ensemble is the simplified treatment of atmospheric aerosols. How aerosols are represented depends on the specific RCM considered, but most of the EURO-CORDEX RCMs employ stationary aerosol climatologies that do not evolve over time. For future scenarios, this could result in an inconsistency with the transiently evolving aerosols in the driving GCMs as prescribed by the RCPs (Chapter 2.2) and might lead to biases in simulated temperature trends [15, 242]. However, estimation of how much this affects the results is not trivial, since the RCMs also inherit the aerosol impact on temperature fields from the GCMs, which can reduce the influence of this inconsistency. Furthermore, the RCM simulations often employ outdated aerosol climatologies, which can enhance their cold temperature bias (e.g., [397, 300]). These issues emphasize the importance of continuous model development and improvement beyond the EURO-CORDEX RCM generation.

GCM	init	RCM	RCP8.5		RCP4.5		RCP2.6	
			0.11°	0.44°	0.11°	0.44°	0.11°	0.44°
ICHEC-EC-EARTH	r1i1p1	KNMI-RACMO22E		◉		◉		○
	r3i1p1	DMI-HIRHAM5	◉	✔	◉	✔	◉	
	r12i1p1	CLMcom-CCLM4-8-17	◉		◉		○	
		CLMcom-CCLM5-0-6		◉		○		○
		SMHI-RCA4	◉	✔	◉	✔	◉	✔
MOHC-HadGEM2-ES	r1i1p1	CLMcom-CCLM4-8-17	◉	✔	◉		○	
		CLMcom-CCLM5-0-6		◉		○		○
		ICTP-RegCM4-3		◉		○		○
		KNMI-RACMO22E		◉		◉		◉
		SMHI-RCA4	◉	✔	◉	✔		◉
MPI-M-MPI-ESM-LR	r1i1p1	CLMcom-CCLM4-8-17	◉	✔	◉	✔	○	
		CLMcom-CCLM5-0-6		◉		○		○
		MPI-CSC-REMO2009	✔	✔	✔	✔	✔	✔
		SMHI-RCA4	◉	✔	◉	✔		◉
	r2i1p1	MPI-CSC-REMO2009	◉	✔	◉	✔	◉	✔
MIROC-MIROC5	r1i1p1	CLMcom-CCLM5-0-6		◉		○		○
		SMHI-RCA4		◉		◉		◉
CCCma-CanESM2	r1i1p1	SMHI-RCA4		◉		◉		○
CSIRO-QCCCE-CSIRO-Mk3-6-0	r1i1p1	SMHI-RCA4		◉		◉		○
IPSL-IPSL-CM5A-MR	r1i1p1	SMHI-RCA4	◉	✔	◉	✔	○	
NCC-NorESM1-M	r1i1p1	SMHI-RCA4		◉		◉		◉
NOAA-GFDL-GFDL-ESM2M	r1i1p1	SMHI-RCA4		◉		◉		○

Table 4.1. Simulations in the CH2018 model database (simulations excluded due to quality reasons not shown). The header indicates the model chains by GCM, initial condition (init), and RCM, as well as the different RCPs and the two horizontal resolutions available. Checkmarks indicate existing simulations, circles mark the simulations used for multi-model combination, and empty dashed circles show the simulations substituted by pattern scaling.

4.2.2. Pattern scaling of RCPs

To fill in missing RCM simulations in the CH2018 ensemble (Table 4.1, dotted empty circles), estimates for the corresponding RCP and time period are derived using a pattern-scaling approach. CH2018 employs a time-shift-based pattern-scaling method using global mean surface temperature (GMT) as a control parameter [154]: An existing RCM simulation is scaled by shifting the time axis to align GMT as simulated by the driving GCMs. Unlike other pattern-scaling methods, this method does not scale the climate change signal but simply shifts the time axis. It is nevertheless referred to as “pattern scaling” here, since it serves a similar purpose [154].

For example, consider the process of scaling a simulation of RCP8.5 to substitute a missing RCM simulation of RCP4.5 for a given GCM-RCM model chain (Figure 4.1). First, the GMT averaged over the 30-year period of interest is taken from the GCM simulation of RCP4.5. Then, the 30-year period with a GMT closest to this value is identified in the GCM simulation of RCP8.5 (1). This time slice is extracted from the RCM simulation for RCP8.5 (2) and substituted for RCP4.5 in the period of interest (3). This procedure makes use of the fact that there is a corresponding GCM run available for all the missing RCM simulations that require substitution by means of pattern scaling.

This method can scale an existing simulation “downward” to a scenario with lower global warming. Because there is a corresponding RCP8.5 simulation for each missing RCP4.5 or RCP2.6 simulation, ensembles with the same number of members for all RCPs can be produced using pattern scaling. Such consistent ensembles for different RCPs are a prerequisite for the comparison of results and the construction of climate projections. However, the time slices associated with the limited time periods produced by pattern scaling do not support analyses requiring transient simulations throughout the century.

The time-shift pattern scaling used here is based on the assumption that the climate state is an instantaneous function of the global mean surface temperature. Presumably, the closer the emission scenarios of the simulation used for pattern scaling and the simulation to be estimated, the better this assumption turns out to be. Accordingly, for pattern scaling to RCP2.6, an RCP4.5 simulation is generally used if available, and for scaling to RCP4.5, an RCP8.5 simulation is used. A list of the pattern-scaling time windows of CH2018 is given in Appendix 1.1. The assumption of climate as a function of global mean temperature implies that climatic variables to a first order are a consequence of warming and are independent of the type of radiative forcing. This is not entirely correct, for example, for mean precipitation, which responds differently to aerosol forcing. However, this error is expected to be small compared to the variability at the scale of interest.

The advantage of the time-shift-based method is that it does not modify the data in any way, but merely extracts a 30-year slice of data with the full daily to interannual variability from an RCM simulation. By the same token, this method can be applied to all available variables without limitation. This contrasts with the method used in CH2011 [56], which scaled the simulated changes *and* their range of variability by the ratio of global mean temperature changes. An additional practical advantage of the new method is that a scaled scenario is completely specified by the time window corresponding to the period of interest (as shown in Table 13.4).

A limitation of this pattern-scaling method is that the 30-year period used here may contain a trend that is too large, as the time slices are extracted from a scenario with stronger and therefore faster warming. Thus, a pattern-scaled time slice will tend to underestimate any future changes for the beginning of the 30-year period and overestimate them toward the end. This limitation does not greatly affect the CH2018 projections, which are based on averages over the 30-year periods. However, a stronger trend may artificially increase the variability and thereby influence climate extremes.

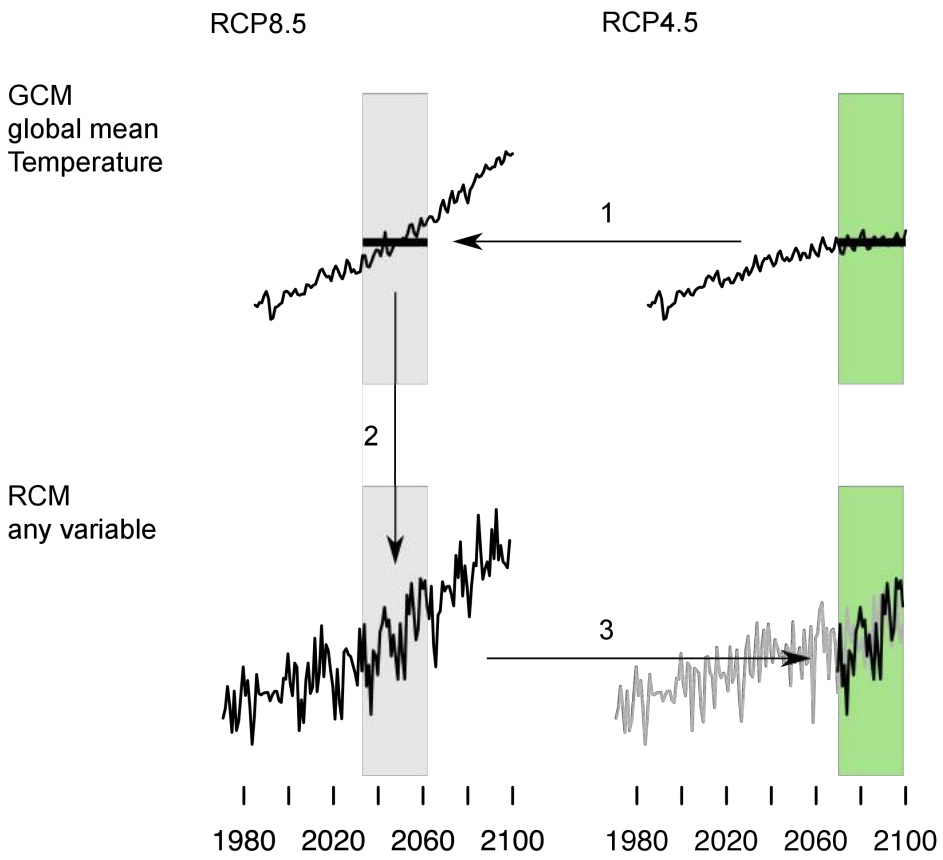

Figure 4.1. Time-shift pattern-scaling approach. The example shows an application scaling surface air temperature for the period 2070 - 2099 from RCP8.5 to RCP4.5 (black). The corresponding RCM simulation for RCP4.5 is shown for comparison (grey). See the text for a discussion.

4.2.3. Pattern scaling from scenarios to warming targets

The pattern-scaling procedure described above can be applied with a slight modification to produce projections for global mean temperature targets such as the 1.5 °C or the 2 °C target. A temperature target prescribes the global mean temperature change with respect to the pre-industrial state. To analyze what this warming means for Europe and Switzerland, it is assumed that the currently observed global warming with respect to the pre-industrial era can be subtracted from the temperature target (i.e., 1.5 °C or 2 °C) to yield the remaining warming. The pre-industrial era is not well-defined, and it has been shown that the choice of the pre-industrial baseline influences the resulting temperature target (e.g., [301, 146]). Here, we use the global mean temperature change between the recent past climate (defined by the CH2018 reference period 1981 - 2010) and the pre-industrial period (defined as 1864 - 1900), which is estimated to be 0.6 °C [237]. This assumption implies that the warming before 1864 is considered to be negligible (e.g., [301]). Thus, the remaining global warming for the 1.5 °C and 2 °C temperature targets is 0.9 °C and 1.4 °C, respectively. This remaining warming is used in step 1 of the scaling procedure shown in Figure 4.1 to estimate the local warming.

The 1.5 °C and 2 °C temperature targets shown in Box 4.1 are produced using this pattern-scaling approach. The application of this method to temperature targets shares the advantages outlined above, but it also has limitations. As mentioned above, there is considerable uncertainty associated with the observed past warming, and combining observational records with model projections and their associated uncertainties is not straightforward. The simulated warming rates differ from the historical warming rate (see also Chapter 7) due to both model biases and natural variability (which is critical on regional scales). However, the approach ensures that the 1.5 °C or 2 °C scenario for any model chain will always be associated with a positive remaining warming, consistent with observations.

4.2.4. Multi-model combination

In order to make robust inferences and to estimate the uncertainty based on the CORDEX model ensemble, a multi-model combination is constructed in CH2018 based on a subset of the available set of simulations (Table 4.1). This multi-model combination set excludes simulations that are strongly interdependent (i.e., simulations with the exact same RCM model version but with two different horizontal resolutions). It should thus retain all relevant data while reducing the sensitivity to the unequal number of simulations from different model chains. The following rules are applied:

- Only the highest available horizontal resolution of each RCM is used.
- To avoid a substantial reduction of the RCM ensemble size, simulations from closely related but not identical RCMs are treated as separate models and kept in the ensemble (e.g., the same RCM but different model versions and different resolutions).
- In one case, two simulations differ only in the initialization of the driving GCM (same GCM, RCM, resolution, and RCP). Only one realization of these very similar simulations is kept, namely the one in which the initial conditions are different from simulations used by other RCMs.

For RCP8.5, a multi-model set of 21 transient simulations is obtained in this way (solid circles in Table 4.1). For RCP4.5 and RCP2.6, missing simulations are substituted through pattern scaling (Chapter 4.2) to obtain the same set of simulations (dashed empty circles in Table 4.1). This multi-model combination ensemble contains simulations at different spatial resolutions (12 km and 50 km). For multi-model combinations at the model grid scale – that is, for the maps of the central estimate shown in this chapter (obtained by the median) – an original averaging method is used. This consists of separately averaging information on the coarser 50-km grid and on the higher-resolution 12-km grid. First, the information on the coarser EUR-44 grid is averaged for all simulations and regridded to the 12-km grid (by remapping the fields using a conservative interpolation method). Then, the fine-scale anomalies from the 12-km simulations are added to the absolute values from the coarser resolution averaging. This avoids any damping of the high-resolution features present in the EUR11 simulations, while conserving the coarse-scale features. The median or any other quantile is computed separately for the low-resolution fields (aggregated EUR-11 components and the EUR-44 simulations) and the high-resolution anomaly fields. The multi-model value is then the sum of the low-resolution and the high-resolution values (equations for the multi-model combination are given in Appendix 1.3).

This procedure allows the consideration of all ensemble members while retaining the high-resolution features present in the EUR-11 simulations. However, the method has two limitations: First, for fields that have a strong nonlinear dependence on elevation, there are systematic differences between the low-resolution fields and the averages of the high-resolution fields. Second, the quantiles of a sum are not exactly equal to the sum of the quantiles. The influence of these two effects on the results presented in this report has been visually checked and was found to be negligible. However, users wishing to adopt the same procedure should ascertain that its applicability for their specific purpose is not restricted by these effects.

This multi-model combination set of 21 simulations per RCP is used for the future climate projections presented in Chapter 4, Chapter 5, and Chapter 6. Maps show the median of the multi-model combination set, and bar plots additionally show the empirical 90 % (5 % - 95 %) quantile range. The empirical quantiles are calculated by assigning cumulative probabilities to the ordered data values of a given variable across the multi-model set. The lowest value is assigned the cumulative probability zero; the highest value, the cumulative probability 1. In between, cumulative probability increases by equal amounts with each value and is interpolated linearly between the data values (see also Chapter 2.7; the equation for the empirical quantiles is given in Appendix 1.4).

4.3. Large-scale European context

The large-scale European warming pattern shows large geographical variations. The increase in mean temperature is stronger during winter in northern Europe and during summer in southern Europe (Figure 4.2). These uneven warming patterns are often referred to as the Polar and Mediterranean amplification, respectively (e.g., [199]). A similar pattern exists for mean precipitation, which increases with warming in the north mainly in winter and decreases in the south, most distinctly in summer (Figure 4.3). This large-scale dipole pattern is quite robust and is seen in the majority of the IPCC GCMs [168]. However, Switzerland is located on or close to the line at which the distinct changes in northern and southern Europe meet, implying a large spread in the future climate projections for the different Swiss regions. The model domain for Switzerland is divided into five climatically nearly homogeneous regions: northeastern Switzerland (CHNE), western Switzerland (CHW), southern Switzerland (CHS), eastern Alps (CHAE), and western Alps (CHAW) (see also Chapter 2.4). The basic climate change patterns over Switzerland suggest a stronger mean temperature increase during the summer season and a slightly enhanced warming over the two Alpine regions, along with an increase in mean precipitation during winter and a decrease during summer. It should be noted, however, that an increase in extreme precipitation is expected for all seasons (see Chapter 6). These changes are accompanied by a reduction in both snowfall and snow cover over the mountainous regions in the country.

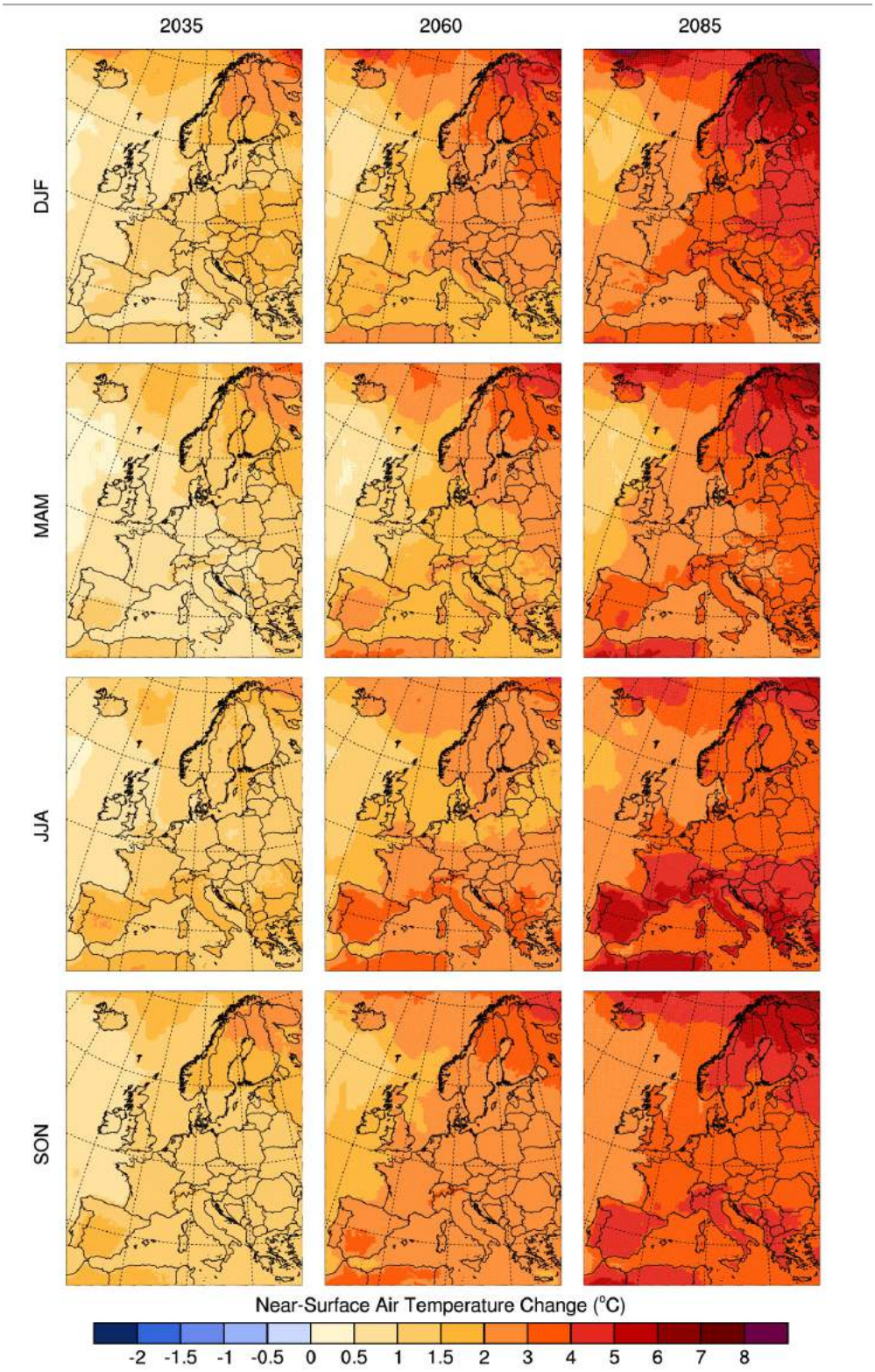

Figure 4.2. Projected future change in median temperature (in °C) over Europe shown by averages centered at 2035, 2060, and 2085 with respect to the reference period 1981 - 2010, for winter (DJF: December - February), spring (MAM: March - May), summer (JJA: June - August), and autumn (SON: September - November). Shown is the multi-model median of the combined simulations of different resolutions from the EURO-CORDEX ensemble (see Chapter 2.1) for the RCP8.5 emission scenario with respect to the reference period 1981 - 2010.

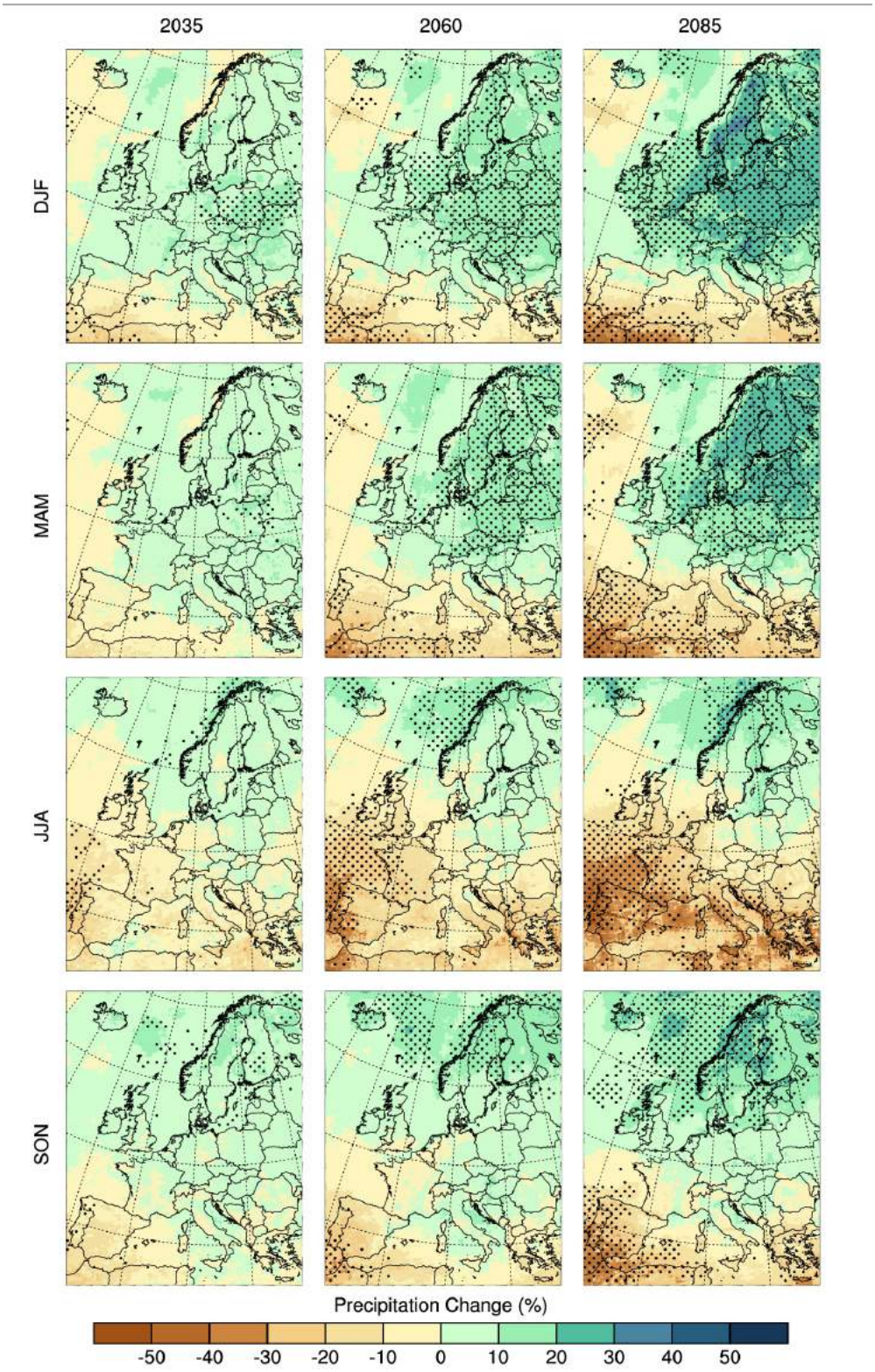

Figure 4.3. Projected future median precipitation change (in %) over Europe by 2035, 2060, and 2085 for winter (DJF: December - February), spring (MAM: March - May), summer (JJA: June - August), and autumn (SON: September - November). Shown is the multi-model median of the combined simulations of different resolutions from the EURO-CORDEX ensemble for the RCP8.5 emission scenario with respect to the reference period 1981 - 2010. Stippling (dots) indicates regions in which at least 90 % of the models agree on the sign of change.

4.4. Seasonal mean changes in temperature

Consistent with the large-scale warming over Europe, Switzerland is projected to experience rising temperatures, in particular during summer, when parts of Switzerland are affected by the Mediterranean amplification.

The regionally aggregated projections for Switzerland (Figure 4.4) consistently show an increase in temperature for all seasons, regions, and emission scenarios. A particularly large increase in temperature is projected at the end of the century (2085) for the RCP8.5 scenario. For this high-emission scenario, the median temperature increase at the end of the century for the model ensemble varies between 3.1 °C and 5.5 °C, depending on the season and region considered. However, when considering the empirical quantile spread (see Chapter 2.7), the lower estimate of the model range shows temperature increases between 2.0 °C and 4.3 °C, whereas the upper bound ranges between an increase of 4.0 °C and 7.3 °C, depending on the region and season.

For the near-term projections (2035), the choice of emission scenario has a minor impact on the temperature projections; the empirical quantile model spread shows a similar range for the three RCPs. The main sources of uncertainties for near-term projections are thus the decadal variability and model imperfections (see Chapter 7; [147]). Over the course of the 21st century, the projections from the different emission scenarios diverge. At the end of the century (2085), the median estimates of the projections from the three RCPs vary by up to 4.6 °C for the different regions and seasons.

For the intermediate scenario RCP4.5, there is only a small increase in the projected temperature change from mid-century (2060) to the end of the century (2085). At the end of the century, the model ensemble projects a median temperature increase of 1.5 - 2.8 °C across the CH2018 regions and seasons. In contrast, the mitigation scenario RCP2.6 shows a smaller temperature change at the end of the century compared to mid-century. The model ensemble mean at the end of the century varies from 0.8 °C to 1.5 °C, depending on the region and season.

The projections indicate that mean temperatures are likely to increase more in summer than in winter. Moreover, the warming is projected to be strongest in southern Switzerland (CHS) and at higher altitudes of the mountainous regions (CHAW and CHAE). At the end of the century (2085), a median summer mean temperature increase of 4.5 °C for northeastern Switzerland is estimated for the RCP8.5 emission scenario, compared to up to a 5.5°C increase in the the eastern and western Alps. In winter, the median increase in mean temperature in these mountain regions is estimated to be up to 3.9 °C, which is similar to the median estimate of 3.8 °C for northeastern Switzerland. The mean temperature increase projected for autumn is similar to that for winter; a smaller increase in mean temperature is projected for spring. The numerical values of the empirical quantile range projections shown in Figure 4.4 are listed in the Appendix (Table 13.3).

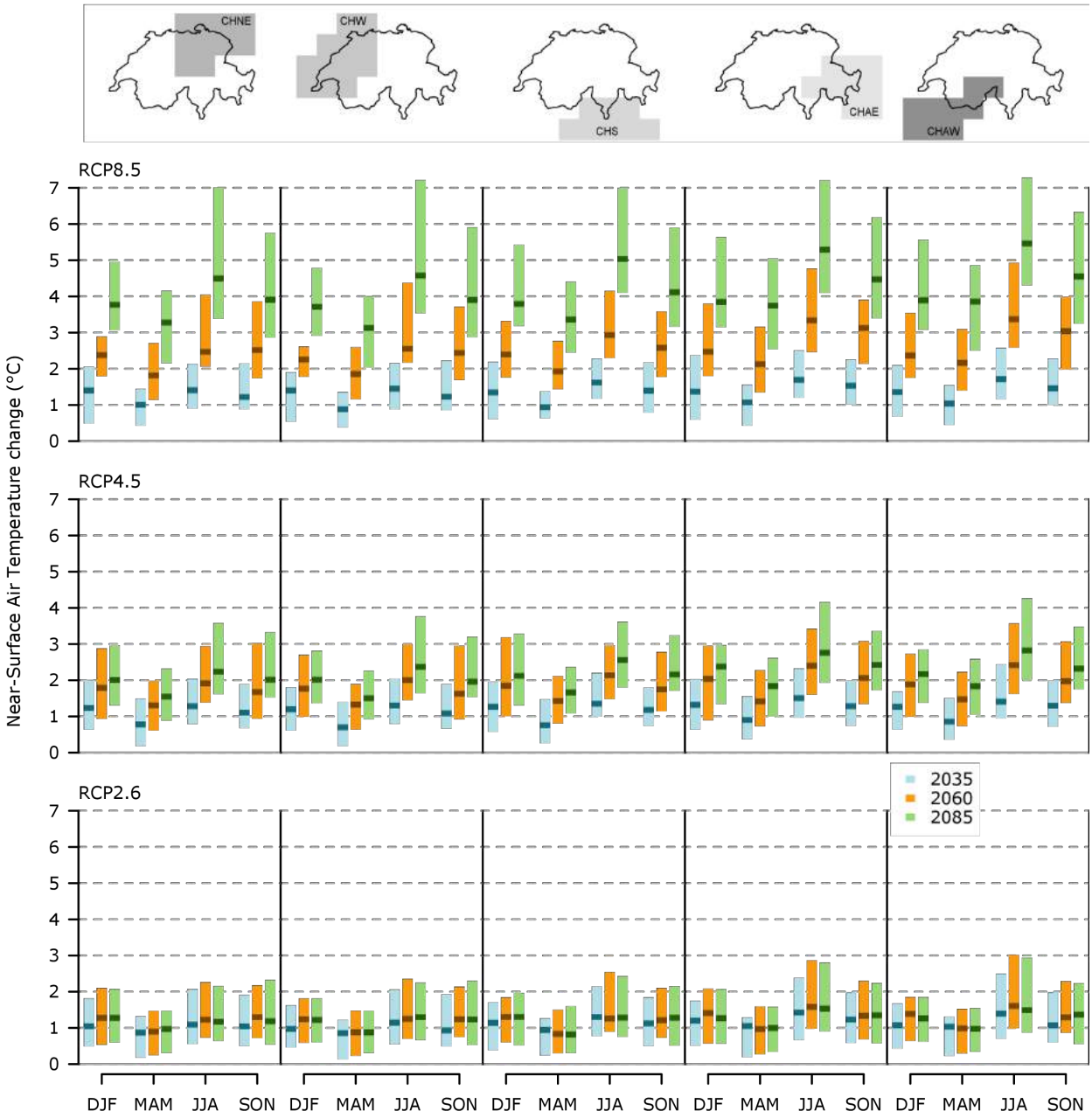

Figure 4.4. Projected future change in median temperature (in °C) for winter (DJF: December - February), spring (MAM: March - May), summer (JJA: June - August), and autumn (SON: September - November) in northeastern Switzerland (CHNE), western Switzerland (CHW), southern Switzerland (CHS), eastern Alps (CHAE), and western Alps (CHAW). Projections are for 30-year averages centred at 2035 (blue), 2060 (orange), and 2085 (green) with respect to the reference period 1981 - 2010. Three emission scenarios are considered: RCP8.5 (top row), RCP4.5 (middle row), and RCP2.6 (bottom row). The lower and upper bounds of the colored bars represent the empirical quantile range, spanning the lower (5 %) and upper (95 %) bounds of the ranked data points (i.e., 90 % of the model ensembles fall within this range). The middle line is the median estimate of the ensemble.

4.5. Seasonal mean changes in precipitation

Mean precipitation changes are projected to increase in northern Europe and decrease in southern Europe. As a result, individual climate simulations may not agree on the sign of precipitation change when they are close to zero, particularly for the near-term projections (2035). Nevertheless, the agreement on the sign of change among the individual models increases with time, especially for the winter season. In the other seasons, individual models project either an increase or a decrease in precipitation amounts. Overall, the large-scale features and multi-model median estimates suggest that mean precipitation over Switzerland will increase during winter and decrease during summer. The estimated changes for spring and autumn are less distinct, but the multi-model median suggests a weak increase in northern Switzerland during spring, whereas no clear changes are seen for autumn.

The empirical quantile range of estimated precipitation changes from the individual simulations is shown in Figure 4.5. Because the single-model estimates of mean precipitation changes vary between the different seasons, regions, and emission scenarios considered, the empirical quantile range also differs and increases over time, most clearly for the RCP8.5 emission scenario. For this scenario, the estimate of (model) median summer precipitation change at the end of the century (2085) varies between regions, from -10 % to -24 % relative to the reference period. It should be noted that for the CHAE region, either an increase or a decrease in median precipitation is consistent with the projected range. At the end of the century (2085), the upper bound of the range indicates an +11 % increase in summer precipitation, while the lower bound indicates a decrease of -27 %. This large spread between the individual model estimates is the result, as discussed above, of Switzerland's location between the two pronounced regions of increase (north) and decrease (south) in precipitation, as well as the fact that these regions are situated differently in each model. Nevertheless, the overall projected range for CHNE and CHW estimates a decrease in the median summer precipitation. Most of the projected range for CHS and CHAW also estimates a decrease in summer precipitation; the upper range estimate indicates only a +2 % increase. The projected precipitation changes in the different Swiss regions are shown in Figure 3.7.

For the winter season, median precipitation is projected to increase in all regions, with the increase varying between +12 % to +22 %, depending on the season and region. The model range is smaller during winter than during summer: The largest upper estimate suggests an increase of 38 % (for the CHS region), whereas the lowest change estimate is a slight reduction of -2 % (for CHAE).

In the transition seasons, spring and autumn, the changes are not amplified as strongly during the 21st century. The upper and lower bounds of the projected ranges do not change overtime, suggesting that the model spread is largely the result of internal variability (see Chapter 4.6 and Chapter 7). However, although the upper and lower bounds of the projected ranges for the different regions often disagree on the sign of the change, there is a tendency toward a slight increase in mean precipitation in spring; for autumn, there is no clear change north of the Alps and a weak decrease south of the Alps.

As with temperature, the choice of emission scenario has little impact on the median precipitation projections for the near term, but it has a large effect on the long-term projections. For instance, in southern Switzerland, the projected changes in summer median precipitation by 2035 are close to zero in all emission scenarios considered, but the projections diverge toward the end of the century (2085). The RCP8.5 emission scenario at the end of the century implies a -23 % decrease in the median precipitation for southern Switzerland. In contrast, the RCP2.6 emission scenario corresponds to a median precipitation decrease of -4 % (see also Box 4.1). All the numerical values for the empirical quantile range projections shown in Figure 4.5 are listed in the Appendix (Table 13.6).

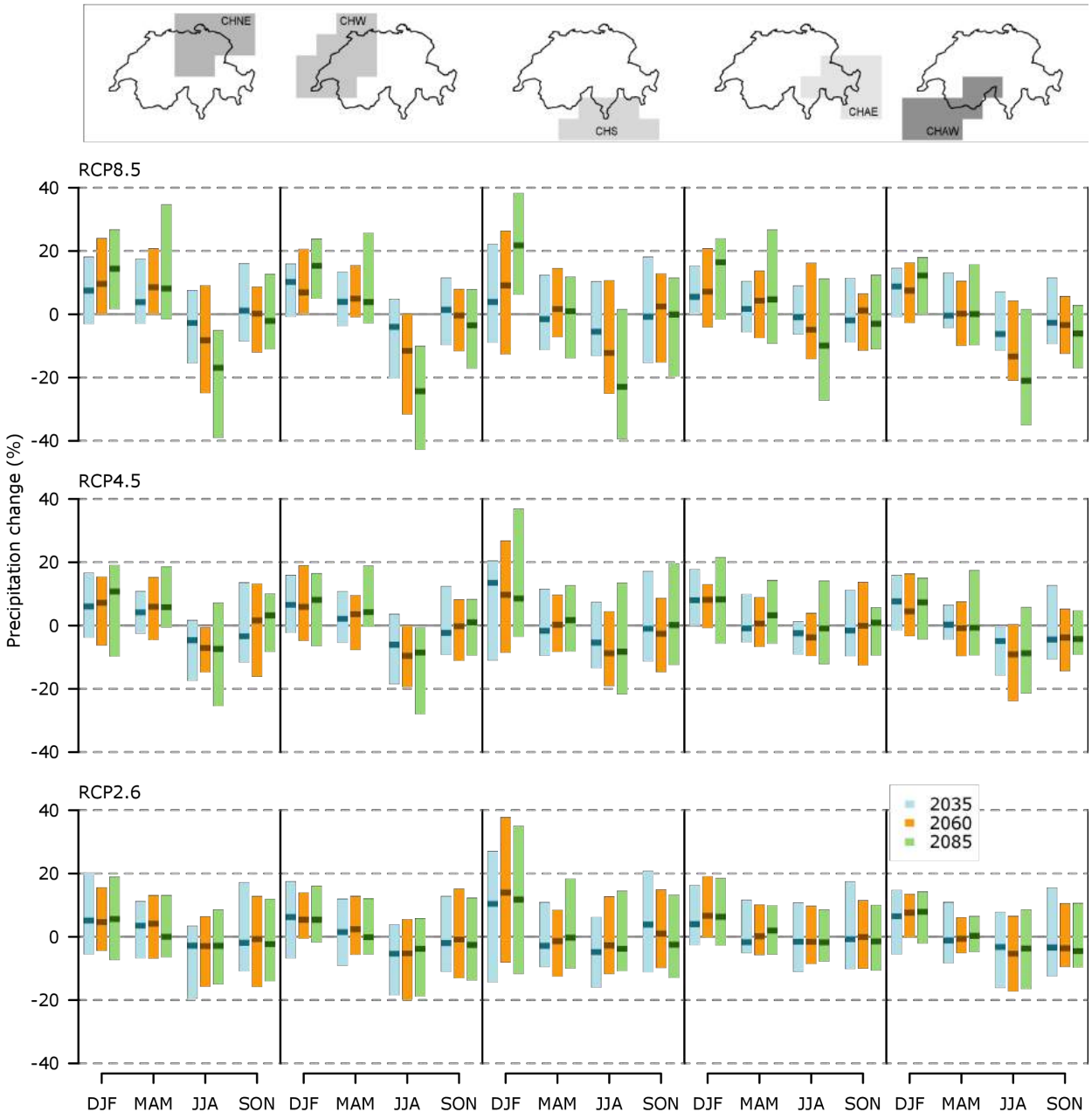

Figure 4.5. Projected precipitation change (in %) for winter (DJF: December - February), spring (MAM: March - May), summer (JJA: June - August), and autumn (SON: September - November) in northeastern Switzerland (CHNE), western Switzerland (CHW), southern Switzerland (CHS), eastern Alps (CHAE), and western Alps (CHAW). Projections are for 30-year averages centered at 2035 (blue), 2060 (orange), and 2085 (green) with respect to the reference period 1981 - 2010. Three emission scenarios are considered: RCP8.5 (top row), RCP4.5 (middle row), and RCP2.6 (bottom row). The lower and upper bounds of the colored bars represent the empirical quantile range, spanning the lower (5 %) and upper (95 %) bounds of the ranked data points (i.e., 90 % of the model ensembles fall within this range). The middle line is the median estimate of the ensemble.

Box 4.1: 1.5 °C and 2 °C temperature targets

With the Paris Agreement of 2015, the nations of the world pledged to keep the increase in the global mean temperature (GMT) “well below” 2.0 °C above pre-industrial levels, and to pursue efforts to limit it to below 1.5 °C [349]. Keeping global warming within this range requires drastic reductions in greenhouse gas emissions. The RCP2.6 scenario pathway is representative of a mitigation scenario aiming to limit the increase in global mean temperature to 2.0 °C (see Chapter 2.2 and [238]). This scenario features a peak in emissions early in the 21st century, followed by a strong reduction, likely limiting the global temperature change to less than 2.0 °C at the end of the century [330]. However, as a result of the varying climate sensitivities of the climate models [191, 192], the spread in the simulated global temperature responses to this scenario is large. Here, a pattern-scaling approach (Chapter 4.2) is used to quantify the temperature and precipitation responses for Switzerland corresponding to the global temperature targets. In Switzerland, the average temperature has increased by 1.5 °C between the pre-industrial era (1864 - 1900) and the reference period (1981 - 2010) [20], a much larger increase than the global mean temperature change of 0.6 °C [237]. The results presented here are for the remaining warming (i.e., the warming that would occur from the reference period until the target is reached); the observed past warming over Switzerland must be added to estimate changes with respect to pre-industrial levels.

The model ensemble from the RCP2.6 emission scenario projects a seasonal median temperature change that is in between or close to the estimated projections from the global temperature targets of 1.5 °C and 2.0 °C (Figure 4.6). For the small spatial scales of Switzerland, the different median estimates overlap mainly due to internal variability and model uncertainty (see Chapter 7 and [147]). The projected warming over Switzerland varies across the different seasons: lowest during spring and highest during winter. For the precipitation changes, all three estimates are similar, with comparable changes projected from the RCP2.6 emission scenario and temperature targets for each season. The largest change is seen during winter, where an increase in precipitation is estimated. During the other seasons, the precipitation changes are close to zero, with a tendency toward an increase in spring and a decrease in summer.

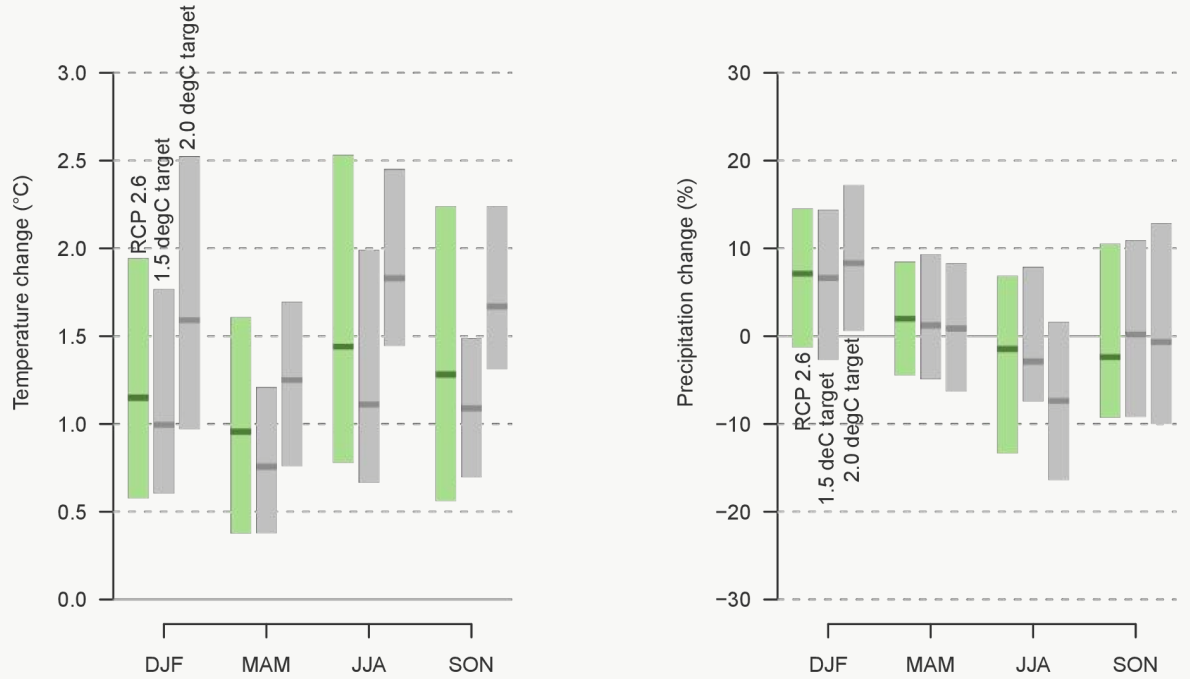

Figure 4.6. Temperature change (°C, left) and relative precipitation change (%, right) for Switzerland (area-weighted mean) with respect to the reference period for RCP2.6 (period 2085) and the two temperature targets of 1.5 °C and 2.0 °C (obtained by means of the pattern-scaled approach).

Note that the uncertainty range for RCP2.6 is wider than for a 2 °C case, as the former quantifies the response to a given forcing (meaning that the global mean temperature response is already uncertain), whereas the latter only quantifies the uncertainty in the regional response and variability, with a fixed global mean.

For simplicity, we focus on RCP2.6 here as an illustrative case of a scenario with global mean warming likely below 2 °C. For this scenario, Switzerland will likely experience a further annual mean warming of 0.6 - 1.9 °C relative to the 1981 - 2010 reference period. Addition of the observed temperature increase (1.5 °C between 1864 - 1900 and 1981 - 2010; [20]) suggests a total warming of 2.1 - 3.4 °C. A difference of 0.5 °C in the global mean temperature target (e.g., between 1.5 °C and 2 °C) would result in a difference of about 0.6 - 0.7 °C in Switzerland. In contrast, for unmitigated emissions, Switzerland may experience a warming up to three times larger than what already has occurred, as shown in Figure 4.4 and Figure 4.5. To assess the climatic impacts of a warming limited to 1.5 °C and/or 2 °C over pre-industrial levels in Switzerland, the projections for RCP2.6 should be used as an analog.

4.6. Changes in snowfall and snow cover

Due to the temperature dependency of the freezing and melting processes, the projected changes in temperature will have a direct impact upon atmospheric and surface cryospheric features such as snowfall and snow cover. The former term denotes the amount of solid precipitation reaching a given surface in the form of snow, whereas the latter describes the surface snowpack itself, which is subject to redistribution of fallen snow (for instance, by wind and avalanches) and to melting. In addition to temperature changes, shifts in the seasonal precipitation regime are likely to influence total winter snowfall. These changes are relevant for the assessment of climate change impacts in Switzerland, as various sectors including tourism, hydropower generation, natural hazards, and road and airfield maintenance are highly dependent on snowfall and snow coverage. A substantial decrease in both snowfall and snow cover in Switzerland, albeit strongly influenced by natural decadal variability, has already been observed in recent decades (Chapter 3.3.4).

Future changes in surface snow cover are assessed in accompanying projects such as Hydro-CH2018 (see Chapter 10). Here, an overview analysis based on the direct output of the EURO-CORDEX RCMs is presented. For this purpose, a dedicated sub-ensemble of EURO-CORDEX that fulfills certain additional criteria is used. For the analysis of snow cover changes, all models are omitted in which, even after spatial filtering, snow cover accumulation throughout a considerable part of the period 1981 - 2099 takes place at high-elevation grid cells (see Chapter 4.2). Such a persistent accumulation of snow cover could be due to cold or wet model biases. For these high-elevation grid cells, it could also be due to the lack of parameterizations of snow removal from high to low elevations (glacier flow). In any case, persistent and unrealistic snow accumulation prevents the proper analysis of snow cover change signals, and the affected models are therefore removed from the analysis, as are models that do not provide snow cover information at all. Furthermore, due to the pronounced height dependency of snow cover and its control by temperature thresholds, the coarsely resolved EUR-44 ensemble is not considered. Only the highly resolved EUR-11 simulations, whose grid-cell orography reaches higher Alpine elevations, are taken into account. Additionally, to ensure a consistent comparison between emission scenarios, only model chains that cover both RCP4.5 and RCP8.5 are considered; pattern scaling is not used here. Due to its small ensemble size, the RCP2.6 emission scenario is omitted completely. For the analysis of snowfall changes, the EUR-11 sub-ensemble employed by [127] is used. For the most part, this sub-ensemble is based on the same selection criteria outlined above, but it does not require the availability of raw RCM snowfall amounts (these are separated from total precipitation based on simulated temperature; see [127] for details). The resulting EURO-CORDEX sub-ensembles are listed in Table 13.5 and Table 13.6. They consist of 18 (snowfall; 9 x RCP4.5, 9 x RCP8.5) and 10 experiments (snow cover; 5 x RCP4.5, 5 x RCP8.5), respectively.

Snowfall changes

The projected seasonal mean temperature and precipitation changes presented in Chapter 4.4 and Chapter 4.5 can be viewed as having opposing effects on mean snowfall sums. On the one hand, a projected mean temperature increase will be associated with a decrease in the snowfall fraction (the contribution of snowfall to total precipitation) and a corresponding increase in the rainfall fraction (the contribution of

rainfall to total precipitation; the latter being the sum of rainfall and snowfall). In the absence of any total precipitation changes, this would lead to a reduction in snowfall sums (total accumulated snowfall). On the other hand, the tendency for increases in total wintertime precipitation might completely or partially offset this temperature effect and lead to higher snowfall sums compared to a non-modified precipitation regime.

Previous studies on past and future snowfall changes in the Alps that are based in part on EURO-CORDEX model output indicate a dominance of the temperature effect over the precipitation effect and therefore project substantial snowfall reductions [75, 266, 316]. A more comprehensive analysis specifically targeting the European Alps has recently been presented by Frei et al. (2018) [127]. Here, this analysis is adopted and a summary for the entire CH2018 domain is presented (Chapter 2.4). As part of their respective microphysics schemes, all EURO-CORDEX RCMs internally discriminate between different precipitation phases. However, the solid precipitation flux at the surface (snowfall flux) is only provided by a few models as a direct model output. To resolve this issue, Frei et al. (2018) [127] developed a method that separates snowfall from total precipitation based on near-surface air temperature and explicitly takes into account RCM subgrid variability. Simulated snowfall sums are additionally bias-corrected against an observation-based reference. For further details, the reader is referred to Frei et al. (2018) [127].

The relative change signals of several snowfall indices for the September - May snowfall season and for the last scenario period 2085 are presented in Figure 4.7 (see the figure caption for details on the indices considered). For both emission scenarios, mean snowfall sums are expected to decrease at all elevations and over the entire winter, except for elevations higher than 2000 m a.s.l. in mid-winter. Domain-mean reductions amount to about 15 % for RCP4.5 and 35 % for RCP8.5. At elevations below 750 m a.s.l. for RCP4.5 and below 1250 m a.s.l. for RCP8.5, more than 50 % of today's mean winter snowfall is lost. Stable or even slightly increasing snowfall sums in mid-winter at high elevations are a consequence of increasing winter precipitation and a slight increase in mean snowfall intensity. At these elevations and at this time of year, both snowfall frequency and snowfall fraction are rather stable due to the fact that temperatures are well below the freezing point even in the future climate. At low to mid-elevations and in the transition seasons, however, snowfall fraction and snowfall frequency strongly decrease, ultimately leading to a decrease in both mean and heavy snowfall (the latter as defined by the 99th all-day snowfall percentile).

Snow cover changes

The widespread decrease in winter snowfall sums described above means reduced snow accumulation at the surface; as such, this decrease will influence surface snow cover, here expressed as snow water equivalent (SWE). Furthermore, rising temperatures can be expected to accelerate the melt process and thus the ablation of the surface snowpack.

The geographical pattern of projected mean September - May SWE changes until the scenario period 2085 (ensemble mean; Figure 4.8) is clearly controlled by elevation. For RCP4.5, SWE reductions of more than 50 % are projected for large regions north and south of the main Alpine ridge. In particular, low-lying areas in northern Italy (Po valley) are affected by SWE losses exceeding 80 %. Changes at medium to high elevations along the main Alpine ridge are less pronounced and typically do not exceed 30 %. For RCP8.5, however, SWE losses of more than 50 % are obtained at medium to high elevations, and large parts of the Alpine forelands experience SWE reductions of more than 80 %, up to almost complete losses in the Po valley south of the Alps.

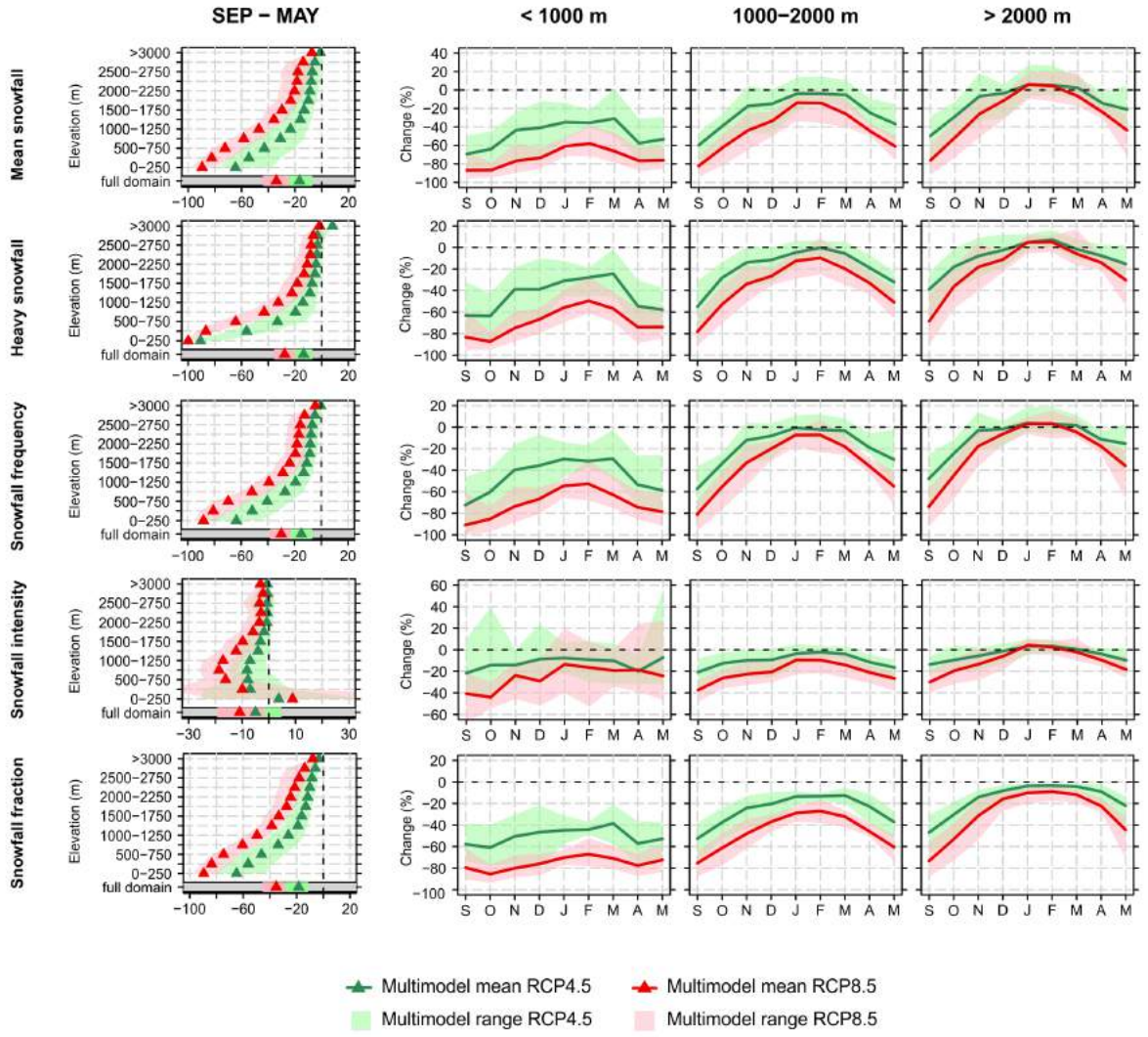

Figure 4.7. Relative change in different snowfall indices for RCPs 4.5 and 8.5 for the entire CH2018 analysis domain and the scenario period 2085. Left column: Changes averaged over 250-m elevation intervals and over the period September - May. Second to fourth column: Monthly changes for three distinct elevation ranges (< 1000 m a.s.l., 1000 - 2000 m a.s.l., > 2000 m a.s.l.). Indices (from top to bottom): Daily mean snowfall, heavy snowfall (99th all-day percentile), daily snowfall frequency (threshold for a snowfall day: snowfall > 1 mm d^{-1}), snowfall intensity (mean snowfall amount on snowfall days), snowfall fraction (snowfall sum divided by total precipitation sum). The triangles indicate ensemble mean values; the shading indicates the ensemble range.

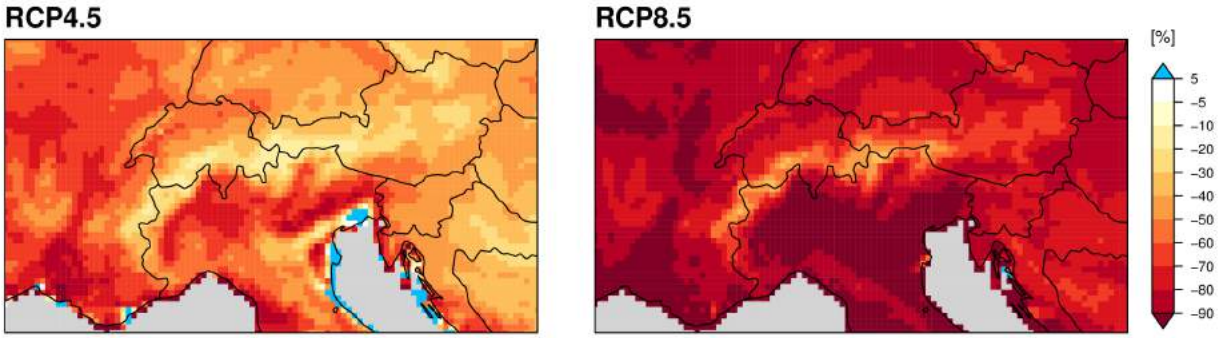

Figure 4.8. Relative change (ensemble mean) in mean September - May snow water equivalent over the Alpine region for RCPs 4.5 (left) and 8.5 (right) and for the scenario period 2085.

The strong elevation dependency of SWE losses is also clearly apparent fromFigure 4.9, which summarizes relative SWE changes by 2085 for 500 m a.s.l. elevation classes and for the combined CH2018 domains only. For both emission scenarios, relative SWE losses are most pronounced at elevations below 1000 m a.s.l. In the case of RCP4.5, a considerable model spread of change signals is seen, with elevation-mean losses ranging from about 40 to 80 %. The spread is considerably reduced for RCP8.5, and models agree on substantial losses between about 85 and 95 %. Moving upward, relative SWE losses become less pronounced but are still substantial. For high elevations above 2500 m a.s.l., SWE losses of about 20±10 % (RCP4.5) and 40±10 % (RCP8.5) are obtained.

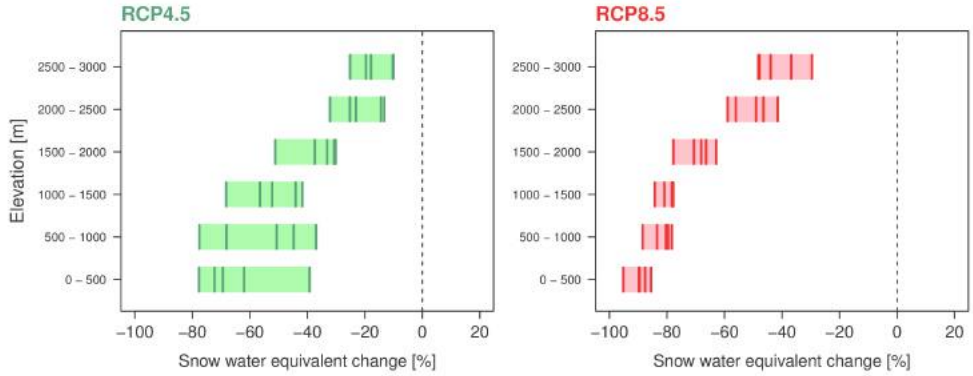

Figure 4.9. Relative change in mean September - May snow water equivalent for the late scenario period 2085 for the combined CH2018 domain, averaged over individual elevation classes. Left: RCP4.5. Right: RCP8.5. The vertical lines indicate the change signals of the individual underlying EURO-CORDEX model chains; the shading indicates the entire ensemble range.

4.7. Uncertainty estimation for seasonal mean quantities

The CH2018 projections are the result of a cascade of processing steps, including the selection of GCMs contributing to the EURO-CORDEX exercise, the combinations with RCMs for dynamical downscaling, the choice of RCM-GCM chains considered for multi-model analysis (Chapter 4.2), and possibly the choice and application of downscaling and bias-correction methods to produce localized projections. Each of these processing steps is associated with uncertainties that eventually add to the overall scientific uncertainty of the climate change signal at the local scale (see, e.g., [374]). Natural variability is another source of uncertainty (Chapter 7). The model selection of GCMs has a large effect on the spread in temperature and precipitation projections across the Alpine region [396]. Likewise, various bias-correction methods can give rise to large uncertainty (e.g., [212]).

This section compares the uncertainty range of the CH2018 climate projections (Chapter 4.4 and Chapter 4.5) to other quantifications of uncertainty based either on other data sources or on other methods in the processing chain. The RCM-based projections are compared to the driving GCMs to measure the effect of dynamical downscaling on the climate change signal. Precisely how the set of 12 GCMs used for dynamical downscaling relates to the uncertainty from the much larger GCM set of CMIP5 models used in IPCC AR5 (38 GCMs) is also investigated [168]. To assess the consistency of the model-based projections with the localized projections of Chapter 5, the effect of quantile mapping as a bias-correction method is analyzed (without downscaling; Chapter 4.2). To isolate the effect of bias correction, quantile mapping applied at the model-grid level is considered, an approach that does not include an implicit downscaling step. Toward the end of the section, the question of uncertainty quantification from a fixed set of model projections and the effects of prior assumptions on the estimated uncertainty range are discussed. For this purpose, the empirical quantiles used for the CH2018 projections are compared to probabilistic estimates obtained with a Bayesian joint analysis of observed and simulated changes (Box 4.2).

4.7.1. Effect of dynamical downscaling

Dynamical downscaling with RCMs modifies the changes projected by the EURO-CORDEX GCMs (Figure 4.10), but in most cases the differences are small, in particular for the median values. For the median temperature change, the RCMs and EURO-CORDEX GCMs project a similar increase. The uncertainty range across models is reduced going from the EURO-CORDEX GCMs to the RCMs, mainly for the summer season. For the estimated median precipitation change, the RCM ensemble projects lower levels of summer drying. For the spring season, the weak precipitation reduction in the EURO-CORDEX GCMs turns into a small increase in the EURO-CORDEX RCMs. Consistent with the anti-correlation between temperature and precipitation projections in summer [101], dynamical downscaling results in less pronounced summer drying. This is in line with an analysis of the interrelation between RCM and GCM projections from the predecessor project ENSEMBLES [396]. However, the model ranges for EURO-CORDEX GCMs (12 GCMs) and EURO-CORDEX RCMs (21 RCM simulations) are not fully comparable due to the different ensemble sizes. Notably, the EURO-CORDEX GCM ensemble is too small to robustly estimate the 90 % quantile range.

4.7.2. Effect of selecting a set of GCMs

Generally speaking, the EURO-CORDEX GCM ensemble spans the range of the spread of the larger IPCC GCM ensemble (Figure 4.10); however, the model range in EURO-CORDEX GCMs is still somewhat smaller, depending on the season and variable considered. No consistent effect on the median projections for the temperature changes can be discerned. Although the IPCC ensemble median indicates a less pronounced wettening in winter and a less pronounced drying in summer in comparison to the EURO-CORDEX median, the two agree remarkably well overall.

A number of studies have attributed the large uncertainty in regional temperature and precipitation projections over central Europe to uncertainty originating from large-scale circulation changes (e.g., [353, 390]), especially during the winter [87, 99]. This implies a large sensitivity of model-based uncertainty estimates to the choice of the GCMs used as boundary conditions. This may explain in part the smaller

uncertainty ranges for the EURO-CORDEX GCMs in temperature and precipitation, along with the reduced number of GCMs. A number of IPCC GCMs lie outside the range spanned by the EURO-CORDEX GCMs at both extremes. In a bivariate perspective, Zubler et al. (2016) [396] showed that there is a clustering of GCMs with two centers: one large group of models clustering around zero precipitation change and a warming between 3°C and 5 °C, and a second (smaller) group consisting predominantly of simulations from the CSIRO model with a warming of around 8 °C and a precipitation reduction of about 30 - 40 %. At this point, observations cannot rule out either of these outcomes by constraining the range of models.

4.7.3. Effect of bias correction with quantile mapping

The effect of applying quantile mapping to the CH2018 RCM simulations on the projected changes is in general quite small and does not exhibit a consistent tendency (Figure 4.11). The largest effects on both the median and the uncertainty range are seen in the winter and summer seasons. In winter, quantile mapping lowers the upper bound of the uncertainty range in temperature change, whereas the median and lower uncertainty estimate are hardly affected at all. This is most prominently seen for the two Alpine regions and for southern Switzerland. For precipitation, quantile mapping increases the median change signal in all regions and tends to inflate the uncertainty. In summer, two opposing effects can be observed for temperature: The upper end of the uncertainty range is raised in the two Alpine regions and lowered elsewhere. For precipitation, the upper bound of the uncertainty is raised, whereas the median remains largely unaffected. The fact that the upper bound of the uncertainty range is more strongly affected than the lower bound is likely related to the non-linear correction of the upper quantiles that often occurs in quantile mapping (Chapter 5). This effect is strongest for the end-of-century period in which the models simulate conditions that systematically exceed the currently observed climatic range. Further details on the modification of the raw models' change signals by quantile mapping are provided in Chapter 5.3.

4.7.4. Effects of different uncertainty quantifications

Uncertainty estimates can be derived from an ensemble of climate model simulations in various ways. Here, uncertainty is quantified by simply calculating empirical quantiles across the set of simulations. It is implicitly assumed that each of the 21 simulations is equally credible and informative. After the strongly interdependent models are removed (see Chapter 4.2.4.), no further weighting is assigned. A number of methods exist to estimate probabilities from multi-model or perturbed physics ensembles [338, 240, 45, 194, 292]. These offer the potential to explore the ensemble more fully and permit calibration based on observations of the climate mean state and trend, thereby improving the skill of the projection relative to a naive multi-model mean. However, there is no consensus on how such weights should best be obtained, and it is possible that more information will be lost by inappropriate weighting than could be gained by optimum weighting [369], in particular when trends are due to internal variability and the number of models is small. Another implicit assumption of the approach followed here is that systematic model biases do not change over time. This is a common assumption that has also been applied, e.g., by the IPCC. More sophisticated methods to quantify uncertainties from ensembles are the focus of ongoing research.

Several alternative methods to quantify model uncertainty and natural variability in climate projections were applied in earlier scenario assessments in Switzerland. In the report "Klimaänderung und die Schweiz 2050" (CH2007; [246]), uncertainties on the regional scale were estimated using probability density functions fitted to RCM simulations and multiplied by uncertainty estimates for global mean change taken from the literature (cf. [122]). In CH2011, the algorithm of Buser et al. (2009) [45] was applied. This method combines observational data with model simulations of past and future climate in a Bayesian framework and yields probabilistic projections [99]. These projections were, however, not interpreted in a probabilistic sense, as uncertainty estimates derived from model data alone are often overconfident [56]. To account for process understanding and observed evidence, as well as model limitations, a more conservative interpretation of the uncertainty range based on (ultimately subjective) expert judgment was provided.

Here, the results of Chapter 4.4 and Chapter 4.5 are compared to the uncertainty quantification using a Bayesian multi-model combination algorithm (Box 4.2). This algorithm allows for bias changes, takes into

account the dependence between RCMs and its drivers, and accounts for internal variability. The Bayesian uncertainty ranges are, however, not fully comparable to the CH2018 empirical quantile ranges: The latter indicates the model spread based on an equal treatment of all models, whereas the Bayesian method considers changes that are common to a majority of models as an indication of the true change (Box 4.2).

The Bayesian median estimates of temperature are systematically lower than the raw RCM medians in all seasons and regions (Figure 4.11). For winter and spring, the difference is about 0.5 °C, and the Bayesian medians are close to the lower bound of the RCM range. Additionally, the Bayesian estimates indicate a smaller uncertainty range. This is especially prominent in the summer and autumn seasons, where the uncertainty toward higher values is reduced, while the lower bound remains similar to that of the raw ensemble. For precipitation, the median estimate is comparable between the three different uncertainty quantifications. However, the Bayesian uncertainty range is somewhat enlarged in winter and markedly reduced in summer; these opposing effects appear to cancel out in the transition seasons, where they are very close to the raw RCM ranges.

From a qualitative perspective, a comparison of the CH2018 projections with other estimates corroborates the findings in Chapter 4.4 and Chapter 4.5 for the end of the century in Switzerland, assuming the RCP8.5 emission scenario:

- A substantial increase in seasonal temperatures, with the median varying between 2.5 °C to 5.5 °C depending on the method and source.
- A median summer drying varying between -23 % to -9 % depending on the method, source, and region.
- A clear tendency toward an increase in winter mean precipitation.

The EURO-CORDEX RCMs provide the best available evidence for future climate change in Switzerland, and the results of these models are generally supported by the Bayesian method and the results from the GCMs. Confidence is lower for the summer season, for which the projections across models differ more. From the similarity of quantile-mapped and raw projections, we conclude that this procedure can be applied to bias-correct climate model data, but more care needs to be taken when interpreting winter and summer changes in bias-corrected data.

Unless otherwise noted, the 90 % ranges for seasonal means determined empirically from the RCMs is interpreted as a “likely” range, implying at least a 66 % probability (as opposed to “very likely”, at least 90 %) of reality falling in between. This increases the estimated uncertainty range over the raw model spread for a given percentile range and accounts for potential structural biases in many or all models. Similar to and consistent with CH2011, the 5th and 95th percentiles can then be used as illustrative upper and lower estimates when exploring the uncertainties of models and variability. This approach – using empirically determined quantiles from the RCMs but assigning a lower likelihood or confidence – is consistent with the IPCC method, in which the two-standard-deviation range is interpreted as “likely”. The advantage of this approach is that various quantities (e.g., changes in extremes) can be determined directly from the ensemble in a consistent way (to the degree that the models are physically consistent). The alternative of scaling or correcting the raw model range before estimating quantiles may be possible for some quantities (see Box 4.2) but would be extremely challenging for others – for example, extremes, as there is no consensus on how to build a statistical model of the biases in these quantities.

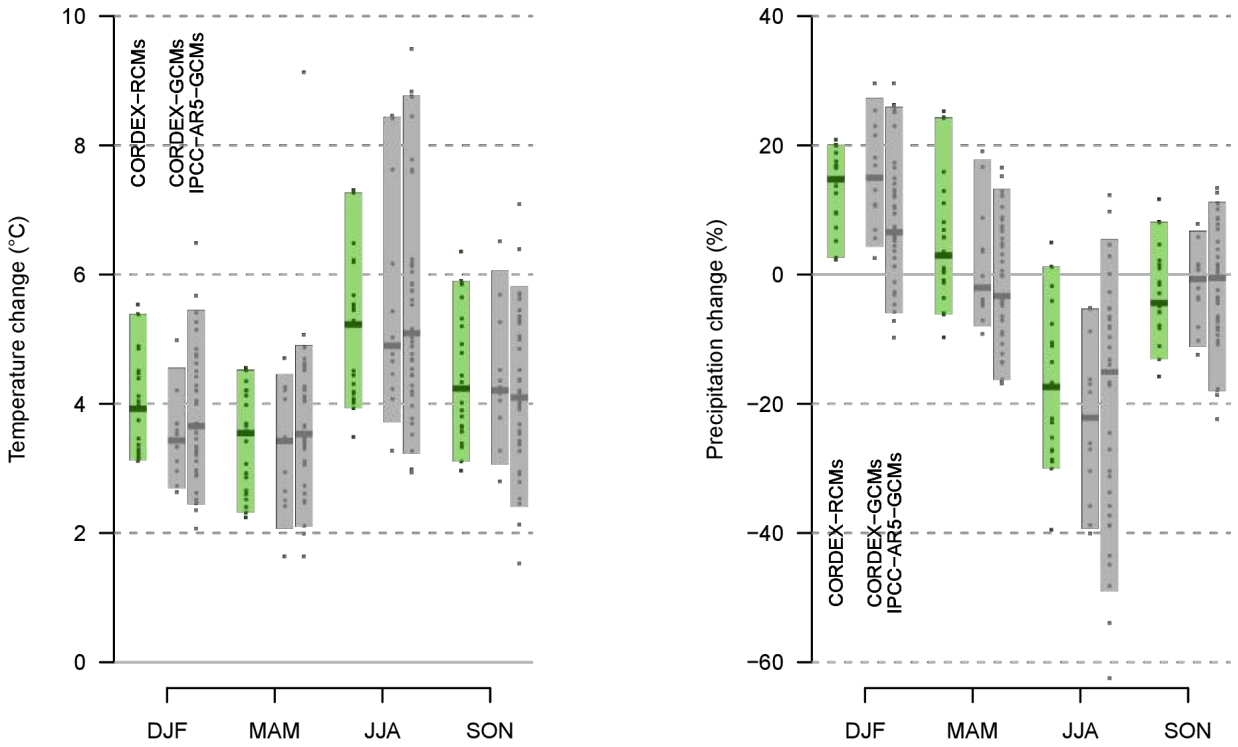

Figure 4.10. Temperature change (°C, left) and relative precipitation change (%, right) for Switzerland projected for the period around 2085 and RCP8.5, based on various model ensembles: the RCM-based CH2018 multi-model projections ("CORDEX-RCMs"), GCM simulations used for EURO-CORDEX ("CORDEX-GCMs"), and GCM simulations used for AR5 of IPCC ("IPCC-AR5-GCMs"). Quantile-based uncertainty ranges (colored bars) and individual models (points) are shown.

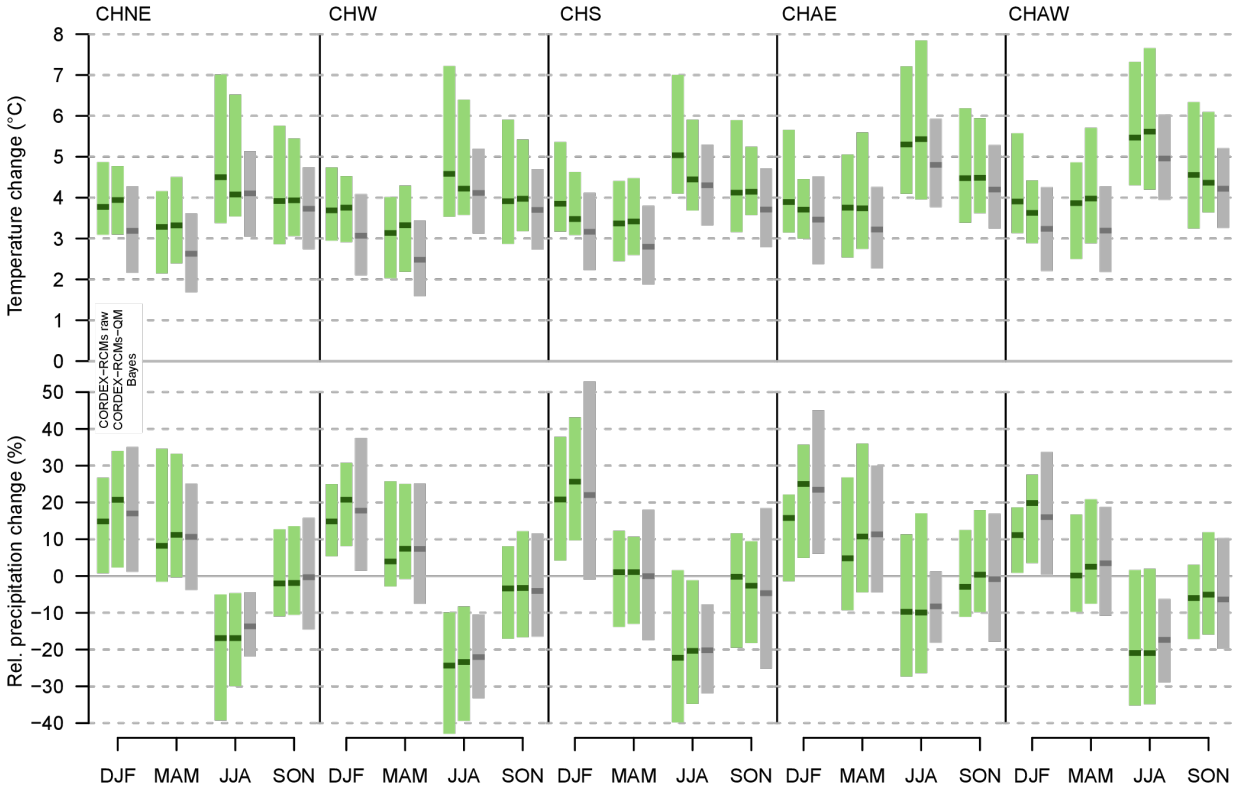

Figure 4.11. Top: Seasonal mean near-surface temperature change (°C) for the five CH2018 regions projected for the period around 2085 and RCP8.5, based on the CORDEX-RCM ensemble and different bias-correction methods: a combination of EUR-11 and EUR-44 RCM-GCM simulations ("CORDEX-RCMs raw"), bias-corrected RCM-GCM simulations using quantile mapping ("CORDEX-RCMs_QM"), and the output of a Bayesian Hierarchical Model ("Bayes"). Bottom: As top, but for seasonal mean precipitation change (%).

4.7.5. Effect of RCM selection

Kotlarski et al. (2014) [197] performed an evaluation of the RCMs used in the EURO-CORDE, finding that the various RCMs are able to capture the main features of the European climate. However, the authors also noted that the RCMs tend to have a cold and wet bias over large parts of Europe for most seasons, as well as a warm and dry bias over southern/southeastern Europe. Several new RCM simulations have subsequently been included in the EURO-CORDEX ensemble. The temperature and precipitation biases from the different RCMs are shown in Appendix 1.8. For each RCM, an ERA-Interim-driven simulation (1989 - 2008) is performed, as well as a historical evaluation simulation driven by the respective GCM (1971 - 2005). To calculate the biases, the E-OBS dataset [150] is used. The bias for the ERA-Interim-driven simulations exhibits the same features as in Kotlarski et al. (2014) [197]: The models tend to have a cold and wet bias over most parts of Europe during the colder months, and a warmer and dryer bias in the warmer months, mostly in south/southeastern Europe. For the GCM-driven historical simulations, the magnitudes of the biases are larger than for the ERA-Interim-driven simulations. Many of the same bias characteristics are seen for the historical simulation, with some exceptions. The summer warm and dry bias is strongest in the simulations driven by the GCM MOHC-HadGEM-ES; the other simulations feature a weaker warm and dry bias or a cold and wet bias.

As discussed above, when only a subset of GCMs are selected for use in dynamical downscaling over Europe, not all of the possible future projections are included in the regional climate estimates. Indeed, not all the GCMs that have been downscaled over Europe are included in the CH2018 ensemble (Chapter 4.2). The exclusion of one GCM-RCM model chain was due to errors in the forcing fields found in the CNRM-CERFACS-CNRM model, in addition to a very strong wet summer bias over southern Europe for the RCMs driven by this particular GCM. By not including the RCMs driven by the CNRM-CERFACS-CNRM, a total of 9 RCM simulations were removed from the model ensemble. In this section, we investigate the effect on the results when these 9 RCM simulations are included. Figure 4.12 compares the estimated changes in temperature and precipitation from the RCM models used for the CH2018 results to the results when the 9 RCM simulations driven by the CNRM-CERFACS-CNRM are included. The main difference is found for the projected summer precipitation. When the RCMs driven by the CNRM-CERFACS-CNRM model are included, the median summer drying is reduced, and even an increase in summer precipitation over Switzerland is possible. Notably, when the CNRM-CERFACS-CNRM simulations are not included, the empirical quantiles are more consistent with the results from the Bayesian analysis (Figure 4.11). The Bayesian method essentially downweights the models with a large bias and consequently results in a more narrow range with a robust projected decrease in summer precipitation, which is similar to the projected change results without the CNRM-driven simulations in the model ensemble (see Figure 4.12).

4.7.6. Conclusion and discussion

Uncertainty in climate simulations originates from model uncertainty, internal variability, and scenario uncertainty ([147]; Chapter 2.7). For the RCP2.6 scenario, the median and range of the projected mean precipitation change are more or less the same over the course of the century. The lack of a clear trend in mean precipitation in RCP2.6 suggests that these uncertainties mainly represent internal variability, whereas the trend in RCP8.5 is coupled with an increase in model spread that is due to climate model uncertainty (Figure 4.5). The near-term projections do not vary much between the different scenarios. Hence, most of the near-term climate uncertainty arises from the decadal variability, not from the choice of emission scenario.

In a context of risk assessment for adaptation, the upper bound of the temperature range for the non-mitigation scenario RCP8.5 is arguably the most relevant case to consider, since the largest impacts are expected with this scenario. Conversely, in the context of quantifying the benefits of mitigation actions, the differences between the central estimates of the reference scenario RCP8.5 and the mitigation scenario RCP2.6 are more informative. In the context of the temperature targets of 1.5 °C and 2 °C, the scaling to these targets sheds light on the implications of such a global temperature change for Switzerland (Box 4.1). For the

most part, the temperature targets fall within the projected temperatures for RCP2.6. This corresponds to the assessment of RCP2.6 as a stringent mitigation scenario with a probability of staying below 2 °C of 66 % or more [169]. For communication purposes, the projections based on this mitigation scenario will be used as an analog for describing a future climate that is 1.5 °C to 2 °C warmer than pre-industrial times.

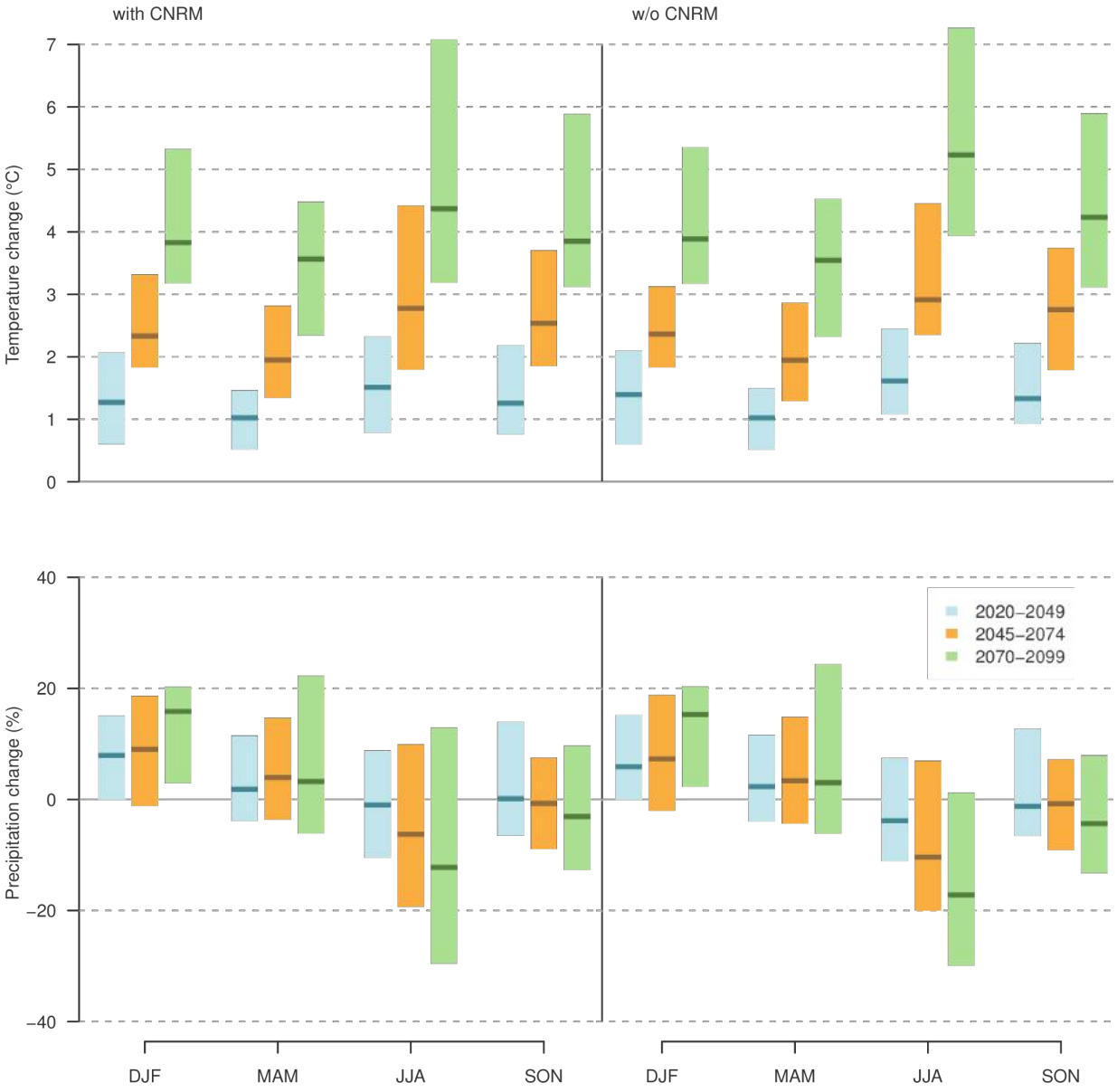

Figure 4.12. Temperature change (°C, top) and relative precipitation change (%, bottom) for Switzerland projected for the period centered around 2085 and RCP8.5, based on two different model ensembles: the full CH2018 multi-model projections (right), and the CH2018 multi-model projections when the RCM simulations driven by the GCM CNRM-CERFACS-CNRM-CM5 are included (left). See Table 4.1 for the list of the different model simulations.

Box 4.2: Bayesian probabilistic estimates

The Bayesian estimates shown in Chapter 4.7 are probabilistic projections of seasonal mean changes in temperature and precipitation obtained from the CH2018 multi-model set (shown by circles in Table 4.1) by means of a statistical method similar to the one used by Kerkhoff et al.(2015) [185]. This method assumes that the seasonal means of observations and of outputs from a multi-model ensemble of climate simulations are independent random draws from a normal distribution whose expected value and standard deviation change slowly over time. It is thus effectively making an "indistinguishable world" assumption for the multidecadal variability and a "truth plus error" assumption [8] with a wide prior for the climatological signal. The expected value corresponds to temperature or precipitation in a typical year, and the standard deviation quantifies how much the actual value can deviate from this expected value. The standard deviation therefore also describes the natural variability from year to year. Based on the available data and some prior assumptions, one can then estimate these expected values and standard deviations and quantify the uncertainty of these estimates. Similarly, one can estimate the change in the average of observations during a future 30-year period compared to a reference period in the past and compute ranges of this change for a given coverage probability.

The underlying assumptions restrict the degrees of freedom for the expected values and standard deviations as a function of time: Standard deviations are assumed to change linearly with time on the logarithmic scale. Expected values are assumed to consist of a smooth trend and decadal variations that change more quickly. We use three degrees of freedom for the trend and four degrees of freedom for decadal variations. In addition, there are soft constraints in the form of prior distributions, which express the belief that differences between expected values and standard deviations of model outputs on the one hand and observations on the other hand will not be too large.

Like any multi-model ensemble, the EURO-CORDEX ensemble upon which this report is based exhibits biases, i.e., systematic differences between simulated model output and observations. By using the raw model changes, one makes an implicit assumption that the bias is constant over time and thus cancels out when the change relative to a reference period is computed. An alternative to this "constant bias" assumption is the "constant relation" assumption [45], which states that models over- or underestimate changes in the long-term mean by the same factor by which they over- or underestimate interannual variability. The Bayesian method includes a continuous interpolation between "constant bias" and "constant relation" and also allows additional bias changes over time.

Because biases are allowed to change over time, and because future observations are unknown, there is a basic identifiability problem: Any change in the future model output can be considered either as a true climate change or simply as an increasing deviation of the model from the truth. To resolve this identifiability issue, we use informative priors for how large the change in the systematic difference between a model and the observations can be. Although these priors still leave considerable freedom to each model, they tend to consider changes that are common to a majority of models as indications of true changes.

The method developed by Kerkhoff et al. (2015) [185] is similar to the methods of Buser et al. (2009) and Fischer et al. (2011) [45, 99] but incorporates several improvements that increase the flexibility and coherence of the method. First, the constant relation assumption after Buser et al. (2010) [46] is included in the analysis. Second, the dependence between an RCM and its driving GCM is explicitly taken into account, whereas Fischer et al. (2011) [99] averaged all RCMs driven by the same GCM. Third, decadal variability and smooth trends are estimated differently. Fourth, the time series of all observations and model outputs is considered instead of two or more time slices of 20 - 30 years. For this report, a modification of the method described in Kerkhoff et al. (2015) [185] that gives more weight to RCMs over GCMs was used.

5. Localized projections

Summary

The climate models employed in CH2018 have a horizontal resolution of 12 or 50 kilometers and are subject to systematic biases. This prevents their direct applicability in climate impact assessments that require accuracy and local representativeness of the climate data. Applying quantile mapping (QM), an established method that incorporates both a statistical downscaling and bias correction step, localized and bias-corrected projections for Switzerland have been produced. These projections are available to end-users and facilitate the assessment of climate change and its impacts at the local scale.

- Three QM datasets have been generated: *QM to stations* targets the scale of individual weather stations, whereas *QM to high-resolution grid* provides projections on a regular 2-km grid. Both products implicitly include a downscaling step and are publicly available for impact applications (the corresponding datasets DAILY-LOCAL and DAILY-GRIDDED are described in Chapter 9). A third dataset is a bias-corrected version of the raw simulations at their original spatial resolution.
- Projections at stations for a complete set of seven meteorological variables are available for 58 stations at daily resolution for the period 1981 to 2099. Depending on the variable considered, more stations are available (e.g. up to 399 for precipitation). Gridded data at 2-km horizontal and daily temporal resolution for the period 1981 to 2099 are available for four variables. In both cases, all climate model chains considered in CH2018 that provide data for the respective variable of interest are covered.
- The projected localized climate change signals are in broad agreement with the raw climate model simulations described in Chapter 4 and Chapter 6. This agreement includes geographical and seasonal variations in the magnitude of change signals for different variables as well as differences among the three forcing scenarios. It also includes model uncertainties (as discussed in Chapter 4) and the chance that future climate change might lie outside the uncertainty range provided by the model ensemble at hand.
- A QM evaluation yields good skill for the present-day climate. However, QM can modify the raw models' climate change signals to some extent. It does not alter the sign of the projected change. This is in line with evidence from the existing scientific literature.
- Although multivariate relationships are not explicitly corrected, univariate QM can represent multivariate indices, as illustrated by the example of a heat stress index (the wet bulb temperature, a combination of temperature and humidity).
- A summary of the limitations and uncertainties of the localized projections is provided. Major uncertainties concern the stationarity of the model bias, climate extremes, and the spatio-temporal correlation in the data products. It is recommended that end-users evaluate the uncertainties and potential limitations for each individual application.

5.1. Introduction

The EURO-CORDEX simulations employed in CH2018 provide data at a spatial resolution of 12 or 50 km (Chapter 2.1). The high-resolution 12-km data in particular represent a considerable added value with respect to the driving GCM and to lower-resolution RCM data [344]. However, in most cases, the direct use of the model output for climate impact assessment and adaptation is not possible due to:

1. the scale gap between the RCM output – which must be interpreted as a spatial average over the respective grid cell's area – and the spatial scale of the impact model applied (often a specific weather station), and
2. the systematic biases inherent to RCM output [184, 197, 326, 335] that would directly translate into biased results of an impact model.

To overcome these limitations, a large number of statistical downscaling (SD) and bias-correction (BC) approaches have been developed [118, 212, 375, 376, 216].

These approaches include the well-established *delta change* method (also referred to as the *change factor* or *perturbation* method), which was employed in the previous Swiss climate scenarios CH2011 [32]. In this approach, a climate change signal ("delta") is computed by comparing raw climate model output for a future scenario and a historical reference period. In a second step, the delta is used to scale observational time series in either an additive or a multiplicative manner. This yields time series at the spatio-temporal scale of the underlying observations for the future period (Figure 5.2, upper part).

The advantages of delta change are its easy implementation and robustness, the possibility of obtaining spatially consistent multi-site scenario series (based on the observed record at multiple sites), and its inter-variable consistency (based on the observed record of several variables at a given site). However, the method is subject to a number of assumptions and limitations. Several of these are illustrated in Figure 5.1, middle panel, for the example of the annual mean temperature series at the Zurich/Fluntern station. The observed record in the reference period (black line) indicates a 30-year annual mean temperature of about 9.4 °C and a slight positive trend. Delta change-based scenarios for three different RCMs are obtained by extracting the simulated climate change signals for annual mean temperature between the reference and the scenario period for the grid cells covering Zurich/Fluntern and by adding this signal to the observed time series (colored lines). The three resulting scenario series have an identical temporal structure that, apart from an offset, mimics the temporal structure of the observations. Potential changes in the temporal structure that might actually be simulated by the underlying RCMs are disregarded by delta change, as are possible changes in the overall interannual variability or in extremes. Furthermore, delta change is a time slice-based approach that does not provide information for times between the reference period and the scenario period. Transient time series can in principle be produced, but would require the application of additional gap-filling methods.

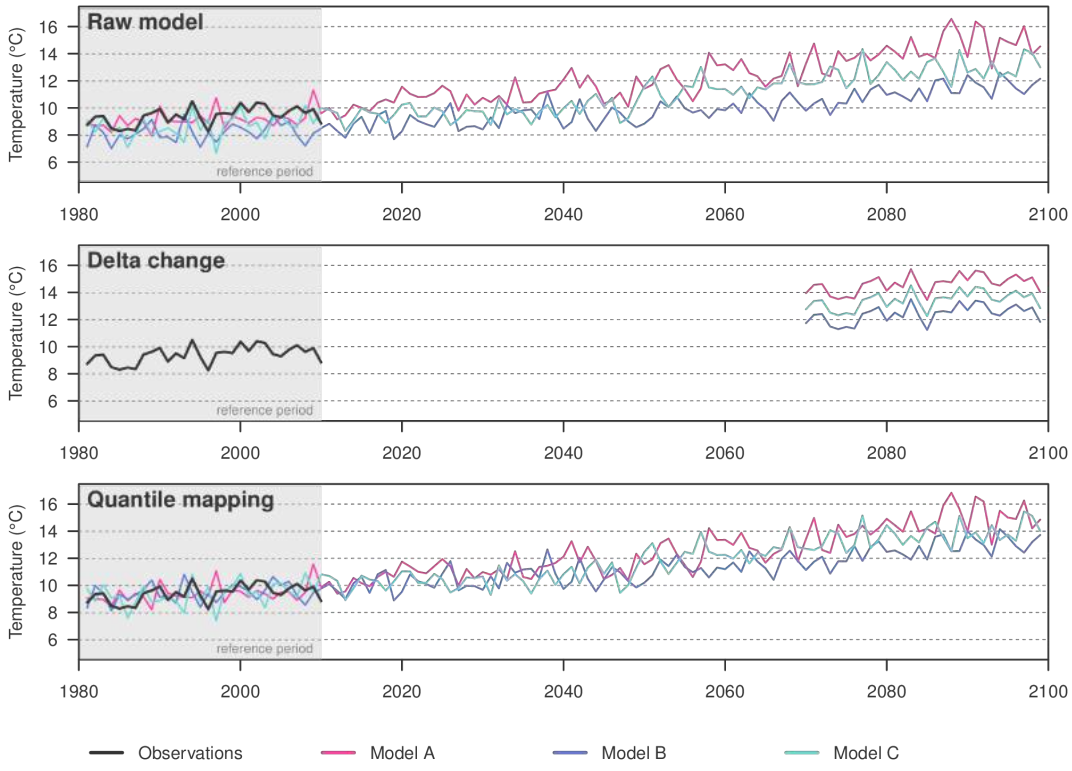

Figure 5.1. Comparison of delta change and quantile mapping for the case of annual mean temperature at the Zurich/Fluntern (SMA) station and for three EURO-CORDEX model chains (referred to as A, B, and C). Top: Observations and raw model output. Middle: Delta-change method, consisting of a simple scaling of the observed time series with the annual mean temperature-change signal between the reference and the scenario period. Bottom: Quantile mapping.

Within CH2018, in order to produce climate projections at a local scale, delta change is replaced by a **bias-correction** approach: quantile mapping (QM; see Chapter 5.2). Bias-correction techniques, also referred to as *model output statistics* (*MOS*), were originally developed in the context of numerical weather forecasting and relate a given variable simulated by a numerical (weather or climate) model to observations of the same variable within a common reference period. Note that in a pure forecasting context, the term MOS has a narrower definition and generally refers to regression methods [394]. In this manner, the simulated values are corrected toward the observations, and systematic model biases are partially removed. In a climate change context, the so-called *correction function* established in the historical calibration period can then be applied to the simulated future time series to produce de-biased scenario time series (Figure 5.2).

Depending on the nature and the temporal resolution of the correction function, different kinds of model biases can be removed (e.g., the simple removal of a temporal mean bias). Bias correction, however, only removes certain bias characteristics (e.g., a bias in the mean); the resulting de-biased time series is typically subject to remaining deficiencies (e.g., biases in the variance or in the temporal sequence). *Bias-correction* approaches are therefore sometimes also referred to as *bias adjustment*, highlighting the fact that biases are adjusted but not entirely removed and might in fact be adjusted toward incorrect, uncertain, or non-representative observations. However, the first notation is used throughout the present report. *Bias correction* as such corrects for systematic model biases but – as long as the reference observations reflect the same spatial scale as the model output – does not produce downscaled output. If, however, the reference observations reflect a smaller spatial scale (for instance. an individual weather station), *bias correction* is implicitly associated with a downscaling step and provides output at higher spatial resolution than the original (weather or climate) model output. This additional downscaling step involves specific assumptions and is associated with potential risks and limitations (Chapter 5.7, [215]).

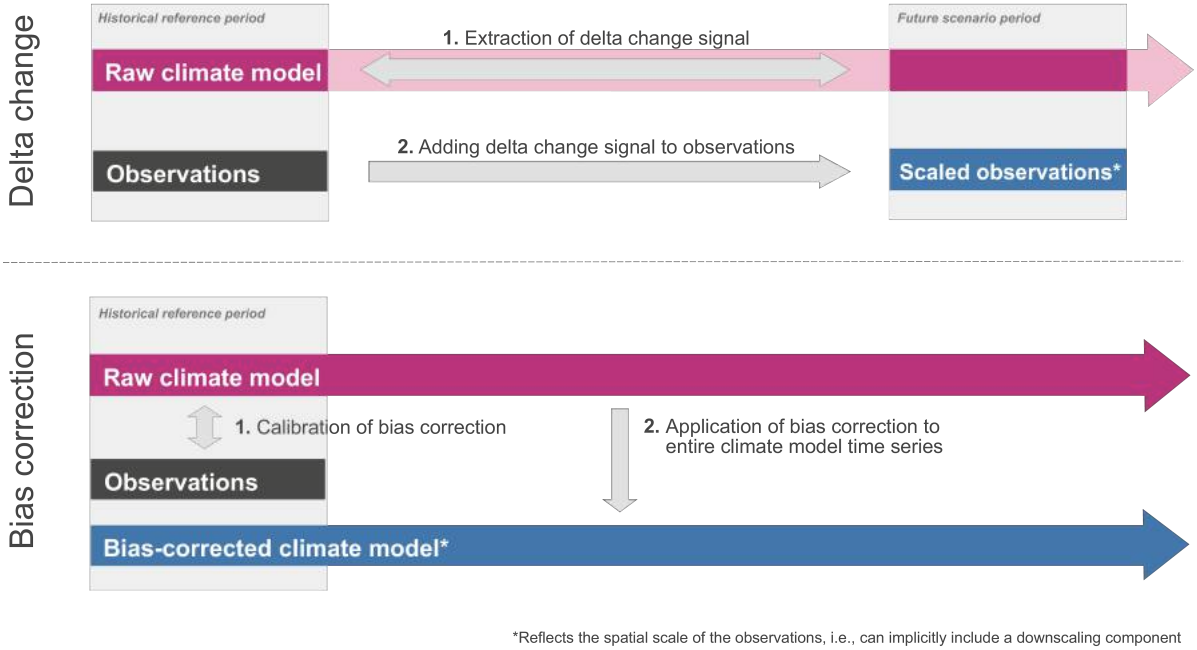

Figure 5.2. Methodological overview of the delta-change (top) and bias-correction approaches (bottom). Blue color: The final climate scenario products that can be employed, for instance, in climate change impact modeling. These reflect the spatial scale of the observations (i.e., they may contain an implicit downscaling component).

5.2. Methods

In CH2018, a variant of quantile mapping (QM) is employed as a bias-correction method (see also [95]). QM has become increasingly popular in recent years and is widely used for purposes of (1) correcting systematic biases in climate model simulations and (2) bridging the scale gap between coarse-resolution climate model output and the site scale. QM originates from the empirical transformation introduced by Panofsky and Brier (1968) [254] and corrects for biases in the distribution of a simulated variable (the *predictor*) by

comparing raw model output to observations (the *predictand*; see Figure 5.3). Simulated and observed distributions are approximately matched by establishing a quantile-dependent correction function that translates simulated quantiles into their observed counterparts. This function is then used to translate a transient simulated time series into a bias-corrected series with a distribution representative of the observed one. The implicit assumption of QM is that a climate model can accurately project ranked categories of the variable of interest (i.e., quantiles) but not its actual values [87]. Simulated and observed quantiles can either be based on the full empirical distribution (non-parametric implementation; e.g., [87, 339]) or on a fitted theoretical distribution (parametric implementation; e.g., [265]).

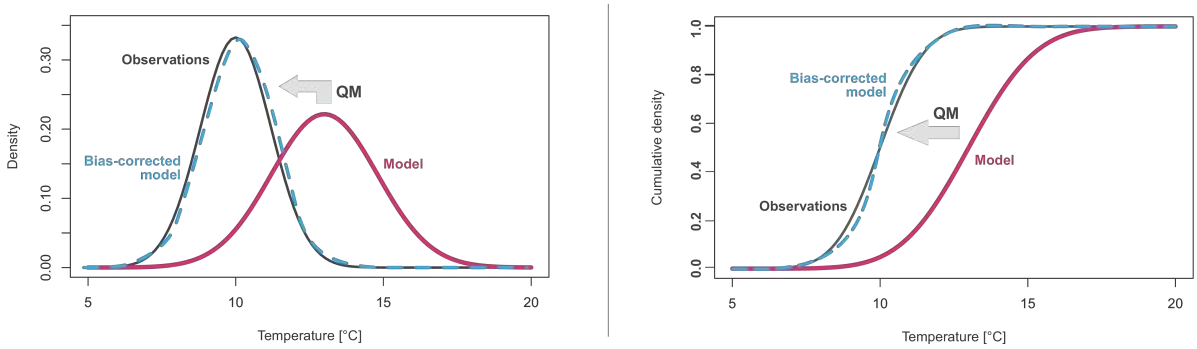

Figure 5.3. The nature of QM (illustrative example): A biased simulated distribution of the predictor (red) is corrected toward an observed distribution of the predictand (black). The raw simulated distribution is subject to both a bias in the mean and a bias in variance. Note that the resulting bias-corrected distribution (blue) typically only approximates the observed one but is not identical to it. This is due to approximations in the QM setup (such as the consideration of a limited number of quantiles during calibration and linear interpolation in between) that also avoid over-parameterizations. Left: Example based on the probability density function (PDF). Right: Example based on the cumulative distribution function (CDF).

A large number of recent studies have documented the applicability and performance of QM in a downscaling context, often finding it to be similar or superior to other statistical downscaling approaches [34, 138, 340, 339, 214, 139]. Several studies have explicitly applied QM as an interface between coarse-resolution and potentially biased climate model output and subsequent climate-impact models [97, 144, 270, 385]. Although QM does not explicitly correct for biased temporal variability in climate model simulations [2], Rajczak et al. (2016) [271] showed that biases in wet day-dry day transition probabilities and in multi-day indices can be removed. Furthermore, Wilcke et al. (2017) [377] found that the separate application of QM to several meteorological variables preserves the inter-variable dependencies represented in the climate model output (although it does not necessarily correct for biased interdependencies). Despite these promising results, limitations regarding the applicability of QM in a downscaling context remain [215]. This is especially true for the attractive property of including both a bias-correction and a downscaling component (depending on the spatial scale of the predictand). The latter adds potential uncertainties and limitations that should be carefully considered and evaluated for any prospective application (Chapter 5.7). In addition, QM can to some extent modify the climate change signal of raw RCM data (e.g., [133]). This feature could be advantageous in the case of non-stationary model biases, but might to some extent be a statistical artifact (see below).

The specific QM variant employed in CH2018 is a non-parametric empirical implementation that has previously been extensively validated [271, 174, 95] and has also been applied to generate input at the site scale for climate-impact studies across Switzerland [270]. In this approach, a simulated value x is corrected toward a value y according to

$$y := F_O^{-1}(F_M(x)),$$

with F_O and F_M denoting the empirical cumulative distribution function of observed and modeled values in the historical calibration period (here, typically 1981 - 2010), respectively, and F_O^{-1} denoting the inverse

of the observational distribution function. The corrected value y thus corresponds to the observed value with the same quantile in the observed distribution as the modeled value x in the modeled distribution. This transformation is accomplished by applying an additive correction function g to the modeled value x:

$$y = x + g(x)$$

The correction function g, in turn, is explicitly and separately derived for 99 percentiles (1st to 99th percentile; $p_{1..99}$) of the modeled distribution in the calibration period according to

$$g(p_i) = F_O^{-1}(F_M(p_i)) - p_i \text{ with } i \in [1..99]$$

The use of 99 percentiles avoids overfitting of the correction function (with respect to, for instance, the use of all empirical quantiles) and has been shown to yield robust results in cross-validation exercises (e.g., [174]). $g(x)$ for an arbitrary simulated value x that does not necessarily correspond to one of the 99th percentiles $p_{1..99}$ is obtained by linear interpolation of the correction function for the adjacent lower p_{low} and upper p_{up} percentiles. Values of x smaller than the 1st percentile of the simulated distribution ($x < p_1$) and larger than the 99th percentile ($x > p_{99}$) are corrected according to the correction function obtained for the 1st and 99th percentile, respectively (constant extrapolation of the correction function). This is a straightforward practice that has been proven to be of similar or even superior performance compared to other, often more complex, extrapolation methods [174]. In this respect, note that, especially for temperature, cases in which such a correction is applied occur frequently in transient climate change scenarios as the climate warms and simulated daily temperatures often exceed present-day records. It should also be noted that the correction function g can strongly depend on the quantile considered, implying different corrections for different parts of the simulated distribution (non-constant correction function). This reflects intensity-dependent climate model biases – for instance, the fact that over parts of the European continent, climate models show positive summer temperature biases that increase with temperature (i.e., larger positive biases for higher temperatures; [58, 31]).

Because the magnitude and direction of climate model biases often depend on the season [197], the correction function g is determined individually for each day of the year using information from a 91-day window centered on the respective day of interest (see also [270]). In the case of precipitation, g implicitly corrects for biases in the wet day frequency (*fre*), as long as it is overestimated by the model (which is typically the case [271]). If, however, *fre* is underestimated by the model, a frequency adaptation is carried out (see [174] for details) to ensure the correct representation of *fre*.

The nature of the resulting QM products, again for the example of annual mean temperatures at Zurich /Fluntern and three climate model chains, is illustrated in Figure 5.1, lower panel. By definition, the bias-corrected 30-year-averaged annual mean temperature in the reference period (grey shading) approximately matches the observed mean of about 9.4 °C. As is obvious from the upper panel, the model biases in mean temperature are corrected. Because the three climate models consist of RCMs that are driven by different free-running GCMs at their lateral boundaries, they are out of phase with one another in a temporal sense, and also out of phase with the observed record. These differences are an expression of natural climate variability and of the fact that the observed record is only one possible realization of the reference period's climate. For all three models, the constructed QM scenario time series is transient (i.e., it covers the entire simulated period 1981 - 2099). In the specific case shown, QM only slightly modifies the overall change signals of the raw models, and therefore the warming magnitudes and future temperature levels of the QM series are similar to those obtained from delta change. Model A shows the strongest warming and Model B the weakest. In contrast to delta change, however, QM is able to capture simulated changes in temporal variability. For example, Model A simulates an increase in interannual temperature variability by the end of the century, which is represented by the QM series. As a consequence, simulated changes in extreme conditions are also better captured by the bias-corrected product than by the delta-change approach.

5.2.1. CH2018 Quantile mapping variants and data products

In CH2018, the same QM implementation is employed in three variants, resulting in three bias-corrected data products at daily resolution (Figure 5.4). More specifically, the three variants differ with respect to the observational reference used for calibration and, as a consequence, with respect to their spatial representativeness. Furthermore, they cover different sets of meteorological variables. All variants are computed for the entire CORDEX RCM ensemble considered in CH2018 (Chapter 4.2). In order to obtain results on a standard date vector, the data of RCMs that internally use a 360- or 365-day calendar were converted to a Gregorian calendar prior to the application of QM. This was achieved by introducing days with missing values into the original model output, randomly distributed throughout the year. For 360-day models, 5 (for non-leap years) or 6 (for leap years) missing-value days were filled in; for 365-day models, one missing-value day was filled in per leap year. For a given GCM-RCM chain, these random dates are identical for all cases (i.e., for all QM variants and all variables), ensuring full temporal consistency between the QM variants and the individual variables within one variant.

QM to stations

This QM variant is the central bias-corrected CH2018 product available to users (the corresponding dataset DAILY-LOCAL is described in Chapter 9). It provides bias-corrected daily scenarios for meteorological stations in Switzerland. The QM reference (predictand) consists of observed station records in the period 1981 - 2010; the predictors are simulated time series of the RCM grid cell that covers the respective station. Here, QM is implicitly associated with a downscaling step. The data product covers four central variables (daily mean temperature, daily minimum temperature, daily maximum temperature, daily precipitation sum) plus three auxiliary variables (daily mean relative humidity, daily mean global radiation, daily mean wind speed). The latter elements are not validated in detail and mainly serve as additional input variables for impact models that explicitly compute the surface energy or water balance. QM is applied separately and independently to each of the seven variables. The number of available stations differs from variable to variable. For the purpose of heat stress projections (Chapter 5.3), QM to stations is also carried out for specific humidity.

QM on RCM grid

This product covers bias-corrected scenarios at the scale of the underlying RCMs – that is, at 12- or 50-km resolution. The reference observations are the gridded products presented in Chapter 2.6. Due to the restricted availability of the observational reference, the calibration period has a length of only 28 years (1981 - 2008). Because the predictor (RCM data) and the predictand (observations aggregated to the RCM grid) reflect the same spatial scale, the QM involves only a bias-correction component, no downscaling. The product covers all grid cells in the five CH2018 regions (Chapter 2.4) and the four variables of daily mean temperature, daily minimum temperature, daily maximum temperature, and precipitation. It is not provided to users by default but is employed for the uncertainty assessment (Chapter 4.7).

QM to high-resolution grid

This product employs 2-km observational grids for the Swiss domain as a reference (Chapter 2.6; the corresponding dataset DAILY-GRIDDED is described in Chapter 9). Prior to the application of QM, the simulated raw model data were bilinearly interpolated from the 12- or 50-km RCM resolution to the observational 2-km grid, and QM was carried out on a grid-cell-by-grid-cell basis. Because the resulting data product has a high spatial resolution of 2 km compared to the coarser RCM resolution, this QM variant is also associated with a downscaling component. The calibration period is 1981 - 2010. The product has been produced for the four meteorological variables of daily mean temperature, daily minimum temperature, daily maximum temperature, and precipitation. Like the observational reference, it exclusively covers the Swiss domain.

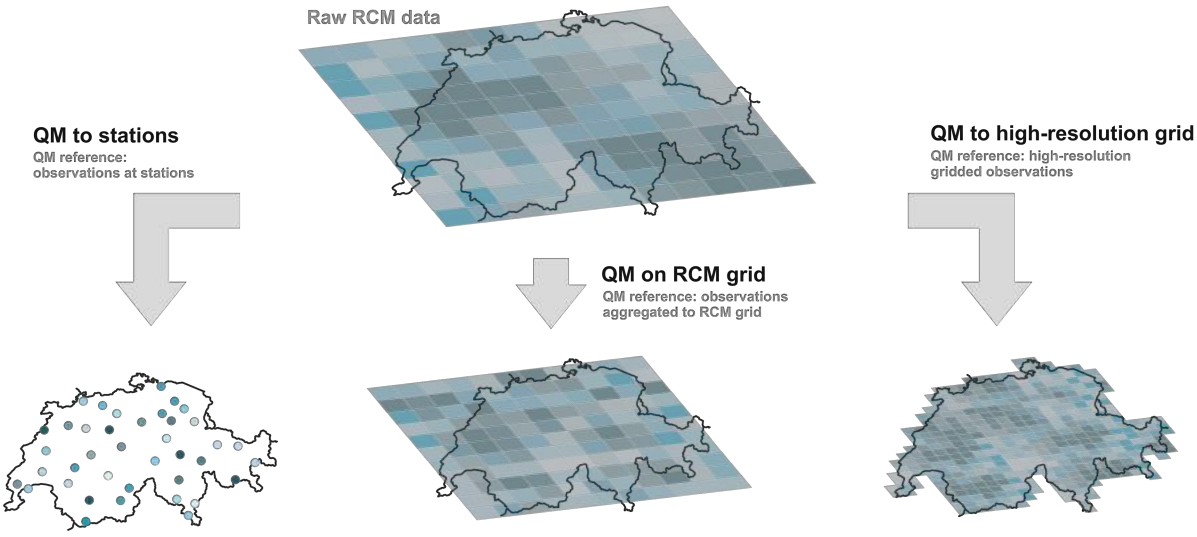

Figure 5.4. QM variants employed within CH2018 and related data products: QM to stations (left), QM on RCM grid (middle), QM to high-resolution grid (right). All variants have been produced for the entire CH2018 RCM ensemble but for different sets of meteorological variables.

5.2.2. Station selection for the bias-corrected scenarios at station scale

Two sets of stations are considered for the QM-to-stations product. The**full set** comprises all Swiss stations that fulfill certain criteria (see below); these scenarios are available for public download. The **illustrative set** represents a subset of the full set and is used for exemplary presentation of the results.

The criterion for a station to be considered in the full set is that daily measurements are available for at least 25 years out of the 30-year-long reference period 1981 - 2010, implying an overall availability of about 83 % of the daily data series. This criterion was applied separately for each of the seven meteorological variables considered, resulting in a variable-dependent number of stations. In most cases, this additionally implies the availability of at least 83 % of data for each individual day of the year. The resulting variable-dependent set of stations is shown in Figure 5.5 (small panels). The number of stations varies from 59 (for global radiation) to 399 (for precipitation).

The illustrative set (i.e., the stations presented in this report) is a subset of the full set, primarily consisting of those 58 stations for which the 83 % data availability criterion (see above) is fulfilled for all seven variables considered (red markers in Figure 5.5, lower right). Depending on the meteorological variable, this basic set of stations is complemented by additional stations from the climatologically important Swiss National Basic Climatological Network (Swiss NBCN; [19]; blue circles in Figure 5.5, lower right panel) that fulfill the 83 % availability criterion for the variable considered. Consequently, the total number of stations in the illustrative set is variable-dependent and ranges from 59 (global radiation) to 68 (mean temperature, minimum temperature, precipitation, relative humidity).

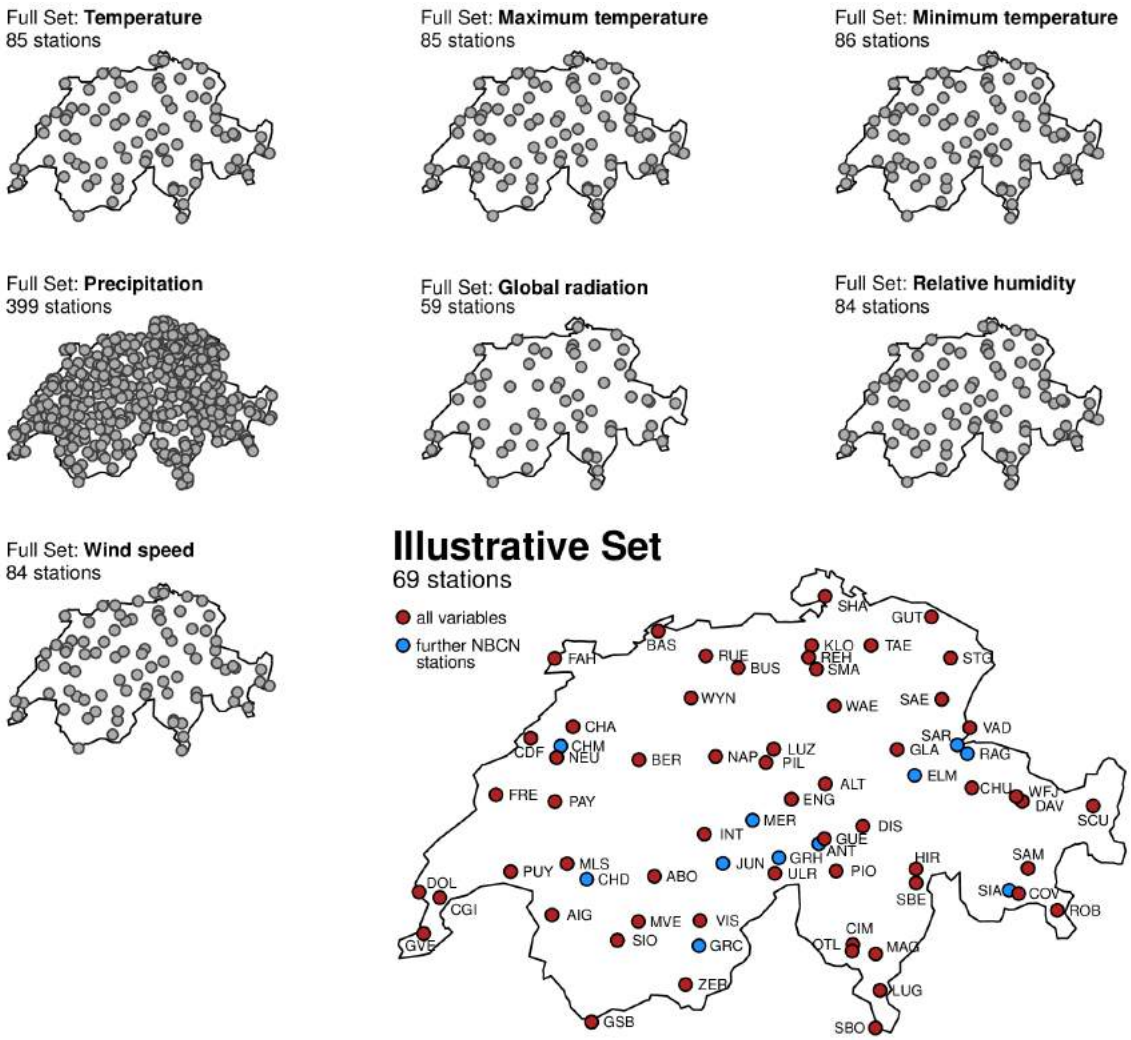

Figure 5.5. Stations covered by the CH2018 bias-corrected scenarios at the station scale. Small panels: Full set, which is available for download. Lower right: Illustrative set, which is considered in this report. For both sets, the size depends on the meteorological variable considered. The station abbreviations in the lower right panel refer to the internal station identifier (also provided in the downloadable datasets).

5.3. Evaluation

5.3.1. QM evaluation in the calibration period

In this section, an illustrative evaluation of seasonal mean temperature and precipitation in raw RCM output and in the quantile-mapped version at the station scale is presented (see [95] for a more detailed evaluation). Both raw RCM output, as represented by the simulated time series of the grid cell covering the respective station, and its station-based quantile-mapped counterpart (QM to stations) are considered. As an exemplary dataset, the ensemble mean of all RCP8.5 simulations is analyzed for all stations in the illustrative set (see above). The evaluation period is identical to the QM calibration period. Thus, certain aspects of this period's climate are represented by the quantile-mapped data by definition. Cross-validation assessments of QM with explicit separation of the calibration and validation periods are provided by, among others, [174, 271, 340].

Figure 5.6 presents the evaluation of seasonal mean temperature. When compared to observations, raw RCM output is subject to substantial biases of up to more than 10 °C (upper row). Especially in the Alpine area, pronounced negative biases are present in all seasons. In part, this systematic bias originates from the scale mismatch between the gridded RCM data representative of the grid cell mean elevation and the station measurements at different elevations. Hence, the large negative biases partially reflect the fact that most stations are located in valleys and at lower elevations than the overlying RCM grid cell. Such biases should

not be confused with systematic model biases at the grid cell scale. The application of QM effectively removes systematic biases (lower row). Although the evaluation is carried out in the QM calibration period itself, small biases of the QM product remain. This is because QM is applied with a 91-day moving window and, in order to avoid overfitting, is trained for 99th percentiles only, with linear interpolation of the correction function in between and constant extrapolation of the correction function below and above (see Chapter 5.2).

Similarly, the evaluation of seasonal mean precipitation sums Figure 5.7 yields considerable biases of raw RCM output that must also be partially attributed to the scale mismatch between gridded RCM data and the point-scale observational reference. For most stations, the raw RCM ensemble mean is subject to a wet bias that can amount to several millimeters per day (upper row). Again, QM effectively removes these systematic biases, and the remaining inaccuracies are generally smaller than 0.5 mm d^{-1} (lower row). In summer, the ensemble mean precipitation of the bias-corrected simulations is systematically smaller than the observed reference. In relative terms, these differences can exceed -10 %. Again, this is due to the approximate nature of the QM correction, as explained above.

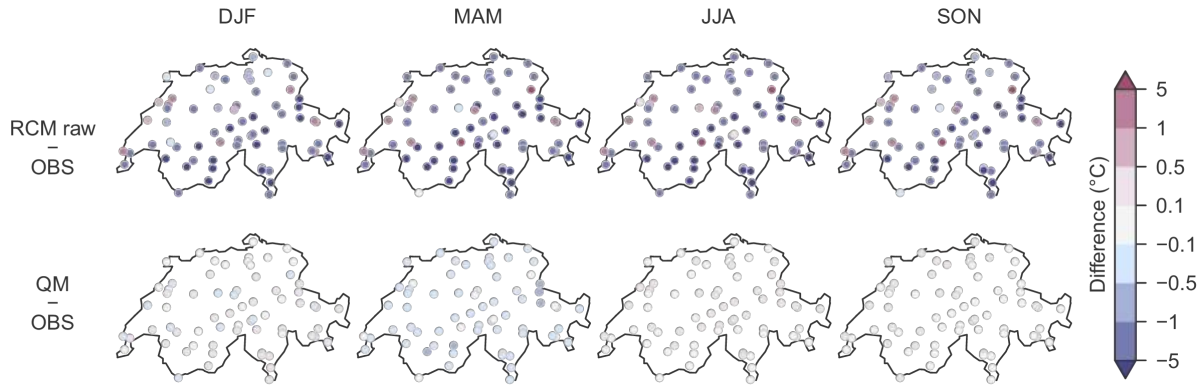

Figure 5.6. Biases in seasonal mean temperature (°C) in the raw RCM output (upper row) and in the quantile-mapped product (QM to stations; lower row). Ensemble mean of all RCP8.5 simulations and for the calibration period 1981 - 2010. In all cases, the raw RCM data refer to the simulated series of those RCM grid cells in which the respective station is located. See Figure 13.23 for the absolute temperature patterns in the observations, in raw RCM data, and in the quantile-mapped product. Note that the biases of individual simulations can be larger than the ensemble mean bias displayed here.

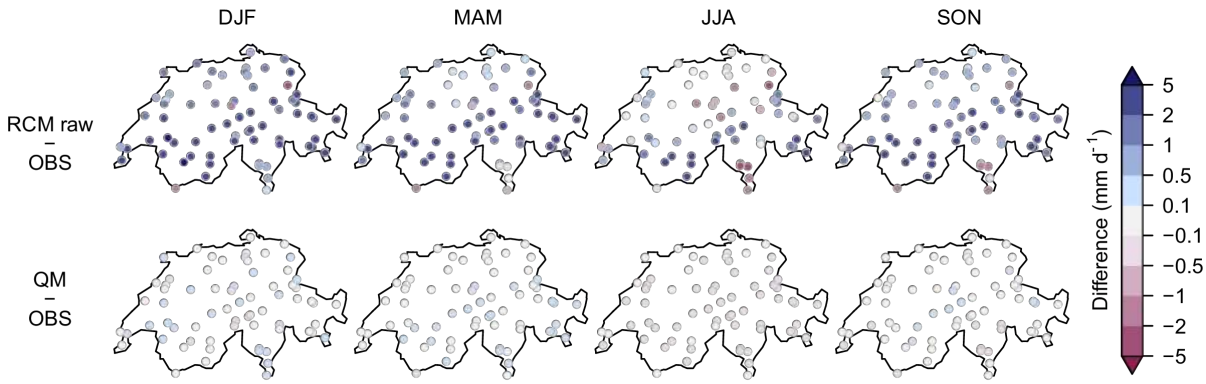

Figure 5.7. As Figure 5.6, but for seasonal mean precipitation (mm d^{-1}). See Figure 13.24 for the absolute precipitation patterns in the observations, in raw RCM data, and in the quantile-mapped product.

5.3.2. Climate change signals in raw and quantile-mapped output

A non-constant QM correction function combined with systematic differences between the distribution of a meteorological variable in the historical reference period and in a future scenario period (for instance, a systematic shift in the temperature distribution due to climate warming) can lead to a modification of the raw model's temperature-change signal by QM [133]. This is evident from the earlier comparison of the overall uncertainty ranges in raw and quantile-mapped model output (Chapter 4.7).

In the case of true intensity-dependent model biases and a systematic shift in the distribution from the reference to the scenario period, a modification of the raw climate change signal could make sense, since the associated non-stationarity of the mean model bias may be realistic. However, such modification of the raw change signal can depend on the specific QM implementation and, in a more general sense and without in-depth analyses, could lack a physical rationale [90, 334]. Furthermore, variance inflation (i.e., the deterministic generation of small-scale variance by QM) can lead to spurious climate trends in cases in which trends in the predictor and/or predictand are small and natural variability is large [211]. This particularly concerns setups in which QM involves a downscaling component (QM to stations and QM to high-resolution grid). Here, the fact that local (observed) PDFs often have a larger variance than simulated PDFs valid for coarse-resolved climate model grid cells leads to variance inflation by QM via a positively sloped, non-constant correction function and, ultimately, to the modification of climate change signals and trends. The underlying question is whether biases in PDFs that are based on high-frequency (e.g., daily) data can be meaningfully applied to low-frequency variability (e.g., trends). The explicit and stochastic consideration of subgrid-scale variance can attenuate these effects [360]. Regarding modifications of the relative change signal of precipitation, an additional underlying reason is the absolute nature of the QM correction function. Even in the case of a constant correction for all percentiles but a strong bias in the raw RCM (positive or negative), QM can considerably modify the relative climate change signal. In such a case, both the reference period's and the scenario period's precipitation are corrected by a similar absolute amount, and the absolute raw climate change signal is maintained by QM. This absolute signal, however, is related to different levels of precipitation in the reference period (due to a strong raw model bias), implying differences in the relative change signal between raw model output and quantile-mapped data (see, e.g., [175]).

For the station-based QM product, the features mentioned above are summarized by Figure 5.8 and Figure 5.10 (see Figure 13.25 and Figure 13.26 for the respective spatial patterns). The temperature changes simulated by the raw model ensemble and the quantile-mapped ensemble qualitatively agree (Figure 13.25). In both cases, the strongest warming occurs in summer (JJA) and over the Alpine ridge. Ensemble median temperature change differences of plus/minus several tenths of a degree can arise for individual stations and seasons; in some cases, differences of more than plus/minus 1°C are found. In winter, QM mostly increases change signals by a few tenths of a degree, whereas temperature changes in summer are generally dampened, especially in the southern parts of the country. Focusing on one station only (Zurich/Fluntern, SMA) but considering change signals in all individual CH2018 model chains, Figure 5.9 reveals that for most cases, seasonal mean temperature changes in the QM product differ by less than 1 °C compared to the raw RCM output (grey-shaded area). Most markers are aligned according to a 1:1 relationship, i.e., (1) seasonal mean changes in raw and in bias-corrected RCMs approximately agree with each other, and (2) comparatively strong (weak) warming in a raw experiment also implies comparatively strong (weak) warming in its quantile-mapped counterpart. Note, however, that maximum absolute deviations from the 1:1 line increase with the overall warming magnitude and tend to be larger for RCP8.5 than for RCP4.5 and RCP2.6. For individual cases and for the strong warming signal of the RCP8.5 scenario (red markers), differences between raw and QM-based change signals can be larger than 1 °C. Also note that for changes in temperature extremes, differences can be expected to be larger than for changes in the mean (e.g., [174]).

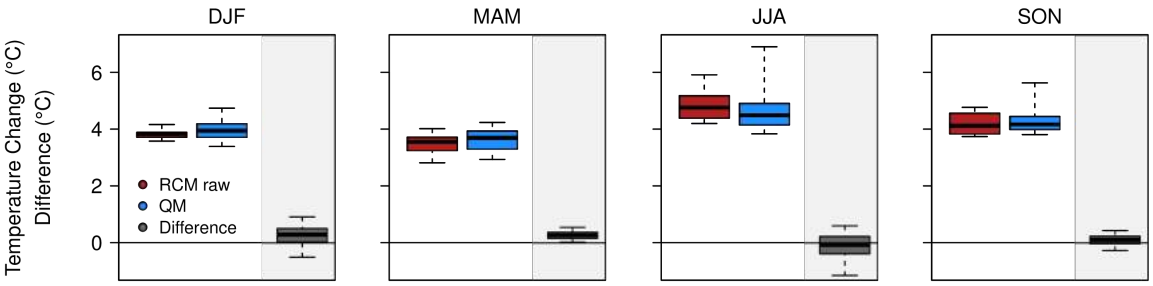

Figure 5.8. Seasonal mean temperature change (°C) in raw RCM output and in the station-based QM product (ensemble median of the multi-model combination) for RCP8.5 and the scenario period 2085. Boxes represent the 25th to 75th percentile range of the change signal at all stations in the illustrative set; whiskers represent the minimum and maximum values. The grey box denotes the range of the change-signal differences (°C) (QM - RCM raw). Raw RCM data refers to the simulated series of those RCM grid cells in which the respective station is located. See Figure 13.25 for the spatial pattern of ensemble median change signals and their differences.

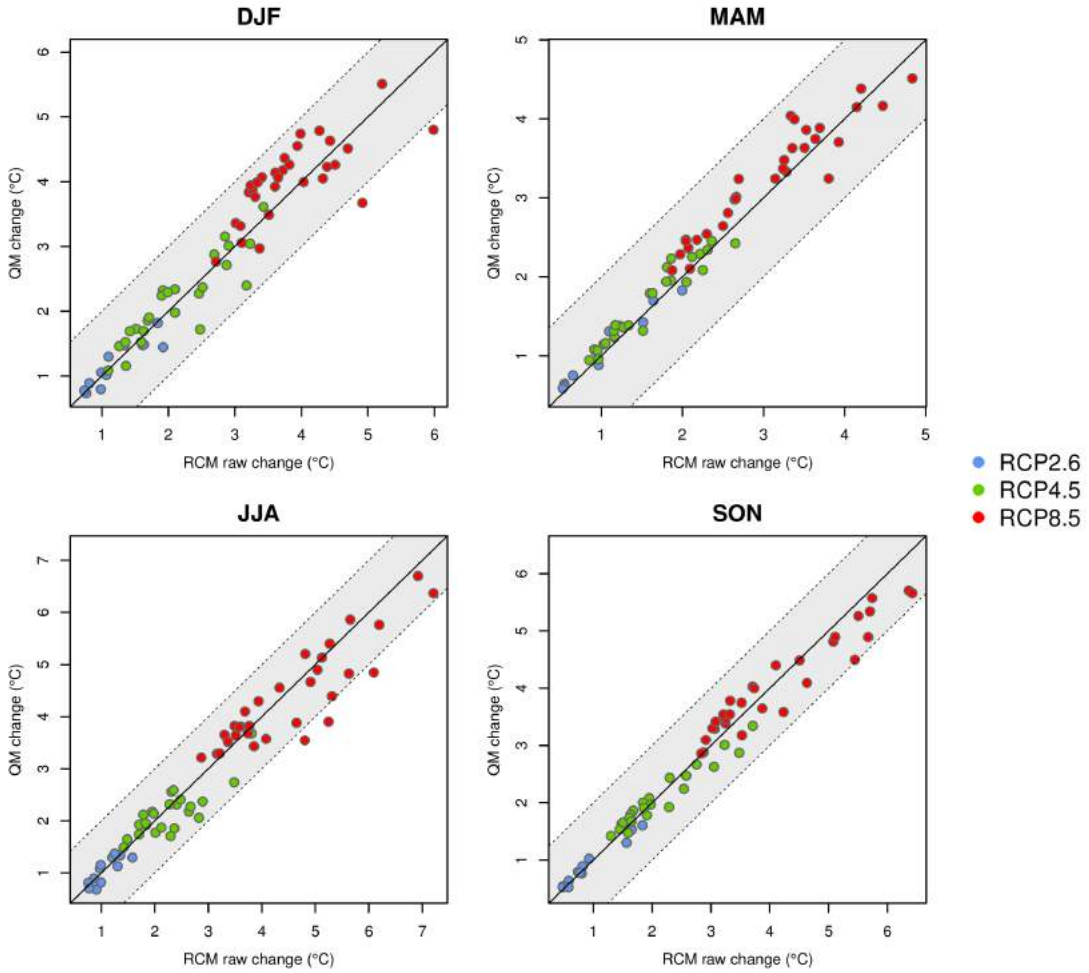

Figure 5.9. Seasonal mean temperature changes for the period 2085 at the station Zurich/Fluntern (SMA) in raw RCM output (x-axis) and in the station-based QM product (y-axis). The individual experiments of the CH2018 RCM ensemble are color-coded according to the emission scenario assumed. Raw RCM data refers to the simulated series of those RCM grid cells in which the respective station is located. The bold black line denotes a 1:1 relationship, i.e., identical change signals in the two datasets. Markers within the grey area indicate an absolute difference in the change signals of less than 1 °C.

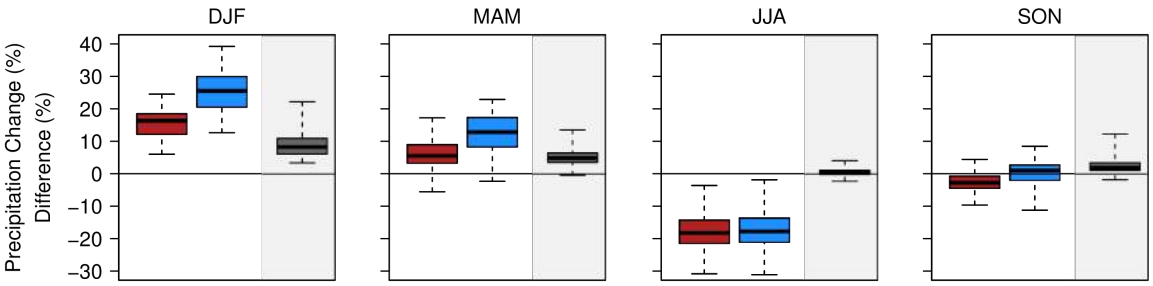

Figure 5.10. As Figure 5.8, but for seasonal mean precipitation changes (%) and the difference between QM and raw RCM output(%, percentage points). See Figure 13.26 for the spatial pattern of ensemble median change signals and their differences.

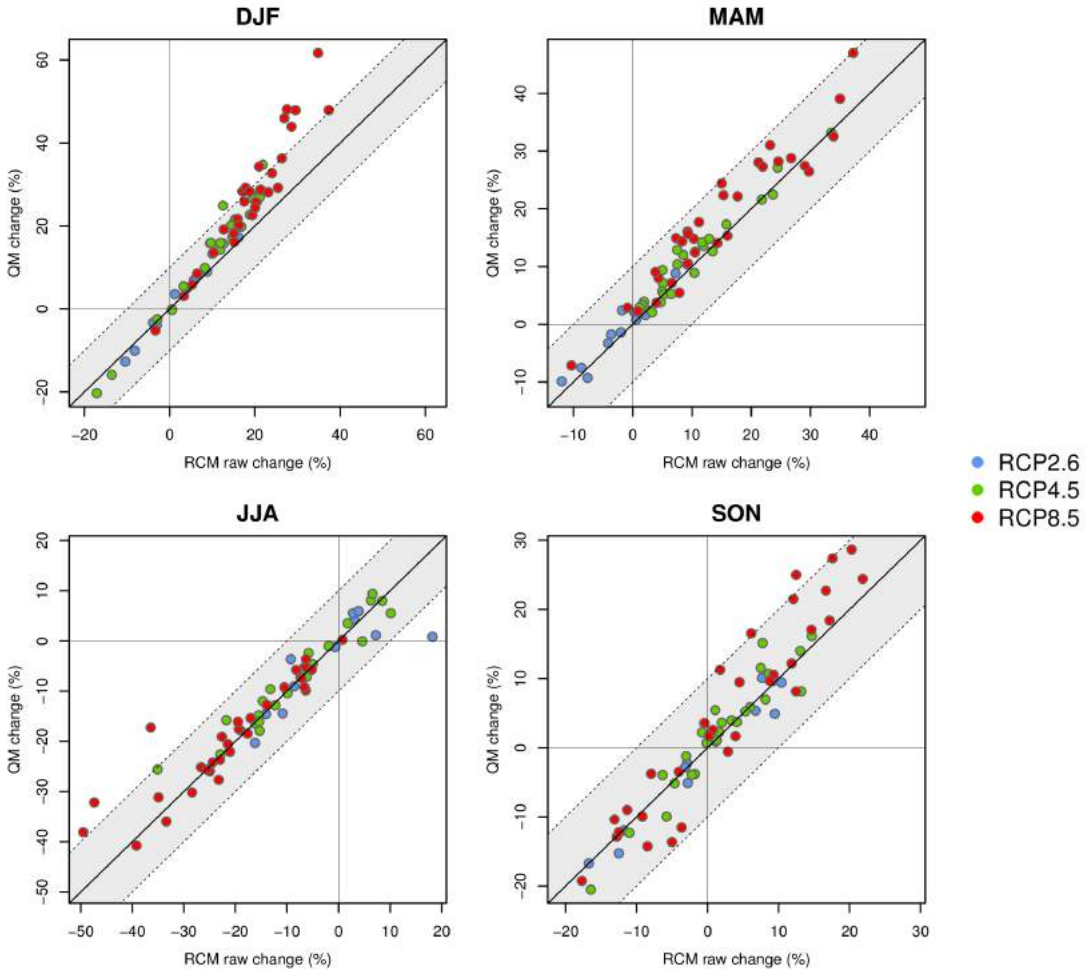

Figure 5.11. As Figure 5.9, but for seasonal mean precipitation changes (%). Markers within the grey area indicate a difference in the change signals between -10 % and 10 %.

With regard to relative changes in seasonal mean precipitation at stations, ensemble median differences mostly lie between 0 % and 20 % (Figure 5.10, Figure 13.26). A notable and systematic feature is an increase in the relative winter precipitation change by QM of about 10 % (percentage points). This systematic modification of the raw change signal is linked to the pronounced wet winter bias of most RCMs in combination with the absolute nature of the QM correction, implying lower precipitation amounts in the reference period in the QM product and an amplification of the relative change signal. For the example of Zurich/Fluntern (Figure 5.11), differences between raw and quantile-mapped change signals for individual model chains amount to less than 10 % (percentage points) in most cases (grey-shaded area). Stronger modifications are obtained for only a few experiments and especially in wintertime.

These results are consistent with the uncertainty estimates in raw and quantile-mapped RCM output as presented in Chapter 4.7. In a general sense, as discussed above, a modification of the raw change signal by QM can lead to more realistic climate change estimates in the case of truly intensity-dependent model biases that are accounted for by QM but not by delta changes derived from raw model data. However, the modification of the climate change signal by QM could to some extent be a statistical artifact. An indication of the latter effect emerges when comparing the spatial change patterns in bilinearly interpolated RCM output and in the QM to high-resolution grid product, especially for temperature (Figure 5.12). Although the broad spatial patterns of change agree, QM tends to amplify temperature changes at high elevations along the Alpine ridge and to dampen change signals in valleys. An additional amplification is visible in the area around Chur in eastern Switzerland. While the former mostly originates from a modification of the raw temperature change in winter, the latter also affects the other seasons.

These features can regionally amplify the elevation dependency of future temperature changes in comparison to raw RCM output. An obvious example is the Ticino region in southern Switzerland, where mountain-valley patterns in the change signal are prominent in the QM product. The reason for these modifications after the application of QM is a systematic dependence of the width of the observed daily temperature distribution on topography. In winter, persistent cold air pools often prevail in the valleys, leading to a rather narrow temperature distribution. In contrast, mountain sites and ridges are exposed to synoptic variability and exhibit a wider distribution. During QM calibration, these differences in distributional widths lead to systematically different slopes of the QM temperature correction function in valleys and in mountain settings. Because temperatures are generally projected to rise in the future and higher quantiles of the reference period's temperature distribution are preferentially sampled, this implies a systematic and topography-dependent difference in the modification of the raw temperature-change signal by QM: Temperature changes in valleys are often dampened (negative slope of the QM correction function), whereas changes on ridges and mountains are amplified (positive slope of the QM correction function; variance inflation). These modifications cannot be explained by physical reasoning in a straightforward manner, as the frequency changes of inversions and the presence of cold air pools are not resolved by the underlying RCMs. The same applies to the amplification of the temperature change by QM in the region around Chur (eastern Switzerland), which is presumably linked to wide temperature distributions in the observations due to frequent Föhn conditions and, again, a positive slope of the QM correction function. These issues also impact the station-based QM product but are less obvious there due to the less systematic sampling of spatial variability.

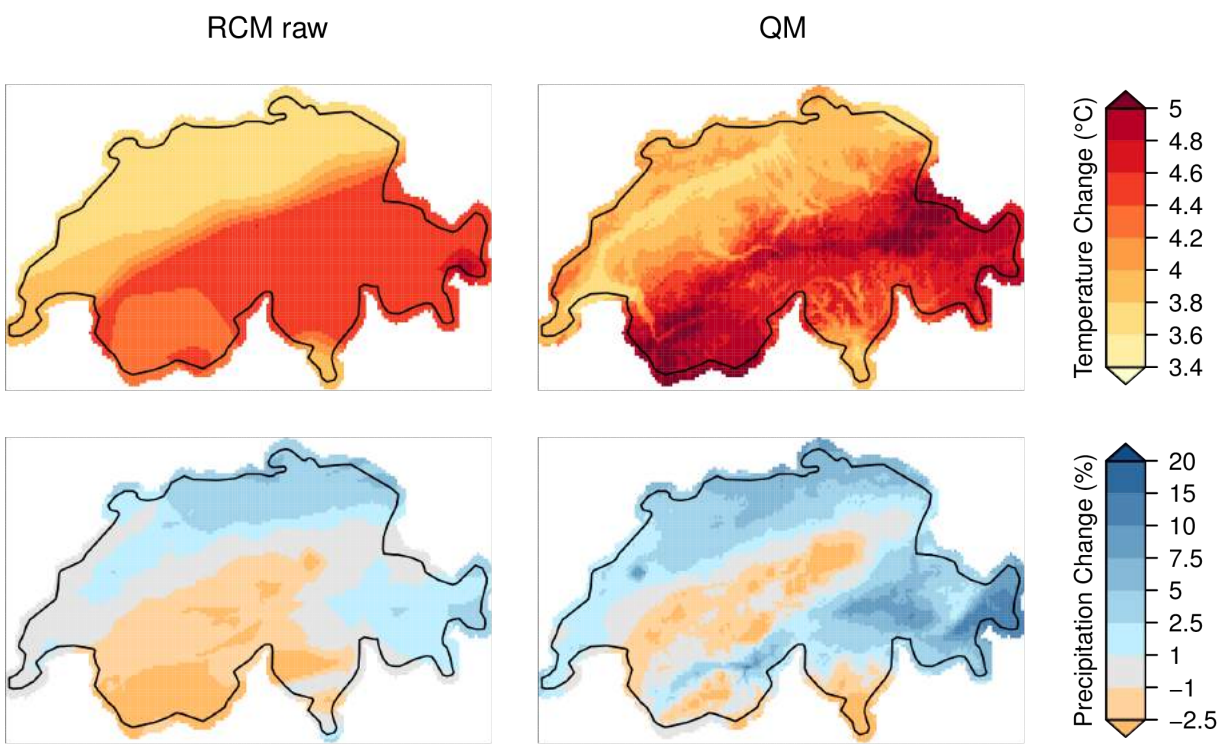

Figure 5.12. Ensemble median changes (multi-model combination) in annual mean temperature (upper row) and annual mean precipitation (lower row) for RCP8.5 and the scenario period 2085 in the QM to high-resolution grid product. Left: RCM raw output bilinearly interpolated to the observational 2-km grid. Right: QM to high-resolution grid.

5.3.3. Downscaling of multivariate indices

In addition to the applications described above, QM is also used to provide climate change projections for a multivariate heat stress index, namely the wet bulb temperature (TW; see Chapter 3.2.1). QM is applied separately to the two input variables of the wet bulb temperature (i.e., daily maximum temperature and daily mean specific humidity). The TW is then calculated from the two bias-corrected components. Several authors have pointed out that inconsistencies in spatio-temporal fields may appear and that the inter-variable dependencies may be modified by QM [90], suggesting the use of more sophisticated multivariate bias-correction methods [362]. However, Wilcke et al. (2013) [377] show that the inter-variable dependencies from the raw RCM data are preserved after QM. Moreover, QM of the input variables is the most common approach for the bias correction of multivariate indices (see, e.g., [387]); for consistency with the rest of the CH2018 report, QM of the input variables is the preferred bias-correction method.

The performance of QM in a multivariate context is evaluated by comparing the distributions of the uncorrected and bias-corrected TW with their observed counterpart. The correction of these two independent variables leads to a good representation of the TW in the present-day climate (Figure 5.13). Similar results are obtained for other RCM-GCM chains and other Swiss stations. Although no cross validation has been applied (separate calibration and validation periods), this evaluation can be considered fair, since the TW is not directly targeted in the calibration of the QM, but it is acknowledged that the evaluation of the QM might be less positive in a full cross-validation experiment.

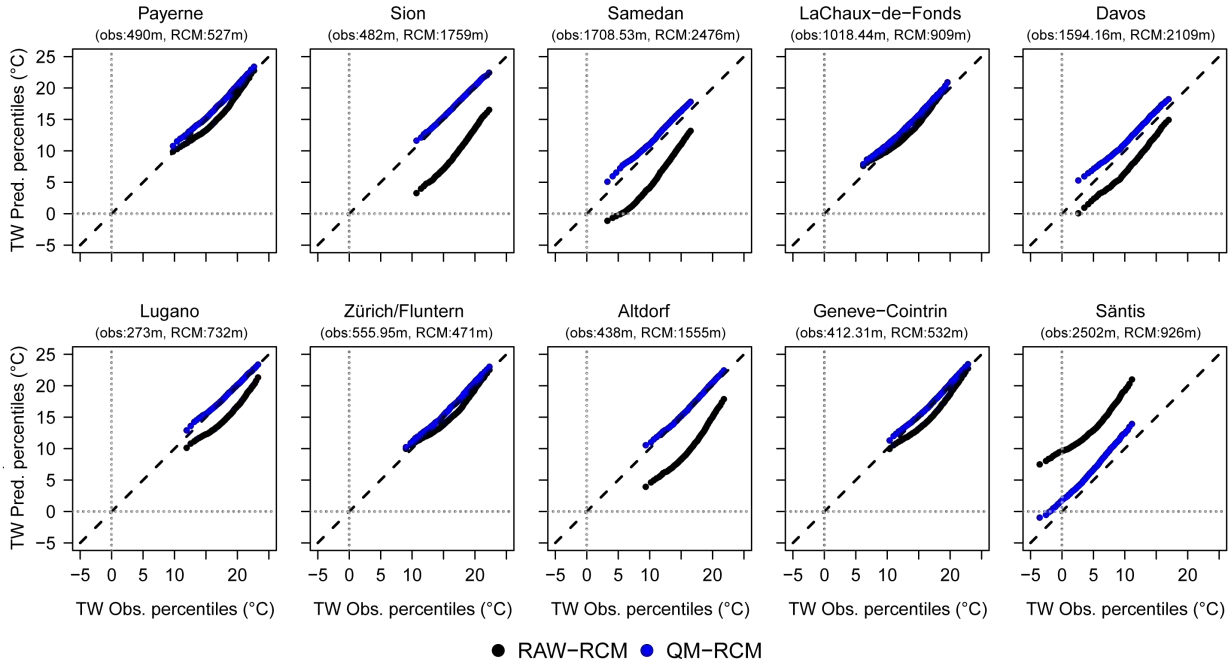

Figure 5.13. Percentiles of the observed and predicted summer wet bulb temperature (quantile-quantile plot) from the uncorrected RCM data (black) and corrected data (blue) for ten representative stations in Switzerland. The RCM data correspond to the closest grid box to the stations from the simulation CLMcom_MPI-M-MPI-ESM-LR for EUR-11 and the reference period. The altitude of the station and the corresponding grid box are given in brackets.

Raw and bias-corrected RCM-GCM simulations are compared in order to investigate the possible effects of QM on the climate change signal of the multivariate index (Figure 5.14). For summer mean and maximum wet bulb temperature, the change signal is consistent between raw and QM data, although it is slightly lower for the bias-corrected data. The differences between raw and QM data are more noticeable for individual model chains and specific stations (see Chapter 5.3). QM has a greater impact on threshold-based indices (i.e., *TWg22*), for which the change signal of the bias-corrected data may double, on average, the raw model's signal. This is an indication of the need to bias-correct data when using absolute-threshold indices: When the raw model data do not reach the threshold (due to, for instance, a systematic cold bias), the climate change signal of the index in raw model data will not be interpretable.

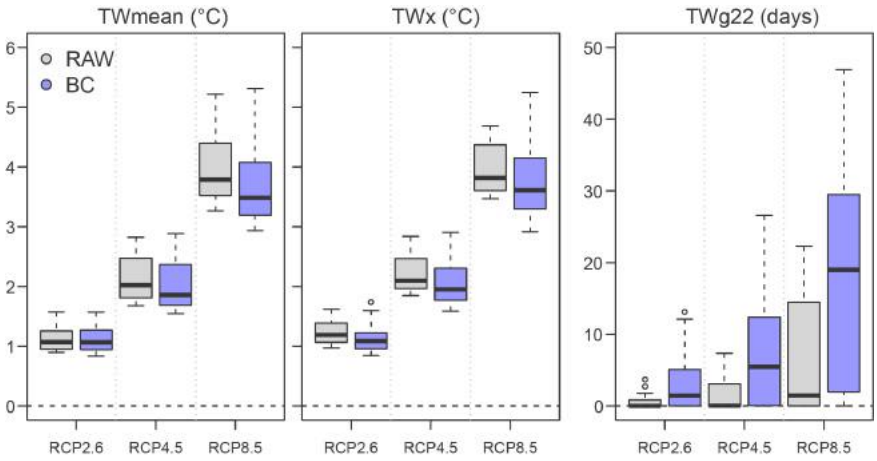

Figure 5.14. Climate change signal of the summer mean (TWmean) and maximum TW (TWx) and number of days with TW > 22 °C (TWg22) for the multi-model ensemble median for the three RCPs (2.6, 4.5, and 8.5 from left to right within each panel) for the uncorrected (grey) and bias-corrected (blue) RCM data. Each box represents the climate change signal for the period 2085 with respect to the reference period across the 67 Swiss stations.

5.4. Temperature

Figure 5.15 presents an overview of the station-based QM scenarios in terms of the seasonal mean temperature change for RCP8.5. These results are closely connected to the regional mean changes presented in Chapter 4.4 and are consistent with them. Up through the first scenario period, change signals at stations are mostly smaller than 2 °C, with typically slightly larger values in summer and autumn and for stations located in the inner regions of the Alps. Warming intensifies with time, and ensemble median warming often surpasses 4 °C for the third scenario period. A comparison to the emission scenarios RCP2.6 and RCP4.5 (Figure 13.27 and Figure 13.28, Appendix 3) indicates that both the intra-annual and the spatial variability of the warming signal are qualitatively similar across emission scenarios and scenario periods. At most stations, the summer season is subject to the strongest warming; temperature increases are typically least pronounced in spring. In spring, summer, and autumn, the strongest warming occurs in inner-Alpine regions, whereas winter warming is most pronounced along the Swiss Plateau north of the main Alpine ridge. These patterns largely agree with the analysis of Chapter 4.4 with certain modifications due to the influence of QM on the raw models' climate change signals (Chapter 5.3).

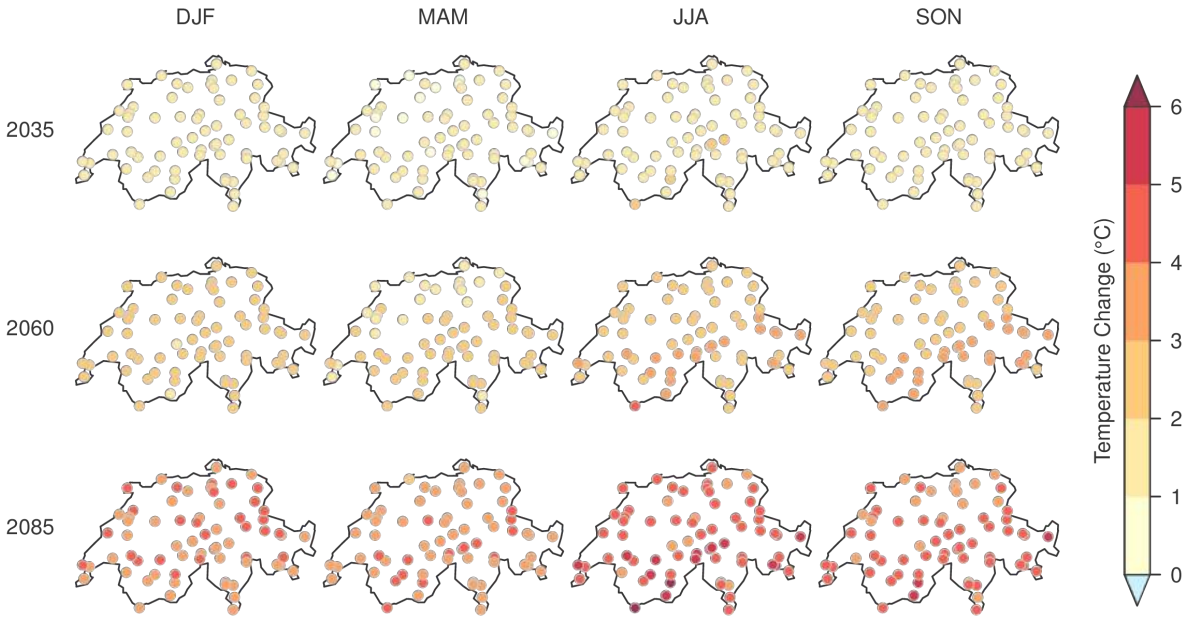

*Figure 5.15. Ensemble median climate change signal for seasonal mean temperature (°C) at stations for all scenario periods and for **RCP8.5** (multi-model combination). See Figure 13.27 and Figure 13.28 for RCP2.6 and RCP4.5, respectively. Note that the model uncertainty of the change signal is not reflected by the ensemble median signal displayed here and can be substantial.*

The temporal evolution of seasonal mean temperature change at the example station of Zurich/Fluntern indicates a similar and continuous increase in ensemble median temperature in all seasons until the end of the century (Figure 5.16). Warming magnitudes are slightly larger in summer and winter than in spring and autumn and amount to 4.5 °C to 5 °C by 2099. The model uncertainty range is considerable and is largest in summer. The temperature change evolution in one individual model experiment (black line) illustrates the fact that interannual climate variability can still lead to substantial temperature fluctuations that are, however, superimposed onto a dominating warming trend. An overview of annual mean temperature changes for RCP8.5 for both the station-based (QM to stations) and the grid-based (QM to high-resolution grid) product as well as the annual cycle of the temperature-change signal at four exemplary sites are provided in Figure 5.17. The grid-based change pattern indicates an amplification of the warming signal with elevation and overall agreement between station-based and grid-based estimates. The elevation-dependent warming, however, must be interpreted with special care (see Chapter 5.7). At the sites of

Zurich/Fluntern and Weissfluhjoch, peak warming occurs in mid-to-late summer, with a secondary maximum in mid-winter. At Lugano and Sion, the annual cycle of the temperature change is less pronounced and peaks in late summer/early autumn. Model uncertainty is large, especially at Weissfluhjoch and Sion. For the former, individual model chains indicate maximum warming signals greater than 9 °C for June, July, August, and September, whereas ensemble median changes amount to about 4.5 °C.

Finally, for the four exemplary sites, Figure 5.18 presents the mean annual cycle of temperature in the observations and for the late scenario period for all RCPs. In accordance with the change signals presented above, the temperature level gradually increases from RCP2.6 to RCP4.5 to RCP8.5 at all sites. For RCP8.5 and the example of Weissfluhjoch, monthly mean temperatures in April and November are close to 0 °C, whereas observations in the reference period indicate temperatures well below the freezing point. In general, climate change will not alter the general shape of the annual cycle for temperature but rather shift it to higher levels. At all sites and for all RCPs, July will still be the warmest month; depending on the site, either January or February will still be the coldest.

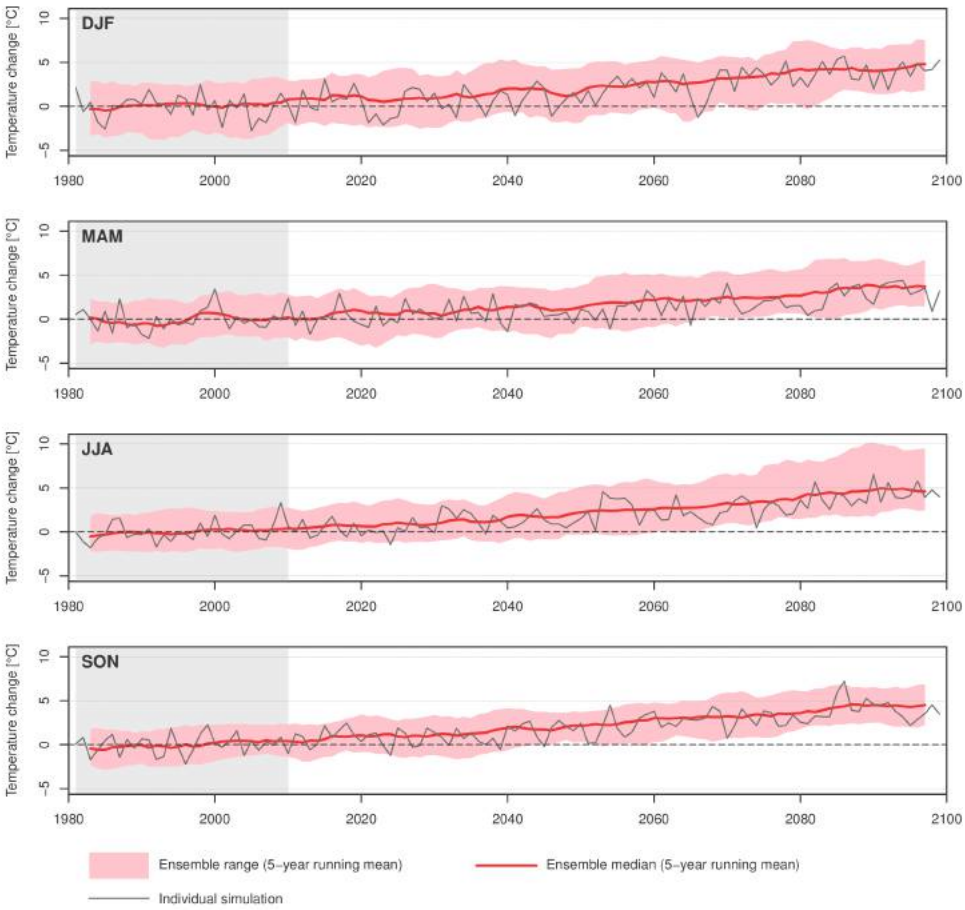

Figure 5.16. Temporal evolution of the seasonal mean temperature change (°C) with respect to the reference period at the Zurich/Fluntern (SMA) station for RCP8.5 (all simulations). The shading indicates the full model range (ensemble minimum to maximum), reflecting model uncertainty; the red line, the ensemble median change. Data were temporally smoothed by applying a 5-year moving window. In addition, the non-smoothed change signal of one individual simulation (MPI-M-MPI-ESM-LR CLMcom-CCLM4-8-17 for EUR-11) is shown.

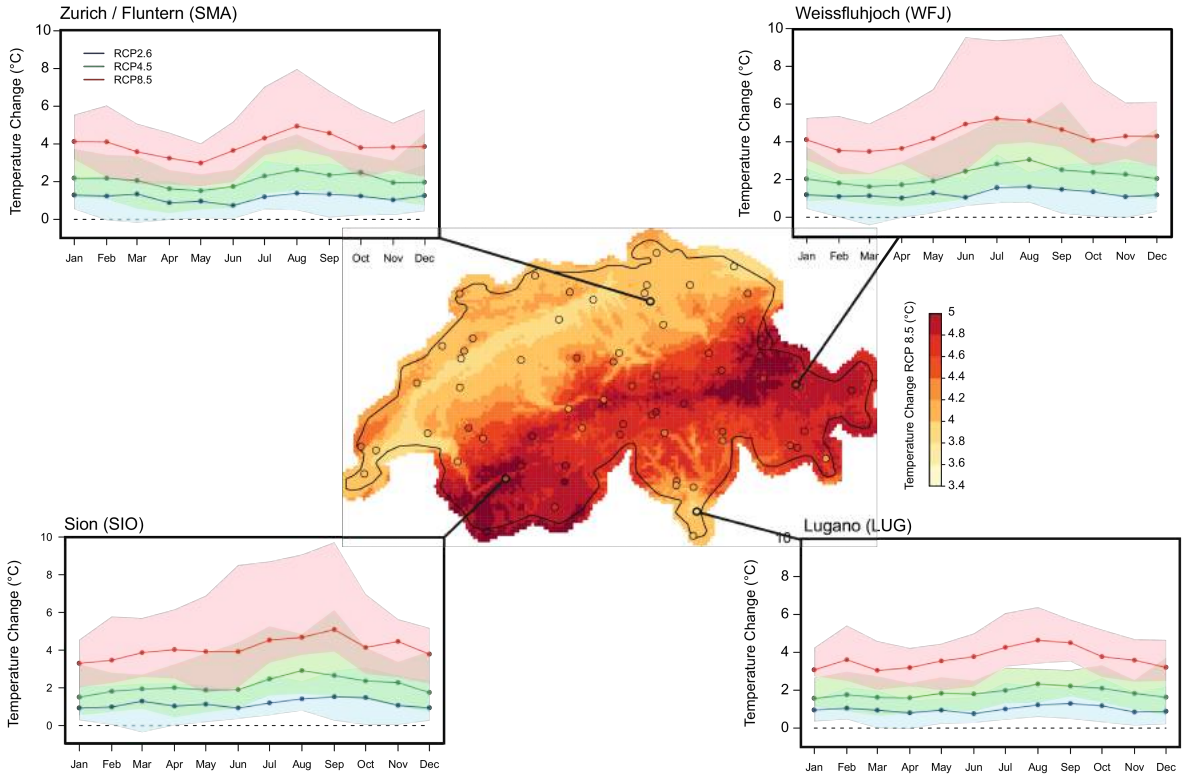

Figure 5.17. Center: Ensemble median annual mean temperature change (multi-model combination) (°C) for RCP8.5 and for the period 2085 at stations (QM to stations) and on the high-resolution grid (QM to high-resolution grid). This map is identical to the upper right panel of Figure 5.12. Note that the model uncertainty of the change signal is not reflected by the ensemble median signal displayed here and can be substantial. Corner panels: Mean annual cycle of the temperature change (multi-model combination) (°C) for all RCPs and the late scenario period at the four exemplary sites. The line indicates the ensemble median change; the shading illustrates the full ensemble range (model uncertainty).

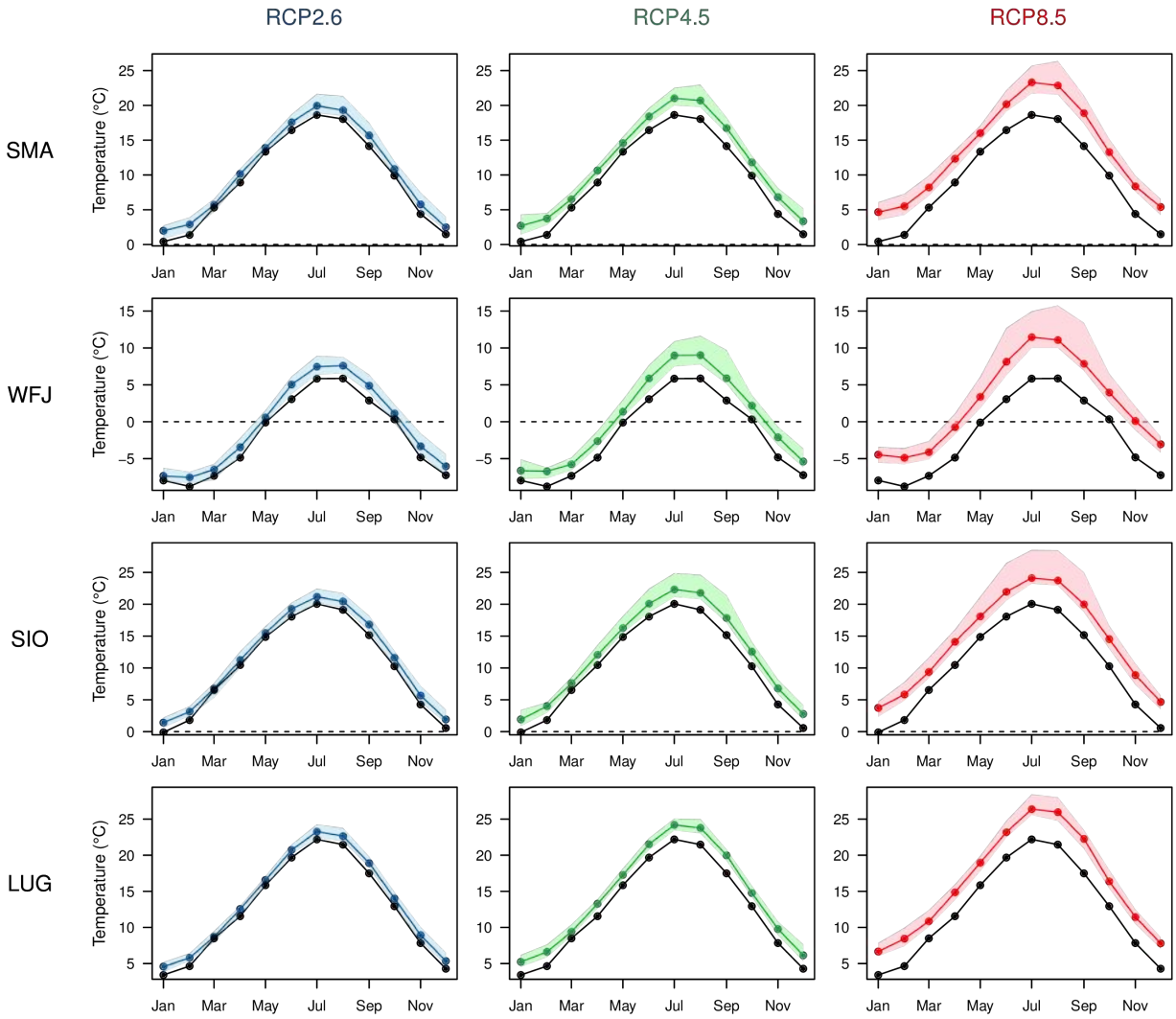

Figure 5.18. Mean annual cycle of temperature (°C) for the reference period (observations, black) and scenario period 2085 (multi-model combination, colored) for all RCPs (columns) and the four exemplary sites of Zurich/Fluntern (SMA), Weissfluhjoch (WFJ), Sion (SIO), and Lugano (LUG). In the case of the RCPs, the line indicates the ensemble median, whereas the shading indicates the full ensemble range (model uncertainty).

Box 5.1: Example application: Evolution of the zero-degree line

Bias-corrected climate model data can, in principle, be employed to derive absolute threshold-based indices and their changes. Chapter 6.3 exploits this possibility in the context of temperature-based indices such as the number of summer days, hot days, and tropical nights. We present here a further application that targets the elevation of the winter (DJF) zero-degree line averaged over the Swiss domain. Elevation dependencies in bias-corrected data must be handled with care (Chapter 5.7), but an approximate analysis of the future evolution of the Swiss domain-mean zero-degree line is possible.

For this purpose and as an exemplary analysis, the CH2018 model ensemble for RCP8.5 and an observation-based 2-km gridded temperature dataset for the Swiss domain available since the year 1864 (an extended version of [123]) are considered. The zero-degree line is determined by a simple least-square linear regression of the 30-year mean winter temperature (moving window) from the observations and the bias-corrected RCM data against grid-cell elevation. For each year, the zero-degree line is obtained by extracting the elevation corresponding to a mean winter temperature of 0°C from the regression equation.

Figure 5.19 presents the results of this analysis. In the observed period from 1874 to 2017, the mean winter zero-degree line rose by about 350 m to 400 m. For RCP8.5, an additional increase of about 400 m to 650 m by mid-century and of about 700 m to 1050 m by the end of the century is projected (ranges refer to model uncertainty). Relating these numbers to the projected winter warming of about 3.5 - 5.5 °C by end of the century and averaged over the country (Chapter 4) translates to an approximate increase in the zero-degree line by about 150 m to 200 m per °C warming. This is well in line with the results found in the observational chapter (Chapter 3) and consistent with theoretical expectations from the moist adiabatic lapse rate.

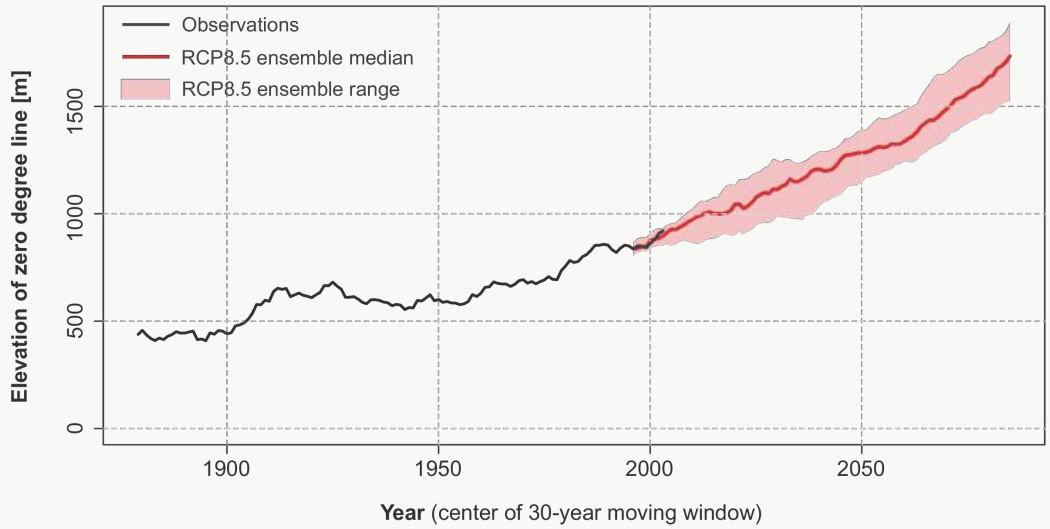

Figure 5.19. Evolution of the mean winter (DJF) zero-degree line in the observations (black) and for RCP8.5 (red). The red line indicates the ensemble median of all RCP8.5 simulations considered in CH2018. The red shading denotes the ensemble range (q5 to q95). Both the observed and the simulated evolution were computed for 30-year moving windows. Note that the underlying observations and the methodology are not identical to those used for the analysis in Figure 3.16.

5.5. Precipitation

An overview of ensemble median seasonal mean precipitation changes in the station-based QM product for RCP8.5 is presented in Figure 5.20 (see Figure 13.29 and Figure 13.30 for RCP2.6 and RCP4.5, respectively). Consistent with Chapter 4.5, the general picture is one of increasing precipitation amounts at most stations in winter, minor changes in spring and autumn, and precipitation decreases in summer. For RCP2.6, even for the latest scenario period (2085), only the winter season shows widespread precipitation changes (increases) of more than 5 %. For RCP4.5 and RCP8.5, the summer drying signal is more pronounced; in the case of RCP8.5, it clearly intensifies toward the end of the century, when most stations show summer precipitation decreases of more than 10 %. In contrast, winter precipitation mostly increases by more than 15 %. No clear spatial pattern of relative precipitation changes can be identified, except for a tendency toward rather strong relative increases in winter precipitation in Ticino and less pronounced increases at inner-Alpine sites. Furthermore, summer drying in the Engadine (eastern Switzerland) is somewhat less pronounced.

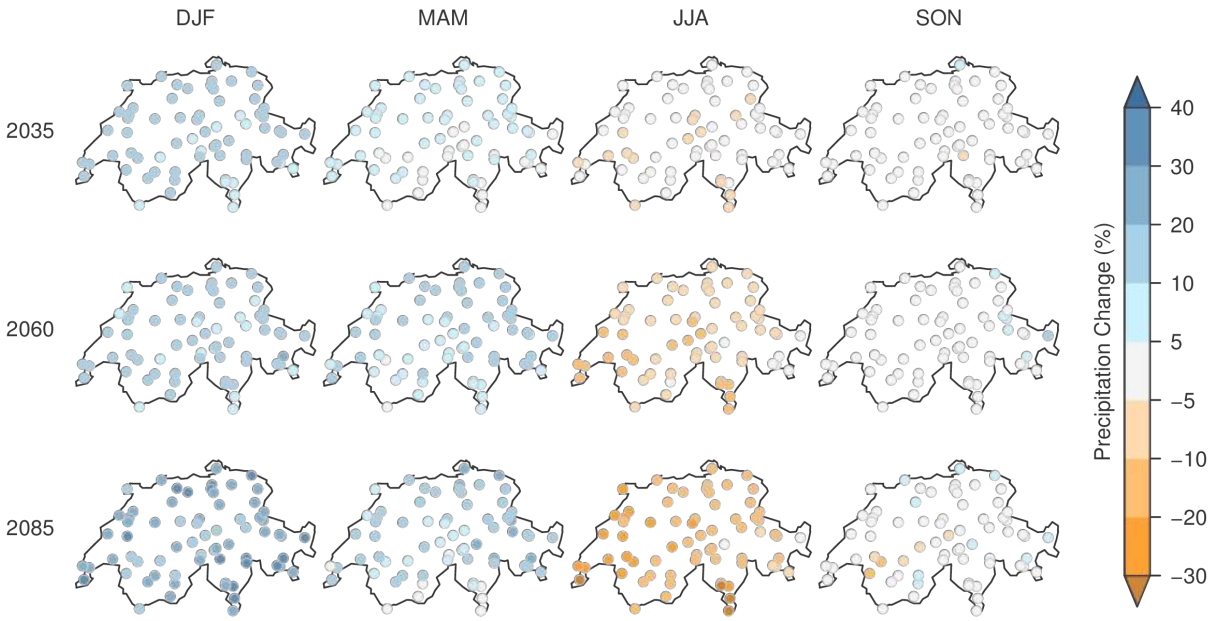

Figure 5.20. Ensemble median climate-change signal for seasonal mean precipitation (%) at stations for all scenario periods and for RCP8.5 (multi-model combination). See Figure 13.29 and Figure 13.30 for RCP2.6 and RCP4.5, respectively. Note that the model uncertainty of the change signal is not reflected by the ensemble median signal displayed here and can be substantial.

Again, Figure 5.21 provides a more detailed picture of the temporal evolution of seasonal mean precipitation changes for the RCP8.5 model ensemble and the example of Zurich/Fluntern. Ensemble median winter precipitation shows a positive trend, yielding an approximate increase of 30 % by the end of the century. In contrast, the ensemble median change in summer precipitation is subject to a slightly negative trend that is, however, less pronounced than the positive trend in winter. Furthermore, there is a tendency toward a slightly positive trend in spring and autumn. In all seasons, model uncertainty and uncertainty due to natural climate variability are large: The ensemble range of change signals, filtered using 5-year moving-window averaging, covers both precipitation increases and decreases throughout the entire period. The considerable influence of natural climate variability is also apparent from the strongly fluctuating annual change signal of one individual experiment (black line).

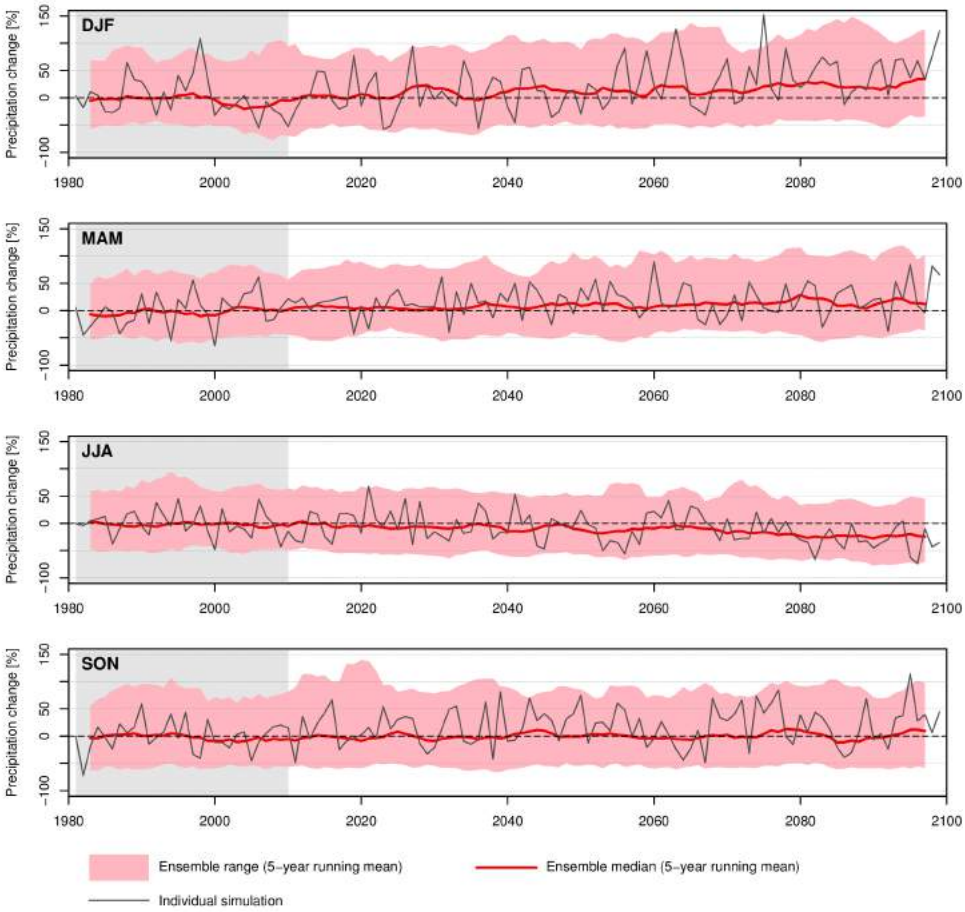

Figure 5.21. Temporal evolution of the seasonal mean precipitation change (%) with respect to the reference period at the Zurich/Fluntern station (SMA) for RCP8.5 (all simulations). The shading indicates the full model range (ensemble minimum to maximum), reflecting model uncertainty; the red line, the ensemble median change. Data were temporally smoothed by applying a 5-year moving window. In addition, the non-smoothed change signal of one individual simulation (MPI-M-MPI-ESM-LR CLMcom-CCLM4-8-17 for EUR-11) is shown.

Relative annual change signals for RCP8.5 in the station-based (QM to stations) and grid-based (QM to high-resolution grid) QM products for the last scenario period approximately agree with each other (Figure 5.22, center). Most parts of Switzerland are subject to increases in ensemble median annual precipitation, with the exception of parts of the western Alps, Valais, and Ticino. The annual cycle of the change signal is qualitatively similar at the four exemplary sites of Zurich/Fluntern, Weissfluhjoch, Lugano, and Sion, with increases during the winter months and decreases during summer. In general, change signals are amplified for RCP8.5 compared to both RCP2.6 and RCP4.5. In contrast to temperature (see above), climate change has the potential to modify the characteristics of the annual cycle of precipitation. This includes shifts in peak precipitation from August to June for Weissfluhjoch and shifts in minimum precipitation from spring to late summer in the case of Sion (Figure 5.23). Note that minor changes in monthly mean precipitation for individual models and even for the ensemble median might not be significant due to the potentially considerable influence of random internal variability [148] .

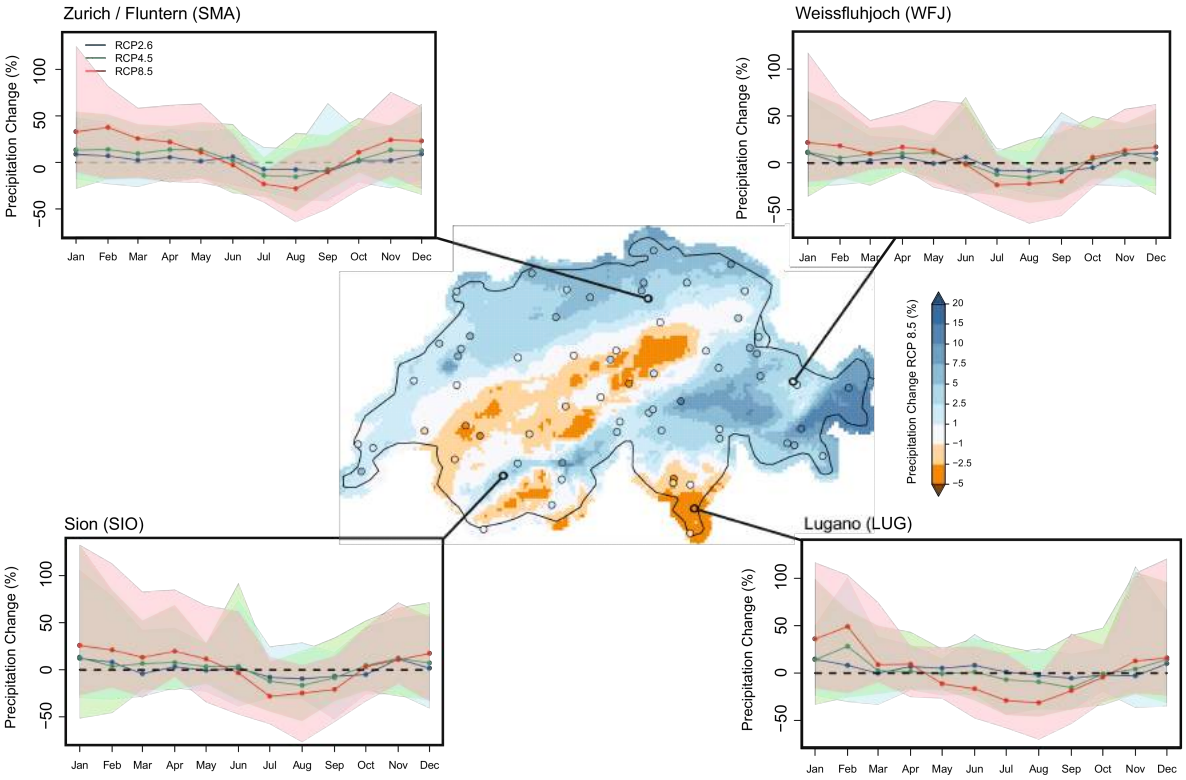

Figure 5.22. Center: Ensemble median annual mean precipitation change (multi-model combination) (%) for RCP8.5 and the period 2085 at stations (QM to stations) and on the high-resolution grid (QM to high-resolution grid). Note that the model uncertainty of the change signal is not reflected by the ensemble median signal displayed here and can be substantial. Corner panels: Mean annual cycle of the precipitation change (multi-model combination) (%) for all RCPs and the late scenario period at the four exemplary sites. The line indicates the ensemble median change; the shading, the full ensemble range.

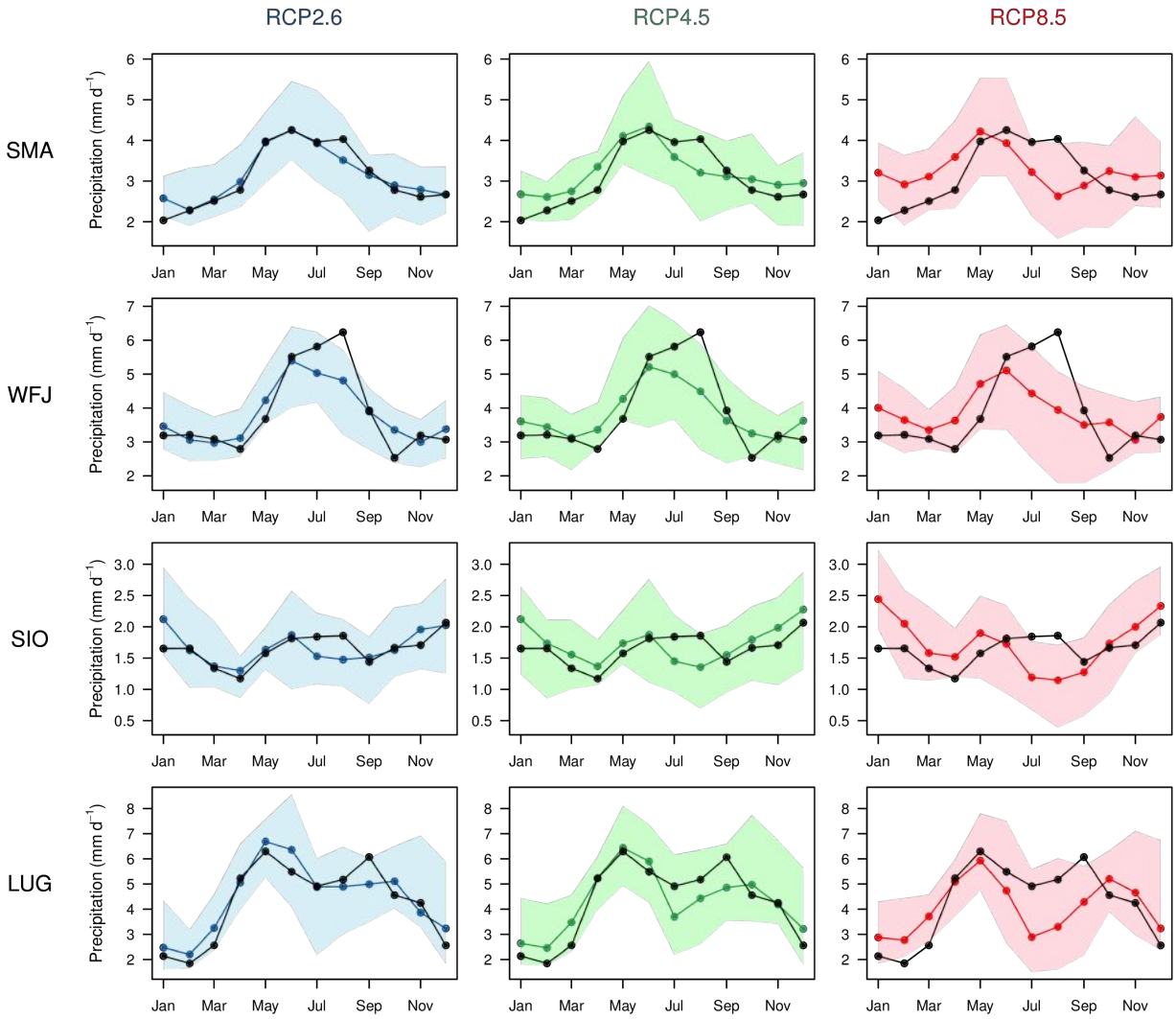

Figure 5.23. Mean annual cycle of precipitation (mm/d) for the reference period (observations, black) and the scenario period 2085 (multi-model combination, colored) for all RCPs (columns) and the four exemplary sites of Zurich/Fluntern (SMA), Weissfluhjoch (WFJ), Sion (SIO), and Lugano (LUG). In the case of the RCPs, the line indicates the ensemble median, whereas the shading indicates the full ensemble range (model uncertainty).

5.6. Additional variables

In the following section, ensemble median change signals in the station-based QM product for the additional variables of daily maximum and minimum temperature, relative humidity, global radiation, and wind speed are summarized (Figure 5.24). Only RCP8.5, the scenario period 2085, and changes in seasonal mean values are considered (see Appendix 3 for other forcing scenarios and periods). Note that the climate change signals of relative humidity, global radiation, and wind speed have not been analyzed in detail or on a physical, process-based level in the context of CH2018. The main purpose of including these auxiliary data is to provide an internally consistent and extended set of meteorological variables for certain impact-related applications.

Ensemble median change signals of daily minimum and maximum temperature are similar to those of daily mean temperature. For minimum temperature, differences of a few tenths of a degree are possible at individual stations. Depending on the station, these differences can be in either direction (i.e., slightly weaker or slightly stronger than mean daily temperature changes). Projected changes in maximum temperature are slightly larger than both mean and minimum temperature changes at most stations; this is especially true in wintertime. Spatial patterns and variability across seasons, however, are very similar. Projected ensemble median changes in relative humidity are small and by the end of the century typically do not exceed ±5 %. Increases are found in inner-Alpine regions in winter, whereas decreases are apparent

in summer over most parts of the country and are most pronounced over parts of the Alps and in Ticino. This pattern qualitatively agrees with the summer precipitation change patterns (see above), indicating a drying of the lower atmosphere along with precipitation decreases.

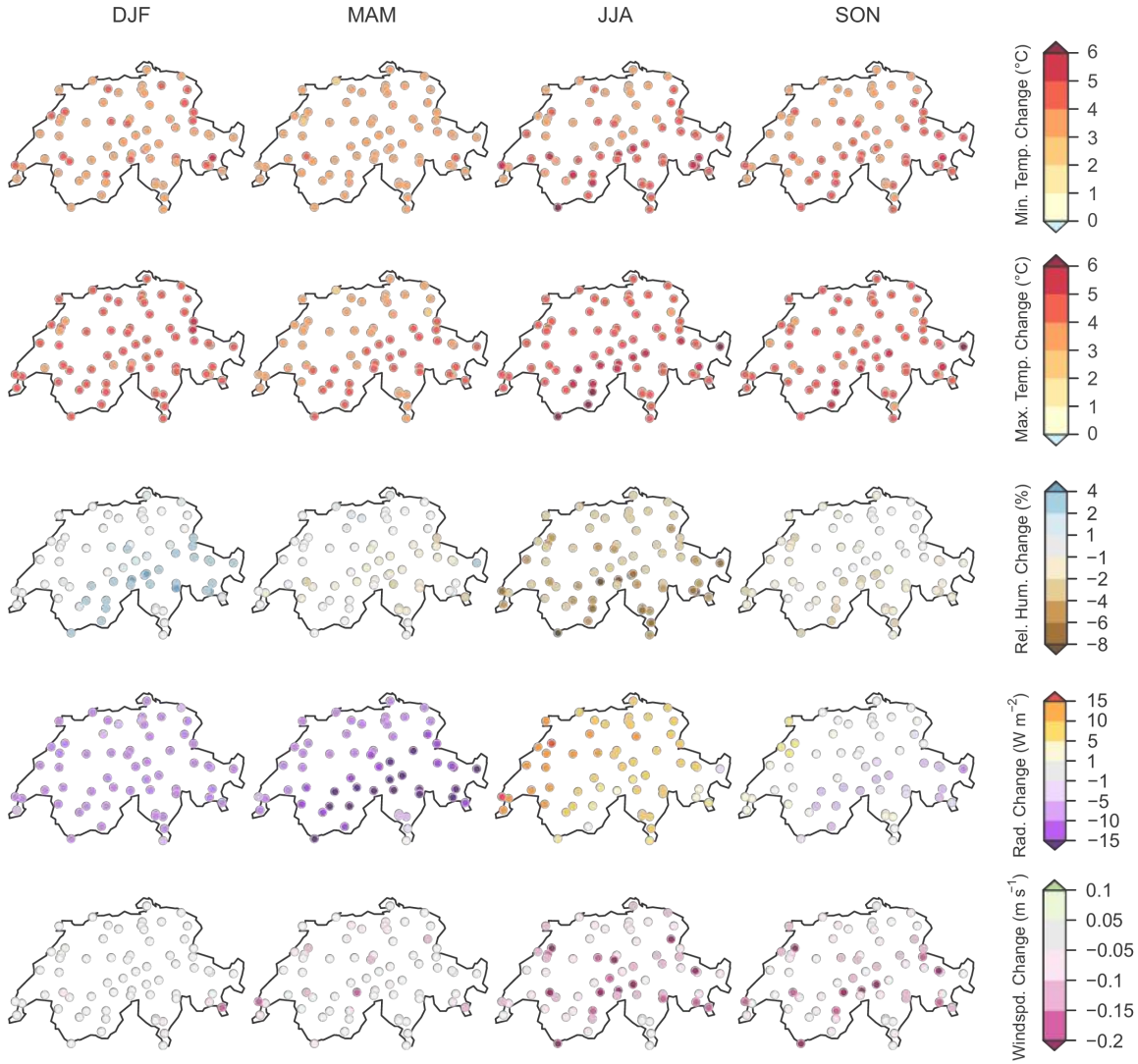

Figure 5.24. Ensemble median seasonal climate change signals at stations for the 2085 period and for ***RCP8.5*** *(multi-model combination). Top to bottom: Daily minimum temperature, daily maximum temperature, relative humidity, global radiation, wind speed. See Appendix 3 for the respective patterns for each scenario period and each forcing scenario. Note that the model uncertainty of the change signal is not reflected by the ensemble median signal displayed here and can be substantial.*

For global radiation (downwelling shortwave radiation at the surface), an increase in summer over most parts of the country and a decrease in winter and spring are obtained. The absolute decrease is stronger in spring than in winter, which presumably is related to the higher absolute amounts of global radiation in spring. Furthermore, the increases are most pronounced for Alpine sites. By the end of the century, increases in summer global radiation can be larger than 15 W m^{-2} at individual locations. Both the winter/spring decrease and the summer increase in global radiation are presumably linked to opposite change signals of total cloud cover (not shown here).

Changes in near-surface wind speed are generally small. Consistent and noticeable signals over most parts of the country are obtained for the summer season and, in part, for spring and autumn as well. In these seasons, mean wind speeds tend to decrease over most parts of Switzerland, but ensemble median decreases typically do not exceed -0.2 m s^{-1}. No consistent spatial pattern of wind speed changes can be identified. Note that wind conditions at the station level are strongly influenced by the local topography,

which is not or is only rudimentarily represented by EURO-CORDEX RCMs. Hence, projected changes in wind conditions at the station scale must be interpreted with special care.

5.7. Limitations

Quantile mapping is an attractive and suitable approach for the generation of transient bias-corrected climate scenarios at different spatial scales. One should, however, be aware of several limitations and potential pitfalls when considering the application of QM-based products. Some of these can actually preclude the application of QM-based products for specific purposes, and thus a careful evaluation of the usability of QM-based scenarios is necessary for any given application. In addition, post-processing by QM adds another level of uncertainty to the overall uncertainties already inherent to climate model simulations (Chapter 4.7), in particular for cases in which QM is associated with a downscaling step (here: QM to stations and QM to high-resolution grid; [215]).

Stationarity of the model bias

When applied in a climate change context, QM is calibrated in the historical reference period and is subsequently applied to the entire simulated time series, including the future scenario period (Figure 5.2). Hence, QM implicitly assumes that the calibrated correction function and, consequently, intensity-dependent climate model biases are stationary in time. Especially under changing climatic conditions, this assumption is uncertain (e.g., [45, 211, 24]). Furthermore, multi-decadal internal climate variability might also have an impact on the stationarity of the identified biases. This is linked to the fact that QM, a purely empirical technique, ignores the underlying physical reasons for climate model biases and is thus affected by different modes of variability in the simulations and in the observed reference [89, 220]. Note, however, that non-stationary biases of simulated mean conditions caused by a systematic shift in the simulated distribution toward conditions subject to different bias characteristics can in principle be accounted for by QM. QM evaluations employing pseudo-realities indicate the validity of the calibrated correction functions also in a future climate [174].

Temporal climatic variability and remaining biases

QM is a distribution-based correction approach that does not alter the principle temporal sequence of the raw climate model output. If temporal variability is strongly distorted in the raw model output (e.g., biased interannual or day-to-day variability or biased trends), remaining biases in the quantile-mapped output are to be expected [2]. For the case of precipitation transition probabilities and multi-day precipitation sums, however, previous work suggests an approximate representation of temporal variability through QM [174, 271], although spell length distributions can remain distorted [215]. Furthermore, due to the approximate nature of the QM correction, the quantile-mapped data can be subject to remaining biases in the calibration period itself, even for seasonally averaged values. These remaining biases are typically small but, in the case of the CH2018 scenarios, they can lead to a systematic underestimation of the reference summer precipitation by several quantile-mapped model chains, for example. This is why bias-correction approaches are nowadays often referred to as *bias adjustment*, highlighting the fact that not all model biases are removed by the correction procedure.

Changes in extremes

The QM correction function for high and low quantiles can be subject to large uncertainties that arise in part from sampling issues due to the limited number of years considered for the calibration of the mapping. Furthermore, the bias of values that lie outside the range of the present-day calibration period (i.e., new extremes that have not yet been observed in the present-day climate) is not explicitly considered in QM. In our setup, a constant extrapolation of the biases for the 1st and 99th percentiles is implemented (Chapter 5.2). Other approaches, both parametric and non-parametric, are possible [174, 140] and might yield different results for changes in extremes. The applicability of QM scenarios to the analysis of changes in extremes must therefore be carefully evaluated, especially for extremes beyond the 1st and 99th percentiles.

Modification of raw climate change signals

The application of QM can modify the raw models' mean climate change signal and the simulated trends [133, 175, 219] (Chapter 5.3). This can be a meaningful feature but could to some extent also represent a statistical artifact. In the context of CH2018, the modification of the raw change signals is minor in most cases, but can be substantial for individual GCM-RCM chains, variables, and meteorological stations/regions (Chapter 5.3). Among other effects, a systematic and topography-controlled modification of the raw models' temperature-change signals by QM has been discovered that partially modifies the elevation dependency of the warming signal and to some degree represents a statistical artifact. In addition, relative precipitation increases in raw model output tend to be amplified by QM, a feature that is directly connected to the positive precipitation bias of many GCM-RCM chains and the absolute nature of the QM correction.

Spatial climate variability

When employed in a downscaling context (here: QM to stations and QM to high-resolution grid), QM can misrepresent spatial climate variability on short timescales [211]. The underlying reason is its deterministic nature when downscaling from coarse climate-model grid cells to local scales, as well as the fact that the predictor information (grid-cell-based simulated values) is translated to finer scales without any randomization that could mimic small-scale variance.

The associated misrepresentation of spatial climate variability at scales finer than the predictor information (i.e., smaller than a climate model grid cell) is illustrated for one example in Figure 5.25, which adopts the analysis presented by [211]. Here, precipitation for one EUR-44 CH2018 model chain has been bias-corrected and downscaled by applying QM for 27 stations that are located in the same climate model grid cell (Panel a). These stations are situated in the Alpine part of Switzerland and are partially separated by major topographic barriers. Panel b (upper part) presents the observed precipitation sums for each station in summer 2000 (June 1 to August 31). On a few days, none of the stations received precipitation, and the entire region was dry. During days with moderate to high precipitation amounts, many stations were affected by rainfall, but in most cases, individual stations recorded no or only minor precipitation amounts. This reflects the small-scale nature of summer convective precipitation in particular, with convective cells moving over certain sites in a region but bypassing others.

The situation is different in the corresponding quantile-mapped product (Panel b, lower part). Here, each individual station closely follows the information provided by the predictor (the simulated value of the raw RCM grid cell; middle part). When the latter indicates no rain (or a low/high quantile of precipitation), each individual station in the quantile-mapped output shows no rain (or a low/high quantile of its precipitation distribution). Spatial climate variability on sub-grid scales is hence considerably underestimated by the QM product, leading, for instance, to an overestimation of high extremes when analyzed in a spatially averaged context (Panel c). At the same time, the frequency of completely dry conditions can be overestimated by QM. Note that a temporal correspondence between observed and simulated precipitation amounts in Panel b is not expected, as observations and GCM-driven simulations are – by definition and due to internal climate variability – out of phase on decadal and shorter timescales.

Regarding QM to a high-resolution grid, a further limitation with respect to spatial climate variability is the observational reference dataset. Its quality depends on the accuracy of the underlying rain-gauge measurements and the capability of the interpolation scheme to reproduce precipitation at ungauged locations. Especially for the observational 2-km precipitation product employed (Chapter 2.6), the effective resolution expressed in terms of the typical inter-station distance (15 - 20 km) is much larger than the nominal 2-km grid spacing [226]. As a consequence, the quantile-mapped product does not fully represent spatial climate variability at the 2-km scale.

The limitations described above affect the downscaled QM products (QM to stations and QM to high-resolution grid) when employed in a multi-site (multi-grid cell) context at daily resolution. This impacts the

summer season with its frequent small-scale convective activity in particular. It can, for instance, be expected to be problematic for spatial hydrological applications that require meteorological input data at daily resolution. Researchers working on such applications are advised to carefully evaluate the spatial variability of the quantile-mapped output before applying the QM scenario product.

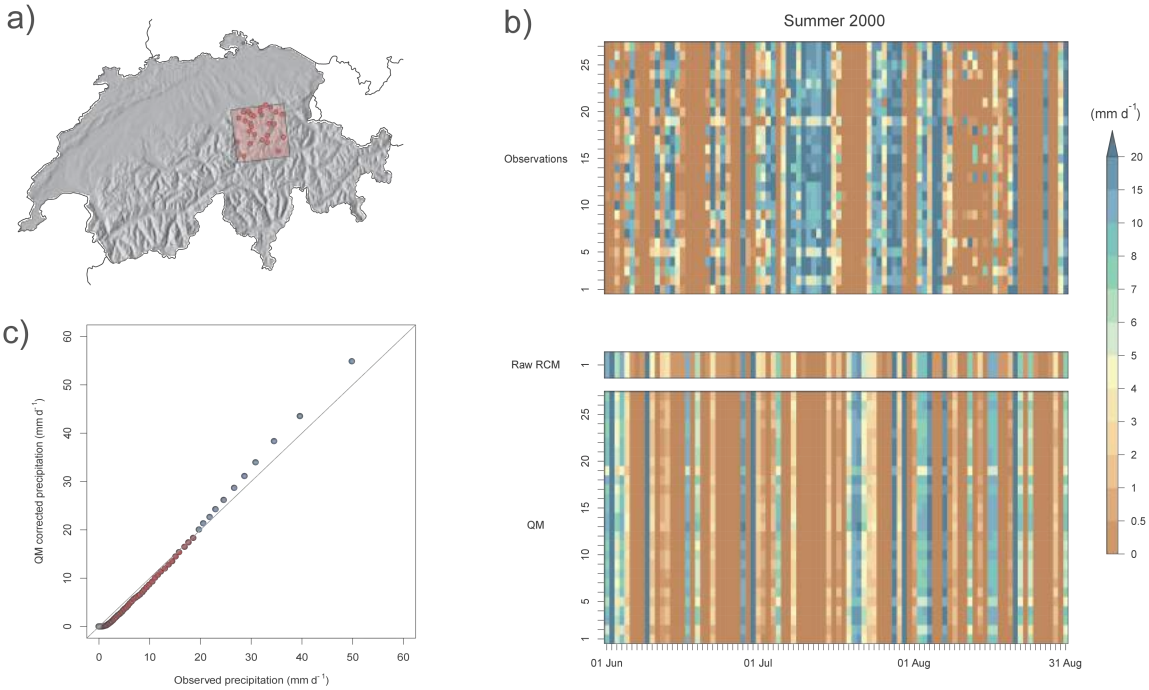

Figure 5.25. Example of the limitations of QM downscaling in a spatial context (based on [211]). Panel a: Location of the 27 stations for which quantile-mapped output is analyzed. All stations are situated within the same EUR-44 climate model grid cell. Panel b, upper part: Observed daily precipitation sums at all 27 stations in summer 2000. Panel b, middle part: Simulated daily grid-cell precipitation in the CH2018 model chain MPI-M-MPI-ESM-LR_CLMcom-CCLM4-8-17 (RCP4.5, EUR-44) in summer 2000. Panel b, lower part: Quantile-mapped precipitation sums for all 27 stations for the same model chain in summer 2000. Panel c: Quantile-quantile plot of observed (x-axis) and quantile-mapped (y-axis) areal daily precipitation sums for the entire QM calibration period 1981 - 2010. Areal daily sums were obtained by averaging the daily values for all 27 stations. Red markers: QM < observations. Blue markers: QM > observations.

Local-scale processes and feedbacks

QM as such is a purely empirical and data-driven approach. When applied in a downscaling context (QM to stations and QM to high-resolution grid), it connects coarse-resolution climate-model information to local-scale conditions without considering the underlying processes that translate a large-scale signal into its local-scale counterpart. If these processes become modified in a climate-change context, QM cannot account for it, as the technique completely relies on the stationarity of the correction function that is calibrated in a historical reference period. Examples of such processes active in Alpine terrain include local- and regional-scale circulation systems (slope and valley winds, Föhn) and elevation-dependent warming signals caused by the snow albedo feedback [198, 384]. See also the comprehensive discussion of these issues by [215]. Furthermore, with regard to elevation-dependent warming, QM-based downscaled projections will be representative of the elevation of the underlying RCM grid cell and not necessarily of the elevation of the target station or the high-resolution grid cell. Moreover, and in both pure bias-correction (QM on RCM grid) and downscaling contexts, intensity-dependent model biases might depend on the large-scale weather conditions, as represented by weather types, for instance [1, 372]. Such features are basically neglected by the QM approach employed here.

Inter-variable consistency

The QM approach utilized in CH2018 is a univariate correction, i.e., it treats each meteorological variable independently. Consequently, inter-variable consistency in the quantile-mapped products is not given a

priori. However, previous work has shown that, as long as inter-variable relationships are not strongly distorted in the raw RCM output, QM generally maintains inter-variable consistency and can to some extent even correct for biased relationships [174, 377]. Here, a favorable evaluation of the multivariate heat stress index considered in CH2018 (the wet bulb temperature) has been presented. Nevertheless, the CH2018 QM products can be subject to misrepresented inter-variable relationships. An obvious example involves individual days on which the quantile-mapped daily maximum temperature can be lower than the quantile-mapped daily mean or daily minimum temperature at specific stations or grid cells. The number of these cases is generally small, however.

Spatial representativeness

QM to stations as employed in CH2018 uses the simulated output of the climate model grid cell in which a given station of interest is located as a predictor. In the case of systematically biased spatial variability in the climate model and, in particular, in the case of strong circulation biases, this grid cell might not be the most representative cell for deriving scenarios for the station of interest [213]. In regions of pronounced topography, representativeness issues can arise even in the absence of systematic climate model biases in spatial variability, solely due to the fact that the climate model topography is only a coarse representation of the true topography. A given station, for instance, may be located along the northern rim of a ridgeline, whereas the overlying climate model grid cell might be located along the southern rim of the coarsened climate model topography and could thus be exposed to different circulation types. Moreover, in the case of elevation-dependent forcings such as the snow albedo feedback, a nearby climate model grid cell at similar elevation might be more representative of a given station than the directly overlying grid cell.

Circulation biases

The presence of large-scale circulation biases in the underlying climate models, such as a misrepresented frequency of weather types or a systematic dislocation of major storm tracks, can cause representativeness issues (see above), but it could also call into question the applicability of QM in general [216]. QM, by definition, corrects for local- to regional-scale biases but does not consider the nature of these biases or their possible relationship to the large-scale flow regime. Previous contributions have shown that climate model biases can depend considerably on the large-scale weather type [1, 264]. Hence, bias-corrected fields might be completely inconsistent with the large-scale flow in the underlying climate model, and bias-corrected fields for a given flow regime might be misrepresented. This potential shortcoming can be expected to affect inter-variable relationships in particular (see above) and to introduce artifacts into spatial climate change patterns. In the context of CH2018, the circulation biases of the climate models employed have not been investigated in detail.

5.8. Conclusions and implications

Empirical quantile mapping (QM) has been applied to all CH2018 climate-model chains to produce bias-corrected and downscaled climate scenario products at different spatial scales and for several meteorological variables. These data can be directly employed in subsequent climate impact assessments. This explicitly includes applications that refer to absolute thresholds of meteorological variables, such as the analysis of frequency changes in days above or below a certain temperature or precipitation threshold.

The primary QM product provides daily scenarios at a large number of individual stations in Switzerland and allows a broad range of applications. It has several advantages compared to the previously employed delta-change approach. These include the consideration of changes in temporal variability and of non-stationary model biases, as well as the direct provision of transient scenarios. A dedicated evaluation of the CH2018 QM implementation reveals satisfactory performance in the present-day climate in terms of the effective removal of mean model biases. Nonetheless, remaining biases might be present for extremes, for daily to interannual climate variability, for small-scale spatial climate variability, or for inter-variable relationships. However, the multivariate heat stress index (the wet bulb temperature) is well represented by its separately bias-corrected and downscaled input variables. The climate change signals derived from the

quantile-mapped product are largely consistent with other CH2018 products.

It should be acknowledged that, similar to all other downscaling and bias-correction methods, QM has a range of potential limitations and might not be applicable in every kind of climate impact research. These limitations mostly originate from the fact that QM is a purely statistical and data-driven method. It does not incorporate physically based knowledge on the processes that are responsible for either model biases or for small-scale climate variability beyond the scale resolved by the underlying climate models. These potential limitations are summarized and illustrated in Chapter 5.7. They especially arise in topographically structured terrain where spatial climate variability is large and relevant processes are not or are only approximately captured by climate models. Please also note that, like the seasonal mean scenarios presented in Chapter 4, the QM-based scenarios are subject to modeling and emission scenario uncertainties, as represented by the projection range of the model ensemble at hand. In particular, this includes the fact that, for a given emission scenario, there is some chance that future climate change will lie outside the uncertainty range of the CH2018 model ensemble.

As a consequence, users of the QM-based scenarios should properly address the sources of uncertainty and should assess the validity of the dataset for each specific application. This should include:

- if possible, the use of QM products derived from all or at least from several GCM-RCM combinations for a given forcing scenario in order to account for climate model uncertainty.
- a proper evaluation of both the QM-based CH2018 scenario product and the individual climate-impact model when driven by QM-based data in a historical reference period. This evaluation should especially consider aspects that are not explicitly corrected for by QM (such as temporal and spatial climate variability) and could also employ dedicated validation frameworks (e.g,. [275]).
- a careful use of QM-based scenarios simultaneously for multiple sites (QM to stations) or multiple grid cells (QM to high-resolution grid). In particular, proper validation of the spatial variability of the QM product at daily scales is essential for applications in which impact models are driven by QM data at the daily scale (e.g., hydrological models).
- a proper evaluation of multivariate relationships in the QM-based product when several variables are simultaneously provided to an impact model (e.g., hydrological models).
- if applicable, the explicit consideration of the fact that downscaled QM products potentially distort the height dependency of the climate change signals as represented by the raw climate model output.

6. Climate extremes and climate indices

Summary

Climate change will modify the frequency, intensity and character of extreme events In the future. This chapter discusses these changes with emphasis given to the long-term climate-change signal (i.e., the forced response), by considering projections for RCP8.5 by the end of the 21st century. However, at the scale of Switzerland, there is substantial decadal and year-to-year variability in extremes, which may dampen or amplify this forced response at timescales of years to decades. Depending on the type of extreme, the forced response will only emerge for a substantial level of anthropogenic warming (i.e. in RCP4.5 and RCP8.5 by the middle to end of the 21st century). The assessment provided in this chapter highlights the following changes in extremes as the most significant:

- More frequent, more intense, and longer-lasting *heatwaves* and *extremely hot days*. Along with central and southern Europe, Switzerland is a hotspot for changes in hot temperature extremes. The anomalous warming of hot extremes is due to increases in the amplitude of natural temperature variations on daily to seasonal timescales. Under RCP8.5, the hottest summer days are projected to warm by 5.4 - 6.1°C in the multi-model median by the end of the 21st century, depending on the region, with a substantial model range (3.9 - 9.4°C) (typical rounded range across models and regions: 4 - 8.5°C; see Chapter 6.4). Changes are substantially lower for RCP4.5 (2.5 - 3.2°C) and RCP2.6 (1.4 - 1.8°C). Likewise, very hot days that currently occur on average on about one day per summer are projected to occur on about 13 - 38 days or during 2 - 5 weeks per summer (typical range across models and regions; see Chapter 6.4).
- More frequent days with *heat stress* (temperature and humidity) and more warm nights as summer temperatures further increase. These changes are largest at low elevations where the population density is typically highest, and heat stress may be further amplified by urban heat island effects. For unmitigated climate change in particular, heat stress is projected to reach levels that have not been observed over the past century in Switzerland. The amplitude of the changes depends on the scenario considered. The number of days with high heat stress increases non-linearly with warming, becoming about 3 - 5 times more frequent for RCP8.5 than for RCP2.6. Under RCP8.5, half of the summer days in low-altitude areas of Ticino might exhibit high heat stress risk by the end of the 21st century (Chapter 6.5).
- Fewer and less intense *cold waves*, *frost days*, and *ice days*. Absolute changes (number of days) are largest at higher elevations and are much more pronounced in the case of non-mitigation scenarios. Given the very high natural internal variability of winter temperatures, cold winter periods will continue to occur for several more decades (Chapter 6.4).
- More frequent and more intense *heavy precipitation events* in all seasons, but particularly in the winter half year. This trend is projected for all event categories, from hourly downpours to multi-day events. The number and intensity of peak events increases much more strongly than mean precipitation, and may increase even in seasons with decreasing mean precipitation. For the RCP8.5 scenario and the end of the century, day-long heavy precipitation events (100-year return levels) are projected to increase by 10 - 25 %, depending on the season and region (multi-model median; Chapter 6.6,Figure 6.21). During the summer season, the projected changes in the intensity of heavy events on daily to hourly time scales are consistent with an increase of 6 - 7 % per degree warming (due to the Clausius-Clapeyron relationship expressing the increase in water holding capacity; Box 6.1). It follows that changes in heavy precipitation intensity increase approximately linearly with the warming and are thus correspondingly smaller for the mitigation scenarios. Confidence in heavy precipitation intensification is now substantially higher, given the evidence from observations and from a new generation of climate models run at unprecedented resolution. However, the EURO-CORDEX simulations still exhibit substantial spread. Along with the warming, there will also be a shift from solid (snow) to liquid (rain) precipitation. The associated intensification of heavy rainfall has implications for the risk of flooding, while the frequency of heavy snowfall events will decrease at low to mid-altitudes (< 2000 m; Chapter 6.6).

- In summer, there is likely a reduction in wet days in RCP8.5 by the end of the century, and the majority of models suggests longer *dry spells* (periods with no rain). Because of the substantial summer warming and the associated increase in evaporative demand, there is likely to be an increase in agricultural droughts (reductions in soil moisture). Relative to temperature and precipitation extremes, the extent of the drying remains rather uncertain (Chapter 6.7).

The RCP8.5 projected changes mentioned above fit into a continental-scale pattern that is in general qualitatively consistent with recent observational trends on a European scale. At the scale of Switzerland, there is significant decadal and year-to-year variability, and a comparison of projected versus observed patterns is difficult.

6.1. Introduction

This chapter covers projections of both climate extremes and climate indices. Here*climate extremes* encompass rare weather and climate events with potentially serious implications for humans, infrastructure, and the environment, whereas *climate indices* describe more frequent events, such as the frequency of warm days (above some absolute threshold, e.g., 25°C). Although these two categories of events are generally very different in terms of impacts, their assessment relies on similar methodologies. Furthermore, there is a smooth transition between the two concepts, depending on the location considered and the threshold employed. For these reasons, these two event categories are addressed in the same chapter. An overview of key climate indicators is provided in Appendix 1.

6.1.1. Extremes in a changing climate

Alterations in the occurrence of extreme events are a key component of climate change. Already the first IPCC Report [163] stated that “changes in the variability of weather and the frequency of extremes will generally have more impact than changes in the mean climate”. However, at that time the assessment of extremes in a changing climate mostly relied on conceptual and theoretical considerations, and extreme events featured on only a handful of pages in the 365-page IPCC report. Since then the understanding of extreme events and the ability to simulate extremes has dramatically improved. The most recent IPCC report [168] features extremes on more than one hundred pages, and extremes were also the subject of an IPCC Special Report [167, 311].

The development of Swiss climate scenarios followed a similar pattern. The early climate scenario reports compiled by the Swiss climate research community (e.g., [245]) offered very little quantitative information. Even in the most recent report [56], the information on climate extremes was synthesized predominantly based on a review of the literature; however, for the first time it also included an early analysis of regional climate model (RCM) simulations (see Chapter 8). In comparison, the information provided in the current chapter is more comprehensive, detailed, and quantitative.

Providing quantitative information about extremes is of great practical importance. This is particularly evident in the case of precipitation and runoff events. To date, the dimensioning of critical infrastructure such as bridges, dams, and urban runoff systems has largely been based on observations collected over recent decades. With the advent of climate change, past observational climatologies increasingly lose value as a guide to the future. Consequently, for infrastructure with lifetimes of many decades, new methodologies must be developed that combine the past observational record with climate-change projections.

In principle, extreme events can be defined for any meteorological variable, or any combination of variables. This report gives consideration to the most relevant extremes, including temperature extremes, heat stress (combining aspects of temperature and humidity), precipitation extremes (for hourly, daily, multi-day, and seasonal events), and droughts. In addition, the literature on wind extremes, hail, and thunderstorms is assessed.

6.1.2. Probability of extreme events

The quantitative definition of extreme events is based on the statistical distribution of the variables of interest. This is illustrated in Figure 6.1 using a schematic figure for daily temperature and precipitation events for current and future climatic conditions. The right-hand tail of the distribution represents extremes and can be are defined based on the exceedance of some threshold (colored areas). The figure demonstrates potential changes that may occur with climate change. It is evident that the occurrence of extremes is closely tied to both the center and the width of the distributions, which in the case of temperature are related to its mean and variability, respectively.

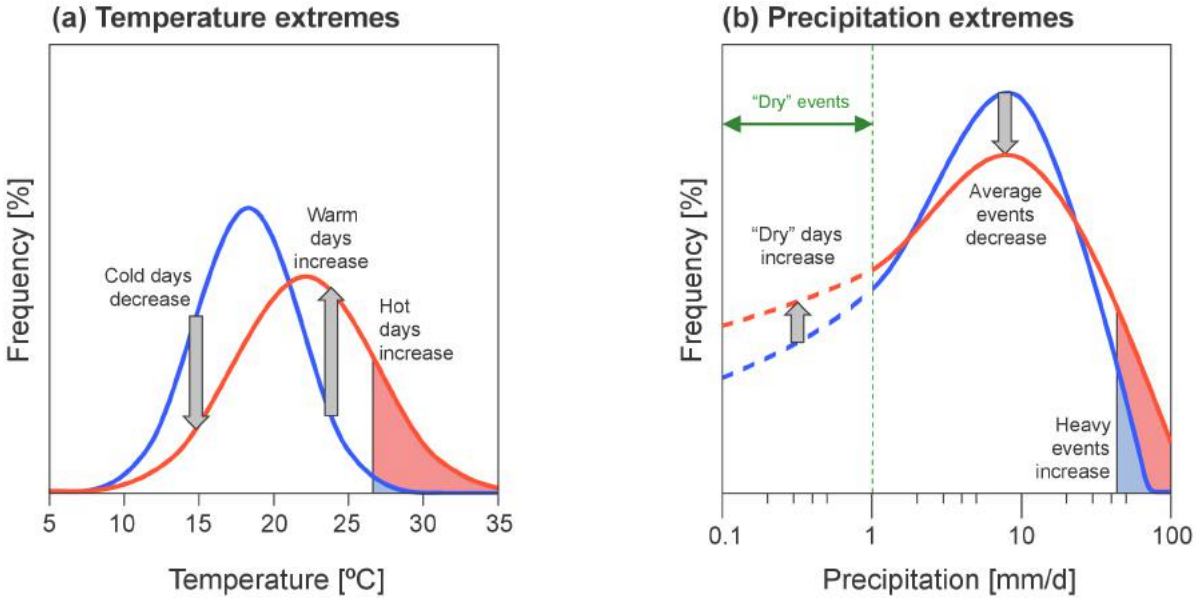

Figure 6.1. Schematic diagram explaining the definition of extreme events for daily (a) temperatures and (b) precipitation using probability density functions (PDFs). Extremes are defined at the tails of the statistical distribution as events exceeding some threshold (colored areas). A shift or change in the distribution with time from the current (blue) to the future (red) distribution leads to changes in the occurrence of extremes. Note that the consideration of precipitation requires the definition of a wet-day threshold (for daily events, usually 1 mm d^{-1}; see the green dashed line in the right-hand panel). The distributions shown are qualitative but are motivated by summer temperatures and precipitation in Zurich. The areas under the PDFs are proportional to the probability of occurrence.

More specifically, the standard deviation of the daily temperature distribution within the summer season typically amounts to 3 - 4 °C. As the expected climate shift is of similar magnitude, associated changes in the probability of hot extremes are very large (compare blue and red areas in Figure 6.1, a). Likewise, because the width of the distribution (which is largely due to natural variations) is large in comparison to the anticipated climate shift, apparent changes in the frequency of extremes may also be caused by chance. Distinguishing natural variations from external (anthropogenic) trends thus represents a challenging task. This difficulty applies to trends in observed (see Chapter 3) as well as simulated climate records (Chapter 6, Chapter 7).

Extreme events may represent a *hazard*, i.e., they have the potential to cause harm, incur damages, or even have catastrophic impacts. However, it is important to note that the definition of “extreme events” utilized in the current report follows a purely statistical concept, using meteorological variables and ignoring potential impacts. The term thus solely represents the hazard component of risk, i.e., the potential of an impact to happen. This is discussed in the next section.

6.1.3. Risk of extreme events

Risks emerge through the interplay of climate- and weather-related hazards, the exposure of goods or people to such hazards, and the specific vulnerability of exposed people, infrastructure, and the environment. Risk can be actively managed, and adaptation allows one to reduce risk, as society shapes exposure and vulnerability. By reducing GHG emissions, one can also indirectly reduce risk, since this

reduces the effect of climate change on the probability of extremes (or hazards).

Risk is the “effect of uncertainty on objectives” [171]. Risk can thus be defined as the combination of the probability of a consequence and its magnitude (i.e., risk = probability x severity). In the simplest case, “x” stands for multiplication, but more generally, it represents a convolution of the respective distributions of probability and severity. According to the IPCC [170], natural hazard risk is the combination and hence a function of hazard, exposure, and vulnerability:

risk = f(hazard, exposure, vulnerability) = probability of hazard x f(intensity of hazard, exposure, vulnerability),

where the last three parameters constitute “severity”.

Here, “hazard” describes weather events such as storms, floods, droughts, or heat waves both in terms of the probability of occurrence as well as the physical intensity. “Exposure” denotes the geographical distribution of people, livelihoods, and assets or infrastructure – generally speaking, of all items potentially exposed to hazards, including ecosystems and their services. “Vulnerability” describes how specific exposure will be affected by a specific hazard; that is, it relates the intensity of a given hazard to its impact, such as wind damage to buildings as a function of wind speed or the effect of a flood on a local community and the livelihoods of its residents.

Risk is best measured in the metrics relevant for decision making, e.g., the number of affected people in the context of evacuation, or the replacement value of buildings in the context of property insurance. Risk models therefore attempt to quantify the parameters determining risk in the way most appropriate for the specific purpose. Depending on the purpose, the level of detail in quantification will vary. For a geographical representation, consider, for example, a local flood model at very high resolution (a few decameters) compared to a drought impact model at 10-km resolution. With regard to the vulnerability resolution, consider a general description of building damage due to wind as a simple function of (gust) wind speed, compared to a detailed flood damage function that depends not only on flood height but also on the building construction type, the number of floors, whether or not there is a basement, etc.

Risk management starts with the joint identification of risks and related parameters by all relevant stakeholders, followed by a risk analysis building on the quantification of hazard, exposure, vulnerability, and a careful evaluation of the combination thereof. This analysis forms the basis for the appraisal of specific adaptation options and adaptation planning. Such a comprehensive approach to risk also allows for measurement, reporting and verification of the effectiveness of adaptation, and thus facilitates constant improvements along the risk management cycle.

The present report focuses on the hazard side, i.e., on the frequency and intensity of physical variables describing meteorological events. Consequently, the results presented in this report should by no means be viewed as a quantification of risk. In order to quantify risk, information about exposure and vulnerability would need to be integrated. Nevertheless, the results presented here will serve as a solid basis for risk-based approaches to decision making in the context of weather and climate.

6.2. Methods

6.2.1. Definition of indices and extremes

As indicated in Figure 6.1, the quantitative definition of extreme events and climate indices is based on the statistical distribution of all events of the category under consideration. For temperature, the statistical distribution of daily temperature approximately follows a bell-shaped (Gaussian) distribution (see Figure 6.1, a). If the distribution is shifted toward warmer temperatures (blue and red curves), as expected with climate change, the frequency of cool days will decrease, whereas hot days may become significatnly more common. As illustrated, the statistical distribution may not only shift, but it may change in other aspects as

well. In the current example, it is assumed that it undergoes an increase in variability (or variance), i.e., the distribution widens. Such changes may be more critical than mere shifts in the distribution [163, 179, 306].

For precipitation (see Figure 6.1, b), the situation is more complex. First, precipitation is not Gaussian distributed, and the nature of its distribution strongly depends upon the region and timescale considered (i.e., daily versus hourly precipitation). Second, the description of the precipitation statistics requires the consideration of dry periods. In practice, a wet-day threshold is introduced (e.g., 1 mm d^{-1} for daily events), and events below this threshold are considered “dry”. The choice of such a wet-day threshold was originally motivated by observational constraints, as standard rain-gauge instruments suffer from substantial errors at low precipitation intensities. The details of the precipitation distribution below this threshold (dashed lines in Figure 6.1, b) are not further considered.

Although the case of precipitation is far more complex than that of temperature, it is nevertheless evident from Figure 6.1 that their behavior under climate change can be qualitatively comparable: Both distributions are shifted toward the right (i.e., temperature experiences a warming and precipitation an intensification). As a result, the frequency of cold days decreases (warm days increases), and the frequency of small precipitation amounts decreases (heavy events increases).

6.2.2. Extreme and climate indices used in CH2018

One of the major challenges of climate change research is to adequately accounting for all possible changes in statistical distributions. To this end, a number of indices that address different event levels (from frequent, normal events to rare, extreme events) are used. A recommended list of indices is available from a WMO-initiated expert team (Expert Team on Climate Change Detection and Indices, ETCCDI; see [392]). The current report uses a carefully selected list of these indices, but deviates in part from the team’s recommendations. In addition, the selection takes into account the recommendations from a user survey [230], which revealed a need for additional information on climate extremes.

The indices considered are best defined using the cumulative distribution function (seeFigure 6.2, b), which expresses the probability that a variable is below (or above) some threshold. There are two classes of indices:

- Frequency indices assess the change in exceedance probability (or exceedance frequency) for a given event size (vertical arrow in Figure 6.2, b). An example of this index is the number of*hot days* (e.g., temperature above 30 °C).
- Intensity indices assess the change in intensity at a given probability level (horizontal arrow in Figure 6.2, b). Percentile indices represent a subset of these indices. For instance, the 99th temperature percentile measures the temperature that on average is exceeded in 1 out of 100 days. Similarly, the 10-year return level of a precipitation event reflects the intensity of a precipitation event that on average occurs once every 10 years.

It is important to note that these two categories of indices are not independent: An increase in one of the measures implies an increase in the other (see Figure 6.2, b). However, relative changes in the two categories are not identical.

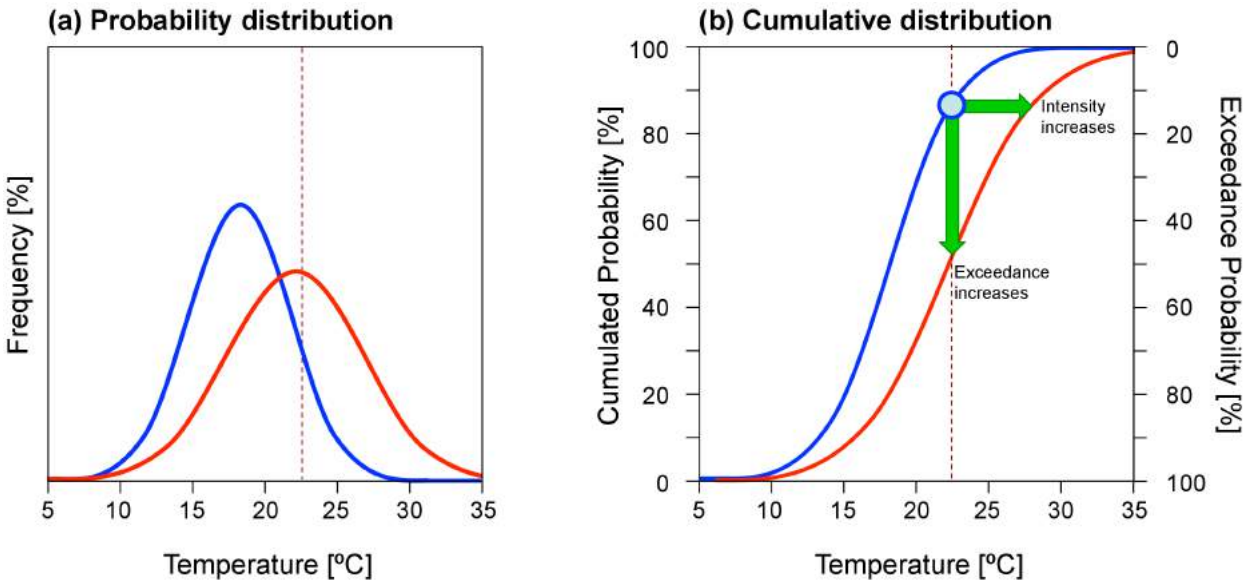

Figure 6.2. Schematic diagram explaining the use of (a) probability density functions (PDFs) and (b) cumulative distribution functions (CDFs) for the analysis of temperature indices and extremes. The CDF can be phrased in terms of the cumulative probability or the exceedance probability (left-hand and right-hand axes, respectively). The green arrows in (b) indicate the two main categories of indices, i.e., frequency indices (measuring the change in exceedance at some fixed intensity) and intensity indices (measuring the change in intensity at some fixed probability).

In the CH2018 project, a large number of different indices have been investigated using observations (Chapter 2) or information from the EURO-CORDEX regional climate models (in this chapter). The indices are summarized in Table 6.1. The optimal choice of an index, as well as the underlying statistical methodology, depends on a number of factors.

Percentile indices are commonly used for temperature and precipitation extremes. These are intensity indices expressing the magnitude of an event that occurs with a given probability. For instance, the 99th percentile of daily temperature refers to temperature events that are exceeded with a probability of 1 %. In the case of daily precipitation, these percentiles may be relative to wet days (within the sample of events with precipitation > 1 mm/day) or relative to all events (wet and dry days). In CH2018, all-day percentiles are used exclusively, as wet-day percentiles are difficult to interpret and may be misleading [305].

Abbreviation	Definition	Unit	Averaging
Temperature extremes			
TXx	Hottest day of the year: Annual maximum of daily Tmax	°C	Annual time-series, 30yr mean
TNn	Coldest night of the year: Annual minimum of daily Tmin	°C	Annual time-series, 30yr mean
TNx	Warmest night of the year: Annual maximum of daily Tmin	°C	Annual time-series, 30yr mean
TXn	Coldest day of the year: Annual minimum of daily Tmax	°C	Annual time-series, 30yr mean
Hot spells			
TXx7d	Hottest week of the year: Maximum 7-day mean of daily Tmax	°C	Annual time-series, 30yr mean
Temperature indices			
TX>25C	Summer days: number of days with Tmax > 25°C	days	Annual time-series, 30yr mean
TX>30C	Hot days: Annual number of days with Tmax > 30°C	days	Annual time-series, 30yr mean
TN>20C	Tropical nights: Annual number of days with Tmin > 20°C	days	Annual time-series, 30yr mean
TN<0C	Frost days: Annual number of days with Tmin < 0°C	days	Annual time-series, 30yr mean
TX<0C	Ice days: Annual number of days with Tmax < 0°C	days	Annual time-series, 30yr mean
Temperature percentiles			
TXp90%	90th percentile of Tmax	°C	Seasonal percentile computed over 30yr
TXp95%	95th percentile of Tmax	°C	Seasonal percentile computed over 30yr
TXp99%	99th percentile of Tmax	°C	Seasonal percentile computed over 30yr
TNp5%	5th percentile of Tmin	°C	Seasonal percentile computed over 30yr
Percentile-temperature exceedances			
TX95P	Hot days: Number of days with Tmax > TXp95% of CTRL	days	Annual time-series, 30yr mean
TX99P	Very hot days: Number of days with Tmax > TXp99% of CTRL	days	Annual time-series, 30yr mean
TN5P	Cold days: Number of days with Tmin < TNp5% of CTRL	days	Annual time-series, 30yr mean
Wet-bulb temperature (based on daily mean temperature and daily mean relative humidity)			
TWx	Maximum of wet-bulb temperature	°C	Annual time-series, 30yr mean
TWg22	Number of days with wet-bulb temperature greater than 22°C	days	Annual time-series, 30yr mean
Precipitation indices			
MEA	Mean daily precipitation	mm/d	Seasonal 30yr mean
FRE	Wet-day frequency: frequency of wet days (R>1mm/day)	fraction	Seasonal 30yr mean
INT	Wet-day intensity: mean precipitation amout on wet days	mm/d	Seasonal 30yr mean
Rx1d	Maximum of 1-day precipitation	mm/d	Seasonal 30yr mean
Rx5d	Maximum of 5-day accumulated precipitation	mm/d	Seasonal 30yr mean
Precipitation Percentiles			
Rp90%	90th all-day percentile of daily precipitation	mm/d	Seasonal percentile computed over 30yr
Rp95%	95th all-day percentile of daily precipitation	mm/d	Seasonal percentile computed over 30yr
Rp99%	99th all-day percentile of daily precipitation	mm/d	Seasonal percentile computed over 30yr
Precipitation return levels for return periods of YY = 5, 10, 20, 50, 100 years (computed using generalized extreme value analysis)			
x1d.YY	YY-year return levels of daily precipitation	mm/d	Seasonal 30yr estimate
x3d.YY	YY-year return levels of 3-day accumulated precipitation	mm/d	Seasonal 30yr estimate
x5d.YY	YY-year return levels of 5-day accumulated precipitation	mm/d	Seasonal 30yr estimate
Drought indices			
CDD	Maximum number of consecutive dry days (R<1mm/day)	days	Seasonal 30yr mean
SPI3	Standardized precipitation index for 3-months acc. precipitation	-	Seasonal 30yr mean
P-E	Precipitation minus evapotranspiration	mm/d	Seasonal 30yr mean
SMA	Standardized soil moisture anomaly	-	Seasonal 30yr mean

Table 6.1. Climate indices and extreme indices used in this study.

6.2.3. Additional aspects

The treatment of climate-model biases depends upon the index under consideration. Some of the indices are defined relative to the statistical distribution of the targeted variable; in this case, bias correction is not always needed. This applies, for instance, to changes in percentiles (such as *Tx90%*) and changes in maximum indices (such as *TXx*). However, if an index relies on an absolute threshold (such as the frequency of summer days *TX>25C*), bias correction is usually required. In CH2018, the standard methodology for bias correction is quantile mapping (see Chapter 5). In this chapter, we use bias-corrected data in Chapter 6.3 and Chapter 6.5 and raw model output in the remaining sections. As bias-correction methodologies require an observational reference, the geographical domain that can be considered varies from index to index. For some of the indices, the results can be assessed over the entire computational domain of the models considered (e.g., for changes in annual maximum temperature); for others, a credible observational reference is available for the area of Switzerland (e.g., for the frequency of summer days); and for still others, bias correction is only feasible where surface observations at stations are available (e.g., heat-stress indices). This explains the heterogeneity of the figures in this chapter.

This chapter uses the same ensemble of EURO-CORDEX simulations as considered in Chapter 4. The temporal evolution of the climate-change signal until 2100 can be directly derived from the transient simulations that mostly cover the period 1950 - 2100. In order to incorporate different emission pathways (RCPs), use is made of the time-shift pattern-scaling approach (Chapter 4.2). This approach enables a consistent treatment across scenarios and projection periods.

6.3. Temperature indices

Rising temperatures will have an effect on the frequency of temperature-related indices such as *summer days* and *frost days* [398, 85, 206]. Here, the projected evolution of temperature threshold indices (see Chapter 4.3.2 Definition of indices and extremes) in Switzerland over the course of the 21st century is presented in terms of spatial patterns of the absolute number of days for the individual scenario periods (maps of the respective change signals can be found in Appendix 3.1). In addition, the results of an explicit analysis of the elevation dependency of the indices' changes are described. This exercise is based on bias-corrected model data (multi-model combination) at stations (QM to stations) and on a 2-km high-resolution grid (QM to high-resolution grid; see Figure 5.4).

Due to the absolute nature of the temperature threshold indices considered, they show a strong elevation dependency expressed by large – and in part sharp – elevation gradients (see also Chapter 3.3.2). This is a direct consequence of the elevation dependency of temperature itself and results in high numbers of *summer days* and *hot days* in the lowlands (typically 20 - 60 *summer days* and 0 - 15 *hot days* on the Swiss Plateau and in Alpine valleys in the reference period) and only very few or no occurrences in regions above 1000 m a.s.l. (Figure 6.6). Conversely, the maximum numbers of *frost days* and *ice days* are found in high-Alpine regions (more than 200 *frost days* and more than 150 *ice days* under present-day conditions), whereas only a few *ice days* are observed in the lowlands (Figure 6.6). *Tropical nights* are only found in the low regions and Föhn valleys under present-day conditions. In general, they occur very rarely, namely about once in 1 to 10 years (Figure 6.5 upper row, Figure 13.47 upper row, and Figure 6.6). It should be noted that such low occurrence frequencies are subject to important sampling uncertainties and should be interpreted cautiously. This is true for both the present-day and the future climate.

According to the projections, climate change will have a distinct effect on all indices considered, in particular for the high RCP8.5 forcing scenario and for the period 2085. Most regions are expected to experience increases in the amounts of *summer days*, *hot days*, and *tropical nights*. The latter will also affect large areas of Switzerland where *tropical nights* do not occur in the present-day climate. All regions of Switzerland are projected to face pronounced decreases in the numbers of *frost days* and *ice days*, which is consistent with the observed trend over the past century (see Chapter 3.3.2). *Ice days* will be rare events in the future climates of Ticino and the Lake Geneva region. Projected changes are, in general, less pronounced

for earlier scenario periods and for RCPs 2.6 and 4.5 (see also Appendix 3.1). A summary of the results for each individual index is provided below.

In the reference period, *hot days* (Figure 6.3, Figure 13.49) only occur at low and middle elevations (up to 20 days per year), but a larger proportion of the country will be affected in the future, including considerable parts of the Alps. The frequency of *hot days* is projected to increase by more than 50 days per year in many low-lying regions for the period 2085 of RCP8.5. On the Swiss Plateau, more than 30 hot days per year are expected for the period 2085 and the RCP8.5 forcing scenario; in Ticino and the Lake Geneva region, more than 50 days per year are expected. These numbers are lower for RCP4.5 and especially for RCP2.6 as well as for earlier scenario periods, but are for most parts of the country still higher than for the present-day reference period.

Summer days (Figure 6.5, Figure 13.46, Figure 13.50) occur regularly in most areas under current conditions (up to more than 50 days per year in low-lying regions), except for elevations above 2000 m a.s.l. (see Figure 6.6). In the future, the lowlands are projected to experience many more *summer days*, with up to 100 days per year in low-lying parts of western and southern Switzerland for RCP8.5. Here, frequency increases of more than 50 days per year are possible. Furthermore, the projections suggest the frequent occurrence of *summer days* over large parts of the Alpine area. For the low-emission scenario RCP2.6, frequency increases of typically fewer than 20 days per year are obtained for the period 2085.

Tropical nights (Figure 6.5, Figure 13.47, Figure 13.51) seldom occur under current conditions and are restricted to only a few locations (e.g., to Ticino and very low-lying urban areas; up to about 10 nights per year). Projections suggest an expansion of areas affected by *tropical nights* in the future for all scenario periods and for all forcing scenarios. In the lowlands and in Ticino in particular, *tropical nights* are projected to become frequent events that can occur on average 10 - 30 times per year for the period 2085 and RCP8.5. Exceptions are high-elevation regions above 1500 - 2000 m a.s.l., where *tropical nights* will continue to be rare events even for the most extreme scenario, RCP8.5. For earlier scenario periods and for the RCPs 2.6 and 4.5, the frequency of *tropical nights* typically increases by fewer than 5 events per year.

Frost days (Figure 6.4, Figure 13.52) currently occur regularly in all regions of Switzerland; at high elevations above 2000 m a.s.l., more than 50 % of all days are *frost days* in the present-day climate. Occurrence frequencies at low elevations are considerably smaller (typically fewer than 100 days per year). For all scenario periods, the number of *frost days* is projected to decrease all across Switzerland, with widespread reductions of more than 20 and in part exceeding 80 days per year by the end of the century. For RCP8.5 and the period 2085, low-lying regions are expected to experience very few *frost days*, but typically more than 25 days per year will be obtained for the forcing scenarios RCP2.6 and RCP4.5 and for earlier scenario periods. High elevations in the Alpine region will also experience fewer *frost days*, but frequencies will still exceed 100 days per year for RCP8.5 and the period 2085.

Ice days (Figure 6.5, Figure 13.48, Figure 13.53) are also a common feature of Switzerland's present-day climate and occur at all locations. They are exceptional in Ticino, but they frequently occur in high-Alpine regions, where *ice day* frequencies can exceed 100 days per year. In the future, the number of*ice days* is projected to decrease substantially in all regions, and lowlands will only rarely experience *ice day* conditions. For RCP8.5 and the period 2085, projections suggest an *ice day* fraction of less than 50 % even in high-Alpine regions. This reduction is less pronounced for earlier scenario periods and for RCPs 2.6 and 4.5.

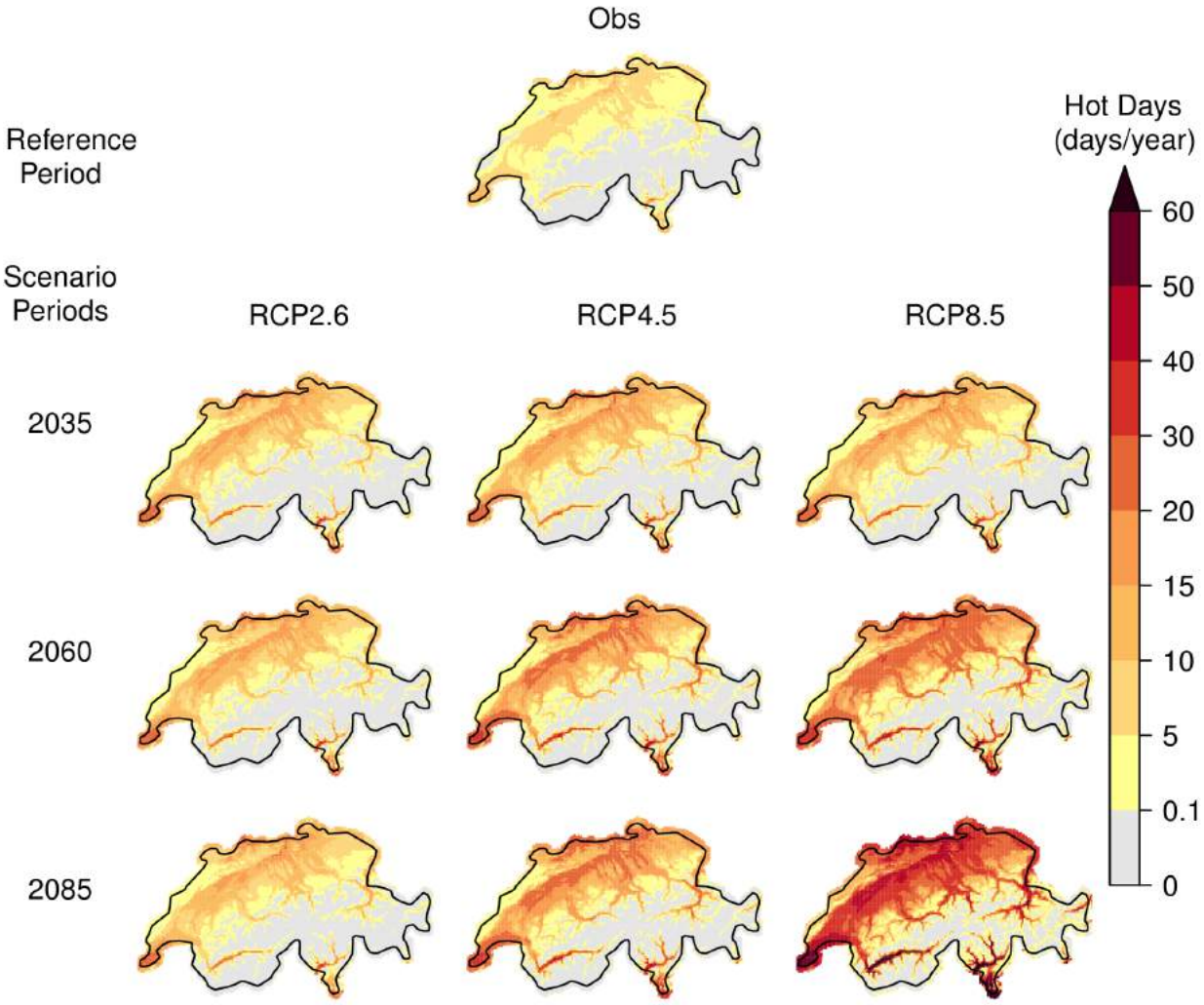

Figure 6.3. Hot days frequency. First row: 2-km observational grid in the reference period 1981 - 2010. Lower rows: Projected ensemble median number (multi-model combination) of the bias-corrected RCM data (QM to high-resolution grid) for the three scenario periods (rows) and the three forcing scenarios (columns). See Figure 13.49 for the respective change signals. Note that the model uncertainty of the change signal is not reflected by the ensemble median number displayed here and can be substantial.

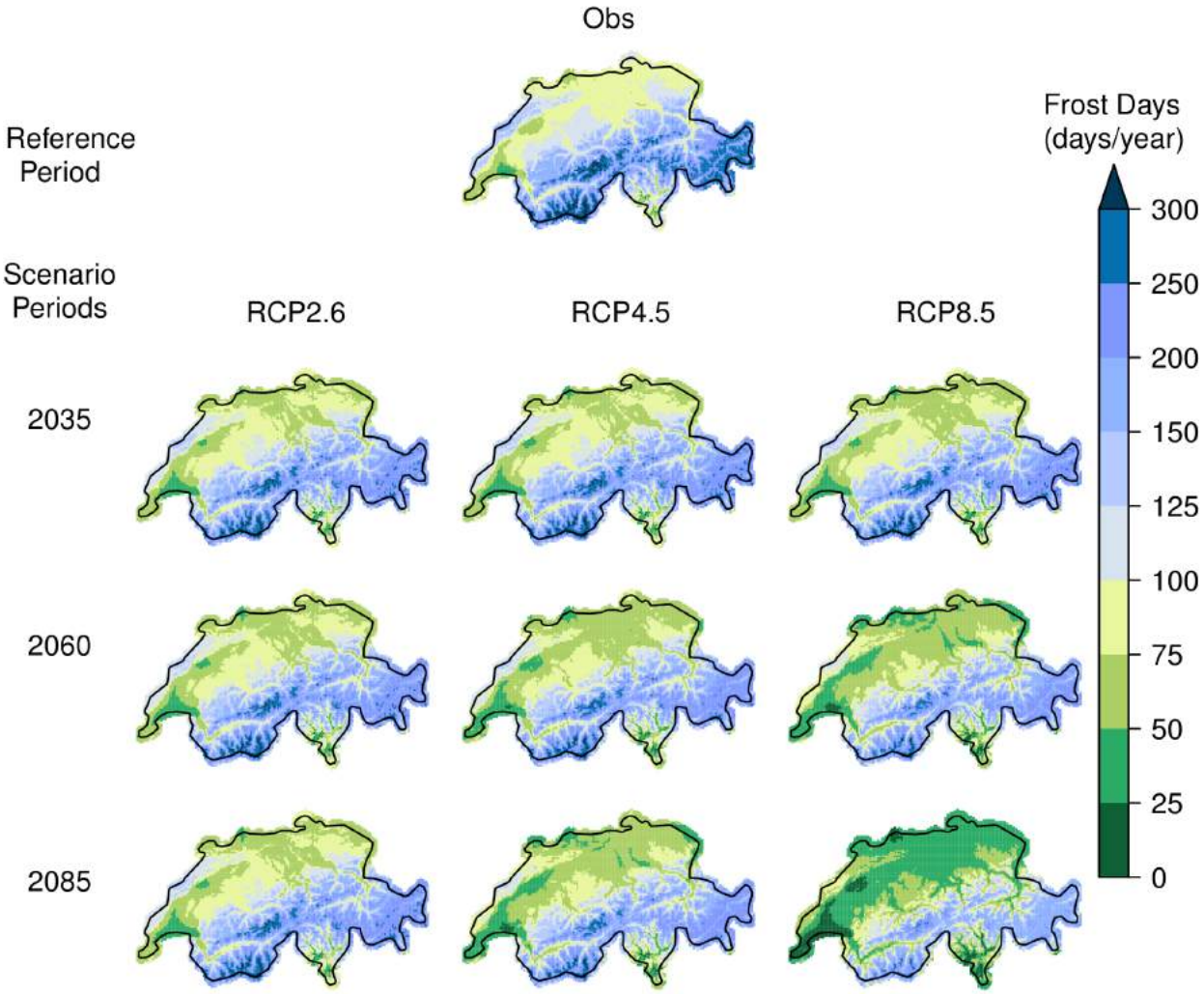

Figure 6.4. As Figure 6.3, but for frost days frequency. See Figure 13.52 for the respective change signals.

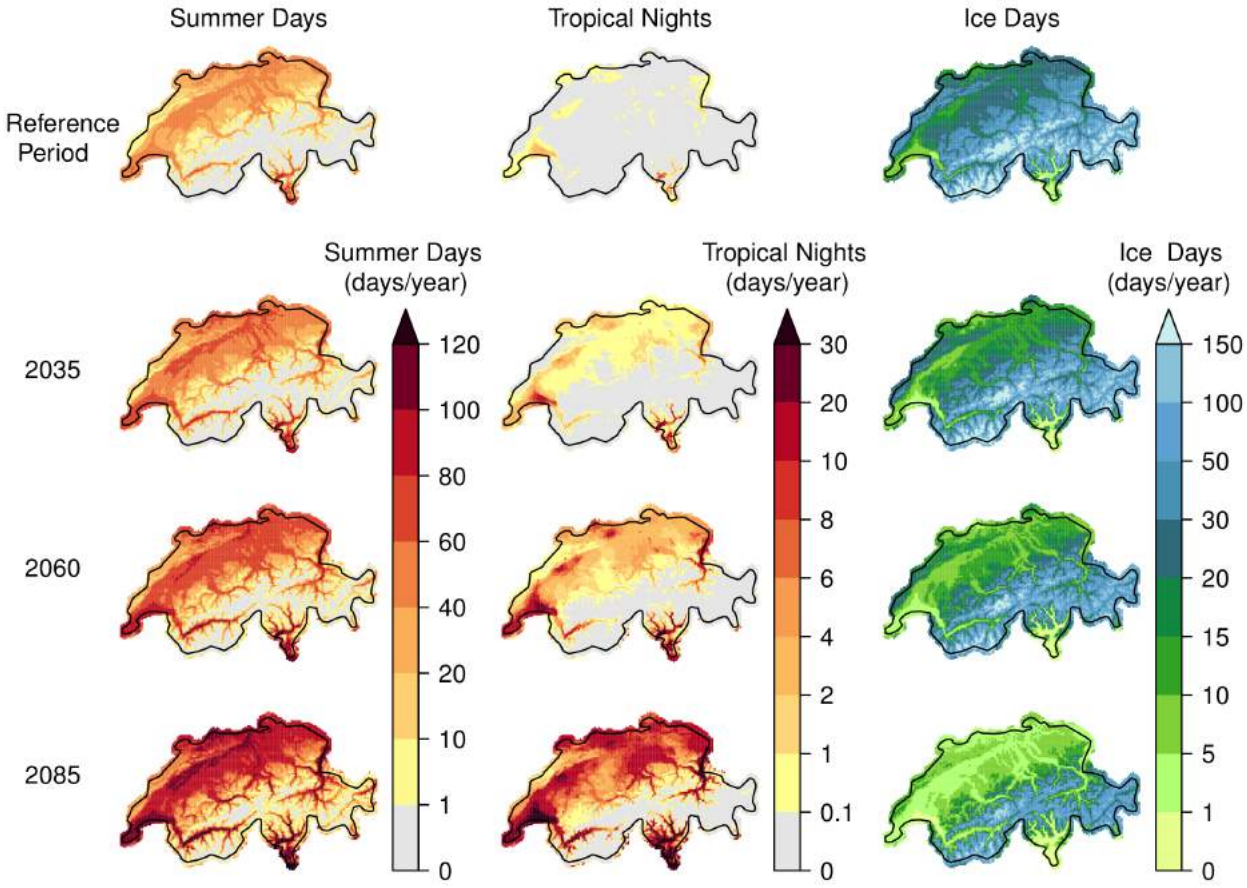

Figure 6.5. Frequency of summer days (left column), tropical nights (middle column), and ice days (right column). First row: 2-km observational grid in the reference period 1981 - 2010. Lower rows: Projected ensemble median number (multi-model combination) of the bias-corrected RCM data (QM to high-resolution grid) for the three scenario periods and for RCP8.5. See Figure 13.46, Figure 13.47, and Figure 13.48 for the full set of forcing scenarios. See Figure 13.50, Figure 13.51, and Figure 13.53 for the respective change signals. Note that the model uncertainty of the change signal is not reflected by the ensemble median number displayed here and can be substantial.

In summary, both present-day occurrences as well as changes in all temperature indices are subject to considerable *elevation dependencies*. These are visualized in Figure 6.6 and Figure 6.7, which show the absolute value and the change in the respective index as a function of elevation for the period 2085. In general, index regimes are expected to be subject to an upward shift following the general warming. However, even under strong forcing (RCP8.5), high elevations above 2500 m a.s.l. will not experience warm or hot conditions (*summer days*, *hot days*, *tropical nights*) although the temperature on the warmest days will also increase strongly relative to the present-day climatology Chapter 6.4. In contrast, low- and mid-elevation regions below 2000 m a.s.l. are expected to experience drastic increases in indices of hot conditions and might even experience events that do not typically occur in the present-day climate. Examples are the future occurrence of *hot days* and *tropical nights* above 1000 m a.s.l. Cold temperature indices drastically decrease across all elevations. These decreases are, in absolute terms, larger at high elevations but in relative terms still very substantial at low elevations. Under RCP8.5 conditions and by the end of the century, regions below 1000 m a.s.l. might no longer experience *ice days*.

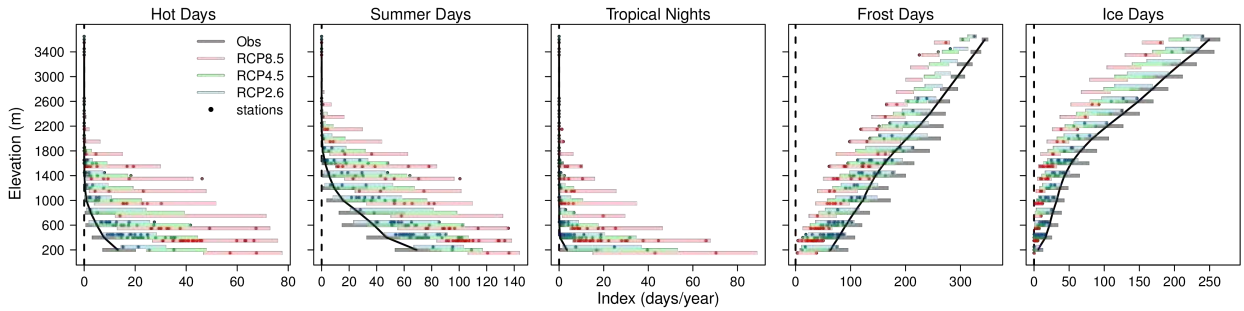

Figure 6.6. Ensemble median frequency (days/year) of the five temperature indices in individual elevation classes (200-m intervals) as represented by bias-corrected data (QM to stations and QM to high-resolution grid; multi-model combination). Black/grey: Observations in the reference period. Color: Bias-corrected data (QM to stations and QM to high-resolution grid) in the late scenario period (2070 - 2099). The points mark the station-based projections (QM to stations; illustrative set); the bars indicate the range of the 2-km observational grid and of the ensemble median of the grid-based QM product (QM to high-resolution grid) in the corresponding elevation class. The black line denotes the elevation-mean number of days in the gridded observations.

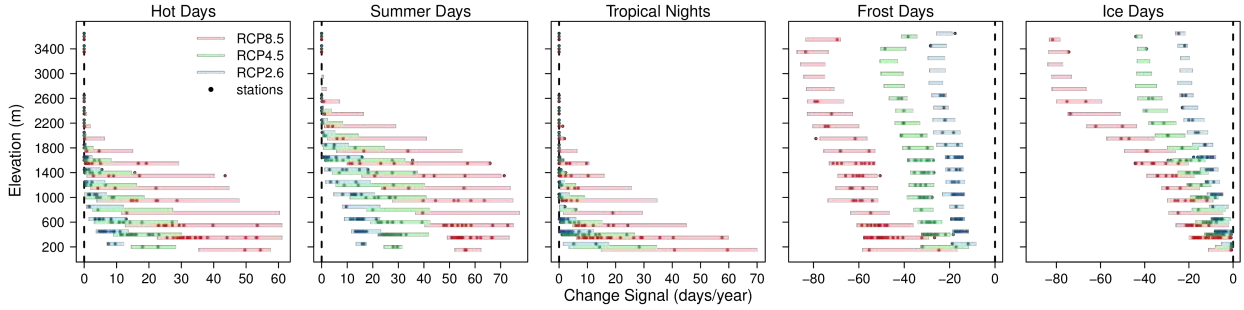

Figure 6.7. Ensemble median change signal (multi-model combination) of the five temperature indices for the late scenario period 2085 and for individual elevation classes (200-m intervals). The points mark the station-based projections (QM to stations; illustrative set); the bars indicate the range of the ensemble median of the 2-km data in the corresponding elevation class.

Finally, turning to the level of individual stations, Figure 6.8, Figure 13.54, and Figure 13.55 present the absolute numbers of the five temperature threshold indices for the reference period and the three scenario periods for the four exemplary sites of Zurich/Fluntern, Weissfluhjoch, Sion, and Lugano. At all four sites, the number of hot events (*hot days*, *summer days*, *tropical nights*) increases with time. In Zurich and Sion, *tropical nights* are basically absent in the present-day climate but can reach important occurrence frequencies by the end of the century for RCP8.5 (about 10 to 20 nights per year for the multi-model ensemble median; Figure 6.8). In Lugano, frequencies of about 10 nights per year already occur today. For RCP8.5, this number might increase to between 60 and 90 nights per year (taking into account model uncertainty) by the end of the century – more than every other summer night. Weissfluhjoch does not experience hot extremes in the present, and even for RCP8.5 future occurrences are only obtained for a few model chains but typically not for the multi-model ensemble median. Conversely, cold extremes are projected to decrease at all sites. For RCP8.5, Lugano might no longer experience any *ice days* at all by 2085.

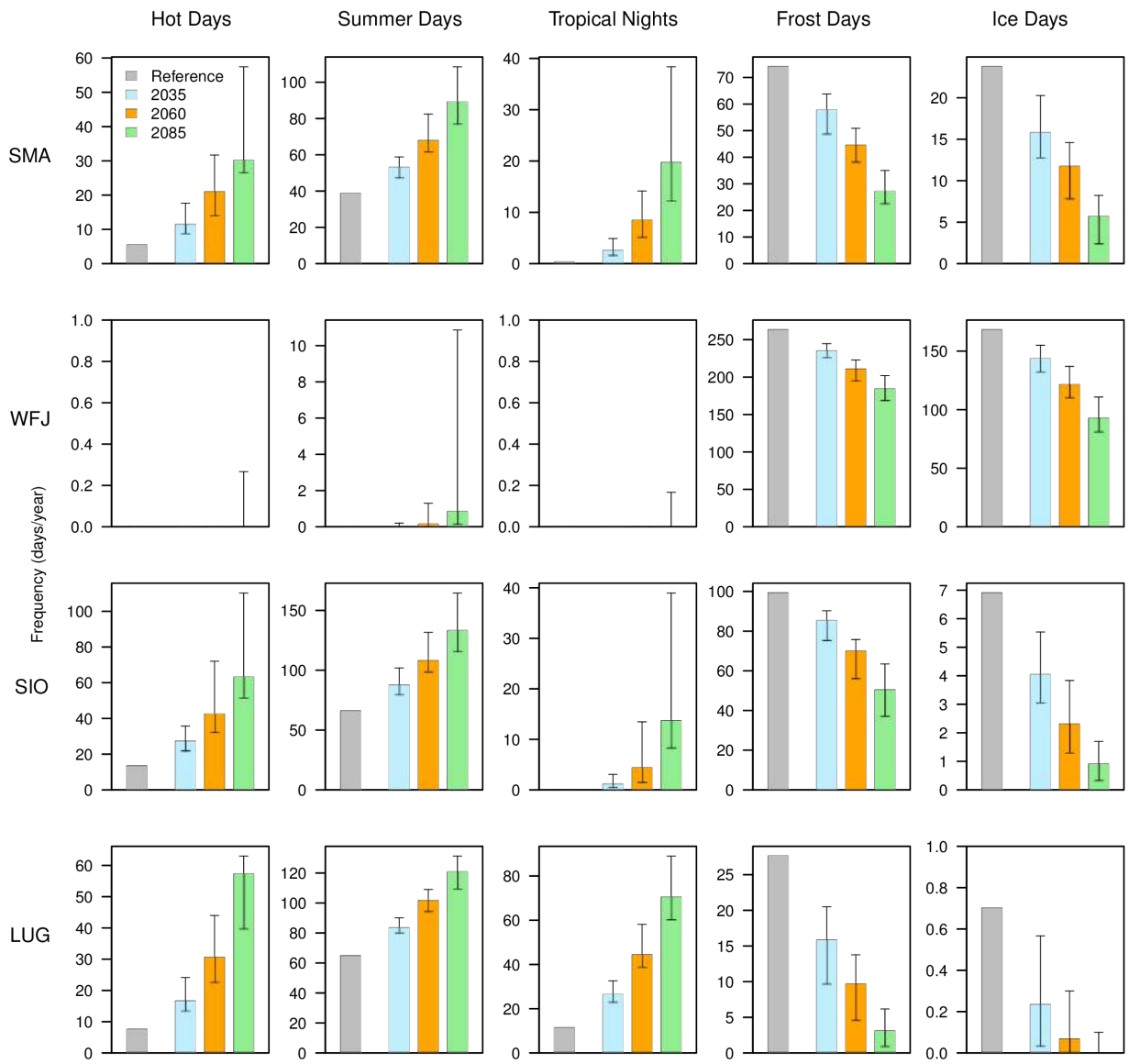

Figure 6.8. Frequency of hot days, summer days, tropical nights, frost days, and ice days in the reference period (observations) and in the three scenario periods (multi-model combination; QM to stations) for RCP8.5 at the four exemplary sites of Zurich/Fluntern (SMA), Weissfluhjoch (WFJ), Sion (SIO), and Lugano (LUG). Bars indicate the ensemble median number; whiskers, the 5 - 95 % model range. See Figure 13.54 and Figure 13.55 for RCP2.6 and RCP4.5.

6.4. Temperature extremes

6.4.1. Heat extremes

Along with increasing summer mean temperatures, hot extremes are virtually certain to increase [66, 311] and become more frequent, intense, and persistent across all land regions globally. Likewise, over Switzerland, heat extremes (here expressed as the maximum temperature of the *hottest day of the year TXx*) are projected to intensify. Depending on the region, the best estimate (multi-model median) for the intensification corresponds to 1.8 - 1.9 °C by 2035, 3.4 - 3.6 °C by 2060, and 5.4 - 6.1 °C by 2085 (Figure 6.10) in RCP8.5, depending on the region. Best estimates for changes are much smaller for RCP4.5 (2.5 - 3.2 °C) and RCP2.6 (1.4 - 1.8 °C). Note that these best estimates include very large uncertainties due to structural and parametric model uncertainties and internal variability. For example, projected *TXx* changes by 2085 for RCP8.5 vary between 3.9 °C and 9.4 °C, depending on the model (typical rounded range across Switzerland 4 - 8.5 °C). The *TXx* changes are consistent with the warming of the *warmest night of the year TNx* (Figure 13.56) and the *hottest week of the year TXx7d* (Figure 13.58), which is a measure of heatwave intensity. The intensification of the *hottest day of the year TXx* (Figure 6.9) is projected to substantially exceed the corresponding summer mean warming (Figure 6.11), an amplification that is consistent with the rest of south-central Europe. This amplification of heat extremes results from enhanced interannual to day-to-day temperature variability and increasing diurnal temperature ranges (Figure 6.11), which is in accordance with earlier generations of regional and global climate models [306, 313, 110, 103, 108, 249, 54]. It has been suggested that the increase in the variability of summer temperatures and in the diurnal temperature range is related to land-atmosphere interactions, including the altered partitioning of sensible and latent heat flux as a result of drying vegetation as well as reduced cloud cover and atmospheric relative humidity [313, 110, 54]. Although the temperature variability increase is robust across models, there is not yet clear observational evidence (Chapter 4.4) [77, 324, 298]. In the European context, the intensification of hot extremes is most pronounced north of the Mediterranean Sea, including France and Switzerland (Figure 6.9). Switzerland thereby forms part of a hotspot region that has experienced one of the strongest intensifications of heat extremes over recent decades [82, 106]; moreover, this region is projected to be one of the areas that will experience the strongest future intensification of hot extremes worldwide [249, 104, 312]. Although the sign of the change is robust (warming), these projections exhibit a large model spread (Figure 6.10) due to uncertainty in the regional mean warming (see section) and due to factors specifically amplifying or damping variability and extremes, such as potential circulation changes [68, 159], land surface feedbacks [358, 356, 110, 359], aerosol forcing [323], and irrigation and land-use changes [73, 341, 155].

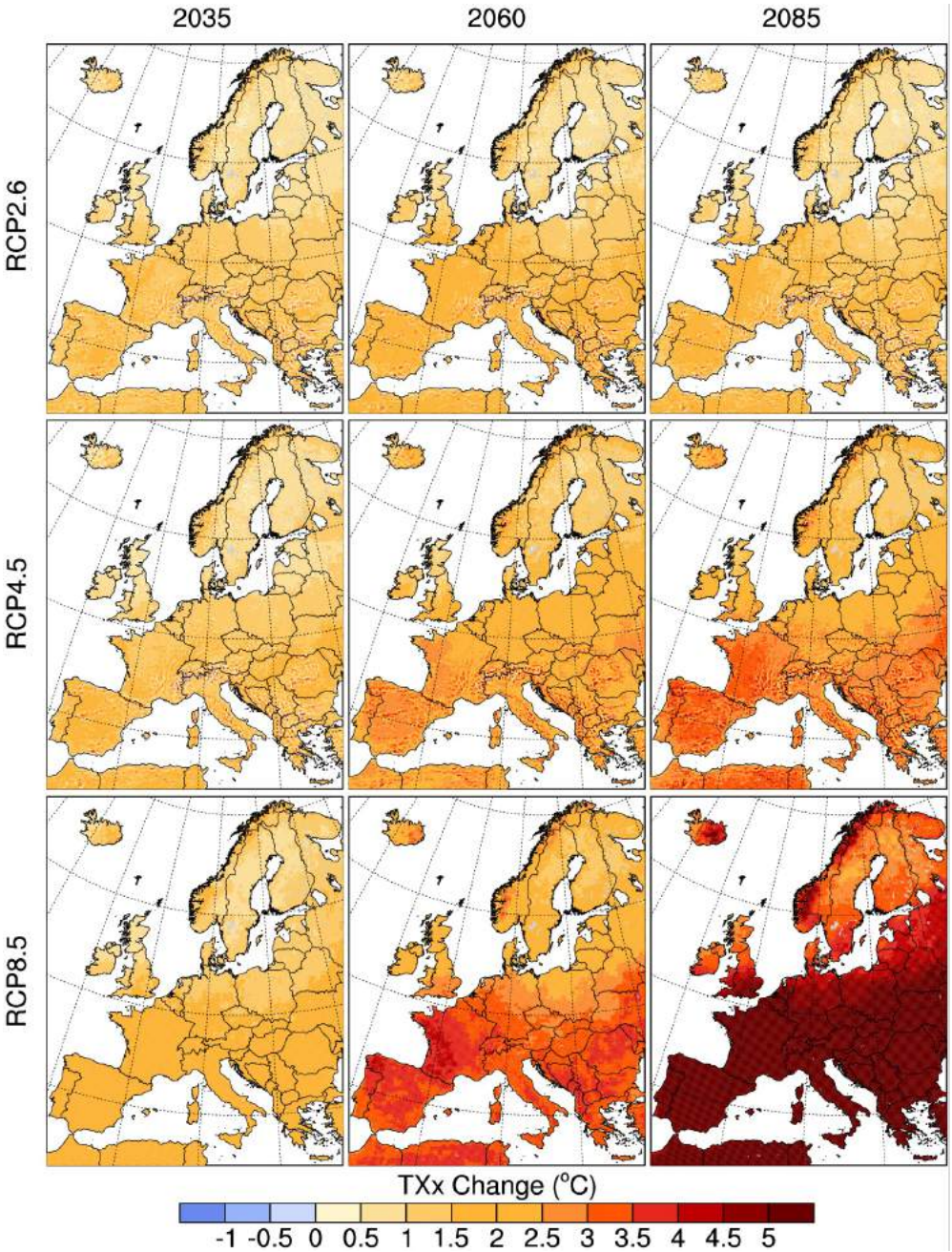

Figure 6.9. Multi-model median change in hot extremes (TXx) by 2035, 2060, and 2085 in RCP2.6, RCP4.5, and RCP8.5 with respect to present-day conditions (°C).

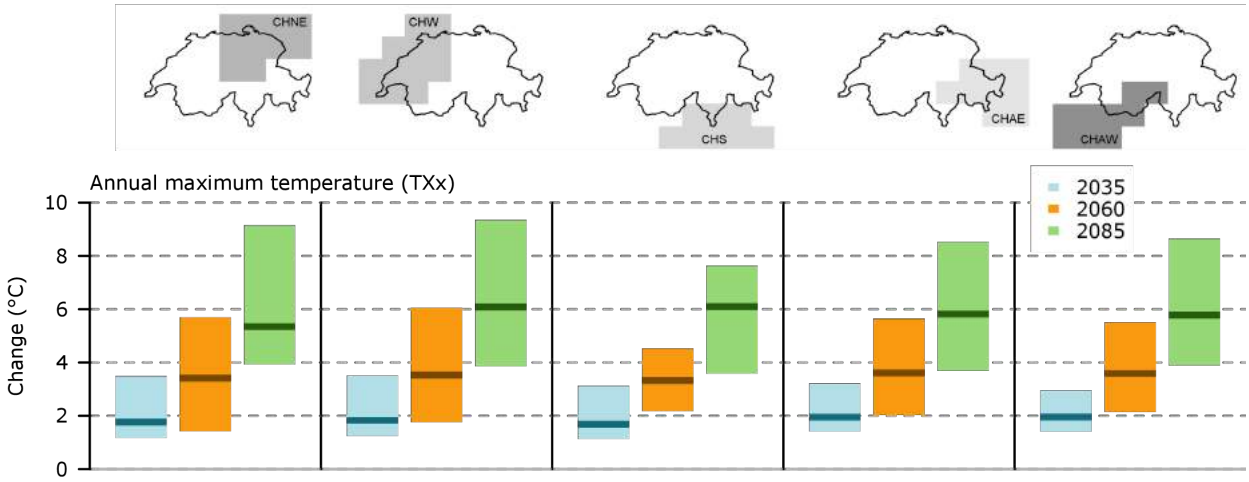

Figure 6.10. Change in hot extremes (TXx) (°C) by 2035, 2060, and 2085 (RCP8.5) averaged across five regions in Switzerland with respect to present-day conditions.

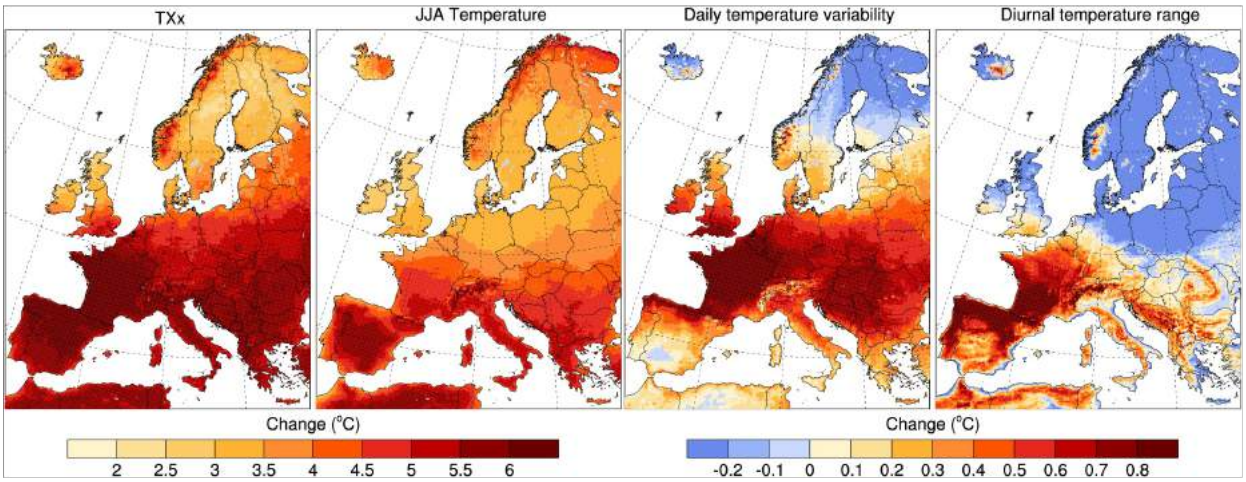

Figure 6.11. Multi-model median change in hot extremes (TXx), summer mean temperature, daily summer temperature variability (standard deviation of daily temperature in summer), and diurnal temperature range (DTR) by 2085 in (RCP8.5) with respect to present-day conditions (°C).

Heat extremes are expected to become not only more intense but also more frequent. The number of*very hot days* (*TX99P*, today expected to occur on about 1 day per summer) is projected to increase in the multi-model median to 2 - 4 days by 2035, 6 - 11 days by 2060, and 13 - 23 days in RCP8.5, depending on the region (Figure 6.13) (typical rounded model range across Switzerland 4 - 18 days by 2060 and 13 - 38 days by 2085 in RCP8.5). Consequently, such *very hot days* are expected to occur during about 2 - 5 weeks per summer season by 2085 rather than on one day per summer today. The increase in the number of *very hot days* is greater over southern Switzerland; this is consistent with the north-south warming gradient over Europe projected to lead to the strongest regional increase in very hot days over southern Europe (Figure 6.12). Likewise, this north-south gradient is consistent with the pattern of *hot days* (*TX95P*) (Figure 13.59) and previous multi-model experiments showing the strongest increase in *very hot days* over the areas of strongest summer warming [103, 11]. *Very hot days* often occur as a cluster of consecutive days, referred to as a heatwave. Models consistently project more frequent, more intense, and longer-lasting heatwaves over Switzerland [25, 103, 249, 60, 285, 322].

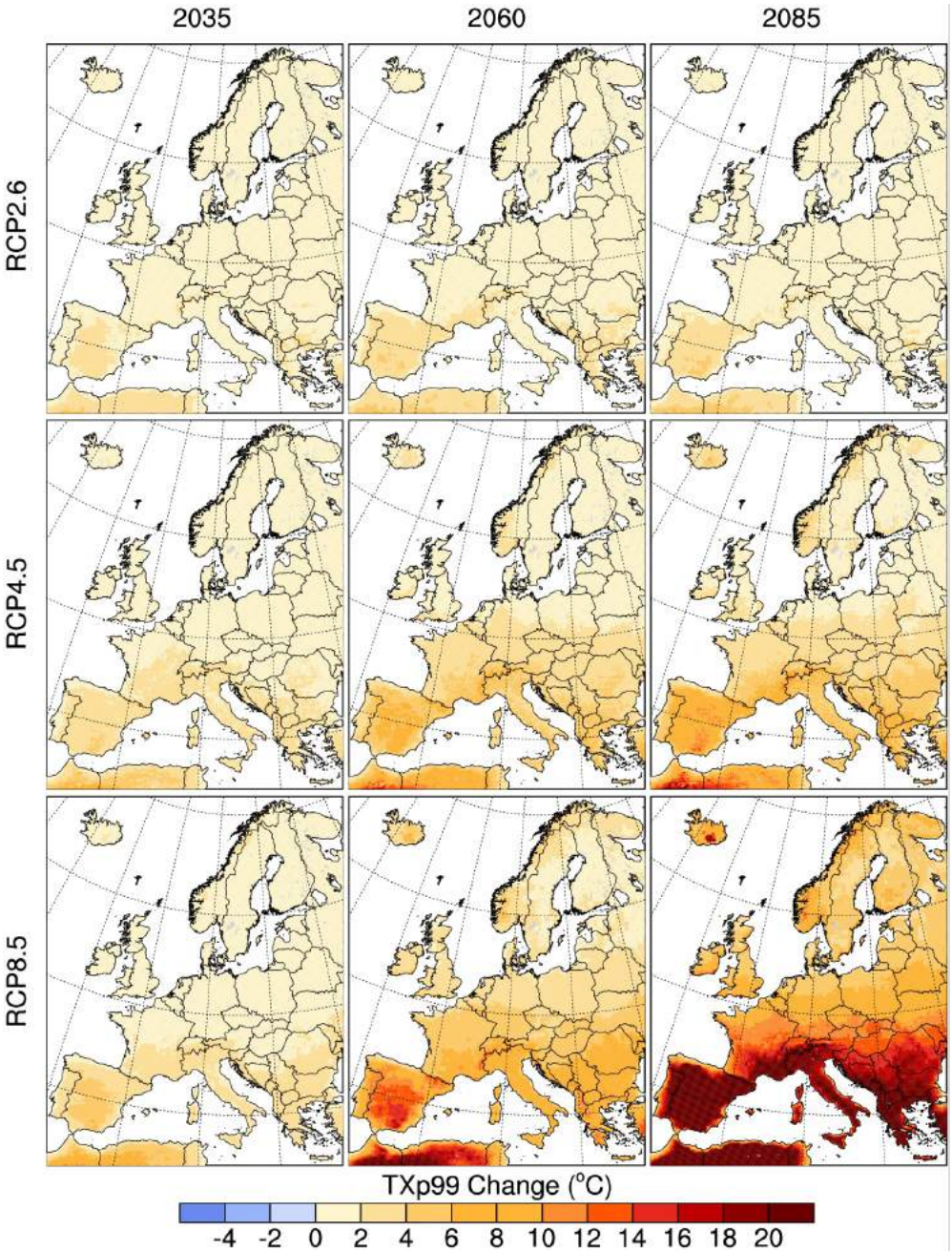

Figure 6.12. Multi-model median change in the number of very hot days (TX99P) by 2035, 2060, and 2085 in RCP2.6, RCP4.5, and RCP8.5 with respect to present-day conditions (days).

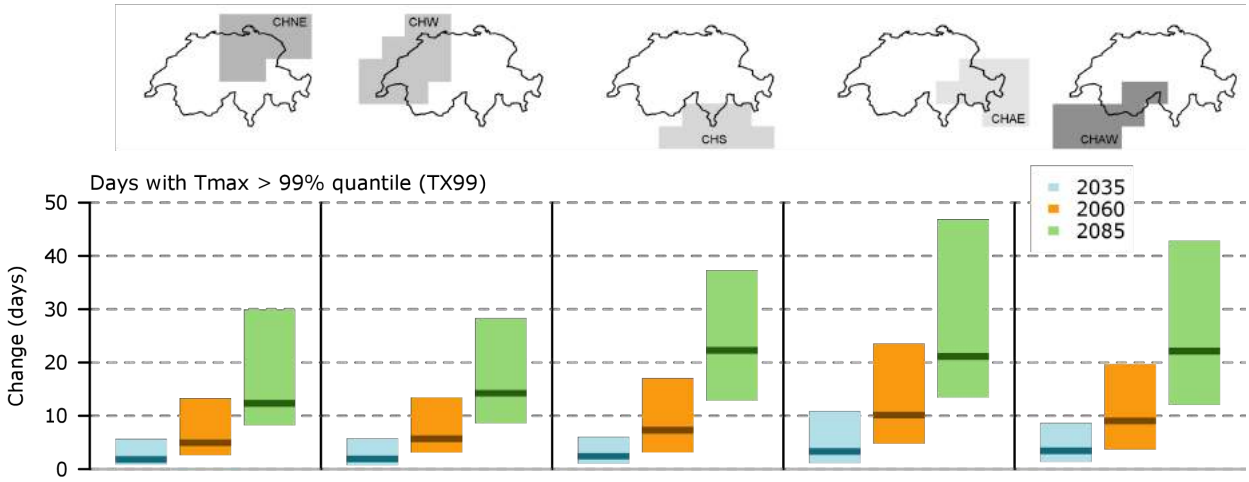

Figure 6.13. Change in the number of very hot days (TX99P (days)) by 2035, 2060, and 2085 (RCP8.5) averaged across five regions in Switzerland with respect to present-day conditions.

6.4.2. Cold extremes

Cold extremes, in contrast to hot extremes, are projected to become less intense and less frequent with warming winter temperatures. Cold extremes in Switzerland (here expressed as *TNn*, the minimum temperature of the *coldest night of the year*) are projected to warm in the multi-model median by 2.0 - 2.3 °C by 2035, by 4.1 - 4.4 °C by 2060, and by 6.2 - 6.9 °C by 2085, depending on the region (Figure 6.15). Changes by 2085 are much smaller for RCP4.5 (3.7 - 4.1°C) and RCP2.6 (2.2 - 2.9 °C). For all best estimates, the model uncertainty is very large, amounting to 3.5 - 11.3 °C for RCP8.5 by 2085. Notably, a substantial fraction of this large uncertainty is related to internal variability [102]. Cold extremes are projected to warm substantially more than the corresponding mean winter temperatures (Figure 6.16), which is consistent with previous regional and global multi-model projections [76, 108, 249]. This amplified warming results from a reduction in the day-to-day winter temperature variability arising from snow-albedo feedbacks [109] and from the relatively strong warming in the source regions of cold-air advection (the continental high-latitudes) due to Arctic amplification and land-sea contrast [76, 308, 158]. Consistent with the north-south warming gradient across Europe (Figure 6.14), cold extremes are projected to warm somewhat more in northern than southern Switzerland. Additionally, very cold days are projected to become less frequent, and cold waves to become shorter. However, given the very high variability of winter temperatures and cold extremes in particular, cold extremes are expected to sporadically occur for several more decades.

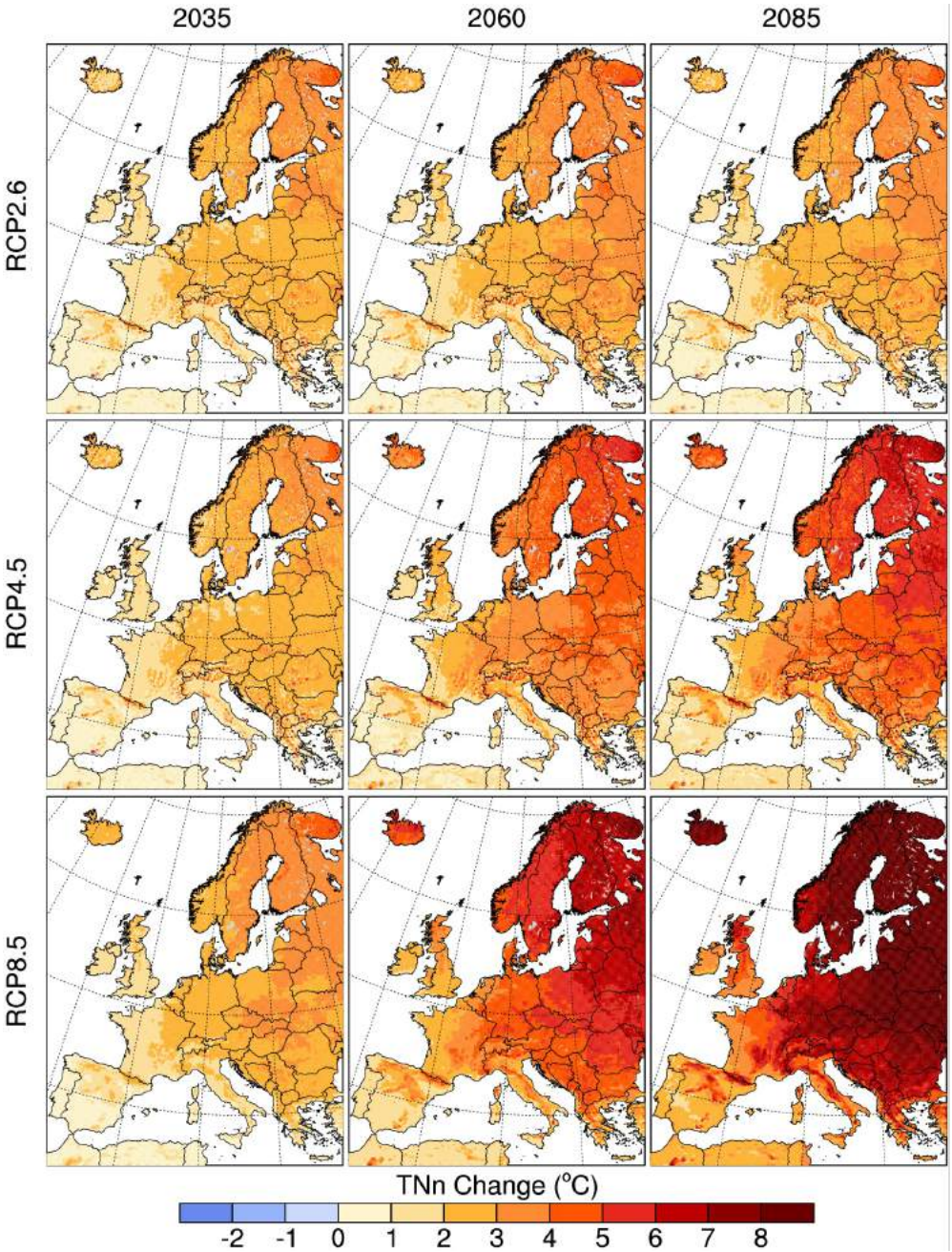

Figure 6.14. Multi-model median change in cold extremes (TNn) by 2035, 2060, and 2085 in RCP2.6, RCP4.5, and RCP8.5 with respect to present-day conditions (°C).

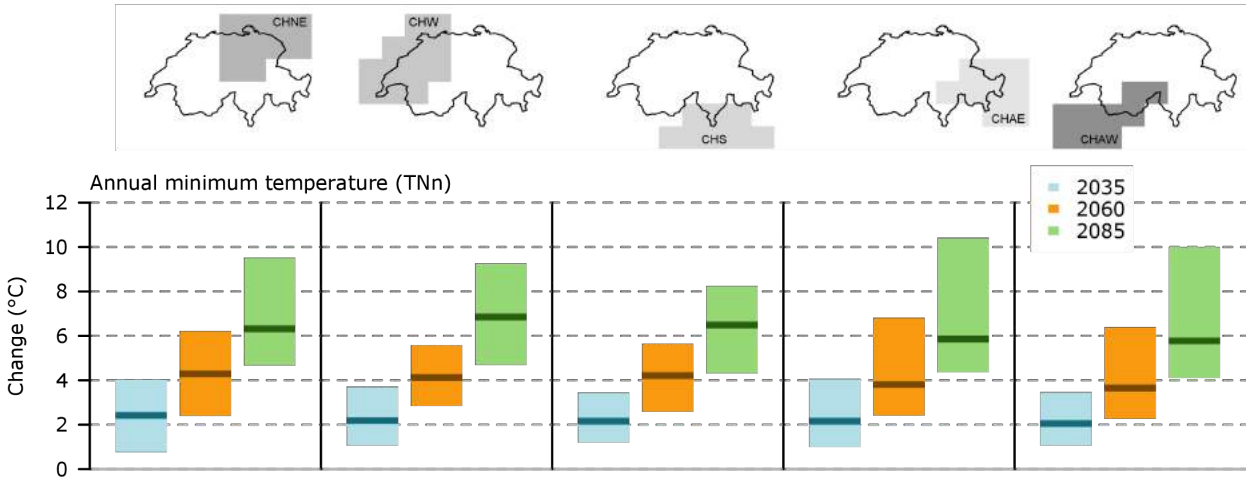

Figure 6.15. Change in cold extremes (TNn) (°C) by 2035, 2060, and 2085 (RCP8.5) averaged across five regions in Switzerland with respect to present-day conditions.

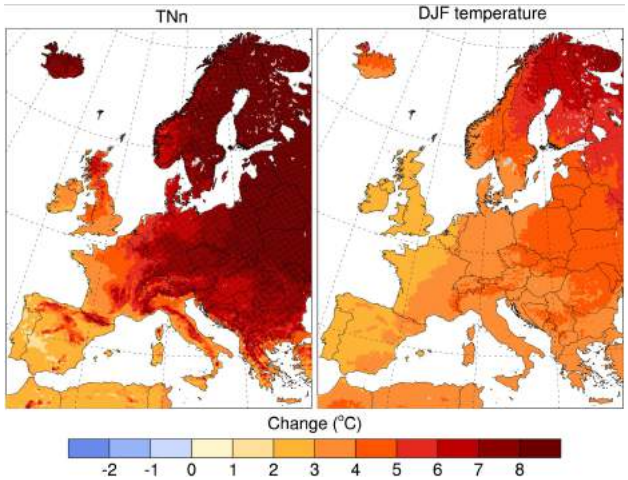

Figure 6.16. Multi-model median change in cold extremes (TNn) and in winter mean temperature by 2085 in (RCP8.5) with respect to present-day conditions (°C).

6.5. Heat stress

An extreme situation can result from a combination of several variables (multivariate extremes; e.g., [4]). This is the case for heat stress, which depends not only on temperature but also on humidity [105]. As explained in Chapter 3.2.1, the wet bulb temperature (TW), based on daily maximum temperature and daily mean specific humidity, is used here to assess heat stress.

The temporal evolution of seasonal maximum wet bulb temperature indicates a continuous increase until the end of the century (Figure 6.17). In the past, in Zurich, Geneva, and Sion, the threshold of 22 °C was only exceeded in extreme summers (e.g., 2003, 2010; black lines), but projected values in these locations are well above that threshold from mid-century onward for RCP8.5.

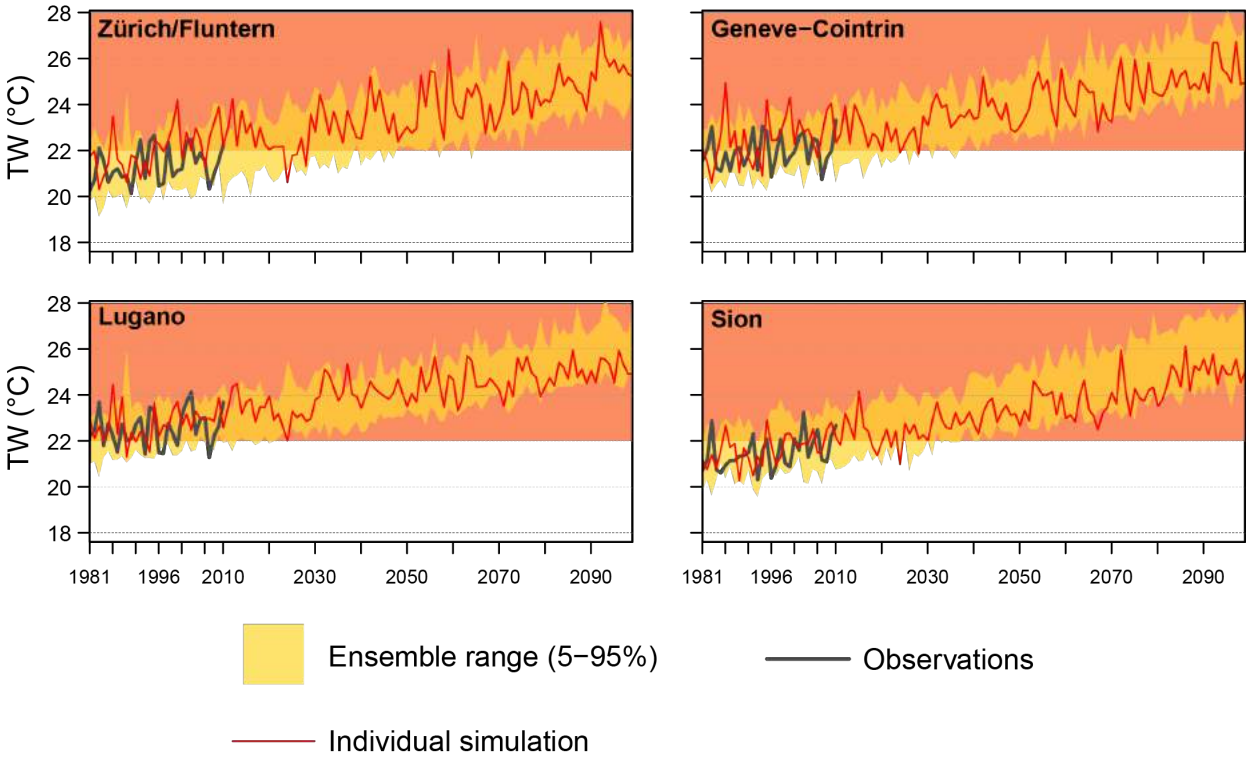

Figure 6.17. Temporal evolution of the summer maximum wet bulb temperature (°C) at four Swiss stations for RCP8.5. The maximum value for each summer is obtained from the maximum daily heat stress values smoothed with a 3-day moving average. Observed values are depicted by the black line, the shading indicates 90 % of the model range, and the red line illustrates an individual simulation (MPI-M-MPI-ESM-LR CLMcom-CCLM4-8-17 for EUR11) as an example.

TW-derived indices are projected to gradually increase over the course of the century at all stations (Figure 6.18). Under scenario RCP8.5, the maximum wet bulb temperature *TWx* increases by 1 - 2 °C, 2 - 3.5 °C, and 3 - 4.5 °C (multi-model median, depending upon the station) in the three scenario periods, respectively. For instance, in Lugano, summer mean and maximum TW are projected to reach 21 - 23 °C and 25 - 27 °C, respectively, in the late 21st century. Heat stress extremes, unlike temperature extremes, show an increase in the upper tail of the distribution similar to the increase in the mean. This absence of amplification of the climate-change signal may be caused by the role of humidity in the TW, since the slight decrease in relative humidity (Figure 13.39) might counteract the larger increase in extreme temperatures. The projected number of summer days with TW >22 °C (*TWg22*) suggests that, on average, more than one-third of summer days will feature severe heat-stress-prone conditions in many locations on the Swiss Plateau (Zurich, Basel, Geneva) and Alpine valleys (Sion, Interlaken, Chur). Ticino is the region with the largest increases in *TWg22*, with increments of up to 15, 30, and 45 days in the three scenario periods, respectively. In mountainous stations, *TWg22* only slightly increases or does not change, since the threshold of 22 °C is hardly ever exceeded (0 - 2 days). These results for *TWg22* are consistent with the findings of [398] for summer days in Switzerland.

Similar regional patterns are found for RCP2.6 and RCP4.5 until mid-century (Figure 13.60, Figure 13.61), also with the largest increases in heat stress indices in Ticino and stations in the lowlands. For RCP2.6, the projected values in the late 21st century scarcely differ from the mid-century values, reaching 19 - 20 °C and 23 - 24 °C for mean and maximum TW in Lugano, respectively. Summer mean and maximum TW are projected to reach 20 - 21 °C and 24 - 25 °C in the late 21st century for RCP4.5. *TWg22* differs substantially between RCP2.6 and RCP8.5 in magnitude and spatial extent, with such summer days about 3 - 5 times more frequent for RCP8.5.

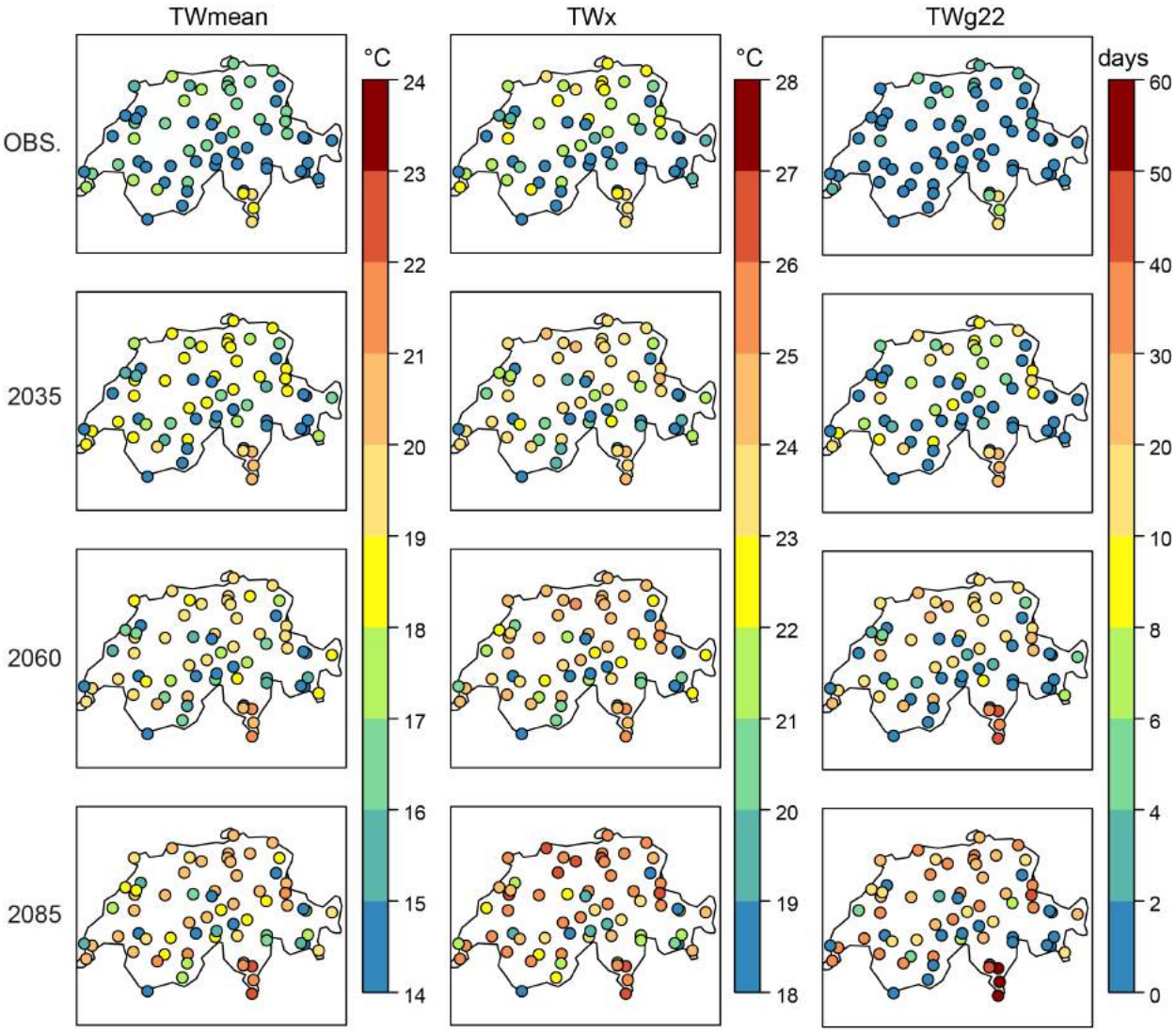

Figure 6.18. Observed values (first row) and climate-change projections (2nd - 4th rows) for summer mean (TWmean) and maximum TW (TWx) temperatures, and the number of days with TW >22 °C (TWg22) for the multi-model ensemble median for the three future periods, for the bias-corrected RCMs (combination of EUR-11 and EUR-44, 20 simulations; see Chapter 5.3) and the RCP8.5 scenario. See Figure 13.60 and Figure 13.61 for RCP2.6 and RCP4.5.

6.6. Precipitation extremes

Heavy and extreme precipitation events are of high relevance, as they may imply risk and damage to environmental and human systems. Mountainous regions like Switzerland are particularly prone to heavy precipitation and its consequences, as is evident from the August 2005 and June 2013 flood events ([228] and Chapter 3.3.3). Because the maximum amount of water vapor in the atmosphere is determined by temperature via the Clausius-Clapeyron relationship, increasing by 6 - 7 % per degree of warming, heavy precipitation events are expected to intensify at a similar rate [125, 7]. Apart from this thermodynamic effect, however, additional processes govern the future frequency and intensity of precipitation, such as changes in large-scale circulation, the occurrence of weather types, and atmospheric stratification [91, 244, 199, 260].

6.6.1. Methodology

Here, precipitation extremes are described by a set of indices that cover a broad range of characteristics. Empirical indices are used to address moderate to heavy precipitation (i.e., events that occur once to a few times per year), and indices based on extreme value statistics are used to address extreme precipitation (i.e., events that occur once per decade or century). All meteorological seasons are treated separately.

The empirical indices include the 90th, 95th, and 99th percentiles of daily precipitation (*p90*, *p95*, and *p99*) considering both wet and dry days [305]. The average maximum single-day event (*Rx1d*) and the average maximum five-day event (5-day precipitation sum, *Rx5d*) are also provided. Precipitation events that are associated with certain return periods (i.e., return levels of one-day events with a 100-year return period, *x1d100*) are estimated using extreme value statistics by fitting Generalized Extreme Value (GEV) distributions to seasonal maxima [64]. The implementation employed in CH2018 has been used in several previous studies [126, 272, 273], and similar implementations are often used in hydrology and infrastructure design. In addition to daily events (*x1dYY*), 3-day and 5-day precipitation events are considered (*x3d*, *x5d*).

6.6.2. Heavy and extreme precipitation events

Previous studies [126, 56, 272] and the most recent climate-model projections (see Figure 6.19 and [273]) agree that heavy and extreme precipitation events will intensify in all seasons and across the majority of the European continent. The most prominent and robust intensifications are found in the cold seasons and in northern Europe. Changes seen in extreme indices do not scale proportionally with changes in mean precipitation (*MEA*; see also Chapter 4) or the *wet-day frequency* (*FRE*). Changes in extreme indices are in most cases stronger than those in mean precipitation, and the wet-day frequency may even exhibit the opposite sign, especially for summer and in southern Europe. Across large parts of Europe and in most seasons, the intensification of extreme events with a return period of 100 years (*x1d100*) lies between +10 % and +30 %. Changes in moderate events (*Rx1d*) exhibit a pronounced north-south gradient pattern that is shifted with the seasonal cycle, with slight decreases in the Mediterranean region, an intensification in Scandinavia, and a transitional region with smaller changes in between. In summer, a reduction in the intensity of moderate events is seen in regions as far north as the greater Alpine region. In general, multi-day events (*Rx5d*) tend to intensify less than single-day events.

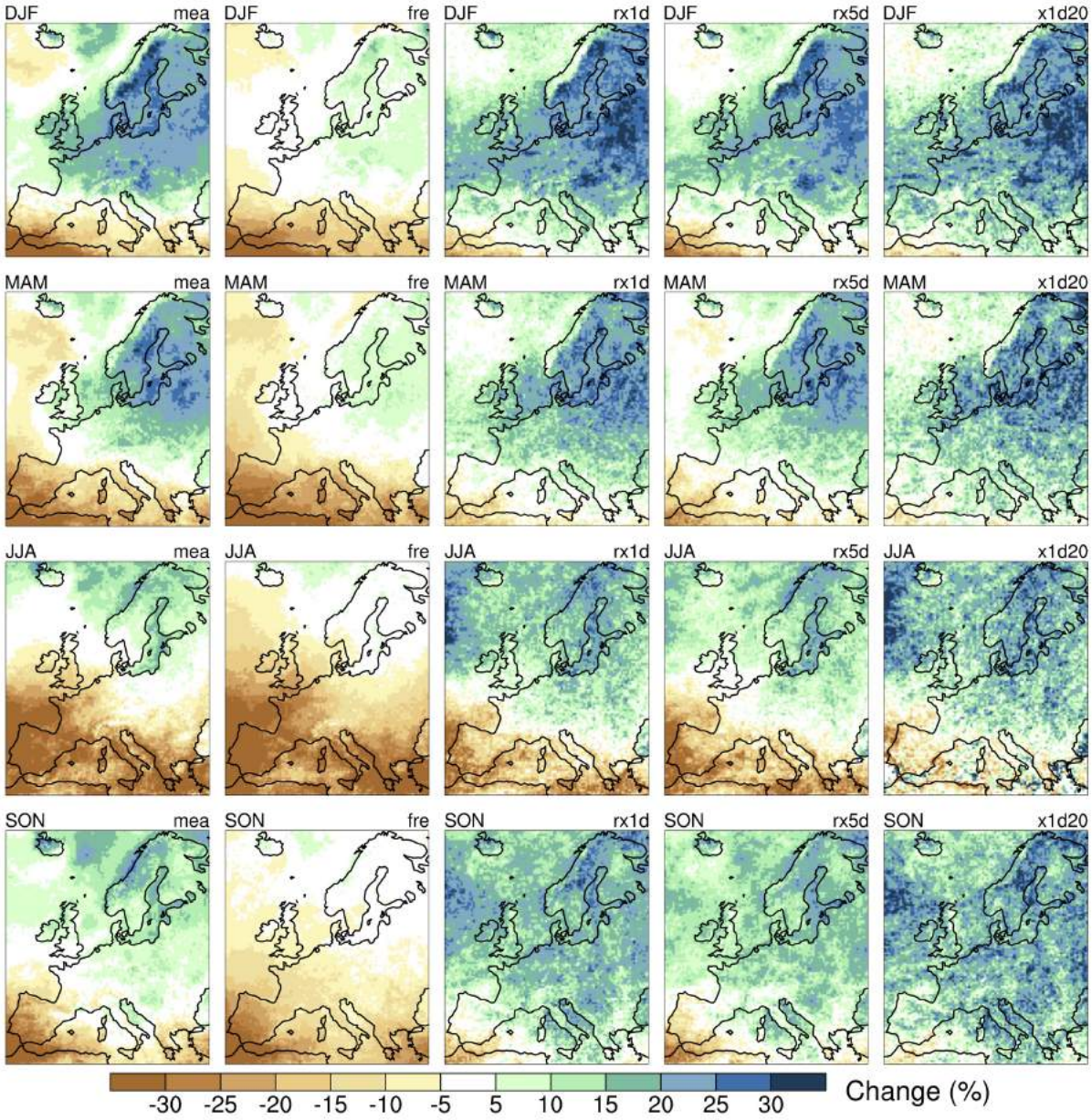

Figure 6.19. Multi-model median projected changes in (from left to right) mean daily precipitation (MEA), wet-day frequency (FRE), the mean seasonal maximum event at the daily (Rx1d) and 5-day aggregated time-scale (Rx5d), and the 20-year return value (x1d20) for each season (from top to bottom) and for RCP8.5 and the period 2085 with respect to the reference period 1981 - 2010. The multi-model ensemble consists of EUR-11 and EUR-44 simulations (see Chapter 4.2).

Heavy precipitation events are projected to intensify in all seasons and regions of Switzerland (Figure 6.20 and Figure 6.21), in particular in northern Switzerland (e.g., CHNE) and in winter (DJF). Uncertainty as indicated by the model spread is larger for extreme (e.g., *x1d100*) than for heavy or moderate events (e.g., *Rx1d*). Model spread is largest in summer (JJA) and in the south (CHS). In summer, moderate events are projected to change little, whereas extremes show a tendency to intensify, although this is not statistically significant. In other seasons, intensification across the spectra of return periods (from heavy to extreme: *Rx1d*, *x1d10*, *x1d100*) is of similar magnitude. It is further projected that in all seasons, single-day events (*Rx1d*, *x1dYY*) intensify more than multi-day events (*Rx5d*, *x5dYY*). Changes in mean seasonal precipitation (*MEA*; see also Chapter 4) scale roughly with changes in the frequency of wet days (*FRE*). However, for the most part, changes in *FRE* and *MEA* do not scale proportionally with changes in heavy and extreme events (see also [98] and Chapter 4). The degree of precipitation intensification increases with time and shows a clear trend by the end of the century. The magnitude of the projected changes depends on the emission scenario chosen (not shown) and is larger for RCP8.5 than for RCP4.5 and RCP2.6. In the near term, internal variability may dominate the response.

Overall, events that could potentially have the most devastating effects and are relevant for infrastructure planning (i.e., *x1d10* and *x1d100*) may intensify strongly in all seasons. Across Switzerland, the intensification of extreme events with a return period of 100 years (*x1d100*) lies between +10 % and +25 %, depending on the season and region (multi-model median by the end of the century in RCP8.5). However, the model spread is substantial, reflecting both internal variability and model uncertainty. At the same time, the majority of models project a reduction in the number of wet days, especially in the warm seasons (i.e., *FRE*; see also Chapter 6.7). This is of particular relevance for energy supply and agriculture. The results presented here are in line with observations from recent decades (see Chapter 3), which show a comparable scaling between mean temperature changes and heavy precipitation indices.

6.6.3. Snowfall fraction and snowfall extremes

Along with warming temperatures, the partitioning between solid (snow) and liquid (rain) precipitation will change in favor of liquid precipitation [127]. Domain and multi-model mean decreases in mean September - May Alpine snowfall by the end of the century are projected to reach about 25 % and 45 % for scenarios RCP4.5 and RCP8.5, respectively. In terms of relative changes, this effect is most pronounced in low-altitude regions (500 - 1000 m a.m.s.l), where the snowfall fraction is projected to decrease by about 70 % under RCP8.5. However, in terms of absolute changes, the effect is more pronounced in mid-altitude regions (1000 - 2000 m a.s.l.), where the corresponding decrease in snowfall is projected at about 0.6 - 1.0 mm/d (RCP8.5 multi-model mean). There are considerable uncertainties in this estimate stemming from the separation of precipitation into snowfall and rainfall.

The decrease in the snowfall fraction will also decrease the probability of large snowfall events in low- to mid-altitude ranges. In contrast, high-elevation regions (> 2000 m a.s.l.) could experience slight snowfall increases in mid-winter for both the RCP8.5 and RCP4.5 emission scenarios, despite the general decrease in the snowfall fraction [127]. These increases in mean and heavy snowfall can be explained by a general increase in winter precipitation.

The projected reduction of the snowfall fraction in low and intermediate altitude ranges is of concern, as it implies – together with the earlier melt of the snowpack – changes in runoff behavior, with increasing mean runoff in winter and early spring and decreasing runoff in late spring and summer [115, 33]. There is evidence that these changes will raise the risk of both floods and low flows, but the behavior will strongly depend upon the catchment considered; this aspect will further be addressed in Hydro-CH2018 (see Chapter 10).

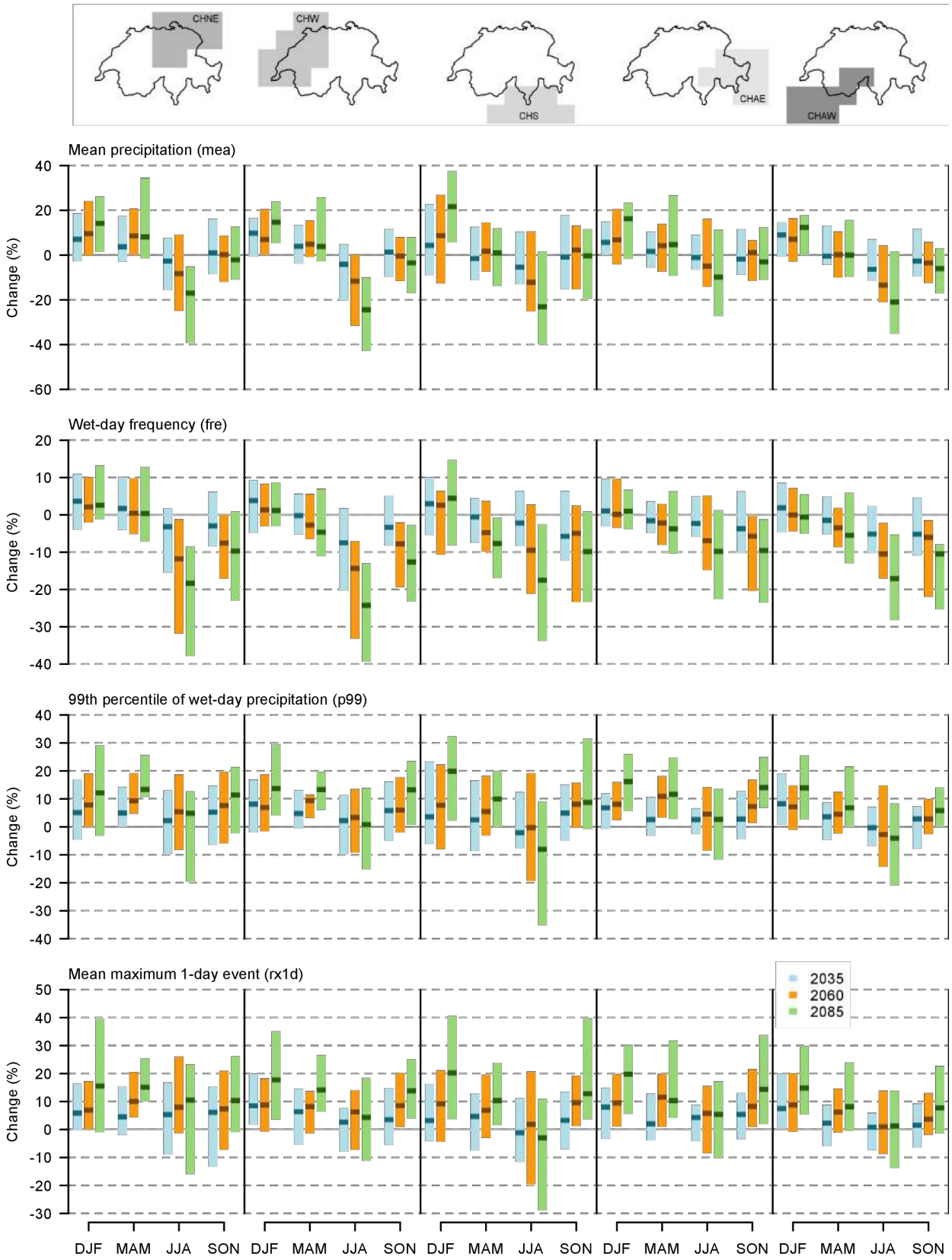

Figure 6.20. Multi-model ensemble projected changes in mean daily precipitation (MEA), wet-day frequency (FRE), the 99th percentile of all-day precipitation (p99), and the mean seasonal maximum daily precipitation event (Rx1d) for all seasons (see x-axis) for the five CH2018 analysis regions, for RCP8.5 and the periods 2035 (blue), 2060 (red), and 2085 (green) with respect to the reference period 1981 - 2010. The multi-model ensemble consists of EUR-11 and EUR-44 simulations (see Chapter 4.2).

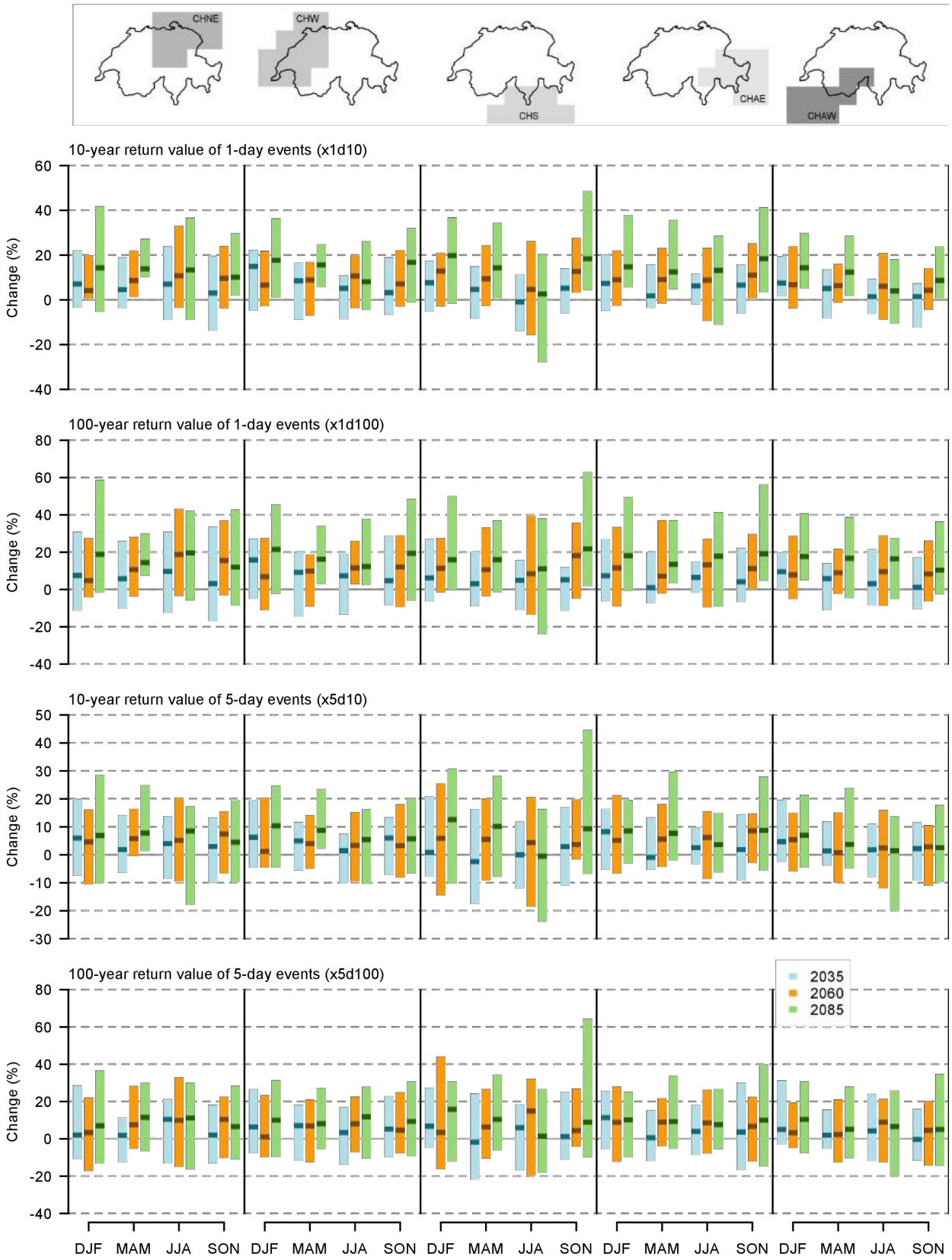

Figure 6.21. Multi-model ensemble projected changes in the intensity of daily events with a return period of 10 years (x1d.10) and 100 years (x1d.100) and the corresponding events for 5-day aggregated precipitation episodes (x5d.10 and x5d.100) at seasonal scale (see x-axis) for the five CH2018 analysis regions, for RCP8.5 and the periods 2035 (blue), 2060 (red), and 2085 (green) with respect to the reference period 1981 - 2010. The multi-model ensemble consists of EUR-11 and EUR-44 simulations (see Chapter 4.2).

Box 6.1: Hourly precipitation extremes & convection-resolving climate simulations

The CH2018 climate-change projections largely rely on Regional Climate Models (RCMs). Due to the models' coarse horizontal resolution (12 km - 50 km), they suffer from limitations associated with small-scale unresolved processes (thunderstorms and rain showers, i.e., convective precipitation) and have difficulties representing the complex topography of Switzerland. Increasing the horizontal resolution of RCMs to the kilometer scale (< 4 km) allows switching off the parameterization of convection, which is one of the key sources of uncertainty in future projections of extreme precipitation. These Convection-Resolving Models (CRMs) are currently in use for Numerical Weather Prediction (NWP), but with recent model developments and advances in computational power, it has become feasible to use such resolutions for climate studies as well.

Some of the first decade-long convection-resolving simulations have been conducted over the southern part of the United Kingdom [183] and over the greater Alpine region [12]. Evaluation of these simulations has revealed that convection-resolving models significantly improve the simulation of precipitation, especially for heavy precipitation on hourly timescales [12, 183]. As an example, Figure 6.22 shows the diurnal cycle of mean precipitation, wet-hour frequency, and heavy precipitation (defined as the 99th percentile of all hours), averaged over 62 surface precipitation stations across Switzerland and simulated by a convection-resolving model at a horizontal resolution of 2.2 km over the greater Alpine region. The convection-resolving model is compared to rain-gauge station observations and a convection-parameterizing model at a horizontal resolution of 12 km. The results from convection-resolving models show great improvements in the timing of precipitation, precipitation frequency, and the simulation of peak heavy precipitation. Convection-parameterizing models tend to produce too frequent precipitation with small intensity, and excessively early precipitation peaks. They are thus inadequate for assessing potential changes in hourly precipitation intensity under conditions of climate change.

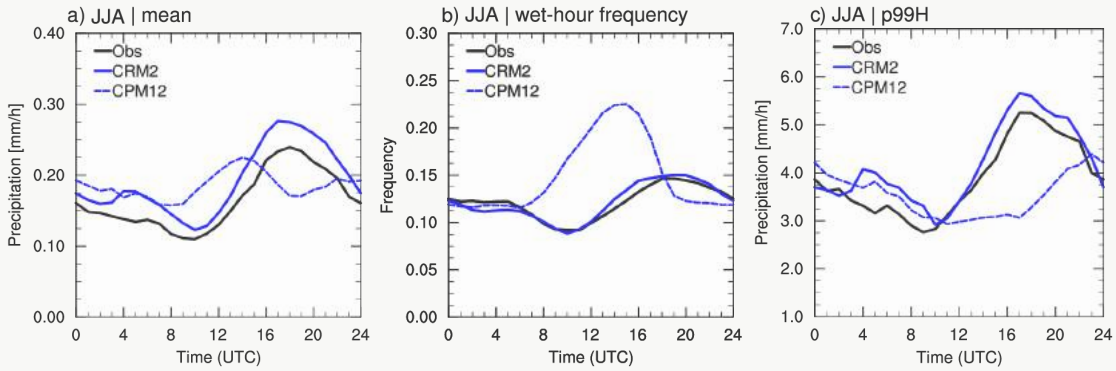

Figure 6.22. Diurnal cycle of (a) mean precipitation, (b) precipitation frequency, and (c) heavy precipitation (defined as the 99th percentile of all hours) obtained in the convection-resolving simulation at 2.2-km horizontal resolution (CRM2), convection-parameterizing simulation at 12-km horizontal resolution (CPM12), and observations from rain-gauge stations. The evaluation is performed for the summer (JJA: June - July - August) season, and the results are averaged over 62 stations across Switzerland. Results are based on 10-year-long high-resolution simulations presented in [12, 13].

Convection-resolving and convection-parameterizing climate-change simulations (driven by one specific RCP8.5 GCM) of summer precipitation over the greater Alpine region are shown in Figure 6.23. Following Ban et al. (2015) [13], relative changes in extreme summer precipitation are expressed in relation to mean temperature change, i.e., as a scaling rate. A comparison of the convection-resolving and convection-parameterizing models shows small differences in changes in extreme precipitation at daily scales, but large differences at hourly timescales. The increase in extreme hourly precipitation is smaller in the convection-resolving model than in the convection-parameterizing model.

Furthermore, the convection-resolving model shows that increases in extreme hourly precipitation, similar to extreme daily precipitation, is actually consistent with the Clausius-Clapeyron rate, i.e., the increase in the most extreme events converges toward a value of about 6.5 % K^{-1} (Figure 6.23) [13]. The convection-parameterizing model suggests that the increase in extreme hourly precipitation may exceed the Clausius-Clapeyron rate; however, this result is not reliable, since the model has difficulties reproducing extreme hourly precipitation [12, 13]. The increase in extreme hourly precipitation in convection-resolving models is also smaller than what might be expected from the present-day scaling found in observations, which exceeds the Clausius-Clapeyron rate (i.e., 6 - 7 %K^{-1}) in the summer season [12]. Thus, the results indicate that convection-resolving model projections are

consistent with theoretical expectations from the Clausius-Clapeyron relationship; moreover, future changes in extreme hourly precipitation cannot be extrapolated from present-day precipitation scaling, but they are likely to follow the Clausius-Clapeyron scaling of 6 - 7 $\%K^{-1}$. This comparatively simple scaling law can be used for a number of climate-change adaptation strategies [13].

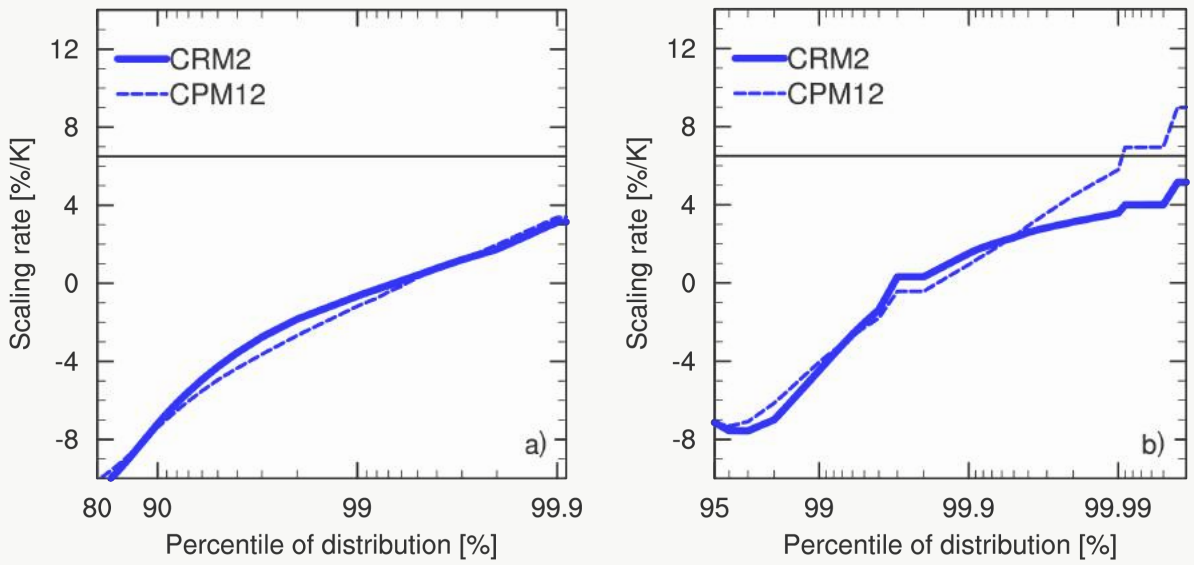

Figure 6.23. Projected changes in precipitation intensity as a function of percentiles, normalized by the local temperature changes for convection-resolving (CRM2, resolution of 2.2 km, solid lines) and convection-parametrizing (CPM12, resolution of 12 km, dashed lines) models [13], calculated for (a) daily precipitation and (b) hourly precipitation, averaged over the greater Alpine region. (From [13]).

The future warming of the atmosphere will also lead to changes in other hazardous convective events, such as tornadoes, hailstorms, and severe thunderstorm winds. Some studies have explored the use of convection-resolving models for the simulation of such events in a future climate, but the results are still very limited. However, they indicate that future increases in summer precipitation over high alpine elevations are associated with enhanced convection, as found in both conventional and convection-resolving climate simulations [132]. Studies over Colorado's mountains indicate that despite more intense convection in a warmer climate and more hail generated within clouds, less hail reaches the surface due to the enhanced melting associated with climate warming [209]. More robust results are found using global and regional climate models, which show that the further warming of the atmosphere will lead to increases in the occurrence of severe thunderstorms [81] and can also result in increases in the frequency of lightning strikes [281].

6.7. Drought indices

Measuring and defining drought is not straightforward, as the term can be defined in various ways, depending on the perspective of the stakeholders. Commonly, one distinguishes between meteorological drought, which refers to a deficit of precipitation, soil moisture drought (often called agricultural drought), which refers to a deficit of (mostly root zone) soil moisture, and hydrological drought, which refers to negative anomalies in streamflow, lake, and/or groundwater levels (e.g., [152]). These multifaceted definitions of drought and the lack of direct measurements of drought-related variables, in particular soil moisture (e.g., [315, 84]), have led to the development of several indices to characterize (meteorological, agricultural, and hydrological) drought (see, e.g., [152, 70]). It should be noted that such indices are not necessarily restricted to depicting dryness, but can also represent wet conditions.

Lack of precipitation is often the primary cause of drought; this is the basis for the definition of meteorological drought indices that reflect the aspect of a water deficit on the supply side (see Figure 6.24). On the demand side, increased evapotranspiration induced by enhanced radiation, wind speed, or a vapor pressure deficit (itself linked to temperature and relative humidity) can further intensify the water shortage and lead to critical soil moisture values and the associated agricultural drought. Under strong drought conditions, however, soil moisture can also become limiting for evapotranspiration, which can restrict

further soil moisture depletion. Furthermore, pre-conditioning (pre-event soil moisture, surface and/or groundwater storage) can contribute to the emergence of agricultural and hydrological droughts. This is related to the inherent characteristic memory of these water stores (e.g., [196, 310, 250]) and their specific response times to drought forcing (e.g., [113]).

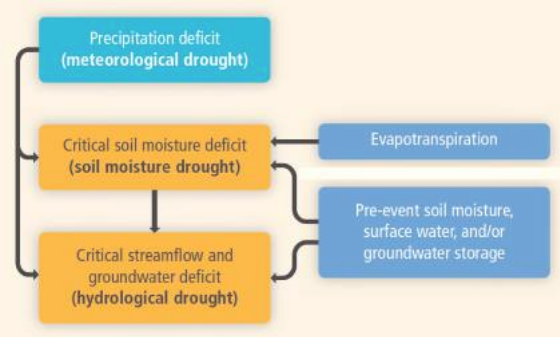

Figure 6.24. Schematic of the different climatic drivers of meteorological, agricultural (soil moisture), and hydrological drought (from [311]). Light blue relates to supply-driven impacts on the different types of drought, dark blue to demand- or storage-driven impacts.

Switzerland has experienced several drought episodes since the beginning of the 20th century. Long-term historical trends are insignificant, although they indicate a tendency toward drying (i.e., negative trend slope of standardized precipitation minus evapotranspiration; see Chapter 3.3.3). Climate change will affect the drivers of drought via the modification of atmospheric circulation and associated precipitation patterns, as well as via changes in radiation, air temperature, atmospheric humidity, and wind (e.g., [314]; see Figure 2 therein). Thus, to investigate the different impacts of climate change on drought, it is appropriate to use indices covering multiple drought definitions (see also [311]). Here, the focus is on meteorological and agricultural drought, as these can be more directly derived from the CH2018 climate model projections than hydrological drought. Two meteorological and two agricultural drought indices are considered (see Table 6.1).

6.7.1. Meteorological drought (precipitation deficits)

The *consecutive dry days* index (*CDD*) shows the maximum number of consecutive days without rain (i.e., below a given threshold, typically 1 mm d^{-1}) within a considered period [128, 6, 337]. Here, *CDD* is calculated on a seasonal timescale (i.e., for DJF, MAM, JJA, or SON as a whole). Another commonly used meteorological drought index is the *standardized precipitation index* (SPI; [222, 205]). This is derived by fitting and transforming a long-term precipitation record into a normal distribution that has zero mean and unit standard deviation. SPI values of -0.5 to -1 correspond to mild droughts, -1 to -1.5 to moderate droughts, -1.5 to -2 to severe droughts, and below -2 to extreme droughts. Similarly, values from 0 to 2 correspond to mildly wet to severely wet conditions, and values above 2 to extremely wet conditions. SPI can be computed over several timescales (e.g., 3, 6, 12, or more months) and thus indirectly considers effects of accumulating precipitation deficits. Here, the 3-month timescale is used (3-month SPI, denoted *SPI3*). The index is calculated separately for each month and then seasonally averaged. SPI only considers the supply of moisture, which is currently sufficient for western to central Europe. However, in southern Europe, the effects of evapotranspiration need to be considered as well for an appropriate representation of water deficit [269].

6.7.2. Agricultural drought (soil moisture deficits)

Precipitation minus evapotranspiration (*P-E*) describes the net flux of water between atmosphere and land by including the influence of both atmospheric supply and demand (Figure 6.24). Here, seasonal averages of *P-E* are considered to represent water availability [136, 47]. Actual evapotranspiration, which results from atmospheric forcing and simulated soil moisture limitation on evapotranspiration, is used; compared to potential evapotranspiration, it is less prone to overprediction [233]. The index is categorized as an agricultural drought index, although it neglects storage changes and runoff. The fact that most of the

CORDEX simulations employ aerosol climatologies that remain constant at late 20th-century levels (see also Chapter 4.2) probably leads to an underestimation of the radiation forcing in the regional projections (see [15]) and the consequent impacts on evapotranspiration. *Standardized soil moisture anomaly* (*SMA*) is an alternative measure for the evaluation of agricultural drought based on simulated total column soil moisture (e.g., [71, 249]). Monthly *SMA* values are calculated with respect to the monthly means of the reference period and standardized by the monthly standard deviations of the reference period [248]; these values are then seasonally averaged. *SMA* integrates the effects of precipitation forcing, simulated evapotranspiration (see above), and simulated soil moisture persistence. Although the soil moisture simulated by (land-surface, hydrological, and climate) models often exhibits strong discrepancies in absolute terms, soil moisture anomalies can be compared by simple scaling and generally match reasonably well (e.g., [195, 248]). Recent studies furthermore suggest that future drought projections should rely on direct climate-model output of the water cycle (e.g., simulated soil moisture, as used for *SMA*), as a posteriori off-line metrics tend to overestimate drying trends (e.g., [26, 234]).

Figure 6.25 shows the ensemble median changes in the meteorological and agricultural drought indices on

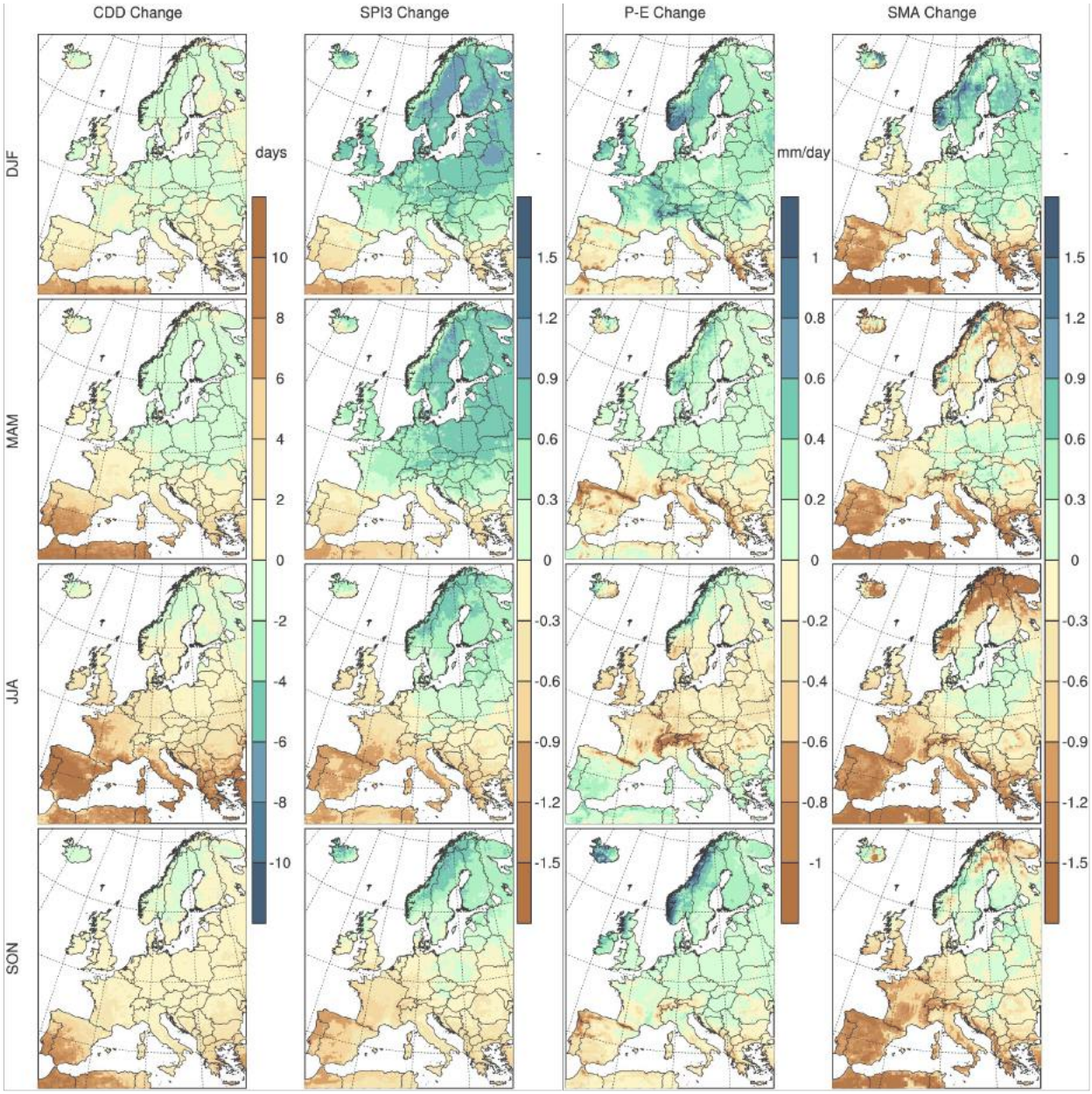

Figure 6.25. Ensemble median changes in the meteorological and agricultural drought indices CDD, SPI3, P-E, and SMA (from left to right) for the different seasons (top to bottom) and the RCP8.5 emission scenario by 2085. The ensemble median is based on a combination of EUR-11 and EUR-44 simulations (Chapter 4.2).

the European scale under the RCP8.5 emission scenario by 2085. *CDD* indicates increasing dry spell lengths in the Mediterranean and western/central Europe. The signal shows a northward shift over the course of the year (i.e., extending further north in summer) and toward the later scenario periods (not shown). Similarly, *SPI3* also displays an intensification and extension of a drying trend in the Mediterranean and western Europe, with stronger and extended signals in summer and again for the later scenario periods (not shown). In northern Europe, *SPI3* shows a wetting trend that is more extended in winter/spring and intensifies in the 2085 scenario period. The European-scale analysis indicates that Switzerland is often in between the drying (in summer/autumn) and wetting signals (in winter/spring). This position within the larger-scale change signals points to the inherent uncertainties associated with regional responses within the CH2018 regions (see below).

The agricultural drought indices *P-E* and *SMA* both show a drying in the Mediterranean and western Europe, again intensified for the 2085 scenario period (not shown) and more extended in summer. Similar to *SPI3*, the agricultural drought indices also indicate a wetting trend in parts of northern Europe, in particular for winter and in the 2085 scenario period. In summer, *P-E* shows effects of water limitation in the southern Mediterranean (e.g., over the Iberian Peninsula), where the net change in the index becomes positive due to a strong decrease in evapotranspiration. Overall, the agricultural drought indices suggest more heterogeneous signals than the solely precipitation-driven meteorological drought indices. For *SMA* (and, to a lesser extent, for *P-E*), topographical effects can be observed as well. Mountainous regions (e.g., in the Alps and in Scandinavia) seem more prone to drying, which appears to be related to carry-over effects due to less snow storage and earlier spring snow melt, in connection with increased runoff (not shown). In parts of Scandinavia, this runoff effect even seems to result in a net soil drying despite increased *P-E*.

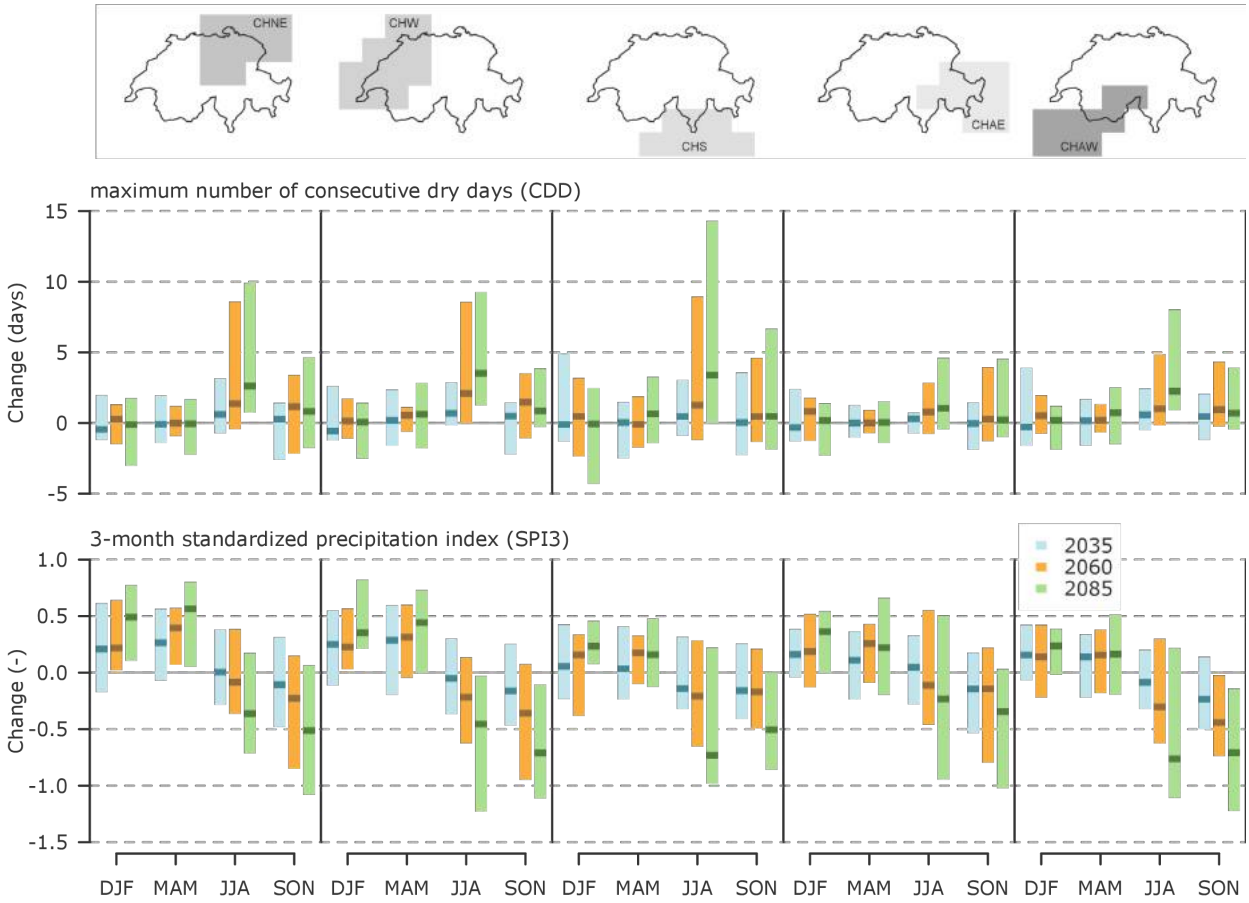

Figure 6.26. Multi-model regional mean changes in the meteorological drought indices CDD (top) and SPI3 (bottom) for the five CH2018 regions and the scenario periods 2035, 2060, and 2085 and RCP8.5. The ensemble median is based on a combination of EUR-11 and EUR-44 simulations (Chapter 4.2). See Figure 13.66 and Figure 13.67 for RCP4.5 and RCP2.6.

For most CH2018 regions (except CHAE) and primarily for the period 2085, *CDD* exhibits a signal toward longer dry spell lengths in summer for RCP8.5 (possible increases of up to 8 - 14 days from the currently observed 11 days on average; Figure 6.26, top). These signals are, however, associated with larger uncertainties, and neither weak nor strong changes can be excluded. The other seasons do not show significant changes in this index. *SPI3* shows a winter/spring wetting that often intensifies by the end of the century (Figure 6.26, bottom). This signal manifests in all CH2018 regions and becomes pronounced for CHNE and CHW in particular; it is less evident in CHS and in the Alpine regions CHAE and CHAW. For summer and autumn, the signal for *SPI3* is less consistent. The median estimate indicates a drying in the later periods for all regions and both seasons. The models project a consistent drying in CHW (summer and autumn) and in CHAW (autumn) for the period 2085, but the signal is associated with uncertainties in the sign of the change in the other regions (i.e., a minority of models also project a wetting). Overall, uncertainty ranges in summer are larger than in other regions, due to the fact that Switzerland is situated in between the larger-scale change wetting and drying signals (see Figure 6.25), with individual models projecting diverse or even opposite responses.

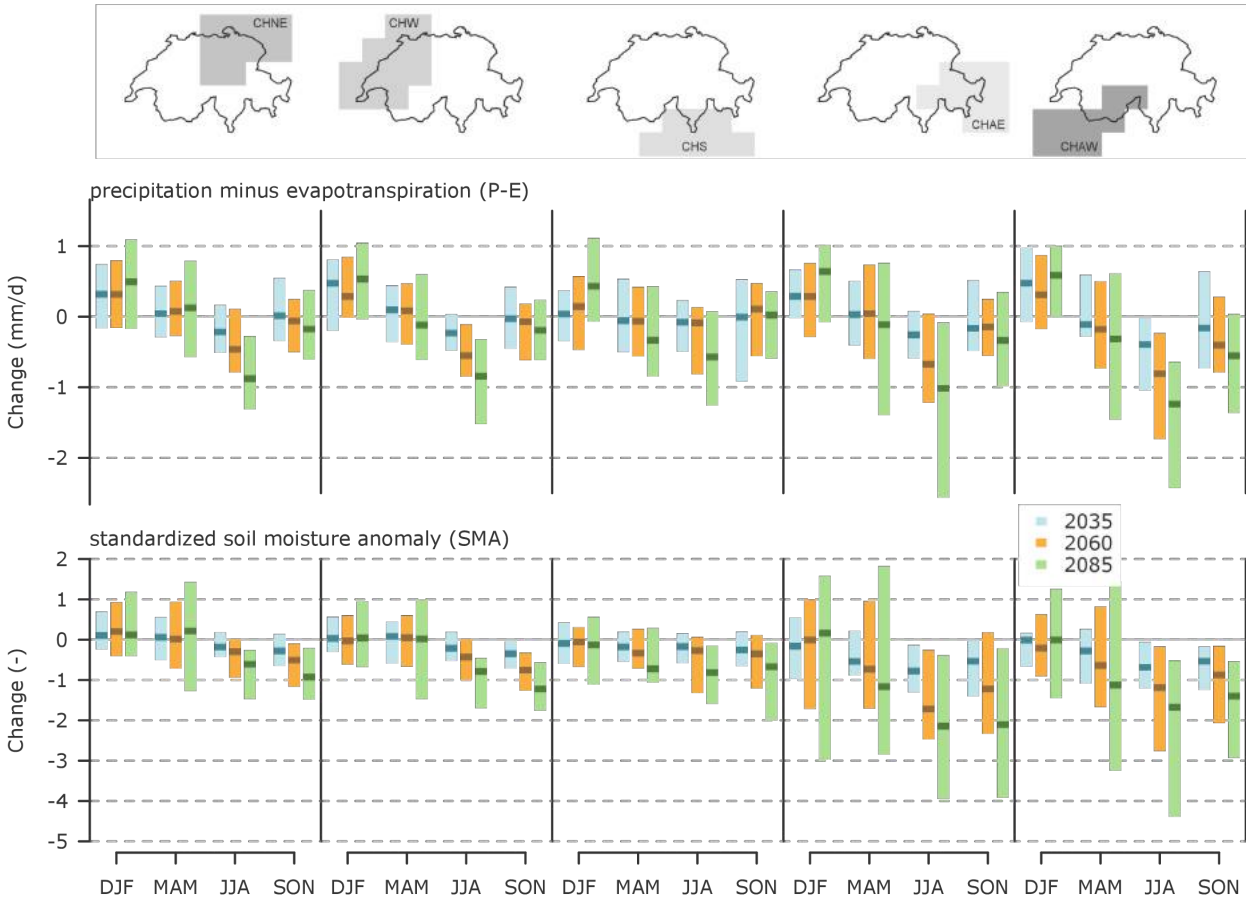

Figure 6.27. Multi-model regional mean changes in the agricultural drought indices P-E (top) and SMA (bottom) for the five CH2018 regions and the scenario periods 2035, 2060, and 2085 and RCP8.5. The ensemble median is based on a combination of EUR-11 and EUR-44 simulations (Chapter 4.2). See Figure 13.66 and Figure 13.67 for RCP4.5 and RCP2.6.

In agreement with *SPI3*, the agricultural drought index *P-E* shows a tendency toward a wetting in winter by the end of the century in all CH2018 regions under RCP8.5 (Figure 6.27, top); however, this signal is not as pronounced, and some models also project insignificant changes. For summer, *P-E* shows a drying, which becomes most evident for the 2085 scenario period (except in CHS, which shows uncertainty in the sign of the change). This summer drying also appears in *SMA* (Figure 6.27, bottom), which exhibits a decrease by the end of the century in all CH2018 regions. In addition, *SMA* also shows a drying in autumn. Overall, the two agricultural drought indices exhibit larger uncertainties in the two Alpine regions, likely associated with the complexity of the underlying snow and precipitation, evapotranspiration, and storage processes that govern the responses of these indices.

Considering RCP2.6 (see Appendix 3.5), the changes for *CDD* and *SPI3* are not robust, with various models projecting opposite signs of change. For RCP4.5, *CDD* exhibits a tendency toward longer dry spell lengths in summer, in particular for the western part of Switzerland (CHW and CHAW). The changes are, however, less strong than for RCP8.5. For *SPI3*, a tendency for spring wetting can be observed in CHNE only in the later two scenario periods under RCP4.5. *P-E* also shows mostly non-robust responses for the lowest emission scenario, while for RCP4.5, an indication of summer drying appears in CHNE, CHW, and CHAW. *SMA* starts to show a tendency toward summer drying for RCP2.6 in CHAE in the 2085 period. This signal intensifies under RCP4.5 and also expands to CHAW under this scenario.

In summary, for Switzerland under RCP8.5, the drought indices considered here show a tendency toward an increase in dry spell lengths (*CDD*) and tendencies toward drying in summer (*SPI3*, *P-E*, *SMA*), as well as wetting in winter (but only when storage effects are neglected, i.e., for *SPI3* and *P-E*). The extent of the drying seems to be partially dependent on the index and on the domain, and the signal is most visible by the end of the century. The clearest responses are observed when effects of atmospheric demand and storage are included in the index (as is the case for *P-E* and *SMA*). Overall, the level of drying remains uncertain, and both insignificant and very strong changes cannot be excluded. This is related to large internal variability and model uncertainties in the representation of key processes (e.g., strength of soil moisture-atmosphere feedbacks, circulation changes), as well as factors such as aerosol forcing, irrigation, and land-use changes that may differ between models and multi-model experiments (see also Table 6.2). It should be noted that the CH2018 domain is often in between the European-scale signals (i.e., winter wetting in northern Europe, summer drying in southern Europe), and thus the responses in the individual Swiss regions depend on their location with respect to the larger-scale signal.

6.8. Wind extremes

A good knowledge of the frequency and geographical distribution of extreme winds is key for the prevention of damage caused by windstorms. Unfortunately, for the highly complex topography of Switzerland, our current knowledge on extreme winds and their evolution over time is still rather limited. As shown in Chapter 3.2.4, near-record wind gusts in Switzerland can be caused by winter storms, summer convection, and flow crossing the main Alpine ridge (Föhn) or deflected flow such as the Bise (cf. Figure 3.11).

To give a preliminary overview of the current state of knowledge regarding wind extremes (especially winter storms), we summarize the findings of earlier studies focusing on Europe and Switzerland. Several review studies have indicated that in the second half of the 21st century, the frequency and intensity of storms, cyclones, and high-impact wind might increase over central and western Europe, resulting in a high potential for associated damages [389, 355, 96, 241]. This is in contrast to southern Europe, where current model projections indicate a future decrease in extratropical storminess [241]. This picture becomes more complicated when one considers only the seven CMIP5 simulations that show the best performance in simulating historical mean wind fields over Europe. In this regard, Colle et al. (2013) [65] found a decrease in cyclone track density and a weakening of cyclones over the western Atlantic storm track. This has been confirmed in a recent study by Wang et al. (2017) [365], although their work is based on a large ensemble with only one climate model. The reason for this diversity of results lies in the nature of the phenomenon being analyzed, as different processes (such as a projected decrease in meridional temperature gradient in the lower troposphere or an increase in humidity) can have opposing impacts on storm track responses. This makes future projections of extratropical cyclones and thus wind extremes a challenge [319].

Another important process leading to high-impact wind extremes is the serial clustering of extratropical storms over the North Atlantic European area [210, 30, 29]. Economou et al. (2015) [88] showed that future changes in serial clustering are generally found to be small and are not consistent across CMIP5 models. Multi-model ensembles of RCMs generated in earlier projects such as PRUDENCE and ENSEMBLES agree with the diverse picture highlighted by the GCM simulations. Still, model studies show that there is some

indication of an intensification of wind extremes over western or central Europe that could also affect northern Switzerland (cf. [25, 278, 303, 83, 134, 252]). The analysis of wind extremes in this report is based on the CORDEX multi-model ensemble, as described in Box 2.1. Like the earlier multi-model ensembles of RCMs, the CORDEX RCMs are able to simulate the large-scale wind patterns above the boundary layer, but are not yet capable of resolving all relevant phenomena causing extreme near-surface (10-m) winds. An evaluation of the 10-m mean wind speed at MeteoSwiss observational sites reveals substantial biases on the annual and seasonal scales during the reference period (1981 - 2010). For example, some of the ensemble members are unable to simulate the spatial structure and the seasonal cycle of the 10-m mean wind field in the complex Alpine topography. Thus, the surface wind data of the CORDEX multi-model ensemble must be treated and interpreted with caution, and we recommend use of this data only after consultation with the authors of the CH2018 report.

To gauge whether there are any signs of trends in the CORDEX wind data over Switzerland, changes in the 98th percentile of daily maximum wind speeds have been computed for the CORDEX multi-model ensemble. The results for the EUR-11 model ensemble show only very small changes over Switzerland in all scenarios and for all time periods. The relative changes in the mean 98th percentile over all grid points in Switzerland in the RCP8.5 scenario range between -1.9 % and +1.8 % depending on the model for the period around 2035, between -1.6 % and 1.8 % around 2060, and between -2.5 % and +1.8 % around 2085. For the other scenarios, the changes are even smaller.

In summary, we conclude that given the complexity of the processes involved in generating wind extremes [319] and the fact that Switzerland is located in an area between projected increases (over central Europe) and decreases (over southern Europe) in storminess, it currently remains unclear whether and how wind extremes over Switzerland will change in response to anthropogenic climate forcing.

6.9. Conclusions and implications

This chapter provides a comprehensive and quantitative assessment of changes in weather and climate extremes in Switzerland. While extreme events are a natural element of the climate system, their frequency, intensity, and character will change in response to climate change. Here, we provide different lines of evidence from observations, models, and theory that demonstrate that many weather and climate extremes are changing significantly with increasing atmospheric greenhouse-gas concentrations and global warming (Table 6.2). Switzerland is expected to experience the following changes in extreme events:

- As average temperatures continue to increase, there will very likely be more frequent, more intense, and longer-lasting heat waves and extremely hot days, weeks, and seasons in all the RCPs considered. Along with central and southern Europe, Switzerland is a hotspot for changes in hot temperature extremes, as it has experienced one of the strongest intensifications of hot extremes worldwide over recent decades and is projected to experience some of the strongest intensifications of hot extremes also with future warming. The magnitude of the changes strongly depends on the RCP and is much larger for RCP8.5 than for RCP4.5 and RCP2.6.
- There will very likely be more frequent days with high heat stress due the combined effects of temperature and humidity, and similar increases are projected for very warm nights. These changes are largest at low elevations where the population density is typically highest, and the heat stress may be further amplified by urban heat island effects. Particularly in RCP4.5 and RCP8.5, heat stress is projected to reach levels that have not been observed over the past century, implying potentially adverse impacts on public health, labor productivity, and livestock. *There will likely be more frequent and intense heavy rainfall events with warming temperatures. Heavy rainfall events are projected to become more frequent and intense in all seasons, but particularly in the winter half year, at a rate that is substantially higher in RCP8.5 than in RCP4.5 and RCP2.6. Heavy rainfall events, from hourly downpours to multi-day periods, continue to increase with warming temperatures, a projected trend for which now also observational evidence exists for daily extremes. The most intense of the events experience the strongest

intensification. At the station or grid-point level, these changes are superimposed by high internal variability and are thus only significant for long periods or high warming levels. The intensification broadly follows the capacity of warmer air to carry about 6 - 7 % more moisture per degree of warming. Confidence in heavy rainfall intensification is now higher, given the evidence from observations and from a new generation of climate models run at unprecedented resolution. Along with a higher snow line, associated with a shift from solid (snow) to liquid (rain) precipitation at higher elevations, the intensification of heavy rainfall has implications for the risk of flooding.

- There is a tendency toward longer dry spells (periods with no rain) in summer (a majority of models in RCP4.5 and RCP8.5) and toward more pronounced agricultural droughts in summer and autumn by the end of the 21st century (likely – most of the models in RCP8.5). The extent of the drying remains uncertain (both insignificant and very strong changes cannot be excluded) and depends in part on the region. Switzerland is located between southern Europe that is projected to experience a severe increase in drought risk, and northern Europe that will receive more winter precipitation.
- There will very likely be fewer and less intense cold waves, *frost days*, and *ice days* with warming mean winter temperatures, particularly in RCP4.5 and RCP8.5. These changes are largest at higher elevations and are potentially amplified by snow-albedo feedbacks. Impacts may be both positive (for instance, due to reduced energy demand for heating or alleviated adverse health effects) and negative (due to an increase in pests). Given the very high natural internal variability of winter temperatures, cold winter periods will continue to occur for several more decades.

By the second half of the 21st century, changes in extremes are highly dependent on the level of warming and thus on the emission scenario. The number of extreme events depends non-linearly on the level of warming, such that any additional degree of warming will have a substantially stronger effect. It should be noted that at the scale of Switzerland, long-term trends in the frequency, intensity, and duration of extreme events are associated with large decadal and multi-decadal variability, which can lead to the absence of certain events for several decades and likewise to a clustering of several severe events in other decades. However, particularly in the long term, the trends in weather and climate extremes are expected to emerge clearly in Switzerland and also consistently affect the neighboring countries. In the near term, the intensity and frequency of extreme heat anomalies will very likely change within decades, whereas changes in the extremes of the water cycle (beyond changes in the snow line) might be dominated by natural fluctuations for several decades.

Type of extreme	Process-based expectation	Observed changes over last decades	Projected changes	LOSU*	Key uncertainties in projections
Hot days and warm nights in summer	More frequent and warmer hot days and warm nights as a result of mean summer warming, strongest increase at low elevations and areas of low variability	More hot days, summer days, warm nights and tropical nights (Section 3.4.2)	More summer days and tropical nights, strong increase in very warm days and nights (Section 4.3.3 and 4.3.4)	Very high	Amplification due to urban heat island effects, soil moisture-temperature feedbacks, circulation changes, and lack of consideration of changes in land use and irrigation.
Heat extremes, summer heatwaves	Increasing intensity of heat extremes and more frequent and longer lasting heatwaves along with summer warming and enhanced variability/amplification through land-atmosphere interactions	Increasing intensity of heat extremes and increasing frequency and duration of heat waves (Section 3.4.2)	Increasing frequency, intensity and duration (Section 4.3.3 and 4.3.4)	High	Circulation changes (persistence of anticyclones, large-scale circulation changes), strength of land-surface atmosphere interactions, precipitation and cloud processes
Heat stress (combination of temperature and humidity)	More frequent and intense heat stress due to higher temperatures and specific humidity which increases despite a weak reduction in relative humidity	?	More intense and more frequent days with high heat stress (Section 4.3.5)	High	Same as for heat extremes, other factors affecting heat stress such as changes in wind, radiation and urban heat island effect
Cold days and nights in winter	Fewer and warmer cold days and nights as a result of mean winter warming, strongest reduction at high elevations and areas of snow melt or shortening snow seasons	Fewer and warmer cold days and nights in winter, fewer frost days and ice days, rising zero degree line (Section 3.4.2)	Fewer and warmer cold days and nights and fewer frost and ice days (Section 4.3.3 and 4.3.4)	Very high	Circulation changes
Winter coldwaves / cold extremes	General decrease along with winter warming potentially amplified by snow albedo feedback and pronounced warming in source region of cold-air advection	Weakly decreasing frequency and duration (Section 3.4.2)	Decreasing frequency, intensity and duration but cold waves will continue to sporadically occur over coming decades (4.3.4)	High	Circulation changes (changes in winter blocking frequency and persistence) and potential effect of Artic amplification and sea-ice melt on midlatudinal weather
Heavy rainfall	More intense as a result of higher water carrying capacity of warmer air	Majority of stations with trends to more frequent and intense heavy rainfall events in all seasons (Section 3.4.3)	More intense and frequent heavy rainfall events in all seasons, in particularly in the cold season, the more intense the events the higher the increase (section 4.3.6)	Medium-high	Large-scale circulation changes, vertical stability and wind, small-scale convective processes
Dry spells / droughts	Increased probability of summer droughts and dry spells due to enhanced evapotranspiration, earlier snow melt and vegetation onset leading to soil drying and potentially more dry days	No robust and significant trend in summer mean precipitation and drought indicators (Section 3.4.3)	More frequent soil moisture droughts (soil moisture droughts) Tendency to more and longer dry spells (meteorological drought) (section 4.3.7)	Medium	Circulation changes (persistence of anticyclones, large-scale circulation changes), precipitation processes, strength of land-surface atmosphere interactions (soil moisture and vegetation feedbacks, convection, boundary layer processes)
Winter storms and extreme wind speeds	Intensification of cyclones due to latent heat release, changes in latitudinal temperature gradient affecting storm tracks	No robust trend but high decadal variability (Section 3.4.5)	No evidence for changes (4.3.8) changes cannot be ruled out	Low	Circulation changes (frequency, intensity and track of cyclones)
Hail	Not clear (Box 4.3)	No observational evidence for changes	No model evidence for changes (spatial scale too small)	Very low	Small-scale convective processes
Tornadoes	Sign not clear, competing effects of decreasing wind shear, and moistening / warming of boundary layer (Box 4.3)	Events of waterspouts and few tornadoes documented, no evidence for changes	No model evidence for changes (spatial scale too small)	Very low	Vertical wind shear, change in convective available potential energy, storm initiation
Intense snow fall events (lowlands)	Sign not clear, winter warming and precipitation increase are competing factors at low altitudes (Box 4.3)	No observational evidence for changes	No model evidence for changes	Low	Circulation changes (frequency and persistence of cross-Alpine flows)

* Level of scientific understanding: This is an index on a 5-step scale (very high, high, medium, low, and very low) designed to characterize the degree of scientific understanding. The index represents a subjective expert judgment about the reliability of the estimate, involving such factors as the significance of observed changes; uncertainties in how model capture the relevant mechanisms, agreement among different models, and theoretical process understanding.

Table 6.2. Synthesis table for different types of extremes. The projections and levels of uncertainty (LOSU) are valid for moderate- to high-emission scenarios and a mid- to end-of-century time period.

7. Natural climate variability, detection, and attribution

Summary

The emerging human-induced influence on climate must be considered against the backdrop of substantial natural (in part solar and volcanic, but mostly internal unforced) variability on timescales of years to decades. This poses challenges in detecting climate change and attributing it to anthropogenic causes, evaluating models against observed trends, and quantifying uncertainties in future changes, in particular on local scales where variability is substantial. Nevertheless, linking observed trends, attribution, model evaluation, and near-term projection are critical steps in establishing confidence in projections. The main findings of this chapter are:

- The observed warming in Switzerland over the past 50 to 100 years is much larger than could plausibly be explained by natural (forced and unforced) climate variability alone. Internal unforced variability alone is extremely unlikely to explain more than half of the observed warming, and the lack of trends in atmospheric variability indicates that not much of the warming can be attributed to variability. The natural forced (solar and volcanic) variability has been demonstrated to be very small at the global scale, and there is no evidence supporting any different conclusion at the scale of Switzerland. Therefore, even when accounting for the potential underestimation of variability in models, it is unlikely that natural variability (internal variability and forced natural variability combined) can explain more than half of the observed warming.
- At least half of the observed annual and seasonal warming in Switzerland over the past 50 to 100 years is likely due to anthropogenic emissions. This conclusion is supported by the unusual magnitude and pace of the past warming relative to natural variability, the attribution of warming to anthropogenic emissions at continental to global scales with very high confidence, and the process understanding of land warming faster than the global average.
- Since warming is predominantly anthropogenic, human influence has likely also contributed to trends seen in many other climate variables that respond to temperature.
- Natural variability is important even in the absence of climate change, and it makes a substantial contribution to the total uncertainty in future changes, in particular for variables other than temperature and on decadal timescales. On local scales, it has been and will remain a limiting factor in attributing past changes to specific forcings, in determining how fast the climate will change in the future, in investigating whether models are capturing the relevant processes, and in utilizing observed changes to evaluate and calibrate model projections using emergent constraints. Changes that have been attributed on continental to global scales often have not emerged from natural variability locally. Notably, relative to the forced trend, the contribution of natural variability continues to decrease as the climate continues to change, leading to the detection and attribution of increasing numbers of variables at smaller scales and with higher confidence.
- Natural forced and internal unforced variability can enhance or partially mask long-term anthropogenic trends. As a consequence, short-term trends are poor indicators of the magnitude of climate change.
- Uncertainties due to internal variability should also be taken into account in adaptation. Decisions regarding adaptation to climate change therefore need to be robust for a wide range of future climate outcomes. Apparent regime shifts, step changes, disaster gaps and the clustering of events, and strong increases or decreases in event frequency or magnitude (when estimated as trends over short periods) are expected to occur on local scales even if the underlying forced changes are gradual.

7.1. Introduction

Long-term anthropogenic changes in climate are superimposed by so-called *natural* variability, the sum of *forced natural* changes due to changes in incoming solar radiation and volcanic eruptions and *unforced internal* (simply *internal* hereafter) variability. Internal variability occurs even in the absence of changes in external forcings and arises from interactions within the atmosphere as well as between the atmosphere, ocean, land surface, and sea ice. Internal variability ranges from high-frequency sub-daily and day-to-day variability (due to the chaotic nature of weather) to interannual (e.g., the North Atlantic Oscillation, NAO) and low-frequency decadal and multi-decadal variations induced primarily by different modes of ocean variability (e.g., the Atlantic Multidecadal Oscillation, AMO). Some of the most dominant modes of internal variability for the climate in Switzerland are discussed in Chapter 3.2. Consequently, the observational record as well as the future evolution of the climate for a given location can be conceptually viewed as a combination of a relatively gradual (but not necessarily linear) long-term change (often referred to as the forced response to external forcings such as atmospheric greenhouse gases and aerosol concentrations or land-use changes) and unforced internal variability occurring on various spatial and temporal scales (Box 7.1). The climate thereby evolves in a fashion similar to housing prices, where gradual increases are superimposed onto largely unpredictable short-term fluctuations. The two components are not necessarily independent, as the forced response can affect the amplitude, patterns, or frequency of internal variability.

Because weather, due to its chaotic nature, is unpredictable beyond a week or two [17], and even low-frequency variations are unpredictable at timescales beyond a few years to a decade [225, 35], internal variability represents an important source of uncertainty in climate projections. The smaller the spatial scale and the shorter the time horizon considered, the greater its uncertainty contribution. Thus, at the scale of Switzerland and the five subregions considered in this report, internal variability is particularly relevant. It is the dominant source of uncertainty for the coming three to four decades [147], the time horizon highly relevant for planning and undertaking adaptation measures in the public and private sectors. Note, however, that such variability would also be present in the absence of anthropogenic climate change. To limit the effect of variability, projections are typically averaged over a 30-year period.

In this chapter, key aspects of internal variability are quantified, and its relevance for understanding and interpreting the observational record and for evaluating and interpreting model simulations of recent decades and projections for the coming decades is discussed. Changes in variability are not assessed. We also focus on separating the forced anthropogenic response from internal variability, assuming that the contributions of solar and volcanic forcings for Europe are as limited as they are for global temperature.

7.2. Methods

As both observations and historical model realizations represent a combination of a forced response to external natural and anthropogenic forcings and unforced internal variability, it is difficult to estimate the pure internal variability. Three methods for obtaining the internal variability are presented here, based on (a) a statistical model fitted to observations for Switzerland, (b) an unforced pre-industrial control simulation of a regional climate model, and (c) a large forced initial-condition ensemble performed with a regional climate model. The two methods based on models allow for a clear separation of forced changes from variability, but suffer from potential biases in the models in terms of their simulated variability compared to observations. The method based on observations utilizes the actual variability of the system, but the separation of that variability from the externally forced changes is difficult.

7.2.1. Observed temperature since the pre-industrial period

The observational estimate of internal variability uses observed Swiss annual mean temperatures for the period 1864 - 2016 (see Chapter 3.3.2) and is based on the method introduced and tested by Thompson et al. (2015) [342]. It employs a simple analytic model to estimate the expected range of trends due to internal climate variability. The analytic model is derived from the standard error of the regression and is based on two statistics of the unforced climate variability: the standard deviation and autocorrelation. By accounting

for autocorrelation, it quantifies the margin of error for a trend in a Gaussian red-noise process. The analytic model is based on the assumptions that (1) the internal variability is adequately modeled as a Gaussian red-noise process and (2) the standard deviation and/or autocorrelation of the internal climate variability do not change in response to anthropogenic forcing [342]. These assumptions do not account for the possibility of climate regimes and regime shifts. Finally, assumptions must be made regarding the forced response. Given the non-linearity of the forcing over the period 1864 - 2016, a third-order polynomial fit has been subtracted to extract internal variability [147]. The conclusions drawn in the following analysis are insensitive to the choice between second-, third-, or fourth-order polynomial fit.

7.2.2. COSMO pre-industrial control simulation

The second approach used to estimate internal variability is based on a 600-year-long pre-industrial GCM control simulation downscaled with the regional model COSMO-CLM. This analysis permits consideration of the time of emergence (the time at which the signal of climate change emerges from the noise of natural climate variability [149]) and the detection of observed trends. The driving GCM is the fully-coupled NCAR-DOE CESM 1.2.2 using the CAM5 atmospheric model run at about 2° horizontal resolution, forced with constant pre-industrial conditions following the CMIP5 protocol. An arbitrarily selected period of 600 years is dynamically downscaled with COSMO-CLM version 5.0.6 run at 0.44° horizontal resolution over the EURO-CORDEX model domain. To estimate average Swiss temperatures, an area-weighted average across all the subregions defined in Chapter 2.4 is used. There is no systematic temperature trend over the course of this entire pre-industrial control simulation. The natural variability calculated from the standard deviation of 15-year average Swiss mean temperatures from the pre-industrial control simulation is consistent and somewhat smaller than the observation-based estimate introduced above (see Figure 7.3, blue bar vs. grey bar).

7.2.3. COSMO initial-condition ensemble (COSMO-IC)

The third approach used to estimate internal variability for the recent past and to interpret projections for the near future relies on an initial-condition ensemble (see [3] for details). The model experiment was performed with the NCAR-DOE CESM 1.0.4 using the CAM4 atmospheric model at a horizontal resolution of about 2°, forced with observed historical radiative forcings up to 2005 and by RCP8.5 thereafter [238]. The experiment consists of 21 simulations starting in 1950 from slightly different atmospheric initial conditions (see [102, 106] for details). The simulations were performed with the exact same model, forced with the same radiative forcings, and share the same initial conditions in all components except for the atmosphere. Thus, the spread among the simulations merely represents the internal variability of the system, similar to the setting used by Deser et al. (2012) and Kay et al. (2015) [79, 180]. To gain insight into the internal variability at the regional scale, the CESM runs were dynamically downscaled over Europe using the regional climate model COSMO-CLM version 4.8 at a resolution of 0.44°. Note that this is a somewhat older version of COSMO-CLM than was used above; the older version significantly overestimates the JJA interannual variability compared to the more recent version [23]. The RCM was run 21 times over the 1950 - 2100 period, each time using a different realization of CESM as the boundary conditions.

Box 7.1: Dynamical adjustment

The observational record of the past century can be viewed as a combination of (a) a forced response to human-induced changes in atmospheric greenhouse gas and aerosol concentrations as well as natural changes in solar and volcanic forcing and (b) internal unforced variability. Due to the effects of internal variability (b), observed past and future climatic trends over Switzerland are likely to depart from the expected forced response (a). For instance, over the period 1989 - 2012, a winter cooling trend was observed over most of Europe (Figure 7.1, a); this phenomenon was particularly pronounced in Switzerland, with –0.55 °C decade^{-1} (Figure 7.2). These negative trends are in sharp contrast to the observed long-term winter warming over the twentieth century and the projected warming in climate models. The effect of atmospheric circulation variability is more pronounced in winter than in other seasons, as the hemispheric latitudinal temperature gradient is higher. As discussed in Chapter 3.1, winter temperatures in Switzerland are strongly affected by modes of atmospheric variability such as the North Atlantic Oscillation and the East Atlantic Pattern. Consequently, a period starting with an unusual clustering of atmospheric circulation conditions favoring warm winters and ending with conditions favoring cold winters can produce a cooling trend purely as a result of atmospheric variability. To what extent this applies to the winter cooling trend during the period 1989 - 2012 can be tested by means of dynamical adjustment, i.e., estimating an adjusted temperature time series by accounting for the temperature variations resulting from changes in the atmospheric circulation. A change in the atmospheric circulation over such a short period can in principle be the result of a change in the external forcing, but there is no evidence for this, neither from climate models nor from the long-term observational record [289]. It is assumed here that it represents unforced internal variability.

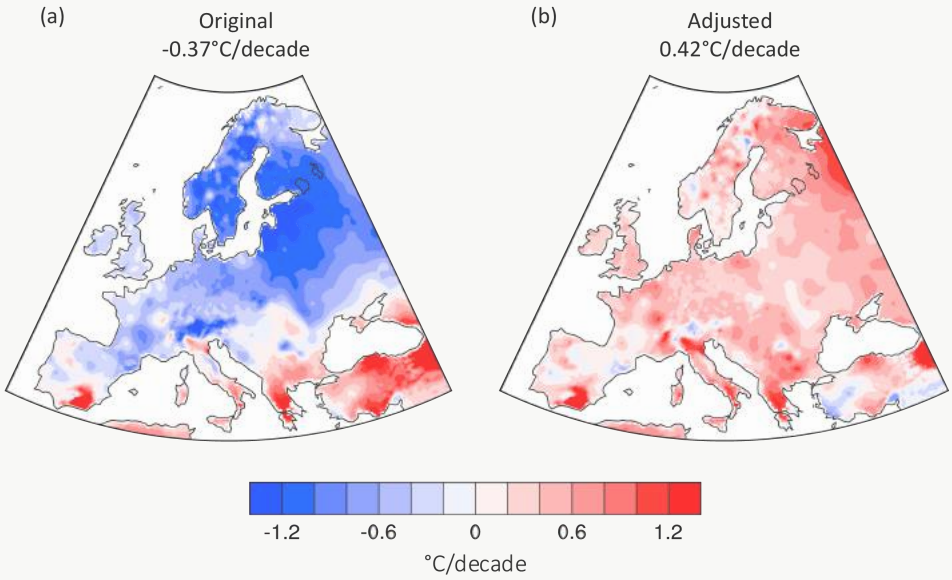

Figure 7.1. Winter temperature trends in the period 1989 - 2012 estimated from the original EOBS data (a) and after removing the effect of circulation (b). Area-weighted average trends are reported at the top of each panel (after [290]).

Dynamical adjustment uses multiple linear regression to remove the effect of atmospheric circulation on temperature as calibrated over the longest available observational record. This assumes that the patterns of circulation variability are not affected much by the anthropogenically forced response, an assumption that is well supported by model evidence. In this way, it can be shown that the negative winter temperature trends in the period 1989 - 2012 were strongly influenced by atmospheric circulation variability [289], whereby heat on the surface of the Earth was redistributed through advection (the transport of air through wind). By accounting for the effect of atmospheric circulation, the 1989 - 2012 winter cooling is reversed to show a positive temperature trend (Figure 7.1 b and Figure 7.2). The temperature response to the first five Empirical Orthogonal Functions (EOFs) of sea-level pressure are removed in this example. These EOFs explain 86.0 % of the overall variance in winter sea-level pressure. The adjusted trend in 1989 - 2012 is consistent with both the forced response estimated by averaging across model simulations and with the observed winter warming over a much longer period. This is consistent with previous analyses attributing part of the changes in Swiss temperatures

over the period 1959 - 2008 to atmospheric circulation [55]. Although variability has affected short-term trends in the past, there is no clear evidence that the long-term warming over the entire 20th century was substantially affected by internal unforced variability.

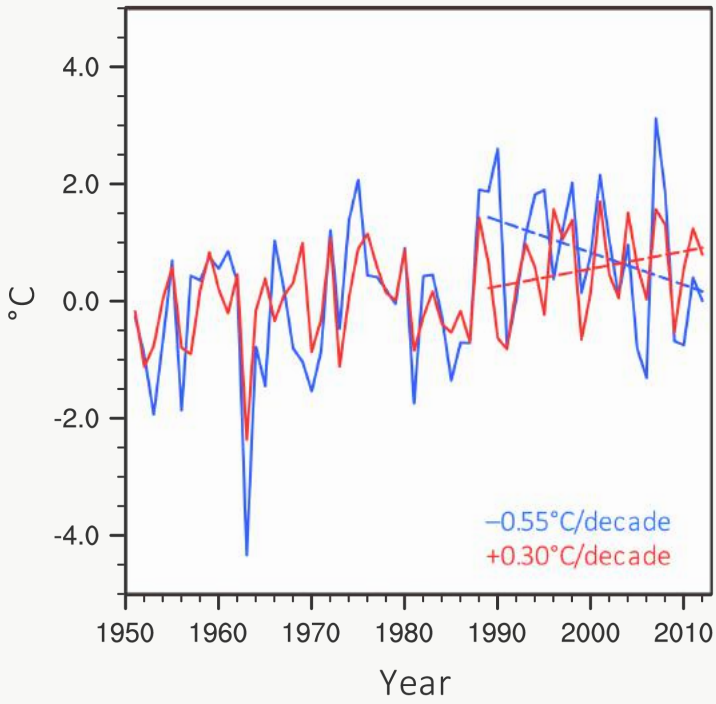

Figure 7.2. Winter temperature anomaly time series over Switzerland (average of 12 MeteoSwiss stations) from the original data (blue) and after removing the effect of circulation (red). The temperature trends in the period 1989 - 2012 are indicated by the dashed lines, and their values are reported in the plot (after [290]).

7.3. Emergence, detection, and attribution

The “detection and attribution” of climate change refers to the process of demonstrating that the observed change is larger than expected from internal variability alone (“detection” or “emerging signal”), and that the signal can be attributed to a specific cause (“attribution”) [27]. Global trends in numerous observed climate variables such as temperature, ocean heat content, heat extremes, and heavy precipitation have been detected, and many of these have already been attributed to anthropogenic forcing. Given the significant role of internal variability, it is much more difficult to detect and attribute climate change signals at the relatively small spatial scale of Switzerland. Swiss annual mean temperatures (illustrated as a 15-year running average in Figure 7.3) have emerged from the range expected from internal variability alone (time-of-emergence framework; see, e.g., [208, 149, 187]) – that is, the current temperatures are significantly different from those expected without natural and anthropogenic forcing. Over the last three decades, 15-year mean temperatures have been continuously warmer than the 4-standard deviation (grey shading in Figure 7.3) range of internal variability, independent of whether this value was estimated based on observations or climate models (see Chapter 7.2). This is consistent with what is found for summer temperatures in Box 3.1. The exact year when Swiss annual mean temperatures emerged from internal variability depends on the length of the moving time window (here, 15 years), the definition of the reference period (here, 1864 - 1900), and the threshold (1 or 2 standard deviations, etc.). However, independent of these choices, the temperatures over the past three decades have emerged from the pre-industrial climate and have increased in accordance with those in the rest of Europe.

For detection and attribution, the first step is to test whether a signal can be detected (i.e., is statistically different) from internal variability. Figure 7.4 demonstrates that all observed Swiss annual mean temperature trends ending in 2016 and starting more than 30 years in the past are significantly larger than

equally long trends caused by internal variability. Internal unforced variability alone is extremely unlikely (< 5 % probability) to explain more than half of the observed warming, assuming no information on the sequence of variability observed. The analysis of variability (dynamical adjustment) can provide further insight: There are no clear trends in atmospheric variability, indicating that little if any of the long-term warming is likely to be attributable to internal variability. The natural forced (solar and volcanic) variability has been demonstrated to be very small at the global scale, and there is no evidence supporting any different conclusion at the scale of Switzerland. All in all, the observed warming in Switzerland over the past 50 to 100 years is much larger than could plausibly be explained by natural (forced and unforced) climate variability alone. Thus, even when accounting for the potential underestimation of variability, it is unlikely (< 33 % probability) that natural variability (internal variability and forced natural variability combined) can explain more than half of the observed warming. The annual mean temperatures in Switzerland are consistent with the trends over Europe, which also cannot be explained by natural factors alone, according to model experiments [331, 190].

The detection approach does not investigate the cause of the detected trend. Formal attribution studies on such small scales for Swiss annual mean temperature using optimal fingerprinting methods do not exist [151]. As a consequence, the attribution statements for Switzerland are based on expert judgement and various other lines of evidence, specifically the unusual magnitude and pace of the past warming relative to natural variability, the attribution of warming to anthropogenic emissions at continental to global scales with very high confidence, and the process understanding of land warming faster than the global average. Attribution for Switzerland is also strongly supported by attribution on larger scales: Changes in mean temperature, the number of warm nights [236] and hot days, the intensity of hot extremes [399, 61], and the magnitude of heavy rainfall extremes [235, 393] have been detected and formally attributed to human influence in large-scale (sub-continental to global) regions including Switzerland. Likewise, it has been suggested that changes in temperature extremes have emerged in recent decades or will emerge in the coming decades in Switzerland as elsewhere [187].

Overall, despite the fact that attribution is more challenging at smaller scales, the physical understanding of increased greenhouse gases leading to warming, combined with attribution results for Europe and the Northern Hemisphere, strongly suggests that at least half of the observed annual and seasonal warming in Switzerland over the past 50 to 100 years is likely due to anthropogenic emissions. Because the warming is predominantly anthropogenic, human influence has likely also contributed to trends seen in many other climate variables that respond to temperature. Parts of the observed increases in *hot days* and *tropical nights*, as well as the trend toward more frequent and intense heat extremes (Chapter 3.3.2), are also likely to be of anthropogenic origin. Similarly, anthropogenic warming has likely contributed to the decrease in snow cover (days with snow pack on the ground) over the past few decades, in particular at low- and medium-elevation sites, and to the retreat of glaciers over the last century. However, these recent trend magnitudes should not be extrapolated into the future, as there are indications that recent trends might have been enhanced by natural decadal variability via extraordinarily strong spring temperature trends [189]. Not all snow variables show clear trends yet – for example, the maximum new snow sums (cf. [299]).

Changes in mean rainfall are too small to be attributable at this point [298]. Heavy precipitation events, in contrast, are increasing in both magnitude and frequency (see Chapter 3.3.3). This increase is consistent with the theory that warmer air can hold more moisture, and hence it is likely to be at least partially the result of anthropogenic warming. Model evidence and observed European-scale [395, 107] as well as hemispheric-scale changes in the water cycle have been formally attributed to human influence [235]. The unusual magnitude and pace of warming, combined with attribution studies on larger scales and with process understanding therefore indicates a human influence on the water cycle, even if this has not yet clearly emerged from variability.

It should be noted that large natural variability can, by chance, produce time series that suggest shifts from positive to negative trends or apparent regime shifts. What may look like a regime shift in recent climate

records in some regions including Switzerland [217, 276, 243] may not be a forced abrupt shift in climate. It is tempting to interpret such behavior and search for a causal and mechanistic interpretation, but there may not be one; likewise, such changes do not necessarily reflect a true regime shift in which the conditions in a multi-modal situation shift from one attractor to another (i.e., a system shifting from one preferred state to another). It could simply be a particular realization of internal variability in which conditions change rapidly at a particular point in time. The CORDEX simulations do not point to regime shifts in the sense of multiple climatic regimes over Switzerland (although there are systems elsewhere that could show such behavior [86]). Apparent abrupt changes in trends, however, often occur as a result of internal variability and at different points in time in different CORDEX simulations (examples shown in Figure 7.5), even though the underlying forced signal is gradual. There is no evidence of a mechanism causing these abrupt changes in the model, nor of multiple equilibria or attractors that are qualitatively different.

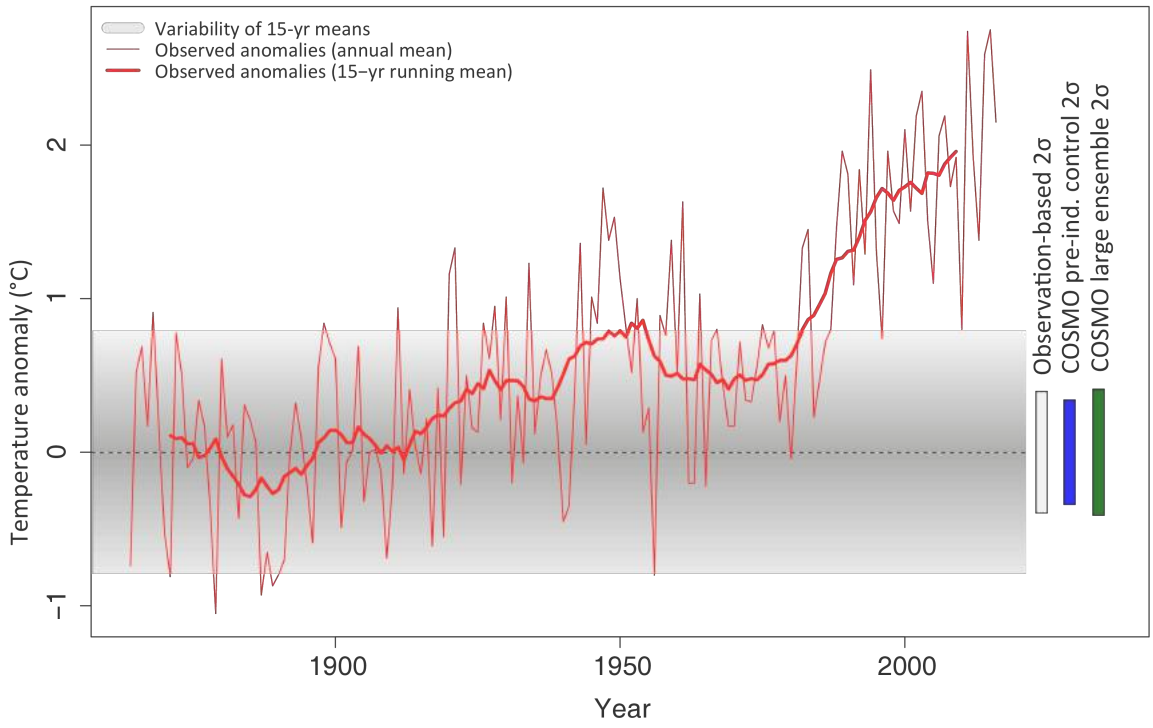

Figure 7.3. Emergence of observed annual (thin red line) and 15-year running mean (thick red line) Swiss mean temperature anomalies (relative to 1864 - 1900). The internal variability of the Swiss annual mean temperature is illustrated with ± 4 standard deviations (grey shading) of 15-year running means calculated from residuals of observations with 3rd-order polynomials removed (± 2 standard deviations shown as the white bar), with ± 2 standard deviations from 15-year running means simulated by a 600-year pre-industrial control simulation performed with COSMO-CLM5-0-6 driven with CCSM4 (blue bar), and by the initial-condition ensemble simulation performed with COSMO-CLM4-8 (green bar) when the ensemble mean has been removed.

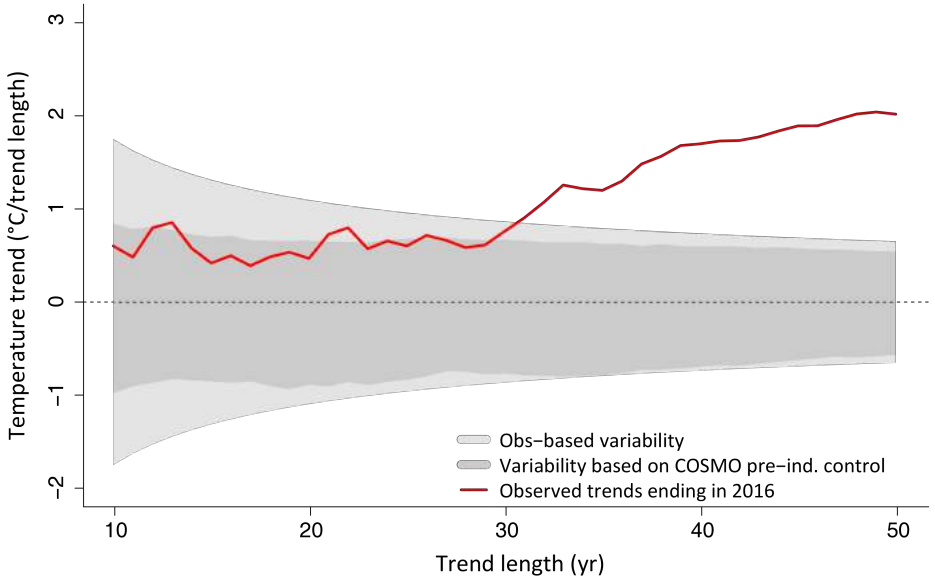

Figure 7.4. Trend magnitudes (in °C over the period length considered, on the x-axis) expected due to internal unforced variability (5 - 95 % confidence interval) as a function of trend length estimated from (dark grey band) a 600-year COSMO-CLM pre-industrial control simulations and (light grey band) residuals of a 3rd-order polynomial fit to Swiss annual mean temperatures 1864 - 2016 following an estimate using the method of Thompson et al. (2015) [342]. The red line shows observed linear trends of varying duration ending in 2016.

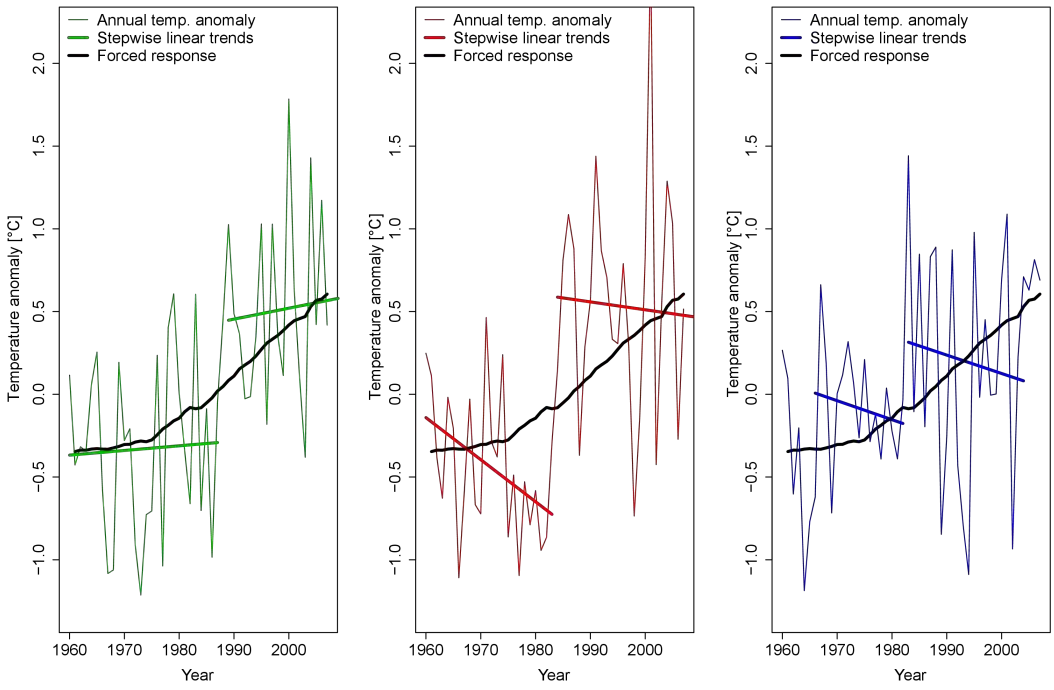

Figure 7.5. Apparent step changes or regime shifts in Swiss annual mean temperatures. The three panels illustrate three selected realizations of historical Swiss annual mean temperature as simulated by three selected members of the COSMO-IC initial-condition ensemble. Trends and colored windows illustrate two periods in which the eye identifies an apparent step change or regime shift. However, what look like regime shifts are actually realizations of internal variability superimposed onto a gradually increasing forced response (21-member mean shown in solid black) that all simulations have in common.

7.4. The challenge of evaluating models on observed trends

Climate models are imperfect representations of the real world. Limited spatial and temporal resolution, a lack of observations with which to evaluate the model, a poor understanding of certain processes, and computational constraints in simulating known processes are among the possible explanations for discrepancies between reality and the climate simulated by models. Even in a perfect case of unlimited computational capacity and observations, internal variability would still be unpredictable on timescales beyond a few years. Hence, an individual realization of weather in a model will not perfectly match the real weather, and models can only be evaluated against reality by comparing climate, i.e., distributions (probability density functions, PDFs) of weather, or for individual time series by considering a noise model for variability. Although the observed mean climate state (the median of the distribution, for example) is often well quantified, this does not provide information about changes in response to forcing. Past trends in response to past forcings (which quantify the sensitivity of the system) are often more directly related to future trends in response to future forcings, but in cases in which variability is large, it will take a long time for a trend to emerge from variability. In other words, trends can be strongly amplified or dampened by natural variability, in particular on local scales and on short timescales.

The use of observed trends for model evaluation is therefore challenging. A single realization of an observed trend will not necessarily agree with the simulated trend, as both are contaminated by variability. In the model world, multiple initial-condition ensemble members can be used to estimate variability and to estimate a forced trend (represented as the average of multiple initial condition members). Consequently, different realizations of the same model may show different trends. Some will agree with observations and others will not, and the relevant question is whether the observed trend or realization is consistent with the distribution of trends in the models at a given confidence level. A simulated trend that differs from an observed trend may indicate a bias in a model or a problem in the observations, but for short-term local trends, the internal (unpredictable) variability is often just as plausible as an explanation. Furthermore, determining the magnitude of variability is a complicated process. It is difficult to estimate variability in observations because the observed changes represent the sum of forced changes and internal variability (i.e., effectively requiring a model-based attribution step to isolate variability) and because the observational record is short. Simulated variability in models on the other hand can be biased. Summer temperature variability over central Europe, for example, is overestimated in many models [110].

An analysis of trends in a 21-member initial-condition ensemble of COSMO-CLM (see Chapter 7.2) shows that the range of 45-year-long trends (red shading) covers most of the range of the EURO-CORDEX models (blue shading in Figure 7.6). The observed warming starting in any year between 1971 and 1980 and ending in 2005 or 2016 is at the lower end of EURO-CORDEX (not shown), but generally falls within or marginally outside the EURO-CORDEX range, such as for the period 1971 - 2016 (black thick line). The difference between the simulated EURO-CORDEX model mean and the observed trend can be due to variability, inadequate forcing assumptions (constant aerosol concentrations are assumed in several models), underestimated warming in models, or any combination of the three. It is difficult to pin down the contributions of the various potential causes. For the apparent reduced warming on a global scale in the period 1998 - 2012 (termed the “hiatus” or the “pause”), for example, several hundred studies have identified a number of mechanisms that contribute to the explanation, including radiative forcing scenarios used in the climate models that turned out to be different in reality, the contribution of natural variability, and biases and incomplete coverage in observation networks (see [223] and references therein).

Not nearly as much work has been done on evaluating modeled and observed precipitation trends at the scale of Switzerland, but the evidence suggests that the absence of summer (JJA) drying over recent decades is consistent with EURO-CORDEX models (Figure 7.7). Variability on interannual to decadal timescales is very large. Even the models that project substantial future summer drying, such as COSMO-CLM, show a few individual simulations with no drying in the past.

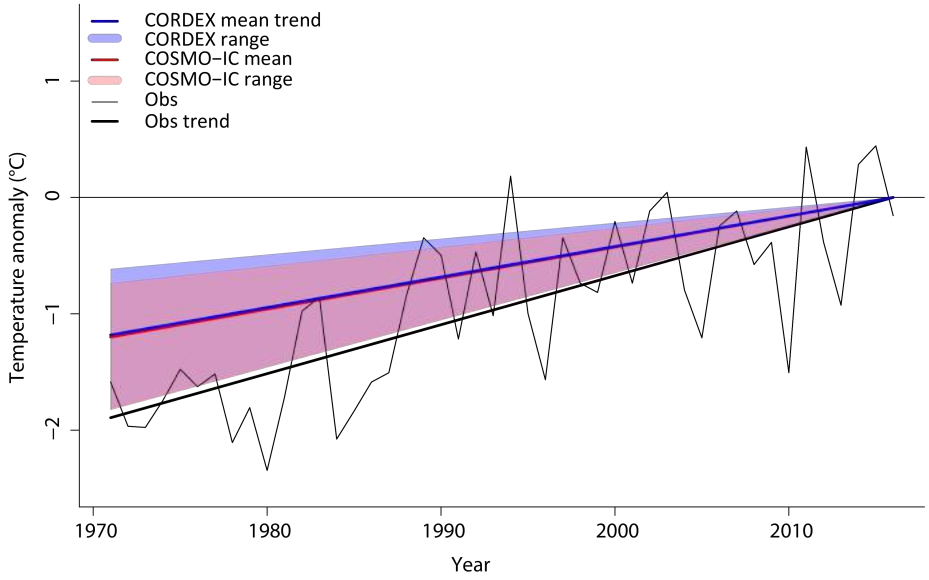

Figure 7.6. Swiss annual temperature trend over the period 1971 - 2016 as observed (black line) and as simulated by COSMO-IC (red solid line, multi-member mean) and min-max range (light red shading), as well as the EURO-CORDEX multi-model mean (blue line) and corresponding range (light blue shading). All trend lines are anchored to end at the same point in 2016.

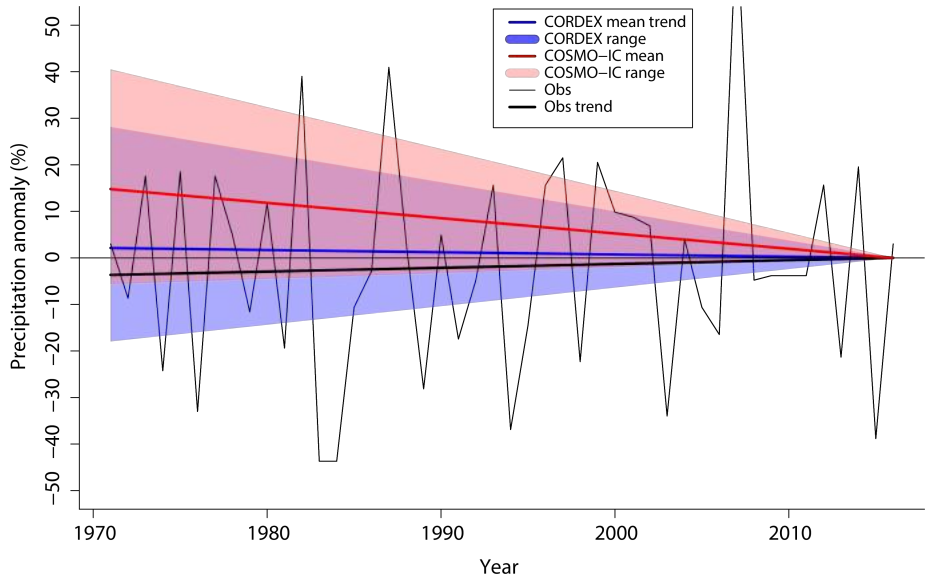

Figure 7.7. Swiss summer precipitation trend (epressed as %/36-yr trend length) over the period 1971 - 2016 as observed (black line) and as simulated by COSMO-IC (red solid line, multi-member mean) and min-max range (light red shading), as well as the EURO-CORDEX multi-model mean (blue line) and corresponding range (light blue shading). All trend lines are anchored to end at the same point in 2016.

7.5. The challenge of near- to mid-term projections

For the same reasons that past observed warming can differ from that simulated in a model, future near-term trends in the real world may strongly deviate from the forced trend (the response to forcing in the absence of variability, estimated by averaging multiple realizations). Even in a high-emission scenario such as RCP8.5, extended periods without warming in Switzerland are possible, as shown in Figure 7.8 (blue line). Likewise, warming could be much faster than anticipated (Figure 7.8, red line) and lead to apparent

stepwise changes. Based on the range of trends in COSMO-IC, the probability of experiencing certain magnitudes for a 26-year trend (green histogram in Figure 7.8) and the associated 5 - 95 % likelihood range are estimated (bars to the right). In addition, the likelihood range of no warming trend is estimated for different period lengths. There is about a 5 % chance of no annual mean warming over a period of 26 years, but the exact probability estimation is sensitive to the estimate of the underlying forced signal (here, the COSMO-IC mean starting in 2018) and internal variability (here, based on COSMO-IC). If variability is estimated from observations or from a pre-industrial control (see Chapter 7.2), there is a 5 % chance of no annual mean warming over 22 years or 26 years, respectively. For individual seasons and locations, the climate may deviate even more strongly from the forced response, as illustrated in Figure 7.9.

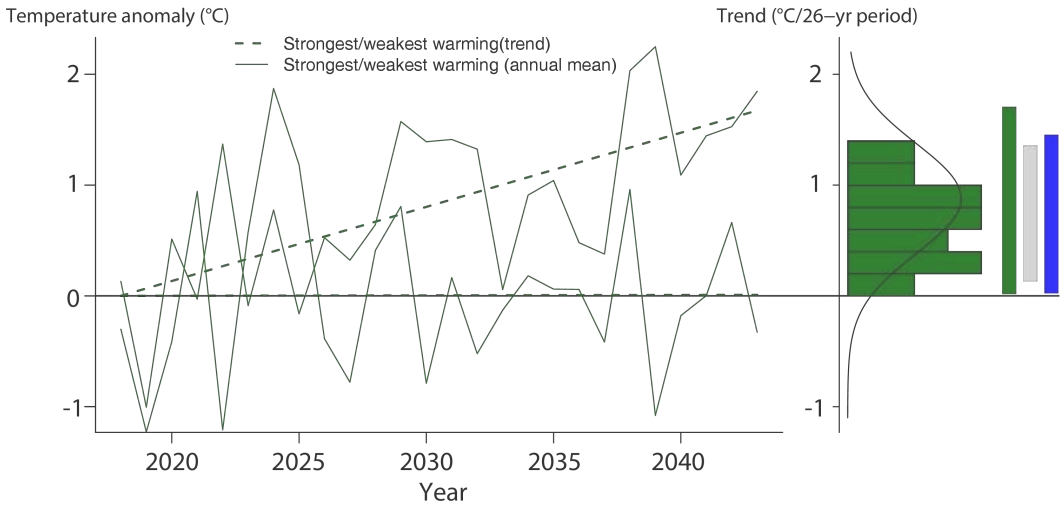

Figure 7.8. Lowest (blue) and highest (red) annual mean temperature trends for the period 2018 - 2043 as simulated by the COSMO-IC ensemble, along with the histogram of the corresponding trends in all 21 members (dark green) and a fitted normal distribution. The bars on the right illustrate the 5 - 95 % range of 26-year trends expected due to internal variability estimated from the COSMO-IC (dark green, 5 - 95 % range: 0.0 - 1.7 °C/26-yr period), the observation-based estimate (grey, 5 - 95 % range: 0.1 - 1.4 °C/26-yr period), and the pre-industrial control simulation (blue, 5 - 95 % range: 0.0 - 1.5 °C/26-yr period) centered around the COSMO-IC multi-member mean trend.

Seasonally, simulations of the same GCM-RCM model chain, forced with the same RCP and differing only in the initial conditions of the driving GCM, simulate opposing temperature trends until 2050 (Figure 7.9). Solely as the result of a different realization of unforced internal variability, one member projects a winter or summer cooling, whereas the other predicts a rapid warming for the respective season in the period 2018 - 2050. Likewise, for precipitation, where variability is even larger, the projected summer drying may occur more rapidly than expected in the long term or not manifest itself for decades (see Figure 7.10). Note that the simulations shown in Figure 7.9 and Figure 7.10 share the same underlying forced response, which implies that the realizations will converge to the same warming or drying by the end of the 21st century.

The different simulations showing opposing trends for Switzerland agree on the hemispheric-scale warming by 2050 seen in the driving model. However, in one realization, the strongest warming by 2050 occurs over Switzerland, whereas northeastern Europe experiences a cooling; the opposite effects are predicted in a different realization. Because the differences between these simulations originate from slightly different initial conditions, these uncertainties are essentially irreducible. This implies that for near- to mid-term local projections, stakeholders must cope with substantial uncertainties. At the scale of Switzerland, these quasi-irreducible uncertainties due to internal variability cover almost the entire multi-model uncertainty range for trends over the coming two decades and still a substantial fraction by the mid-century [282], although they become less important by the end of the 21st century with respect to model and scenario uncertainty (see also [147]). Note that, generally speaking, the smaller the spatial scale and the shorter the time horizon,

the larger the uncertainty contribution due to internal variability. Furthermore, this contribution is larger for extremes than for annual or seasonal means. Thus, particularly when interpreting the projections in Chapter 6 on extremes, it is crucial to keep in mind that trends over a few decades may be reversed. The occurrence of extremes in a certain decade may also be the opposite of the expected long-term changes determined by the forced response that is reflected in the change in return periods.

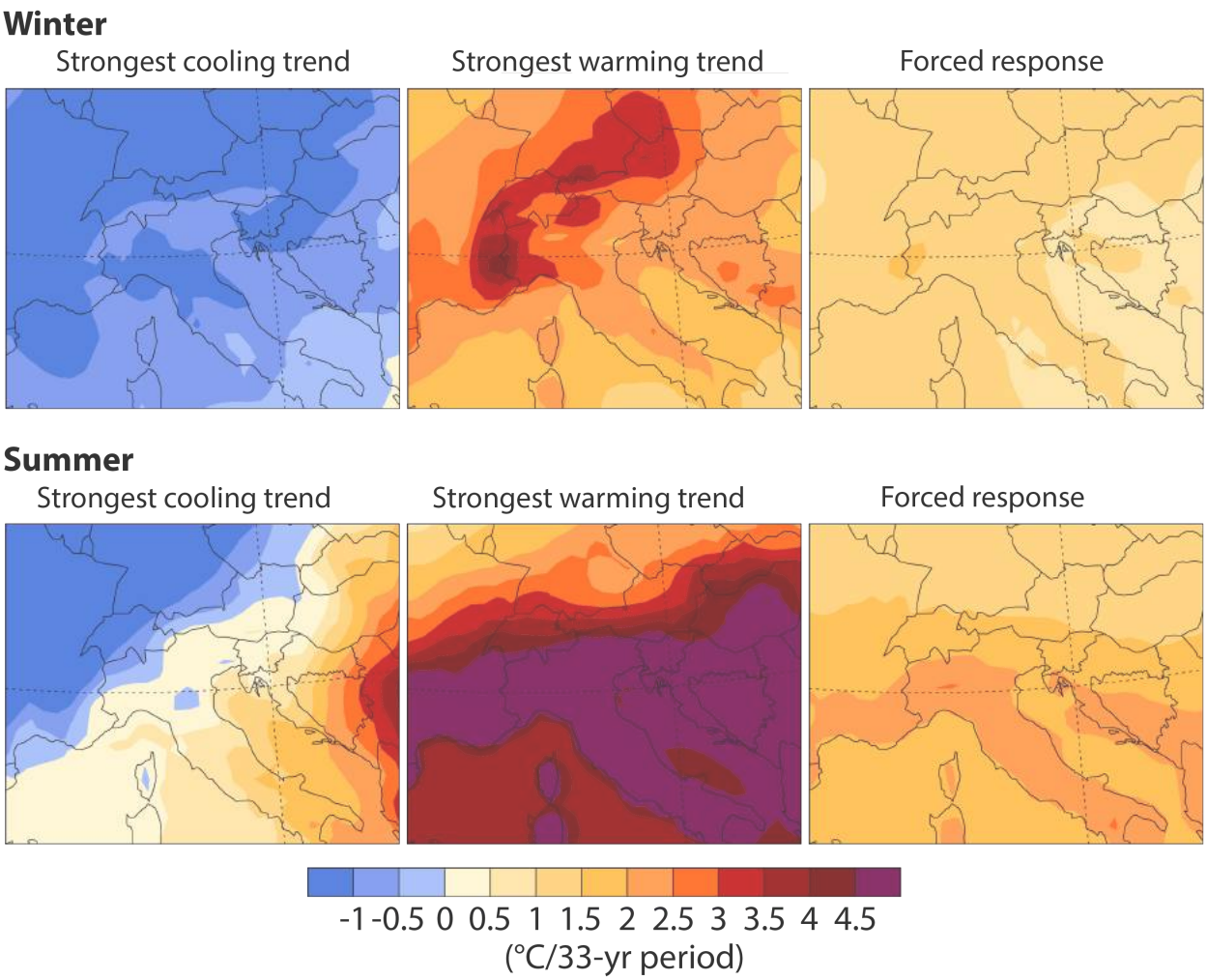

Figure 7.9. Projected winter (top) and summer (bottom) temperature trends for the 33-year period 2018 - 2050 as simulated by the members exhibiting the lowest and highest Swiss area average trends, as well as the forced response calculated as the 21-member average of the COSMO-CLM driven with lateral boundary conditions and sea-surface temperatures from the NCAR-DOE CESM model forced with RCP8.5 (see Chapter 7.2). The simulations are based on the exact same model chain using the same RCP and differ only in the initial conditions of the driving GCM. Note that the range for JJA may be biased, as the GCM-RCM chain is known to overestimate observed interannual summer temperature variability [358, 108, 45, 184, 185].

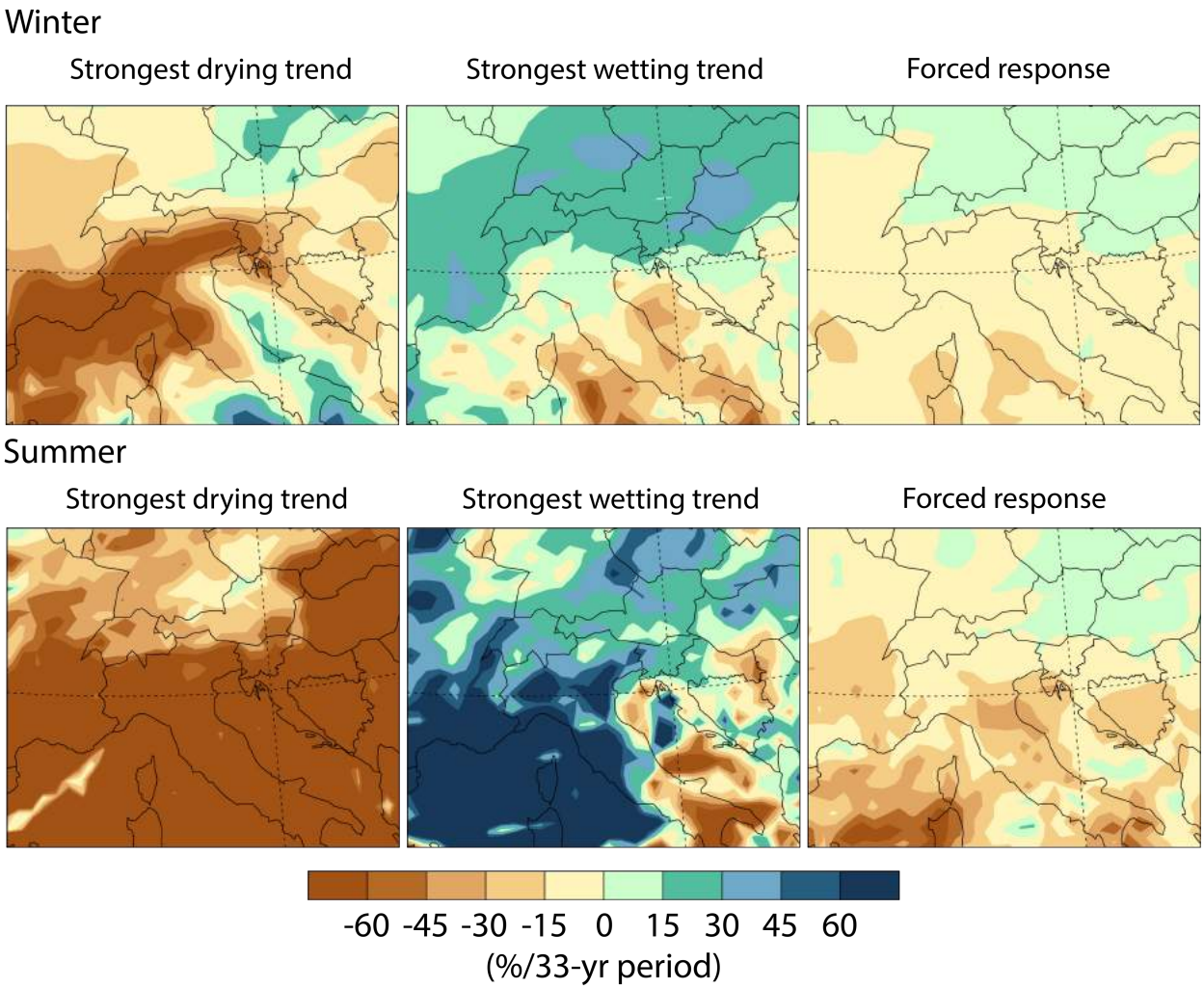

Figure 7.10. Same as Figure 7.9, but for precipitation.

7.6. Conclusions

In summary, natural variability is important, even in the absence of climate change, and on local scales it is a major contributor to the total uncertainty in future changes. It has been and will remain a limiting factor in attributing past changes to specific forcings, in determining how fast the climate will change in the future, in investigating whether models are capturing the relevant processes, and in using observed changes to evaluate and constrain model projections. The role of variability is more pronounced for precipitation and extremes than for mean temperature.

Nevertheless, there is clear evidence that observed changes in the climate of Switzerland cannot be explained by natural variability alone, and the evidence from other regions in Europe and globally strongly supports the conclusion that a large fraction of the changes are of anthropogenic origin, with variability modulating the long-term trends in either direction.

Given the confounding effect of natural variability, particularly over the next few decades, climate model projections of trends in temperature and precipitation are best expressed in probabilistic terms or as ranges with an associated likelihood. The implication is that uncertainties due to internal variability should be taken into account – also in adaptation. Apparent regime shifts, step changes, disaster gaps and the clustering of events, and strong increases or decreases in the frequency or magnitude of events (when estimated as trends over short periods) are expected to occur on local scales. The longer the time period and the larger the area averaged across, the smaller the variability will be, and the closer the actual realization (either modeled or observed) will be to the underlying forced trend. Aggregation over longer periods or climatically similar stations or grid points can improve the signal [102, 106]. The challenges for scientists involve explaining to the public and the stakeholders the long-term forced trends in the presence of

significant short-term fluctuations (“it’s not happening today in my backyard”); stakeholders, for their part, must find ways to deal with a large range of future climate outcomes. The emerging climate model evidence and deeper understanding of climate variability presented in this chapter reinforce the need for monitoring networks with adequate resources that are coupled to national frameworks for periodic risk assessment and the adaptive management of emergent climate threats and opportunities.

8. Comparison with earlier climate change scenarios in Switzerland

Summary

CH2018 supersedes the previous scenario assessments CH2011 and CH2007 (OcCC (2007)). Major changes in the methods employed have been made, mostly related to the implementation of advanced scientific developments. Although there are also some quantitative differences in the climate change projections, the CH2018 scenarios generally confirm the findings of CH2011.

- In particular, many of the quantitative differences between CH2018 and CH2011 are related to precipitation. The new scenarios indicate wetter winters and a less pronounced summer drying. In addition, model spread and thus uncertainty ranges have increased with the new set of scenarios. Nevertheless, the CH2018 scenarios are fully compatible with the “expert judgement” interpretation of CH2011 that the projected ranges encompass the actual changes with a likelihood of 66 % (for temperature) and 50 % (for precipitation).
- CH2018 incorporates higher-resolution climate simulations (12 km as opposed to 25 km in CH2011), allowing for a better representation of relevant processes (especially in Alpine terrain). In addition, the set contains simulations at a resolution of 50 km. The ensemble size has increased by half, with 21 RCM simulations (14 in CH2011) using 9 GCMs combined with 7 different RCMs, facilitating more comprehensive coverage of model uncertainty.
- CH2018 considers three emission scenarios from the IPCC AR5: one mitigation scenario (RCP2.6) and two non-mitigation scenarios (RCP4.5 and RCP8.5). This is similar to CH2011, which explored three comparable scenarios (see also Figure 2.4).
- In contrast to CH2011, CH2018 provides transient projections that include simulated daily to interannual variability and cover a set of additional variables (minimum and maximum temperature, relative humidity, radiation, and wind).
- Other innovations of CH2018 include an assessment of projected changes in climate extremes and impact-relevant indices (Chapter 6), as well as a detailed chapter on observed climate variability and trends (Chapter 3) and natural variability (Chapter 7).
- Based on the in many ways novel and methodologically improved data basis, as well as the differences identified between CH2011 and CH2018, it is highly recommended that researchers and stakeholders re-assess the quantitative impacts of potential climate change using this new reference data.

The CH2018 scenarios supersede the previous generations of Swiss climate scenarios OcCC2007 [246] and CH2011 [56] (Chapter 1). Scientific advances have led to a number of new methods and an extended range of climate information and data products (Chapter 8.1). These changes are also reflected in quantitative differences, raising the question of how such differences should be interpreted and whether impact assessments and adaptation plans need to be updated (Chapter 8.2).

8.1. Differences in methods and products

Table 8.1 summarizes the main technical, methodological, and conceptual differences. The most important of these are:

Climate simulations

The new simulations are largely based on newer generations of the same regional and global models used in previous reports. However, the increase in computing power over the last ten years has enabled successive climate scenario generations to be based on progressively improving ensembles of regional climate simulations (Chapter 4.2). Transient simulations up to 2100 have replaced the time-slice simulations used in CH2007. Horizontal resolution has increased by a factor of two with each generation of regional climate model ensembles, reaching 12 km in the EURO-CORDEX ensemble used for CH2018.

The number of available simulations has nearly doubled (21 simulations compared to 14 in CH2011), in part due to the addition of computationally less expensive simulations at a resolution of 50 km. These improvements provide more spatial detail, better physical representation of atmospheric processes, and more comprehensive coverage of climate model uncertainty. This last improvement is partially due to the increased number of global climate simulations included. However, the larger number of scenarios and simulations at different resolutions, combined with the increased variety of data products, has also made it more complex to quantify uncertainties in a consistent fashion.

Emission scenarios

Whereas CH2007 used one probabilistic projection for the time period around 2050, CH2018 separately considers two non-mitigation scenarios (RCP8.5 and RCP4.5) and one mitigation scenario (RCP2.6) (see also Chapter 2.2 and Figure 2.4). CH2011 employed a similar setup with three scenarios. However, two scenarios were simply derived by pattern scaling from the projections following the older SRES scenario A1B [164]. In contrast, the EURO-CORDEX dataset used in CH2018 includes simulations for all three RCPs. Pattern scaling is still used to complement the simulation ensemble and to derive projections for the policy targets of 1.5 °C and 2 °C above pre-industrial temperatures.

Uncertainty estimation

CH2007 relied on literature estimates of global-scale uncertainty and derived regional uncertainty estimates from RCM simulations probabilistically. CH2018 used Bayesian projections in combination with an expert judgement of probability. CH2018 quantifies uncertainty directly from climate simulations, owing to the improved coverage of the model ensemble (see above).

Localized projections

Climate projections at the local scale, which are particularly important for impact research, already formed part of the CH2011 scenarios (for mean temperature and precipitation). As an improvement over CH2011, CH2018 provides transient projections that include simulated daily to interannual variability. The localized projections were produced using the well-established quantile mapping method for downscaling and bias correction (Chapter 5). The CH2018 localized projections also cover a set of additional variables (minimum and maximum temperature, relative humidity, radiation, and wind).

Climate indices and extremes

An important advancement of CH2018 is the quantitative analysis of changes in the frequency and intensity of extreme weather events directly based on the EURO-CORDEX climate simulations. The discussion of extreme events in CH2007 and CH2011 was primarily qualitative and literature-based, although in the wake of CH2011, a number of temperature-based climate indices were made available to the user community [398]. CH2018 includes indices that quantify moderate to rare extremes relevant to a broad range of climate change impacts and affected sectors (health, agriculture, infrastructure, etc.).

Observations of past trends and variability

Observations of climatological variables are key to the understanding of future changes. In CH2018, observational data from direct measurements as well as reconstructions based on proxy data are discussed. This is a major improvement over the previous generation of climate scenarios, which touched on the observed record and past trends only marginally.

User Interactions

Another advantage of CH2018 over previous assessments is the integration of user needs right from the start by means of a comprehensive survey of users across Switzerland and the establishment of a “sounding board” group of representatives from research and governmental institutions to accompany the project (Box 2.2). In CH2011, user engagement was limited to one workshop with certain representatives of the user community.

Table 8.1. Methods and characteristics of the scenario assessments CH2018, CH2011, and CH2007. The numbers given for CH2011 refer to the simulations that covered the full period 1951 - 2100; for the period up until 2050, six additional simulations were considered in CH2011.

	CH2018	CH2011	CH2007
Model Ensemble	Euro-CORDEX [177, 198]	EU FP6 ENSEMBLES [352]	EU FP5 PRUDENCE [59]
Resolution	12 km (0.11°) and 50 km	25 km (0.22°)	50 km (0.44°)
Number of Simulations	26 (12 at 12 km, 14 at 50 km)	14	16
Number of GCMs	13	6	2
Number of RCMs	9	10	8
Simulation Period	1971 - 2100	1951 - 2100	1961 - 1990 and 2071 - 2100
Scenario Periods	2020-2049 (“2035”), 2045 - 2074 (“2060”), 2070 - 2099 (“2085”)	2020-2049 (“2035”), 2045 - 2074 (“2060”), 2070 - 2099 (“2085”)	2030, 2050, 2070
Reference Period	1981 - 2010	1980 - 2009	1990
Model Regions	Five regions (CHNE, CHW, CHS, CHAE, CHAW)	Three regions (CHNE, CHW, CHS) with later extensions to the Alps (CHAE, CHAW) [100]	Two regions (northern and southern Switzerland)
Emission Scenarios	RCP8.5 (no mitigation, 26 simulations), RCP4.5 (no mitigation, 19 simulations, 7 estimated by pattern scaling), and RCP2.6 (mitigation, 8 simulations, 18 estimated by pattern scaling); separate assessment of scenarios	SRES A1B (no mitigation) only, A2 (no mitigation, estimated by pattern scaling), and RCP3PD (mitigation, identical to RCP2.6, estimated by pattern scaling); separate assessment of scenarios	A2 and B2 with scaling for 35 non-mitigation emission scenarios; joint assessment of emission scenarios
Information on Climate Extremes	quantitative (based on Euro-CORDEX)	qualitative (literature review)	qualitative (literature review)
Climate Indices	Several moderate and extreme climate indices of temperature and precipitation	High-resolution temperature-based indices in CH2011+ extension series [398]	-
Localized Projections	Transient time-series 1971 - 2099 with daily variability, based on quantile mapping [270, 271]	30-yr mean change in annual cycle (daily resolution), based on delta-change method [32]	-
Available Local Datasets	Daily Temperature (min./max./mean), Precipitation, Humidity, Radiation, Wind	Daily Temperature (mean), Precipitation	-

	CH2018	CH2011	CH2007
Data in Digital Format	Data products of model variables and derived quantities (see Chapter 9)	Climate scenarios of seasonal means, regional scenarios at daily resolution, gridded scenarios at daily resolution [398], local scenarios at daily resolution	-
Uncertainty Estimation	Empirical quantiles (5 %, 50 %, 95 %) of model spread	Bayesian approach [99]	Empirical PDF modeling and global scaling [122]
Observations	Extensive discussion of past and current climate (Chapter 3)	Short section on past trends and variability	Short section on past trends; interpretation of future changes in terms of current climate
User Interaction	User survey [230], stakeholder dialog, and sounding board	Climate scenario workshop (March 2010)	-

8.2. Quantitative comparison of CH2018 and CH2011

It is important to evaluate whether conclusions from different generations of climate scenario assessments are consistent. Many impact studies and potential adaptation measures depend not only on the qualitative behavior of change but also on changes in quantitative terms. The following summary of overall consistencies and differences between CH2018 and CH2011 serves as a guide for users, also in relation to questions of whether a potential reconsideration of the evaluation of climate impacts is necessary. Projected seasonal mean changes in temperature and precipitation from CH2011 and CH2018 are presented in a comparative manner in Figure 8.1 for the example of northeastern Switzerland (CHNE). Figure 8.1 illustrates results for two different emission scenarios: the non-mitigation scenarios with the highest emissions (RCP8.5 for CH2018 and A2 for CH2011; see also Chapter 2.2) and a mitigation scenario (RCP2.6; Figure 8.1). It should be noted that from a scientific point of view, a direct comparison of the disseminated quantiles is not straightforward for a number of reasons: differences in emission scenarios and the projected global mean warming, differences in the quantification of uncertainty, and differences in both the model runs selected and the number of simulations considered. However, from a user perspective, a direct comparison of the disseminated data products is instructive, as it provides a quick overview of the main differences and similarities between the two initiatives.

There is overall qualitative agreement between CH2018 and CH2011, especially with regard to the median changes in temperature. Quantitative differences appear in the median precipitation projections, especially in summer and winter. There are also distinct differences in the model spread between CH2018 and CH2011 projections, with the spread mostly being larger in the updated CH2018 scenarios (Figure 8.1). This could be related to the larger ensemble used in CH2018, in particular because more GCMs were involved; additionally, in contrast to CH2011, no Bayesian post-processing was applied, a step that potentially down-weights outlying simulations. In all of the simulations, signals emerge more distinctly with time and increasing greenhouse gas concentrations. Figure 8.1 presents changes for the scenario periods 2035, 2060, and 2085, but the following discussion focuses on the period 2085 only.

8.2.1. Temperature

The CH2018 projections indicate significantly increasing temperatures in all seasons, with particularly pronounced increases in summer (Figure 8.1, top row).

Overall, the median projected temperature increase is in line with CH2011. For instance, in summer, the median signal from CH2018 is +4.5 °C around 2085 for northeastern Switzerland, compared to +4.4 °C in CH2011. However, model ranges are markedly larger in CH2018 compared to CH2011 (+3.4 to +7.0 °C in CH2018 vs. +3.1 to +5.6 °C in CH2011), primarily due to an increase in the upper end minus median difference; the median minus lower end difference remains unchanged. This is especially the case in summer and autumn. For summers at the end of the century, the uncertainties for RCP8.5 are larger by a factor of about 1.4 than in A2-driven CH2011 scenarios.

8.2.2. Precipitation

The CH2018 projections indicate increasing winter and spring precipitation, stable conditions in autumn, and a tendency toward a reduction in summertime precipitation (Figure 8.1, bottom row).

The distinct ***summer drying*** – which was projected to be considerable in the two previous assessment reports – is still present, though slightly less pronounced. The strongest reductions in precipitation were projected in CH2007 (median: -23 %, range: -41 % to -9 % for the northern side of the Alps for the time period around 2070), but CH2011 also showed a reduction in summer precipitation across the full range of the projections (median -21 %, range: -33 % to -10 % around 2085 for northeastern Switzerland). This is still the case in CH2018, although the range is larger (-17 %, range: -40 % to -4 %). It should be noted that some of the EURO-CORDEX model chains even exhibit increasing summer precipitation (the simulations driven by the GCM CNRM), but these have been excluded from the CH2018 simulation set due to quality issues (Chapter 4.2 and Chapter 4.7).

The new scenarios also project a considerable ***winter wetting***, which was only seen in the southerly regions CHS and CHAE in CH2011. The CH2007 scenarios exhibited this winter signal as well (median: +16 %, range: +1 % to +42 %), in contrast to CH2011, which showed no clear tendency (median: +3 %, range: -11 % to +18 %). The increase in winter precipitation seen in CH2018 already emerges in the near-term future period (median: +8 %, range: -4% to +19 %) and becomes substantial by the end of the century (median: +14 %, range: -1 % to +27 %).

For the most part, the similarities and differences discussed above for the scenarios RCP8.5 and A2 are also seen for RCP2.6, although the magnitude of change is lower and the associated model spread is smaller (Figure 8.1, right). This is the case, for instance, for the projected increase in winter precipitation, which is clearly visible in CH2018 (median: +6 %, range: -8 % to +19 %), whereas the change in CH2011 was insignificant.

Studies in the scientific literature comparing the regional climate model ensembles ENSEMBLES (the data basis of CH2011) and EURO-CORDEX (the data basis of CH2018) support the overall consistencies and thereby strengthen previous knowledge about projected European climate change [177, 273]. However, certain differences related to summer and winter precipitation have been identified [273]. On the European scale, the reductions in summer precipitation projected by EURO-CORDEX models are not as large as previously found, in particular across central and southern Europe including the Alps. Conversely, across central and northern Europe, winter precipitation is projected to increase more strongly.

Implications for the use of the CH2018 climate scenarios

Although previous results from earlier climate change scenarios in Switzerland are mostly confirmed by CH2018 in a qualitative sense, some deviations have been found, such as the winter and summer precipitation changes and the differing model ranges. It is therefore generally recommended that users re-assess quantitative impacts with this new reference scenario data. Impact applications that are sensitive to potential summer drying and/or increasing winter precipitation might benefit most from such an update. In addition, the new data products and improved methods facilitate broader applicability for impact applications.

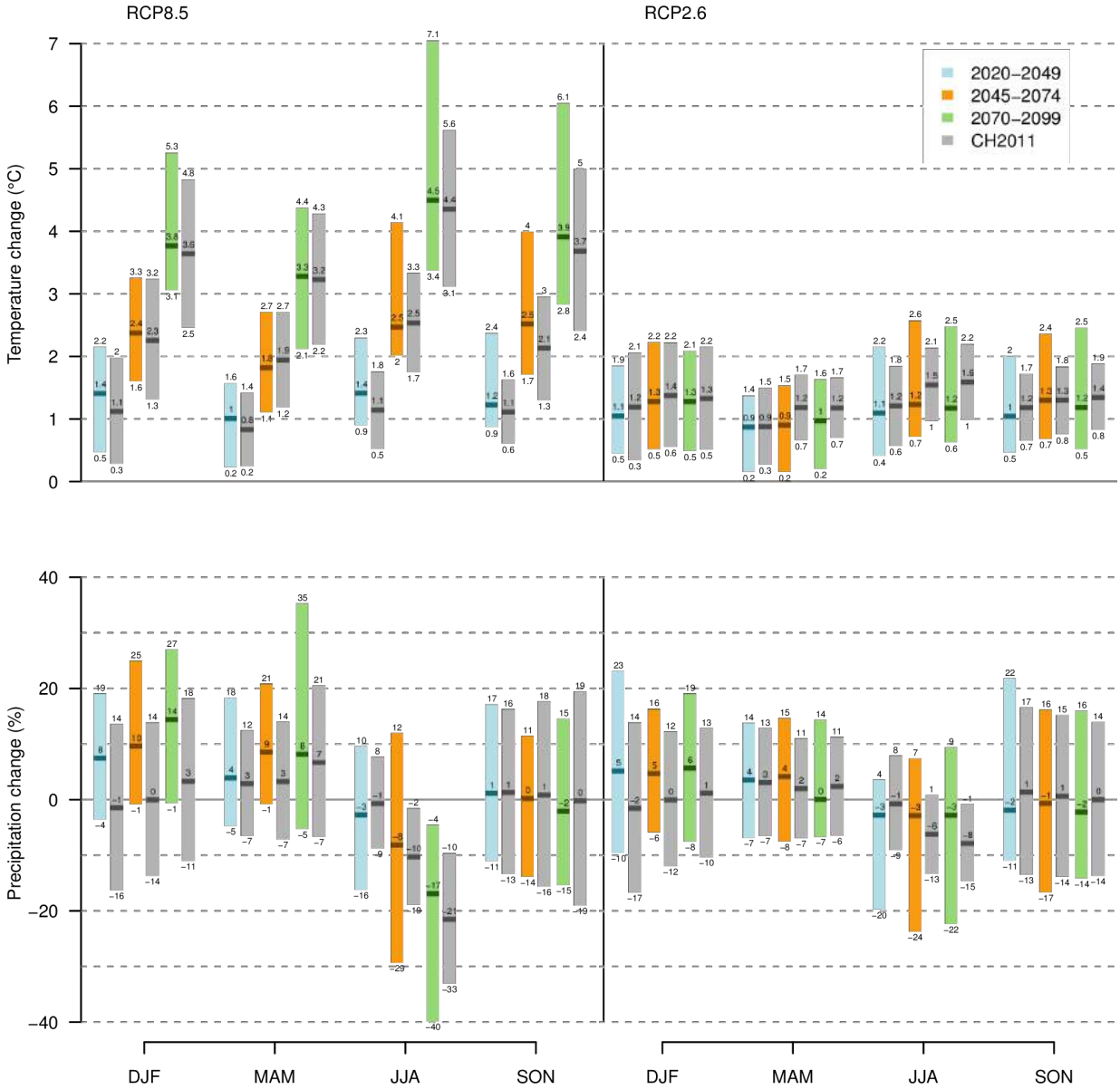

Figure 8.1. Seasonal mean changes in temperature (top) and precipitation (bottom) as described in Chapter 4 (colored) against those from CH2011 (grey). Shown are the changes for northeastern Switzerland at the three future time periods for the reference scenario RCP8.5 (left) and the mitigation scenario RCP2.6 (right). To compare the changes from CH2018 at RCP8.5 to earlier findings, the uncertainty estimates from CH2011 based on the SRES A2 scenario are displayed.

9. The CH2018 scenario datasets

Summary

A number of datasets for the climate-change projections presented in this report are available for use in impact research and practical applications. All datasets are based on the emission scenarios RCP2.6, RCP4.5, and RCP8.5.

Two datasets contain transient daily time series of model variables that have been downscaled to produce absolute values at a local scale. These data are primarily useful for research purposes and are available upon request (see contact form):

- DAILY-LOCAL includes daily mean, maximum, and minimum temperature, precipitation, relative humidity, global radiation, and near-surface wind speed, downscaled to MeteoSwiss station locations.
- DAILY-GRIDDED includes daily mean, maximum, and minimum temperature and precipitation, downscaled to a 2 km x 2 km grid.

The remaining datasets contain 30-year average changes in seasonal or annual mean variables and indices. These datasets are geared toward practical application, especially in the context of adaptation to climate change. They are available for download from www.climate-scenarios.ch:

- SEASONAL-REGIONAL contains mean temperature and precipitation changes for each season and for each of five climatically nearly homogeneous regions covering Switzerland.
- INDEX-LOCAL contains changes in climate indices including seasonal mean wet bulb temperature, maximum wet bulb temperature, and the number of days of wet bulb temperature above 20 °C for MeteoSwiss station locations. INDEX-LOCAL is derived from the DAILY-LOCAL dataset.
- INDEX-REGIONAL provides seasonal mean changes in indices of temperature and precipitation extremes, precipitation frequency, and drought for the same five regions as in SEASONAL-REGIONAL.
- INDEX-GRIDDED contains gridded annual temperature indices including hot days, summer days, tropical nights, frost days, and ice days for a 2 km x 2 km grid. INDEX-GRIDDED is derived from the DAILY-GRIDDED dataset.

The available datasets for the CH2018 scenarios are derived from the EURO-CORDEX ensemble of regional climate simulations (Chapter 2 and Chapter 4). The methodological steps to derive the different datasets are shown in Figure 9.1. CH2018 provides six different datasets (Table 9.1). All datasets are provided separately for the three emission scenarios RCP2.6, RCP4.5, and RCP8.5.

The datasets DAILY-LOCAL and DAILY-GRIDDED are primarily research-oriented (Table 9.2). They correspond to the localized projections described in Chapter 5 and consist of model variables that are statistically downscaled to individual meteorological station sites or to a high-resolution grid using the quantile-mapping method. Both datasets include transient time series of daily data covering the period 1981 through 2099, which are derived from 31 model chains for RCP8.5, 25 for RCP4.5, and 12 for RCP2.6. Additionally, 30-year time slices are provided for RCP4.5 (5) and RCP2.6 (13) for the model chains that have not been run with these emission scenarios. These are derived through pattern scaling of existing simulations (Chapter 4.2).

The DAILY-LOCAL and DAILY-GRIDDED datasets are extensive and detailed, and as such are suitable as input for models of climate change impact that explicitly resolve time-dependent processes. They require scientific insight for correct use and interpretation, as they contain not only robust features but also random variation that is not necessarily related to climate change. Furthermore, owing to the statistical downscaling method applied, these data entail a range of potential limitations and might not be suitable for every kind of impact research (Chapter 5.7). The DAILY-LOCAL and DAILY-GRIDDED datasets are available upon request.

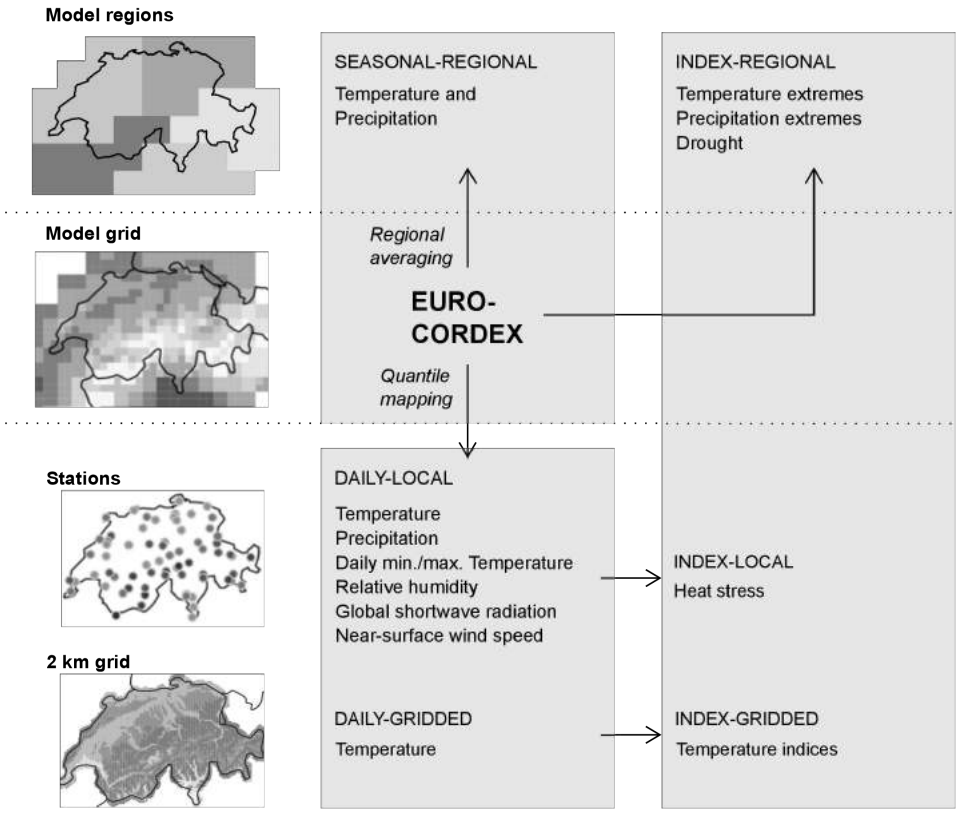

Figure 9.1. Overview of the methodological steps to derive the CH2018 datasets.

The remaining datasets are also useful for practical applications that do not involve a detailed analysis of the climate data, e.g., for adaptation planning by cantonal or federal authorities. They consist of aggregate results and indices derived from the first two datasets or directly from the model output (Table 9.3).

The dataset SEASONAL-REGIONAL provides 30-year averages of the seasonally and regionally averaged changes in temperature and precipitation, similar to the dataset included in the earlier CH2011 climate scenarios [56] (Chapter 8). The remaining datasets, INDEX-LOCAL, INDEX-REGIONAL, and INDEX-GRIDDED, are 30-year averages of derived indices describing extreme events and other specific aspects of the climate simulations (Table 9.3). These aggregated results are provided either as absolute values for the CH2018 periods 2035, 2060, and 2085, as well as the reference period 1981 - 2010 (INDEX-GRIDDED), or as changes for the future periods with respect to the reference period (SEASONAL-REGIONAL, INDEX-LOCAL, INDEX-REGIONAL). The model spread in these variables/indices is commonly summarized by the median and empirical 5 % and 95 % quantiles of the CH2018 multi-model ensemble (Chapter 2.7).

The datasets of seasonal and annual means and indices are considered robust, as most of the variations on short timescales are filtered out by the 30-year averaging. They have been derived with the intention of extracting salient information on mean changes, changes in extreme events, or changes with respect to the exceedance of relevant temperature thresholds. In contrast to the daily data, they are geared toward practical applications of the CH2018 climate scenarios, especially in the context of adaptation to climate change. To optimize dissemination, these datasets are available for download from the CH2018 website (see below). The selection of indices provided is based on a list recommended by an expert team [392] and a user survey conducted at the beginning of the CH2018 project [230] (see also Chapter 4.3.2 Definition of indices and extremes). Despite their user-oriented nature, the application of these datasets requires careful interpretation that takes into account the uncertainty assessments for the individual parameters provided in this report (Chapter 4, Chapter 5, and Chapter 6). Chapter 10.4 provides further guidance on best practices in using these data.

Dissemination of the CH2018 data:

- All datasets listed in Table 9.2 are available upon request (see contact form).
- All datasets listed in Table 9.3 are available free of charge from the CH2018 website (www.climate-scenarios.ch).

Dataset	Spatial resolution	Temporal resolution	Time coverage	Range	Values	Source / Method	Chapter
DAILY-LOCAL	Stations	Daily	Transient 1981-2099*	26 Simulations*	Absolute	Quantile Mapping	5
DAILY-GRIDDED	2km x 2km	Daily	Transient 1981-2099*	26 Simulations*	Absolute	Quantile Mapping	5
SEASONAL-REGIONAL	CH2018-regions	Seasonal	30-year-period mean	Quantiles	Change	Model output	4
INDEX-LOCAL	Stations	Seasonal/annual**	30-year-period mean	Quantiles	Change	Quantile Mapping	6
INDEX-REGIONAL	CH2018-regions	Seasonal/annual**	30-year-period mean	Quantiles	Change	Model output	6
INDEX-GRIDDED	2km x 2km	Seasonal/annual**	30-year-period mean	Quantiles	Absolute	Quantile Mapping	6

*Including pattern-scaled 30-year time slices for RCP4.5 (7 members) and RCP2.6 (18 members), which are not transient (Chapter 4.2.1)
**Annual values are provided for season-specific indices

Table 9.1. Overview of the available CH2018 datasets.

DAILY-LOCAL	Unit	Number of stations
Mean near-surface Temperature	°C	85
Daily minimum near-surface Temperature	°C	86
Daily maximum near-surface Temperature	°C	85
Precipitation	mm/day	399
Relative Humidity	%	84
Global Radiation	W/m^2	59
Wind speed*	m/s	84
DAILY-GRIDDED	**Unit**	**Horizontal resolution**
Tmean, Tmin, Tmax	°C	2 km x 2 km
Precipitation	mm/day	2 km x 2 km

* Wind data are not reliable for projections despite agreement with observations in the reference period (Chapter 6.8).

Table 9.2. Datasets available upon request, including localized projections at meteorological stations (DAILY-LOCAL) and on a high-resolution grid (DAILY-GRIDDED).

SEASONAL-REGIONAL	Report Chapter		Unit
Basic variables	4		
Mean near-surface Temperature			°C
Precipitation			%
INDEX-LOCAL	Report Chapter	Number of stations	Unit
Heat stress indices	6.5	83	
Mean Wet Bulb Temperature (TWmean)			°C
Max. Wet Bulb Temperature (TWx)			°C
Wet Bulb Temperature > 22°C (TWg22)			days
INDEX-REGIONAL	Report Chapter		Unit
Temperature extremes	6.4		
Hottest temperature per year (TXx)			°C
Number of very hot days (TX99p)			days
Coldest temperature per year (TNn)			°C
Precipitation frequency	6.6		
Wet-day frequency (fre)			%
Precipitation extremes	6.6		
99th percentile of daily precipitation (p99)			%
maximum precipitation event per year (rx1d)			%
maximum 5-day precipitation per year (rx5d)			%
Intensity of daily precipitation with 10 yr return period (rx1d10)			%
Intensity of daily precipitation with 100 yr return period (rx1d100)			%
Intensity of 5-day preciptiation 10 yr return period (rx5d10)			%
Intensity of 5-day preciptiation 100 yr return period (rx5d100)			%
Drought indices	6.7		
Maximum number of consecutive dry days (CDD)			days
Standardized Preciptiation index (SPI)			%
Preciptiation minus evapotranspiration (P-E)			mm/day
Standardized soil moisture anomaly (SMA)			%
INDEX-GRIDDED	Report Chapter		Unit
Temperature indices	6.3		
Hot Days			days
Summer Days			days
Tropical Nights			days
Frost Days			days
Ice Days			days

Table 9.3. Datasets available for download, including projections (SEASONAL-REGIONAL) and climate indices (INDEX-REGIONAL) aggregated to the five CH2018 regions of Switzerland, as well as indices at meteorological stations (INDEX-LOCAL) and on a high-resolution grid (INDEX-GRIDDED). The information on the aggregated data with the suffix "REGIONAL" also applies to the corresponding data fields on the native grid of the regional climate models (available upon request).

10. The CH2018 scenarios in use

Summary

As the most up-to-date collection of climate change information on Switzerland, the CH2018 scenarios are an important source of data for impact research and practical adaptation issues. The CH2018 scenarios are discussed for illustrative use cases to foster understanding as well as to demonstrate the wide application of the CH2018 data products.

- So-called “climate analogs” suggest that the future Swiss climate is similar to the present-day climate near the northern Mediterranean coastline.
- An application to runoff shows that decadal variability strongly modulates the long-term change. Thus, the transient evolution of climate variables should be taken into account in order to develop realistic expectations.
- Snow pack is a complex quantity formed by the interplay of a number of variables. Simulations for the Swiss Alps reveal that due to compensating effects, the combination of temperature and precipitation change is still an adequate predictor of the response.
- Weather generators are promising tools in efforts to overcome some of the limitations of the downscaling method used in CH2018. The recently developed Advanced WEather GENerator (AWE-GEN-2d) provides impact-relevant climatic variables at a high temporal and spatial resolution and is evaluated within the sister project Hydro-CH2018 for hydrological downscaling applications in a climate change context.
- A stakeholder dialog has been initiated to provide continued support and close interaction with users of the CH2018 scenarios. As a kind of “climate service”, this stakeholder dialog prepares the groundwork for an ongoing interaction between providers and users of the CH2018 scenarios under the umbrella of the recently founded National Center for Climate Services (NCCS).
- Due to the complexity of the CH2018 climate scenarios, there is no single physically consistent scenario for “strong climate change”. The most drastic changes in summer hot spells, extreme winter precipitation, or any other parameter are not all found in the same simulations. Thus, the behavior of the individual simulations should be considered when deriving an impact-specific climate change scenario from the range of CH2018 projections.

As the most up-to-date collection of climate change information on Switzerland, the CH2018 scenarios are an important data source for impact research and practical adaptation issues. To foster understanding as well as to demonstrate the wide application and ensure consistent treatment of the CH2018 data products, this chapter describes illustrative cases of the CH2018 scenarios in use (Chapter 10.1, Chapter 10.2), comments on the process of engaging with stakeholders to achieve a broader application of the scenarios (Chapter 10.3), and provides some guidance on their use (Chapter 10.4).

In order to better communicate and improve understanding of changing climatic conditions, such as “2.5 °C warmer and 20 % precipitation decrease”, the development and use of climate analogs is demonstrated (Chapter 10.1). These climate analogs express the projected changes in temperature and precipitation in terms of existing climates in other regions of Europe today.

In the following section, a first application of CH2018 scenarios in hydrology is discussed (Chapter 10.2). Because a lack of precipitation and low-flow conditions result in substantially reduced water availability and will likely challenge the current allocation of water use and rights, a case study (Chapter 10.2.1) looks into the use of CH2018 data in such an application context. It shows how the transient nature of the localized CH2018 projections yield a richer picture of expected impacts, depicting the compound influences

of trend and variability. Given the relevance of snow conditions in the Alpine region, not least for ski tourism, the CH2018 scenarios are applied for a snow pack analysis (Chapter 10.2.2). These simulations demonstrate the application of CH2018 data in a multivariate context, using snow as an example of a complex entity formed through the interplay of precipitation with the environmental variables of temperature, sunlight, and wind. The hydrological example applications confirm the improvements in and better usability of the new CH2018 projections. Some of the remaining limitations of the downscaling method used in CH2018 can be addressed using *weather generators*. These statistical models that mimic natural variability on top of projected changes are discussed as an example of applying CH2018 data in technical development (Chapter 10.2.3).

Most users are not so much interested in the climate as such, but in the performance of the systems and infrastructures they are responsible for and depend upon. Such users thus care about the *impact* of weather and climate (see also the section about risk, Chapter 6). Consequently, in parallel to the development of the new climate scenarios, a dialog with public and private stakeholders has been established to facilitate optimal use of the CH2018 results. This dialog will continue past 2018 under the umbrella of the Swiss National Center for Climate Services (NCCS) and is pursued in the spirit of co-development of knowledge and co-design of decision-support systems (Chapter 10.3). Impact researchers who are not climate modelers will presumably be working together with regional climate modelers who have expertise in generating impact scenarios. Accordingly, the present chapter is intended as a contribution to this collaboration, aimed at a mutually beneficial improvement of understanding and the co-development of truly connected impact chains. This will not only further our knowledge, but also improve decision-making in the context of optimizing the performance of complex systems. Many such applications will consider only a subset of the complex CH2018 scenario data, as the entire range of projections may not be manageable computationally, or may not be relevant for a specific question. A section on best practices (Chapter 10.4) at the end of this chapter outlines how to make a selection of data with due care for consistency and robustness.

10.1. Analogs for the future Swiss climate

The projected climate changes in Switzerland as outlined in Chapter 4 can lead to significant modifications of the present-day temperature and precipitation climate. However, it can be difficult to grasp the meaning and consequences of, for instance, a 2.5 °C temperature increase in wintertime or a 20 % summer precipitation decrease. To better illustrate such changes, climate analogs can be useful. Climate analogs are locations that currently experience a climate that is similar to the projected (i.e., the future) climate of a given site of interest. The recent work by Dahinden et al. (2017) [69] introduced a method to identify such analogs based on the normalized similarity of climatological seasonal mean values of temperature and precipitation between the projected climate for a site of interest and the present-day climate of a potential analog.

Here, a modified version of this technique is applied to identify climate analogs for individual sites in Switzerland. Modifications concern (1) the bootstrapped use of the standard deviation of seasonal mean values for the reference site in the period 1981 - 2010 instead of the standard deviation in a pre-industrial control climate, (2) the use of ensemble median projections instead of individual model projections, and (3) the application of a dissimilarity threshold of 4 instead of 2, implying a less strict exclusion of poor analogs (see Equations 1 and 2 in [69]). For this purpose, the localized scenarios of Chapter 5 (QM to stations), the ensemble-median projected climate for RCP8.5, and the late scenario period (2085) are used. As potential analogs, 2472 stations in Europe for which the present-day climate of the reference period 1981 - 2010 can be derived based on available daily observation data are considered (data sources: ECAD, GSOD, and the automated MeteoSwiss network).

Figure 10.1 presents the results in terms of combined temperature and precipitation analogs for the four sites of Zurich/Fluntern, Weissfluhjoch, Lugano, and Sion. For all stations except Weissfluhjoch, the best analogs are found at more southerly latitudes and are mostly located in the Mediterranean region.

Exceptions are the third- and fifth-ranked analogs for Zurich Fluntern, which are located on the coast of the Black Sea (Sochi and Tuapse, Russia). For the high-Alpine site of Weissfluhjoch, the climate analogs are found in the Alpine region itself, but are located at lower elevations.

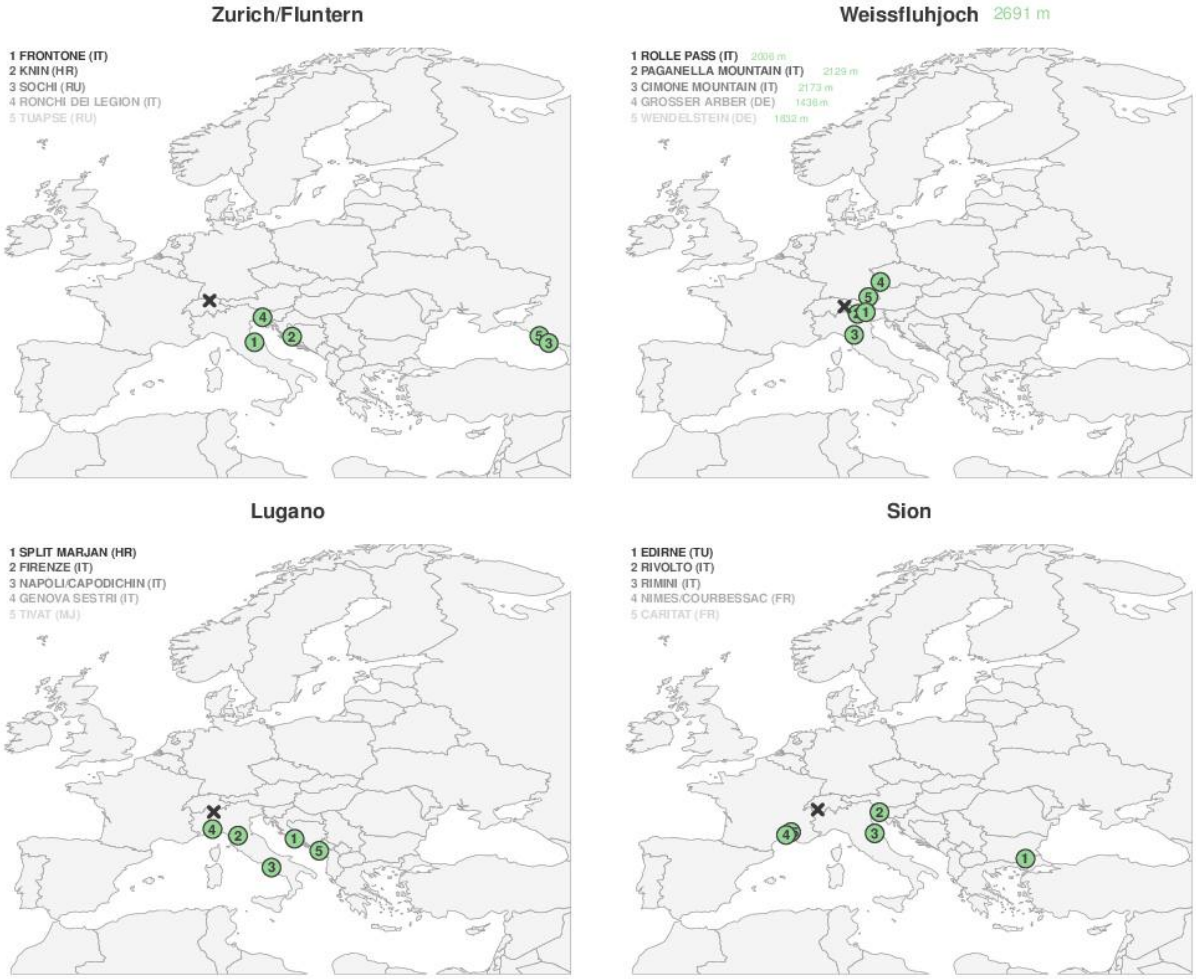

Figure 10.1. Combined temperature and precipitation climate analogs for the 2085 scenario period based on the ensemble median of all model chains for RCP8.5 and on the localized scenarios (QM to stations). Each panel presents the analogs for one of the four sites of Zurich/Fluntern, Weissfluhjoch, Lugano, and Sion (marked by a black cross). The names in the upper left part of each panel represent the five best analogs (top/black to bottom/grey indicating decreasing quality of the analogs in terms of their similarity to the projected climate for the respective site of interest). In addition, elevation information is provided for the site of Weissfluhjoch and its five analogs.

If projected future precipitation is disregarded and only temperature conditions are considered, the best climate analogs are typically found at even more southerly locations (Figure 10.2). For these analog stations, present-day temperature conditions are close to the projected climate at Swiss sites for RCP8.5 at the end of the century, but drier climates than projected for the Swiss sites typically prevail. This difference in precipitation is the reason why these sites are typically not among the combined temperature and precipitation analogs. For Zurich/Fluntern, the five best temperature analogs are located in the Spanish highlands and in Croatia on the Adriatic coast. The best analogs for Lugano and Sion are mostly found along the Mediterranean coastline. For Weissfluhjoch, again, geographically closer analogs that are located at lower elevations are found. An outstanding exception is the Russian site of Vajda-Guba, situated on a peninsula in the Barents Sea, which is the third-best temperature analog for Weissfluhjoch. This site is located at a much lower elevation compared to the other four analogs for Weissfluhjoch, but it has a similar temperature climate due to its northerly location.

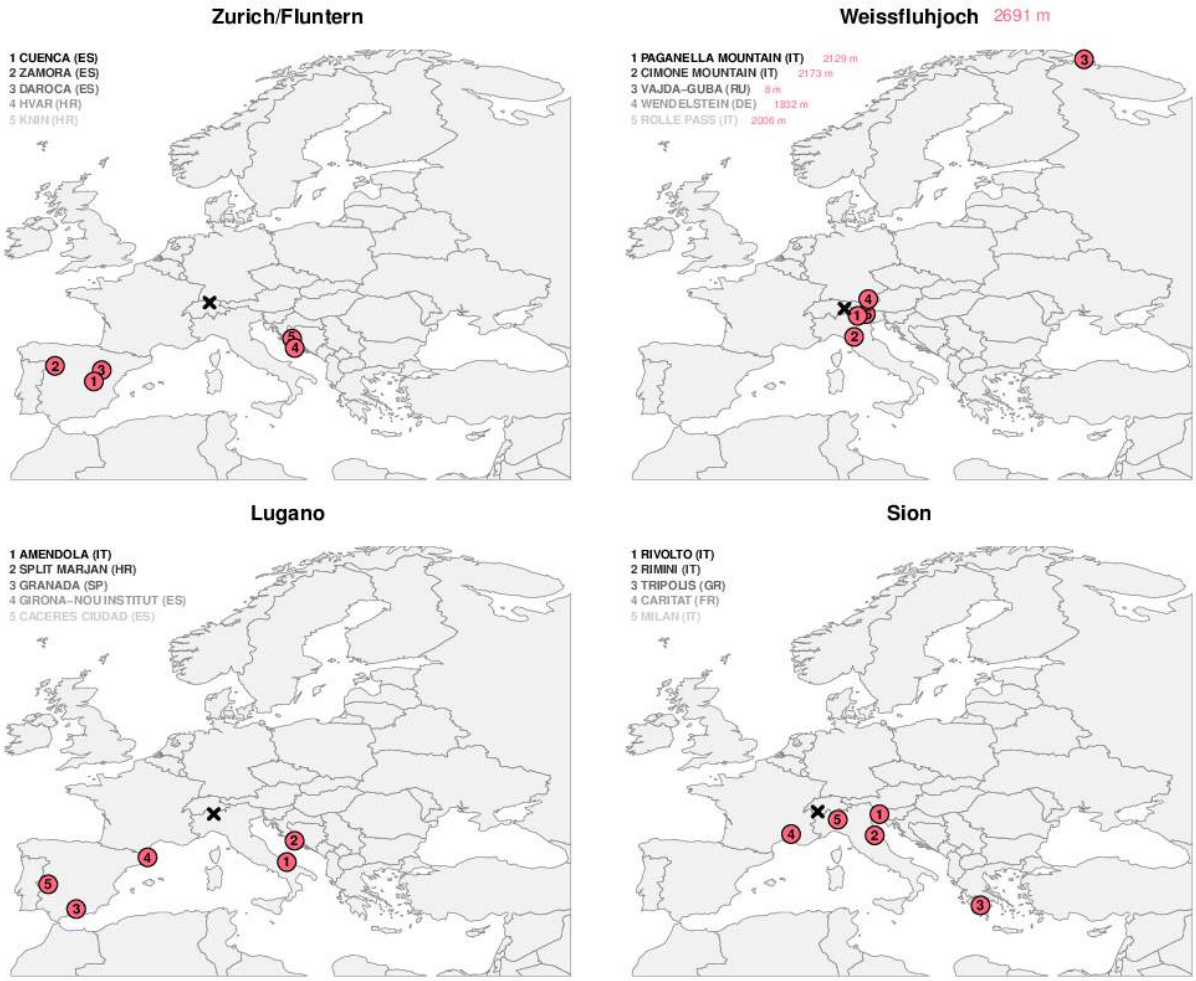

Figure 10.2. Temperature-only climate analogs for the 2085 scenario period based on the ensemble median of all model chains for RCP8.5 and on the localized scenarios (QM to stations). Each panel presents the analogs for one of the four sites of Zurich/Fluntern, Weissfluhjoch, Lugano, and Sion (marked by a black cross). The names in the upper left part of each panel represent the five best analogs (top/black to bottom/grey indicating decreasing quality of the analogs in terms of their similarity with the projected climate for the respective site of interest). In addition, elevation information is provided for the site of Weissfluhjoch and its five analogs.

It should be noted that these results provide an illustrative but only approximate picture of future climate change in Switzerland. Only seasonal mean values of temperature and precipitation are considered and, furthermore, only one similarity measure. Different variables and metrics might be more informative for specific applications. There are indeed limitations: Although temperature and precipitation may change to make a site's climate more similar to that of another, the amount of radiation or insolation (which depends crucially on latitude) will not. In addition, the final set of best analogs depends on the sample of all potential analogs considered (2471 sites in Europe in our case). Still, the results presented are considered to be useful for communicating the possible future of the Swiss climate in an illustrative manner.

10.2. Use cases in a hydrological context

Experience with the previous generation of Swiss Climate Scenarios, CH2011, has revealed a number of difficulties with the practical application of the data in research and adaptation, some of which could have been avoided through early interactions with users [287]. Below, two example applications of the CH2018 data products that have been produced in close collaboration between providers and users of the climate scenarios are presented. Both examples represent typical use cases in hydrology and illustrate the benefits and limitations of the new CH2018 scenario data. The station data of the DAILY-LOCAL dataset (Chapter 9) serves as the input of the impact models in both cases. The first example explores future changes in low-flow conditions for a typical Swiss catchment and sheds light on the benefit of continuous transient time series. This investigation is a contribution from the project "Hydro-CH2018", a sister project of CH2018 that

aims to produce hydrological scenarios for Switzerland, a further “focus area” of the National Center for Climate Services. The second example explores the benefit of incorporating additional variables beyond temperature and precipitation. Both examples show the applicability and the capabilities of the CH2018 data, but also reveal certain limitations still present that call for future scientific developments. One appealing technique for overcoming some of these limitations involves weather generators. In Switzerland, two types of weather generators developed in the context of hydrology are presented in (Chapter 10.2.3).

10.2.1. Transient projections of summer streamflow in the Thur basin

Background

The summer droughts of 2003 and 2015, and to a lesser extent 2011, are today regarded as extraordinary events for Switzerland that provide an indication of what might be normal by the mid-21st century (see [117]). Indeed, projections based on the CH2011 scenarios [56] revealed a strong intensification of hydrological droughts on the Swiss Plateau, especially for the second half of this century [115]. With the new CH2018 scenarios and their improved representation of changes in dry periods and updated summer temperatures and precipitation projections, an enhanced quality of summer streamflow projections is achievable. Furthermore, transient projections until the end of the century facilitate assessment of the direction of change, the variability of summer streamflow, and the speed of change under climate change conditions. This study presents a first glance at summer streamflow development for the Thur river.

The setting of the study

The hydrological model WaSiM-ETH Version 9.10 is applied to the Thur catchment. Calibrating the model against the observed discharge at Andelfingen (calibration period: 1991 - 1999) yields very good results, although a slight overestimation of low flow is inevitable. For details of the model validation, please refer to [288].

Because the bias-corrected CH2018 scenarios (see Chapter 5) provide the highest quality only for temperature and precipitation, here empirical, temperature-derived evapotranspiration estimates (Hamon equation) are used instead of complex evapotranspiration algorithms, which require the projection of less trustworthy meteorological variables (e.g., wind speed). It should be noted that this approach is still the subject of an ongoing discussion in the scientific community, as the Hamon equation is based on (past) empirical relationships that may not hold under future climate conditions. Here, input data quality is favored over the uncertain effect of empirical algorithms.

Data from various meteorological stations for temperature (4 stations) and precipitation (9 stations) within and around the catchment are used to interpolate the required spatial fields that drive the hydrological model for the reference period 1981 - 2010. Climate model data downscaled for the same stations but running from now until the end of the century (1981 - 2099) (see Chapter 5) are subsequently likewise interpolated. An interpolation technique that introduces as little artifact as possible is chosen. These long, transient time series of meteorological fields enable a transient simulation of hydrological responses. As each parameter at each station is bias-corrected independently, slight spatial inconsistencies can occur and likely affect the interpolated fields. The magnitude of this effect is unknown, but first tests suggest only marginal effects on the interpolated fields. Nevertheless, this issue must be considered when interpreting the results. To avoid arbitrary simulation results, all 9 ensemble members of the EUR-11 models under the RCP8.5 emission scenario are used (Table 4.1) rather than a selection of models. This approach captures climate model uncertainties and a wide range of the seasonal to decadal natural climate variability inherent in each model run. Summer streamflow is defined as the mean streamflow during July, August, and September. This selection is based on the current runoff regime type of the tributaries of the Thur that indicate a propensity for low flow especially during the late summer period.

Projected summer streamflow until the end of the century

Figure 10.3 depicts the mean summer streamflow for the measured discharge data (black), modeled discharge based on meteorological observations (red), and modeled discharge based on the downscaled 9 EUR-11 simulations (shaded areas; median: blue line). The hydrological model captures the range of summer streamflow values and broadly matches the observations. The overestimation of low flows found in the validation results thus does not affect the mean summer values. In contrast, the climate model data-driven simulations slightly underestimate (on average 3.4-6.0 $m^3 s^{-1}$ or -8 %) the summer streamflow (compared to the reference run). Note that differences between climate model data-driven hydrological simulations and the observation-based hydrological simulation for summer streamflow for an individual year should not be interpreted, as they result from different climate variabilities inherent in each model. Rather, only long-term climatological differences should be interpreted, either as a) biases, meaning the differences between climate model-driven simulations and the reference run, and the observations, respectively, or b) as a change signal – that is, the difference in streamflow between two time periods of the scenario run.

The summer streamflow values driven by the EUR-11 climate models reveal a median decrease of ~54 % from 42 $m^3 s^{-1}$ (reference period) to 19 $m^3 s^{-1}$ (2085) in the Thur catchment from the present day until the end of the century. This decrease is approximately linear, with considerable year-to-year variability and small decadal changes (Figure 10.3). The total ensemble spread (on average 52 $m^3 s^{-1}$) and the interquantile range (IQR, on average 22 $m^3 s^{-1}$) of these simulations are considerable yet quite stable over the entire simulation period. This reflects climate model uncertainty and natural climate variability.

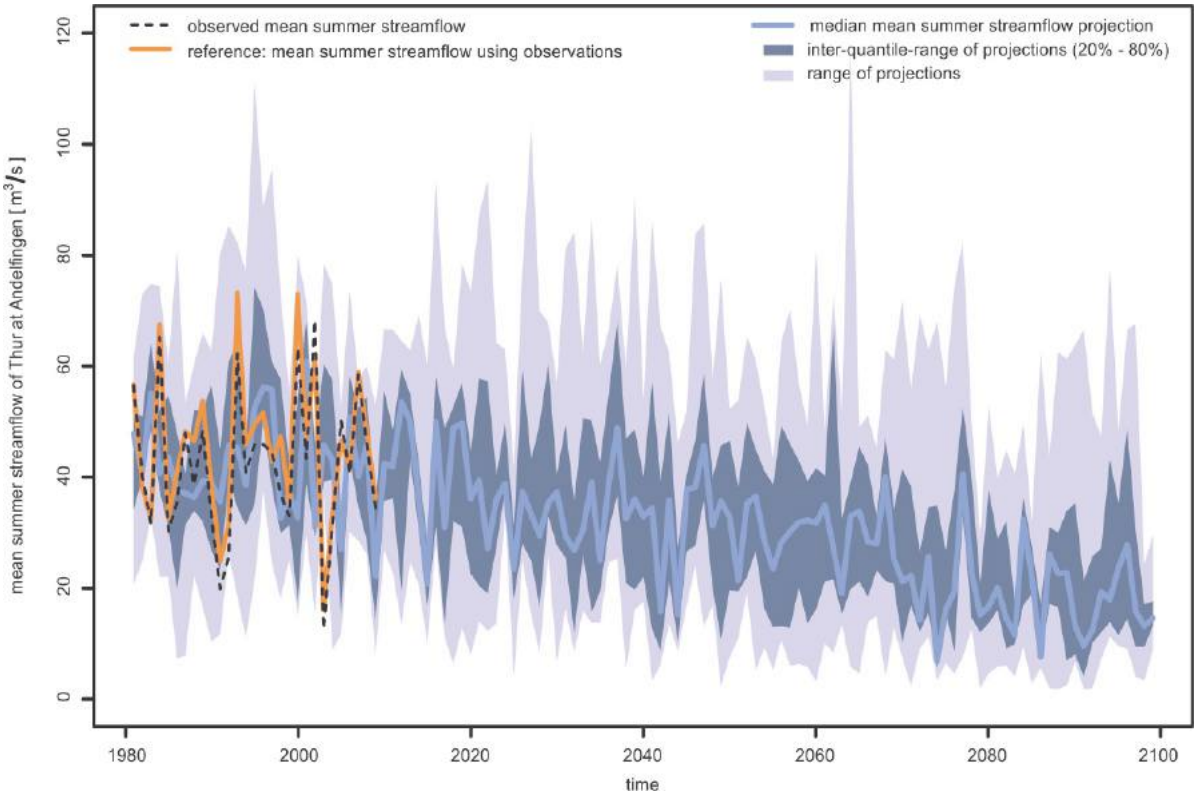

Figure 10.3. Summer streamflow in the Thur catchment for the period 1981 - 2100 represented by the ensemble median (blue line) with the interquantile range (blue shadings) and ensemble spread (purple shadings). The observed discharge (black line) and the simulated discharge driven by meteorological observations (red line) for the reference period 1981 - 2010 serve as benchmarks.

What is new?

The decline in the summer streamflow of the river Thur can likely be linked to a combination of decreased summer precipitation, enhanced evapotranspiration, and longer dry spells. In part, this decline was known from hydrologic scenarios based on CH2011 [115]. Unlike in the earlier study, an intensification of the

climate change signal after mid-century is not projected; rather, the results show a steady decline starting in the present day. The transient simulations provide users an indication of the magnitude of the change in summer streamflow, the development of the change rate, and especially the year-to-year variability. Whether this summer streamflow projection holds for other drought-related indices must be addressed in further studies. This applies, for example, to *Q347*, a politically important index of low-flow conditions used in the Swiss national water protection law (Art. 4, Swiss Water Protection Act). Such information is relevant to discussions regarding how often an official *Q347* value should be updated or which value should be used in future water concessions. A comprehensive application of the new climate scenarios to transiently project this and many other hydrological parameters under climate change conditions for Switzerland is being conducted within the Hydro-CH2018 initiative led by the Federal Office of the Environment.

10.2.2. The projected snow pack in the Alps toward the end of the century

Background

The snow pack in the Alps, as in any other mountain region, is a key component of the hydrologic cycle, storing water from the winter and releasing it in spring and early summer, when environmental and agricultural demands for water are usually greatest. The size of the snow pack can be expressed in snow water equivalent (SWE), which is the amount of water obtained from melting a sample of snow. SWE is expressed as the equivalent depth of water (mm w.e.) in that unit area. In most river basins in the Alps, snow is currently the largest component of water storage and is vulnerable to climate change due to its high temperature sensitivity. This study investigates how SWE develops with the projected changes in the main meteorological variables that determine the accumulation and ablation of the snow pack in the Alpine valley of Davos at roughly 1500 m a.s.l.

The setting of the study

The physical snow model SNOWPACK (version 3.41) and MeteoIO (version 2.6.1) were applied for pre-processing to calculate SWE [203, 18]. For the reference period (1981 - 2010), the following measured meteorological variables in hourly resolution were used: air temperature, precipitation, relative humidity, global radiation, and wind speed. Precipitation values have been corrected for under-catch in the case of sub-zero temperatures. Because SNOWPACK needs sub-daily values as input, the CH2018 scenarios (available only in daily resolution) could not be applied directly. For this reason, daily change values were calculated for each meteorological variable based on the difference or ratio between the daily values of the reference period and the scenario period. These delta values (i.e., one value per day) could then be used to perturb the measured meteorological variables in order to enable modeling of the SWE for the scenario period (2085) under the assumption of the RCP8.5 emissions. The annual cycle of these daily change values is based on bias-corrected seasonal scenarios at the station scale (see Chapter 5). The absolute mean annual cycles in both the calibration and scenario periods have been smoothed, taking the four seasonal means and interpolating them to 366 values with a spline-smoothing function. The change signal was applied on a daily basis: additive for temperature and wind and multiplicative for precipitation, relative humidity, and global radiation. Because CH2018 provides no information about longwave downward radiation, this important variable was parameterized with air temperature and relative humidity; as a result, longwave radiation is automatically enhanced in the scenario period due to the increasing air temperature and relative humidity. Three manually chosen climate model chains were used in order to demonstrate the possible variability originating from the choice of the climate model. The three model chains can be distinguished primarily by their low, medium, or high temperature response over the CHAE region.

Snow water equivalent at the end of the century

For the reference period, SNOWPACK is successfully able to model the annual SWE cycle (Figure 10.4). There is only a small overestimation in the accumulation period (November - mid-March) and a small underestimation in the ablation period (mid-March - April). The maximum SWE currently occurs in the middle of March, with values of about 260 mm. For the end of the century (2070 - 2099), the three climate model chains all show a clear change toward lower SWE values and a shorter period with snow on the

ground. The maximum SWE seems to occur only about a week earlier. However, there is a large spread between the climate model chain with the greatest temperature sensitivity and that with the smallest. The decrease in maximum SWE varies between 10 and 60 %, that of seasonal mean SWE (Nov – Apr) between 40 and 80 %, and that of the snow cover period between 1 and 2.5 months. A comparison between the lowest SWE projection (red curve) and the currently observed minimum values during snow-scarce winters (not shown) reveals that such a – nowadays extreme – SWE evolution might be normal toward the end of the century.

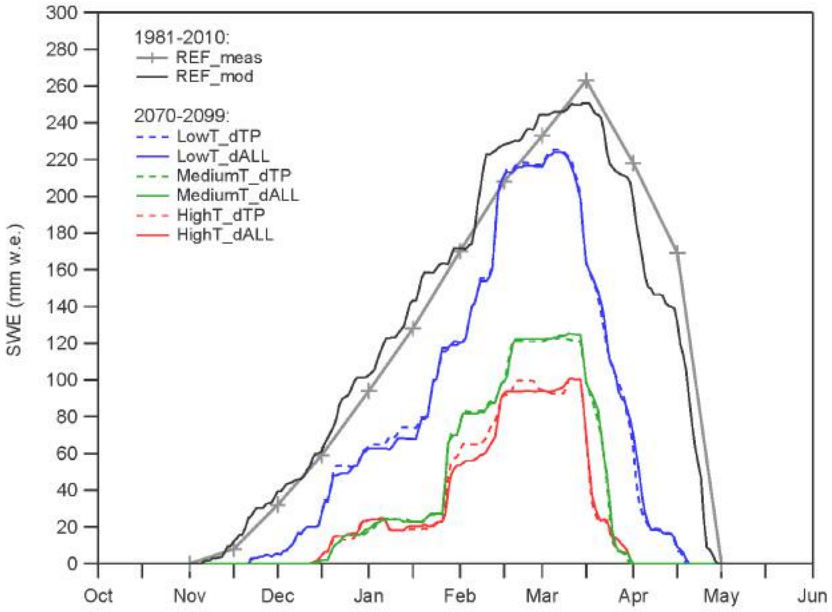

Figure 10.4. Mean SWE evolution for the 1981 - 2010 period (grey and black) and toward the end of the century in Davos at 1590 m a.s.l. for three climate model chains with differing temperature sensitivity. The low response is simulated by the ECEARTH-HIRHAM GCM-RCM model chain (blue), the medium response by IPSL-RCA (green), and the high response by HADGEM-CCLM5 (red). The dashed colored lines represent the future mean SWE evolution when only the projected temperature and precipitation changes are considered (dTP). The solid colored curves represent the future mean SWE evolution when the changes in global radiation, relative humidity, and wind speed (i.e., in all meteorological input variables) are also considered (dAll).

What is new?

The future decrease in SWE in the Alps due to climate change is not new and has thus far been explained by the dominating role of temperature, which determines whether snow or rain falls and how fast a snow pack melts. However, there was always the question of the impact of changes in relative humidity, global radiation, and/or wind speed. The CH2018 scenarios allow for the first time separate investigation of the impacts of changes in most of the major meteorological variables that are needed to force a physical snow model. The projected changes in these meteorological variables generally have the same sign (but different amplitude) for all three chosen climate model chains. With the exception of temperature, the spread among the different variables is relatively small – mainly due to the fact that the agreement between the various model chains is better in winter compared to summer.

The following changes in future SWE toward the end of the century are found for the RCP8.5 scenario when wind speed, global radiation, and relative humidity are modified individually for each of the three climate models (i.e., without changing temperature or precipitation). The projected changes for wind speed are very small and mostly negative. This implies that there are a few occasions with slightly less erosion and less snow melt, which increases the mean (Nov - Apr) SWE by about 8 %. The projected increase in precipitation is accompanied by a 5 - 10 % decrease in global radiation and a 1 - 5 % increase in relative humidity. This is physically meaningful in the sense that there are known processes that can explain these changes: Increasing precipitation may cause more cloudiness and more periods with high relative humidity values. On its own, the decrease in global radiation causes about a 13 % increase in SWE. Similarly, the increase in

relative humidity alone results in a 6 - 9 % increase in SWE. It can be concluded that the impacts of the projected changes in global radiation, relative humidity, and wind speed are positive, almost model-independent, and, assuming linearity, sum up to an increase in SWE of almost 30 %. However, these individual changes are not independent of one another, and because the projected increases in global radiation and relative humidity cause a strong increase in downward longwave radiation, the combined effect (i.e., when considering the changes in all meteorological input variables) is almost the same as when considering only air temperature and precipitation. This has the advantage that earlier simulations, which only considered changes in temperature and precipitation are not obsolete.

The question remains whether these results are also valid for lower and higher elevations, or whether there is an elevation dependence for certain variables due to physical processes that become more or less relevant at lower or higher elevations. Additionally, this case study demonstrates that sub-daily CH2018 scenarios would be preferable for impact models that need to consider the daily evolution of the meteorological variables.

10.2.3. Weather generators

Localized projections of climate variables derived using the quantile mapping method have a number of limitations (Chapter 5.7), including the misrepresentation of spatial climate variability on short timescales and the lack of ensured intervariable consistency. Both are key concerns for hydrological applications. The severity of these limitations, however, depends on the specific impact considered.

Weather generators are promising tools in efforts to overcome some of these limitations. Weather generators are essentially statistical models to mimic the observed record. Once calibrated for a given location, they can generate an arbitrary number of synthetic time series of current weather that are all consistent with observations [142, 186, 383]. This ensemble of stochastically generated time series then allows researchers to investigate natural variability at the local scale. For the use of weather generators as a downscaling tool, the calibrated parameters of the generator are perturbed with changes derived from climate models. In this way, changes in the temporal correlation structure (e.g., alterations in the dry-wet sequences) can be incorporated. A further advantage of weather generators is their physical consistency between several variables, achieved by conditioning dependent atmospheric variables on the dry/wet state of a given day. In Switzerland, two different kinds of weather generators with differing levels of complexity have been developed over recent years to serve the hydrological community.

A weather generator for use as a downscaling model was recently developed in Switzerland [181] to address specific scientific questions such as the comparison of stochastic uncertainty with other sources of uncertainty. To serve a broad segment of the impact community, the degree of complexity and associated calibration requirements of this weather generator was purposely kept low. The generator consists of several Richardson-type weather generators calibrated at several stations. The time series are generated in such a way that the spatial correlation structure of observations (and hence the spatial amount of precipitation over a catchment) is preserved [382]. The precipitation model was extended by conditioning daily temperature on the generated precipitation state. The weather generator has been extensively validated [181] and took part in the validation experiments of the COST VALUE initiative (http://www.value-cost.eu). A key advantage of the Keller et al. weather generator is the incorporation of the spatial correlation structure of daily precipitation (Figure 10.5). It performs well for mean conditions and moderate indices. Limitations include a somewhat weaker performance for extreme value statistics and an underestimation of interannual variability. In Keller et al. (2017) [182], the weather generator was tested in a climate change context and applied to a hydrological model for an intercomparison of different downscaling methods [288].

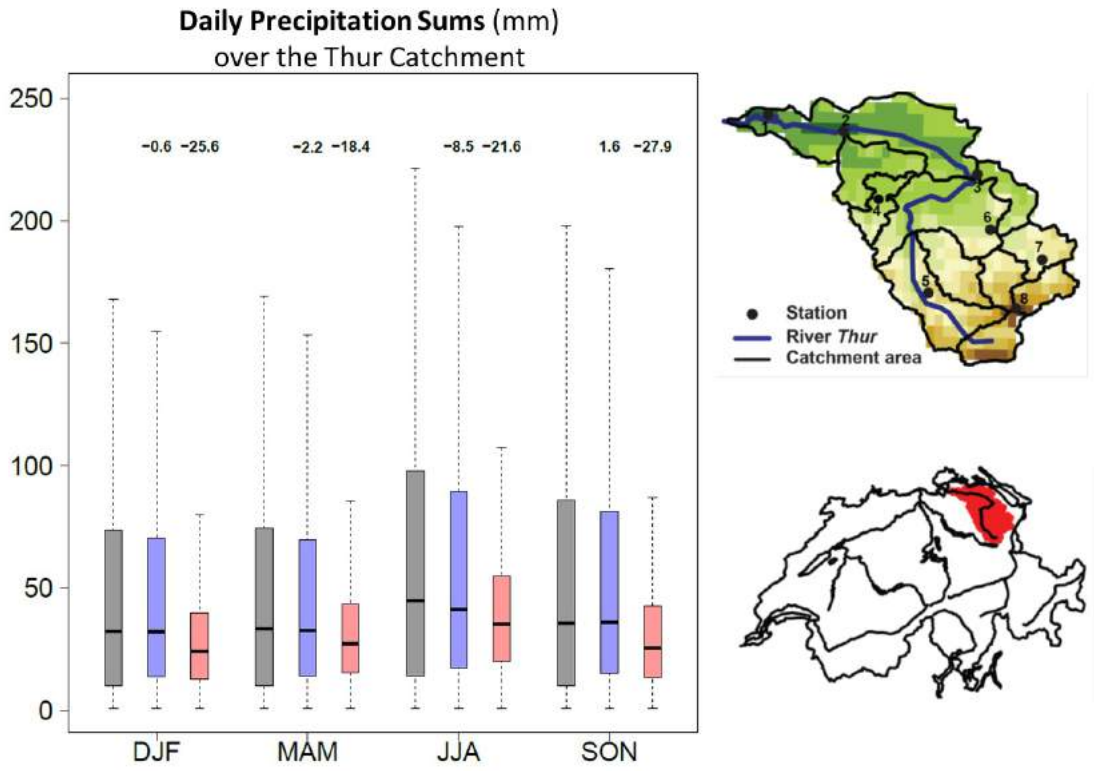

Figure 10.5. Daily non-zero precipitation sums over the catchment for the four seasons during the period 1961 - 2011. The daily precipitation intensity of the eight stations is summed, and days with an area sum of zero are excluded. Box plots of observed daily sums (grey), simulated time series accounting for the spatial structure (blue), and uncorrelated time series in space (red) are shown. The weather generator was run 100 times over a 51-year time period. The numbers (in percentage) above the blue and red boxes represent the relative deviation of the simulated median from the observed median. Figure from [181].

A need often expressed by climate change impact researchers is that for sub-daily input data on several physically consistent variables. The weather generator of Keller et al. (2015) [181] is not designed for such applications, and hence more complex tools are required.

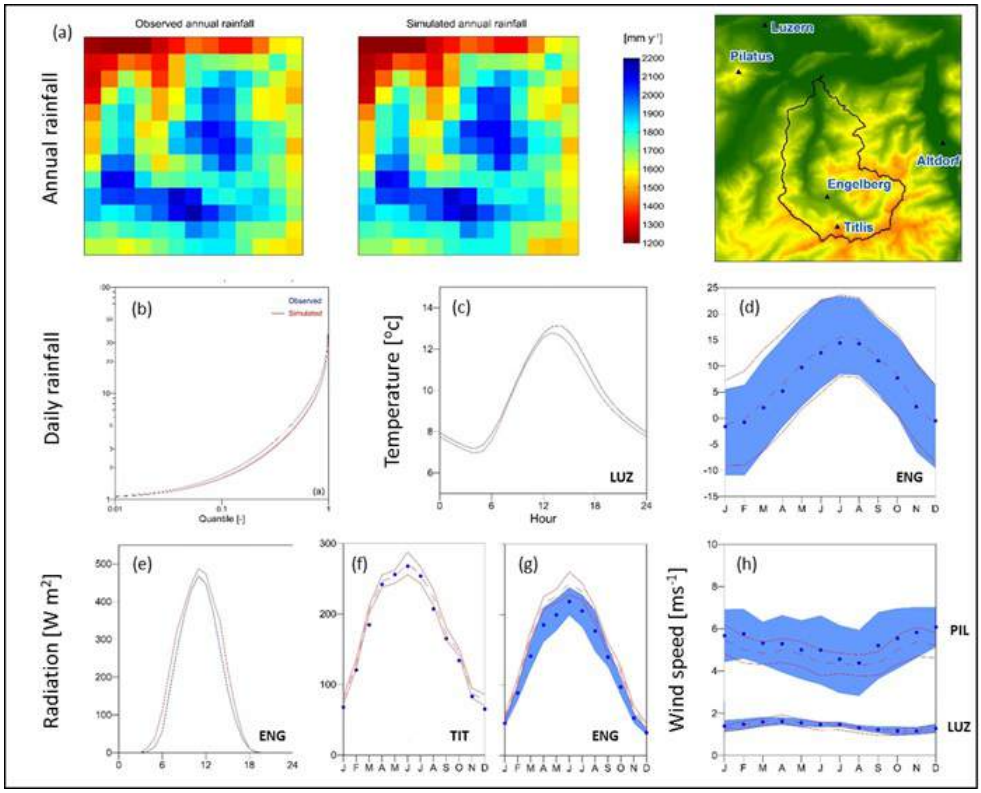

Figure 10.6. Example of present climate representation (1981 - 2012) by AWE-GEN-2d for the Engelberg area. (a) Median observed annual rainfall and mean of the median of the simulated ensemble; (b) inverse cumulative distribution function of the daily rain intensity over a given 2 x 2 km^2 grid cell; (c) observed and simulated average daily cycle of near-surface (2 m) air temperature for Luzern station; (d) observed and simulated near-surface (2 m) air temperature for each month for Engelberg station (blue dots and red dashed lines represent observed and simulated median values, respectively, and bounded blue and red areas represent observed and simulated 5 - 95 % quantile range, respectively); (e) observed and simulated average daily cycle of incoming shortwave radiation for Engelberg station; (f) and (g) observed and simulated incoming shortwave radiation for each month for Titlis and Engelberg stations, respectively; and (h) observed and simulated near-surface wind speed, considering terrain effects, for each month for Pilatus and Luzern stations. The climate ensemble was generated using 50 realizations of 30 years each (figures from [256]). The same datasets were used for the calibration and validation of the model.

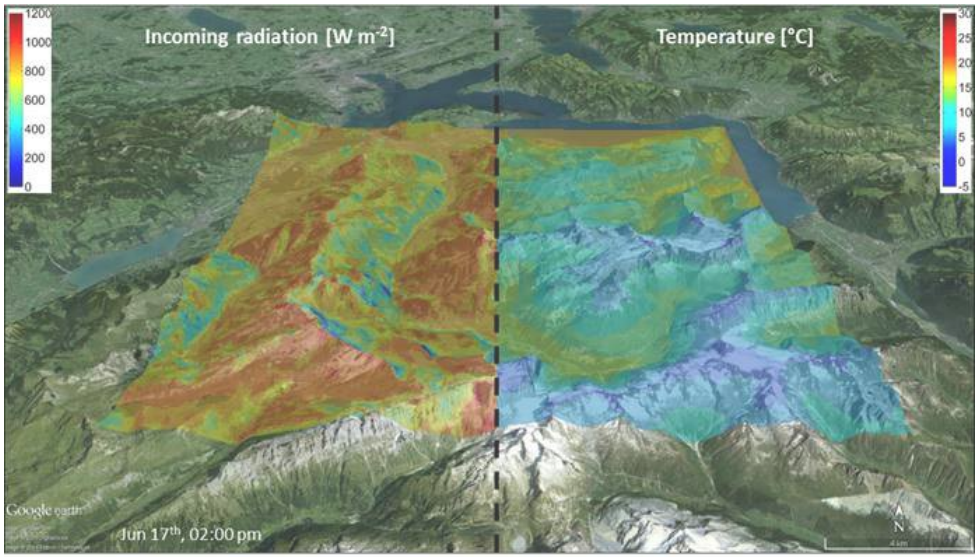

Figure 10.7. Example of a high-resolution simulation with AWE-GEN-2d. Incoming shortwave radiation (left) and temperature (right) are simulated for a spatial resolution of 100 x 100 m^2 and a temporal resolution of 1 h.

One such more complex tool is the new stochastic Advanced WEather GENerator for a 2-dimensional grid (AWE-GEN-2d), which was recently presented by Peleg et al. (2017) [256]. In fact, it is a substantial evolution and combination of four preceding models: (i) AWE-GEN (Advanced WEather GENerator [176, 93]), (ii) STREAP (Space-Time REalizations of Areal Precipitation [255]), (iii) HiReS-WG (High-Resolution Synoptically conditioned Weather Generator [257]), and (iv) WINDS model [44]. AWE-GEN-2d combines physical and stochastic approaches to simulate key climate variables (e.g., precipitation, cloud cover, near-surface air temperature, solar radiation, vapor pressure, atmospheric pressure, and near-surface wind) at high spatial and temporal resolution. The use of combined stochastic-physical methods makes it possible for researchers to account for the dependence between meteorological variables and to simulate them at sub-daily temporal scales; this typically exceeds the capabilities of empirical-statistical weather generators because the statistical correlations at sub-daily scales are complex to model. AWE-GEN-2d is used to simulate the impact of future climate scenarios and their variability on hydrological scenarios in Switzerland as part of the Hydro-CH2018 initiative.

AWE-GEN-2d requires spatially distributed data for calibration. These include time series from ground stations, gridded data from remote sensing, and areal averaged data from reanalysis products. The resolution of the calibration data determines the resolution of the simulated fields (e.g., 2 km x 2 km and 5 min for precipitation when using the MeteoSwiss weather radar composite, and 100 m x 100 m and 1 h for other climate variables when using hourly data from ground stations).

AWE-GEN-2d is parsimonious in terms of computational demand and is therefore particularly suitable for studies in which exploring internal climatic variability at multiple spatial and temporal scales is fundamental. The model is suitable for studying the impacts of stochastic climate variability, spatial heterogeneity, and temporal and spatial resolutions of climate forcing, as well as for climate downscaling. In this respect, the model can also be conveniently used in the context of climate change by modifying the model parameters using climate data derived from dynamical climate models. For Hydro-CH2018, the model is re-parameterized to be consistent with the projections of the present report. The re-parameterization of the sub-daily climate variable is achieved by scaling the parameters of the climate models from daily to hourly resolution. The use of AWE-GEN-2d as a stochastic downscaling technique can allow the investigation of the role of natural variability in future climate scenarios (e.g., [94]). This enables an explicit quantification of the uncertainty associated with the natural variability of climate, which cannot be explored either by direct use of climate model scenarios or by any other common downscaling techniques. However, although the model can reproduce the variability related to the chaotic nature of climate (i.e., for stationary climate), it cannot reproduce multi-decadal variability when this is associated with deterministic non-stationary processes such as changes in ocean circulation, changes in atmospheric circulation, volcanic activity, changes in carbon dioxide concentration, solar cycle variability, or poor sampling of low-frequency periodic processes.

Applications of the model include modeling of environmental systems in which high spatial and temporal resolution of meteorological forcing is crucial for the correct simulation of hydrological, ecological, agricultural, and geomorphological processes. Due to its convenient re-parameterization for the future climate, it can also be efficiently used in climate impact and adaptation studies at the river-basin scale.

The weather generator was calibrated and validated for the Engelberg region, an area with complex topography in the Swiss Alps (see [256]). Model tests show that the climate variables are generated by AWE-GEN-2d with a level of accuracy sufficient for most practical applications. Examples of the model's high-resolution outputs and performance are given in Figure 10.6. Further details can be found at: http://www.hyd.ifu.ethz.ch/forschung/models/awe-gen-2d.html.

10.3. Stakeholder dialog

ETH Zurich, MeteoSwiss, and the University of Bern have been preparing and running model simulations to provide new climate scenarios to Swiss citizens in general and to the Swiss adaptation and mitigation community and climate-impact modellers more specifically. Feedback from the European climate scenarios community was gathered at an early stage in a two-day workshop. This was complemented by an external study on users' needs [230]. This study highlighted the fact that only approximately half of the respondents (all of whom had a professional interest in climate change) had made use of CH2018's predecessor, CH2011 [56]. When asked about specific variables, actual use dropped to about a quarter of respondents [230 p. 36]. Depending on the variable, another quarter to a third of respondents had skimmed the brochure or the variables (ibid.). The study also revealed that the use of the summary was equally high for scientists and practitioners, whereas the background report was used predominantly by the scientists [230 p. 37]. In order to meet producers' (and users') expectations, the study concluded with five recommendations for CH2018: namely, to i) address a more diverse set of users, ii) allocate more resources for dissemination, iii) provide personal advice, iv) incorporate information on the impacts of climate change, and v) provide an online platform to access the raw data [230].

Since 2017, a stakeholder dialog has been running alongside the development of the climate scenarios. This dialog has brought together scientists and both public and private organizations that anticipate or experience impacts of climate change. Taking on board the recommendations of the report on users' needs [230], the CH2018 stakeholder dialog enables the exchange of experiences among stakeholders and between stakeholders and climate scientists. The structure and process of the stakeholder dialog are based on the experiences of other countries producing climate scenarios, as well as on the CH2018 predecessor CH2011 [325]. It is also inspired by the experiences of the authors with similar processes in the context of climate adaptation studies [328].

However, because the modeling activities had proceeded beyond a stage at which larger stakeholder requests could be incorporated, the influence of the stakeholder dialog on modeling decisions was restricted to the recommendations of the MeteoSwiss (2016) report [230]. Consequently, in the dialogs, emphasis was placed on questions regarding presentation, delivery, support, and additional products. To a great extent, the stakeholder dialog thus focuses on enhancing understanding and improving the decision-making context of individual users in relation to climate change. Hence, the stakeholder dialogs represent an important contribution in transforming the scenarios from "pure" climate information into a climate service. As a forum for discussion and reflection, the stakeholder dialogs should ideally be able to improve understanding also among the stakeholders as to where climate-critical thresholds and decision-restraining factors are located in their activities. Thus, the dialog itself can be seen as a climate service as well.

The stakeholder dialog has three phases. In phase one, a pilot project with exploratory interviews and discussions with a subset of stakeholders was completed in early Summer 2017. The goal was to discuss the current use of climate information and services, as well as to solicit feedback on a draft process of the stakeholder dialog. In this pilot phase, the dialog team met with six individual organizations including federal and cantonal administrations, an industry association, a non-governmental organization, and a private infrastructure utility. The pilot phase with exploratory interviews represents the innermost circle in Figure 10.8.

Based on the insight derived from phase one to focus more on the use of a particular variable rather than on many, phase two revolves around urban heat. The reasons for selecting this issue include high scientific confidence as well as its links to many sectors through urban adaptation. In phase two, "pull-style dialogs" with key stakeholders began in Spring 2018. The selection of these "key" stakeholders was based on the Swiss Federal Council's adaptation strategy [114], which identifies "the greatest challenges in adapting to climate change in Switzerland" according to the vulnerabilities of sectors to key climatic changes [114 p. 8]. For example, some of the challenges the energy sector faces are related to "greater heat stress in

agglomerations and cities" (ibid.). The stakeholder selection process sought to encompass a number of relevant challenges and sectors, as well as to include a heterogeneous sample of organization forms, ranging from federal and cantonal administrations to the private sector, industry associations, and NGOs. To ensure that key stakeholders were involved in the dialogs, active efforts by the team to ensure their inclusion were made – the "pull-style" method. Additionally, various other relevant organizations have been notified of the ongoing dialogs and invited to join on a voluntary basis. This approach is referred to as the "push-style" (see Figure 10.8).

In phase three, a quantitative survey of stakeholders including questions on their usage of and needs regarding climate services was sent out in the first half of 2018. These stakeholders are located in the outer circle of the CH2018 stakeholder dialog (Figure 10.8). About 500 organizations, mainly organized interest groups from the private sector and NGOs, as well as municipal, cantonal, and federal administration officials, were targeted as recipients of the survey. Other activities, such as workshops and training sessions, were held in close consultation with the stakeholders in phase two. At the time of this report's publication, the evaluation of the collected data from the CH2018 stakeholder dialog is still ongoing.

Although the CH2018 project ends in Autumn 2018, the established interactions and dialogs should be continued and possibly institutionalized. The National Centre for Climate Services (NCCS) is committed to ensuring that climate information and climate services will be used by the federal, cantonal, and municipal administrations, as well as by civil-society groups and private-sector unions and associations. In the long term, the NCCS will be the knowledge broker for enquiries on climate services and will engage in various networking activities to ensure the inclusion of stakeholders.

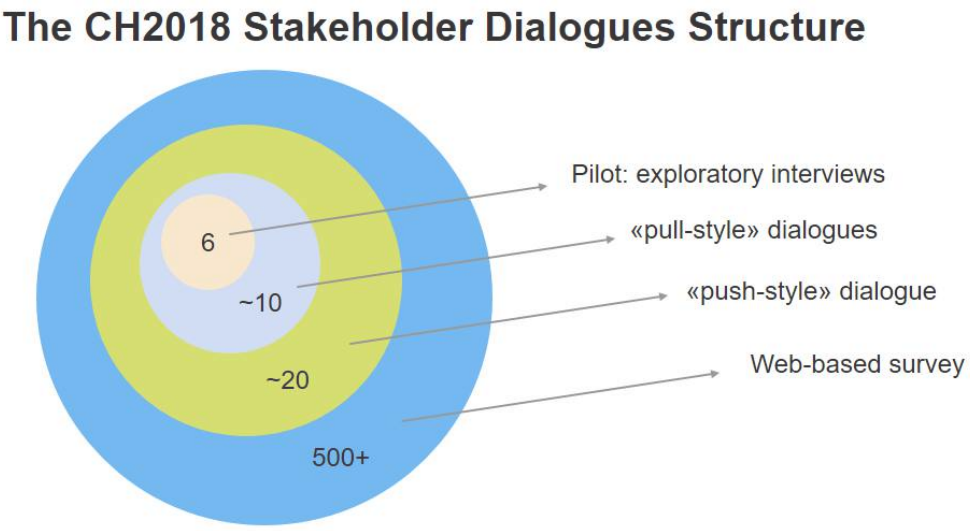

Figure 10.8. Schematic depiction of the CH2018 Stakeholder Dialogs. Inner circle: In phase one, the dialog process and structure was tested through exploratory interviews with six organizations. Inner-middle circle: Based on the Swiss adaptation strategy [114], active efforts to include approximately 10 key stakeholders in the dialogs were made in a "pull-style" fashion to ensure their participation in the process. Outer-middle circle: An additional set of stakeholders was informed about the process using a "push-style" method. The initiative to join the dialog remains with the respective organizations. Outer circle: A larger set of organizations, ranging from Swiss municipalities to organized sector interest groups, were asked about their use of climate information through a web-based survey.

10.4. Best practices for scenario selection

The CH2018 projections consist of a complex set of data. The 30-year averaged model data and indices listed in Table 9.3 and presented in chapters 4 to 6 vary along three different dimensions: time periods, RCPs, and climate-uncertainty quantiles. The CH2018 projections can thus be illustrated by a "scenario cube" [57] (Figure 10.9). The scenario cube represents the full complexity of the climate simulations in aggregated form. When working with the aggregated CH2018 datasets, considering the entire cube ensures that all information contained in the projections will be used. However, this is not always possible due to limited resources, nor is it always necessary in order to extract the information of interest.

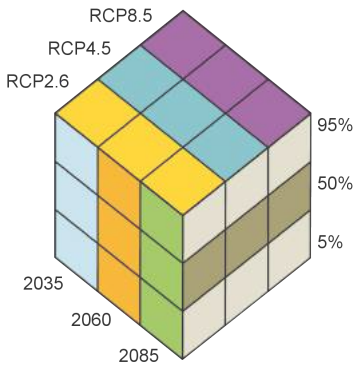

Figure 10.9. Scenario cube illustrating the possible combinations of time period, forcing scenario, and climate uncertainty inherent in the CH2018 projections (after [57]).

Because the climate projections are based on somewhat arbitrarily selected emission scenarios or RCPs, best practice does not necessarily require the consideration of all possible combinations covered by the scenario cube. In the context of adaptation to climate change, it is not crucial where the uncertainty originates (anthropogenic forcing or climate uncertainty). Rather, the relevant information concerns the full range of possible future outcomes from the lower end of the RCP2.6 mitigation scenario projection to the upper end of the RCP8.5 high-emission scenario projection. The statement, for example, that "global surface temperature change by the end of the 21st century is unlikely to exceed 2 °C for RCP2.6" [169] is not very informative for adapting to climate change, since the non-mitigation scenarios must be considered as a possible future outcome as well. In an adaptation context, it therefore makes sense to define an "adaptation scenario" – a climate change scenario defined in much the same way as the RCPs, i.e., by the conscious selection of a meaningful and consistent set of outcomes within the projected ranges. For example, a scenario for risk-adverse adaptation could be defined by taking the upper end of the projected summer temperature range for RCP8.5, i.e., the highest of the values displayed in Figure 4.4 in each region (this corresponds to choosing one element of the scenario cube). Because the projected ranges represent the statistics of the whole climate model ensemble available, this selection is robust. A similar approach was used to define the "Starker Klimawandel" (strong climate change) scenario in the Swiss Federal Council's strategy for climate change adaptation [116].

The difficulty with defining a climate change scenario in this way is that a strong change in summer temperature does not imply a similarly strong change in winter temperature, nor a similarly strong change in other seasons, or in variables other than temperature (Figure 10.10). In other words, the projections assessed for a given variable, index, or season are not necessarily correlated. For example, although the simulations with strong summer drying highlighted in Figure 10.10 exhibit a pronounced winter wetting, the correlation between summer and winter precipitation is not generally very high.

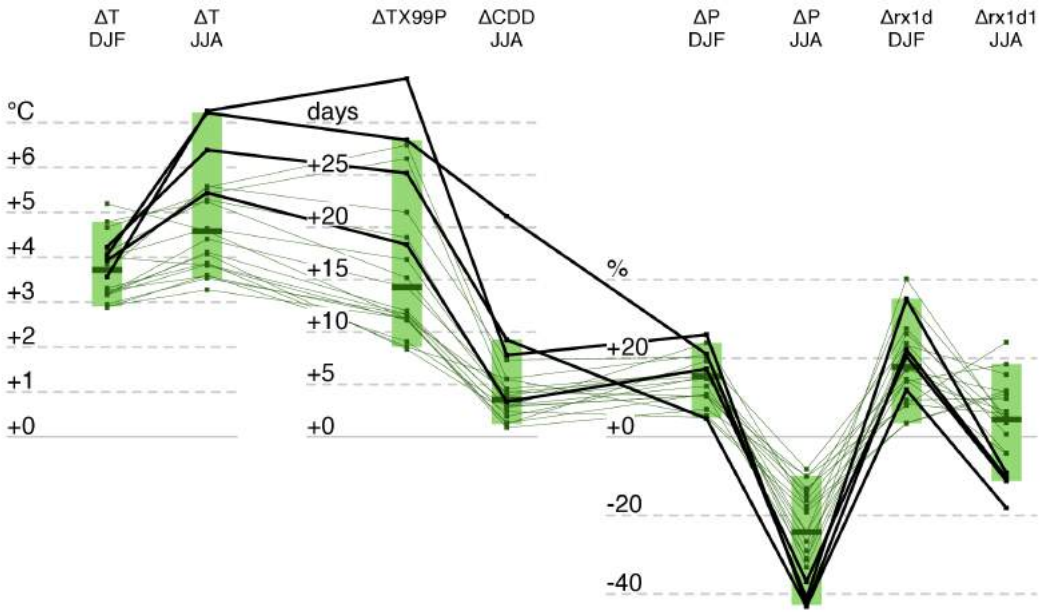

Figure 10.10. CH2018 projection ranges for different variables/indices and seasons (DJF/JJA) for the region CHW and RCP8.5 at the end of the century, including changes in seasonal mean temperature (ΔT), very hot days (ΔTX99P), consecutive dry days (ΔCDD), seasonal mean precipitation (ΔP), and mean seasonal 1-day precipitation maximum (Δrx1d). Fine lines correspond to individual simulations connected across the different changes (circles in Table 4.1). Bold lines indicate the simulations showing the strongest summer drying (ΔP JJA). The data corresponds to the SEASONAL-REGIONAL and INDEX-REGIONAL datasets (Chapter 9).

Without further investigation, a climate change scenario can therefore only be defined for one variable, region, and season in order to avoid physically improbable combinations that are not supported by the underlying simulations. This might be enough to assess some climate impacts that essentially depend on a single climate variable. However, impacts may result from the interplay between different variables or from the interaction across different seasons of the year, calling for multivariate, multi-seasonal scenarios. These scenarios should be plausible combinations of different variables (as well as plausible combinations across different seasons or regions), i.e., they should be consistent. To derive a consistent climate change scenario, one must look for underlying climate simulations that simulate the day-to-day variation in different climatic variables in a physically consistent manner. For the example of summer temperature change, the climate simulations often exhibit a strong summer warming in combination with a strong reduction in summer precipitation (Figure 10.10). This would justify the definition of a “strong climate change” scenario as a combination of upper-end temperature change and lower-end precipitation change, as it was indeed defined in the aforementioned adaptation strategy [116]. With the addition of other variables and indices, the definition of a scenario becomes more complex, as there may be both strongly correlated and largely uncorrelated parameters. This means that there is no single physically consistent scenario for “strong climate change”. This can also be seen from Figure 10.10. To reduce complexity, four different possible manifestations of “strong climate change” in Switzerland have been summarized using four alternative climate change scenarios. The CH2018 climate scenarios focus on qualitatively diverse changes:

1. *Dry summers*: decrease in summer precipitation and increase in summer temperature and in the maximum number of *consecutive dry days* (*CDD*)
2. *More hot days*: increase in the temperature of the *hottest day of the year* (*TXx*) and in the number of *very hot days* (*TX99P*).
3. *Heavy precipitation*: increase in frequency and intensity of rare (*rx1d*) to extreme (*x1d100*) precipitation events

4. *Snow-scarce winters*: reduction in snow cover and frequency of snowfall and rise of zero-degree line due to rising winter temperature

Each of these scenarios is designed to represent the scope of possible changes that could plausibly occur within the range of projections in CH2018, assuming no mitigation of climate change. Accordingly, the scenarios are generally defined by the "likely range" of the projections (Chapter 4.7.4) for RCP8.5 and period 2060 (see Table 13.1). The exception to this rule is the scenario *heavy precipitation*, which is defined by the central projected values (the multi-model-median). This is because the projected range is strongly influenced by statistical uncertainty (as opposed to climate model uncertainty). For scenarios 1, 2, and 4, the median over the five CH2018 regions is used as a representative value for Switzerland as a whole. For scenario 3, the maximum change over the five CH2018 regions is taken.

Each of the four scenarios, however, only combines those changes that coexist in a subset of the CH2018 ensemble. For example, the simulations with pronounced dryness in summer (scenario 1) are not the same as those with a strong increase in heavy precipitation in winter (scenario 3). It should be noted that these scenarios represent the changes that can result from a superposition of both forced change and natural variation (Chapter 7), since the distinction between the two is irrelevant for the purposes of adaptation.

Complementing the four scenarios of "strong climate change", one scenario for "weak climate change" has been defined: *When climate mitigation takes hold*. This scenario describes the four manifestations of climate change (scenarios 1 - 4) in the case of an ambitious mitigation path compliant with the 2 °C target (Chapter 2.2, Table 13.3).

In summary, the CH2018 climate scenarios depict the range of possible climatic changes in Switzerland. This range encompasses the scope of climate mitigation from a coordinated worldwide effort exhausting all mitigation options to a complete failure to mitigate, as well as the scientific uncertainty of climate simulation (Chapter 2.7).

The climate change scenarios outlined above show that "strong climate change" or "weak climate change" can mean different things, and different impacts will stand out in each scenario. Thus, in order to select the correct scenario for the study of a certain type of impact, a good understanding of its causes is necessary. First, a quantitative knowledge of the main climatic phenomena causing various impacts is required; these may be appropriately captured by model variables or derived indices, depending on the level of detail of the impact analysis. Second, the sensitivity of the impact system must be known (e.g., in the form of an impact model, impact response surfaces, etc.). The sensitivity of the impact system is often derived by studying climatic impacts under current or past climate conditions. This analysis should also reveal which part of the projected range of climatic changes is of interest (median, extreme case, lower quantile, etc.). Finally, the formulation of the impact model used determines whether individual simulations are needed or whether the statistics of the model ensemble (i.e., quantiles) provided by the CH2018 projections are sufficient for an impact analysis (e.g., the 95 % quantile of summer temperature increase).

Applications in research on the impacts of climate change typically require coherent time series of several variables and high temporal and spatial resolution. This calls for the use of individual simulations, which are available for the model variables listed in Table 9.2. As discussed above, physical consistency is essentially ensured in this case (except that quantile mapping can potentially destroy some of the multivariate structure). However, by selecting just a few individual simulations, one loses information on robustness (e.g., the simulation with the largest temperature increase is not necessarily the one with the strongest summer drying). In other words, the selected simulations do not cover the entire scenario cube. For a robust impact assessment, however, one should retain as much spread as possible in the parameters to which impacts are sensitive (e.g., changes in winter temperature and summer precipitation). A ranking of individual simulations can be useful as a basis for selecting a small simulation set that meets this requirement. Table 10.1 shows a simulation ranking for six climatic parameters selected from the CH2018

projections.

GCM	init	RCM	DJF ΔT (°C)	JJA ΔT (°C)	ΔTX99P (days)	JJA ΔCDD (days)	DJF ΔP (%)	JJA ΔP (%)	DJF Δrx1d (%)	JJA Δrx1d1 (%)
ICHEC-EC-EARTH	r1i1p1	KNMI-RACMO22E	3.2	4.1	8.4	2.4	4.9	-19	3.5	11
	r3i1p1	DMI-HIRHAM5	2.9	3.3	11	1.3	11	-10	8.0	24
	r12i1p1	CLMcom-CCLM4-8-17	3.2	4.4	14	4.6	16	-29	26	4.4
		CLMcom-CCLM5-0-6	3.2	3.8	12	3.0	13	-24	35	4.9
		SMHI-RCA4	4.1	5.3	19	2.8	11	-31	22	-11
MOHC-HadGEM2-ES	r1i1p1	CLMcom-CCLM4-8-17	4.0	7.2	28	21	21	-41	35	-9.2
		CLMcom-CCLM5-0-6	3.7	5.6	21	7.4	20	-31	40	3.6
		ICTP-RegCM4-3	3.8	5.6	28	5.5	5.4	-18	9.4	9.7
		KNMI-RACMO22E	4.8	5.2	15	3.6	15	-15	28	0.70
		SMHI-RCA4	4.7	5.4	27	4.3	10	-14	17	11
MPI-M-MPI-ESM-LR	r1i1p1	CLMcom-CCLM4-8-17	3.3	3.9	8.6	5.5	21	-33	24	-4.1
		CLMcom-CCLM5-0-6	3.3	3.6	11	4.2	16	-27	14	-4.3
		SMHI-RCA4	4.0	4.6	17	3.9	17	-24	18	4.1
	r2i1p1	MPI-CSC-REMO2009	2.9	3.6	9.1	2.8	24	-18	3.5	12
MIROC-MIROC5	r1i1p1	CLMcom-CCLM5-0-6	4.0	3.8	11	1.2	19	-8.2	23	16
		SMHI-RCA4	5.2	4.6	11	0.89	7.0	-10.0	15	6.5
CCCma-CanESM2	r1i1p1	SMHI-RCA4	3.6	7.3	34	7.8	26	-43	22	-10
CSIRO-QCCCE-CSIRO-Mk3-6-0	r1i1p1	SMHI-RCA4	4.2	6.4	25	9.3	4.6	-43	12	-18
IPSL-IPSL-CM5A-MR	r1i1p1	SMHI-RCA4	3.9	5.4	18	3.4	17	-37	20	-11
NCC-NorESM1-M	r1i1p1	SMHI-RCA4	3.2	4.1	12	2.9	11	-16	14	18
NOAA-GFDL-GFDL-ESM2M	r1i1p1	SMHI-RCA4	3.0	3.5	12	1.9	15	-13	8.3	5.9

Table 10.1. Ranking of individual simulations underlying the CH2018 projections (multi-model set indicated by circles in Table 4.1) according to different variables/indices for different seasons (DJF/JJA) for the region CHW and RCP8.5 at the end of the century. Shown are changes in seasonal mean temperature (ΔT), very hot days (ΔTX99P), consecutive dry days (ΔCDD), seasonal mean precipitation (ΔP), and mean seasonal 1-day precipitation maximum (Δrx1d). For each parameter, the colored areas indicate the four highest values (pink), lowest values (yellow), and values closest to the median (grey). Note that this ranking depends on the region considered and does not generally apply to the localized datasets derived by quantile mapping.

11. Final remarks and outlook

A comprehensive and quantitative overview of the results for past and future trends and variability is given in the Executive Summary. In this chapter, we offer some final remarks focusing on new aspects covered in the CH2018 assessment. We also provide an outlook over some developments that can be expected for the next round of the Swiss national climate scenario assessment.

11.1. Final remarks

The CH2018 report is the final outcome of the Swiss national climate scenario assessment, which is based on the IPCC framework for the global and continental scales and translates information to the local scale. It results from a joint effort by several Swiss institutions under the umbrella of the National Center for Climate Services (NCCS) that have provided a wide range of expertise on scientific, operational, and computational levels while ensuring the appropriate inclusion of stakeholder needs (cf. Chapter 10 and [230]). The report supplies the most accurate, up-to-date, and coherent climate information available to support assessments of climate impacts and decisions about adaptation and mitigation in Switzerland. Building upon previous scenario efforts, it assesses in-depth past and future changes in the physical climate system in Switzerland.

The provision of climate information at a regional to local scale is essential from a user perspective. However, it poses several challenges for the scenario producers, in particular for Switzerland, as the country's complex Alpine topography results in a large number of small-scale processes. To tackle this complicated problem, the CH2018 project has made use of a new generation of regional climate models at higher spatial resolution and improved model physics (compared to the previous assessment CH2011). The ensemble of regional climate model chains considered has also been expanded. In addition, several new methodologies such as statistical downscaling have been developed and applied (cf. Chapter 2).

The CH2018 results include continuous time series, more regionalized information, and quantitative estimates of changes in extremes. As one example of the project's innovations, it is now possible to provide users with continuous daily time series of several variables as gridded datasets with 2-km resolution. Additional efforts have been made to publish the information for decision-makers and stakeholders in user-friendly formats with a brochure containing the key results and a web site providing regional and localised information (climate-scenarios.ch). Another way of illustrating future climate conditions is by means of analogs (Chapter 10.1). The results will also be available as complete datasets (e.g., for impact modelers) and in graphical format in a comprehensive web atlas.

For the first time in the history of the Swiss national climate scenario assessments, the reference climate and recent variability and trends have been discussed in detail (cf. Chapter 3). This is crucial for the interpretation of the future climate change signal. For temperature, the past and future warming emerges clearly from the natural variability (cf. Box 11.1), but for other variables (for example for mean precipitation and wind speed), the change signal lies within the range of the present climate. This type of information is critical for users and decision-makers in their deliberations over whether adaptation to present climate variations might be sufficient or whether the change must be taken into account for planning purposes.

Box 11.1: Temperature evolution 1864 - 2099

The temperature evolution from the year 1864 (when systematic observations began) to the future year 2099 is shown in Figure 11.1. The projected warming of the annual mean at the end of the century (2070 - 2099) relative to the reference period (1981 - 2010) ranges from 0.6 to 1.9 °C under the optimistic RCP2.6 emission scenario to 3.3 to 5.4°C under the business-as-usual scenario RCP8.5. The temperature curves of the two scenarios begin to diverge around the year 2030. The warming over Switzerland is markedly stronger than in the global mean. The figure also confirms that the climate models are able to reproduce the current climate variability reasonably well. Another important point is that natural variability is large and strongly modulates the forced anthropogenic trend. Even in a high-emission scenario such as RCP8.5, extended periods (up to 3 decades) without warming in Switzerland are possible; however, the warming could also be much faster than anticipated (cf. Chapter 7).

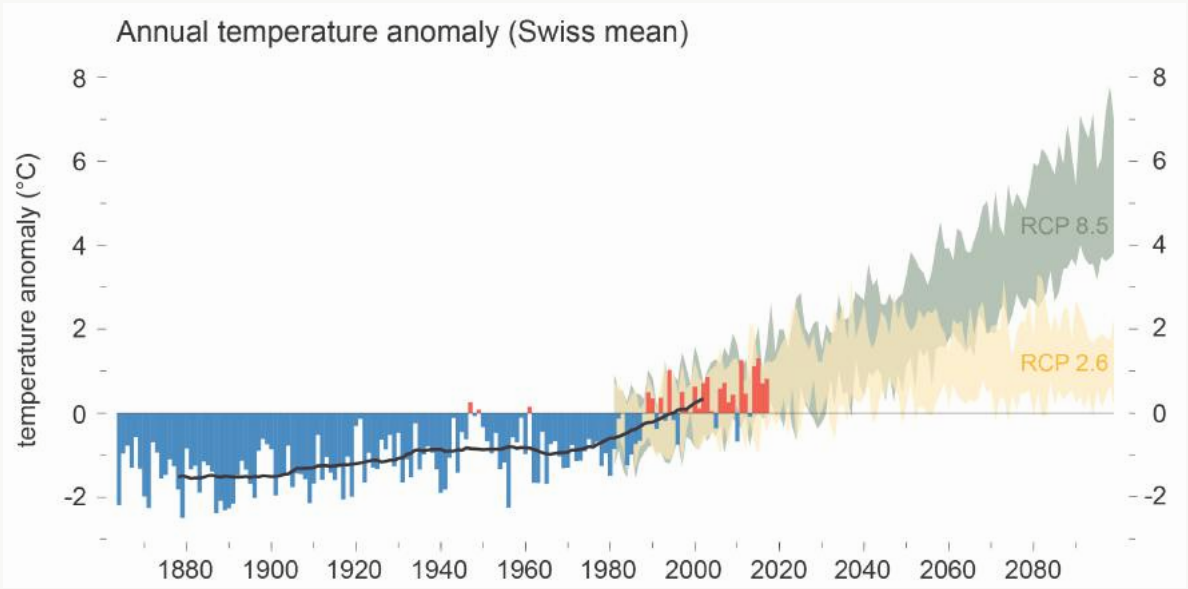

Figure 11.1. Evolution of Swiss annual mean temperature from 1864 to 2099, shown as deviation (°C) from the baseline 1981 - 2010. The bars show the observations from 1864 to 2017 (negative anomalies in blue, positive anomalies in red). The green (orange) shading shows the projected (5th to 95th percentile) range using the RCP8.5 (RCP2.6) scenario.

11.2. Outlook

The provision of Swiss climate change scenarios is a federal mandate of MeteoSwiss and will continue in close collaboration with academic institutions. A new generation of global climate scenarios is already underway in the context of the CMIP6 framework [92]. CORDEX is closely associated with these activities [141] and will produce new sets of downscaled climate projections. For the next round of the national scenarios, which we expect to take place in 6 to 8 years, a number of additional improvements can be expected in the following areas:

- There will be another few years of observational data. Although climate change in Switzerland has emerged in terms of mean warming, changes in many other variables (e.g., summer precipitation) and extremes are only about to emerge. The additional data will enable us to better distinguish between natural variations and anthropogenic climate change. In addition, the compilation and homogenization of past data will continue. These activities will improve critical datasets of several key variables (e.g., snowfall and snow cover).
- In general, the resolution of and parameterizations in global coupled climate models will continue to be refined. This work is already well underway under the umbrella of CMIP6 [92]. It is hoped that this will reduce some of the key uncertainties stemming from the global climate system. For instance, a considerable fraction of the uncertainties related to large-scale mean warming (see Figure 4.4) stems from global model uncertainties.

- Most of the detailed scenario information prepared for the current report is based upon regional climate models (RCMs) running at grid-space resolutions between 10 and 50 km. Currently, major research activities are in progress to refine the horizontal resolution to around 2 km, and one such high-resolution model simulation has been included in the current report (see Box 6.1). These high resolutions enable an explicit (rather than parameterized) representation of deep convection, refined parameterizations of key processes (in particular, cloud microphysics and land-surface schemes), and improved simulations of critical mesoscale phenomena (including Föhn and mountain-valley winds).
- Even higher-resolution and improved regional climate model experiments will be subject to remaining systematic model biases and in many cases will not yet target the impact-relevant spatial scales. Further post-processing in terms of statistical downscaling and bias correction will therefore be necessary. In CH2018, quantile mapping (QM) is used for this purpose (see Chapter 2.5 and Chapter 5.2); additionally, the option to employ weather generators is discussed (see Chapter 10.2.3). Both approaches are subject to caveats and limitations, and further developments – including dedicated statistical downscaling model intercomparison studies – are ongoing and will likely lead to methodological improvements. The same is true for the emerging field of *Climate Information Distillation*, which, among other objectives, seeks to make optimal and robust use of available climate-projection ensembles.
- An even more comprehensive integration of user requirements will be instrumental in further shaping future scenario requirements. The use of climate scenarios for impact studies and adaptation strategies has only just begun. During the second phase of the federal pilot program on climate adaptation (2019 - 2022), the CH2018 scenarios provide the basis for practical applications across several sectors in Switzerland. These efforts will reveal new requirements of the user community that will guide the development of the next phase of national climate scenarios.
- Moreover, as the National Centre for Climate Services (NCCS) evolves as an institution, the dialog between the producers and users of climate scenarios will be strengthened in the coming years. In order for the NCCS to become a true network agent and knowledge broker between academia as well as the public and private sector, a communications strategy has been designed and rolled out. The communications formats and channels range, inter alia, from annual national forums via sectoral and thematic workshops to an interactive web portal. Enhancing dialogues at all levels and across sectors serves not only the development of a next generation of climate scenarios, but is also a prerequisite for the co-development of further downstream climate services.
- Finally, the further development of the Swiss climate scenarios will also benefit from interactions and collaborations with similar ongoing scenario and adaptation activities in other countries (such as UKCP18 in the United Kingdom, KNMI'14 scenarios in the Netherlands, ReKlies-De in Germany, and ÖKS15 in Austria). In addition, the implementation of the Copernicus Climate Change Service and its Climate Data Store will likely provide an important resource supporting the development of national climate change scenarios in a coherent manner across European countries.

References

1. N. Addor, M. Rohrer, R. Furrer, and J. Seibert (2016), "Propagation of biases in climate models from the synoptic to the regional scale: Implications for bias adjustment," *Journal of Geophysical Research*, vol. 121.
2. N. Addor and J. Seibert (2014), "Bias correction for hydrological impact studies – beyond the daily perspective," *Hydrological Processes*, vol. 28, pp. 4823–4828.
3. N. Addor and E. M. Fischer (2015), "The influence of natural variability and interpolation errors on bias characterization in RCM simulations," *Journal of Geophysical Research: Atmospheres*, vol. 120, no. 19.
4. A. AghaKouchak, L. Cheng, O. Mazdiyasni, and A. Farahmand (2014), "Global warming and changes in risk of concurrent climate extremes: Insights from the 2014 California drought," *Geophysical Research Letters*, vol. 41, no. 24, pp. 8847–8852.
5. C. D. Ahrens (2012), *Meteorology today: an introduction to weather, climate, and the environment*, Cengage Learning 296 pp.
6. L. V. Alexander, X. Zhang, T. C. Peterson, J. Caesar, B. Gleason, A. M. G. Klein Tank, M. Haylock, D. Collins, B. Trewin, F. Rahimzadeh, A. Tagipour, K. Rupa Kumar, J. Revadekar, G. Griffiths, L. Vincent, D. B. Stephenson, J. Burn, E. Aguilar, M. Brunet, M. Taylor, M. New, P. Zhai, M. Rusticucci, and J. L. Vazquez-Aguirre (2006), "Global observed changes in daily climate extremes of temperature and precipitation," *Journal of Geophysical Research*, vol. 111, no. D05109.
7. M. R. Allen and W. J. Ingram (2002), "Constraints on future changes in climate and the hydrologic cycle," *Nature*, vol. 419, no. 6903, pp. 224–232.
8. J. D. Annan and J. C. Hargreaves (2010), "Reliability of the CMIP3 ensemble,"*Geophysical Research Letters*, vol. 37, no. 2.
9. C. Appenzeller, M. Begert, E. Zenklusen, and S. C. Scherrer (2008), "Monitoring climate at Jungfraujoch in the high Swiss Alpine region," *Science of the Total Environment*, vol. 391, no. 2, pp. 262–268.
10. S. Bader and S. Fukutome (2015), "Milde und kalte Bergwinter," Arbeitsbericht MeteoSchweiz, 254, 10 pp.
11. J. Ballester, F. Giorgi, and X. Rodó (2010), "Changes in European temperature extremes can be predicted from changes in PDF central statistics," *Climatic Change*, vol. 98, no. 1, pp. 277–284.
12. N. Ban, J. Schmidli, and C. Schär (2014), "Evaluation of the convection-resolving regional climate modeling approach in decade-long simulations," *Journal of Geophysical Research: Atmospheres*.
13. N. Ban, J. Schmidli, and C. Schär (2015), "Heavy precipitation in a changing climate: Does short-term summer precipitation increase faster?," *Geophysical Research Letters*, vol. 42, pp. 1165–1172.
14. A. G. Barnston and R. E. Livezey (1987), "Classification, seasonality and persistence of low-frequency atmospheric circulation patterns," *Monthly Weather Review*, vol. 115, no. 6, pp. 1083–1126.
15. B. Bartók, M. Wild, D. Folini, D. Lüthi, S. Kotlarski, C. Schär, R. Vautard, S. Jerez, and Z. Imecs (2016), "Projected changes in surface solar radiation in CMIP5 global climate models and in EURO-CORDEX regional climate models for Europe," *Climate Dynamics*.
16. A. Bauder, M. Funk, and M. Huss (2007), "Ice-volume changes of selected glaciers in the Swiss Alps since the end of the 19th century.," *Ann. Glaciol.*, vol. 46, pp. 145–149.
17. P. Bauer, A. Thorpe, and G. Brunet (2015), "The quiet revolution of numerical weather prediction," *Nature*, vol. 525, pp. 47–55.
18. M. Bavay and T. Egger (2014), "MeteoIO 2.4. 2: a preprocessing library for meteorological data," *Geoscientific Model Development*, vol. 7, no. 6, pp. 3135–3151.

19. M. Begert, G. Seiz, N. Foppa, T. Schlegel, C. Appenzeller, and G. Müller (2007), “Die Überführung der klimatolgischen Referenzstationen der Schweiz in das Swiss National Basic Climatological Network (Swiss NBCN),” Arbeitsberichte der MeteoSchweiz 215, 43 pp.

20. M. Begert and C. Frei (2018), “Long-term area-mean temperature series for Switzerland - Combining homogenized station data and high resolution grid data,” *International Journal of Climatology*, vol. 38, no. 6, pp. 2792–2807.

21. M. Begert, T. Schlegel, and W. Kirchhofer (2005), “Homogeneous temperature and precipitation series of Switzerland from 1864 to 2000,” *International Journal of Climatology*, vol. 25, no. 1, pp. 65–80.

22. M. Begert, G. Seiz, T. Schlegel, M. Musa, G. Baudraz, and M. Moesch (2003), “Homogenisierung von Klimamessreihen der Schweiz und Bestimmung der Normwerte 1961—1990,” Schlussbericht des Projektes NORM90, Veröffentlichungen der MeteoSchweiz, 67, 170 pp.

23. O. Bellprat, S. Kotlarski, D. Lüthi, R. De Elìa, A. Frigon, R. Laprise, and C. Schär (2016), “Objective Calibration of Regional Climate Models: Application over Europe and North America,” *Journal of Climate*, vol. 29, pp. 819–838.

24. O. Bellprat, S. Kotlarski, D. Lüthi, and C. Schär (2013), “Physical constraints for temperature biases in climate models,” *Geophysical Research Letters*, vol. 40, pp. 4042–4047.

25. M. Beniston, D. B. Stephenson, O. B. Christensen, C. A. T. Ferro, C. Frei, S. Goyette, K. Halsnaes, T. Holt, K. Jylhä, B. Koffi, and others (2007), “Future extreme events in European climate: an exploration of regional climate model projections,” *Climatic change*, vol. 81, no. 1, pp. 71–95.

26. A. Berg, J. Sheffield, and P. C. D. Milly (2017), “Divergent surface and total soil moisture projections under global warming,” *Geophysical Research Letters*, vol. 44, no. 1, pp. 236–244.

27. N. L. Bindoff, P. A. Stott, K. M. AchutaRao, M. R. Allen, N. Gillett, D. Gutzler, K. Hansingo, G. Hegerl, Y. Hu, S. Jain, I. I. Mokhov, J. Overland, J. Perlwitz, R. Sebbari, and X. Zhang (2013), “Detection and Attribution of Climate Change: from Global to Regional,” in *Climate Change 2013: The Physical Science Basis. Contribution of Working Group I to the Fifth Assessment Report of the Intergovernmental Panel on Climate Change*, Cambridge, United Kingdom and New York, NY, USA, pp. 867–952.

28. K. Blazejczyk, Y. Epstein, G. Jendritzky, H. Staiger, and T. B. (2012), “Comparison of UTCI to selected thermal indices,” *International Journal of Biometeorology*, vol. 56, no. 3, pp. 515–535.

29. R. Blender, C. C. Raible, and C. L. E. Franzke (2017), “Vorticity and geopotential height extreme values in ERA-Interim data during boreal winters,” *Quarterly Journal of the Royal Meteorological Society* , vol. 143, no. 703, pp. 634–640.

30. R. Blender, C. C. Raible, and F. Lunkeit (2015), “Non-exponential return time distributions for vorticity extremes explained by fractional Poisson processes,” *Quarterly Journal of the Royal Meteorological Society*, vol. 141, no. 686, pp. 249–257.

31. F. Boberg and J. H. Christensen (2012), “Overestimation of Mediterranean summer temperature projections due to model deficiencies,” *Nature Climate Change*.

32. T. Bosshard, S. Kotlarski, T. Ewen, and C. Schär (2011), “Spectral representation of the annual cycle in the climate change signal,” *Hydrology and Earth System Sciences*, vol. 15, pp. 2777–2788.

33. T. Bosshard, S. Kotlarski, M. Zappa, and C. Schär (2014), “Hydrological climate-impact projections for the Rhine river: GCM-RCM uncertainty and separate temperature and precipitation effects,” *Journal of Hydrometeorology*, vol. 15, no. 2, pp. 697–713.

34. J. Boée, L. Terray, F. Habets, and E. Martin (2007), “Statistical and dynamical downscaling of the Seine basin climate for hydro-meteorological studies,” *International Journal of Climatology*, vol. 27, pp. 1643–1655.

35. G. Branstator and H. Teng (2010), “Two Limits of Initial-Value Decadal Predictability in a CGCM,” *Journal*

of Climate, vol. 23, pp. 6292–6311.

36. E. Brocard, P. Jeannet, M. Begert, G. Levrat, R. Philipona, G. Romanens, and S. C. Scherrer (2013), "Upper air temperature trends above Switzerland 1959—2011," *Journal of Geophysical Research: Atmospheres*, vol. 118, no. 10, pp. 4303–4317.

37. M. Brunet, J. Asin, J. Sigró, M. Bañón, F. García, E. Aguilar, J. E. Palenzuela, T. C. Peterson, and P. Jones (2011), "The minimization of the screen bias from ancient Western Mediterranean air temperature records: an exploratory statistical analysis," *International Journal of Climatology*, vol. 31, no. 12, pp. 1879–1895.

38. D. Brändli (1996), "Schwere Winterstürme über der Schweiz 1500—1995," Universität Bern, 40 pp.

39. S. Brönnimann (2016), "Das vergangene Klima," in *Brennpunkt Klima Schweiz. Grundlagen, Folgen und Perspektiven.*, vol. 11, no. 5, A. der Wissenschaften Schweiz, Ed. Swiss Academies Reports, pp. 32–33.

40. S. Brönnimann, C. Appenzeller, M. Croci-Maspoli, J. Fuhrer, M. Grosjean, R. Hohmann, K. Ingold, R. Knutti, M. A. Liniger, C. C. Raible, R. Röthlisberger, C. Schär, S. C. Scherrer, K. Strassmann, and P. Thalmann (2014), "Climate change in Switzerland: a review of physical, institutional, and political aspects," *WIRES Climate Change*, vol. 5, no. 4, pp. 461–481.

41. S. Brönnimann and D. Krämer (2016), *Tambora and the "Year Without a Summer" of 1816. A Perspective on Earth and Human Systems Science*, Geographica Bernensia G90, 48 pp.

42. S. Brönnimann, O. Martius, H. von Waldow, C. Welker, J. Luterbacher, G. P. Compo, P. D. Sardeshmukh, and T. Usbeck (2012), "Extreme winds at northern mid-latitudes since 1871," *Meteorologische Zeitschrift*, vol. 21, no. 1, pp. 13–27.

43. S. Brönnimann, E. Xoplaki, C. Casty, A. Pauling, and J. Luterbacher (2007), "ENSO influence on Europe during the last centuries," *Climate Dynamics*, vol. 28, no. 2-3, pp. 181–197.

44. M. Burlando, L. Carassale, E. Georgieva, C. F. Ratto, and G. Solari (2007), "A simple and efficient procedure for the numerical simulation of wind fields in complex terrain," *Boundary-layer meteorology*, vol. 125, no. 3, pp. 417–439.

45. C. M. Buser, H. R. Künsch, D. Lüthi, M. Wild, and C. Schär (2009), "Bayesian multi-model projection of climate: bias assumptions and interannual variability," *Climate Dynamics*, vol. 33, no. 6, pp. 849–868.

46. C. M. Buser, H. R. Künsch, and C. Schär (2010), "Bayesian multi-model projections of climate: generalization and application to ENSEMBLES results," *Climate Research*, vol. 4, pp. 227–241.

47. M. P. Byrne and P. A. O'Gorman (2015), "The Response of Precipitation Minus Evapotranspiration to Climate Warming: Why the 'Wet-Get-Wetter, Dry-Get-Drier' Scaling Does Not Hold over Land," *Journal of Climate*, vol. 28, no. 20, pp. 8078–8092.

48. R. Böhm, P. D. Jones, J. Hiebl, D. Frank, M. Brunetti, and M. Maugeri Jul. (2010), "The early instrumental warm-bias: a solution for long central European temperature series 1760—2007," *Climatic Change*, vol. 101, no. 1, pp. 41–67.

49. U. Büntgen, D. C. Frank, D. Nievergelt, and J. Esper (2006), "Summer temperature variations in the European Alps, AD 755-2004," *Journal of Climate*, vol. 19, no. 21, pp. 5606–5623.

50. P. Calanca (2007), "Climate change and drought occurrence in the Alpine region: How severe are becoming the extremes?," *Global and Planetary Change*, vol. 57, no. 1, pp. 151–160.

51. A. Casanueva Vicente, C. Rodríguez Puebla, M. D. Frías Domínguez, N. González Reviriego, and others (2014), "Variability of extreme precipitation over Europe and its relationships with teleconnection patterns," vol. 18, pp. 709–725.

52. A. Casanueva, S. Kotlarski, and S. et al Herrera (2016), "Daily precipitation statistics in a EURO-CORDEX RCM ensemble: added value of raw and bias-corrected high-resolution simulations," *Climate Dynamics*,

vol. 47, pp. 719–737.

53. C. Casty, D. Handorf, and M. Sempf (2005), “Combined winter climate regimes over the North Atlantic/European sector 1766—2000,” *Geophysical Research Letters*, vol. 32, no. 13.

54. J. Cattiaux, H. Douville, R. Schoetter, S. Parey, and P. Yiou (2015), “Projected increase in diurnal and interdiurnal variations of European summer temperatures,” *Geophysical Research Letters*, vol. 42, no. 3, pp. 899–907.

55. P. Ceppi, S. C. Scherrer, A. M. Fischer, and C. Appenzeller (2012), “Revisiting Swiss temperature trends 1959—2008,” *International Journal of Climatology*, vol. 32, no. 2, pp. 203–213.

56. CH2011 (2011), *Swiss Climate Change Scenarios CH2011*, published by C2SM, MeteoSwiss, ETH, NCCR Climate, and OcCC, Zurich, Switzerland, 88 pp., ISBN: 9783033030657. Available from www.ch2011.ch.

57. CH2014-Impacts (2014), *Toward Quantitative Scenarios of Climate Change Impacts in Switzerland*, Bern, Switzerland: OCCR, FOEN, MeteoSwiss, C2SM, Agroscope, and ProClim, 136 pp.

58. J. H. Christensen, F. Boberg, O. B. Christensen, and P. Lucas-Picher (2008), “On the need for bias correction of regional climate change projections of temperature and precipitation,” *Geophysical Research Letters*, vol. 35, no. L20709.

59. J. H. Christensen and O. B. Christensen May (2007), “A summary of the PRUDENCE model projections of changes in European climate by the end of this century,” *Climatic Change*, vol. 81, no. 1, pp. 7–30.

60. N. Christidis, G. S. Jones, and P. A. Stott (2015), “Dramatically increasing chance of extremely hot summers since the 2003 European heatwave,” *Nature Climate Change*, vol. 5, no. 1, pp. 46–50.

61. N. Christidis, P. A. Stott, and S. J. Brown (2011), “The role of human activity in the recent warming of extremely warm daytime temperatures,” *Journal of Climate*, vol. 24, no. 7, pp. 1922–1930.

62. P. Ciais, C. Sabine, G. Bala, L. Bopp, V. Brovkin, J. Canadell, A. Chhabra, R. DeFries, J. Galloway, M. Heimann, C. Jones, C. Le Quéré, R. B. Myneni, S. Piao, and P. Thornton (2013), “Carbon and Other Biogeochemical Cycles,” in *Climate Change 2013: The Physical Science Basis. Contribution of Working Group I to the Fifth Assessment Report of the Intergovernmental Panel on Climate Change*, Cambridge, United Kingdom and New York, NY, USA, pp. 465–570.

63. S. Coccolo, J. Kämpf, J.-L. Scartezzini, and D. Pearlmutter (2016), “Outdoor human comfort and thermal stress: A comprehensive review on models and standards,” *Urban Climate*, vol. 18, pp. 33–57.

64. S. Coles (2004), *An introduction to statistical modeling of extreme values*, 3Rd print., London, United Kingdom: Springer, 208 pp.

65. B. A. Colle, Z. Zhang, K. A. Lombardo, E. Chang, P. Liu, and M. Zhang (2013), “Historical evaluation and future prediction of eastern North American and western Atlantic extratropical cyclones in the CMIP5 models during the cool season,” *Journal of Climate*, vol. 26, no. 18, pp. 6882–6903.

66. M. Collins, R. Knutti, J. Arblaster, J.-L. Dufresne, T. Fichefet, P. Friedlingstein, X. Gao, W. J. Gutowski, T. Johns, G. Krinner, and others (2013), “IPCC 2013, WG1, Chapter 12: Long-term climate change: projections, commitments and irreversibility.”

67. G. P. Compo, J. S. Whitaker, P. D. Sardeshmukh, N. Matsui, R. J. Allan, X. Yin, B. E. Gleason, R. S. Vose, G. Rutledge, P. Bessemoulin, and others (2011), “The Twentieth Century Reanalysis Project,” *Quarterly Journal of the Royal Meteorological Society*, vol. 137, no. 654, pp. 1–28.

68. D. Coumou, V. Petoukhov, S. Rahmstorf, S. Petri, and H. J. Schellnhuber (2014), “Quasi-resonant circulation regimes and hemispheric synchronization of extreme weather in boreal summer,” *Proceedings of the National Academy of Sciences*, vol. 111, no. 34, pp. 12331–12336.

69. F. Dahinden, E. M. Fischer, and R. Knutti (2017), “Future local climate unlike currently observed anywhere,” *Environmental Research Letters*, vol. 12, no. 8.

70. A. Dai (2011), "Drought under global warming: A review," *Wiley Interdisciplinary Reviews: Climate Change*, vol. 2, pp. 45–65.

71. A. Dai (2012), "Increasing drought under global warming in observations and models," *Nature Climate Change*, vol. 3, no. 1, pp. 52–58.

72. R. Davies-Jones (2008), "An Efficient and Accurate Method for Computing the Wet-Bulb Temperature along Pseudoadiabats," *Monthly Weather Review*, vol. 136, no. 7, pp. 2764–2785.

73. E. L. Davin, S. I. Seneviratne, P. Ciais, A. Olioso, and T. Wang (2014), "Preferential cooling of hot extremes from cropland albedo management," *Proceedings of the National Academy of Sciences*, vol. 111, no. 27, pp. 9757–9761.

74. C. R. de Freitas and E. A. Grigorieva (2015), "A comprehensive catalogue and classification of human thermal climate indices," *International Journal of Biometeorology*, vol. 59, no. 1, pp. 109–120.

75. H. de Vries, G. Lenderink, and E. van Meijgaard (2014), "Future snowfall in western and central Europe projected with a high-resolution regional climate model ensemble," *Geophysical Research Letters*, vol. 41, pp. 4294–4299.

76. H. De Vries, R. J. Haarsma, and W. Hazeleger (2012), "Western European cold spells in current and future climate," *Geophysical Research Letters*, vol. 39, no. 4.

77. P. M. Della-Marta, J. Luterbacher, H. von Weissenfluh, E. Xoplaki, M. Brunet, and H. Wanner (2007), "Doubled length of Western European summer heat waves since 1880," *Journal of Geophysical Research: Atmospheres*, vol. 112, no. D15103.

78. B. Denis, R. Laprise, D. Caya, and J. Cote (2002), "Downscaling ability of one-way-nested regional climate models: the Big-Brother experiment," *Climate Dynamics*, vol. 18, pp. 627–646.

79. C. Deser, R. Knutti, S. Solomon, and A. S. Phillips (2012), "Communication of the role of natural variability in future North American climate," *Nature Climate Change*, vol. 2, pp. 775–779.

80. A. Di Luca, D. Argueso, J. P. Evans, R. de Elia, and R. Laprise (2016), "Quantifying the overall added value of dynamical downscaling and the contribution from different spatial scales," *Journal of Geophysical Research: Atmospheres*, vol. 121, pp. 1575–1590.

81. N. S. Diffenbaugh, M. Scherer, and R. J. Trapp (2013), "Robust increases in severe thunderstorm environments in response to greenhouse forcing," *Proc. Natl. Acad. Sci.*, vol. 110, no. 41, pp. 16361–16366.

82. M. G. Donat, L. V. Alexander, H. Yang, I. Durre, R. Vose, R. J. H. Dunn, K. M. Willett, E. Aguilar, M. Brunet, J. Caesar, and others (2013), "Updated analyses of temperature and precipitation extreme indices since the beginning of the twentieth century: the HadEX2 dataset," *Journal of Geophysical Research: Atmospheres*, vol. 118, no. 5, pp. 2098–2118.

83. M. G. Donat, G. C. Leckebusch, S. Wild, and U. Ulbrich (2011), "Future changes in European winter storm losses and extreme wind speeds inferred from GCM and RCM multi-model simulations," *Natural Hazards and Earth System Sciences*, vol. 11, no. 5, p. 1351.

84. W. A. Dorigo, W. Wagner, R. Hohensinn, S. Hahn, C. Paulik, A. Xaver, A. Gruber, M. Drusch, S. Mecklenburg, P. van Oevelen, A. Robock, and T. Jackson (2011), "The International Soil Moisture Network: a data hosting facility for global in situ soil moisture measurements," *Hydrology and Earth System Sciences*, vol. 15, no. 5, pp. 1675–1698.

85. A. Dosio (2016), "Projections of climate change indices of temperature and precipitation from an ensemble of bias-adjusted high-resolution EURO-CORDEX regional climate models," *Journal of Geophysical Research: Atmospheres*, vol. 121, no. 10, pp. 5488–5511.

86. S. Drijfhout, S. Bathiany, C. Beaulieu, V. Brovkin, M. Claussen, C. Huntingford, M. Scheffer, G. Sgubin, and D. Swingedouw (2015), "Catalogue of abrupt shifts in Intergovernmental Panel on Climate Change climate models," *Proceedings of the National Academy of Sciences*, vol. 112, no. 43, pp. E5777–E5786.

87. M. Déequée, D. P. Rowell, D. Lüthi, F. Giorgi, J. H. Christensen, B. Rockel, D. Jacob, E. Kjellström, M. de Castro, and B. van den Hurk (2007), "An intercomparison of regional climate simulations for Europe: assessing uncertainties in model projections," *Climatic Change*, vol. 81, pp. 53–70.

88. T. Economou, D. B. Stephenson, J. G. Pinto, L. C. Shaffrey, and G. Zappa (2015), "Serial clustering of extratropical cyclones in a multi-model ensemble of historical and future simulations," *Quarterly Journal of the Royal Meteorological Society*, vol. 141, no. 693, pp. 3076–3087.

89. J. M. Eden, M. Widmann, D. Grawe, and S. Rast (2012), "Skill, Correction, and Downscaling of GCM-Simulated Precipitation," *Journal of Climate*, vol. 25, pp. 3970–3984.

90. U. Ehret, E. Zehe, V. Wulfmeyer, K. Warrach-Sagi, and J. Liebert (2012), "HESS Opinions 'Should we apply bias correction to global and regional climate model data?,'" *Hydrology and Earth System Sciences*, vol. 16, pp. 3391–3404.

91. S. Emori and S. J. Brown (2005), "Dynamic and thermodynamic changes in mean and extreme precipitation under changed climate," *Geophysical Research Letters*, vol. 32, no. 17.

92. V. Eyring, S. Bony, G. A. Meehl, C. A. Senior, B. Stevens, R. J. Stouffer, and T. K. E. (2016), "Overview of the Coupled Model Intercomparison Project Phase 6 (CMIP6) experimental design and organization.," *Geosci. Model Dev.*, vol. 9.

93. S. Fatichi, V. Y. Ivanov, and E. Caporali (2011), "Simulation of future climate scenarios with a weather generator," *Advances in Water Resources*, vol. 34, no. 4, pp. 448–467.

94. S. Fatichi, V. Y. Ivanov, A. Paschalis, N. Peleg, P. Molnar, S. Rimkus, J. Kim, P. Burlando, and E. Caporali (2016), "Uncertainty partition challenges the predictability of vital details of climate change," *Earth's Future*, vol. 4, no. 5, pp. 240–251.

95. I. Feigenwinter, S. Kotlarski, A. Casanueva, A. M. Fischer, C. Schwierz, and M. A. Liniger (2018), "Exploring quantile mapping as a tool to produce user-tailored climate scenarios for Switzerland," MeteoSwiss, Technical Report 270.

96. F. Feser, M. Barcikowska, O. Krueger, F. Schenk, R. Weisse, and L. Xia (2015), "Storminess over the North Atlantic and northwestern Europe—A review," *Quarterly Journal of the Royal Meteorological Society*, vol. 141, no. 687, pp. 350–382.

97. D. Finger, G. Heinrich, A. Gobiet, and A. Bauder (2012), "Projections of future water resources and their uncertainty in a glacierized catchment in the Swiss Alps and the subsequent effects on hydropower production during the 21st century," *Water Resources Research*, vol. 48, no. W02521.

98. A. M. Fischer, D. E. Keller, M. A. Liniger, J. Rajczak, C. Schär, and C. Appenzeller (2015), "Projected changes in precipitation intensity and frequency in Switzerland: a multi-model perspective," *International Journal of Climatology*, vol. 35, no. 11, pp. 3204–3219.

99. A. M. Fischer, A. P. Weigel, C. M. Buser, R. Knutti, H. R. Künsch, M. A. Liniger, C. Schär, and C. Appenzeller (2012), "Climate change projections for Switzerland based on a Bayesian multi-model approach," *International Journal of Climatology*, vol. 32, pp. 2348–2371.

100. A. M. Fischer, M. Liniger, and C. Appenzeller (2015), "Climate scenarios of seasonal means: extensions in time and space," in *CH2011+*, Zurich, Switzerland, vol. CH2011 Extension Series No. 2, 18 pp.

101. A. M. Fischer, M. Liniger, and C. Appenzeller (2016), "Climate scenarios of seasonal means: correlations of change estimates," in *CH2011+*, Zurich, Switzerland, vol. CH2011 Extension Series No. 3, 19 pp, no. 3.

102. E. M. Fischer, U. Beyerle, and R. Knutti (2013), "Robust spatially aggregated projections of climate extremes," *Nature Climate Change*, vol. 3, no. 12, pp. 1033–1038.

103. E. M. Fischer and C. Schär (2010), "Consistent geographical patterns of changes in high-impact European heatwaves," *Nature Geoscience*, vol. 3, no. 6, pp. 398–403.

104. E. M. Fischer, J. Sedlacek, E. Hawkins, and R. Knutti (2014), “Models agree on forced response pattern of precipitation and temperature extremes,” *Geophysical Research Letters*, vol. 41, no. 23, pp. 8554–8562.

105. E. M. Fischer, K. W. Oleson, and D. M. Lawrence (2012), “Contrasting urban and rural heat stress responses to climate change,” *Geophysical Research Letters*, vol. 39, no. 3.

106. E. M. Fischer and R. Knutti (2014), “Detection of spatially aggregated changes in temperature and precipitation extremes,” *Geophysical Research Letters*, vol. 41, no. 2, pp. 547–554.

107. E. M. Fischer and R. Knutti (2016), “Observed heavy precipitation increase confirms theory and early models,” *Nature Climate Change*, vol. 6, no. 11, pp. 986–991.

108. E. M. Fischer, J. Rajczak, and C. Schär (2012), “Changes in European summer temperature variability revisited,” *Geophysical Research Letters*, vol. 39, no. 19.

109. E. M. Fischer, D. M. Lawrence, and B. M. Sanderson (2011), “Quantifying uncertainties in projections of extremes — a perturbed land surface parameter experiment,” *Climate dynamics*, vol. 37, no. 7-8, pp. 1381–1398.

110. E. M. Fischer and C. Schär (2009), “Future changes in daily summer temperature variability: driving processes and role for temperature extremes,” *Climate Dynamics*, vol. 33, no. 7-8, p. 917.

111. E. M. Fischer, S. I. Seneviratne, P. L. Vidale, D. Lüthi, and C. Schär (2007), “Soil moisture — atmosphere interactions during the 2003 European summer heat wave,” *Journal of Climate*, vol. 20, no. 20, pp. 5081–5099.

112. M. Fischer, M. Huss, and H. M (2015), “Surface elevation and mass changes of all Swiss glaciers 1980–2010,” *The Cryosphere*, vol. 9, pp. 525–540.

113. A. K. Fleig, L. M. Tallaksen, H. Hisdal, and D. M. Hannah (2011), “Regional hydrological drought in north-western Europe: linking a new Regional Drought Area Index with weather types,” *Hydrological Processes*, vol. 25, no. 7, pp. 1163–1179.

114. FOEN (2012), “Adaptation to climate change in Switzerland: Goals, challenges and fields of action First part of the Federal Council’s strategy. Adopted on 2 March 2012,” Federal Office for the Environment, Berne, Switzerland.

115. FOEN (2012), *Auswirkungen der Klimaänderung auf Wasserressourcen und Gewässer. Synthesebericht zum Projekt “Klimaänderung und Hydrologie in der Schweiz” (CCHydro)*, Bern, Schweiz: Federal Office for the Environment, 76 pp.

116. FOEN (2014), *Anpassung an den Klimawandel in der Schweiz. Aktionsplan 2014–2019, Zweiter Teil der Strategie des Bundesrates*, Bern, Schweiz: Federal Office for the Environment, 100 pp.

117. FOEN (2016), “Hitze und Trockenheit im Sommer 2015. Auswirkungen auf Mensch und Umwelt.,” in *Umwelt-Zustand Nr. 1629*, Bern, Schweiz: Federal Office for the Environment, 108 pp.

118. H. J. Fowler, S. Blenkinskop, and C. Tebaldi (2007), “Linking climate change modelling to impacts studies: recent advances in downscaling techniques for hydrological modelling,” *International Journal of Climatology*, vol. 27, pp. 1547–1578.

119. K. Fraedrich (1994), “An ENSO impact on Europe?,” *Tellus A*, vol. 46, no. 4, pp. 541–552.

120. D. Frank, U. Büntgen, R. Böhm, M. Maugeri, and J. Esper (2007), “Warmer early instrumental measurements versus colder reconstructed temperatures: shooting at a moving target,” *Quaternary Science Reviews*, vol. 26, no. 25, pp. 3298–3310.

121. J. Franke, S. Brönnimann, J. Bhend, and Y. Brugnara (2017), “A monthly global paleo-reanalysis of the atmosphere from 1600 to 2005 for studying past climatic variations,” *Scientific Data*, vol. 4.

122. C. Frei (2004), “Die Klimazukunft der Schweiz - Eine probabilistische Projektion,” MeteoSchweiz, 2004, 16 pp.

123. C. Frei (2014), “Interpolation of temperature in a mountainous region using nonlinear profiles and non-Euclidean distances,” *International Journal of Climatology*, vol. 34, no. 5, pp. 1585–1605.

124. C. Frei and C. Schär (2001), “Detection probability of trends in rare events: Theory and application to heavy precipitation in the Alpine region,” *Journal of Climate*, vol. 14, no. 7, pp. 1568–1584.

125. C. Frei, C. Schär, D. Lüthi, and H. C. Davies (1998), “Heavy precipitation processes in a warmer climate,” *Geophysical Research Letters*, vol. 25, no. 9, pp. 1431–1434.

126. C. Frei, R. Schöll, S. Fukutome, J. Schmidli, and P. L. Vidale (2006), “Future change of precipitation extremes in Europe: Intercomparison of scenarios from regional climate models,” *Journal of Geophysical Research: Atmospheres*, vol. 111, no. D6.

127. P. Frei, S. Kotlarski, M. A. Liniger, and C. Schär (2018), “Future snowfall in the Alps: projections based on the EURO-CORDEX regional climate models,” *The Cryosphere*, vol. 12, no. 1, pp. 1–24.

128. P. Frich, L. V. Alexander, P. Della-Marta, B. Gleason, M. Haylock, A. M. G. Klein Tank, and T. Peterson (2002), “Observed coherent changes in climatic extremes during the second half of the twentieth century,” *Climate Research*, vol. 19, no. 3, pp. 193–212.

129. S. Fukutome and A. Schindler (2015), “MeteoSwiss extreme value analyses: User manual and documentation,” Technical Report MeteoSwiss, 255.

130. F. Giorgi, C. Jones, and G. R. Arsar (2009), “Addressing climate information needs at the regional level: the CORDEX framework,” *WMO Bulletin*, vol. 58, no. 3, pp. 175–183.

131. F. Giorgi and L. O. Mearns (1999), “Introduction to special section: Regional climate modeling revisited,” *Journal of Geophysical Research: Atmospheres*, vol. 104, pp. 6335–52.

132. F. Giorgi, C. Torma, E. Coppola, N. Ban, C. Schar, and S. Somot (2016), “Enhanced summer convective rainfall at Alpine high elevations in response to climate warming,” *Nature Geosci*, vol. 9, no. 8, pp. 584–589.

133. A. Gobiet, M. Suklitsch, and G. Heinrich (2015), “The effect of empirical-statistical correction of intensity-dependent model errors on the climate change signal,” *Hydrology and Earth System Sciences*, vol. 19, pp. 4055–4066.

134. S. Goyette (2011), “Synoptic conditions of extreme windstorms over Switzerland in a changing climate,” *Climate dynamics*, vol. 36, no. 5-6, pp. 845–866.

135. M. Graf, S. C. Scherrer, C. Schwierz, M. Begert, O. Martius, C. C. Raible, and S. Brönnimann (2018), “Near-surface mean wind in Switzerland: Climatology, climate model evaluation and future scenarios,” *International Journal of Climatology*, vol. submitted.

136. P. Greve and S. I. Seneviratne (2015), “Assessment of future changes in water availability and aridity,” *Geophysical Research Letters*, vol. 42, no. 13, pp. 5493–5499.

137. B. Grisogono and D. Belušić (2009), “A review of recent advances in understanding the meso-and microscale properties of the severe Bora wind,” *Tellus A*, vol. 61, no. 1, pp. 1–16.

138. L. Gudmundsson, J. B. Bremnes, J. E. Haugen, and T. Engen-Skaugen (2012), “Technical Note: Downscaling RCM precipitation to the station scale using statistical transformations – a comparison of methods,” *Hydrology and Earth System Sciences*, vol. 16, pp. 3383–3390.

139. J. M. Gutiérrez, D. Maraun, M. Widmann, R. Huth, E. Hertig, R. Benestad, O. Rössler, J. Wibig, R. Wilcke, S. Kotlarski, D. San Martín, S. Herrera, J. Bedia, A. Casanueva, R. Manzanas, M. Iturbide, M. Vrac, M. Dubrovsky, J. Ribalaygua, J. Pórtoles, O. Räty, J. Räisänen, B. Hingray, D. Raynaud, M. J. Casado, P. Ramos, T. Zerenner, M. Turco, T. Bosshard, P. Štěpánek, J. Bartholy, R. Pongracz, D. E. Keller, A. M. Fischer, R. M. Cardoso, P. M. M. Soares, B. Czernecki, and C. Pagé (2018), “An intercomparison of a large ensemble of statistical downscaling methods over Europe: Results from the VALUE perfect predictor cross-validation experiment,” *International Journal of Climatology*.

140. O. Gutjahr and G. Heinemann (2013), “Comparing precipitation bias correction methods for high-resolution regional climate simulations using COSMO-CLM,” *Theoretical and Applied Climatology*, vol. 114, pp. 511–529.

141. W. J. Gutowski Jr., F. Giorgi, B. Timbal, A. Frigon, D. Jacob, H.-S. Kang, K. Raghavan, B. Lee, C. Lennard, G. Nikulin, E. O’Rourke, M. Rixen, S. Solman, T. Stephenson, and F. Tangang (2016), “WCRP COordinated Regional Downscaling EXperiment (CORDEX): a diagnostic MIP for CMIP6,” *Geoscientific Model Development*, vol. 9, pp. 4087–4095.

142. D. Gyalistras, H. von Storch, A. Fischlin, and M. Beniston (1994), “Linking GCM-simulated climatic changes to ecosystem models: case studies of statistical downscaling in the Alps,” *Climate Research*, vol. 4, pp. 167–189.

143. W. Haeberli, M. Hoelzle, F. Paul, and M. Zemp (2007), “Integrated monitoring of mountain glaciers as key indicators of global climate change: the European Alps,” *Annals of Glaciology*, vol. 46, pp. 150–160.

144. S. Hagemann, C. Chen, J. O. Haerter, J. Heinke, D. Gerten, and C. Piani (2011), “Impact of a Statistical Bias Correction on the Projected Hydrological Changes Obtained from Three GCMs and Two Hydrology Models,” *Journal of Hydrometeorology*, vol. 12, pp. 556–578.

145. J. Hansen, R. Ruedy, M. Sato, and K. Lo (2010), “Global surface temperature change,”*Reviews of Geophysics*, vol. 48, no. 4.

146. E. Hawkins, P. Ortega, E. Suckling, A. Schurer, G. Hegerl, P. Jones, M. Joshi, T. Osborn, V. Masson-Delmotte, J. Mignot, P. Thorne, and G. van Oldenborgh (2017), “Estimating changes in global temperature since the pre-industrial period,” *Bulletin of the American Meteorological Society*.

147. E. Hawkins and R. Sutton (2009), “The potential to narrow uncertainty in regional climate predictions,” *Bulletin of the American Meteorological Society*, vol. 90, no. 8, pp. 1095–1107.

148. E. Hawkins and R. Sutton (2011), “The potential to narrow uncertainty in projections of regional precipitation change,” *Climate Dynamics*, vol. 37, pp. 407–418.

149. E. Hawkins and R. Sutton (2012), “Time of emergence of climate signals,”*Geophysical Research Letters*, vol. 39, no. 1.

150. M. R. Haylock, N. Hofstra, A. M. G. Klein Tank, E. J. Klok, P. D. Jones, and M. New (2008), “A European daily high-resolution gridded data set of surface temperature and precipitation for 1950—2006,” *Journal of Geophysical Research: Atmospheres*, vol. 113, no. D20.

151. G. C. Hegerl, K. Hasselmann, U. Cubasch, J. F. B. Mitchell, E. Roeckner, R. Voss, and J. Waszkewitz (1997), “Multi-fingerprint detection and attribution analysis of greenhouse gas, greenhouse gas-plus-aerosol and solar forced climate change,” *Climate Dynamics*, vol. 13, pp. 613–634.

152. R. R. Heim Aug. (2002), “A Review of Twentieth-Century Drought Indices Used in the United States,” *Bulletin of the American Meteorological Society*, vol. 83, no. 8, pp. 1149–1165.

153. H. J. H. Hendricks Franssen and S. C. Scherrer (2008), “Freezing of lakes on the Swiss plateau in the period 1901-2006,” *International Journal of Climatology*, vol. 28, no. 4, pp. 421–433.

154. N. Herger, B. M. Sanderson, and R. Knutti (2015), “Improved pattern scaling approaches for the use in climate impact studies,” *Geophysical Research Letters*, vol. 42, no. 9, pp. 3486–3494.

155. A. L. Hirsch, M. Wilhelm, E. L. Davin, W. Thiery, and S. I. Seneviratne (2017), “Can climate-effective land management reduce regional warming?,” *Journal of Geophysical Research*, vol. 122, no. 4, pp. 2269–2288.

156. M. Hirschi, S. I. Seneviratne, V. Alexandrov, F. Boberg, C. Boroneant, O. B. Christensen, H. Formayer, B. Orlowsky, and P. Stepanek (2011), “Observational evidence for soil-moisture impact on hot extremes in southeastern Europe,” *Nature Geoscience*, vol. 4, no. 1, pp. 17–21.

157. N. Hofstra, M. New, and C. McSweeney (2010), “The influence of interpolation and station network

density on the distributions and trends of climate variables in gridded daily data," *Climate dynamics*, vol. 35, no. 5, pp. 841–858.

158. C. R. Holmes, T. Woollings, E. Hawkins, and H. De Vries (2016), "Robust future changes in temperature variability under greenhouse gas forcing and the relationship with thermal advection," *Journal of Climate*, vol. 29, no. 6, pp. 2221–2236.

159. D. E. Horton, N. C. Johnson, D. Singh, D. L. Swain, B. Rajaratnam, and N. S. Diffenbaugh (2015), "Contribution of changes in atmospheric circulation patterns to extreme temperature trends," *Nature*, vol. 522, no. 7557, pp. 465–469.

160. C. Huggel, M. Carey, J. J. Clague, and A. Kääb, Eds. (2015),*The High-Mountain Cryosphere - Environmental Changes and Human Risks*, Cambridge, United Kingdom: Cambridge University Press, 363 pp.

161. J. W. Hurrell (1995), "Decadal trends in the North Atlantic Oscillation: regional temperatures and precipitation," *Science*, vol. 269, no. 5224, pp. 676–679.

162. M. Huss (2012), "Extrapolating glacier mass balance to the mountain-range scale: the European Alps 1900–2100," *The Cryosphere*, vol. 6, pp. 713–727.

163. IPCC (1990), "Climate Change. Intergovernmental Panel on Climate Change." Cambridge University Press, 365 pp.

164. IPCC (2000), "Special Report on Emissions Scenarios." Cambridge University Press, 570 pp, Geneva, Switzerland.

165. IPCC (2001), *Climate Change 2001: The Scientific Basis.Contribution of Working Group I to the Third Assessment Report of the Intergovernmental Panel on Climate Change*, Cambridge, United Kingdom and New York, NY, USA: Cambridge University Press, 881 pp.

166. IPCC (2007), *Climate Change 2007: The Scientific Basis.Contribution of Working Group I to the Fourth Assessment Report of the Intergovernmental Panel on Climate Change*, Cambridge, United Kingdom and New York, NY, USA: Cambridge University Press, 996 pp.

167. IPCC (2012), *Intergovernmental Panel on Climate Change Special Report on Managing the Risks of Extreme Events and Disasters to Advance Climate Change Adaptation*, Cambridge, United Kingdom and New York, NY, USA: Cambridge University Press, pp 582.

168. IPCC (2013), *Climate Change 2013: The Physical Science Basis. Contribution of Working Group I to the Fifth Assessment Report of the Intergovernmental Panel on Climate Change*, Cambridge, United Kingdom and New York, NY, USA: Cambridge University Press, 1535 pp.

169. IPCC (2013), "Summary for Policymakers," in *Climate Change 2013: The Physical Science Basis. Contribution of Working Group I to the Fifth Assessment Report of the Intergovernmental Panel on Climate Change*, Cambridge, United Kingdom and New York, NY, USA, pp. 1–30.

170. IPCC (2014), "Summary for Policymakers," in *Climate Change 2014: Impacts, Adaptation, and Vulnerability. Part A: Global and Sectoral Aspects. Contribution of Working Group II to the Fifth Assessment Report of the Intergovernmental Panel on Climate Change*, Cambridge, United Kingdom and New York, NY, USA, pp. 1–32.

171. ISO (2009), "ISO 31000:2009 Risk management —- Principles and guidelines," International Organization for Standardization.

172. F. A. Isotta, R. Vogel, and C. Frei (2015), "Evaluation of European regional reanalyses and downscalings for precipitation in the Alpine region," *Meteorologische Zeitschrift*, vol. 24, pp. 15–37.

173. F. A. Isotta, C. Frei, V. Weilguni, M. Percec Tadic, P. Lassegues, B. Rudolf, V. Pavan, C. Cacciamani, G. Antolini, S. M. Ratto, L. Maraldo, S. Micheletti, V. Bonati, C. Lussana, C. Ronchi, E. Panettieri, G. Marigo, and G. Vertacnik (2014), "The climate of daily precipitation in the Alps: development and analysis of a high-resolution grid dataset from pan-Alpine rain-gauge data," *International Journal of Climatology*,

vol. 34, no. 5, pp. 1657–1675.

174. M. Ivanov and S. Kotlarski (2017), “Assessing distribution-based climate model bias correction methods over an alpine domain: added value and limitations,” *International Journal of Climatology*, vol. 37, pp. 2633–2653.

175. M. A. Ivanov, J. Luterbacher, and S. Kotlarski (2018), “Climate Model Biases and Modification of the Climate Change Signal by Intensity-Dependent Bias Correction,” *Journal of Climate*, vol. 31, no. 16, pp. 6591–6610.

176. V. Y. Ivanov, R. L. Bras, and D. C. Curtis (2007), “A weather generator for hydrological, ecological, and agricultural applications,” *Water resources research*, vol. 43, no. 10.

177. D. Jacob, J. Petersen, B. Eggert, A. Alias, O. B. Christensen, L. M. Bouwer, A. Braun, A. Colette, M. Déqué, G. Georgievski, E. Georgopoulou, A. Gobiet, L. Menut, G. Nikulin, A. Haensler, N. Hempelmann, C. Jones, K. Keuler, S. Kovats, N. Kröner, S. Kotlarski, A. Kriegsmann, E. Martin, E. van Meijgaard, C. Moseley, S. Pfeifer, S. Preuschmann, C. Radermacher, K. Radtke, D. Rechid, M. Rounsevell, P. Samuelsson, S. Somot, J. F. Soussana, C. Teichmann, R. Valentini, R. Vautard, B. Weber, and P. Yiou (2014), “EURO-CORDEX: New high-resolution climate change projections for European impact research,” *Regional Environmental Change*, vol. 14, no. 2, pp. 563–578.

178. P. Jones Mar. (2016), “The reliability of global and hemispheric surface temperature records,” *Advances in Atmospheric Sciences*, vol. 33, no. 3, pp. 269–282.

179. R. W. Katz and B. G. Brown (1992), “Extreme events in a changing climate: variability is more important than averages,” *Climatic change*, vol. 21, no. 3, pp. 289–302.

180. J. E. Kay, C. Deser, A. Phillips, A. Mai, C. Hannay, G. Strand, J. M. Arblaster, S. C. Bates, G. Danabasoglu, J. Edwards, and others (2015), “The Community Earth System Model (CESM) large ensemble project: A community resource for studying climate change in the presence of internal climate variability,” *Bulletin of the American Meteorological Society*, vol. 96, no. 8, pp. 1333–1349.

181. D. E. Keller, A. M. Fischer, C. Frei, M. A. Liniger, C. Appenzeller, and R. Knutti (2015), “Implementation and validation of a Wilks-type multi-site daily precipitation generator over a typical Alpine river catchment,” *Hydrology and Earth System Sciences*, vol. 19, pp. 2163–2177.

182. D. E. Keller, A. M. Fischer, M. A. Liniger, C. Appenzeller, and R. Knutti (2017), “Testing a weather generator for downscaling climate change projections over Switzerland,” *International Journal of Climatology*, vol. 37, pp. 928–942.

183. E. J. Kendon, N. M. Roberts, C. A. Senior, and M. J. Roberts (2012), “Realism of rainfall in a very high-resolution regional climate model,” *J. Climate*, vol. 25 (17), pp. 5791–5806.

184. C. Kerkhoff, H. R. Künsch, and C. Schär Jul. (2014), “Assessment of Bias Assumptions for Climate Models,” *Journal of Climate*, vol. 27, no. 17, pp. 6799–6818.

185. C. Kerkhoff, H. R. Künsch, and C. Schär (2015), “A Bayesian Hierarchical Model for Heterogeneous RCM-GCM Multimodel Ensembles,” *Journal of Climate*, vol. 28, pp. 6249–6266.

186. C. G. Kilsby, P. D. Jones, A. Burton, A. C. Ford, H. J. Fowler, C. Harpham, P. James, A. Smith, and R. L. Wilby (2007), “A daily weather generator for use in climate change studies,” *Environmental Modelling & Software*, vol. 22, pp. 1705–1719.

187. A. D. King, M. G. Donat, E. M. Fischer, E. Hawkins, L. V. Alexander, D. J. Karoly, A. J. Dittus, S. C. Lewis, and S. E. Perkins (2015), “The timing of anthropogenic emergence in simulated climate extremes,” *Environmental Research Letters*, vol. 10, no. 9, p. 094015.

188. T. Kjellstrom, I. Holmer, and B. Lemke (2009), “Workplace heat stress, health and productivity – an increasing challenge for low and middle-income countries during climate change.,” *Global Health Action*, vol. 2.

189. G. Klein, Y. Vitasse, C. Rixen, C. Marty, and M. Rebetez (2016), “Shorter snow cover duration since 1970 in the Swiss Alps due to earlier snowmelt more than to later snow onset,” *Climatic Change*, vol. 139, no. 3-4, pp. 637–649.

190. T. R. Knutson, F. Zeng, and A. T. Wittenberg (2013), “Multimodel assessment of regional surface temperature trends: CMIP3 and CMIP5 twentieth-century simulations,” *Journal of Climate*, vol. 26, no. 22, pp. 8709–8743.

191. R. Knutti and M. A. A. Rugenstein (2015), “Feedbacks, climate sensitivity, and the limits of linear model,” *Philosophical Transactions of the Royal Society*, no. 373.

192. R. Knutti, M. Rugenstein, and G. C. Hegerl (2017), “Beyond climate sensitivity,” *in print, Nature Geoscience*.

193. R. Knutti, R. Furrer, C. Tebaldi, J. Cermak, and G. A. Meehl (2010), “Challenges in combining projections from multiple climate models,” *Journal of Climate*, vol. 23, no. 10, pp. 2739–2758.

194. R. Knutti, J. Sedlàcek, B. M. Sanderson, R. Lorenz, E. M. Fischer, and V. Eyring (2017), “A climate model projection weighting scheme accounting for performance and interdependence,” *Geophysical Research Letters*, vol. 44, no. 4, pp. 1909–1918.

195. R. D. Koster, Z. Guo, R. Yang, P. A. Dirmeyer, K. Mitchell, and M. J. Puma (2009), “On the Nature of Soil Moisture in Land Surface Models,” *Journal of Climate*, vol. 22, no. 16, pp. 4322–4335.

196. R. D. Koster and M. J. Suarez Dec. (2001), “Soil moisture memory in climate models,” *Journal of Hydrometeorology*, vol. 21, pp. 558–570.

197. S. Kotlarski, K. Keuler, O. B. Christensen, A. Colette, M. Déequée, A. Gobiet, K. Goergen, D. Jacob, D. Lüthi, E. van Meijgaard, G. Nikulin, C. Schär, C. Teichmann, R. Vautard, K. Warrach-Sagi, and V. Wulfmeyer (2014), “Regional climate modeling on European scales: a joint standard evaluation of the EURO-CORDEX RCM ensemble,” *Geoscientific Model Development*, vol. 7, no. 4, pp. 1297–1333.

198. S. Kotlarski, D. Lüthi, and C. Schär (2015), “The elevation dependency of 21st century European climate change: an RCM ensemble perspective,” *International Journal of Climatology*, vol. 35, pp. 3902–3920.

199. N. Kröner, S. Kotlarski, E. Fischer, D. Lüthi, E. Zubler, and C. Schär (2016), “Separating climate change signals into thermodynamic, lapse-rate and circulation effects: theory and application to the European summer climate,” *Climate Dynamics*, pp. 1–16.

200. H. Kunz, S. C. Scherrer, M. A. Liniger, and C. Appenzeller May (2007), “The evolution of ERA-40 surface temperatures and total ozone compared to observed Swiss time series,” *Meteorologische Zeitschrift*, vol. 16, no. 2, pp. 171–181.

201. M. Langner, K. Scherber, and W. R. Endlicher (2013), “Indoor heat stress: An assessment of human bioclimate using the UTCI in different buildings in Berlin,” *Die Erde*, vol. 144, no. 3-4, pp. 260–273.

202. J. H. Lawrimore, M. J. Menne, B. E. Gleason, C. N. Williams, D. B. Wuertz, R. S. Vose, and J. Rennie (2011), “An overview of the Global Historical Climatology Network monthly mean temperature data set, version 3,” *Journal of Geophysical Research: Atmospheres*, vol. 116, no. D19.

203. M. Lehning, P. Bartelt, B. Brown, and C. Fierz (2002), “A physical SNOWPACK model for the Swiss avalanche warning: Part III: Meteorological forcing, thin layer formation and evaluation,” *Cold Regions Science and Technology*, vol. 35, no. 3, pp. 169–184.

204. B. Lemke and T. Kjellstrom (2012), “Calculating workplace WBGT from meteorological data: a tool for climate change assessment.,” *Ind Health*, vol. 50, no. 4, pp. 267–278.

205. B. Lloyd-Hughes and M. A. Saunders (2002), “A drought climatology for Europe,” *International Journal of Climatology*, vol. 22, no. 13, pp. 1571–1592.

206. A. Lustenberger, R. Knutti, and E. M. Fischer (2013), “The potential of pattern scaling for projecting temperature-related extreme indices,” *International Journal of Climatology*.

207. J. Magnusson, D. Gustafsson, F. Hüsler, and T. Jonas (2014), “Assimilation of point SWE data into a distributed snow cover model comparing two contrasting methods,” *Water resources research*, vol. 50, no. 10, pp. 7816–7835.

208. I. Mahlstein, R. Knutti, S. Solomon, and R. W. Portmann (2011), “Early onset of significant local warming in low latitude countries,” *Environmental Research Letters*, vol. 6, no. 3.

209. K. Mahoney, M. A. Alexander, G. Thompson, J. J. Barsugli, and J. D. Scott (2012), “Changes in hail and flood risk in high-resolution simulations over Colorado’s mountains,” *Nature Clim. Change*, vol. 2, no. 2, pp. 125–131.

210. P. J. Mailier, D. B. Stephenson, C. A. T. Ferro, and K. I. Hodges (2006), “Serial clustering of extratropical cyclones,” *Monthly weather review*, vol. 134, no. 8, pp. 2224–2240.

211. D. Maraun (2013), “Bias Correction, Quantile Mapping, and Downscaling: Revisiting the Inflation Issue,” *Journal of Climate*, vol. 26, pp. 2137–2143.

212. D. Maraun, F. Wetterhall, A. M. Ireson, R. E. Chandler, E. J. Kendon, M. Widmann, S. Brienen, H. W. Rust, T. Sauter, M. Themessl, V. K. C. Venema, K. P. Chun, C. M. Goodess, R. G. Jones, C. Onof, M. Vrac, and I. Thiele-Eich (2010), “Precipitation downscaling under climate change: Recent developments to bridge the gap between dynamical models and the end user,” *Reviews of Geophysics*, vol. 48.

213. D. Maraun and M. Widmann (2015), “The representation of location by a regional climate model in complex terrain,” *Hydrology and Earth System Sciences*, vol. 19, pp. 3449–3456.

214. D. Maraun, R. Huth, J. M. Gutiérrez, D. S. Martín, M. Dubrovsky, A. Fischer, E. Hertig, P. M. M. Soares, J. Bartholy, R. Pongrácz, M. Widmann, M. J. Casado, P. Ramos, and J. Bedia (2017), “The VALUE perfect predictor experiment: evaluation of temporal variability,” *International Journal of Climatology*.

215. D. Maraun, T. G. Shepherd, M. Widmann, G. Zappa, D. Walton, J. M. Gutierrez, S. Hagemann, I. Richter, P. M. M. Soares, A. Hall, and L. O. Mearns Nov. (2017), “Towards process-informed bias correction of climate change simulations,” *Nature Clim. Change*, vol. 7, no. 11, pp. 764–773.

216. D. Maraun and M. Widmann (2018), *Statistical Downscaling and Bias Correction for Climate Research*, Cambridge University Press.

217. C. Marty (2008), “Regime shift of snow days in Switzerland,” *Geophysical research letters*, vol. 35, no. 12.

218. C. Marty, A.-M. Tilg, and T. Jonas (2017), “Recent Evidence of Large-Scale Receding Snow Water Equivalents in the European Alps,” *Journal of Hydrometeorology*, vol. 18, no. 4, pp. 1021–1031.

219. E. P. Maurer and D. W. Pierce (2014), “Bias correction can modify climate model simulated precipitation changes without adverse effect on the ensemble mean,” *Hydrology and Earth System Sciences*, vol. 18, pp. 915–925.

220. E. P. Maurer, D. L. Ficklin, and W. Wang (2016), “Technical Note: The impact of spatial scale in bias correction of climate model output for hydrologic impact studies,” *Hydrology and Earth System Sciences*, vol. 20, pp. 685–696.

221. R. W. McColl (2005), *Encyclopedia of World Geography*, vol. 1, New York, NY, USA: Facts on File, 919 pp.

222. T. B. McKee, N. J. Doesken, and J. Kleist. (1993), “The relationship of drought frequency and duration to time scales,” Anaheim, California, USA.

223. I. Medhaug, M. B. Stolpe, E. M. Fischer, and R. Knutti (2017), “Reconciling controversies about the ‘global warming hiatus’,” *Nature*, vol. 545, no. 7652, pp. 41–47.

224. G. A. Meehl, T. F. Stocker, W. D. Collins, P. Friedlingstein, A. T. Gaye, J. M. Gregory, A. Kitoh, R. Knutti, J. M. Murphy, A. Noda, S. C. B. Raper, I. G. Watterson, A. J. Weaver, and Z.-C. Zhao (2007), “Chapter 10: Global Climate Projections,” in *Climate Change 2007: The Physical Science Basis. Contribution of Working Group I to the Fourth Assessment Report of the Intergovernmental Panel on Climate Change*, S. Solomon, D. Qin, M.

Manning, Z. Chen, M. Marquis, K. B. Averyt, M. Tignor, and H. L. Miller, Eds. Cambridge Univ. Press, United Kingdom and New York, NY, USA.

225. G. A. Meehl, L. Goddard, G. Boer, R. Burgman, G. Branstator, C. Cassou, S. Corti, G. Danabasoglu, F. Doblas-Reyes, E. Hawkins, A. Karspeck, M. Kimoto, A. Kumar, D. Matei, J. Mignot, R. Msadek, A. Navarra, H. Pohlmann, M. Rienecker, T. Rosati, E. Schneider, D. Smith, R. Sutton, H. Teng, G. J. van Oldenborgh, G. Vecchi, and S. Yeager (2014), "Decadal Climate Prediction: An Update from the Trenches," *Bulletin of the American Meteorological Society*, vol. 95, no. 2, pp. 243–267.

226. MeteoSchweiz (2016), "Documentation of MeteoSwiss Grid-Data Products. Daily Precipitation (final analysis): RhiresD," MeteoSchweiz, 4 pp.

227. MeteoSwiss (1980), "Klimaregionen der Schweiz. In: Die Beobachtungsnetze der Schweizerischen Meteorologischen Anstalt. Konzept 1980.," Arbeitsberichte der MeteoSchweiz, 93.

228. MeteoSwiss (2006), "Starkniederschlagsereignis August 2005," Arbeitsbericht MeteoSchweiz, 211, 63 pp.

229. MeteoSwiss (2011), "Weather Type Classification at MeteoSwiss - Introduction of new automatic classification schemes," Arbeitsbericht MeteoSchweiz, 235, 48 pp.

230. MeteoSwiss (2016), "Analyse der Nutzerbedürfnisse zu nationalen Klimaszenarien," Fachbericht MeteoSchweiz, 258, 92 pp, 258.

231. MeteoSwiss (2018), "Klimareport 2017," Bundesamt für Meteorologie und Klimatologie MeteoSchweiz, 84 pp.

232. MeteoSwiss (2018), "Hitze und Trockenheit im Sommer 2018," Fachbericht MeteoSchweiz, to appear.

233. P. C. D. Milly and K. A. Dunne (2016), "Potential evapotranspiration and continental drying,"*Nature Climate Change*, vol. 6, no. 10, pp. 946–949.

234. P. C. D. Milly and K. A. Dunne (2017), "A Hydrologic Drying Bias in Water-Resource Impact Analyses of Anthropogenic Climate Change," *JAWRA Journal of the American Water Resources Association*, vol. 53, no. 4, pp. 822–838.

235. S.-K. Min, X. Zhang, F. W. Zwiers, and G. C. Hegerl (2011), "Human contribution to more-intense precipitation extremes," *Nature*, vol. 470, no. 7334, pp. 378–381.

236. S. Morak, G. C. Hegerl, and J. Kenyon (2011), "Detectable regional changes in the number of warm nights," *Geophysical Research Letters*, vol. 38, no. 17.

237. C. P. Morice, J. J. Kennedy, N. A. Rayner, and P. D. Jones (2012), "Quantifying uncertainties in global and regional temperature change using an ensemble of observational estimates: The HadCRUT4 data set," *Journal of Geophysical Research: Atmospheres*, vol. 117, no. D8101.

238. R. H. Moss, J. A. Edmonds, K. A. Hibbard, M. R. Manning, S. K. Rose, and et al. van Vuuren D.P. (2010), "The next generation of scenarios for climate change research and assessment," *Nature*, vol. 463, pp. 747–756.

239. B. Mueller and S. I. Seneviratne (2012), "Hot days induced by precipitation deficits at the global scale," *Proceedings of the National Academy of Sciences*, vol. 109, no. 31, pp. 12398–12403.

240. J. M. Murphy, D. M. H. Sexton, D. N. Barnett, G. S. Jones, M. J. Webb, M. Collins, and D. A. Stainforth Aug. (2004), "Quantification of modelling uncertainties in a large ensemble of climate change simulations," *Geophysical Research Letters*, vol. 430, pp. 768–772.

241. T. Mölter, D. Schindler, A. T. Albrecht, and U. Kohnle (2016), "Review on the projections of future storminess over the North Atlantic European Region," *Atmosphere*, vol. 7, no. 4, p. 60.

242. P. Nabat, S. Somot, M. Mallet, A. Sanchez-Lorenzo, and M. Wild (2014), "Contribution of anthropogenic sulfate aerosols to the changing Euro-Mediterranean climate since 1980," *Geophysical Research Letters*, vol. 41, pp. 5605–5611.

243. R. P. North, D. M. Livingstone, R. E. Hari, O. Köster, P. Niederhauser, and R. Kipfer (2013), "The physical

impact of the late 1980s climate regime shift on Swiss rivers and lakes," *Inland Waters*, vol. 3, no. 3, pp. 341–350.

244. P. A. O'Gorman and T. Schneider (2009), "The physical basis for increases in precipitation extremes in simulations of 21st-century climate change," *Proceedings of the National Academy of Sciences*, vol. 106, no. 35, pp. 14773–14777.

245. OcCC (2003), "Extremereignissse und Klimaänderung," Organe Consultatif pour les Changement Climatiques, 88 pp, Bern, Schweiz.

246. OcCC (2007), "Klimaänderung und die Schweiz 2050; Erwartete Auswirkungen auf Umwelt, Gesellschaft und Wirtschaft," OcCC and ProClim, 172 pp.

247. T. R. Oke (2002), *Boundary Layer Climates*, London, United Kingdom: Routledge.

248. B. Orlowsky and S. I. Seneviratne (2013), "Elusive drought: uncertainty in observed trends and short- and long-term CMIP5 projections," *Hydrology and Earth System Sciences*, vol. 17, no. 5, pp. 1765–1781.

249. B. Orlowsky and S. Seneviratne (2012), "Global changes in extreme events: regional and seasonal dimension," *Climatic Change*, vol. 110, no. 3, pp. 669–696.

250. R. Orth and S. I. Seneviratne Aug. (2012), "Analysis of soil moisture memory from observations in Europe," *Journal of Geophysical Research*, vol. 117, no. D15.

251. R. Orth, J. Zscheischler, and S. I. Seneviratne (2016), "Record dry summer in 2015 challenges precipitation projections in Central Europe," *Scientific reports*, vol. 6.

252. S. D. Outten and I. Esau (2013), "Extreme winds over Europe in the ENSEMBLES regional climate models," *Atmospheric Chemistry and Physics*, vol. 13, no. 10, pp. 5163–5172.

253. J. S. Pal and E. A. B. Eltahir (2016), "Future temperature in southwest Asia projected to exceed a threshold for human adaptability," *Nature Climate Change*, vol. 6, pp. 197–200.

254. H. A. Panofsky and G. W. Brier (1968), *Some Applications of Statistics to Meteorology*, Earth and Mineral Sciences Continuing Education, College of Earth and Mineral Sciences.

255. A. Paschalis, P. Molnar, S. Fatichi, and P. Burlando (2013), "A stochastic model for high-resolution space-time precipitation simulation," *Water Resources Research*, vol. 49, no. 12, pp. 8400–8417.

256. N. Peleg, S. Fatichi, A. Paschalis, P. Molnar, and P. Burlando (2017), "An advanced stochastic weather generator for simulating 2-D high-resolution climate variables," *Journal of Advances in Modeling Earth Systems*, vol. 9, pp. 1595–1627.

257. N. Peleg and E. Morin (2014), "Stochastic convective rain-field simulation using a high-resolution synoptically conditioned weather generator (HiReS-WG)," *Water Resources Research*, vol. 50, no. 3, pp. 2124–2139.

258. N. Pepin, R. S. Bradley, H. F. Diaz, M. Baraër, E. B. Caceres, N. Forsythe, H. Fowler, G. Greenwood, M. Z. Hashmi, X. D. Liu, J. R. Miller, L. Ning, A. Ohmura, E. Palazzi, I. Rangwala, W. Schöner, I. Severskiy, M. Shahgedanova, M. B. Wang, S. N. Williamson, and D. Q. Yang (2015), "Elevation-dependent warming in mountain regions of the world," *Nature Climate Change*, vol. 5, no. 5, pp. 424–430.

259. P. Pettre (1982), "On the problem of violent valley winds," *Journal of the Atmospheric Sciences*, vol. 39, no. 3, pp. 542–554.

260. S. Pfahl, P. A. O'Gorman, and E. M. Fischer (2017), "Understanding the regional pattern of projected future changes in extreme precipitation," *Nature Climate Change*, vol. 7, pp. 423–427.

261. C. Pfister (1999), *Wetternachhersage. 500 Jahre Klimavariationen und Naturkatastrophen*, Bern, Schweiz: Haupt Verlag.

262. C. Pfister (2009), "The' Disaster Gap' of the 20th Century and the Loss of Traditional Disaster Memory," *GAIA*, vol. 18, no. 3, pp. 239–246.

263. A. Philipp, C. Beck, R. Huth, and J. Jacobeit (2016), “Development and comparison of circulation type classifications using the COST 733 dataset and software,” *International Journal of climatology*, vol. 36, no. 7, pp. 2673–2691.

264. C. Photiadou, B. van den Hurk, A. van Delden, and A. Weerts Jan. (2016), “Incorporating circulation statistics in bias correction of GCM ensembles: hydrological application for the Rhine basin,” *Climate Dynamics*, vol. 46, no. 1, pp. 187–203.

265. C. Piani, J. Haerter, and E. Coppola (2010), “Statistical bias correction for daily precipitation in regional climate models over Europe,” *Theoretical and Applied Climatology*, vol. 99, pp. 187–192.

266. M. Piazza, J. Boé, L. Terray, C. Pagé, E. Sanchez-Gomez, and M. Déquée (2014), “Projected 21st century snowfall changes over the French Alps and related uncertainties,” *Climatic Change*, vol. 122, pp. 583–594.

267. A. F. Prein, A. Gobiet, and H. et al. Truhetz (2016), “Precipitation in the EURO-CORDEX 0.11° and 0.44° simulations: high resolution, high benefits?,” *Climate Dynamics*, vol. 46, pp. 383–412.

268. C. C. Raible, S. Brönnimann, R. Auchmann, P. Brohan, T. L. Frölicher, H.-F. Graf, P. Jones, J. Luterbacher, S. Muthers, R. Neukom, and others (2016), “Tambora 1815 as a test case for high impact volcanic eruptions: Earth system effects,” *Wiley Interdisciplinary Reviews: Climate Change*, vol. 7, no. 4, pp. 569–589.

269. C. C. Raible, O. Bärenbold, and J. J. Gómez-Navarro (2017), “Drought indices revisited — improving and testing of drought indices in a simulation of the last two millennia for Europe,” *Tellus A: Dynamic Meteorology and Oceanography*, vol. 69, no. 1.

270. J. Rajczak, S. Kotlarski, N. Salzmann, and C. Schär (2016), “Robust climate scenarios for sites with sparse observations: a two-step bias correction approach,” *International Journal of Climatology*, vol. 36, pp. 1226–1243.

271. J. Rajczak, S. Kotlarski, and C. Schär (2016), “Does quantile mapping of simulated precipitation correct for biases in transition probabilities and spell lengths?,” *Journal of Climate*, vol. 29, no. 5, pp. 1605–1615.

272. J. Rajczak, P. Pall, and C. Schär (2013), “Projections of extreme precipitation events in regional climate simulations for Europe and the Alpine Region,” *Journal of Geophysical Research: Atmospheres*, vol. 118, no. 9, pp. 3610–3626.

273. J. Rajczak and C. Schär (2017), “Projections of Future Precipitation Extremes over Europe: A Multimodel Assessment of Climate Simulations,” *Journal of Geophysical Research: Atmospheres*, vol. 122, pp. 1–28.

274. M. Rebetez and M. Reinhard (2008), “Monthly air temperature trends in Switzerland 1901—2000 and 1975—2004,” *Theoretical and Applied Climatology*, vol. 91, no. 1, pp. 27–34.

275. J. C. Refsgaard, H. Madsen, V. Andréassian, K. Arnbjerg-Nielsen, T. A. Davidson, M. Drews, D. P. Hamilton, E. Jeppesen, E. Kjellström, J. E. Olesen, T. O. Sonnenborg, D. Trolle, P. Willems, and J. H. Christensen Jan. (2014), “A framework for testing the ability of models to project climate change and its impacts,” *Climatic Change*, vol. 122, no. 1, pp. 271–282.

276. P. C. Reid, R. E. Hari, G. Beaugrand, D. M. Livingstone, C. Marty, D. Straile, J. Barichivich, E. Goberville, R. Adrian, Y. Aono, and others (2016), “Global impacts of the 1980s regime shift,” *Global Change Biology*, vol. 22, no. 2, pp. 682–703.

277. H. Richner, B. Dürr, T. Gutermann, and S. Bader (2014), “The use of automatic station data for continuing the long time series (1864 to 2008) of foehn in Altdorf,” *Meteorologische Zeitschrift*, vol. 23, no. 2, pp. 159–166.

278. B. Rockel and K. Woth (2007), “Extremes of near-surface wind speed over Europe and their future changes as estimated from an ensemble of RCM simulations,” *Climatic Change*, vol. 81, no. 1, pp. 267–280.

279. G. Roe (2009), “Feedbacks, Timescales, and Seeing Red,” *Annual Review of Earth and Planetary Sciences*, vol. 37, pp. 93–115.

280. R. Rohde, R. Muller, R. Jacobsen, S. Perlmutter, A. Rosenfeld, J. Wurtele, J. Curry, C. Wickhams, and M. S. (2011), "A New Estimate of the Average Earth Surface Land Temperature Spanning 1753 to 2011," *Geoinfor Geostat: An Overview*, vol. 1, no. 1.

281. D. M. Romps, J. T. Seeley, D. Vollaro, and J. Molinari Nov. (2014), "Projected increase in lightning strikes in the United States due to global warming," *Science*, vol. 346, no. 6211, pp. 851–854.

282. S. Rosser (2013), "Limits of regional predictability due to internal variability," Master Thesis, ETH Zürich, 56 pp.

283. Y. Rosskopf and S. C. Scherrer (2017), "On the relationship between fog and low stratus and weather types over the Swiss Plateau," Technical Report MeteoSwiss, 266.

284. M. Rummukainen (2016), "Added value in regional climate modeling," *Wiley Interdisciplinary Reviews: Climate Change*, vol. 7, pp. 145–159.

285. S. Russo, J. Sillmann, and E. M. Fischer (2015), "Top ten European heatwaves since 1950 and their occurrence in the coming decades," *Environmental Research Letters*, vol. 10, no. 12, p. 124003.

286. J. Räisänen (2007), "How reliable are climate models?," *Tellus*, vol. 59A, pp. 2–29.

287. O. Rössler, A. M. Fischer, H. Huebener, D. Maraun, R. E. Benestad, P. Christodoulides, P. M. M. Soares, R. M. Cardoso, C. Pagé, H. Kanamaru, F. Kreienkamp, and D. Vlachogiannis (2017), "Challenges to link climate change data provision and user needs: Perspective from the COST-action VALUE," *International Journal of Climatology*.

288. O. Rössler, A. Fischer, S. Kotlarski, D. Keller, M. Liniger, and R. Weingartner (2017), "Spoilt for Choice: Which downscaling approach to use for hydrological projections," *International Journal of Climatology*, vol. submitted.

289. C. Saffioti, E. M. Fischer, and R. Knutti (2017), "Improved consistency of climate projections over Europe after accounting for atmospheric circulation variability," *Journal of Climate*, no. 2017.

290. C. Saffioti, E. M. Fischer, S. C. Scherrer, and R. Knutti (2016), "Reconciling observed and modeled temperature and precipitation trends over Europe by adjusting for circulation variability," *Geophysical Research Letters*, vol. 43, no. 15, pp. 8189–8198.

291. A. Sanchez-Lorenzo and M. Wild (2012), "Decadal variations in estimated surface solar radiation over Switzerland since the late 19th century," *Atmospheric Chemistry and Physics*, vol. 12, no. 18, pp. 8635–8644.

292. B. N. Sanderson, M. Wehner, and R. Knutti (2017), "Skill and independence weighting for multi-model assessments," *Geoscientific Model Development*, vol. 10, no. 6, pp. 2379–2395.

293. S. C. Scherrer, P. Ceppi, M. Croci-Maspoli, and C. Appenzeller (2012), "Snow-albedo feedback and Swiss spring temperature trends," *Theoretical and applied climatology*, vol. 110, no. 4, pp. 509–516.

294. S. C. Scherrer and C. Appenzeller (2006), "Swiss Alpine snow pack variability: major patterns and links to local climate and large-scale flow," *Climate Research*, vol. 32, no. 3, pp. 187–199.

295. S. C. Scherrer and C. Appenzeller (2014), "Fog and low stratus over the Swiss Plateau- a climatological study," *International Journal of Climatology*, vol. 34, no. 3, pp. 678–686.

296. S. C. Scherrer, C. Appenzeller, and M. Laternser (2004), "Trends in Swiss Alpine snow days: The role of local-and large-scale climate variability," *Geophysical Research Letters*, vol. 31, no. 13215.

297. S. C. Scherrer, M. Begert, M. Croci-Maspoli, and C. Appenzeller (2016), "Long series of Swiss seasonal precipitation: regionalization, trends and influence of large-scale flow," *International Journal of Climatology*, vol. 36, no. 11, pp. 3673–3689.

298. S. C. Scherrer, E. M. Fischer, R. Posselt, M. A. Liniger, M. Croci-Maspoli, and R. Knutti (2016), "Emerging trends in heavy precipitation and hot temperature extremes in Switzerland," *Journal of Geophysical*

Research: Atmospheres, vol. 121, no. 6, pp. 2626–2637.

299. S. C. Scherrer, C. Wüthrich, M. Croci-Maspoli, R. Weingartner, and C. Appenzeller (2013), "Snow variability in the Swiss Alps 1864—2009," *International journal of climatology*, vol. 33, no. 15, pp. 3162–3173.

300. M. Schultze and B. Rockel (2017), "Direct and semi-direct effects of aerosol climatologies on long-term climate simulations over Europe," *Climate Dynamics*.

301. A. P. Schurer, M. E. Mann, E. Hawkins, S. F. B. Tett, and G. C. Heger (2017), "Importance of the pre-industrial baseline for likelihood of exceeding Paris goals," *Nature Climate Change*, vol. 7.

302. M. Schwarb, C. Daly, C. Frei, and C. Schär (2001), "Mean annual precipitation throughout the European Alps, 1971—1990," *Hydrologic atlas of Switzerland (Plate 2.6)*, pp. 2–6.

303. C. Schwierz, P. Köllner-Heck, E. Z. Mutter, D. N. Bresch, P.-L. Vidale, M. Wild, and C. Schär (2010), "Modelling European winter wind storm losses in current and future climate," *Climatic Change*, vol. 101, no. 3-4, pp. 485–514.

304. C. Schär, H. C. Davies, and H. Wanner (1998), "Present Alpine climate," in *Views from the Alps: Regional perspectives on climate change*, P. Cebon, U. Dahinden, H. C. Davies, D. M. Imboden, and C. C. Jäger, Eds. Boston, USA: MIT Press, pp. 21–72.

305. C. Schär, N. Ban, E. M. Fischer, J. Rajczak, J. Schmidli, C. Frei, F. Giorgi, T. R. Karl, E. J. Kendon, A. M. G. Klein Tank, P. A. O'Gorman, J. Sillmann, X. Zhang, and F. W. Zwiers (2016), "Percentile indices for assessing changes in heavy precipitation events," *Climatic Change*, vol. 137, no. 1, pp. 201–216.

306. C. Schär, P. L. Vidale, D. Lüthi, C. Frei, C. Häberli, M. A. Liniger, and C. Appenzeller (2004), "The role of increasing temperature variability in European summer heatwaves," *Nature*, vol. 427, no. 6972, pp. 332–336.

307. SCNAT (2016), *Brennpunkt Klima Schweiz. Grundlagen, Folgen und Perspektiven*, vol. 11 (5), Swiss Academies Reports.

308. J. A. Screen (2014), "Arctic amplification decreases temperature variance in northern mid-to high-latitudes," *Nature Climate Change*, vol. 4, no. 7, pp. 577–582.

309. S. I. Seneviratne, R. Orth, S. Jörg-Hess, S. Kruse, I. Seidl, M. Stähli, M. Zappa, J. Seibert, M. Staudinger, K. Stahl, and M. Weiler (2013), "Trockenheit in der Schweiz - Ergebnisse des NFP-61-Projekts DROUGHT-CH," *Aqua & Gas*, vol. 9, pp. 38–47.

310. S. I. Seneviratne, R. D. Koster, Z. Guo, P. A. Dirmeyer, E. Kowalczyk, D. Lawrence, P. Liu, C. H. Lu, D. Mocko, K. W. Oleson, and D. Verseghy (2006), "Soil Moisture Memory in AGCM Simulations: Analysis of Global Land-Atmosphere Coupling Experiment (GLACE) Data," *Journal of Hydrometeorology*, vol. 7, no. 5, pp. 1090–1112.

311. S. I. Seneviratne, N. Nicholls, D. Easterling, C. M. Goodess, S. Kanae, J. Kossin, Y. Luo, J. Marengo, K. McInnes, M. Rahimi, M. Reichstein, A. Sorteberg, C. Vera, and X. Zhang (2012), "Changes in climate extremes and their impacts on the natural physical environment," in *Managing the Risks of Extreme Events and Disasters to Advance Climate Change Adaptation*, C. B. Field, V. Barros, T. F. Stocker, D. Qin, D. J. Dokken, K. L. Ebi, M. D. Mastrandrea, K. J. Mach, G.-K. Plattner, S. K. Allen, M. Tignor, and P. M. Midgley, Eds. Cambridge, United Kingdom and New York, NY, USA.: Cambridge University Press, pp. 109–230.

312. S. I. Seneviratne, M. G. Donat, A. J. Pitman, R. Knutti, and R. L. Wilby (2016), "Allowable CO2 emissions based on regional and impact-related climate targets," *Nature*, vol. 529, no. 7587, pp. 477–483.

313. S. I. Seneviratne, D. Lüthi, M. Litschi, and C. Schär (2006), "Land-atmosphere coupling and climate change in Europe," *Nature*, vol. 443, no. 7108, pp. 205–209.

314. S. I. Seneviratne (2012), "Climate science: Historical drought trends revisited," *Nature*, vol. 491, no. 7424, pp. 338–339.

315. S. I. Seneviratne, T. Corti, E. L. Davin, M. Hirschi, E. B. Jaeger, I. Lehner, B. Orlowsky, and A. J. Teuling (2010), “Investigating soil moisture-climate interactions in a changing climate: A review,” *Earth-Science Reviews*, vol. 99, no. 3-4, pp. 125–161.

316. G. Serquet, C. Marty, and M. Dulex J.-P.and Rebetz (2011), “Seasonal trends and temperature dependence of the snowfall/precipitation-day ratio in Switzerland,” *Geophysical Research Letters*, vol. 38, p. L07703.

317. SGHL and CHy (2011), *Auswirkungen der Klimaänderung auf die Wasserkraftnutzung – Synthesebericht. Beiträge zur Hydrologie der Schweiz*, no. 38, Bern, Schweiz: Schweizerische Gesellschaft für Hydrologie und Limnologie (SGHL) und Hydrologische Kommission (CHy), 28 pp.

318. R. Shapiro (1970), “Smoothing, filtering, and boundary effects,” *Reviews of Geophysics*, vol. 8, no. 2, pp. 359–387.

319. T. A. Shaw, M. Baldwin, E. A. Barnes, R. Caballero, C. I. Garfinkel, Y.-T. Hwang, C. Li, P. A. O’Gorman, G. Rivière, I. R. Simpson, and A. Voigt Aug. (2016), “Storm track processes and the opposing influences of climate change,” *Nature Geoscience*, vol. 9, pp. 656–664.

320. J. Sheffield, E. F. Wood, and M. L. Roderick (2012), “Little change in global drought over the past 60 years,” *Nature*, vol. 491, pp. 435–438.

321. S. C. Sherwood and M. Huber (2010), “An adaptability limit to climate change due to heat stress,” *Proceedings of the National Academy of Sciences*, vol. 107, no. 21, pp. 9552–9555.

322. J. Sillmann, V. V. Kharin, F. W. Zwiers, X. Zhang, and D. Bronaugh (2013), “Climate extremes indices in the CMIP5 multimodel ensemble: Part 2. Future climate projections,” *Journal of Geophysical Research: Atmospheres*, vol. 118, no. 6, pp. 2473–2493.

323. J. Sillmann, L. Pozzoli, E. Vignati, S. Kloster, and J. Feichter (2013), “Aerosol effect on climate extremes in Europe under different future scenarios,” *Geophysical Research Letters*, vol. 40, no. 10, pp. 2290–2295.

324. C. Simolo, M. Brunetti, M. Maugeri, and T. Nanni (2011), “Evolution of extreme temperatures in a warming climate,” *Geophysical Research Letters*, vol. 38, no. 16.

325. M. Skelton, J. J. Porter, S. Dessai, D. N. Bresch, and R. Knutti (2017), “The social and scientific values that shape national climate scenarios: A comparison of the Netherlands, Switzerland and the UK,” *Regional Environmental Change*, vol. 3, no. 1.

326. G. Smiatek, H. Kunstmann, and A. Senatore (2016), “EURO-CORDEX regional climate model analysis for the Greater Alpine Region: Performance and expected future change,” *Journal of Geophysical Research*, vol. 121.

327. R. B. Smith (1987), “Aerial observations of the Yugoslavian bora,” *Journal of the Atmospheric Sciences*, vol. 44, no. 2, pp. 269–297.

328. M. Souvignet, F. Wieneke, L. Müller, and D. N. Bresch (2016), “Economics of Climate Adaptation (ECA) - Guidebook for Practitioners,” *Materials on Development Financing*, vol. 6.

329. M. Sprenger, B. Dürr, and H. Richner (2016), “From weather observations to atmospheric and climate sciences in Switzerland,” S. Willemse and M. Furger, Eds. Zurich, Switzerland: vdf, pp. 215–247.

330. T. F. Stocker, D. Qin, G.-K. Plattner, L. V. Alexander, S. K. Allen, N. L. Bindoff, F.-M. Bréon, J. A. Church, U. Cubasch, S. Emori, P. Forster, P. Friedlingstein, N. Gillett, J. M. Gregory, D. L. Hartmann, E. Jansen, B. Kirtman, R. Knutti, K. Krishna Kumar, P. Lemke, J. Marotzke, V. Masson-Delmotte, G. A. Meehl, I. I. Mokhov, S. Piao, V. Ramaswamy, D. Randall, M. Rhein, M. Rojas, C. Sabine, D. Shindell, L. D. Talley, D. G. Vaughan, and S.-P. Xie (2013), “Technical Summary,” in *Climate Change 2013: The Physical Science Basis. Contribution of Working Group I to the Fifth Assessment Report of the Intergovernmental Panel on Climate Change*, Cambridge, United Kingdom and New York, NY, USA, pp. 33–115.

331. P. A. Stott (2003), “Attribution of regional-scale temperature changes to anthropogenic and natural causes,” *Geophysical Research Letters*, vol. 30, no. 14.

332. P. Stucki, S. Brönnimann, O. Martius, C. Welker, M. Imhof, N. von Wattenwyl, and N. Philipp (2014), "A catalog of high-impact windstorms in Switzerland since 1859," *Natural Hazards and Earth System Sciences*, vol. 14, no. 11, pp. 2867–2882.

333. R. Stull (2011), "Wet-Bulb Temperature from Relative Humidity and Air Temperature," *Journal of Applied Meteorology and Climatology*, vol. 50, no. 11, pp. 2267–2269.

334. M. B. Switanek, P. A. Troch, C. L. Castro, A. Leuprecht, H.-I. Chang, R. Mukherjee, and E. M. C. Demaria (2017), "Scaled distribution mapping: a bias correction method that preserves raw climate model projected changes," *Hydrology and Earth System Sciences*, vol. 21, pp. 2649–2666.

335. S. L. Sørland, C. Schär, D. Lüthi, and E. Kjellström (2018), "Bias patterns and climate change signals in GCM-RCM model chains," *Environmental Research Letters*, vol. 13, no. 7.

336. K. E. Taylor, R. J. Stouffer, and M. G.A. (2022), "An Overview of CMIP5 and the Experiment Design," *Bulletin of the American Meteorological Society*, vol. 93, pp. 485–498.

337. C. Tebaldi, K. Hayhoe, J. M. Arblaster, and G. A. Meehl Dec. (2006), "Going to the Extremes. An Intercomparison of Model-Simulated Historical and Future Changes in Extreme Events," *Climatic Change*, vol. 79, no. 3—4, pp. 185–211.

338. C. Tebaldi and R. Knutti Aug. (2007), "The use of the multi-model ensemble in probabilistic climate projections," *Philosophical Transactions of the Royal Society A*, vol. 365, no. 1857, pp. 2053–2075.

339. M. Themessl, A. Gobiet, and G. Heinrich (2012), "Empirical-statistical downscaling and error correction of regional climate models and its impact on the climate change signal," *Climatic Change*, vol. 112, pp. 449–468.

340. M. J. Themessl, A. Gobiet, and A. Leuprecht (2011), "Empirical-statistical downscaling and error correction of daily precipitation from regional climate models," *International Journal of Climatology*, vol. 31, pp. 1530–1544.

341. W. Thiery, E. L. Davin, D. M. Lawrence, A. L. Hirsch, M. Hauser, and S. I. Seneviratne (2017), "Present-day irrigation mitigates heat extremes," *Journal of Geophysical Research*, vol. 122, no. 3, pp. 1403–1422.

342. D. W. J. Thompson, E. A. Barnes, C. Deser, W. E. Foust, and A. S. Phillips (2015), "Quantifying the role of internal climate variability in future climate trends," *Journal of Climate*, vol. 28, no. 16, pp. 6443–6456.

343. C. W. Thornthwaite (1948), "An approach toward a rational classification of climate," *Geographical review*, vol. 38, no. 1, pp. 55–94.

344. C. Torma, F. Giorgi, and E. Coppola (2015), "Added value of regional climate modeling over areas characterized by complex terrain—Precipitation over the Alps," *Journal of Geophysical Research*, vol. 120.

345. M. Trachsel, C. Kamenik, M. Grosjean, D. McCarroll, A. Moberg, R. Bràzdil, U. Büntgen, P. Dobrovolny, J. Esper, D. C. Frank, M. Friedrich, R. Glaser, I. Larocque-Tobler, K. Nicolussi, and D. Riemann (2012), "Multi-archive summer temperature reconstruction for the European Alps, AD 1053—1996," *Quaternary Science Reviews*, vol. 46, pp. 66–79.

346. K. E. Trenberth, A. Dai, R. M. Rasmussen, and D. B. Parsons (2003), "The changing character of precipitation," *Bulletin of the American Meteorological Society*, vol. 84, no. 9, pp. 1205–1217.

347. A. Umbricht, S. Fukutome, M. A. Liniger, C. Frei, and A. C. (2013), "Seasonal variation of daily extreme precipitation in Switzerland," Scientific Report MeteoSwiss, 97.

348. UNDP (2016), "Climate change and Labour: impacts of heat in the workplace. ," Geneva, CVF Secretariat, United Nations Development Program.

349. UNFCCC (2015), "Adoption of the Paris Agreement," no. FCCC/CP/2015/10/Add.1., Paris, France.

350. T. Usbeck, T. Wohlgemuth, C. Pfister, R. Volz, M. Beniston, and M. Dobbertin (2010), "Wind speed measurements and forest damage in Canton Zurich (Central Europe) from 1891 to winter 2007,"

International Journal of Climatology, vol. 30, no. 3, pp. 347–358.

351. E. J. M. van den Besselaar, A. Sanchez-Lorenzo, M. Wild, A. M. G. Klein Tank, and A. T. J. de Laat (2015), "Relationship between sunshine duration and temperature trends across Europe since the second half of the twentieth century," *Journal of Geophysical Research: Atmospheres*, vol. 120, no. 20, pp. 10,823–10,836.

352. P. van der Linden and J. F. B. Mitchell (2009), "ENSEMBLES:Climate Change and its Impacts: Summary of research and results from the ENSEMBLES project," Met Office Hadley Center, Exeter, UK.

353. A. P. Van Ulden and G. J. Van Oldenborgh (2006), "Large-scale atmospheric circulation biases and changes in global climate model simulations and their importance for climate change in Central Europe," *Atmospheric Chemistry and Physics*, vol. 6, no. 4, pp. 863–881.

354. R. Vautard, A. Gobiet, D. Jacob, M. Belda, A. Colette, M. Déqué, J. Fernández, M. García-Díez, K. Goergen, I. Güttler, T. Halenka, T. Karacostas, E. Katragkou, K. Keuler, S. Kotlarski, S. Mayer, E. van Meijgaard, G. Nikulin, M. Patarčić, J. Scinocca, S. Sobolowski, M. Suklitsch, C. Teichmann, K. Warrach-Sagi, V. Wulfmeyer, and P. Yiou (2013), "The simulation of European heat waves from an ensemble of regional climate models within the EURO-CORDEX project," *Climate Dynamics*, vol. 41, pp. 2555–2575.

355. R. Vautard, A. Gobiet, S. Sobolowski, E. Kjellström, A. Stegehuis, P. Watkiss, T. Mendlik, O. Landgren, G. Nikulin, C. Teichmann, and others (2014), "The European climate under a 2°C global warming," *Environmental Research Letters*, vol. 9, no. 3.

356. R. Vautard, P. Yiou, F. D'Andrea, N. de Noblet, N. Viovy, C. Cassou, J. Polcher, P. Ciais, M. Kageyama, and Y. Fan (2007), "Summertime European heat and drought waves induced by wintertime Mediterranean rainfall deficit," *Geophysical Research Letters*, vol. 34, no. L07711, pp. 1–5.

357. S. M. Vicente-Serrano, S. Beguería, and J. I. López-Moreno (2010), "A multiscalar drought index sensitive to global warming: the standardized precipitation evapotranspiration index," *Journal of climate*, vol. 23, no. 7, pp. 1696–1718.

358. P. L. Vidale, D. Lüthi, R. Wegmann, and C. Schär (2007), "European summer climate variability in a heterogeneous multi-model ensemble," *Climatic Change*, vol. 81, no. Suppl 1, pp. 209–232.

359. M. M. Vogel, R. Orth, F. Cheruy, S. Hagemann, R. Lorenz, B. J. J. M. van den Hurk, and S. I. Seneviratne (2017), "Regional amplification of projected changes in extreme temperatures strongly controlled by soil moisture-temperature feedbacks," *Geophysical Research Letters*, vol. 44, no. 3, pp. 1511–1519.

360. C. Volosciuk, D. Maraun, M. Vrac, and M. Widmann (2017), "A combined statistical bias correction and stochastic downscaling method for precipitation," *Hydrology and Earth System Sciences*, vol. 21, pp. 1693–1719.

361. L. von Dach (2008), "Nebelhäufigkeit in der Schweiz - Entwicklung und Trends im Winterhalbjahr von 1864 bis 2006," Diploma Thesis, University of Bern, 147 pp.

362. M. Vrac and P. Friederichs Jan. (2015), "Multivariate—Intervariable, Spatial, and Temporal—Bias Correction," *Journal of Climate*, vol. 28, no. 1, pp. 218–237.

363. G. T. Walker and E. W. Bliss (1932), "World weather V," *Memoirs of the Royal Meteorological Society*, vol. 4, pp. 53–84.

364. J. M. Wallace and D. S. Gutzler (1981), "Teleconnections in the geopotential height field during the Northern Hemisphere winter," *Monthly Weather Review*, vol. 109, no. 4, pp. 784–812.

365. J. Wang, H.-M. Kim, and E. K. M. Chang (2017), "Changes in Northern Hemisphere Winter Storm Tracks under the Background of Arctic Amplification," *Journal of Climate*, vol. 30, no. 10, pp. 3705–3724.

366. H. Wanner and M. Furger (1990), "The bise—climatology of a regional wind north of the Alps," *Meteorology and Atmospheric Physics*, vol. 43, no. 1, pp. 105–115.

367. H. Wanner, J. Beer, J. Bütikofer, T. J. Crowley, U. Cubasch, J. Flückiger, H. Goosse, M. Grosjean, F. Joos, J. O.

Kaplan, and others (2008), “Mid-to Late Holocene climate change: an overview,” *Quaternary Science Reviews*, vol. 27, no. 19, pp. 1791–1828.

368. H. Wanner, S. Brönnimann, C. Casty, D. Gyalistras, J. Luterbacher, C. Schmutz, D. B. Stephenson, and E. Xoplaki (2001), “North Atlantic Oscillation—concepts and studies,” *Surveys in Geophysics*, vol. 22, no. 4, pp. 321–381.

369. A. Weigel, R. Knutti, M. Liniger, and C. Appenzeller (2010), “Risks of Model Weighting in Multimodel Climate Projections,” *Journal of Climate*, vol. 22, pp. 4175–4191.

370. C. Welker and O. Martius (2014), “Decadal-scale variability in hazardous winds in northern Switzerland since end of the 19th century,” *Atmospheric Science Letters*, vol. 15, no. 2, pp. 86–91.

371. S. Westra, L. V. Alexander, and F. W. Zwiers (2013), “Global increasing trends in annual maximum daily precipitation,” *Journal of Climate*, vol. 26, no. 11, pp. 3904–3918.

372. F. Wetterhall, F. Pappenberger, Y. He, J. Freer, and H. L. Cloke (2012), “Conditioning model output statistics of regional climate model precipitation on circulation patterns,” *Nonlinear Processes in Geophysics*, vol. 19, pp. 623–633.

373. K. Whan, J. Zscheischler, R. Orth, M. Shongwe, M. Rahimi, E. O. Asare, and S. I. Seneviratne (2015), “Impact of soil moisture on extreme maximum temperatures in Europe,” *Weather and Climate Extremes*, vol. 9, pp. 57–67.

374. R. L. Wilby and S. Dessai (2010), “Robust adaptation to climate change,” *Weather*, vol. 65, pp. 180–185.

375. R. L. Wilby and H. J. Fowler (2011), “Regional Climate Downscaling,” in *Modelling the Impact of Climate Change on Water Resources*, F. Fung, A. Lopez, and M. New, Eds. Blackwell Publishing Ltd., pp. 34–85.

376. R. L. Wilby and T. M. L. Wigley (1997), “Downscaling general circulation model output: a review of methods and limitations,” *Progress in Physical Geography*, vol. 21, no. 4, pp. 530–548.

377. R. A. Wilcke, T. Mendlik, and A. Gobiet (2013), “Multi-variable error correction of regional climate models,” *Climatic Change*, vol. 120, pp. 871–887.

378. M. Wild (2009), “Global dimming and brightening: A review,” *Journal of Geophysical Research: Atmospheres*, vol. 114, no. D10.

379. M. Wild (2016), “Decadal changes in radiative fluxes at land and ocean surfaces and their relevance for global warming,” *Wiley Interdisciplinary Reviews: Climate Change*, vol. 7, no. 1, pp. 91–107.

380. M. Wild, H. Gilgen, A. Roesch, A. Ohmura, C. N. Long, E. G. Dutton, B. Forgan, A. Kallis, V. Russak, and A. Tsvetkov (2005), “From dimming to brightening: Decadal changes in solar radiation at Earth’s surface,” *Science*, vol. 308, no. 5723, pp. 847–850.

381. D. A. Wilhite (2000), “Drought: A Global Assessment,” D. A. Wilhite, Ed. London, United Kingdom: Routledge, pp. 3–18.

382. D. S. Wilks (1998), “Multisite generalization of a daily stochastic precipitation generation model,” *Journal of Hydrology*, vol. 210, pp. 178–191.

383. D. S. Wilks and R. L. Wilby (1999), “The weather generation game: a review of stochastic weather models,” *Prog. Phys. Geogr.*, vol. 23, pp. 329–357.

384. K. J.-P. M. Winter, S. Kotlarski, S. C. Scherrer, and C. Schär (2017), “The Alpine snow-albedo feedback in regional climate models,” *Climate Dynamics*, vol. 48, pp. 1109–1124.

385. A. W. Wood, L. R. Leung, V. Sridhar, and D. P. Lettenmaier (2004), “Hydrologic implications of dynamical and statistical approaches to downscaling climate model outputs,” *Climatic Change*, vol. 62, pp. 189–216.

386. J. Xiang, P. Bi, D. Pisaniello, and A. Hansen (2014), “Health Impacts of Workplace Heat Exposure: An Epidemiological Review,” *Industrial Health*, vol. 52, no. 2, pp. 91–101.

387. W. Yang, M. Gardelin, J. Olsson, and T. Bosshard Sep. (2015), “Multi-variable bias correction: application of forest fire risk in present and future climate in Sweden,” *Natural Hazards and Earth System Science*, vol. 15, no. 9, pp. 2037–2057.

388. S. Yue, P. Pilon, and G. Cavadias (2002), “Power of the Mann—Kendall and Spearman’s rho tests for detecting monotonic trends in hydrological series,” *Journal of Hydrology*, vol. 259, no. 1, pp. 254–271.

389. G. Zappa, L. C. Shaffrey, K. I. Hodges, P. G. Sansom, and D. B. Stephenson (2013), “A multimodel assessment of future projections of North Atlantic and European extratropical cyclones in the CMIP5 climate models,” *Journal of Climate*, vol. 26, no. 16, pp. 5846–5862.

390. G. Zappa and T. G. Shepherd (2017), “Storylines of Atmospheric Circulation Change for European Regional Climate Impact Assessment,” *Journal of Climate*, vol. 30, no. 16, pp. 6561–6577.

391. M. Zemp, W. Haeberli, H. M, and F. Paul (2006), “Alpine glaciers to disappear within decades?,” *Geophysical Research Letters*, vol. 33, no. L13504.

392. X. Zhang, L. Alexander, G. C. Hegerl, P. Jones, A. K. Tank, T. C. Peterson, B. Trewin, and F. W. Zwiers (2011), “Indices for monitoring changes in extremes based on daily temperature and precipitation data,” *Wiley Interdisciplinary Reviews: Climate Change*, vol. 2, no. 6, pp. 851–870.

393. X. Zhang, H. Wan, F. W. Zwiers, G. C. Hegerl, and S.-K. Min (2013), “Attributing intensification of precipitation extremes to human influence,” *Geophysical Research Letters*, vol. 40, no. 19, pp. 5252–5257.

394. T. Zhao, J. C. Bennett, Q. J. Wang, A. Schepen, A. W. Wood, D. E. Robertson, and M.-H. Ramos (2017), “How Suitable is Quantile Mapping For Postprocessing GCM Precipitation Forecasts?,” *Journal of Climate*, vol. 30, no. 9, pp. 3185–3196.

395. O. Zolina, C. Simmer, S. K. Gulev, and S. Kollet (2010), “Changing structure of European precipitation: longer wet periods leading to more abundant rainfalls,” *Geophysical Research Letters*, vol. 37, no. 6.

396. E. M. Zubler, A. M. Fischer, F. Fröb, and M. A. Liniger (2016), “Climate change signals of CMIP5 general circulation models over the Alps – impact of model selection,” *International Journal of Climatology*, vol. 36, pp. 3088–3104.

397. E. M. Zubler, U. Lohmann, D. Lüthi, and C. Schär (2011), “Intercomparison of aerosol climatologies for use in a regional climate model over Europe ,” *Geophysical Research Letters*, vol. 38.

398. E. M. Zubler, S. C. Scherrer, M. Croci-Maspoli, M. A. Liniger, and C. Appenzeller (2014), “Key climate indices in Switzerland; expected changes in a future climate,” *Climatic change*, vol. 123, no. 2, pp. 255–271.

399. F. W. Zwiers, X. Zhang, and Y. Feng (2011), “Anthropogenic influence on long return period daily temperature extremes at regional scales,” *Journal of Climate*, vol. 24, no. 3, pp. 881–892.

Appendix A:

A.1. Appendix: Key climate indicators

Table 13.1. Changes in key climate indicators for RCP8.5. The columns show regional averages for Northeastern Switzerland (CHNE), western Switzerland (CHW), southern Switzerland (CHS), the western Swiss Alps (CHAW), and the eastern Swiss Alps (CHAE), as well as the median value across all regions (CH).

Year	CHNE	CHW	CHS	CHAE	CHAW	CH
Annual mean temperature (°C)						
2035	+1.2 (+0.7 to +1.7)	+1.2 (+0.7 to +1.6)	+1.4 (+0.9 to +1.9)	+1.5 (+0.9 to +2.0)	+1.5 (+1.0 to +2.0)	+1.4 (+0.9 to +1.9)
2060	+2.3 (+1.8 to +3.2)	+2.3 (+1.8 to +3.1)	+2.6 (+2.0 to +3.3)	+2.8 (+2.0 to +3.7)	+2.8 (+2.0 to +3.6)	+2.6 (+2.0 to +3.3)
2085	+3.9 (+3.0 to +5.0)	+3.8 (+3.0 to +5.0)	+4.3 (+3.3 to +5.4)	+4.5 (+3.4 to +5.7)	+4.5 (+3.4 to +5.6)	+4.3 (+3.3 to +5.4)
Summer temperature (°C)						
2035	+1.4 (+0.9 to +2.1)	+1.5 (+0.9 to +2.2)	+1.6 (+1.2 to +2.3)	+1.7 (+1.2 to +2.5)	+1.7 (+1.2 to +2.6)	+1.6 (+1.2 to +2.3)
2060	+2.5 (+2.1 to +4.1)	+2.6 (+2.2 to +4.4)	+2.9 (+2.3 to +4.2)	+3.3 (+2.5 to +4.8)	+3.4 (+2.6 to +4.9)	+2.9 (+2.3 to +4.4)
2085	+4.5 (+3.4 to +7.0)	+4.6 (+3.5 to +7.2)	+5.0 (+4.1 to +7.0)	+5.3 (+4.1 to +7.2)	+5.5 (+4.3 to +7.3)	+5.0 (+4.1 to +7.2)
Summer precipitation (%)						
2035	-3 (-15 to +8)	-4 (-20 to +5)	-5 (-13 to +10)	-1 (-6 to +9)	-6 (-11 to +7)	-4 (-13 to +8)
2060	-8 (-25 to +9)	-11 (-32 to +0)	-12 (-25 to +11)	-5 (-14 to +16)	-13 (-21 to +4)	-11 (-25 to +9)
2085	-17 (-39 to -5)	-24 (-43 to -10)	-23 (-40 to +2)	-10 (-27 to +11)	-21 (-35 to +2)	-21 (-39 to +2)
Consecutive Dry Days (CDD) (days)						
2035	+1 (-1 to +3)	+1 (-0 to +3)	+0 (-1 to +3)	+0 (-1 to +1)	+1 (-1 to +2)	+1 (-1 to +3)
2060	+1 (-0 to +9)	+2 (+0 to +9)	+1 (-1 to +9)	+1 (-1 to +3)	+1 (-0 to +5)	+1 (-0 to +9)
2085	+3 (+1 to +10)	+4 (+1 to +9)	+3 (+0 to +14)	+1 (-0 to +5)	+2 (+1 to +8)	+3 (+1 to +9)

Year	CHNE	CHW	CHS	CHAE	CHAW	CH
Hottest day of the year (*TXx*) (°C)						
2035	+1.8 (+1.2 to +3.5)	+1.8 (+1.2 to +3.5)	+1.7 (+1.1 to +3.1)	+2.0 (+1.4 to +3.2)	+2.0 (+1.4 to +3.0)	+1.8 (+1.2 to +3.2)
2060	+3.4 (+1.4 to +5.7)	+3.5 (+1.8 to +6.1)	+3.3 (+2.2 to +4.5)	+3.6 (+2.0 to +5.7)	+3.6 (+2.1 to +5.5)	+3.5 (+2.0 to +5.7)
2085	+5.4 (+3.9 to +9.2)	+6.1 (+3.9 to +9.4)	+6.1 (+3.6 to +7.6)	+5.8 (+3.7 to +8.5)	+5.8 (+3.9 to +8.7)	+5.8 (+3.9 to +8.7)
Very hot days (*TX99P*) (days)						
2035	+2 (+1 to +6)	+2 (+1 to +6)	+2 (+1 to +6)	+3 (+1 to +11)	+3 (+1 to +9)	+2 (+1 to +6)
2060	+5 (+3 to +13)	+6 (+3 to +13)	+7 (+3 to +17)	+10 (+5 to +24)	+9 (+4 to +20)	+7 (+3 to +17)
2085	+12 (+8 to +30)	+14 (+9 to +28)	+22 (+13 to +37)	+21 (+13 to +47)	+22 (+12 to +43)	+21 (+12 to +37)
Winter temperature (°C)						
2035	+1.4 (+0.5 to +2.1)	+1.4 (+0.5 to +1.9)	+1.4 (+0.6 to +2.2)	+1.4 (+0.6 to +2.4)	+1.4 (+0.7 to +2.1)	+1.4 (+0.6 to +2.1)
2060	+2.4 (+1.8 to +2.9)	+2.3 (+1.8 to +2.6)	+2.4 (+1.8 to +3.3)	+2.5 (+1.8 to +3.8)	+2.4 (+1.7 to +3.5)	+2.4 (+1.8 to +3.3)
2085	+3.8 (+3.1 to +5.0)	+3.7 (+2.9 to +4.8)	+3.8 (+3.2 to +5.4)	+3.9 (+3.1 to +5.6)	+3.9 (+3.1 to +5.6)	+3.8 (+3.1 to +5.4)
Winter precipitation (%)						
2035	+8 (-3 to +18)	+10 (-1 to +16)	+4 (-9 to +22)	+6 (+0 to +15)	+9 (-1 to +15)	+8 (-1 to +16)
2060	+10 (+0 to +24)	+7 (+0 to +21)	+9 (-13 to +26)	+7 (-4 to +21)	+8 (-3 to +16)	+8 (-3 to +21)
2085	+14 (+2 to +27)	+15 (+5 to +24)	+22 (+6 to +38)	+17 (-2 to +24)	+12 (+0 to +18)	+15 (+2 to +24)

Year	CHNE	CHW	CHS	CHAE	CHAW	CH
Annual maximum daily precipitation event (Summer) (%)						
2035	+5 (-9 to +17)	+3 (-8 to +8)	-1 (-12 to +11)	+4 (-4 to +9)	+1 (-7 to +6)	+3 (-8 to +9)
2060	+8 (-1 to +26)	+6 (-7 to +14)	+2 (-20 to +21)	+6 (-9 to +16)	+1 (-9 to +14)	+6 (-9 to +16)
2085	+11 (-16 to +23)	+4 (-11 to +18)	-3 (-29 to +11)	+5 (-10 to +17)	+1 (-14 to +14)	+4 (-14 to +17)
Annual maximum daily precipitation event (Winter) (%)						
2035	+6 (-0 to +16)	+9 (+2 to +20)	+3 (-4 to +16)	+8 (-3 to +15)	+8 (+1 to +20)	+8 (-0 to +16)
2060	+7 (+0 to +17)	+9 (-1 to +18)	+9 (-4 to +21)	+10 (+1 to +20)	+9 (-1 to +20)	+9 (-1 to +20)
2085	+16 (-1 to +40)	+18 (+3 to +35)	+20 (+4 to +41)	+20 (+6 to +30)	+15 (+5 to +30)	+18 (+4 to +35)
100-year return levels of one-day precipitation events (Summer) (%)						
2035	+10 (-13 to +31)	+7 (-14 to +19)	+5 (-11 to +16)	+7 (-2 to +15)	+3 (-9 to +22)	+7 (-11 to +19)
2060	+19 (-4 to +43)	+12 (+3 to +26)	+9 (-14 to +39)	+13 (-10 to +27)	+10 (-9 to +29)	+12 (-9 to +29)
2085	+20 (-6 to +42)	+12 (+2 to +38)	+11 (-24 to +38)	+18 (-9 to +41)	+17 (-5 to +27)	+17 (-6 to +38)
100-year return levels of one-day precipitation events (Winter) (%)						
2035	+8 (-11 to +31)	+16 (-5 to +27)	+6 (-6 to +27)	+7 (-6 to +27)	+10 (+1 to +20)	+8 (-6 to +27)
2060	+5 (-4 to +28)	+7 (-11 to +28)	+12 (-2 to +28)	+12 (-9 to +34)	+8 (-5 to +29)	+8 (-5 to +28)
2085	+19 (-2 to +59)	+22 (-2 to +46)	+16 (-0 to +50)	+18 (-1 to +50)	+18 (+5 to +41)	+18 (-1 to +50)

Table 13.2. Changes in key climate indicators for RCP4.5. The columns show regional averages for Northeastern Switzerland (CHNE), western Switzerland (CHW), southern Switzerland (CHS), the western Swiss Alps (CHAW), and the eastern Swiss Alps (CHAE), as well as the median value across all regions (CH).

Year	CHNE	CHW	CHS	CHAE	CHAW	CH
Annual mean temperature (°C)						
2035	+1.2 (+0.6 to +1.6)	+1.0 (+0.6 to +1.6)	+1.3 (+0.7 to +1.6)	+1.3 (+0.7 to +1.9)	+1.2 (+0.8 to +1.8)	+1.2 (+0.7 to +1.6)
2060	+1.6 (+1.0 to +2.6)	+1.7 (+1.0 to +2.6)	+1.8 (+1.2 to +2.7)	+1.9 (+1.2 to +2.8)	+1.8 (+1.2 to +2.8)	+1.8 (+1.2 to +2.7)
2085	+2.0 (+1.4 to +2.8)	+2.0 (+1.4 to +2.7)	+2.1 (+1.5 to +3.1)	+2.3 (+1.5 to +3.2)	+2.2 (+1.5 to +3.2)	+2.1 (+1.5 to +3.1)
Summer temperature (°C)						
2035	+1.3 (+0.8 to +2.0)	+1.3 (+0.8 to +2.0)	+1.4 (+1.0 to +2.2)	+1.5 (+1.0 to +2.3)	+1.4 (+0.9 to +2.4)	+1.4 (+0.9 to +2.2)
2060	+1.9 (+1.4 to +2.9)	+2.0 (+1.4 to +3.0)	+2.1 (+1.5 to +3.0)	+2.4 (+1.6 to +3.4)	+2.4 (+1.6 to +3.6)	+2.1 (+1.5 to +3.0)
2085	+2.2 (+1.6 to +3.6)	+2.4 (+1.6 to +3.8)	+2.6 (+1.8 to +3.6)	+2.8 (+1.9 to +4.2)	+2.8 (+2.0 to +4.3)	+2.6 (+1.8 to +3.8)
Summer precipitation (%)						
2035	-5 (-17 to +2)	-6 (-19 to +4)	-5 (-13 to +7)	-2 (-9 to +1)	-5 (-16 to -0)	-5 (-16 to +2)
2060	-7 (-15 to -1)	-9 (-19 to -0)	-9 (-19 to +4)	-4 (-10 to +4)	-9 (-24 to +0)	-9 (-19 to +0)
2085	-7 (-25 to +7)	-8 (-28 to -1)	-8 (-22 to +14)	-1 (-12 to +14)	-9 (-21 to +6)	-8 (-22 to +7)
Consecutive Dry Days (CDD) (days)						
2035	+1 (-0 to +2)	+1 (+0 to +2)	+1 (-1 to +3)	+0 (-0 to +2)	+1 (+0 to +2)	+1 (-0 to +2)
2060	+1 (+0 to +5)	+1 (+1 to +4)	+1 (+0 to +4)	+0 (-0 to +2)	+1 (+0 to +3)	+1 (+0 to +4)
2085	+1 (-0 to +5)	+2 (+1 to +5)	+1 (-0 to +6)	+1 (-1 to +2)	+1 (+0 to +4)	+1 (-0 to +5)

Year	CHNE	CHW	CHS	CHAE	CHAW	CH
Hottest day of the year (*TXx*) (°C)						
2035	+1.4 (+0.8 to +2.5)	+1.5 (+0.8 to +2.6)	+1.3 (+0.5 to +2.4)	+1.5 (+1.0 to +2.5)	+1.5 (+0.7 to +2.4)	+1.5 (+0.8 to +2.5)
2060	+2.3 (+1.4 to +4.5)	+2.3 (+1.4 to +4.4)	+2.3 (+1.3 to +3.7)	+2.6 (+1.3 to +4.1)	+2.6 (+1.3 to +4.1)	+2.3 (+1.3 to +4.1)
2085	+2.5 (+1.6 to +4.9)	+2.8 (+2.0 to +5.1)	+2.7 (+1.5 to +4.1)	+2.9 (+1.5 to +5.0)	+3.2 (+2.0 to +4.7)	+2.8 (+1.6 to +4.9)
Very hot days (*TX99P*) (days)						
2035	+2 (+1 to +4)	+3 (+1 to +4)	+2 (+1 to +6)	+3 (+1 to +7)	+3 (+1 to +8)	+3 (+1 to +6)
2060	+4 (+2 to +7)	+5 (+1 to +8)	+6 (+2 to +10)	+7 (+2 to +12)	+7 (+2 to +13)	+6 (+2 to +10)
2085	+4 (+2 to +10)	+5 (+3 to +11)	+6 (+3 to +13)	+9 (+3 to +13)	+8 (+3 to +14)	+6 (+3 to +13)
Winter temperature (°C)						
2035	+1.2 (+0.6 to +2.0)	+1.2 (+0.6 to +1.8)	+1.3 (+0.6 to +2.0)	+1.3 (+0.6 to +2.0)	+1.3 (+0.6 to +1.7)	+1.3 (+0.6 to +2.0)
2060	+1.8 (+0.9 to +2.9)	+1.8 (+1.0 to +2.7)	+1.9 (+1.0 to +3.2)	+2.0 (+0.9 to +3.0)	+1.9 (+1.0 to +2.7)	+1.9 (+1.0 to +2.9)
2085	+2.0 (+1.3 to +3.0)	+2.0 (+1.4 to +2.8)	+2.1 (+1.3 to +3.3)	+2.4 (+1.3 to +3.0)	+2.2 (+1.4 to +2.9)	+2.1 (+1.3 to +3.0)
Winter precipitation (%)						
2035	+6 (-4 to +17)	+7 (-2 to +16)	+14 (-11 to +21)	+8 (+0 to +18)	+8 (-2 to +16)	+8 (-2 to +17)
2060	+7 (-6 to +15)	+6 (-5 to +19)	+10 (-9 to +27)	+8 (-1 to +13)	+5 (-3 to +16)	+7 (-5 to +16)
2085	+11 (-10 to +19)	+8 (-7 to +17)	+9 (-4 to +37)	+8 (-6 to +22)	+7 (-4 to +15)	+8 (-6 to +19)

Year	CHNE	CHW	CHS	CHAE	CHAW	CH
Annual maximum daily precipitation event (Summer) (%)						
2035	+2 (-10 to +12)	-0 (-6 to +9)	-3 (-11 to +9)	+2 (-5 to +8)	-2 (-6 to +4)	-0 (-6 to +9)
2060	+0 (-10 to +18)	+2 (-6 to +8)	-4 (-16 to +7)	+3 (-9 to +9)	-1 (-11 to +5)	+0 (-10 to +8)
2085	+6 (-6 to +21)	+6 (-8 to +13)	+4 (-15 to +19)	+6 (-3 to +17)	-0 (-6 to +10)	+6 (-6 to +17)
Annual maximum daily precipitation event (Winter) (%)						
2035	+7 (-6 to +15)	+8 (-3 to +18)	+6 (-4 to +17)	+9 (-3 to +13)	+11 (-2 to +13)	+8 (-3 to +15)
2060	+8 (-5 to +17)	+8 (-2 to +18)	+10 (+0 to +19)	+6 (+1 to +16)	+6 (-2 to +13)	+8 (-2 to +17)
2085	+9 (-4 to +16)	+8 (-4 to +18)	+9 (-7 to +26)	+10 (-0 to +23)	+7 (-2 to +21)	+9 (-4 to +21)
100-year return levels of one-day precipitation events (Summer) (%)						
2035	+8 (-6 to +24)	+5 (-8 to +20)	+4 (-20 to +24)	+7 (-6 to +16)	+4 (-7 to +14)	+5 (-7 to +20)
2060	+8 (-11 to +37)	+5 (-14 to +22)	+4 (-14 to +20)	+8 (-13 to +19)	+2 (-10 to +13)	+5 (-13 to +20)
2085	+12 (-9 to +38)	+13 (-6 to +24)	+9 (-13 to +31)	+15 (+0 to +33)	+8 (-6 to +24)	+12 (-6 to +31)
100-year return levels of one-day precipitation events (Winter) (%)						
2035	+4 (-8 to +27)	+11 (-6 to +24)	+13 (-3 to +23)	+9 (-9 to +31)	+8 (-3 to +20)	+9 (-6 to +24)
2060	+3 (-8 to +24)	+10 (-7 to +28)	+12 (-5 to +35)	+12 (-1 to +37)	+9 (-1 to +18)	+10 (-5 to +28)
2085	+7 (-0 to +30)	+12 (-8 to +32)	+11 (-7 to +50)	+13 (-3 to +54)	+11 (-7 to +26)	+11 (-7 to +32)

Table 13.3. Changes in key climate indicators for RCP2.6. The columns show regional averages for Northeastern Switzerland (CHNE), western Switzerland (CHW), southern Switzerland (CHS), the western Swiss Alps (CHAW), and the eastern Swiss Alps (CHAE), as well as the median value across all regions (CH).

Year	CHNE	CHW	CHS	CHAE	CHAW	CH
Annual mean temperature (°C)						
2035	+1.0 (+0.5 to +1.5)	+1.0 (+0.5 to +1.5)	+1.1 (+0.6 to +1.6)	+1.2 (+0.7 to +1.7)	+1.1 (+0.6 to +1.7)	+1.1 (+0.6 to +1.6)
2060	+1.2 (+0.6 to +1.8)	+1.1 (+0.6 to +1.8)	+1.2 (+0.7 to +1.9)	+1.4 (+0.7 to +2.0)	+1.3 (+0.7 to +2.1)	+1.2 (+0.7 to +1.9)
2085	+1.1 (+0.6 to +1.8)	+1.0 (+0.5 to +1.8)	+1.2 (+0.6 to +1.9)	+1.3 (+0.7 to +2.1)	+1.2 (+0.7 to +2.1)	+1.2 (+0.6 to +1.9)
Summer temperature (°C)						
2035	+1.1 (+0.6 to +2.1)	+1.2 (+0.5 to +2.1)	+1.3 (+0.8 to +2.1)	+1.4 (+0.7 to +2.4)	+1.4 (+0.7 to +2.5)	+1.3 (+0.7 to +2.1)
2060	+1.2 (+0.7 to +2.3)	+1.3 (+0.7 to +2.4)	+1.3 (+0.9 to +2.5)	+1.6 (+1.0 to +2.9)	+1.6 (+1.0 to +3.0)	+1.3 (+0.9 to +2.5)
2085	+1.2 (+0.6 to +2.2)	+1.3 (+0.7 to +2.3)	+1.3 (+0.7 to +2.4)	+1.5 (+0.9 to +2.8)	+1.5 (+0.9 to +2.9)	+1.3 (+0.7 to +2.4)
Summer precipitation (%)						
2035	-3 (-20 to +3)	-5 (-19 to +4)	-5 (-16 to +6)	-1 (-11 to +11)	-3 (-16 to +8)	-3 (-16 to +6)
2060	-3 (-16 to +6)	-5 (-20 to +6)	-3 (-12 to +13)	-1 (-9 to +10)	-5 (-17 to +7)	-3 (-16 to +7)
2085	-3 (-15 to +9)	-4 (-19 to +6)	-4 (-11 to +15)	-2 (-8 to +9)	-4 (-17 to +9)	-4 (-15 to +9)
Consecutive Dry Days (CDD) (days)						
2035	+1 (-1 to +4)	+1 (-0 to +3)	+1 (-1 to +5)	+0 (-1 to +2)	+0 (-0 to +2)	+1 (-1 to +3)
2060	+1 (-1 to +4)	+1 (-1 to +3)	+0 (-1 to +6)	+0 (-1 to +3)	+1 (-0 to +3)	+1 (-1 to +3)
2085	+1 (-1 to +4)	+1 (-0 to +3)	+0 (-1 to +6)	+0 (-0 to +3)	+1 (-0 to +3)	+1 (-0 to +3)

Year	CHNE	CHW	CHS	CHAE	CHAW	CH
Hottest day of the year (*TXx*) (°C)						
2035	+1.4 (+0.6 to +3.1)	+1.4 (+0.8 to +3.1)	+1.2 (+0.6 to +2.4)	+1.5 (+0.8 to +2.6)	+1.5 (+0.9 to +2.6)	+1.4 (+0.8 to +2.6)
2060	+1.5 (+0.7 to +3.5)	+1.6 (+1.0 to +3.5)	+1.6 (+0.7 to +2.8)	+1.8 (+1.0 to +3.2)	+1.8 (+1.0 to +3.2)	+1.6 (+1.0 to +3.2)
2085	+1.7 (+0.4 to +3.4)	+1.4 (+0.7 to +3.4)	+1.4 (+0.8 to +2.8)	+1.8 (+0.7 to +3.2)	+1.8 (+0.8 to +3.1)	+1.7 (+0.7 to +3.2)
Very hot days (*TX99P*) (days)						
2035	+1 (+0 to +5)	+2 (+0 to +5)	+2 (+0 to +5)	+2 (+0 to +9)	+2 (+1 to +6)	+2 (+0 to +5)
2060	+2 (+0 to +7)	+2 (+0 to +6)	+2 (+0 to +8)	+3 (+1 to +10)	+3 (+1 to +10)	+2 (+0 to +8)
2085	+2 (+1 to +7)	+2 (+1 to +7)	+2 (+0 to +7)	+3 (+1 to +11)	+2 (+1 to +9)	+2 (+1 to +7)
Winter temperature (°C)						
2035	+1.1 (+0.5 to +1.8)	+1.0 (+0.5 to +1.6)	+1.1 (+0.4 to +1.7)	+1.2 (+0.5 to +1.8)	+1.1 (+0.4 to +1.7)	+1.1 (+0.5 to +1.7)
2060	+1.3 (+0.5 to +2.1)	+1.2 (+0.6 to +1.8)	+1.3 (+0.6 to +1.8)	+1.4 (+0.6 to +2.1)	+1.4 (+0.6 to +1.9)	+1.3 (+0.6 to +1.9)
2085	+1.3 (+0.6 to +2.1)	+1.2 (+0.6 to +1.8)	+1.3 (+0.5 to +2.0)	+1.3 (+0.6 to +2.1)	+1.3 (+0.6 to +1.9)	+1.3 (+0.6 to +2.0)
Winter precipitation (%)						
2035	+5 (-6 to +20)	+6 (-7 to +18)	+10 (-14 to +27)	+4 (-3 to +16)	+7 (-6 to +15)	+6 (-6 to +18)
2060	+5 (-4 to +16)	+5 (-1 to +14)	+14 (-8 to +38)	+7 (-0 to +19)	+8 (-0 to +14)	+7 (-1 to +16)
2085	+6 (-7 to +19)	+5 (-2 to +16)	+12 (-12 to +35)	+6 (-3 to +19)	+8 (-2 to +14)	+6 (-3 to +19)

Year	CHNE	CHW	CHS	CHAE	CHAW	CH
Annual maximum daily precipitation event (Summer) (%)						
2035	+1 (-7 to +15)	-0 (-11 to +11)	-4 (-13 to +8)	+1 (-4 to +10)	-2 (-6 to +5)	-0 (-7 to +10)
2060	+5 (-10 to +14)	+2 (-6 to +10)	-2 (-11 to +6)	+5 (-3 to +11)	-3 (-9 to +6)	+2 (-9 to +10)
2085	+3 (-9 to +17)	+3 (-8 to +16)	-2 (-16 to +10)	+3 (-5 to +11)	-2 (-8 to +23)	+3 (-8 to +16)
Annual maximum daily precipitation event (Winter) (%)						
2035	+4 (-4 to +18)	+7 (-5 to +17)	+4 (-12 to +15)	+6 (-6 to +15)	+8 (-2 to +18)	+6 (-5 to +17)
2060	+4 (-9 to +15)	+5 (-6 to +21)	+8 (-6 to +24)	+7 (-4 to +21)	+8 (-3 to +18)	+7 (-6 to +21)
2085	+3 (-6 to +16)	+6 (-3 to +20)	+9 (-9 to +21)	+8 (-3 to +15)	+10 (-2 to +18)	+8 (-3 to +18)
100-year return levels of one-day precipitation events (Summer) (%)						
2035	+6 (-14 to +28)	+3 (-10 to +26)	+1 (-12 to +27)	+5 (-9 to +22)	+5 (-9 to +12)	+5 (-10 to +26)
2060	+6 (-6 to +24)	+5 (-5 to +20)	-1 (-18 to +16)	+8 (-4 to +17)	+1 (-9 to +16)	+5 (-6 to +17)
2085	+6 (-11 to +25)	+6 (-8 to +20)	+5 (-20 to +24)	+5 (-3 to +21)	+4 (-8 to +33)	+5 (-8 to +24)
100-year return levels of one-day precipitation events (Winter) (%)						
2035	+4 (-10 to +27)	+4 (-11 to +29)	+10 (-8 to +26)	+6 (-13 to +36)	+9 (-3 to +22)	+6 (-10 to +27)
2060	-1 (-11 to +21)	+7 (-9 to +28)	+14 (-4 to +34)	+8 (-10 to +47)	+7 (-1 to +26)	+7 (-9 to +28)
2085	+5 (-11 to +22)	+3 (-6 to +24)	+14 (-9 to +34)	+7 (-8 to +36)	+8 (-2 to +27)	+7 (-8 to +27)

A.2. Appendix: Seasonal mean changes

A.2.1. Pattern-scaling list of time windows

GCM	init	target scenario	source scenario	2020-2049	2045-2074	2070-2099
CNRM-CERFACS-CNRM-CM5	r1i1p1	rcp26	rcp45	2017-2046	2029-2058	2030-2059
			rcp85	2012-2041	2020-2049	2021-2050
		rcp45	rcp85	2014-2043	2031-2060	2041-2070
		1.5 degC	rcp26			2030-2059
			rcp45			2024-2053
			rcp85			2017-2046
		2.0 degC	rcp45			2045-2074
			rcp85			2030-2059
ICHEC-EC-EARTH	r12i1p1/	rcp26	rcp45	2014-2043	2023-2052	2020-2049
	r3i1p1/		rcp85	2008-2037	2014-2043	2012-2041
	r1i1p1	rcp45	rcp85	2012-2041	2028-2057	2037-2066
		1.5 degC	rcp26			2030-2059
			rcp45			2019-2048
			rcp85			2011-2040
		2.0 degC	rcp45			2042-2071
			rcp85			2027-2056
MOHC-HadGEM2-ES	r1i1p1	rcp26	rcp45	2021-2050	2028-2057	2025-2054
			rcp85	2014-2043	2019-2048	2017-2046
		rcp45	rcp85	2013-2042	2031-2060	2040-2069
		1.5 degC	rcp26			2005-2034
			rcp45			2009-2038
			rcp85			2005-2034
		2.0 degC	rcp26			2029-2058
			rcp45			2025-2054
			rcp85			2017-2046
MPI-M-MPI-ESM-LR	r1i1p1	rcp26	rcp45	2016-2045	2018-2047	2014-2043
			rcp85	2011-2040	2012-2041	2009-2038
		rcp45	rcp85	2013-2042	2027-2056	2033-2062
		1.5 degC	rcp26			2039-2068
			rcp45			2020-2049
			rcp85			2013-2042
		2.0 degC	rcp45			2051-2080
			rcp85			2029-2058
MPI-M-MPI-ESM-LR	r2i1p1	rcp26	rcp45	2017-2046	2020-2049	2014-2043
		rcp45	rcp85	2013-2042	2028-2057	2034-2063
		1.5 degC	rcp26			2038-2067
		2.0 degC	rcp45			2045-2074
IPSL-IPSL-CM5A-MR	r1i1p1	rcp26	rcp45	2013-2042	2022-2051	2019-2048
		rcp45	rcp85	2015-2044	2028-2057	2037-2066
		1.5 degC	rcp45			2011-2040
		2.0 degC	rcp45			2031-2060
MIROC-MIROC5	r1i1p1	rcp26	rcp45	2017-2046	2026-2055	2026-2055
			rcp85	2012-2041	2019-2048	2020-2049
		rcp45	rcp85	2015-2044	2029-2058	2037-2066
		1.5 degC	rcp26			2025-2054
			rcp85			2015-2044
		2.0 degC	rcp45			2047-2076
			rcp85			2030-2059
NCC-NorESM1-M	r1i1p1	rcp26	rcp45	2015-2044	2021-2050	2022-2051
		rcp45	rcp85	2015-2044	2028-2057	2037-2066
		1.5 degC	rcp45			2023-2052
		2.0 degC	rcp45			2055-2084
CCCma-CanESM2	r1i1p1	rcp26	rcp45	2018-2047	2028-2057	2027-2056
		rcp45	rcp85	2014-2043	2029-2058	2036-2065
		1.5 degC	rcp45			2009-2038
		2.0 degC	rcp45			2024-2053
CSIRO-QCCCE-CSIRO-Mk3-6-0	r1i1p1	rcp26	rcp45	2020-2049	2027-2056	2031-2060
		rcp45	rcp85	2018-2047	2036-2065	2043-2072
		1.5 degC	rcp45			2016-2045
		2.0 degC	rcp45			2030-2059
NOAA-GFDL-GFDL-ESM2M	r1i1p1	rcp26	rcp45	2013-2042	2019-2048	2019-2048
		rcp45	rcp85	2015-2044	2027-2056	2032-2061
		1.5 degC	rcp45			2036-2065
		2.0 degC	rcp85			2038-2067

Table 13.4. Table of time windows for pattern scaling (the corresponding time slice is extracted from the source scenario and substituted into the target scenario).

A.2.2. Spatial smoothing of RCM fields

For spatial smoothing, the operator `cdo smooth9` from the CDO package (https://code.mpimet.mpg.de/projects/cdo) was employed for each individual model output time step. The `smooth9` operator replaces a given grid cell value with the weighted average of a spatial 3x3 grid cell halo using the weights of 0.24 for the grid cell itself, 0.12 for the lateral neighbor cells, and 0.07 for the diagonal neighbor cells. This is very close to the optimal spatial filter proposed by Shapiro (1970) [318] and is conservative in the sense that large-scale spatial averages are retained.

A.2.3. Multi-model combination equations

The multi-model combination must account for different spatial resolutions (i.e., EUR-44 versus EUR-11) and for the different computational grids used by the models (i.e., rotated latitude/longitude coordinates versus other geographical projections). Consider M simulations φ^m at EUR-44 resolution and N simulations ψ^n at EUR-11 resolution, where m and n denote the index of the respective simulations. The grid cells of the EUR-44 grid are denoted by B_i and those of the EUR-11 grid by C_k. The current treatment considers various native model grids. The fields on their native grids are then denoted by φ_i^m and ψ_k^n, respectively. To derive a multi-model map of a certain quantile Q (e.g., the median) across this ensemble, the average of the EUR-11 fields on the standard EUR-44 grid is defined as

$$\bar{\psi}_i^n = \sum_k \frac{|B_i \cap C_k|}{|B_i|} \psi_k^n,$$

where $|B_i|$ is the area of grid cell B_i and $|B_i \cap C_k|$ is the area of the intersection of the grid cells B_i and C_k. The associated anomaly fields (relative to the EUR-44 mean) are defined on the grid of non-empty intersections $B_i \cap C_k$ by

$$\tilde{\psi}_{ik}^n = \psi_k^n - \bar{\psi}_i^n$$

The quantile map $\bar{\Phi}_{ik}$ is then obtained by applying the quantile function Q separately to the high-resolution and low-resolution components and adding the results:

$$\bar{\Phi}_{ik} = Q(\bar{\psi}_i^1, \ldots, \bar{\psi}_i^N, \varphi_i^1, \ldots, \varphi_i^M) + Q(\tilde{\psi}_{ik}^1, \ldots, \tilde{\psi}_{ik}^N).$$

This procedure keeps all ensemble members and retains the high-resolution features present in the EUR-11 simulations. It has, however, two limitations: First, for some fields (e.g., those with a strong nonlinear dependence on elevation), there are systematic differences between the low-resolution fields φ_i^m and the averages $\bar{\psi}_i^n$ of the high-resolution fields. When this is the case, it is not appropriate to compute a quantile of the combined ensemble and it is better to use only the high-resolution fields. The maps shown in this report were visually checked to ensure that such systematic differences were not present. If this method is applied to other fields not presented in this report, such a check is recommended. Second, in contrast to the mean, the quantiles of a sum are not exactly equal to the sum of the quantiles, and it is difficult to predict how large this difference may be. However, for checking, one can compare the quantiles $Q(\bar{\psi}_k^1, \ldots, \bar{\psi}_k^N)$ to the sum $Q(\psi_i^1, \ldots, \psi_i^N) + Q(\tilde{\psi}_{ik}^1, \ldots, \tilde{\psi}_{ik}^N)$ for indices i and k where $B_i \cap C_k$ is not empty.

A.2.4. Empirical quantile equation

The empirical quantiles used for the medians and uncertainty ranges of the CH2018 projections are calculated as follows. Let vector x_i be a vector of simulated values (e.g., 30-year mean temperatures for a given season and model region), with i ranging over the 21 simulations of the multi-model combination set. The cumulative probability p is assigned to the ordered data values x_i by equal partition of the interval 0-1 and is interpolated linearly in between. Thus, the quantile q for probability p is given by

$$q(p) = x_j(1 - (p(n-1) \mod 1) + x_{j+1}(p(n-1) \mod 1),$$

$$j(p) = \mathit{floor}((n-1)p + 1),$$

where y mod 1 denotes the fractional part of y and $\mathit{floor}(y)$ denotes the greatest integer that is less than or equal to y.

A.2.5. Seasonal mean changes in temperature

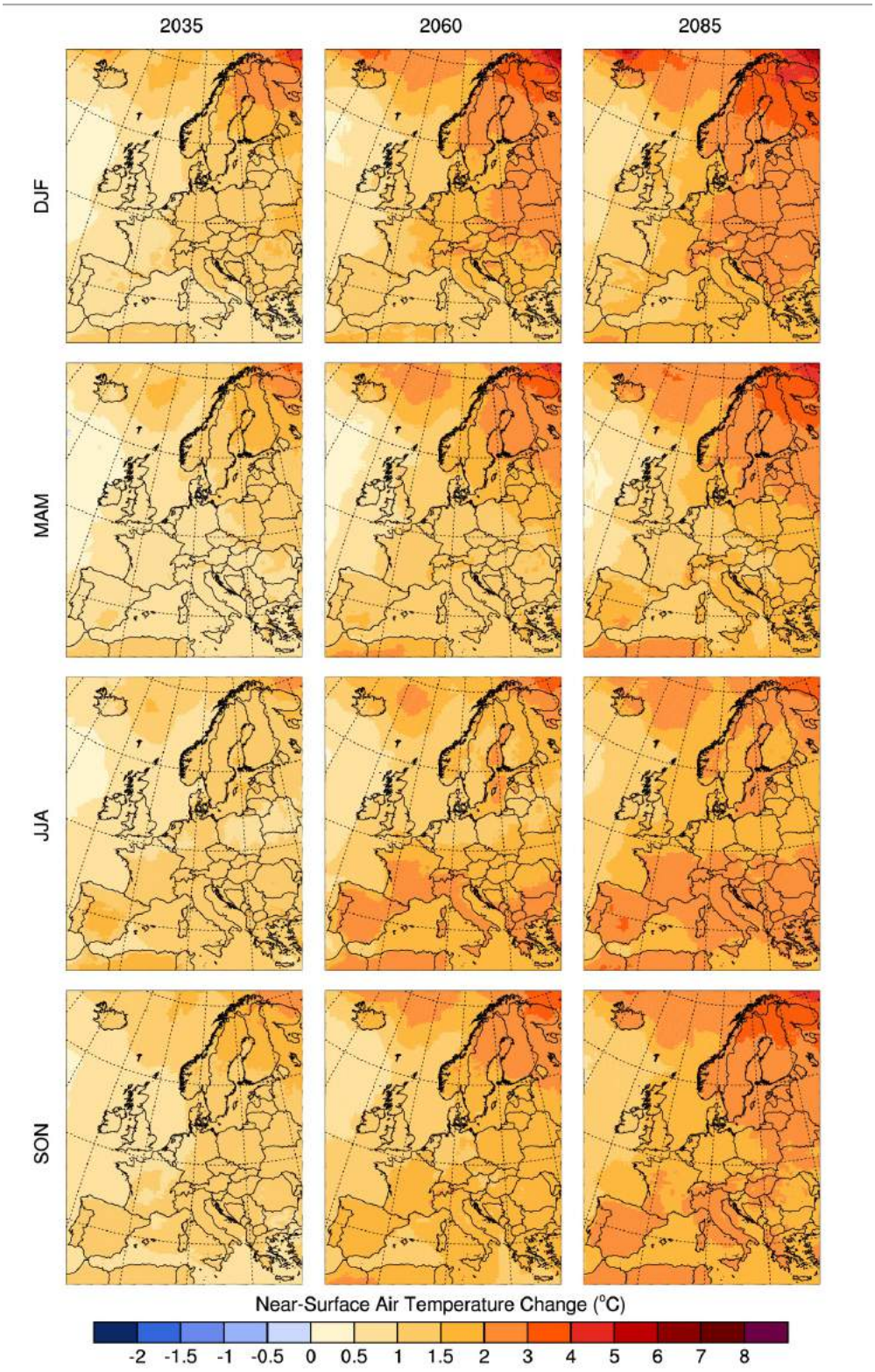

Figure 13.1. Projected future change in temperature (in °C) over Europe by 2035, 2060, and 2085 for winter (DJF: December - February), spring (MAM: March - May), summer (JJA: June - August), and autumn (SON: September - November). Shown is the multi-model median of the combined simulations at different resolutions from the EURO-CORDEX ensemble (see Chapter 2.1) for the RCP4.5 emission scenario with respect to the reference period 1981 - 2010.

Figure 13.2. As Figure 13.1, but for RCP2.6.

			Estimates 2035			Estimates 2060			Estimates 2085		
Region	**Season**	**Scenario**	**lower**	**med.**	**upper**	**lower**	**med.**	**upper**	**lower**	**med.**	**upper**
CHNE	DJF	RCP8.5	0.49	1.41	2.06	1.79	2.38	2.89	3.07	3.77	4.96
		RCP4.5	0.64	1.24	2.01	0.93	1.79	2.89	1.3	2.01	2.96
		RCP2.6	0.49	1.05	1.82	0.53	1.28	2.11	0.59	1.28	2.08
	MAM	RCP8.5	0.43	1.01	1.45	1.14	1.82	2.71	2.15	3.28	4.16
		RCP4.5	0.18	0.78	1.49	0.61	1.31	1.99	0.88	1.56	2.33
		RCP2.6	0.18	0.88	1.32	0.24	0.91	1.47	0.3	0.98	1.47
	JJA	RCP8.5	0.9	1.42	2.13	2.06	2.48	4.05	3.38	4.5	7.01
		RCP4.5	0.79	1.29	2.04	1.38	1.92	2.94	1.61	2.25	3.58
		RCP2.6	0.55	1.1	2.08	0.73	1.23	2.27	0.64	1.18	2.16
	SON	RCP8.5	0.87	1.23	2.15	1.74	2.52	3.86	2.86	3.92	5.76
		RCP4.5	0.68	1.12	1.89	0.94	1.68	3.03	1.52	2.02	3.33
		RCP2.6	0.5	1.05	1.92	0.72	1.3	2.18	0.54	1.19	2.33
CHW	DJF	RCP8.5	0.54	1.41	1.91	1.78	2.26	2.62	2.91	3.72	4.79
		RCP4.5	0.61	1.21	1.8	0.99	1.77	2.71	1.36	2.02	2.82
		RCP2.6	0.46	0.98	1.63	0.58	1.25	1.82	0.6	1.23	1.82
	MAM	RCP8.5	0.38	0.89	1.36	1.16	1.86	2.6	2.03	3.14	4.01
		RCP4.5	0.18	0.7	1.4	0.64	1.33	1.9	0.92	1.51	2.26
		RCP2.6	0.13	0.86	1.22	0.23	0.89	1.48	0.3	0.88	1.47
	JJA	RCP8.5	0.87	1.46	2.16	2.17	2.56	4.38	3.53	4.58	7.22
		RCP4.5	0.79	1.31	2.05	1.45	2.01	2.99	1.64	2.38	3.77
		RCP2.6	0.54	1.15	2.06	0.69	1.26	2.36	0.66	1.3	2.25
	SON	RCP8.5	0.85	1.24	2.23	1.69	2.45	3.72	2.87	3.91	5.91
		RCP4.5	0.66	1.09	1.9	0.92	1.63	2.96	1.53	1.96	3.21
		RCP2.6	0.49	0.94	1.93	0.75	1.25	2.14	0.52	1.24	2.3
CHS	DJF	RCP8.5	0.61	1.35	2.2	1.76	2.4	3.32	3.18	3.8	5.43
		RCP4.5	0.57	1.27	1.96	1.01	1.85	3.19	1.3	2.13	3.29
		RCP2.6	0.38	1.15	1.71	0.6	1.31	1.85	0.52	1.31	1.97
	MAM	RCP8.5	0.63	0.94	1.38	1.43	1.93	2.77	2.45	3.37	4.41
		RCP4.5	0.26	0.76	1.48	0.8	1.43	2.12	1.08	1.67	2.37
		RCP2.6	0.24	0.95	1.27	0.3	0.84	1.51	0.3	0.83	1.6
	JJA	RCP8.5	1.17	1.63	2.29	2.29	2.94	4.15	4.1	5.04	7
		RCP4.5	1	1.36	2.21	1.48	2.14	2.96	1.8	2.57	3.62
		RCP2.6	0.77	1.31	2.15	0.89	1.27	2.54	0.75	1.29	2.44
	SON	RCP8.5	0.78	1.4	2.18	1.77	2.59	3.58	3.16	4.12	5.9
		RCP4.5	0.74	1.19	1.8	1.14	1.75	2.79	1.71	2.17	3.24
		RCP2.6	0.5	1.13	1.85	0.73	1.22	2.11	0.51	1.29	2.16
CHAE	DJF	RCP8.5	0.59	1.38	2.38	1.8	2.48	3.8	3.15	3.86	5.64
		RCP4.5	0.64	1.33	2.03	0.89	2.04	2.96	1.34	2.39	2.97
		RCP2.6	0.51	1.21	1.75	0.57	1.42	2.09	0.56	1.28	2.07
	MAM	RCP8.5	0.43	1.08	1.56	1.35	2.13	3.16	2.54	3.75	5.05
		RCP4.5	0.37	0.91	1.56	0.73	1.42	2.28	1	1.84	2.62
		RCP2.6	0.19	1.06	1.29	0.27	0.98	1.6	0.33	1.01	1.59
	JJA	RCP8.5	1.2	1.7	2.51	2.46	3.34	4.77	4.1	5.3	7.21
		RCP4.5	0.96	1.51	2.33	1.6	2.41	3.43	1.93	2.77	4.17
		RCP2.6	0.66	1.43	2.39	0.98	1.59	2.87	0.9	1.54	2.81
	SON	RCP8.5	1.01	1.54	2.26	2.13	3.13	3.91	3.39	4.48	6.19
		RCP4.5	0.74	1.29	1.99	1.34	2.06	3.09	1.72	2.43	3.37
		RCP2.6	0.59	1.23	1.99	0.68	1.34	2.3	0.58	1.36	2.24
CHAW	DJF	RCP8.5	0.68	1.37	2.1	1.75	2.37	3.55	3.08	3.9	5.57
		RCP4.5	0.64	1.27	1.69	0.99	1.89	2.73	1.37	2.18	2.85
		RCP2.6	0.42	1.08	1.68	0.64	1.39	1.86	0.62	1.27	1.86
	MAM	RCP8.5	0.45	1.04	1.55	1.4	2.17	3.1	2.5	3.87	4.86
		RCP4.5	0.36	0.86	1.51	0.73	1.48	2.24	1.05	1.84	2.59
		RCP2.6	0.22	1.04	1.31	0.29	1	1.53	0.34	0.98	1.55
	JJA	RCP8.5	1.16	1.72	2.58	2.58	3.37	4.93	4.3	5.47	7.32
		RCP4.5	0.94	1.42	2.44	1.62	2.43	3.57	2.02	2.83	4.27
		RCP2.6	0.7	1.4	2.5	0.99	1.61	3.02	0.87	1.49	2.94
	SON	RCP8.5	1	1.47	2.29	1.98	3.05	3.99	3.25	4.56	6.34
		RCP4.5	0.71	1.3	1.99	1.37	1.98	3.07	1.75	2.33	3.48
		RCP2.6	0.6	1.08	1.99	0.87	1.3	2.3	0.55	1.37	2.24

Table 13.3. Projected future change in mean temperature (in °C) for winter (DJF: December - February), spring (MAM: March - May), summer (JJA: June - August), and autumn (SON: September - November) in the northeastern Alps (CHNE), western Switzerland (CHW), southern Switzerland (CHS), eastern Alps (CHAE), and western Alps (CHAW) as shown in Figure 4.4. Projections are for 30-year averages centered at 2035, 2060, and 2085 with respect to the reference period 1981 - 2010. Three emission scenarios are considered: RCP8.5, RCP4.5, and RCP2.6. The lower (5 %), medium (50% = median), and upper (95 %) quantiles are shown.

A.2.6. Seasonal mean changes in precipitation

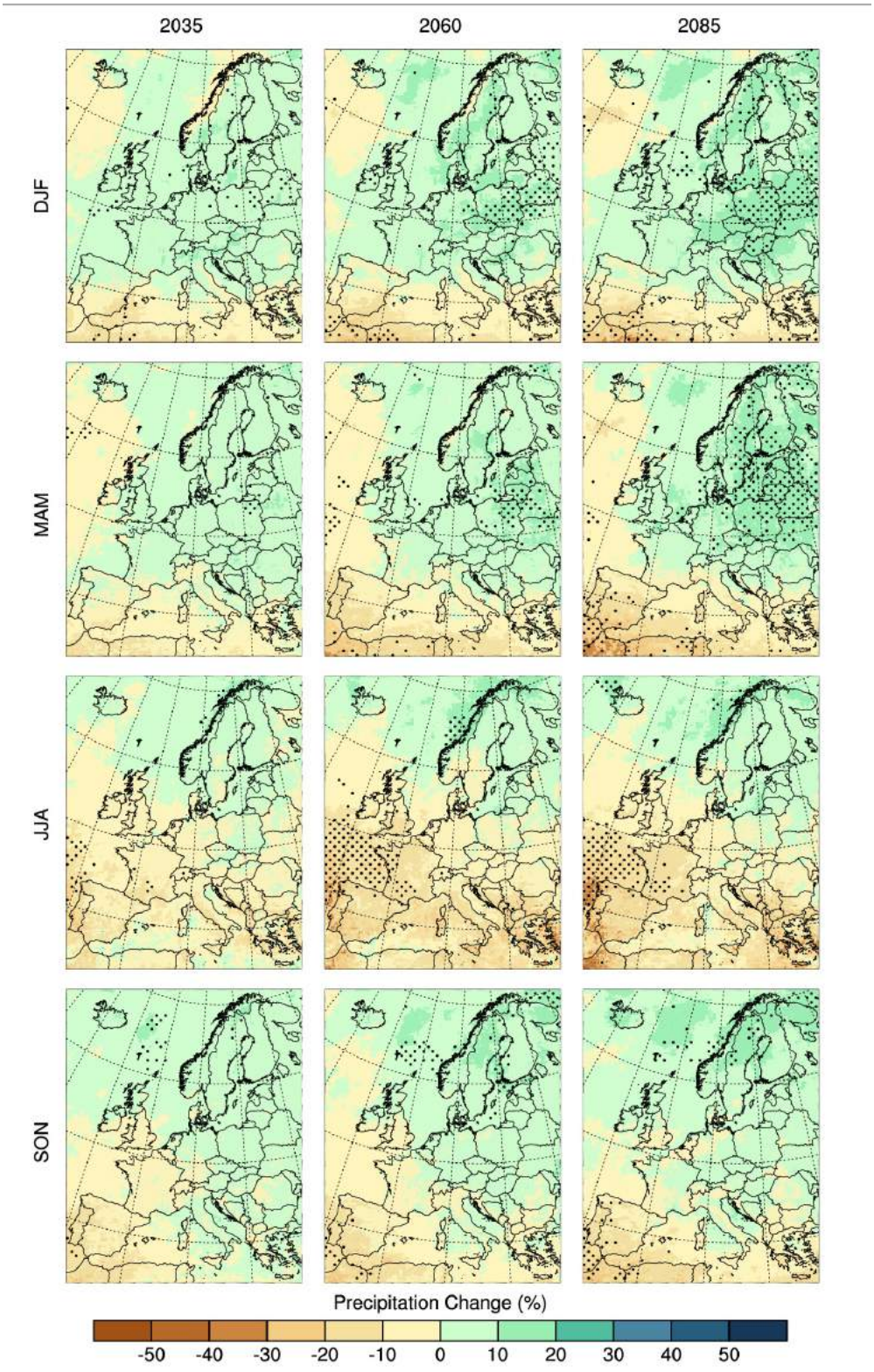

Figure 13.4. Projected future precipitation change (in %) over Europe by 2035, 2060, and 2085 for winter (DJF: December - February), spring (MAM: March - May), summer (JJA: June - August), and autumn (SON: September - November). Shown is the multi-model median of the combined simulations at different resolutions from the EURO-CORDEX ensemble for the RCP4.5 emission scenario with respect to the reference period 1981 - 2010. Stippling (dots) indicates regions where at least 90 % of the models agree on the sign of the change.

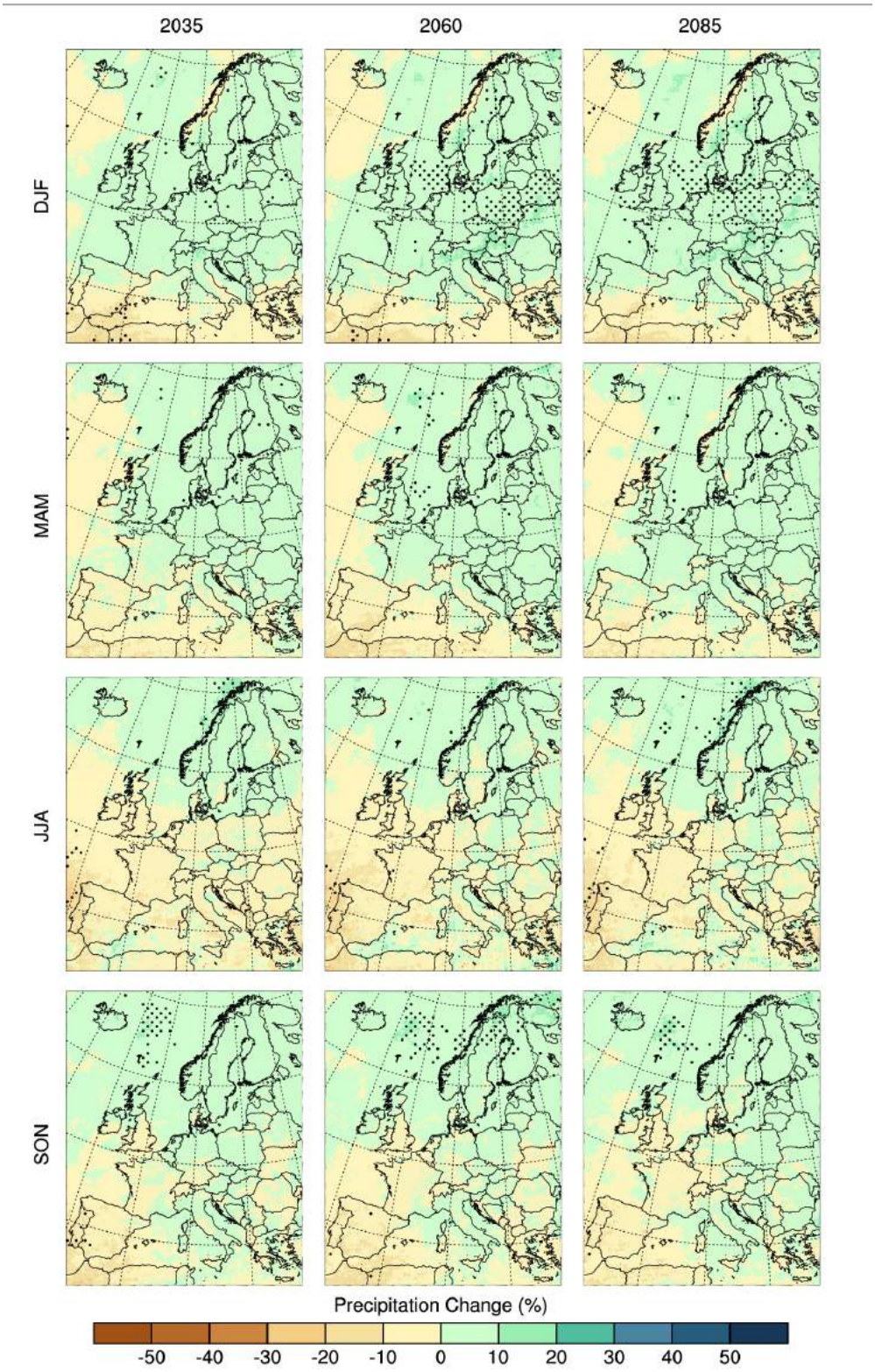

Figure 13.5. As Figure 13.4, but for RCP2.6.

			Estimates 2035			Estimates 2060			Estimates 2085		
Region	Season	Scenario	lower	med.	upper	lower	med.	upper	lower	med.	upper
CHNE	DJF	RCP8.5	-3.1	7.5	18.2	0.1	9.7	24.1	1.6	14.5	26.8
		RCP4.5	-3.8	6.1	16.7	-6.3	7.3	15.5	-9.8	10.8	19.2
		RCP2.6	-5.5	5.2	20.3	-4.4	4.7	15.6	-7.3	5.7	19
	MAM	RCP8.5	-3	3.9	17.5	0.2	8.6	20.9	-1.5	8.2	34.7
		RCP4.5	-2.6	4.3	10.9	-4.6	6	15.3	-0.7	5.9	18.7
		RCP2.6	-6.8	3.6	11.3	-6.9	4.2	13.2	-6.5	0.1	13.2
	JJA	RCP8.5	-15.5	-2.7	7.6	-24.9	-8.1	9.2	-39	-16.9	-5
		RCP4.5	-17.5	-4.6	1.8	-14.8	-7	-0.6	-25.4	-7.3	7.3
		RCP2.6	-19.5	-2.7	3.5	-15.8	-2.8	6.5	-15	-2.7	8.6
	SON	RCP8.5	-8.6	1.2	16.2	-12.1	0.2	8.7	-11.1	-2	12.8
		RCP4.5	-11.7	-3.3	13.7	-16.2	1.7	13.3	-8.3	3.3	10.1
		RCP2.6	-10.9	-1.8	17.2	-15.8	-0.6	12.9	-14.1	-2.2	12
CHW	DJF	RCP8.5	-0.8	10.3	16	0.4	7	20.6	4.9	15.4	23.9
		RCP4.5	-2.3	6.6	16	-4.8	6	19	-6.5	8.2	16.5
		RCP2.6	-6.8	6.3	17.6	-0.6	5.5	14	-1.8	5.5	16.1
	MAM	RCP8.5	-3.8	4	13.4	-1	5	15.5	-2.9	4	25.7
		RCP4.5	-5.4	2.3	10.8	-7.7	3.7	9.6	-0.4	4.3	18.9
		RCP2.6	-9.2	1.6	12.1	-5.7	2.4	13	-5.6	0	12.2
	JJA	RCP8.5	-20.3	-3.9	4.9	-31.6	-11.4	0.2	-42.8	-24.2	-10
		RCP4.5	-18.5	-6	3.7	-19.4	-9.5	-0.1	-28	-8.5	-0.6
		RCP2.6	-18.6	-5.2	3.9	-19.8	-5.1	5.6	-18.9	-3.7	5.9
	SON	RCP8.5	-9.7	1.5	11.6	-11.7	-0.3	8	-17.2	-3.4	7.9
		RCP4.5	-9.2	-2.3	12.5	-11.2	-0.2	8.3	-9.4	1.1	8.4
		RCP2.6	-11	-1.9	12.9	-13.1	-0.8	15.2	-13.8	-2.4	12.3
CHS	DJF	RCP8.5	-9	4	22.2	-12.7	9.2	26.4	6.2	21.8	38.4
		RCP4.5	-11	13.6	20.6	-8.6	9.8	26.9	-3.6	8.6	36.9
		RCP2.6	-14.4	10.5	27.2	-8.1	14.1	37.9	-11.8	11.9	35.1
	MAM	RCP8.5	-11.3	-1.5	12.5	-7.2	1.7	14.6	-13.9	1	11.9
		RCP4.5	-9.5	-1.6	11.6	-8.3	0.3	9.8	-8.2	1.8	12.7
		RCP2.6	-9.5	-2.7	11	-12.6	-1.3	8.5	-10	-0.2	18.4
	JJA	RCP8.5	-13.1	-5.4	10.5	-25.1	-12.1	10.8	-39.5	-22.8	1.6
		RCP4.5	-13.5	-5.3	7.5	-19.1	-8.7	4.5	-21.8	-8.2	13.6
		RCP2.6	-16	-4.8	6.2	-11.8	-2.6	12.8	-10.9	-3.7	14.6
	SON	RCP8.5	-15.4	-0.7	18.2	-15.2	2.5	12.9	-19.7	0	11.6
		RCP4.5	-11.3	-0.9	17.2	-14.7	-2.5	8.7	-12.5	0.3	19.6
		RCP2.6	-11.2	3.9	20.9	-9.9	1.1	15	-13	-2.4	13.3
CHAE	DJF	RCP8.5	0.5	5.6	15.3	-4.1	7.2	20.9	-1.7	16.6	24
		RCP4.5	0.4	8.1	17.8	-0.8	8.2	13	-5.7	8.3	21.6
		RCP2.6	-2.6	4.1	16.3	-0.2	6.7	19.2	-2.7	6.4	18.6
	MAM	RCP8.5	-5.7	1.7	10.5	-7.5	4.4	13.8	-9.3	4.8	26.8
		RCP4.5	-5.3	-0.8	9.9	-6.8	0.7	8.9	-5.7	3.3	14.4
		RCP2.6	-5.1	-1.6	11.7	-5.8	0.3	10.2	-5.6	2.1	9.9
	JJA	RCP8.5	-6.4	-0.8	9.1	-14.2	-4.8	16.3	-27.3	-9.8	11.3
		RCP4.5	-9.1	-2.4	1.3	-9.6	-3.7	4	-12.2	-0.8	14.2
		RCP2.6	-11.1	-1.5	10.8	-8.6	-1.5	9.8	-7.8	-1.6	8.7
	SON	RCP8.5	-8.9	-1.9	11.4	-11.5	1.2	6.6	-11	-2.9	12.5
		RCP4.5	-9.7	-1.5	11.2	-12.6	0.1	13.8	-9.4	0.9	5.7
		RCP2.6	-10.1	-0.6	17.5	-10	0	11.6	-10.7	-1.4	10.1
CHAW	DJF	RCP8.5	-0.9	8.9	14.7	-2.8	7.6	16.4	0.2	12.3	18.1
		RCP4.5	-1.6	7.7	16	-3.3	4.6	16.5	-4.4	7.4	15.1
		RCP2.6	-5.5	6.6	14.8	-0.2	7.7	13.6	-2.1	8	14.4
	MAM	RCP8.5	-4.4	-0.3	13.2	-10	0.2	10.6	-9.8	0.1	15.8
		RCP4.5	-4.5	0.4	6.6	-9.7	-0.7	7.6	-9.4	-0.6	17.5
		RCP2.6	-8.4	-1	11	-5.1	-0.6	6.1	-4.8	0.4	6.6
	JJA	RCP8.5	-11.5	-6.1	7.1	-21	-13.3	4.4	-35.1	-20.9	1.6
		RCP4.5	-15.7	-4.8	-0.4	-23.9	-9.1	0.4	-21.5	-8.7	5.8
		RCP2.6	-16.2	-3.1	7.9	-17.2	-5.2	6.7	-16.5	-3.6	8.6
	SON	RCP8.5	-9.4	-2.6	11.6	-12.5	-3.3	5.8	-17	-6	2.9
		RCP4.5	-10.7	-4.4	12.8	-14.4	-3.7	5.3	-9.2	-4.2	4.8
		RCP2.6	-12.5	-3.2	15.6	-9.5	-3.5	10.6	-9.7	-4.4	10.7

Table 13.6. As in Table 13.3, but for precipitation change (%) (as shown in Figure 4.5).

A.2.7. Snowfall and snow cover changes

Table 13.5. List of the EUR-11 sub-ensemble employed for the analysis of snowfall changes (see also [127]).

GCM	init	RCM	Emission scenario
ICHEC-EC-EARTH	r12i1p1	CLMcom-CCLM4-8-17	RCP4.5, RCP8.5
ICHEC-EC-EARTH	r3i1p1	DMI-HIRHAM5	RCP4.5, RCP8.5
ICHEC-EC-EARTH	r12i1p1	SMHI-RCA4	RCP4.5, RCP8.5
IPSL-IPSL-CM5A-MR	r1i1p1	SMHI-RCA4	RCP4.5, RCP8.5
MOHC-HadGEM2-ES	r1i1p1	CLMcom-CCLM4-8-17	RCP4.5, RCP8.5
MOHC-HadGEM2-ES	r1i1p1	SMHI-RCA4	RCP4.5, RCP8.5
MPI-M-MPI-ESM-LR	r1i1p1	CLMcom-CCLM4-8-17	RCP4.5, RCP8.5
MPI-M-MPI-ESM-LR	r1i1p1	MPI-CSC-REMO2009	RCP4.5, RCP8.5
MPI-M-MPI-ESM-LR	r1i1p1	SMHI-RCA4	RCP4.5, RCP8.5

Table 13.6. List of the EUR-11 sub-ensemble employed for the analysis of snow cover changes.

GCM	init	RCM	Emission scenario
ICHEC-EC-EARTH	r12i1p1	CLMcom-CCLM4-8-17	RCP4.5, RCP8.5
MOHC-HadGEM2-ES	r1i1p1	CLMcom-CCLM4-8-17	RCP4.5, RCP8.5
MPI-M-MPI-ESM-LR	r1i1p1	CLMcom-CCLM4-8-17	RCP4.5, RCP8.5
MPI-M-MPI-ESM-LR	r1i1p1	MPI-CSC-REMO2009	RCP4.5, RCP8.5
MPI-M-MPI-ESM-LR	r2i1p1	MPI-CSC-REMO2009	RCP4.5, RCP8.5

A.2.8. Model biases

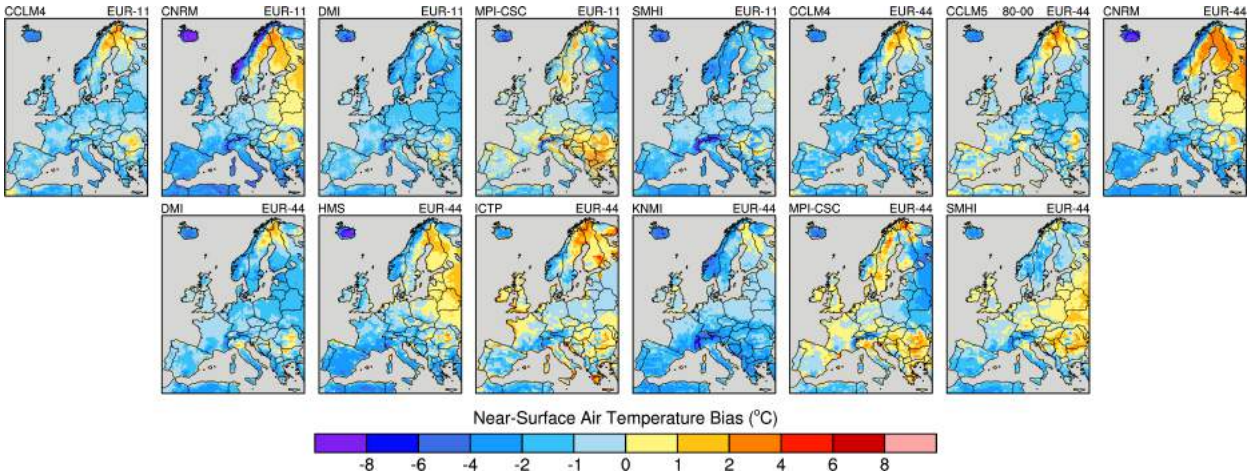

Figure 13.7. Winter (DJF) temperature bias (1989 - 2008) of ERA-Interim-driven runs. The E-OBS dataset [150] is used to calculate the model bias.

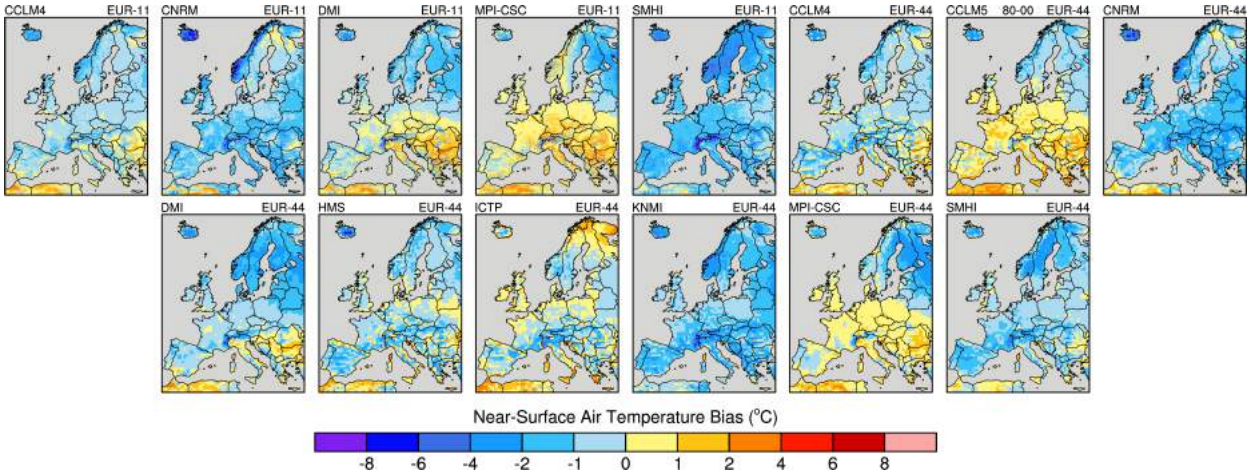

Figure 13.8. As Figure 13.7, but for spring (MAM).

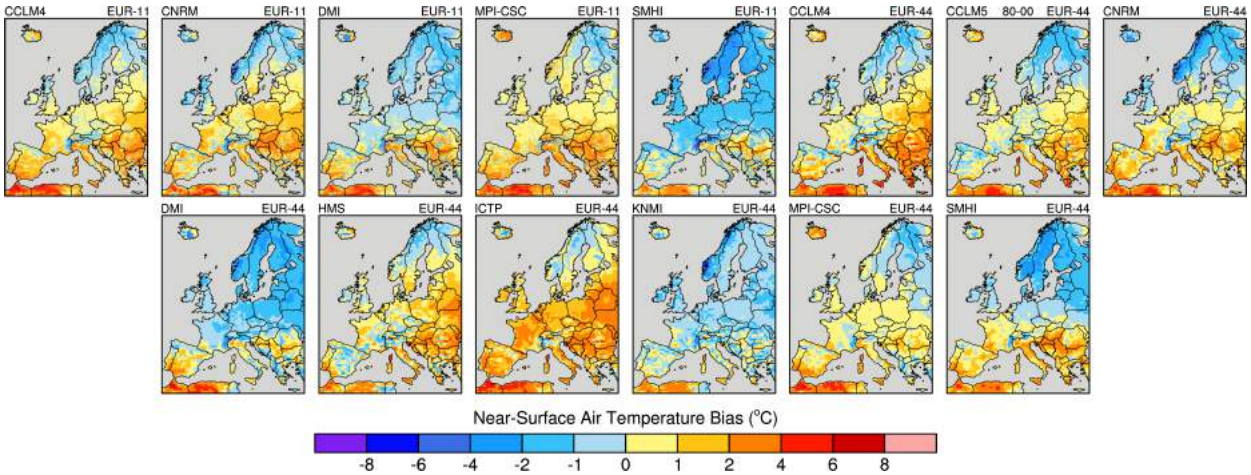

Figure 13.9. As Figure 13.7, but for summer (JJA).

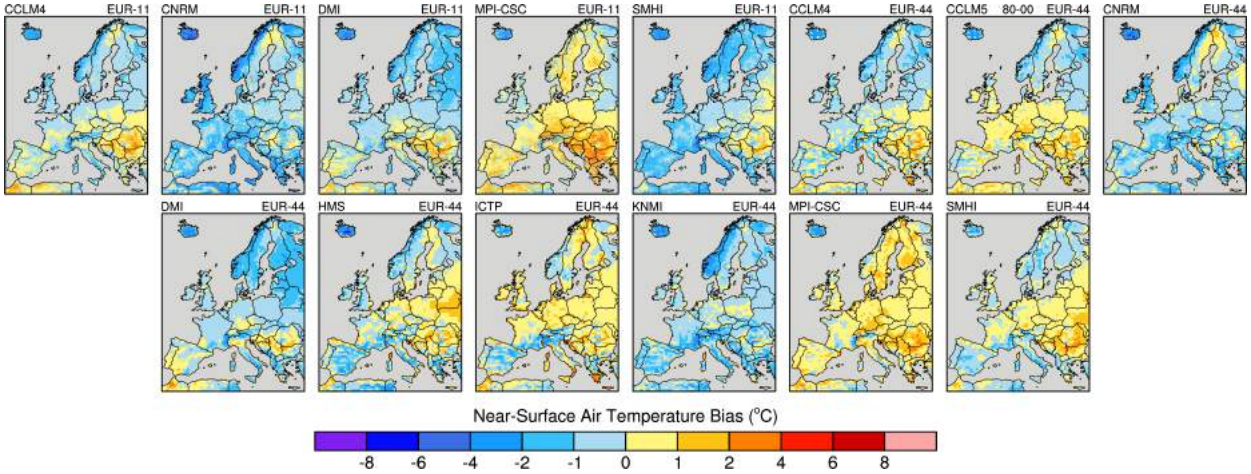

Figure 13.10. As Figure 13.7, but for autumn (SON).

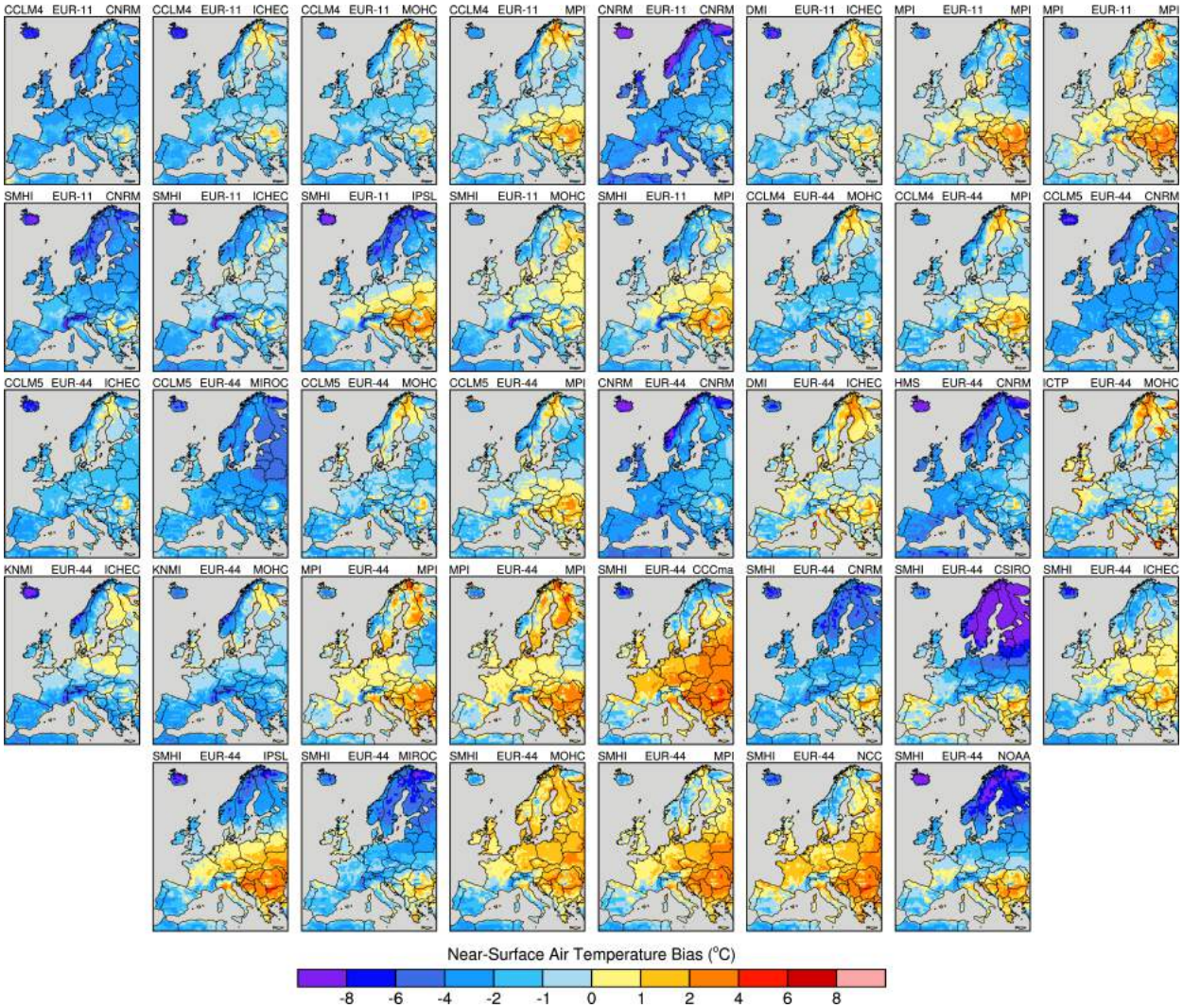

Figure 13.11. Winter (DJF) temperature bias (1981 - 2008) of historical simulations. The E-OBS dataset [150] is used to calculate the model bias.

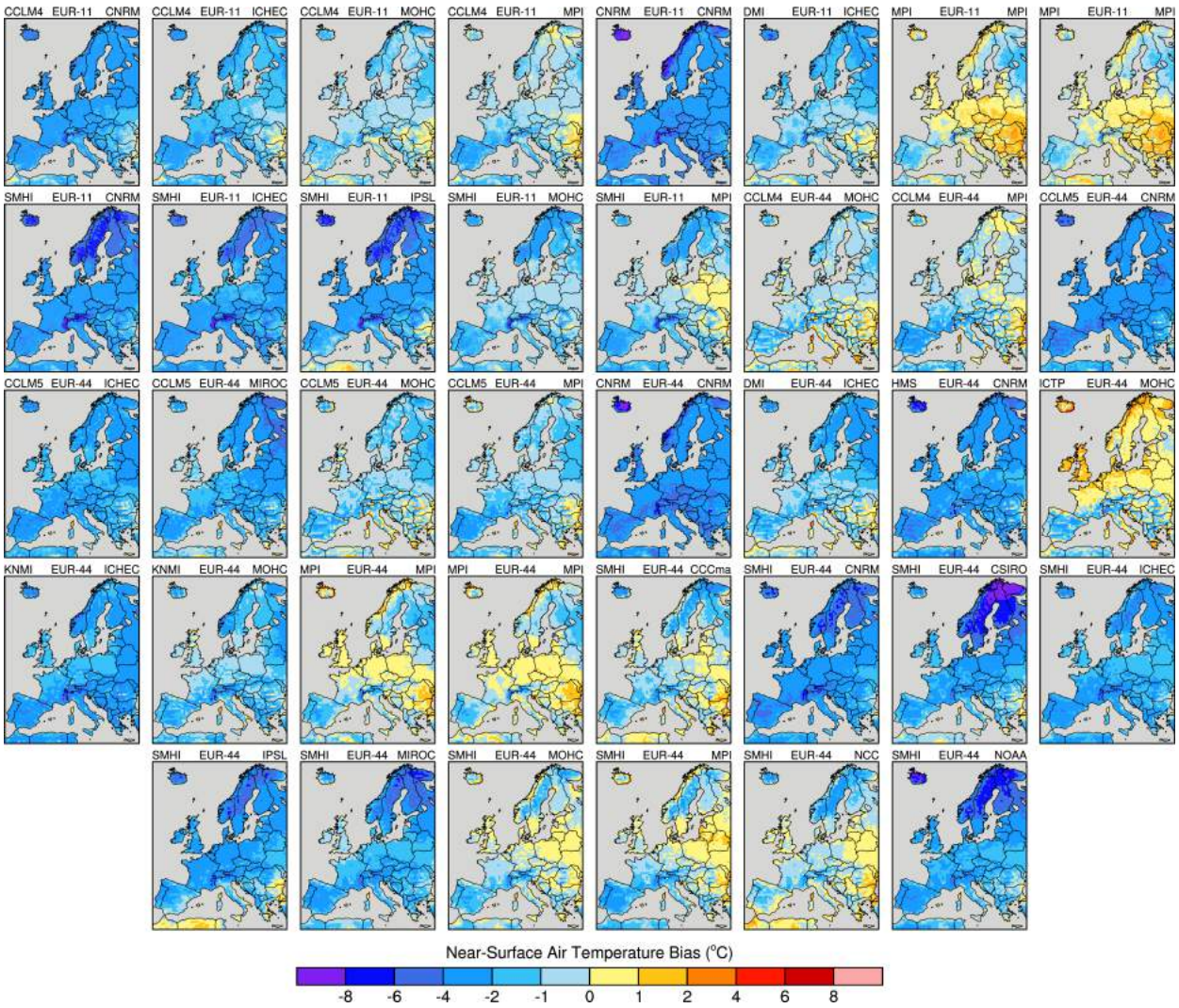

Figure 13.12. As Figure 13.11, but for spring (MAM).

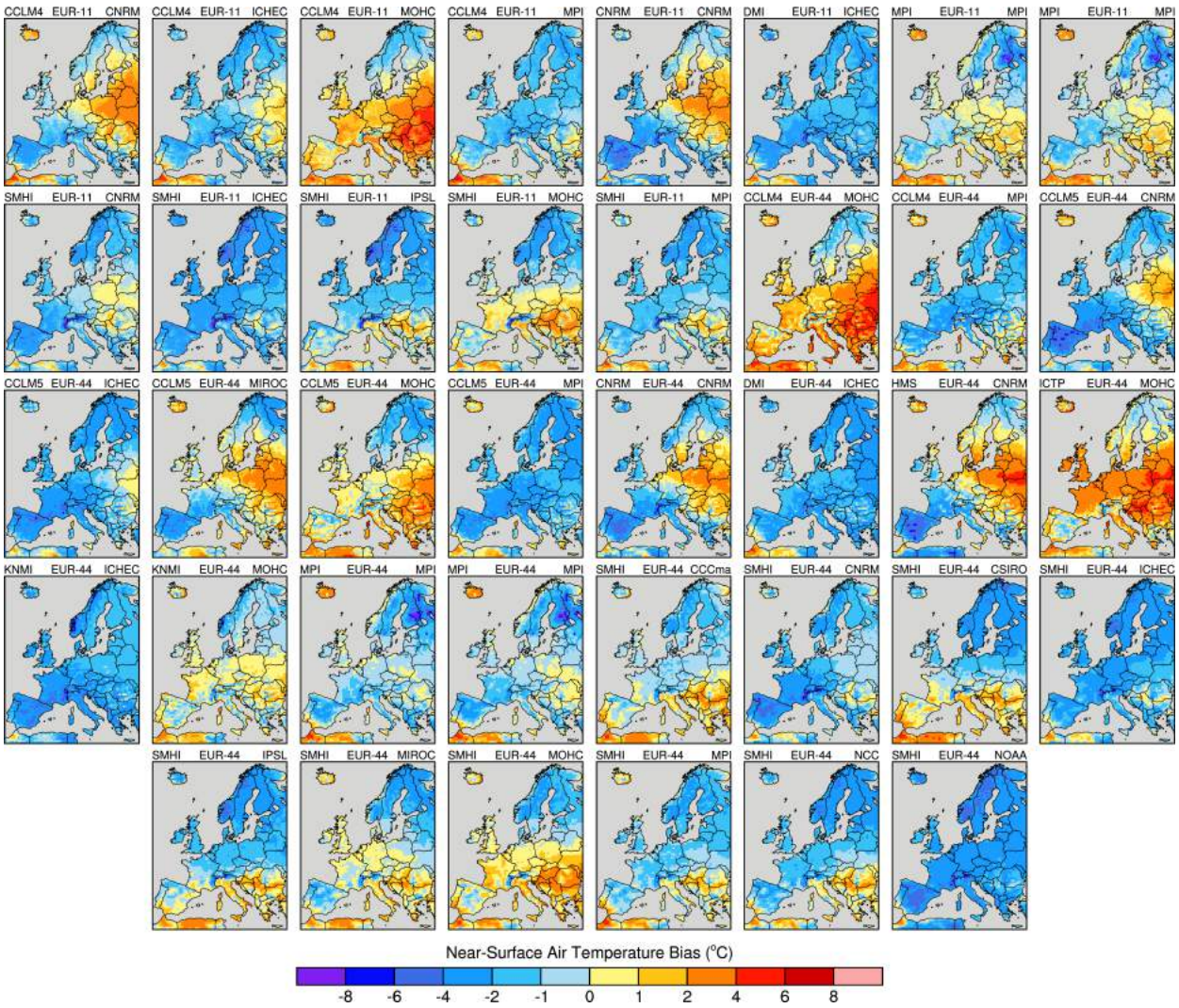

Figure 13.13. As Figure 13.11, but for summer (JJA).

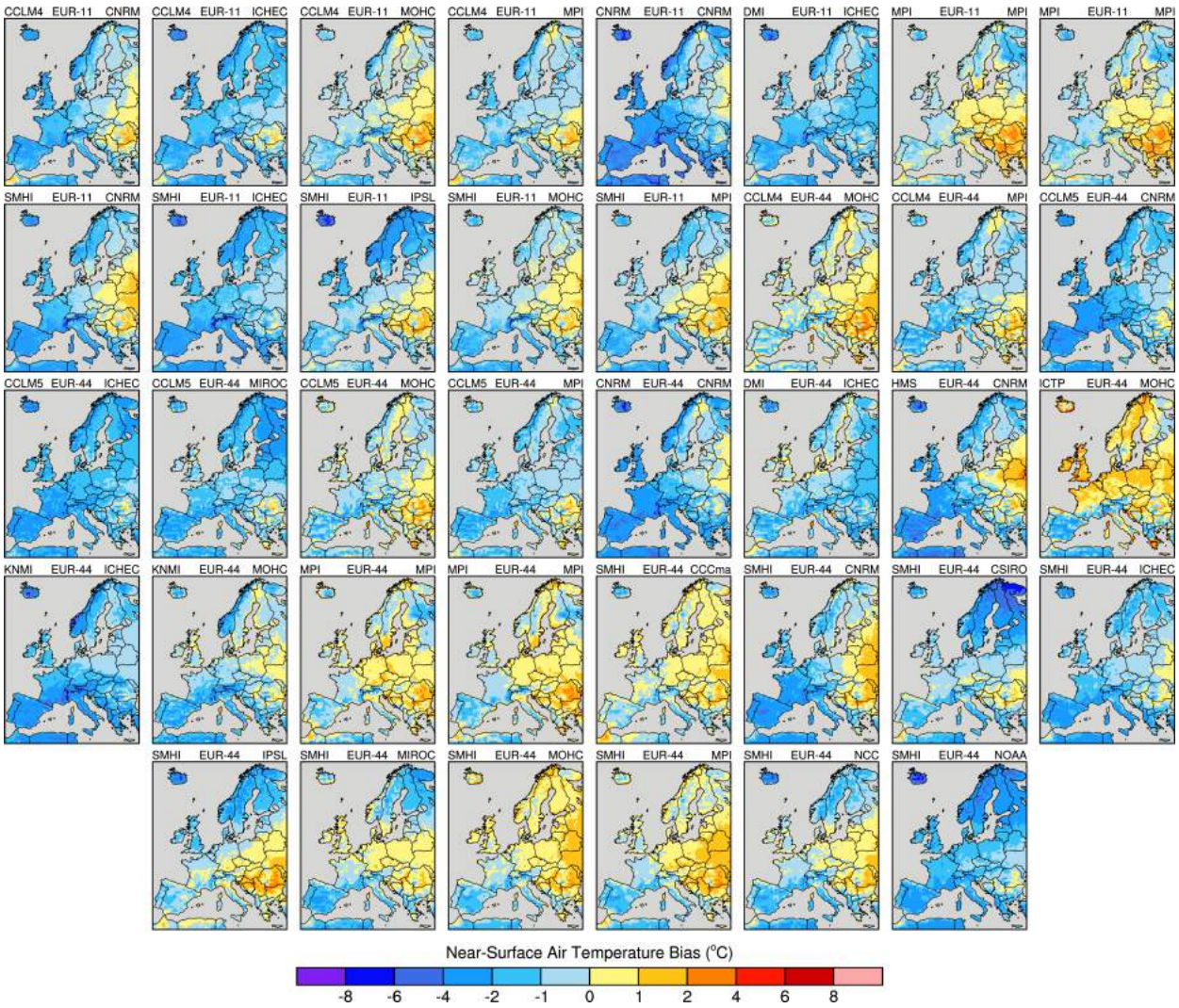

Figure 13.14. As Figure 13.11, but for autumn (SON).

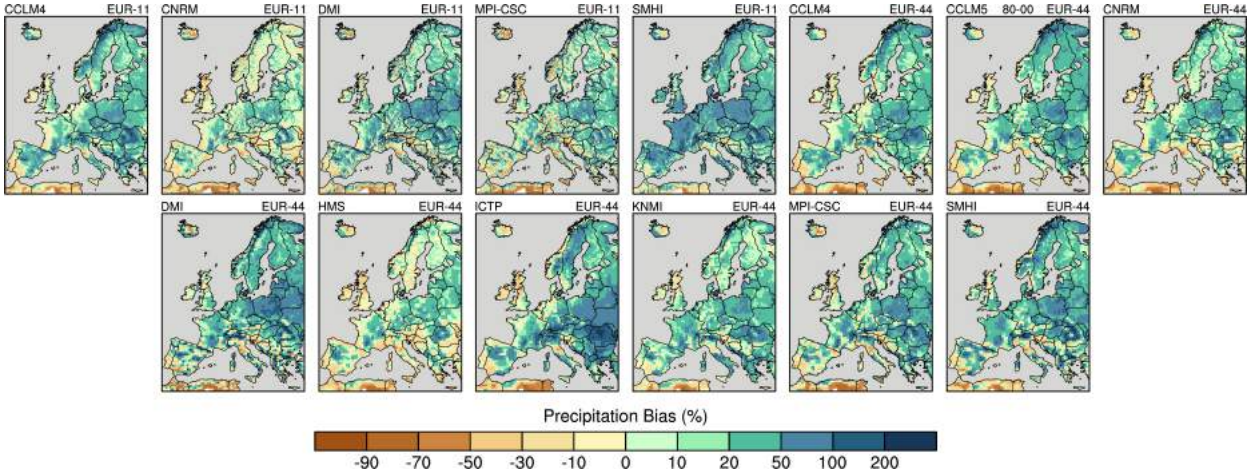

Figure 13.15. Winter (DJF) precipitation bias (1989 - 2008) of ERA-Interim-driven runs. The E-OBS dataset [150] is used to calculate the model bias.

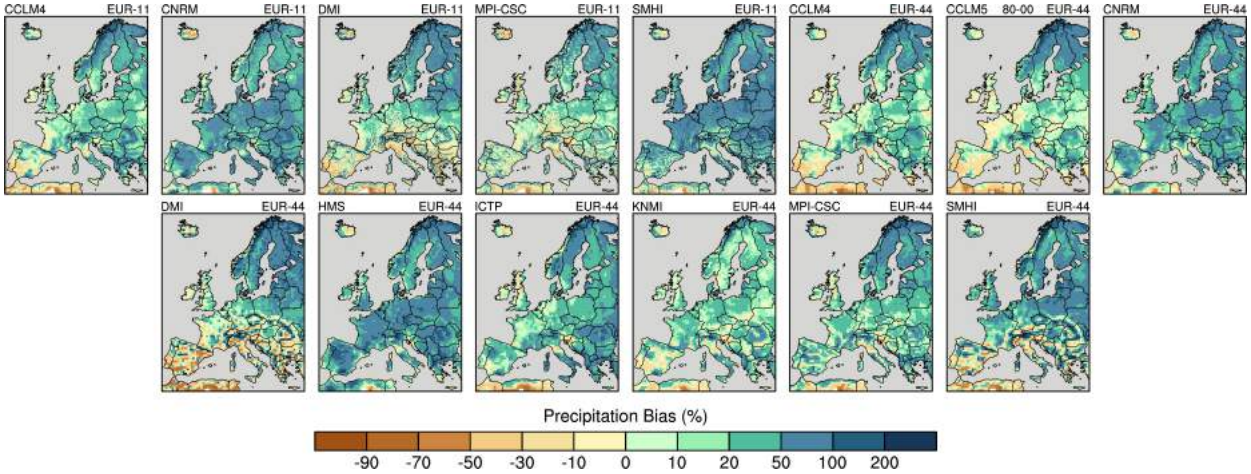

Figure 13.16. As Figure 13.15, but for spring (MAM).

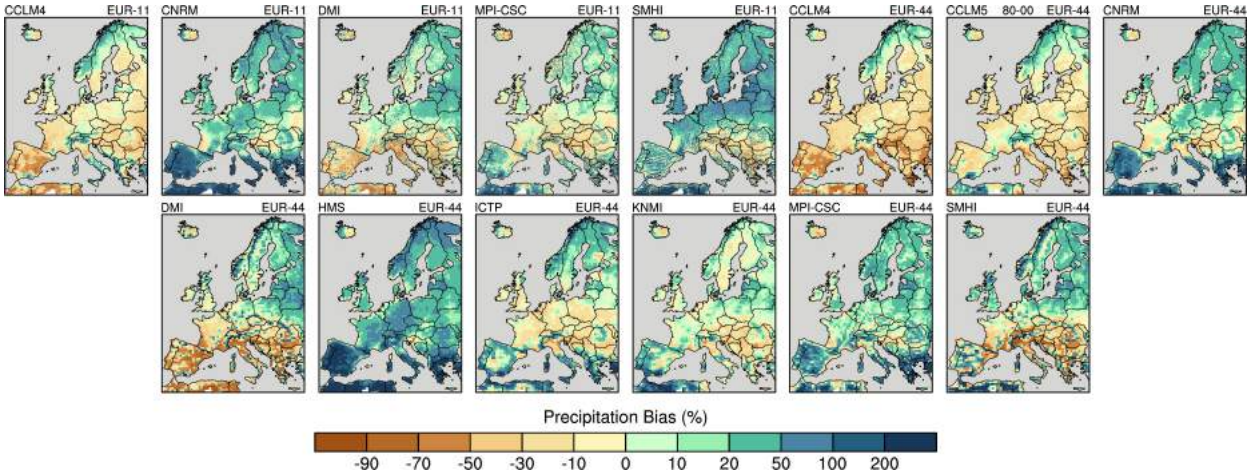

Figure 13.17. As Figure 13.15, but for summer (JJA).

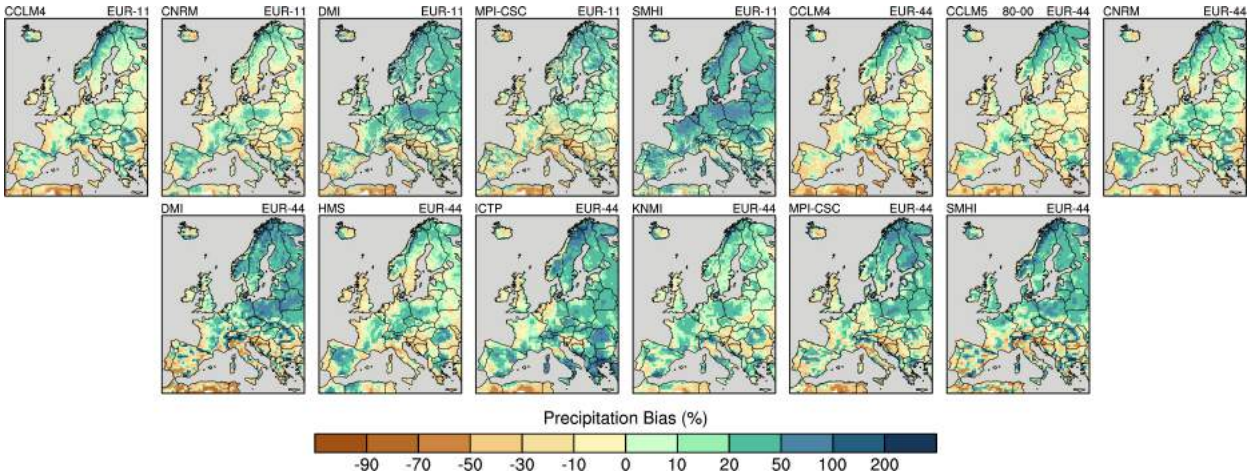

Figure 13.18. As Figure 13.15, but for autumn (SON).

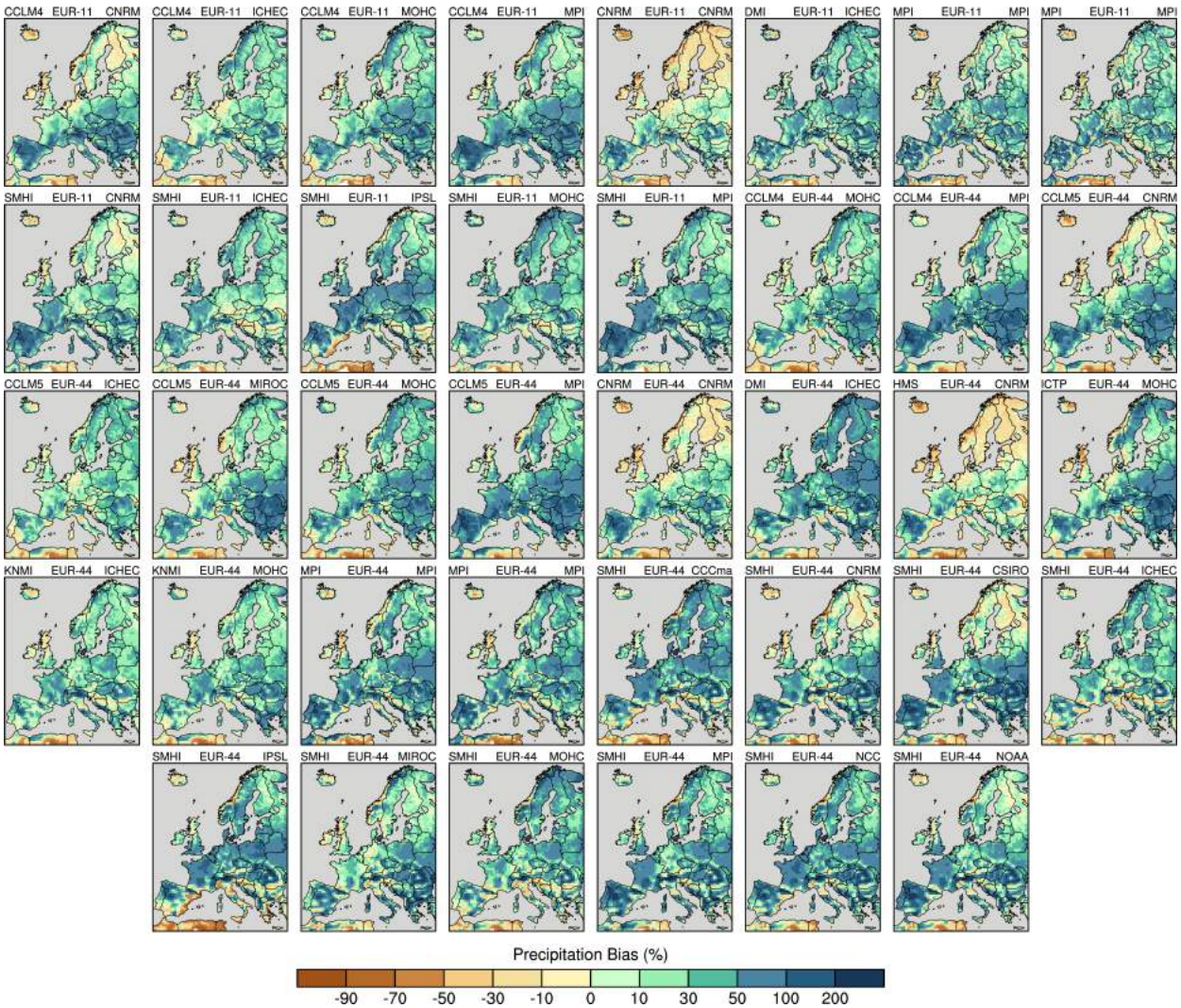

Figure 13.19. Winter (DJF) precipitation bias (1981 - 2008) of historical simulations. The E-OBS dataset [150] is used to calculate the model bias.

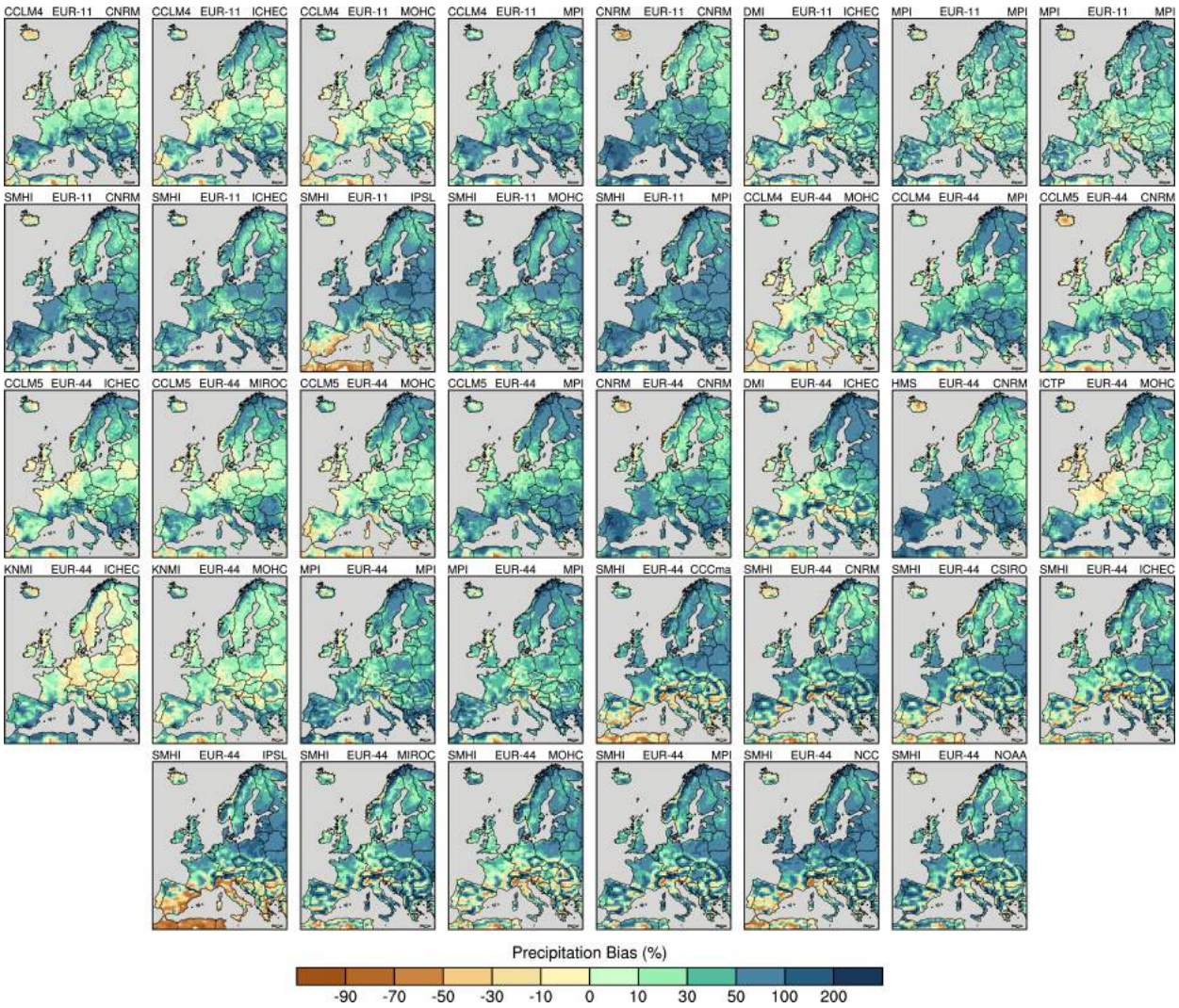

Figure 13.20. As Figure 13.19, but for spring (MAM).

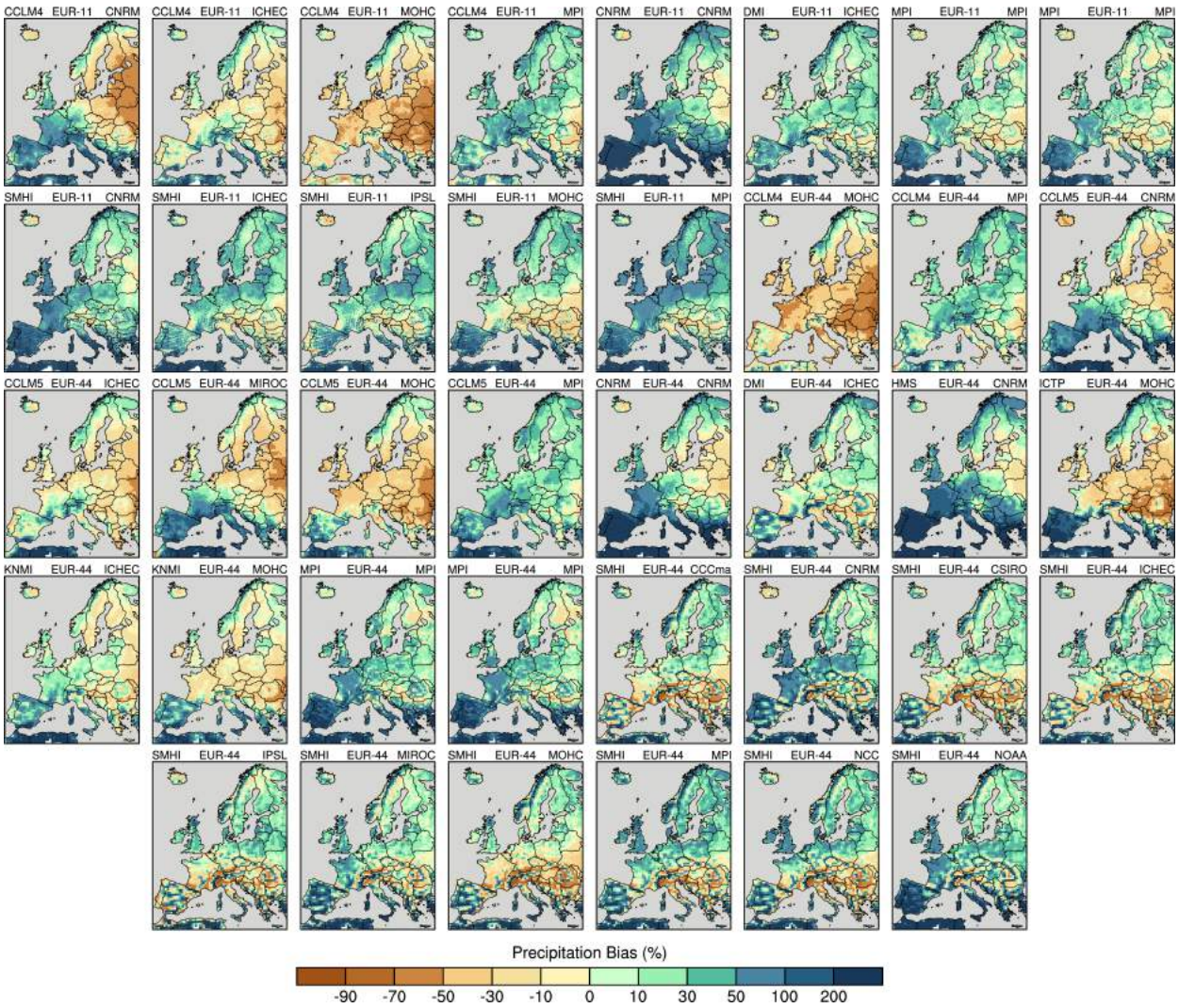

Figure 13.21. As Figure 13.19, but for summer (JJA).

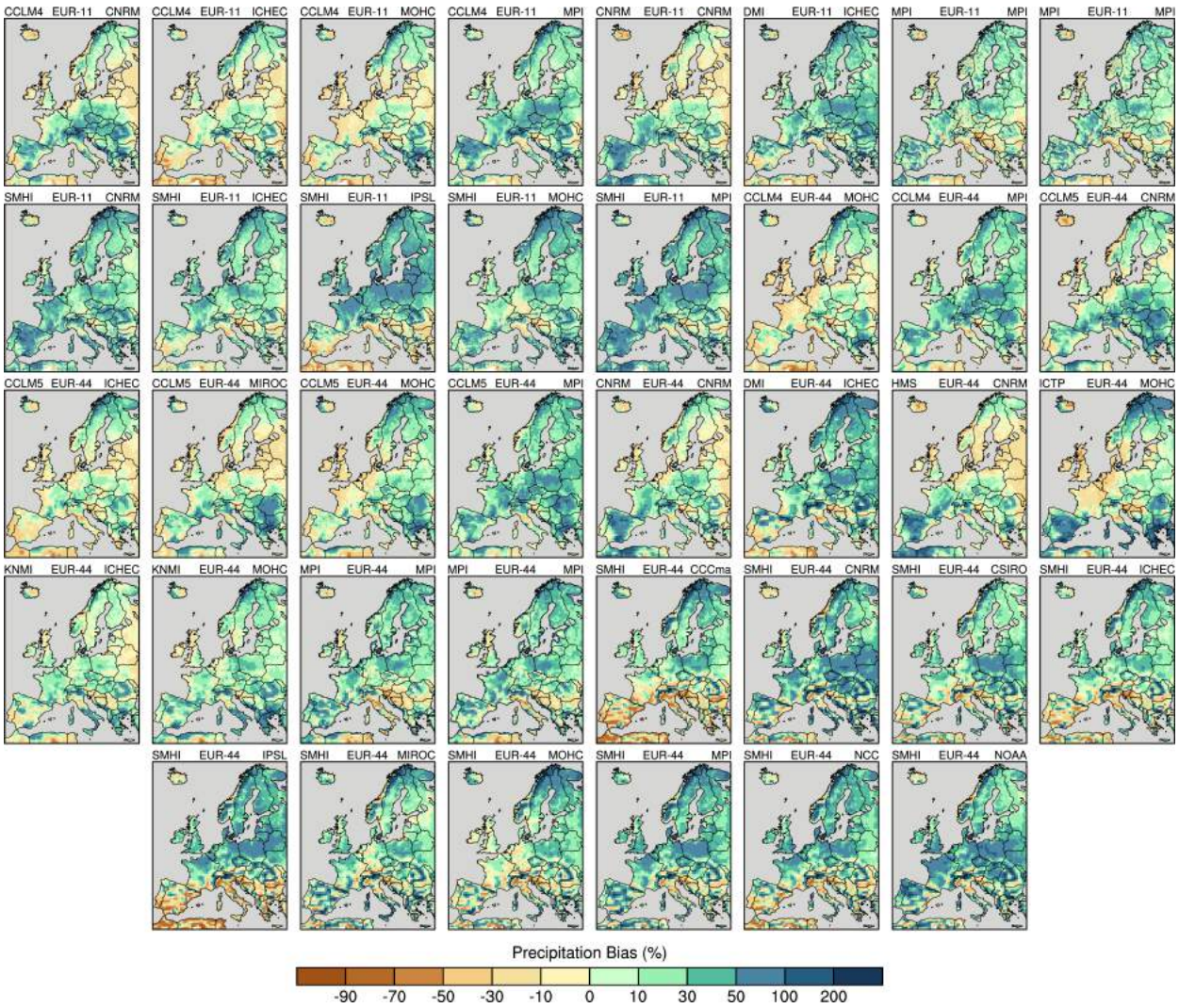

Figure 13.22. As Figure 13.19, but for autumn (SON).

A.3. Appendix: Localized Scenarios

A.3.1. Evaluation

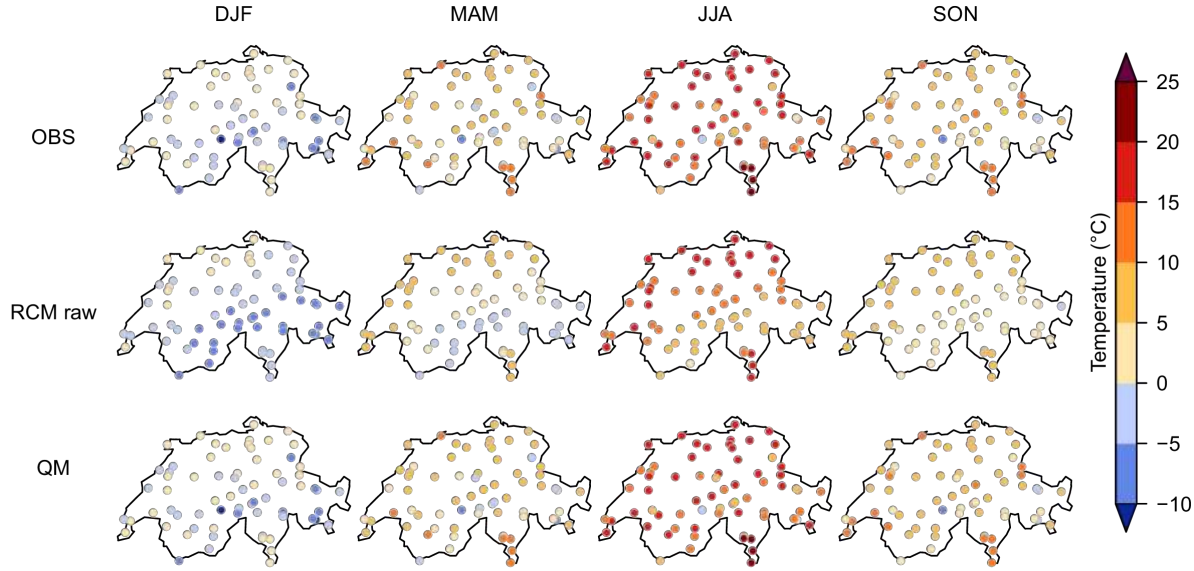

Figure 13.23. Spatial pattern of seasonal mean temperature (°C) in the observations (first row), in RCM raw data (second row), and in the quantile-mapped product (third row). Ensemble mean of all RCP8.5 simulations and for the calibration period 1981 - 2010. In all cases, "raw RCM data" refers to the simulated series of those RCM grid cells in which the respective station is located.

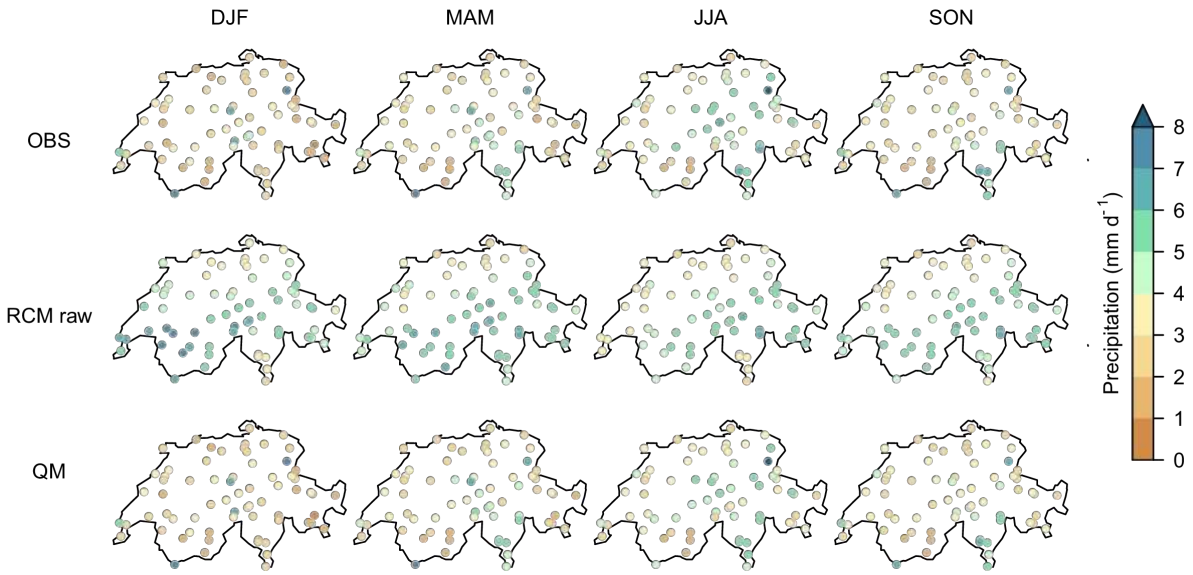

Figure 13.24. As Figure 13.23, but for seasonal mean precipitation (mm/d).

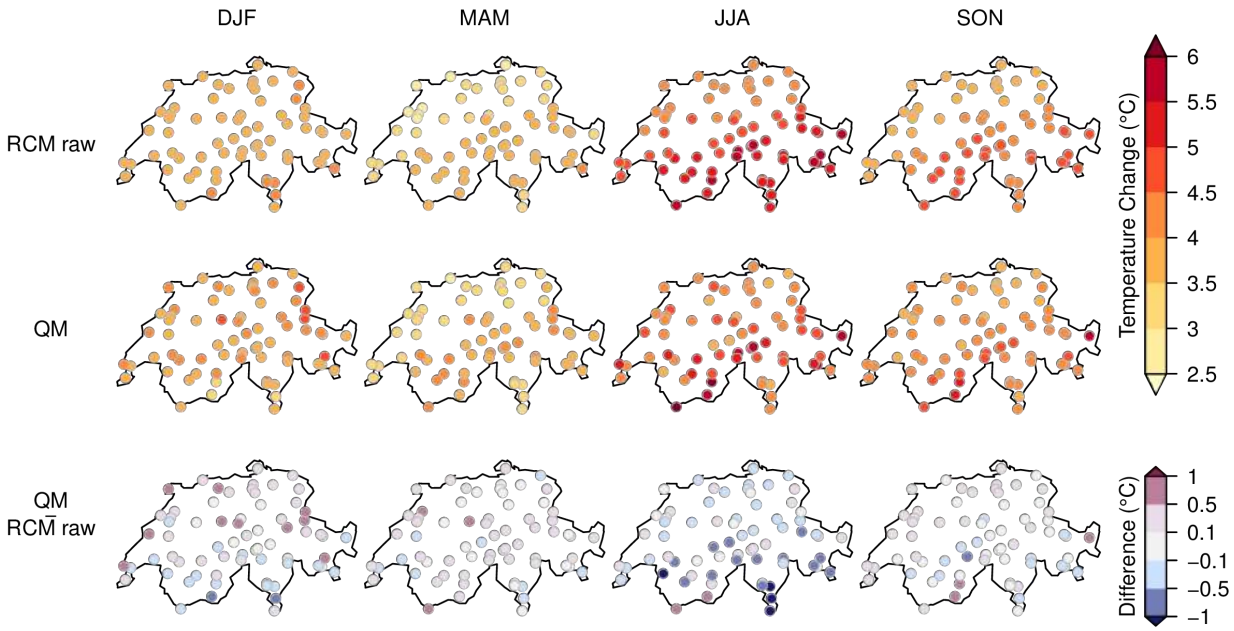

Figure 13.25. Spatial pattern of seasonal mean temperature changes (°C) by the end of the century (ensemble median for RCP8.5) in raw RCM output (upper row) and in the station-based QM product (middle row). Lower row: Difference between QM and raw climate change signals. In all cases, "raw RCM data" refers to the simulated series of those RCM grid cells in which the respective station is located.

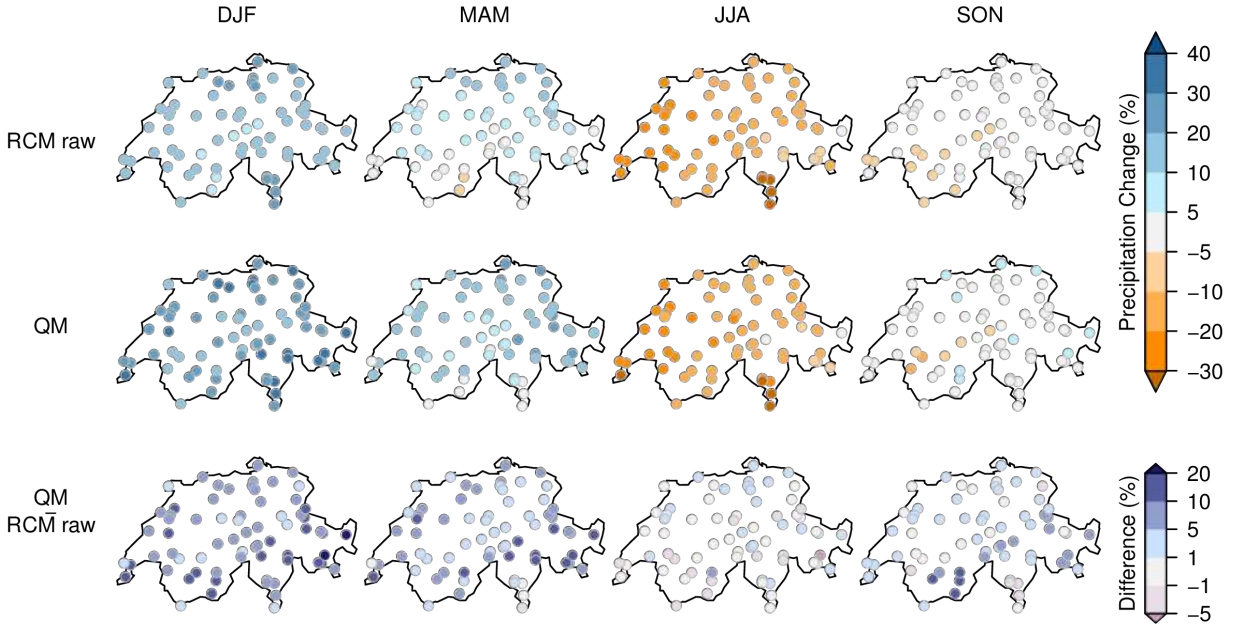

Figure 13.26. As Figure 13.25, but for seasonal mean precipitation changes (%) and the differences between raw RCM output and quantile-mapped data (%).

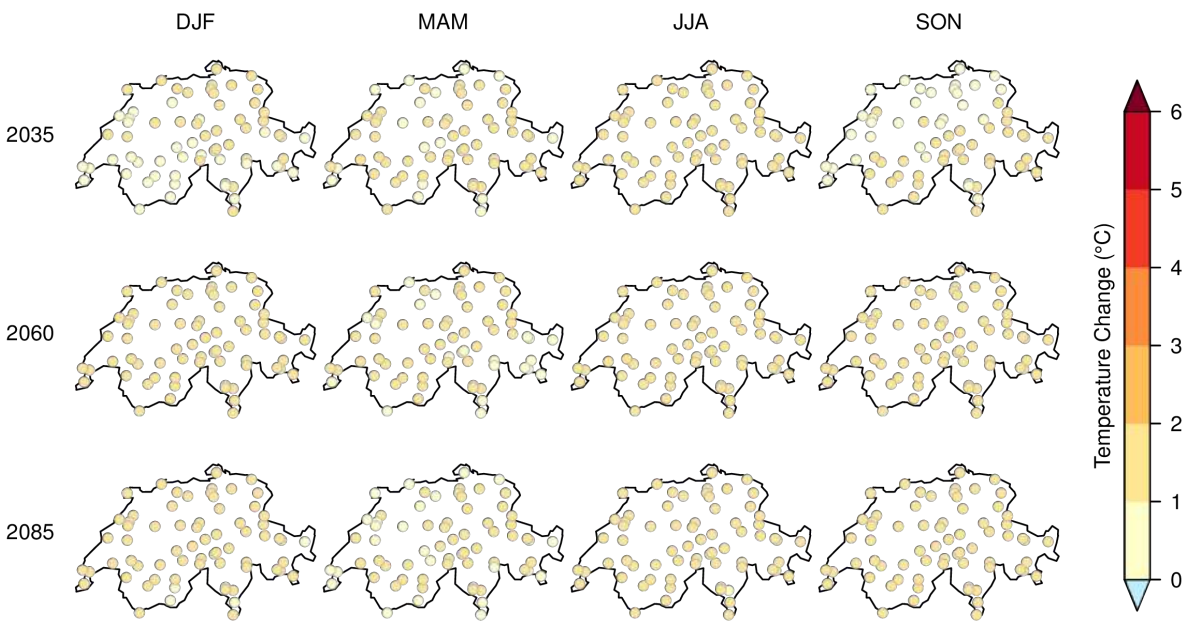

*Figure 13.27. Ensemble median climate change signal for seasonal mean temperature (°C) at stations for all scenario periods and for **RCP2.6** (multi-model combination). Note that the model uncertainty of the change signal is not reflected by the ensemble median signal displayed here and can be substantial.*

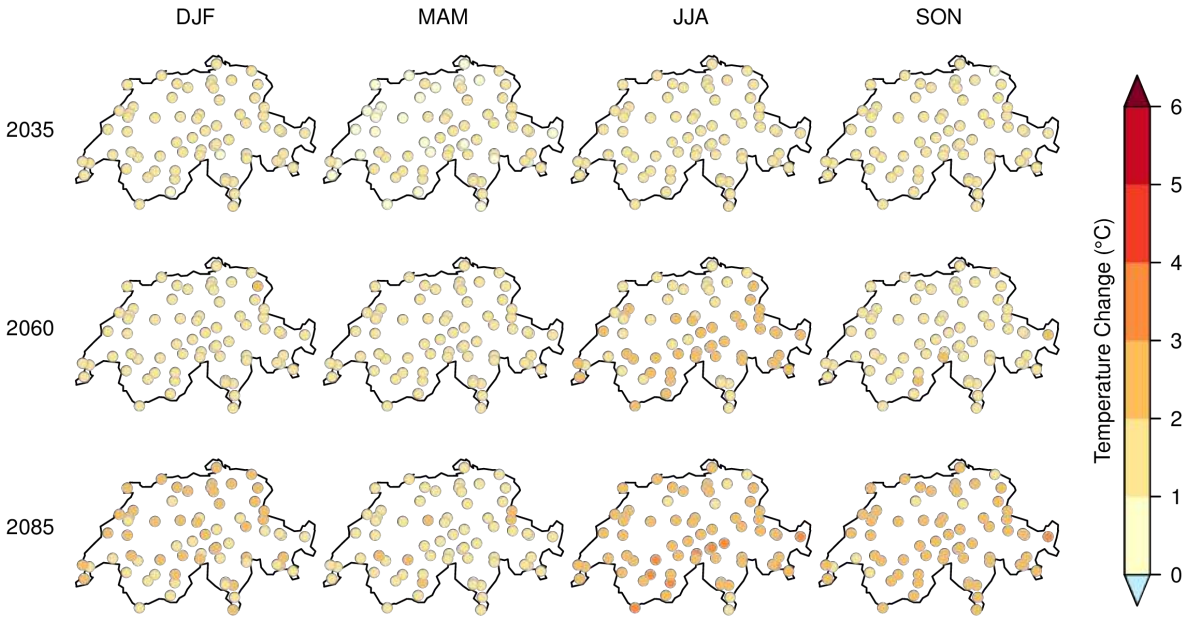

*Figure 13.28. As Figure 13.27, but for **RCP4.5**.*

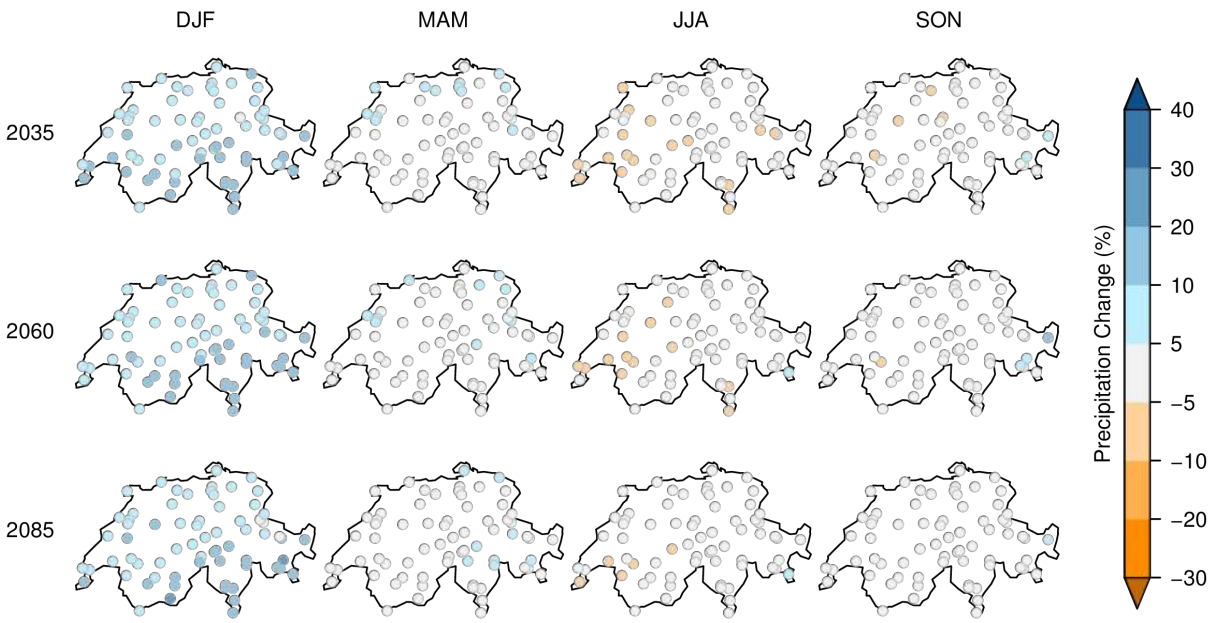

*Figure 13.29. Ensemble median climate change signal for seasonal mean precipitation (%) at stations for all scenario periods and for **RCP2.6** (multi-model combination). Note that the model uncertainty of the change signal is not reflected by the ensemble median signal displayed here and can be substantial.*

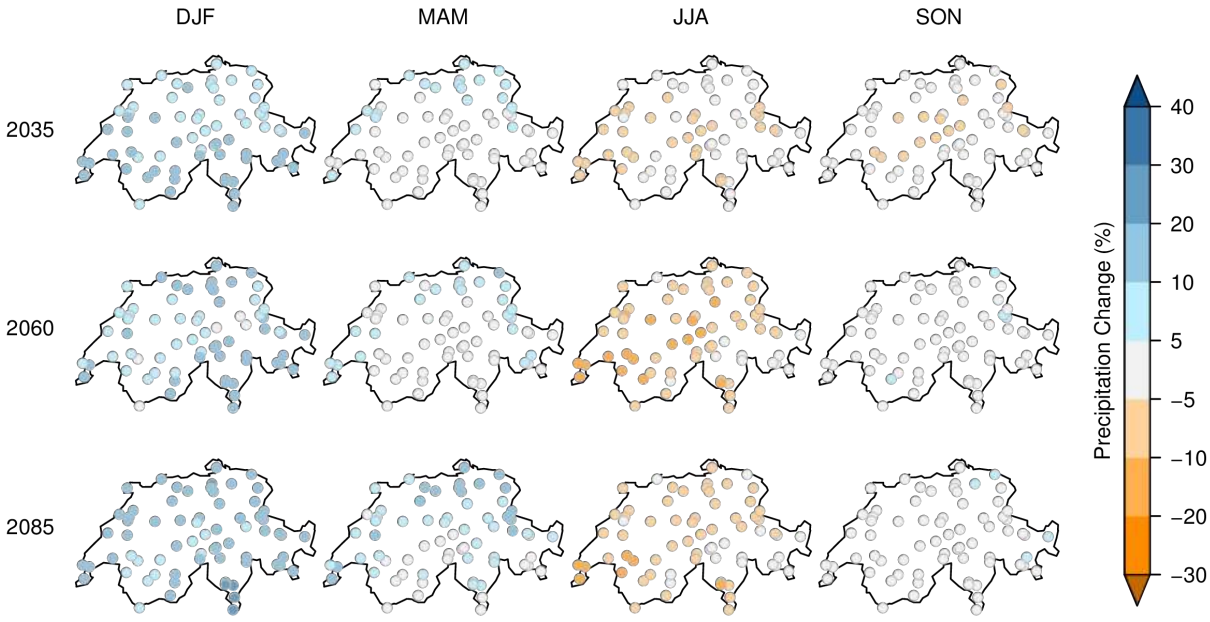

*Figure 13.30. As Figure 13.29, but for **RCP4.5**.*

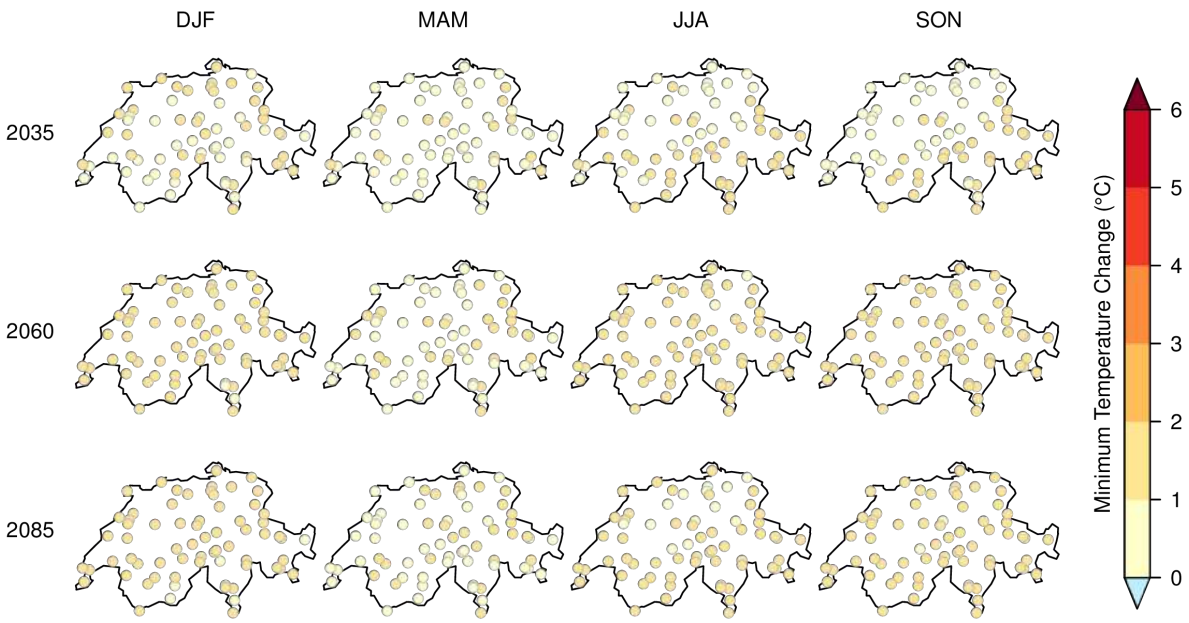

*Figure 13.31. Ensemble median climate change signal for the seasonal mean daily minimum temperature (°C) at stations for all scenario periods and for **RCP2.6** (multi-model combination). Note that the model uncertainty of the change signal is not reflected by the ensemble median signal displayed here and can be substantial.*

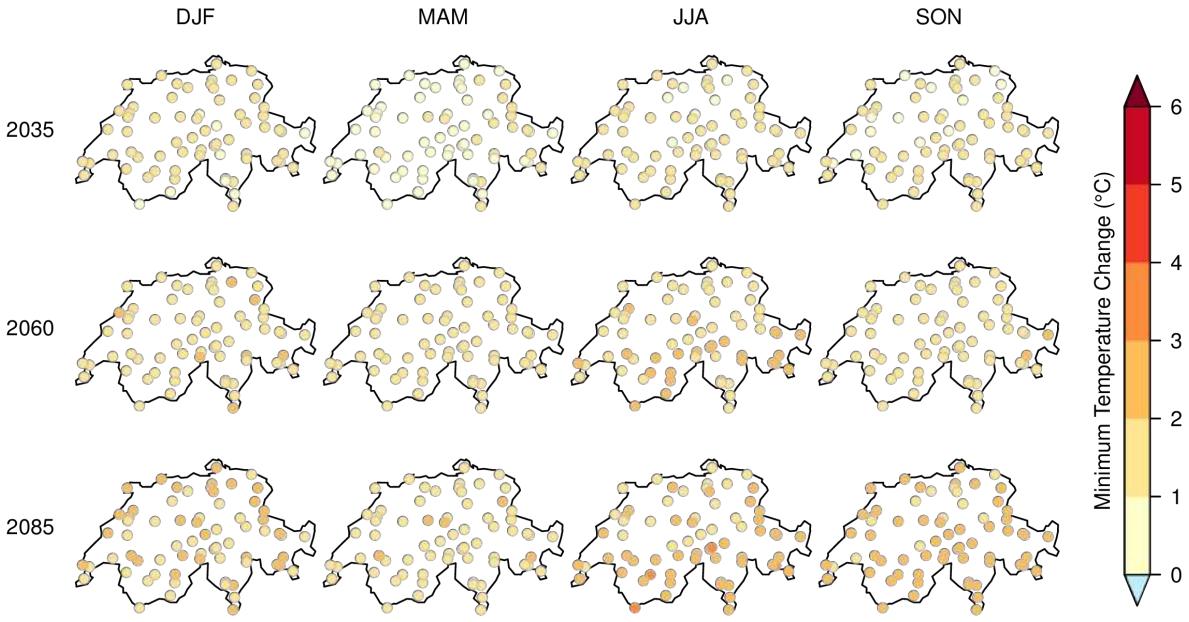

*Figure 13.32. As Figure 13.31, but for **RCP4.5**.*

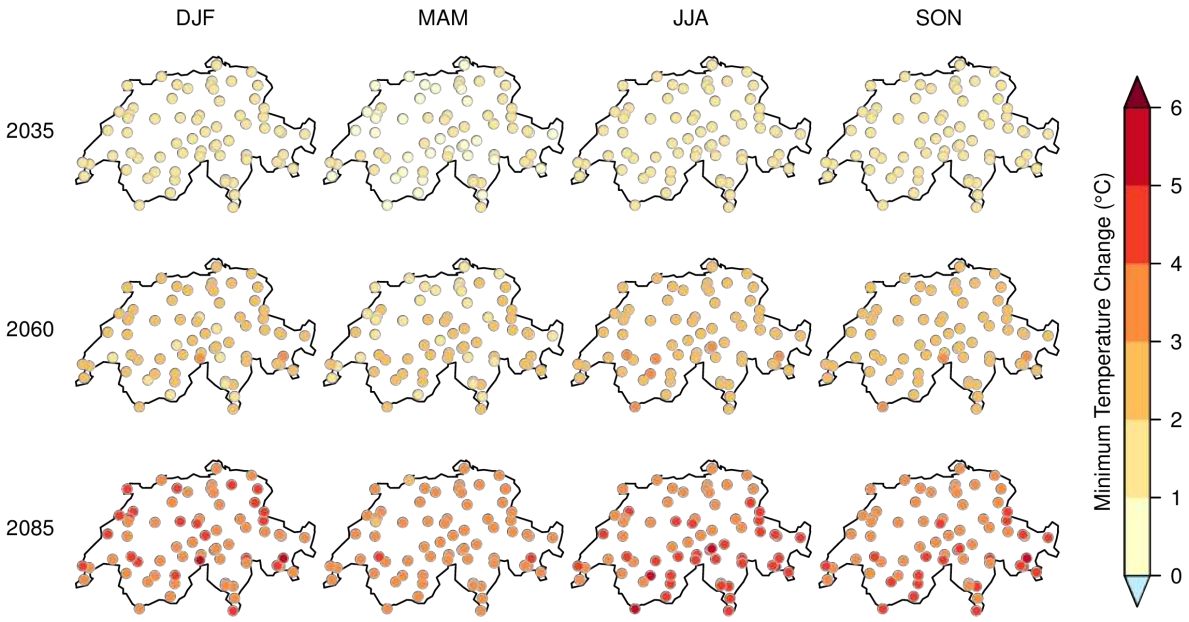

*Figure 13.33. As Figure 13.31, but for **RCP8.5**.*

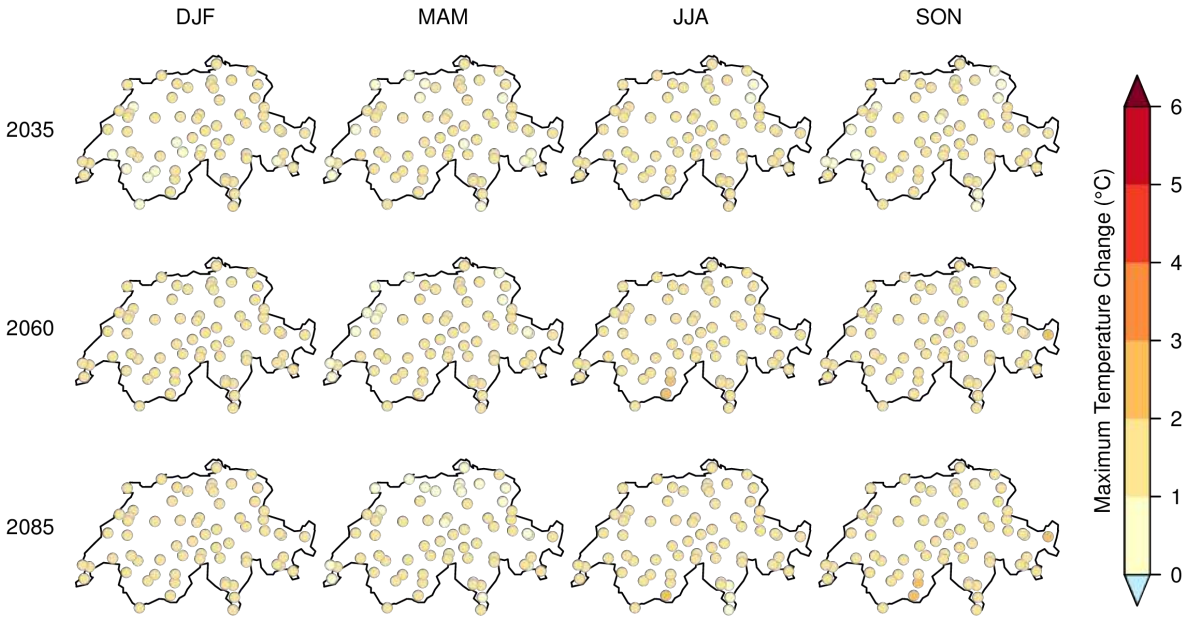

*Figure 13.34. Ensemble median climate change signal for the seasonal mean daily maximum temperature (°C) at stations for all scenario periods and for **RCP2.6** (multi-model combination). Note that the model uncertainty of the change signal is not reflected by the ensemble median signal displayed here and can be substantial.*

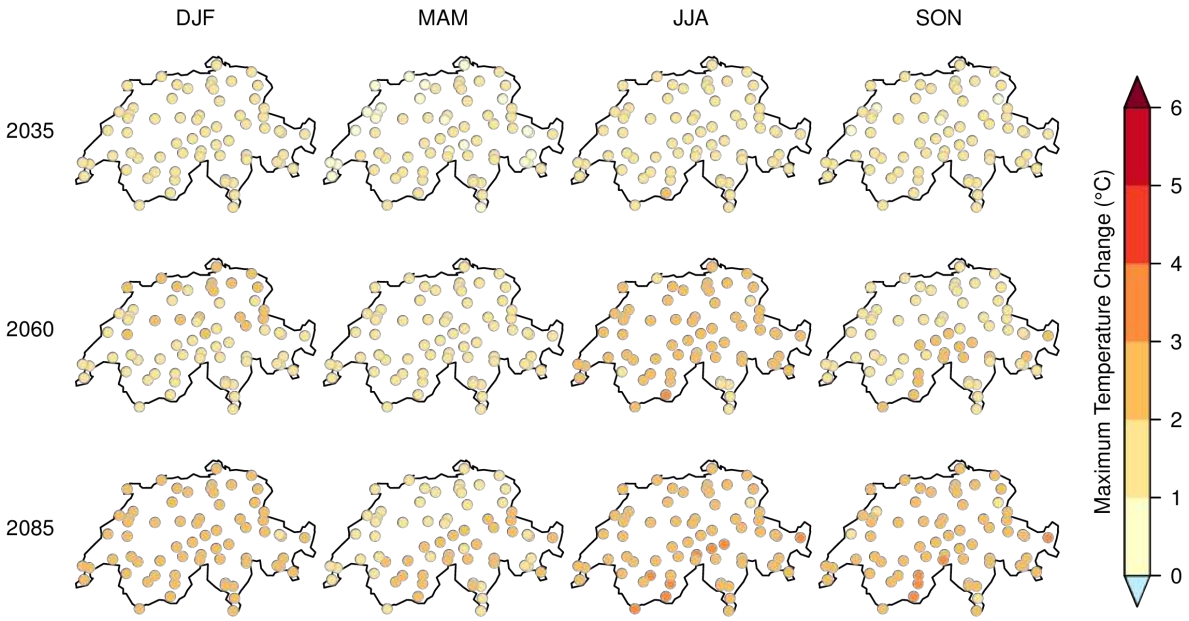

*Figure 13.35. As Figure 13.34, but for **RCP4.5**.*

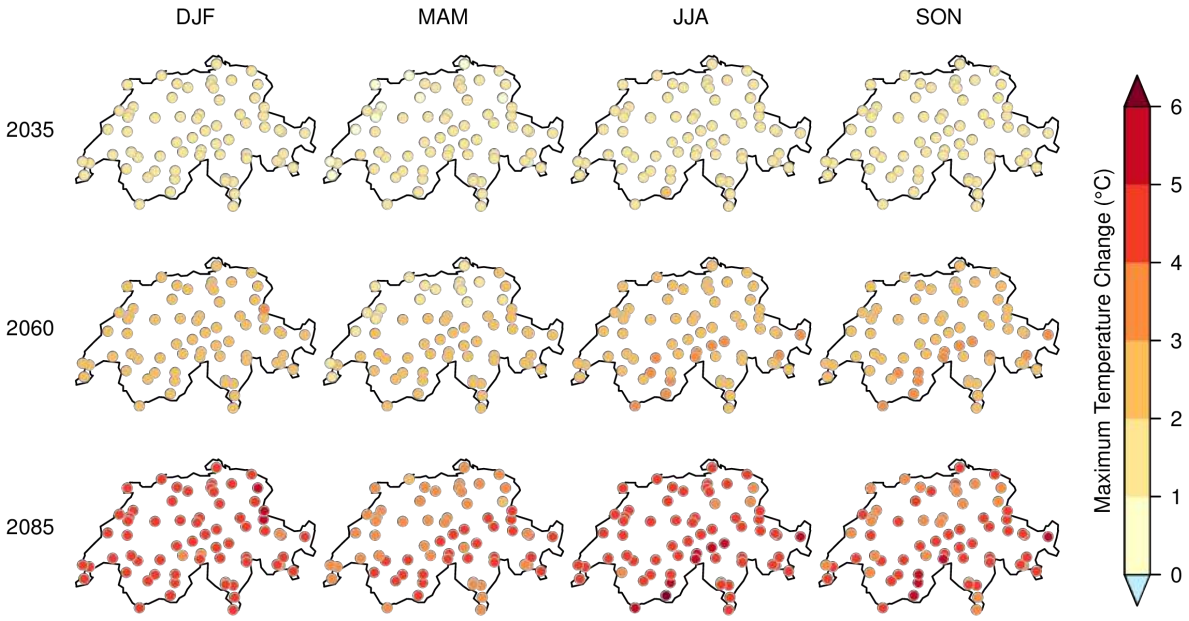

*Figure 13.36. As Figure 13.34, but for **RCP8.5**.*

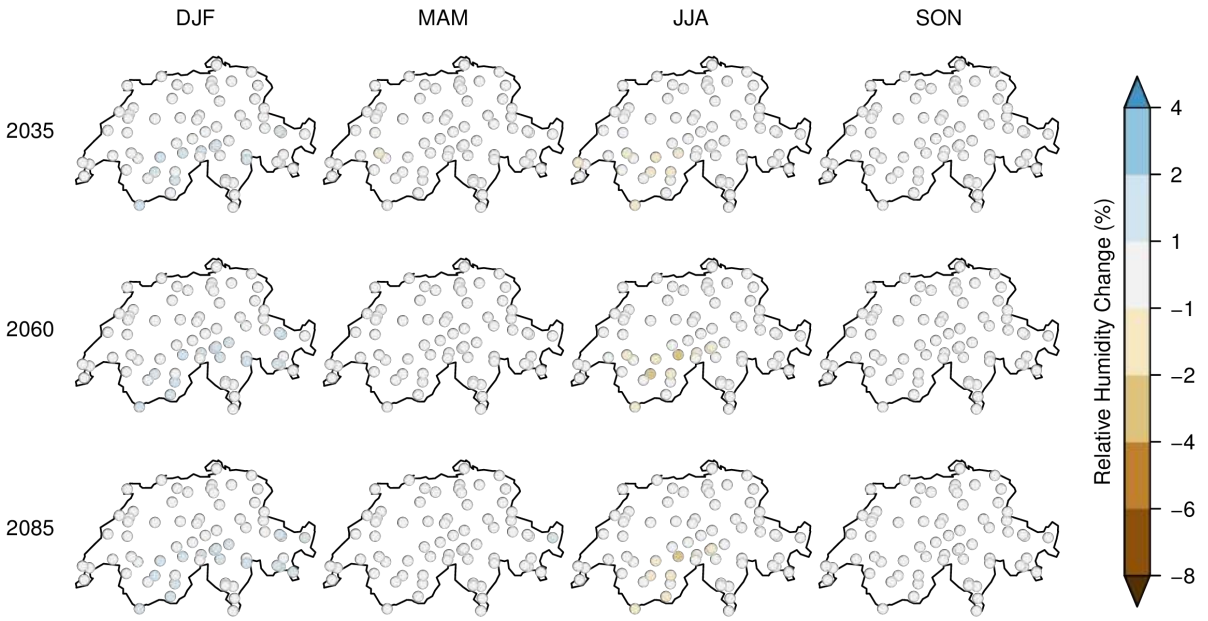

*Figure 13.37. Ensemble median climate change signal for seasonal mean relative humidity (absolute %) at stations for all scenario periods and for **RCP2.6** (multi-model combination). Note that the model uncertainty of the change signal is not reflected by the ensemble median signal displayed here and can be substantial.*

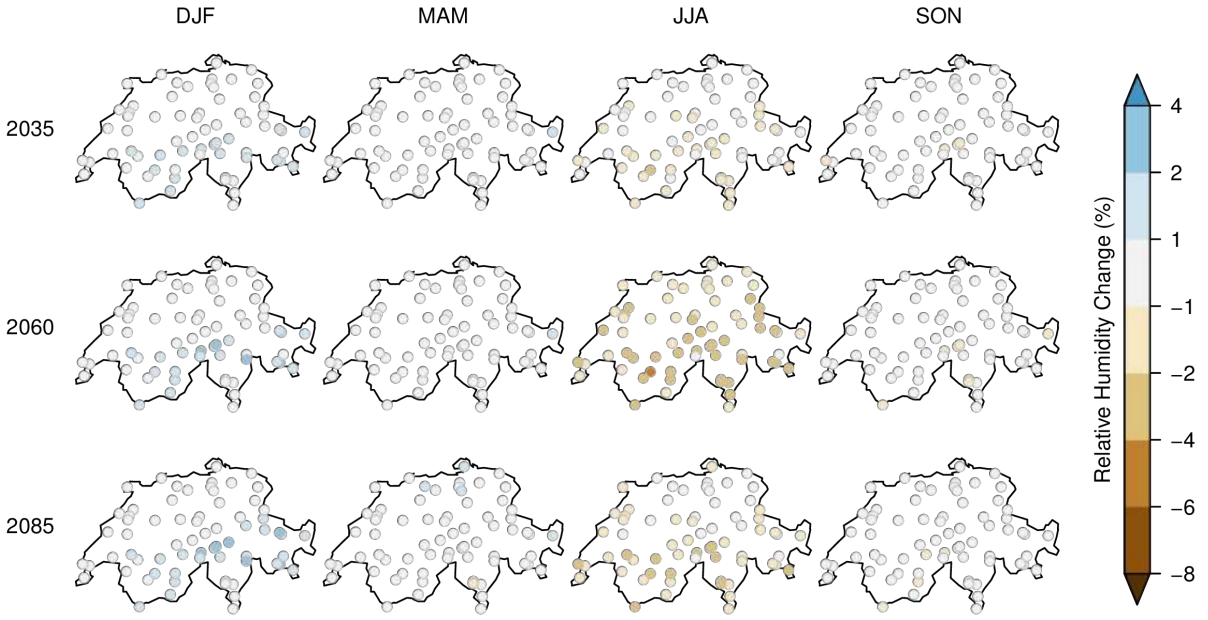

*Figure 13.38. As Figure 13.37, but for **RCP4.5**.*

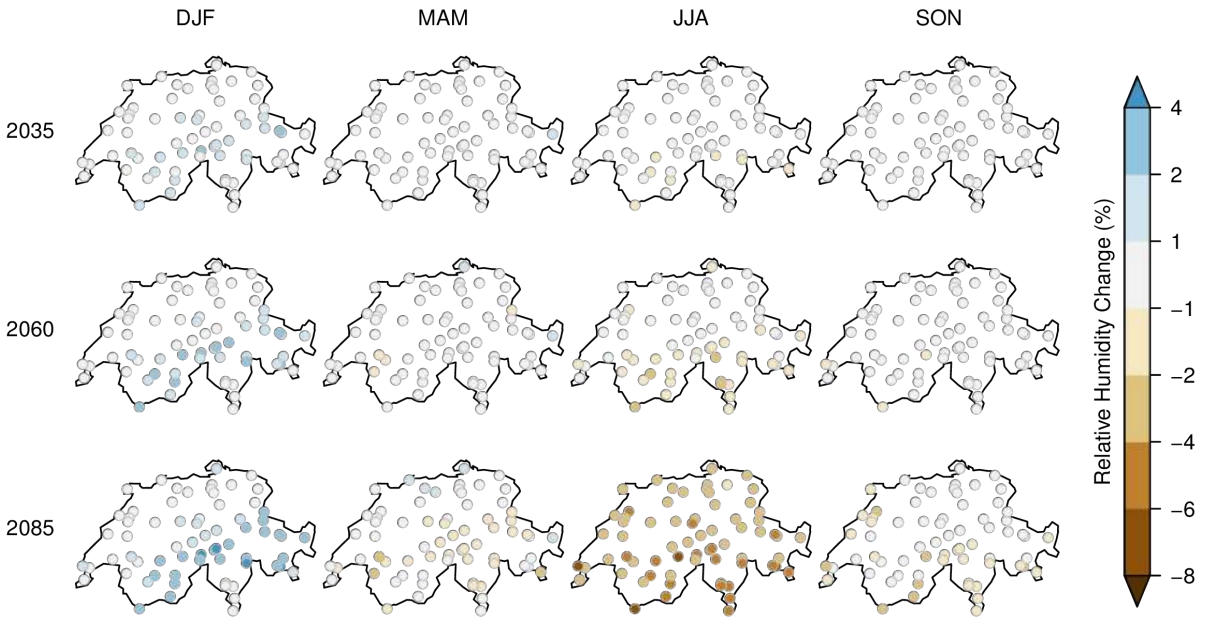

*Figure 13.39. As Figure 13.37, but for **RCP8.5**.*

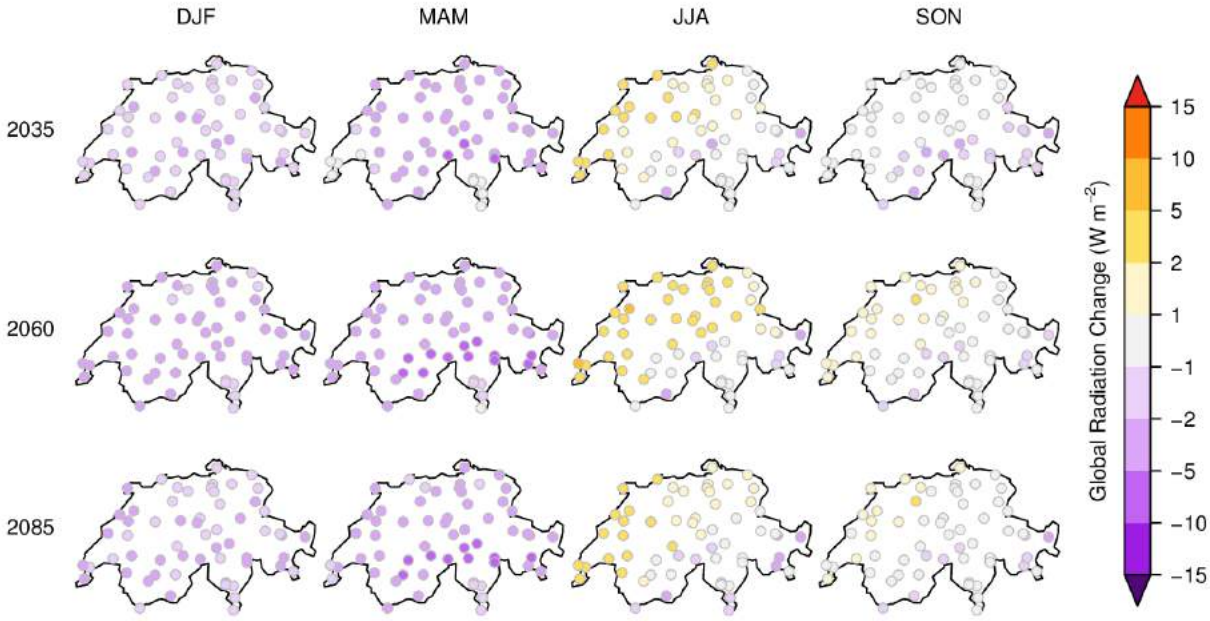

*Figure 13.40. Ensemble median climate change signal for seasonal mean global radiation (W m $^{-2}$) at stations for all scenario periods and for **RCP2.6** (multi-model combination). Note that the model uncertainty of the change signal is not reflected by the ensemble median signal displayed here and can be substantial.*

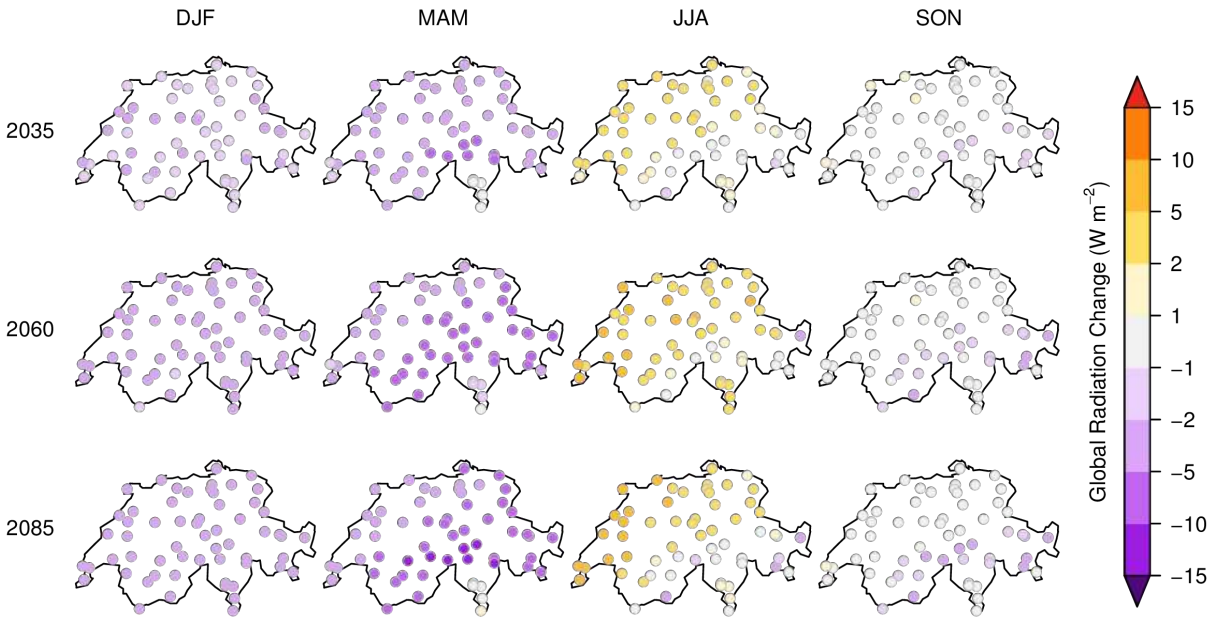

*Figure 13.41. As Figure 13.40, but for **RCP4.5**.*

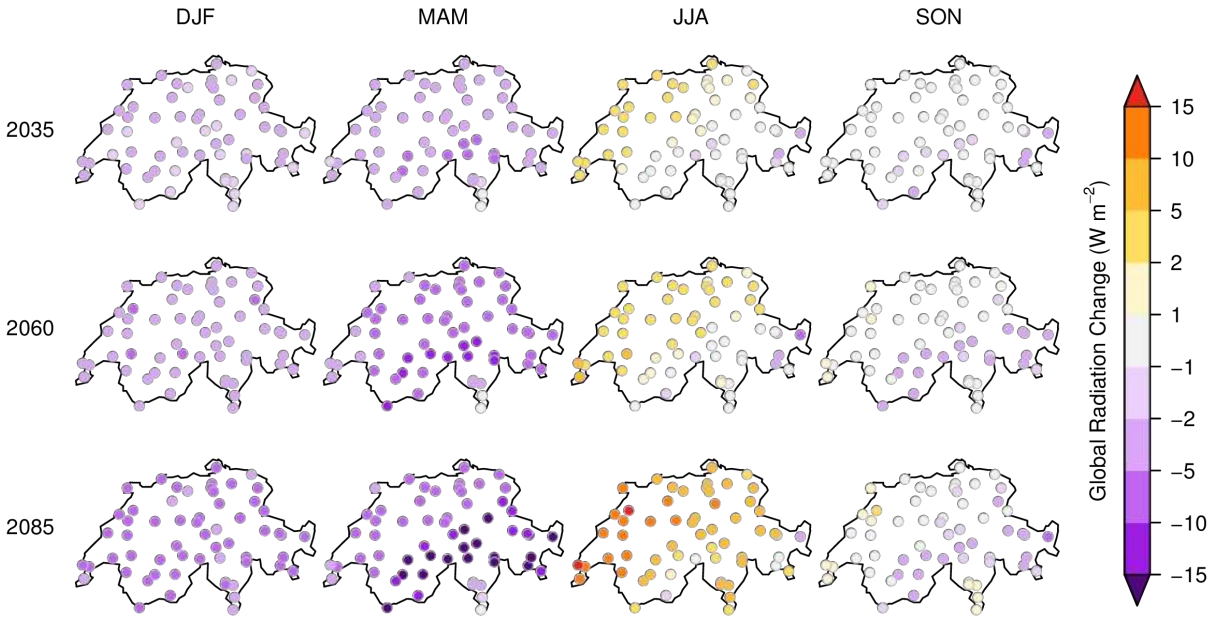

*Figure 13.42. As Figure 13.40, but for **RCP8.5**.*

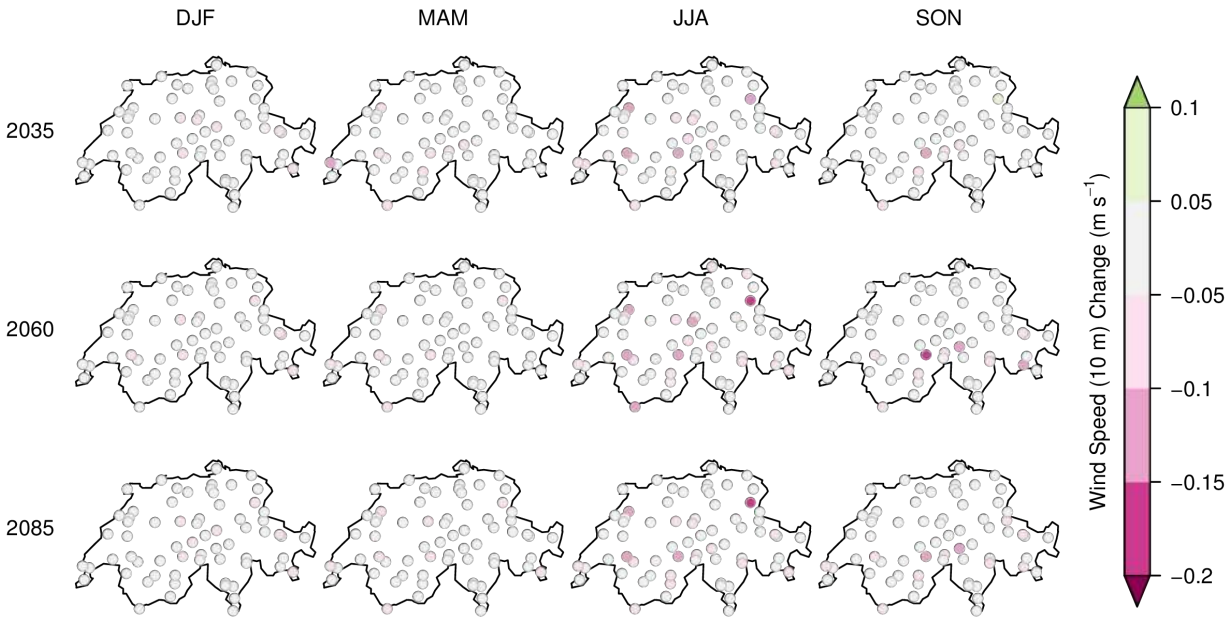

*Figure 13.43. Ensemble median climate change signal for seasonal mean 10-m wind speed (m s $^{-1}$) at stations for all scenario periods and for **RCP2.6** (multi-model combination). Note that the model uncertainty of the change signal is not reflected by the ensemble median signal displayed here and can be substantial.*

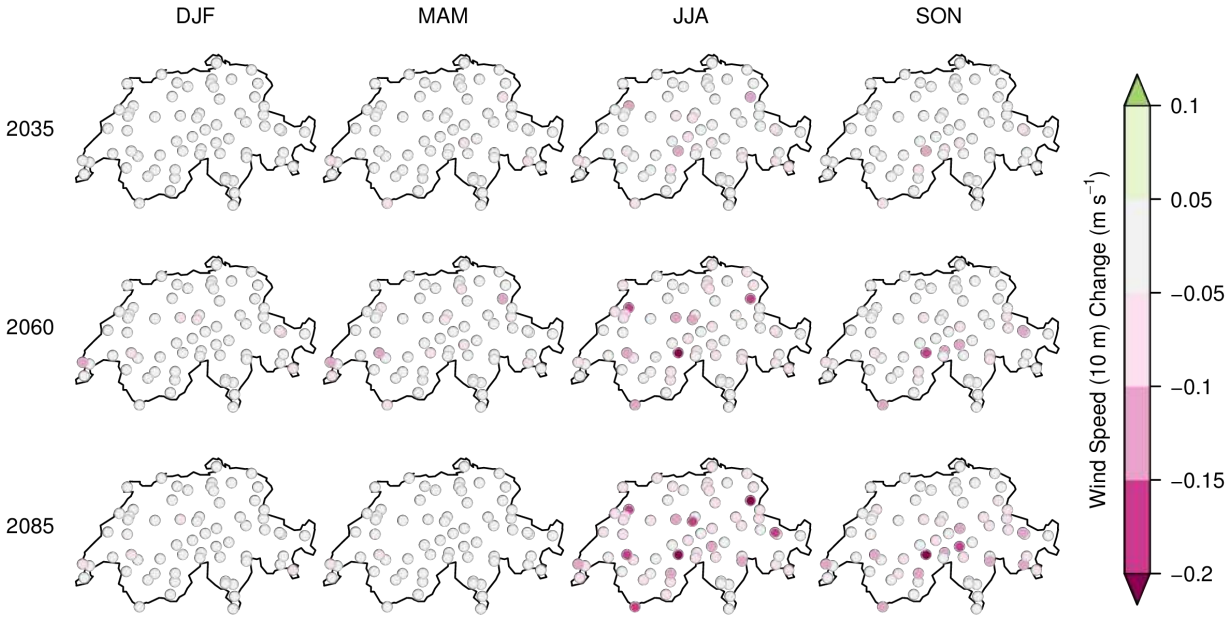

*Figure 13.44. As Figure 13.43, but for **RCP4.5**.*

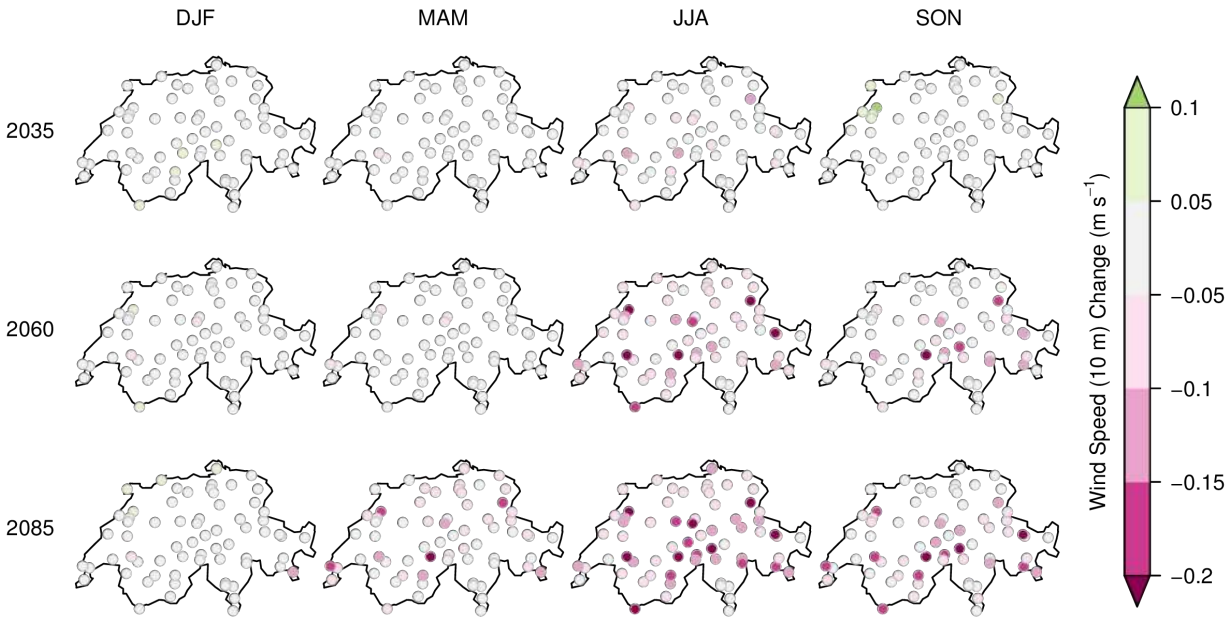

*Figure 13.45. As Figure 13.43, but for **RCP8.5**.*

A.4. Appendix: Climate extremes and indices

A.4.1. Temperature indices

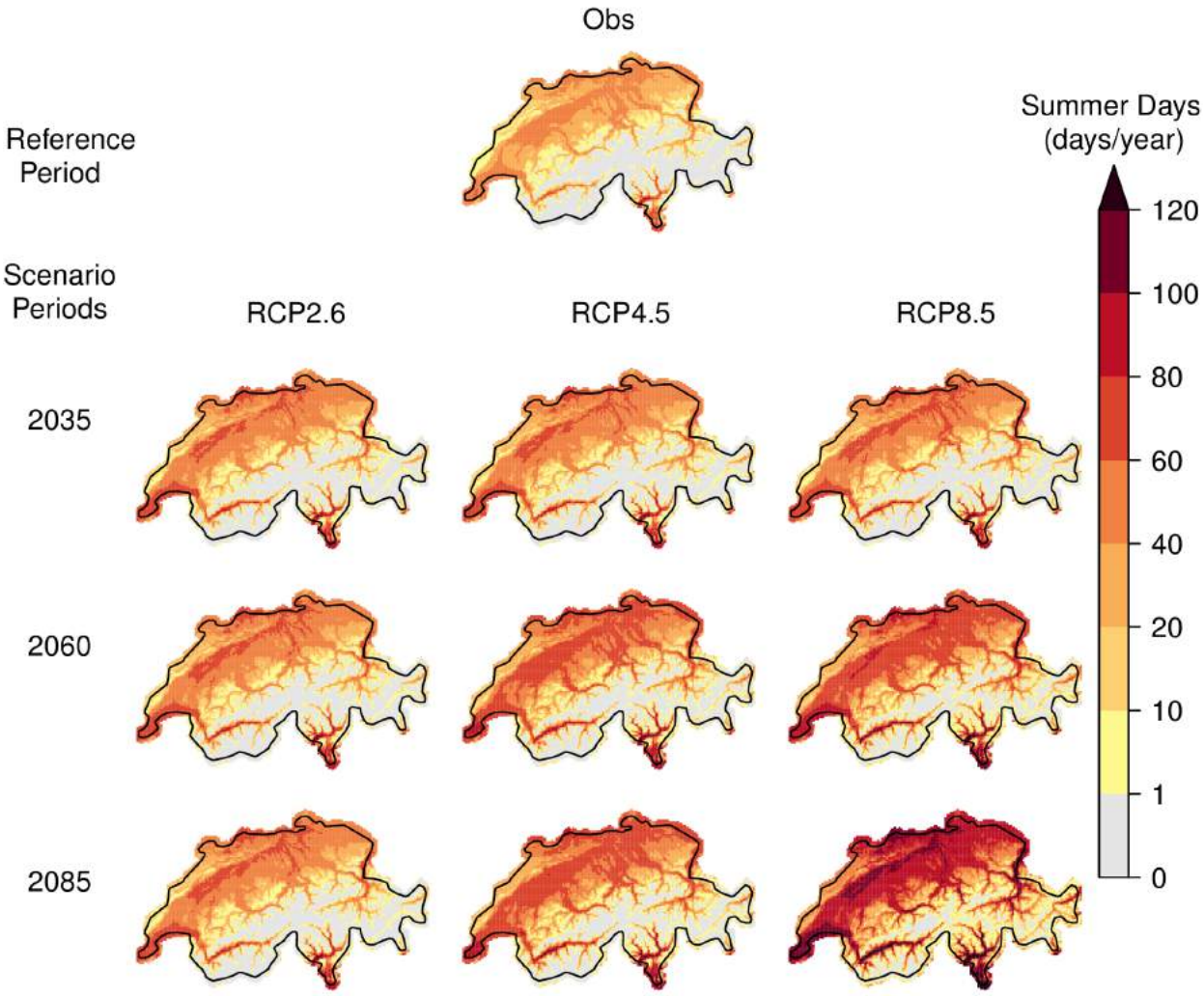

Figure 13.46. Summer days frequency. Top: 2-km observational grid in the reference period 1981 - 2010. Lower rows: Projected ensemble median number (multi-model combination) of the bias-corrected RCM data (QM to high-resolution grid) for the three scenario periods (rows) and the three forcing scenarios (columns). See Figure 13.50 for the corresponding change signals. Note that the model uncertainty of the change signal is not reflected by the ensemble median number displayed here and can be substantial.

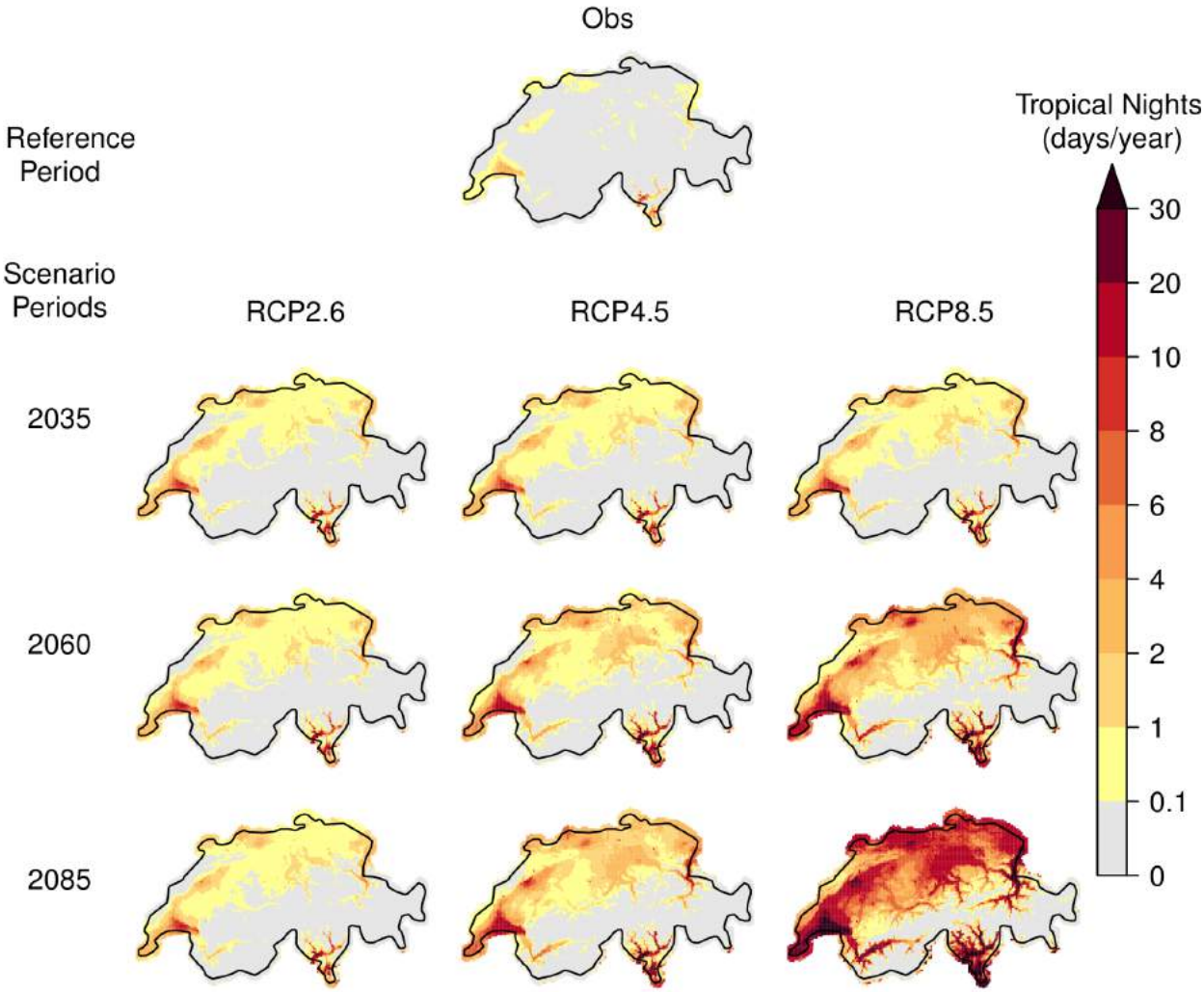

Figure 13.47. As Figure 13.46, but for tropical nights frequency. See Figure 13.51 for the corresponding change signals.

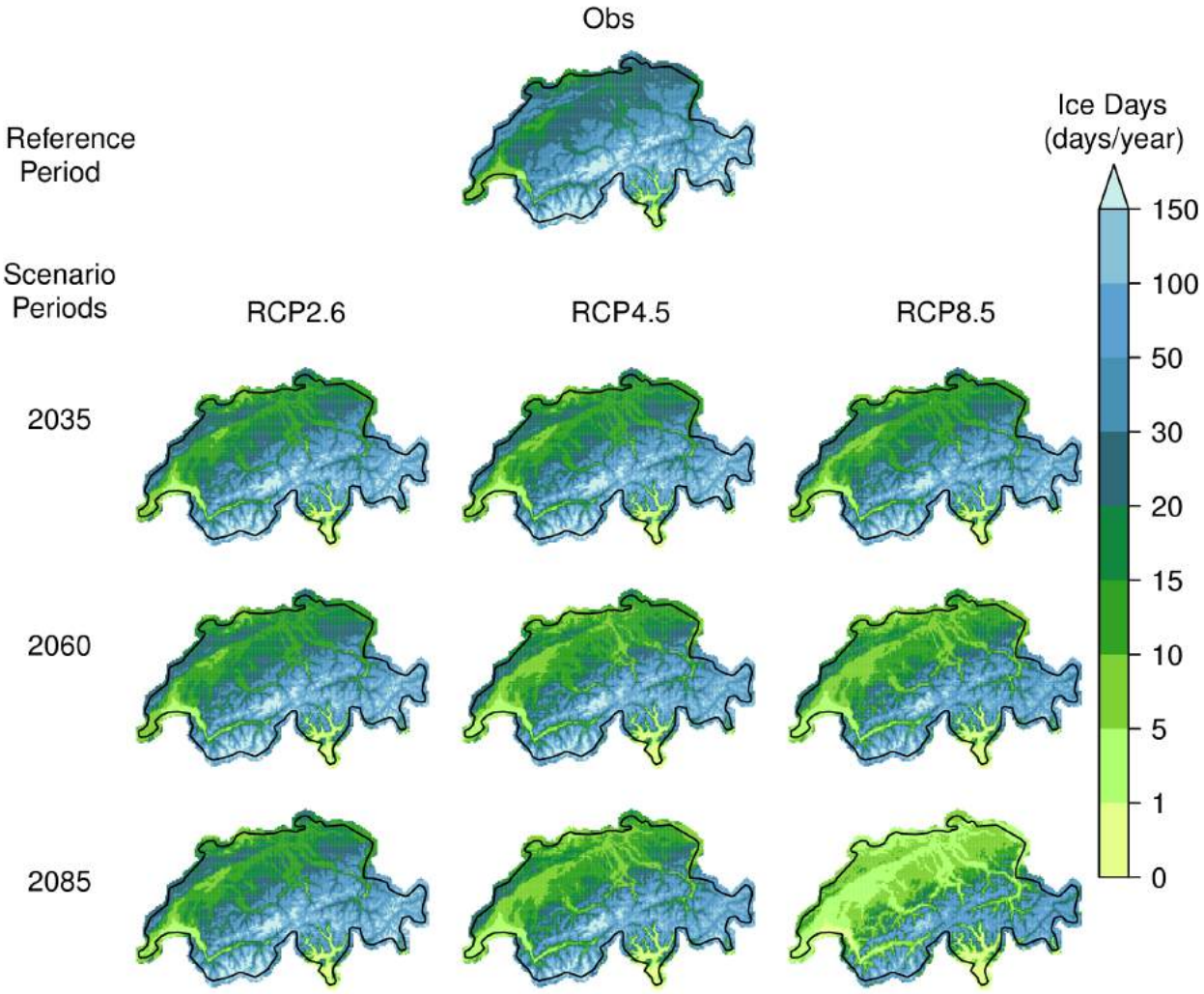

Figure 13.48. As Figure 13.46, but for ice days frequency.

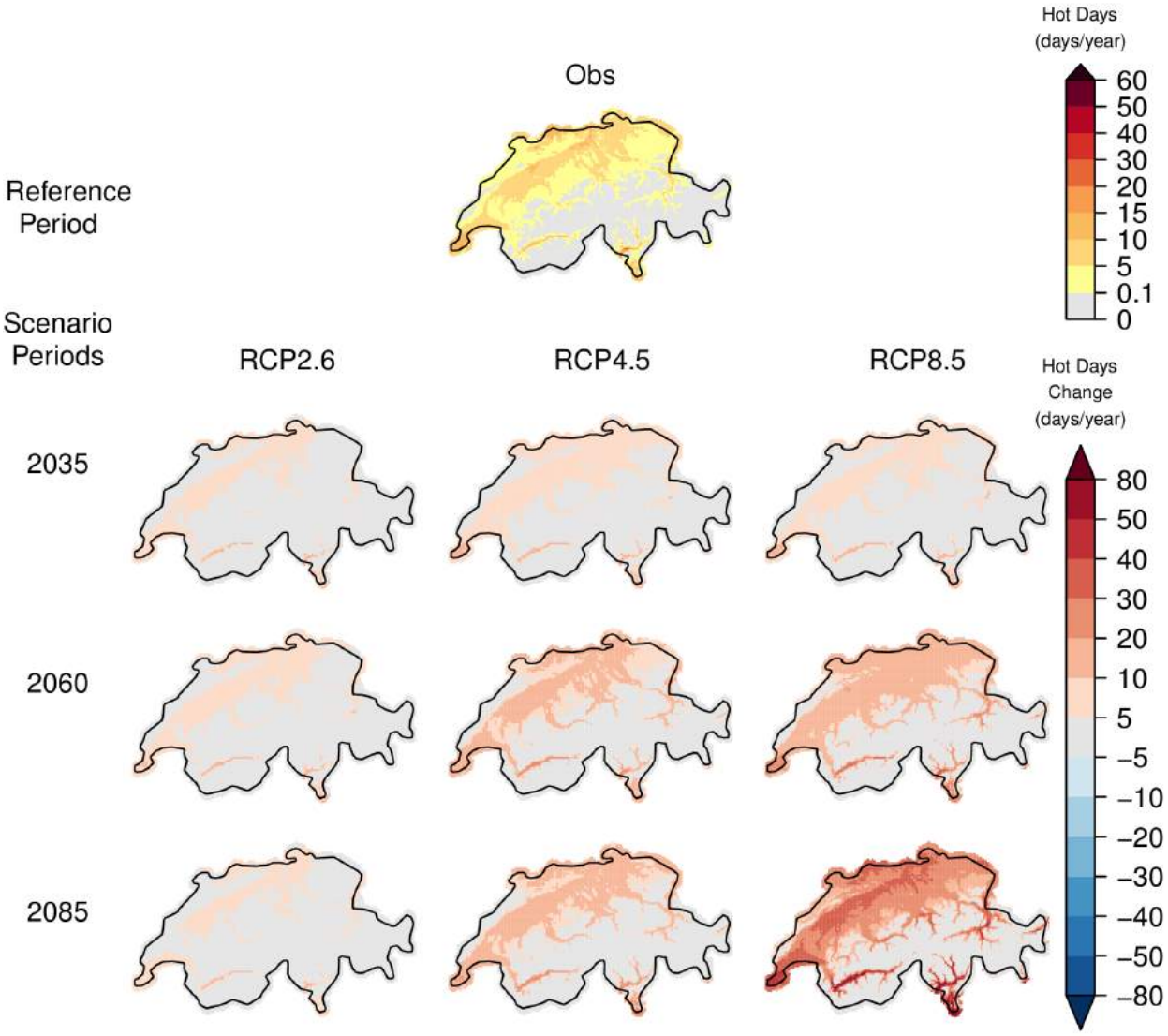

Figure 13.49. Top: Hot days frequency in the 2-km observational grid for the reference period 1981 - 2010. Lower rows: Projected ensemble median change (multi-model combination) of the hot days frequency in the bias-corrected RCM data (QM to high-resolution grid) for the three scenario periods (rows) and the three emission scenarios (columns). Note that the model uncertainty of the change signal is not reflected by the ensemble median change displayed here and can be substantial.

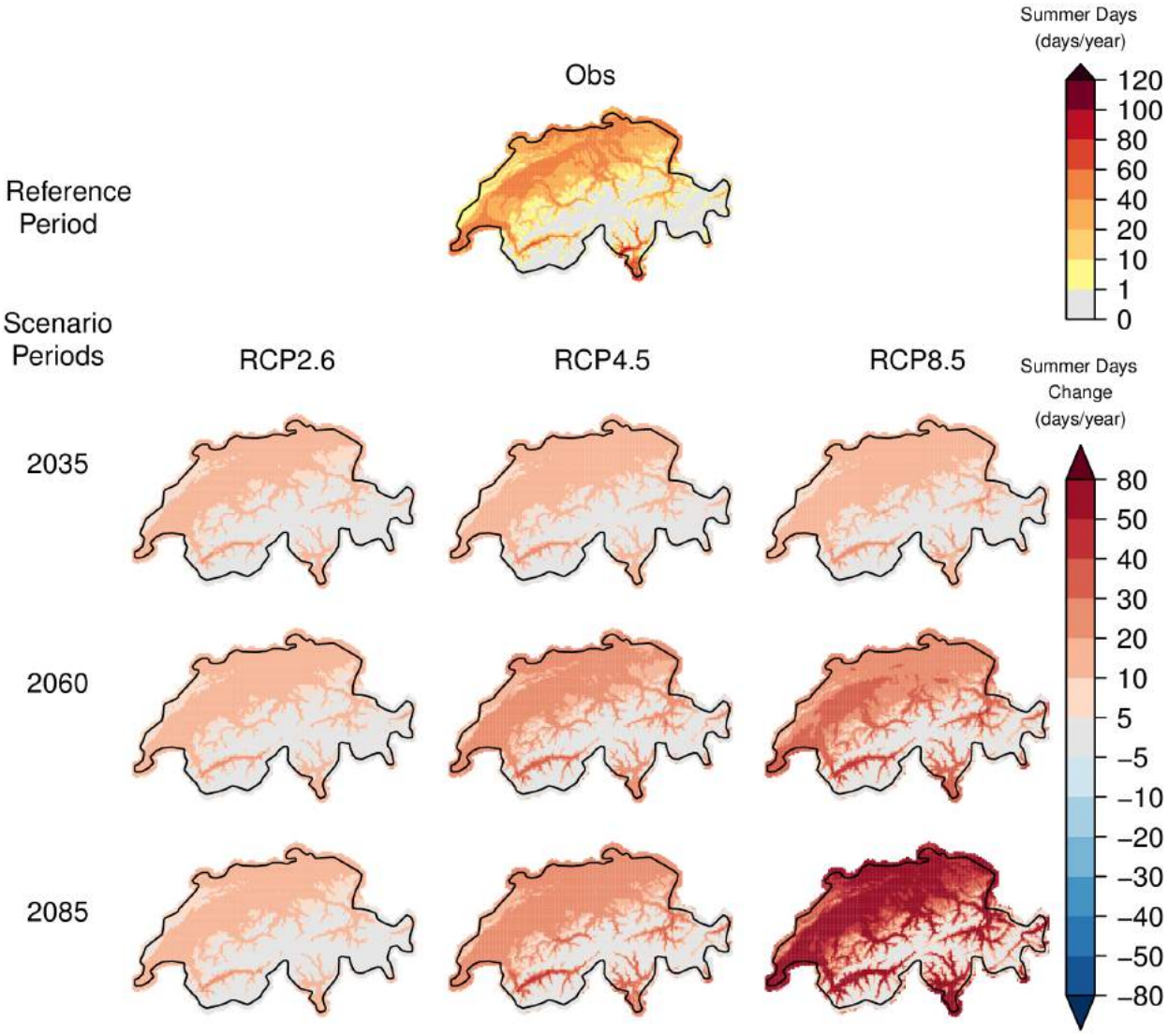

Figure 13.50. As Figure 13.49, but for summer days frequency.

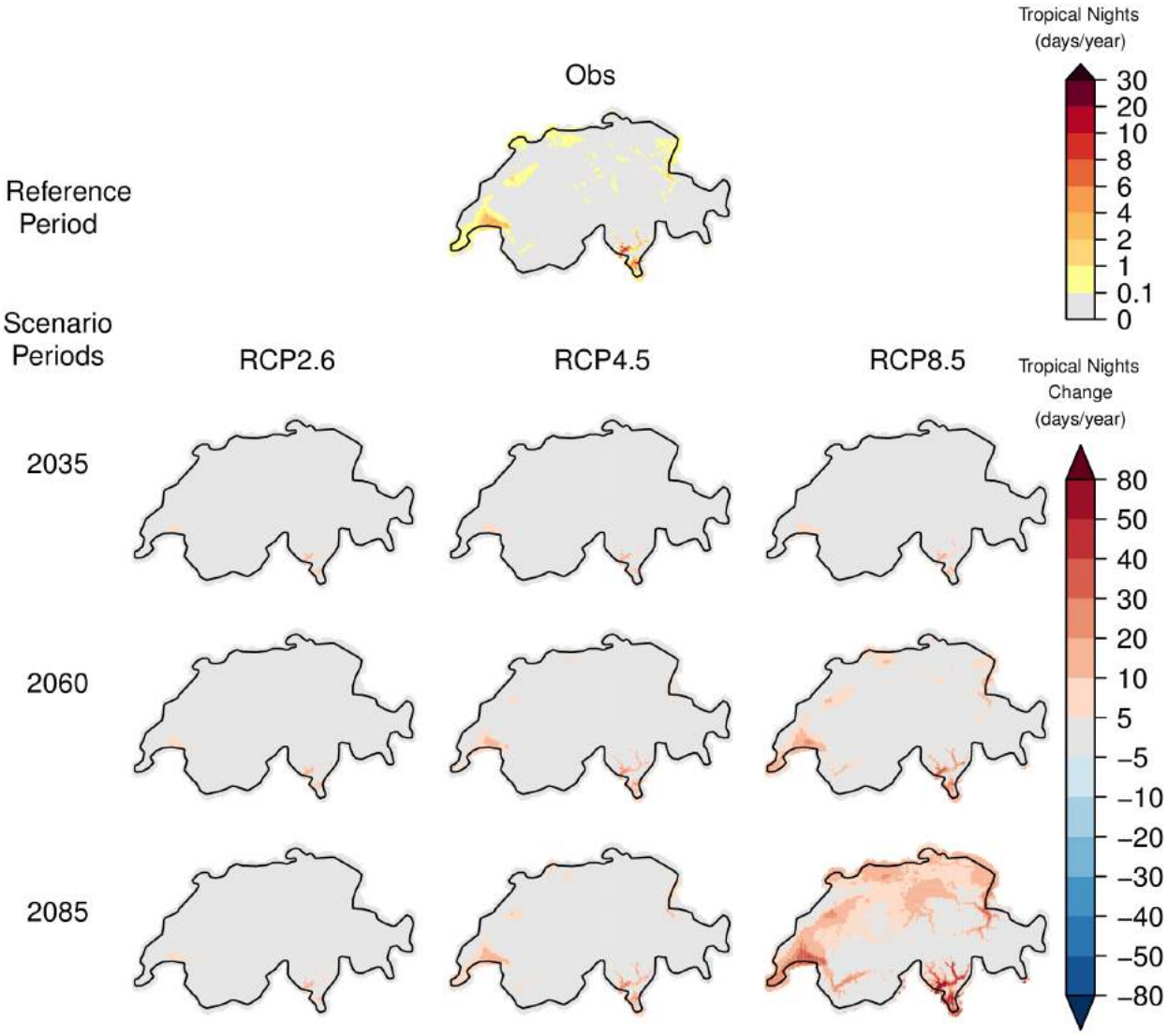

Figure 13.51. As Figure 13.49, but for tropical nights frequency.

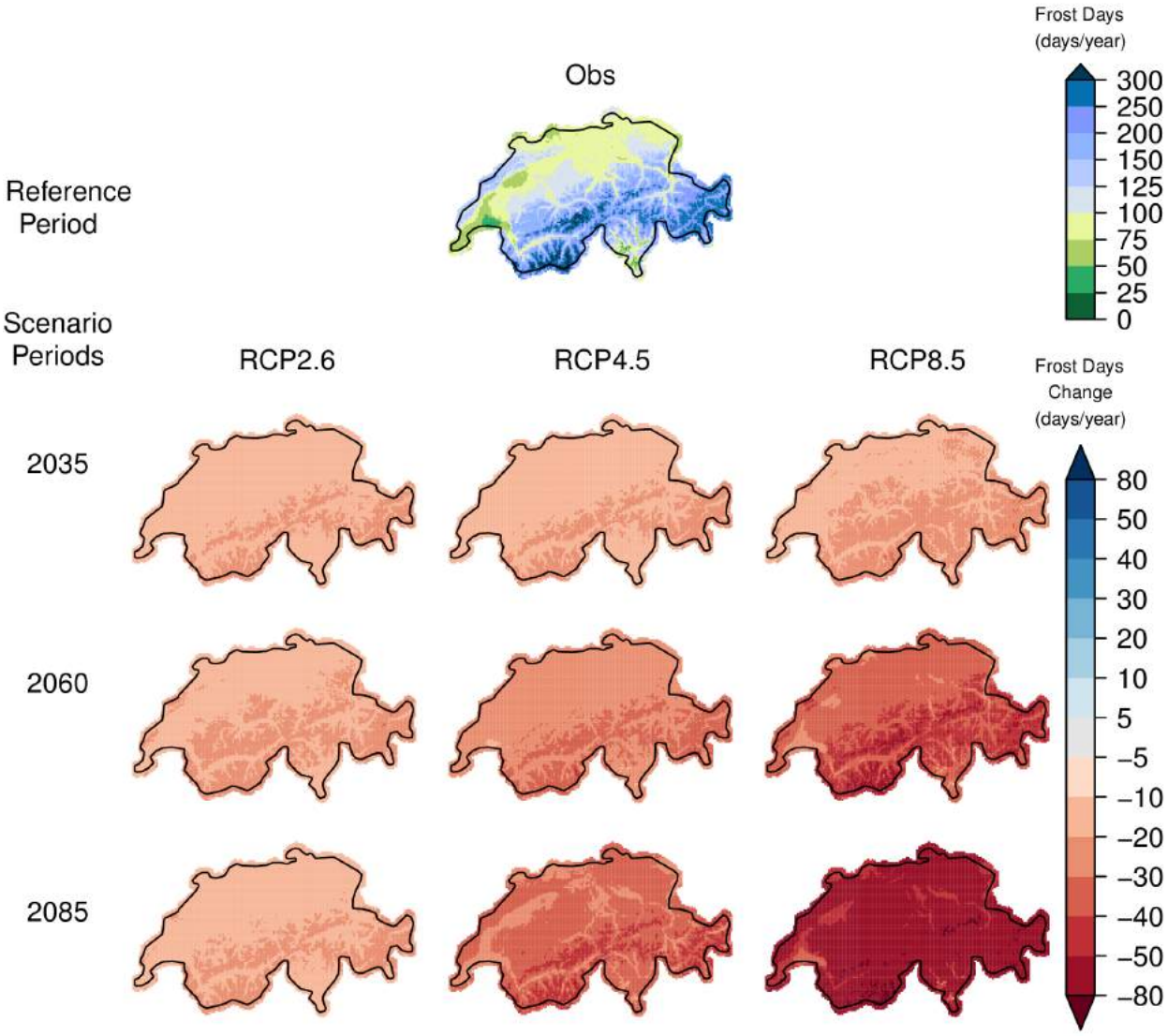

Figure 13.52. As Figure 13.49, but for frost days frequency.

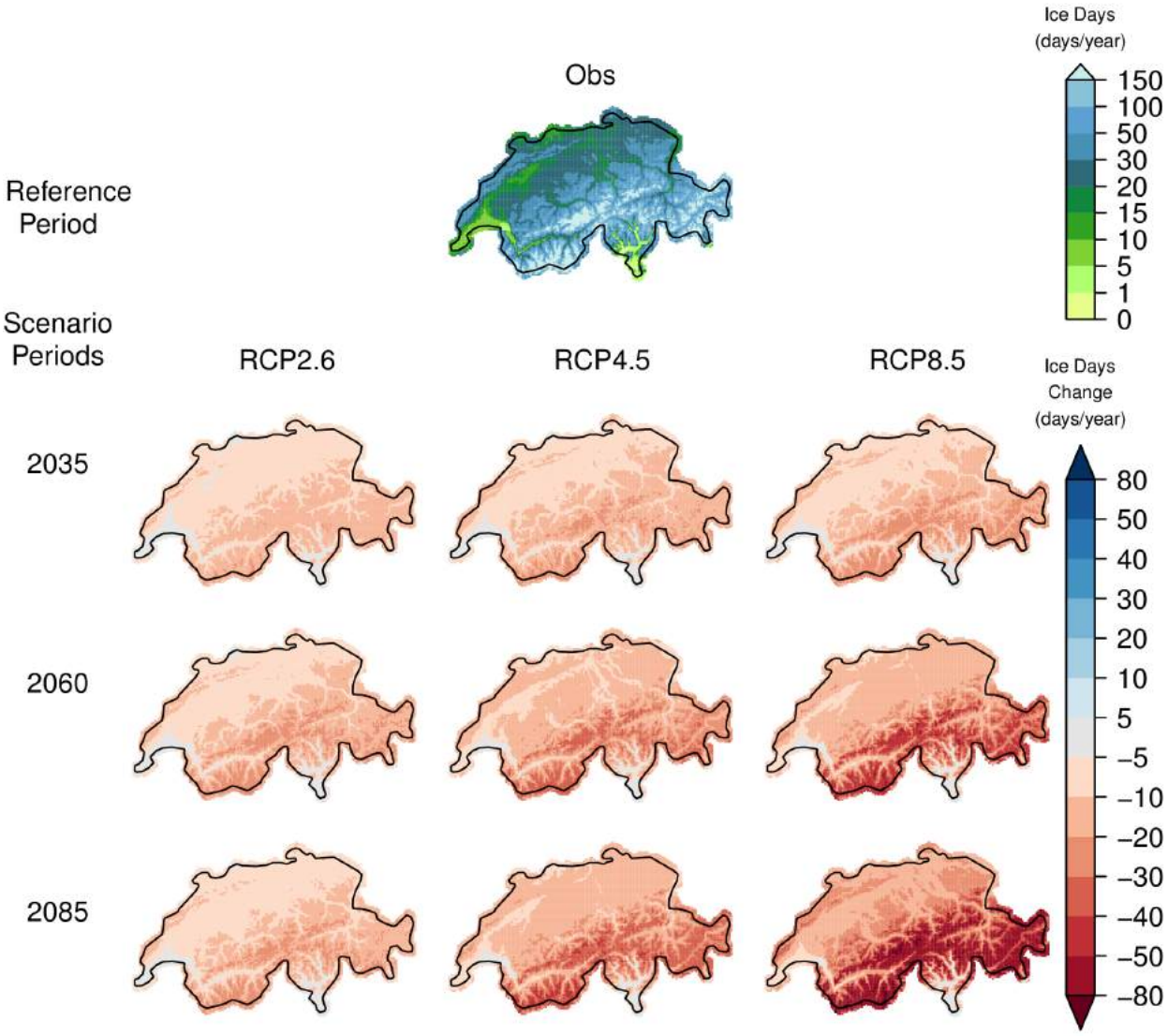

Figure 13.53. As Figure 13.49, but for ice days frequency.

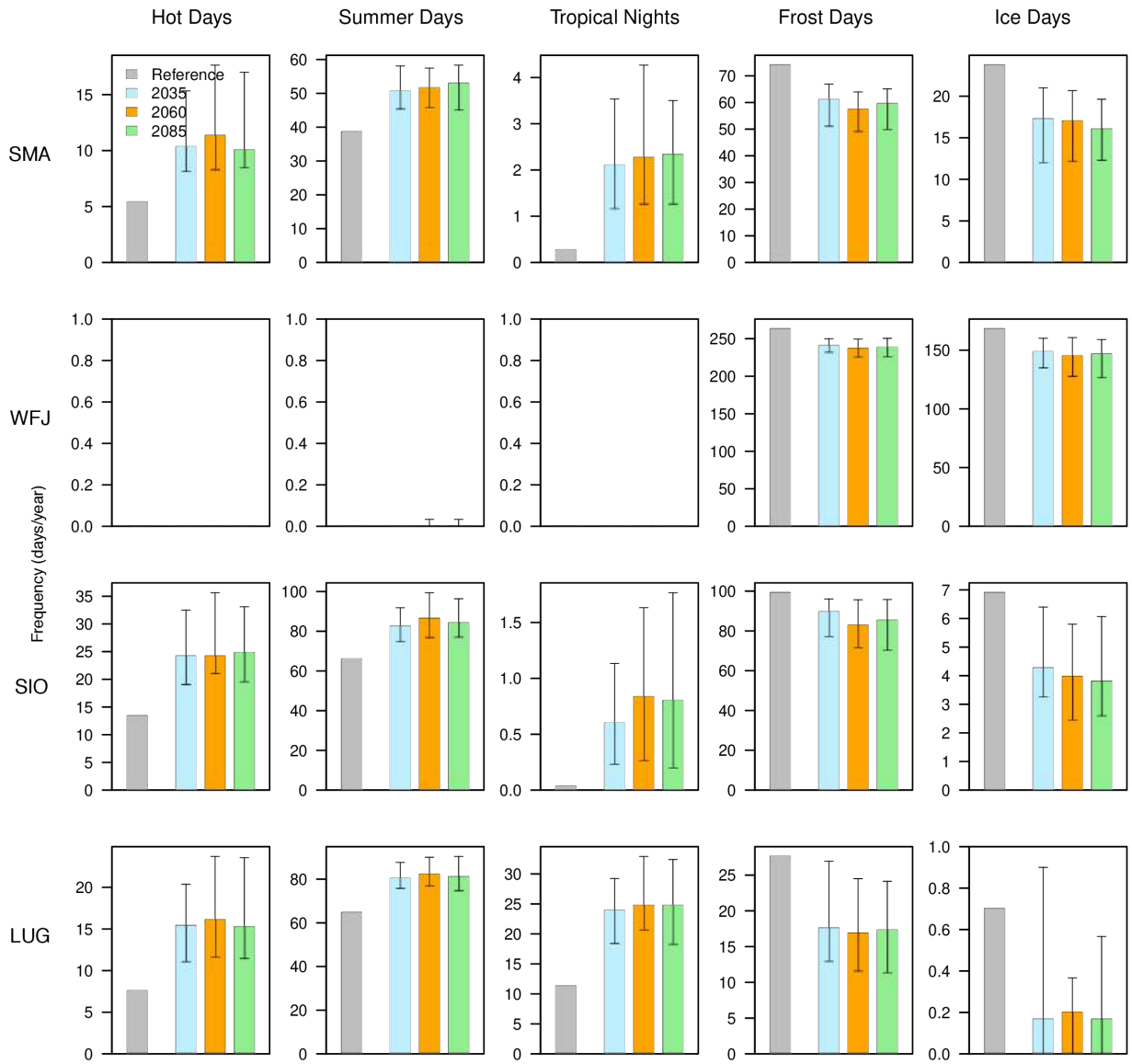

Figure 13.54. Frequency of hot days, summer days, tropical nights, frost days, and ice days in the reference period (observations) and in the three scenario periods (multi-model combination; QM to stations) for RCP2.6 at the four exemplary sites Zurich/Fluntern (SMA), Weissfluhjoch (WFJ), Sion (SIO), and Lugano (LUG). Bars indicate the ensemble median frequency; whiskers, the 5 - 95 % model range.

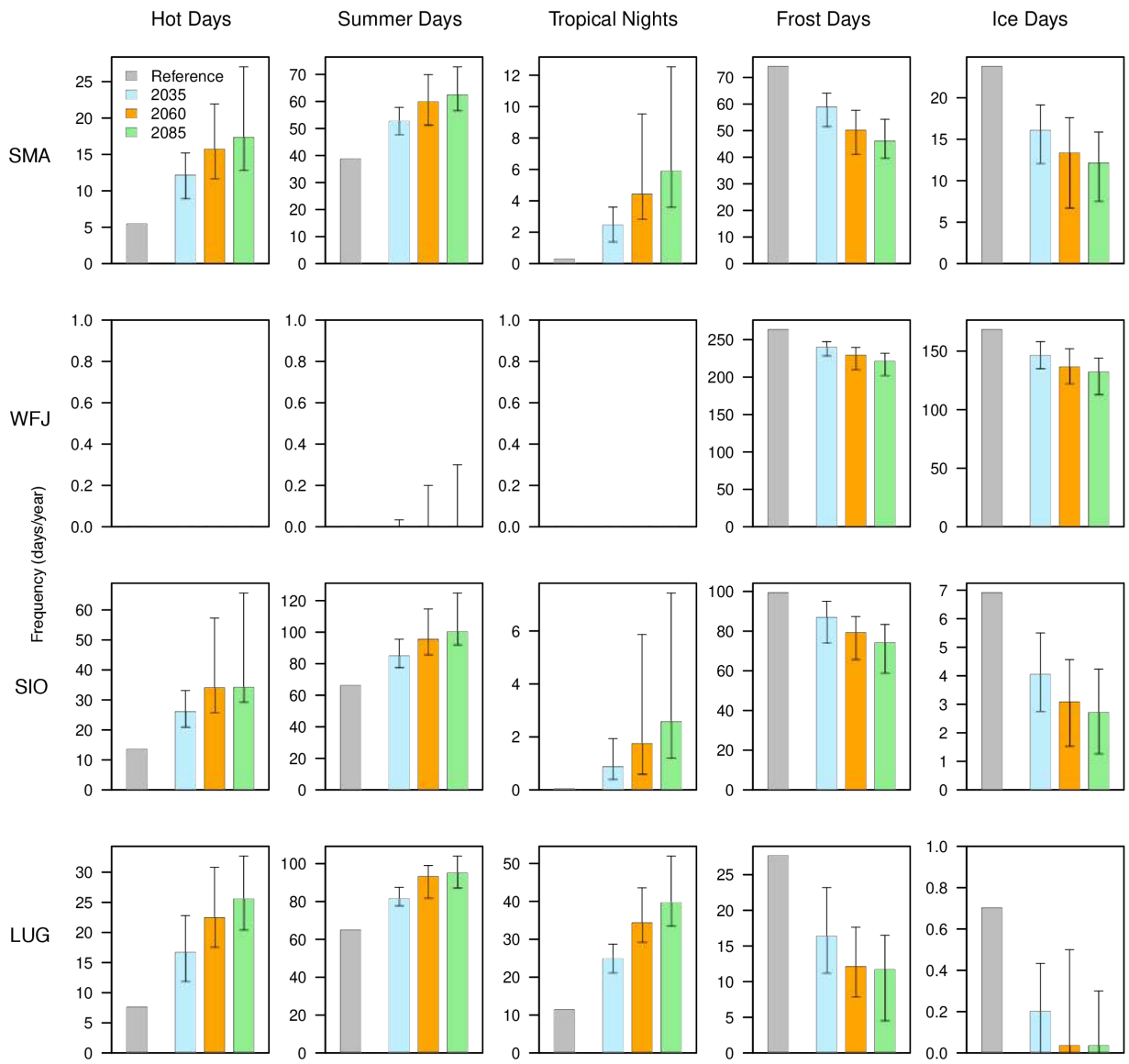

Figure 13.55. As Figure 13.54, but for RCP4.5.

A.4.2. Temperature extremes

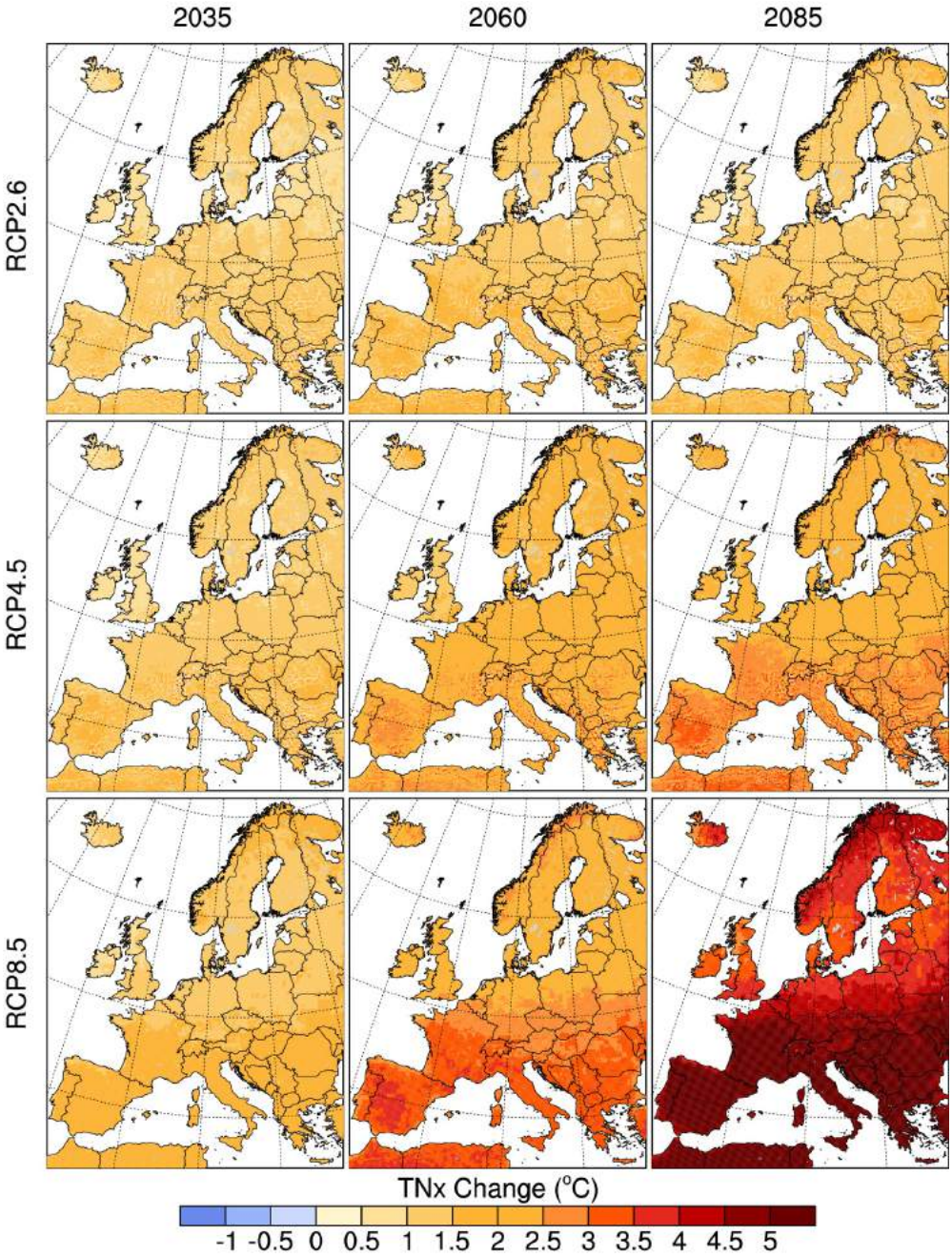

Figure 13.56. Multi-model median change in warmest night (TNx) by 2035, 2060, and 2085 in RCP2.6, RCP4.5, and RCP8.5 with respect to present-day conditions (°C).

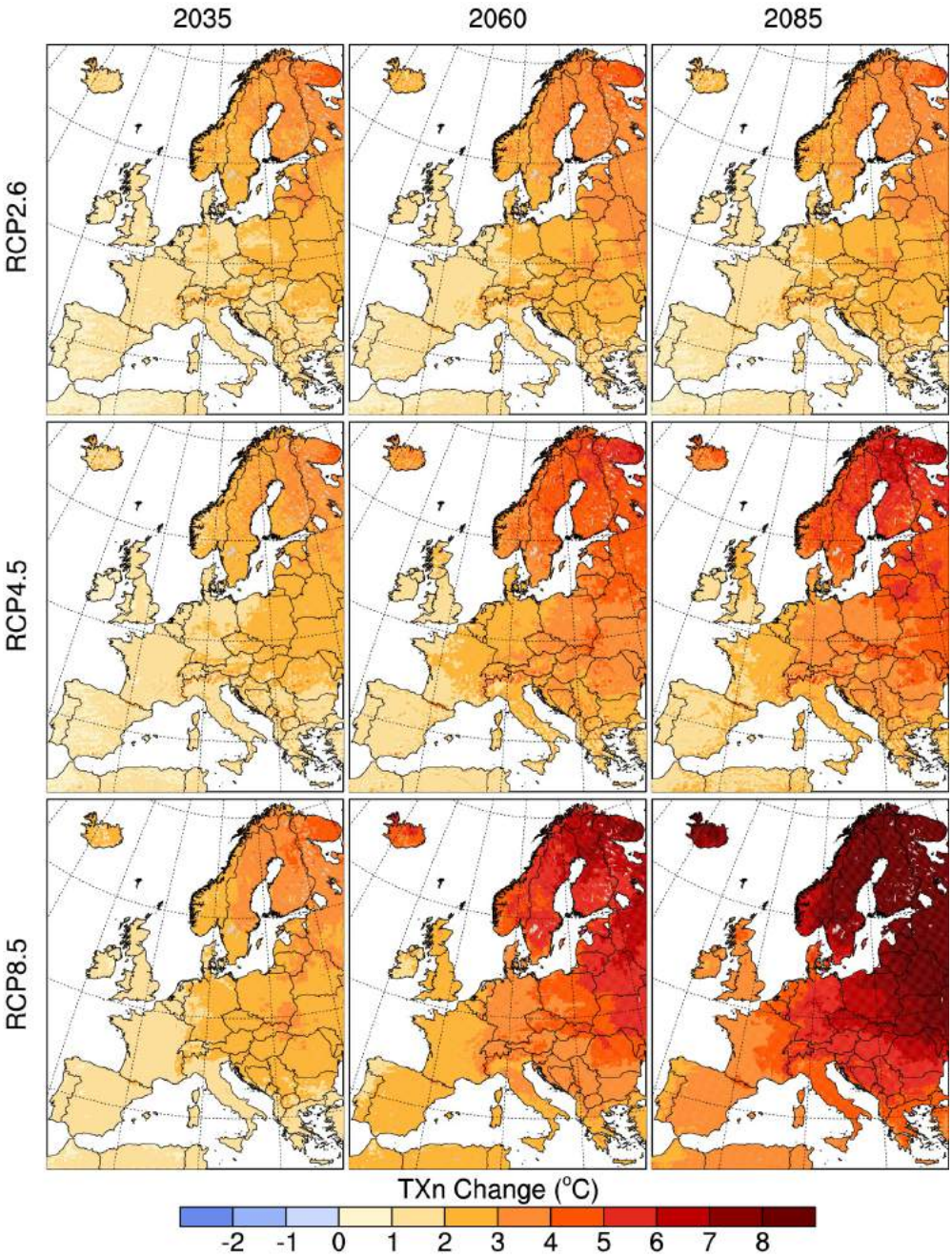

Figure 13.57. Multi-model median change in coldest daytime maximum (TXn) by 2035, 2060, and 2085 in RCP2.6, RCP4.5, and RCP8.5 with respect to present-day conditions (°C).

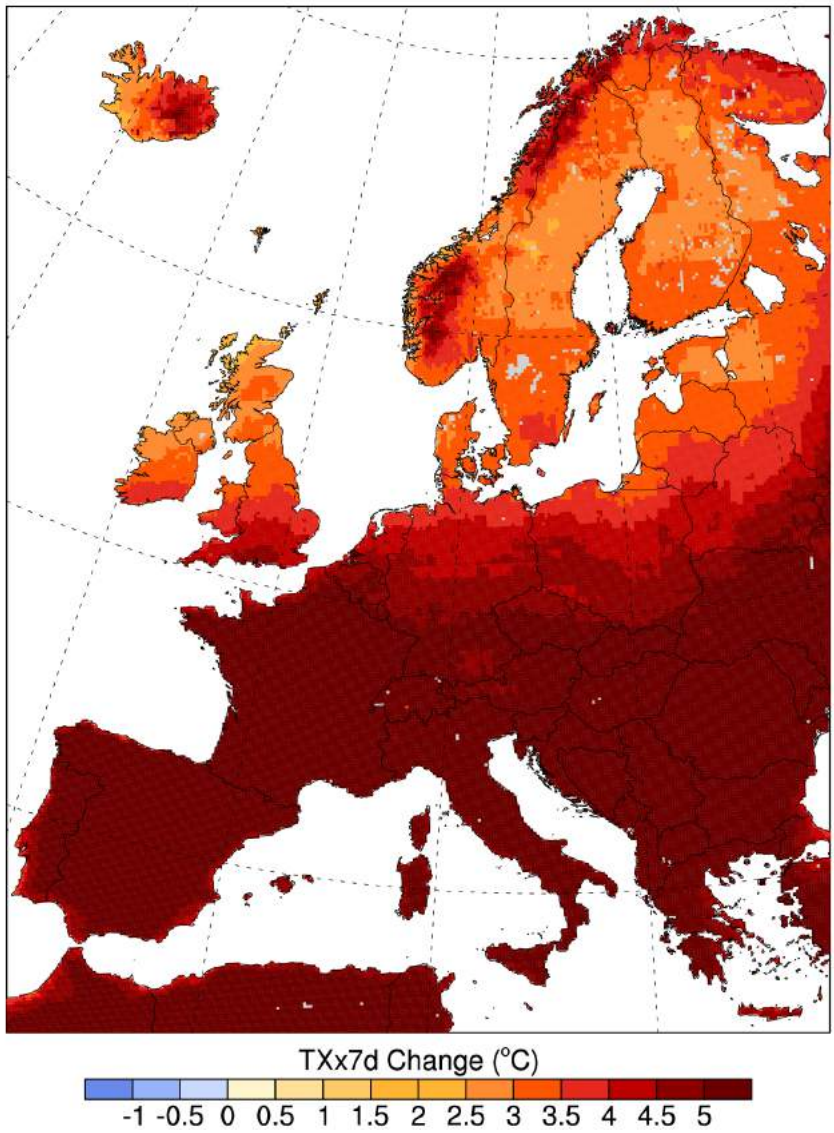

Figure 13.58. Multi-model median change in hottest mean 7-day (TXx7d) by 2085 in RCP8.5 with respect to present-day conditions (°C).

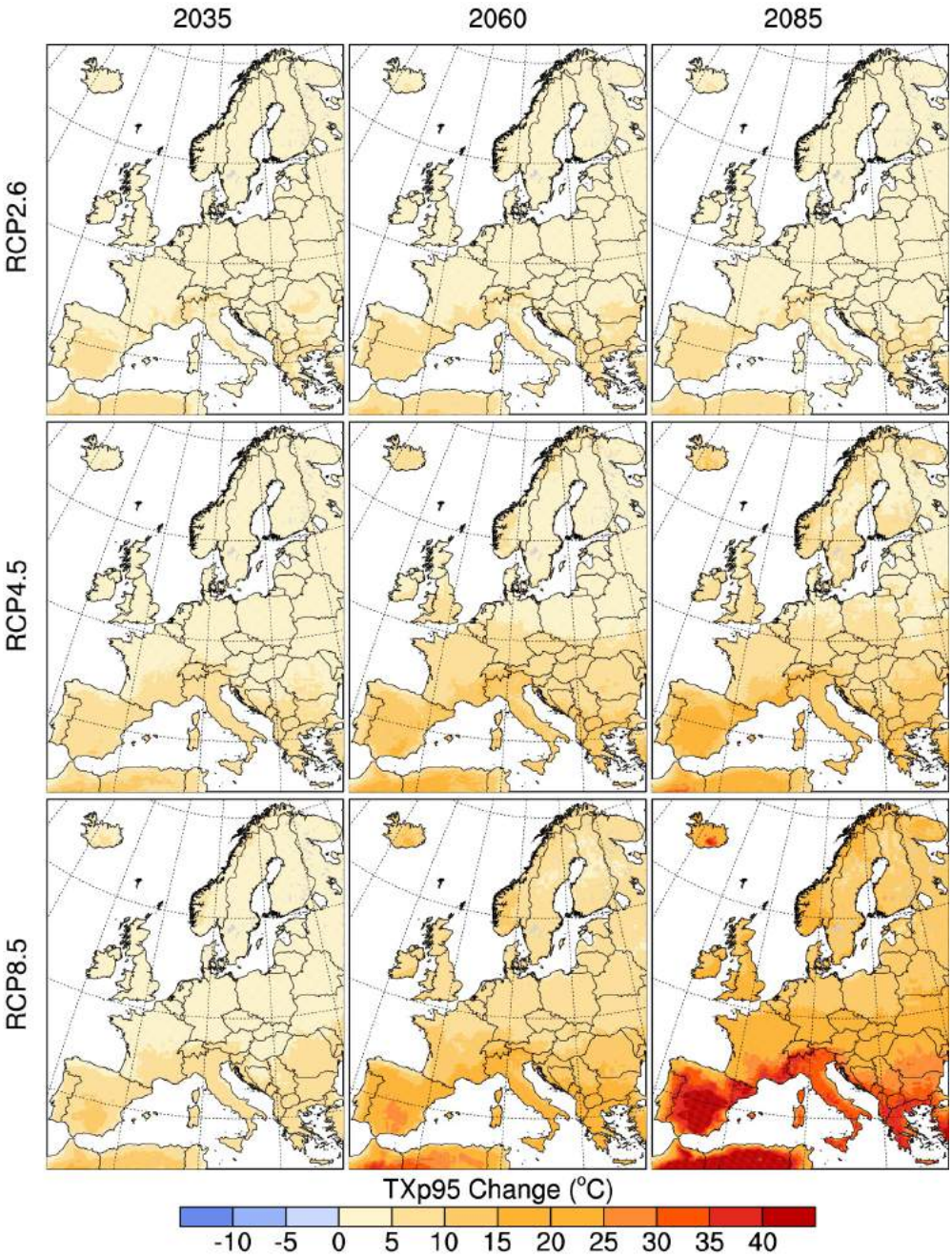

Figure 13.59. Multi-model median change in number of hot days (TX95P) by 2035, 2060, and 2085 in RCP2.6, RCP4.5, and RCP8.5 with respect to present-day conditions (days)

A.4.3. Heat stress indices

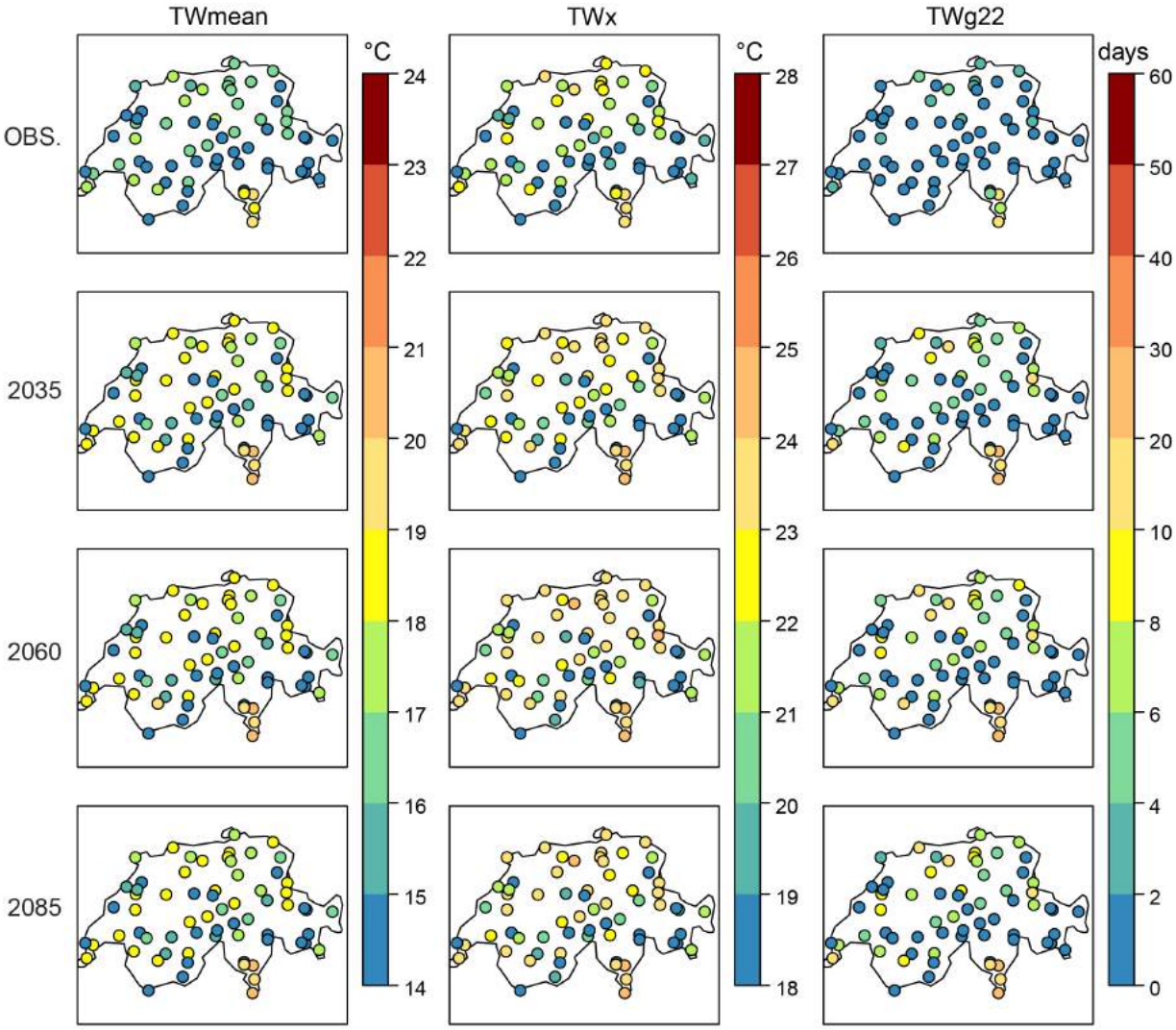

Figure 13.60. Observed values (first row) and climate change projections of summer mean (TWmean) and maximum TW (TWx) and the number of days with TW >22 °C (TWg22) for the multi-model ensemble median for the three future periods (2nd - 4th rows) for the bias-corrected RCMs (combination of EUR-11 and EUR-44, 20 simulations; see Chapter 5.3) and the RCP2.6 scenario.

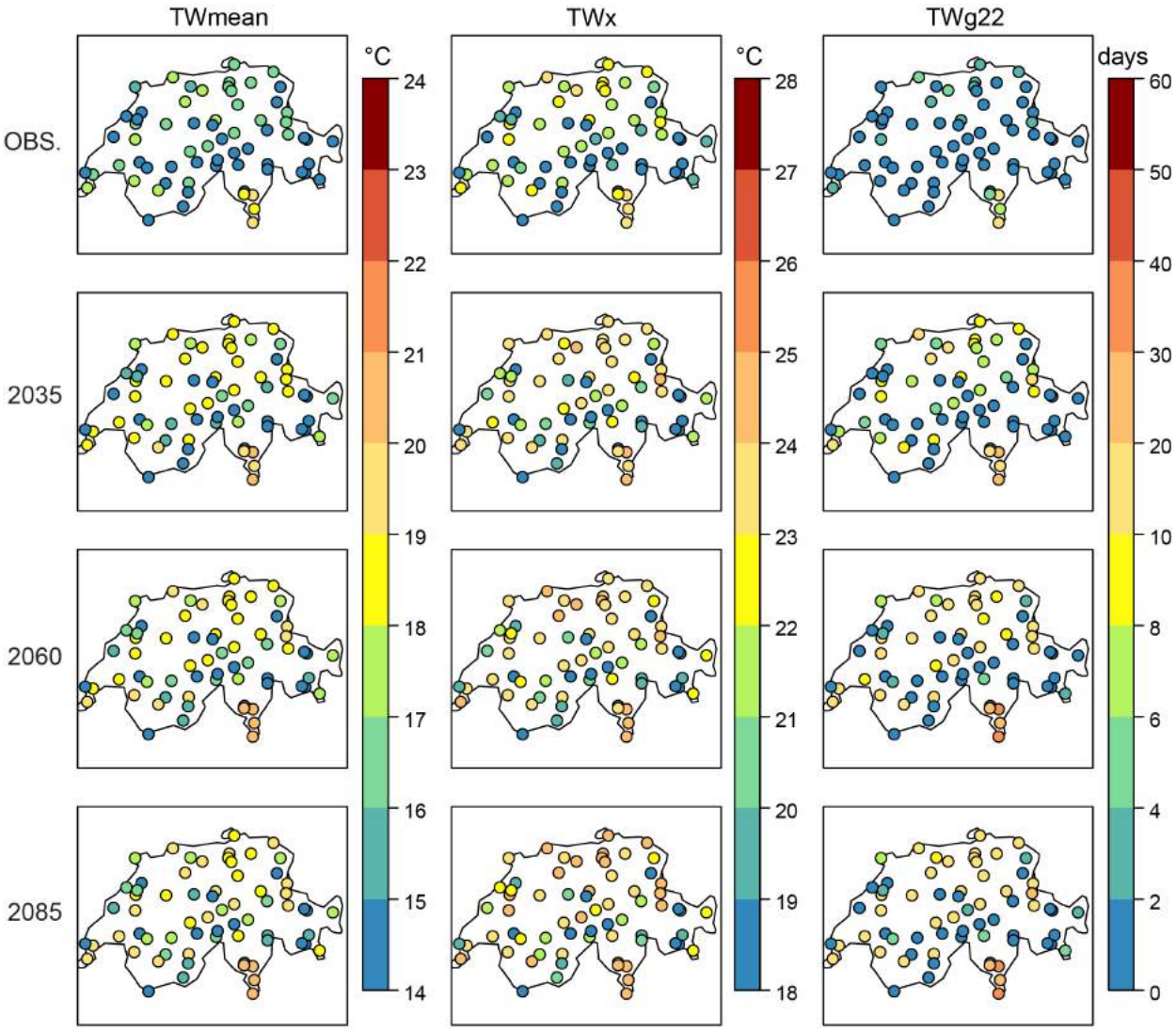

Figure 13.61. As Figure 13.60, but for RCP4.5.

A.4.4. Precipitation extremes

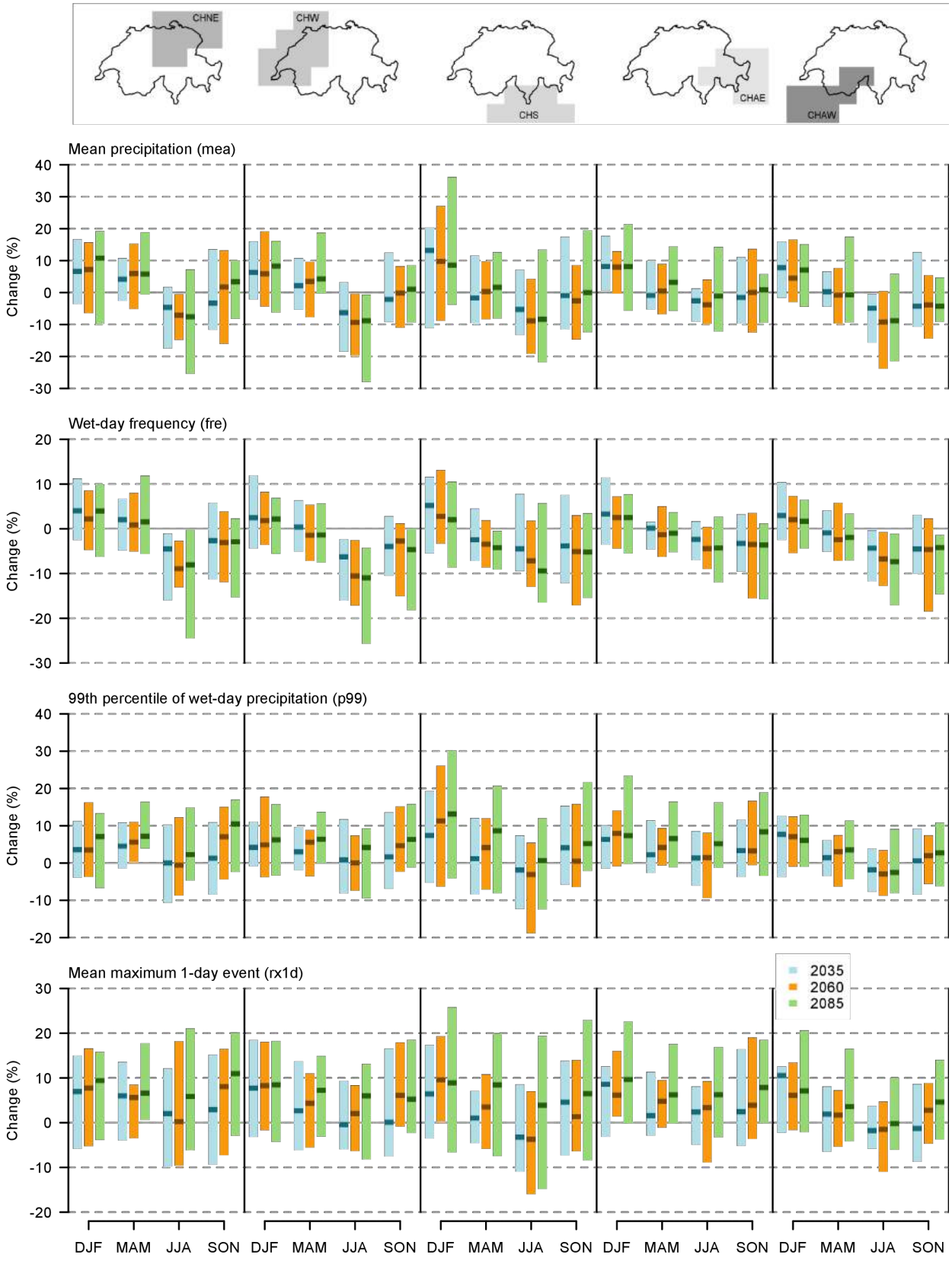

Figure 13.62. Multi-model ensemble estimates of projected change for the five CH2018 analysis regions for the periods 2035 (blue), 2060 (red), and 2085 (green) with respect to 1981 - 2010 in mean precipitation (MEA), the wet-day frequency (FRE), the 99th percentile of all-day precipitation (p99), and the mean annual maximum daily precipitation event (Rx1d) at seasonal scale (see x-axis). The multi-model ensemble constitutes of EUR-11 and EUR-44 simulations forced by the RCP 4.5 emission scenario (see Chapter 4.2).

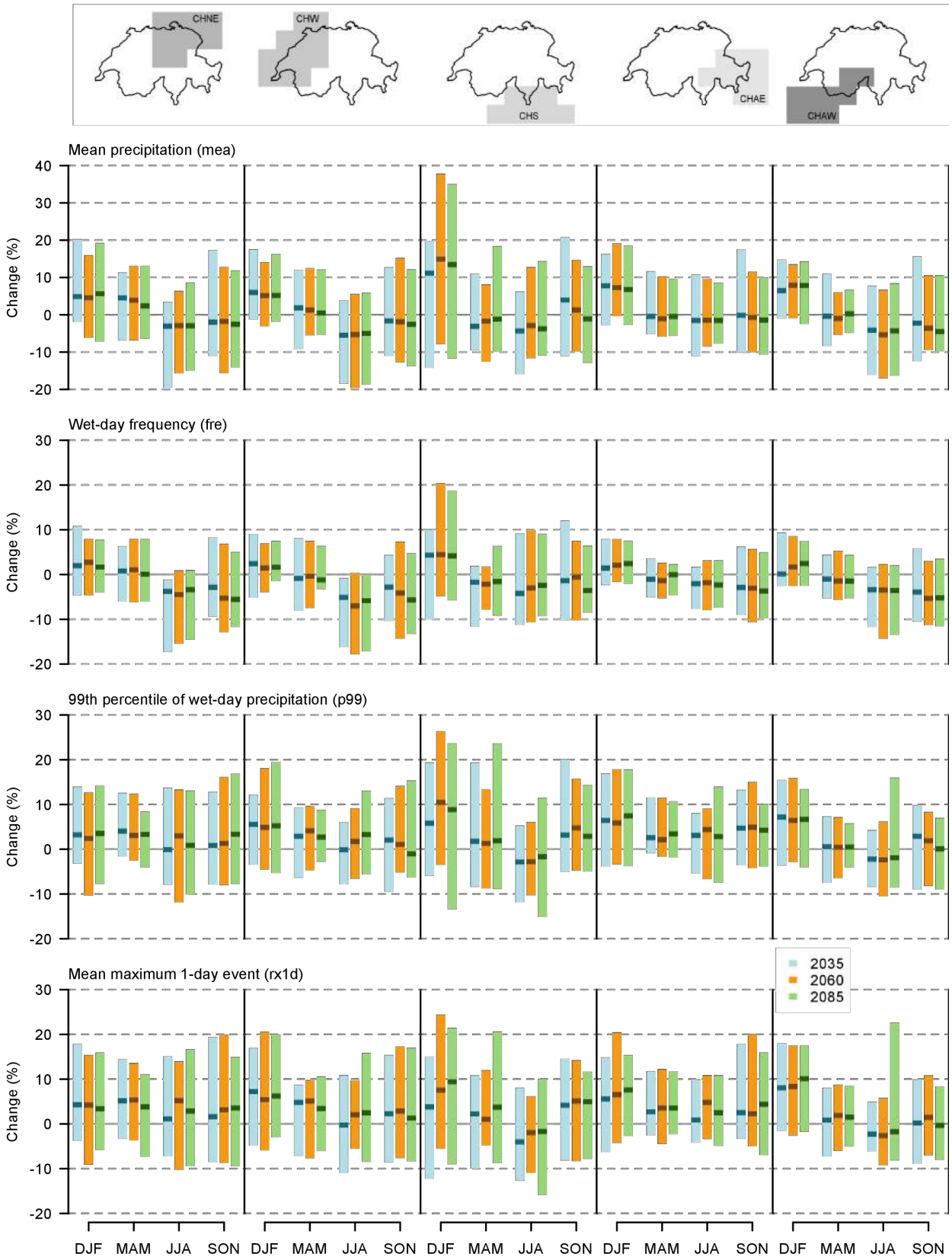

Figure 13.63. As Figure 13.62, but for RCP2.6.

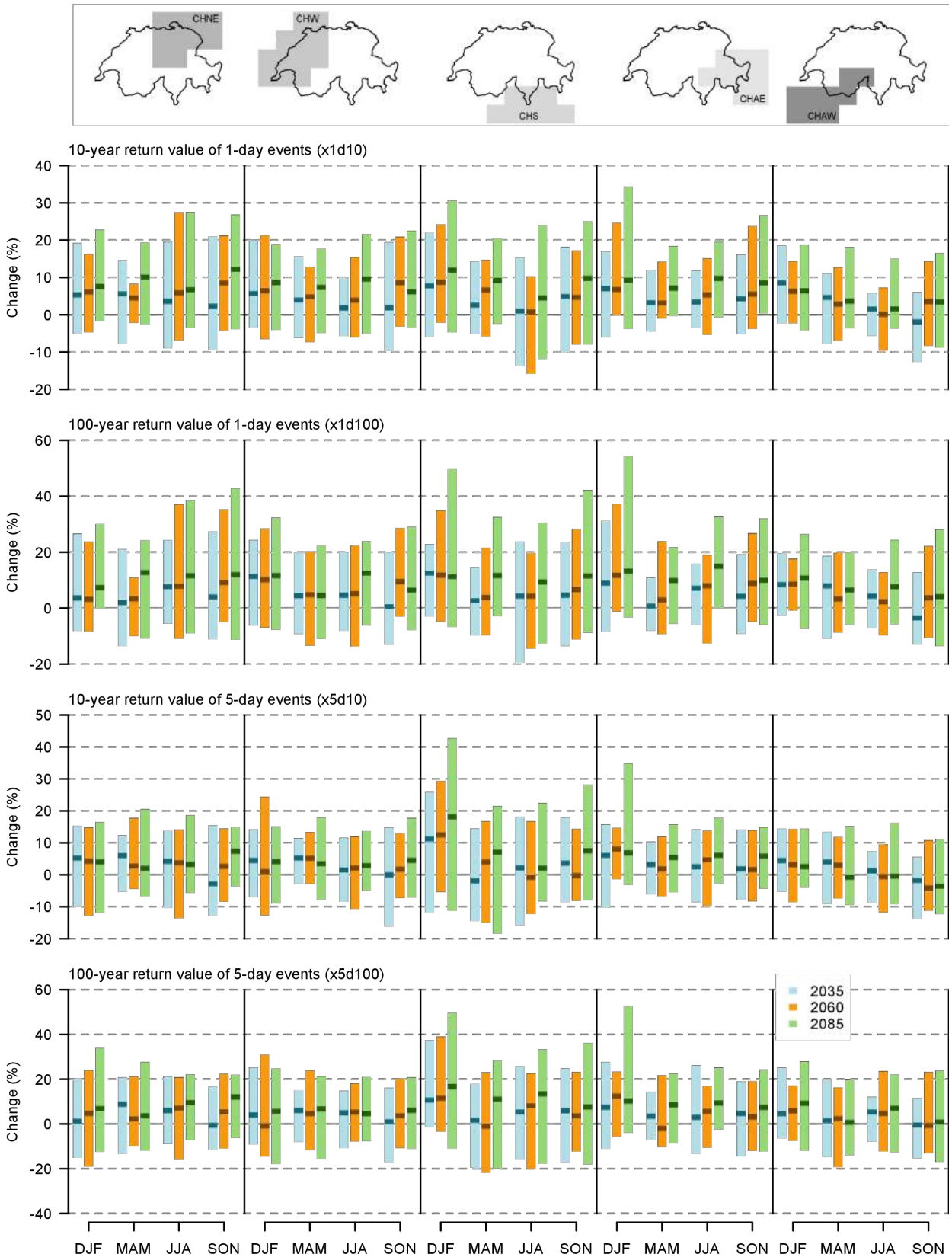

Figure 13.64. Multi-model ensemble estimates of projected change for the five CH2018 analysis regions for the periods 2035 (blue), 2060 (red), and 2085 (green) with respect to 1981 - 2010 in the intensity of daily events with a return period of 10 (x1d10) and 100 years (x1d100) and the corresponding events for 5-day aggregated precipitation episodes (x5d10 and x5d100) at seasonal scale (see x-axis). The multi-model ensemble consists of EUR-11 and EUR-44 simulations forced by the RCP 4.5 emission scenario (see Chapter 4.2).

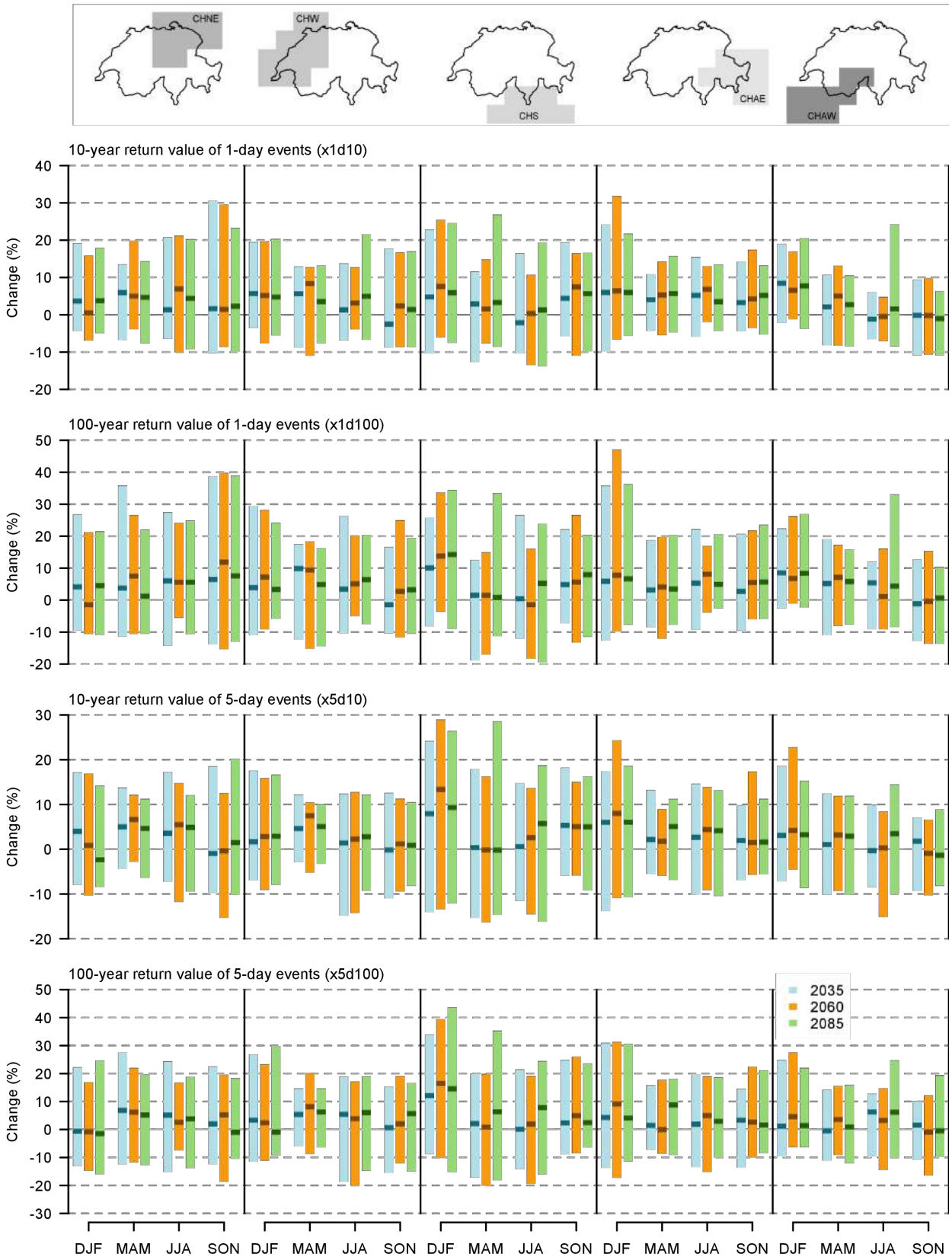

Figure 13.65. As Figure 13.64, but for RCP2.6.

A.4.5. Drought indices

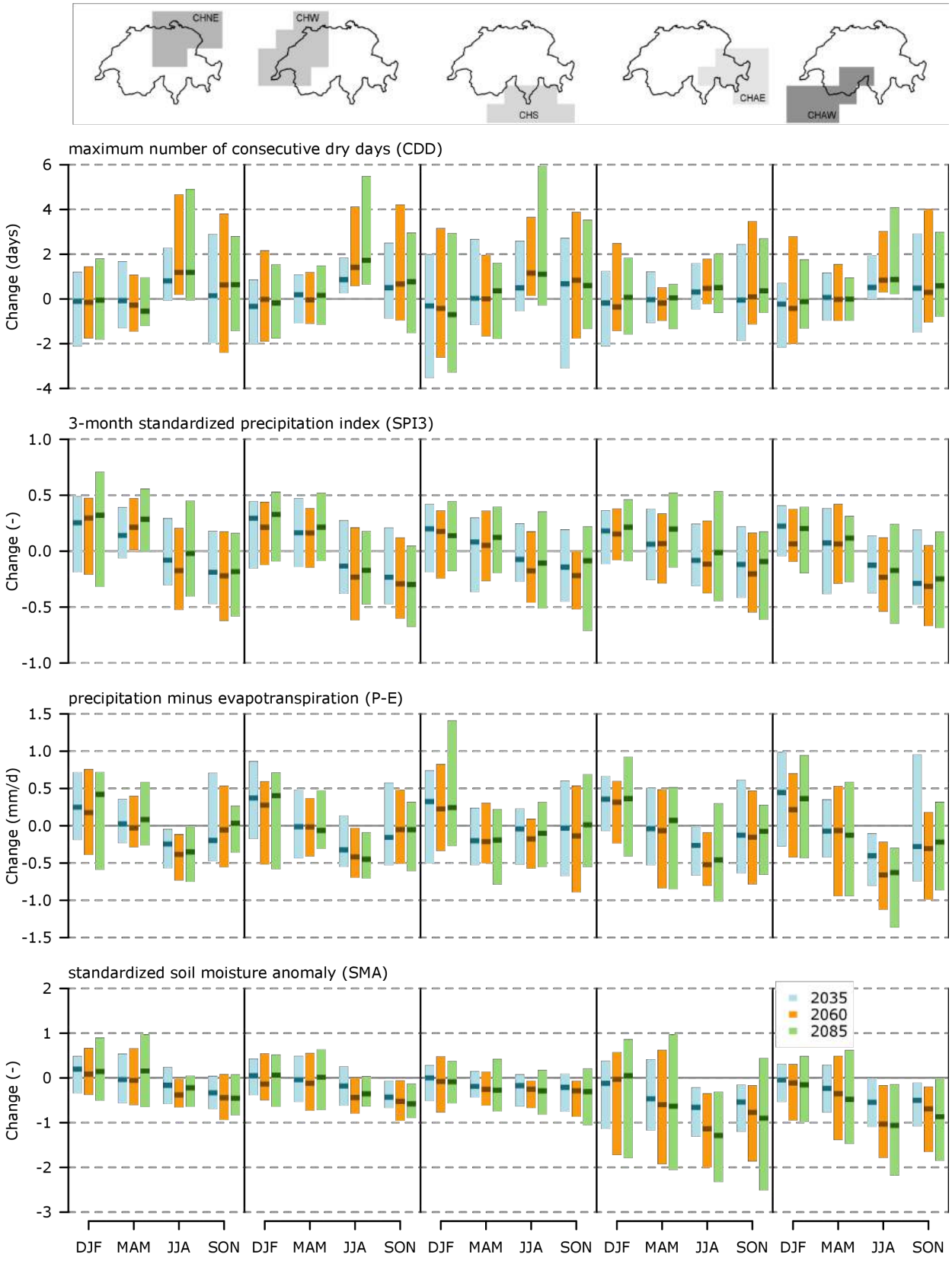

Figure 13.66. Multi-model regional mean changes in the meteorological drought indices CDD (1st row), SPI3 (2nd row), P-E (3rd row), and SMA (4th row) for the five CH2018 regions and the scenario periods 2035, 2060, and 2085 and RCP4.5. The ensemble median is based on a combination of EUR-11 and EUR-44 simulations (Chapter 4.2).

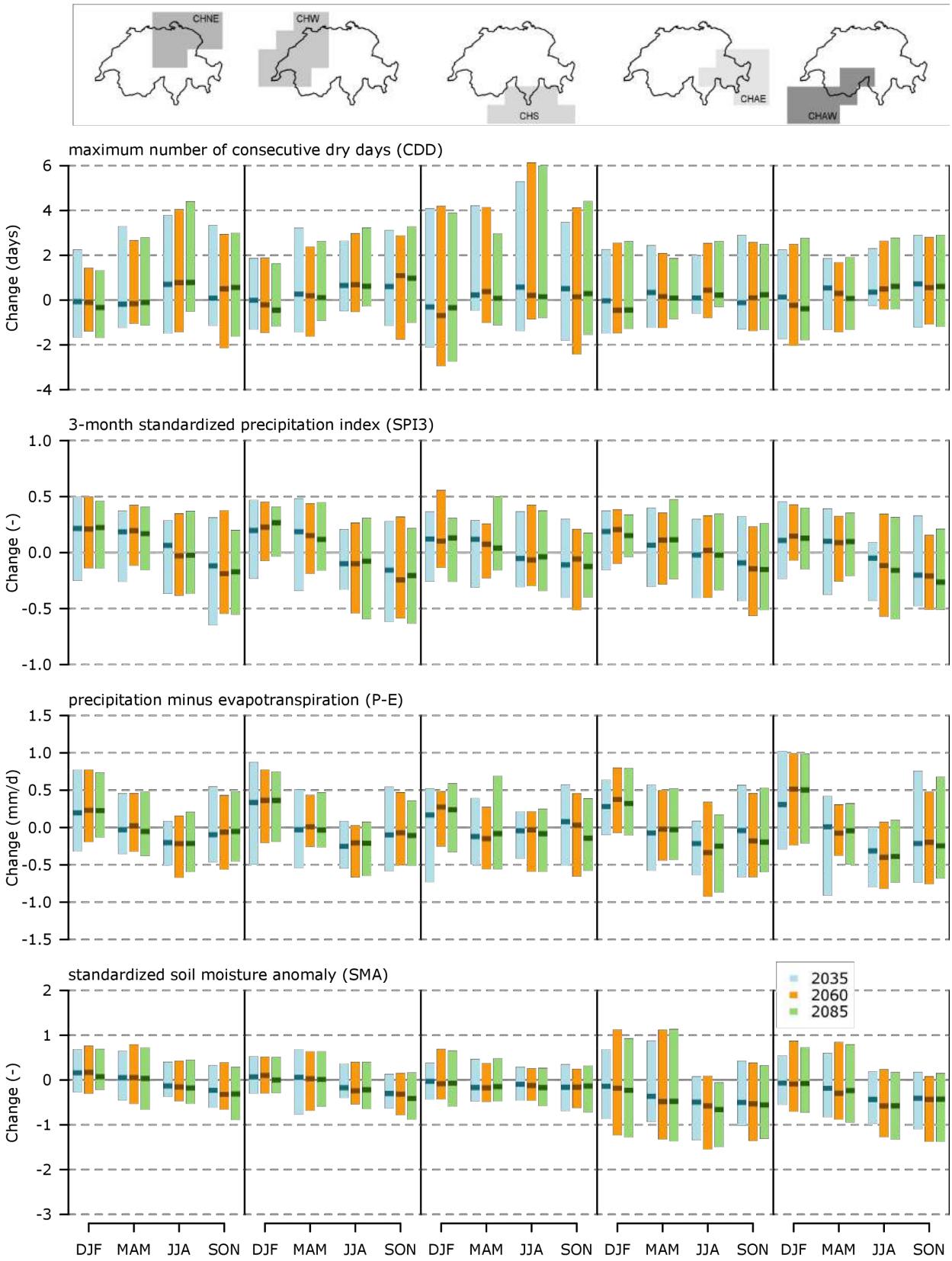

Figure 13.67. As Figure 13.66, but for RCP2.6.